

2016

# FORECASTING FOR CONTROL AND ENVIRONMENTAL IMPACTS OF WAVE ENERGY CONVERTERS

Monk, Kieran

<http://hdl.handle.net/10026.1/5292>

---

<http://dx.doi.org/10.24382/4262>

Plymouth University

---

*All content in PEARL is protected by copyright law. Author manuscripts are made available in accordance with publisher policies. Please cite only the published version using the details provided on the item record or document. In the absence of an open licence (e.g. Creative Commons), permissions for further reuse of content should be sought from the publisher or author.*

# Copyright Statement

This copy of the thesis has been supplied on condition that anyone who consults it is understood to recognise that its copyright rests with its author and that no quotation from the thesis and no information derived from it may be published without the author's prior consent.



FORECASTING FOR CONTROL AND ENVIRONMENTAL  
IMPACTS OF WAVE ENERGY CONVERTERS

by

KIERAN ÜMIT MONK

A thesis submitted to Plymouth University

in partial fulfilment for the degree of

DOCTOR OF PHILOSOPHY

School of Marine Science and Engineering

June 2015

# Acknowledgments

I would like to thank my PhD supervisors at Plymouth University; Dr. Daniel Conley, Dr. Qingping Zou and Professor Deborah Greeves, for their continued contributions throughout this process. In particular I would like to thank them for their faith in me and for supporting my decision to change topic and embark on an unpredictable path with regards to the Pico project. Also, thanks go to Plymouth University for supporting the research financially and for the resources that were made available to me. This is in addition to the transient but always entertaining and supportive postgraduates in the coastal engineering and coastal processes research groups that form part of the school of marine science and engineering.

Part of this body of work was conducted in collaboration with WAVEC – offshore renewables, Lisbon, and thanks go to Frank Neumann for giving me the opportunity to work with the Pico project. Professor Antonio Sarmiento and Dr. Ana Brito-Melo and the other staff at WAVEC – offshore renewables for their continued support and for giving me the freedom to investigate topics that interest me as well as unlimited access to the Pico plant and data.

On the Pico plant operations side, I thank Victor Winands for his technical support and mentoring. Without his support and expertise it is likely that the all-important field test would not have been accomplished. His commitment to the Pico project has been remarkable.

I would like to acknowledge Professor John Ringwood and Francesco Paparella at Maynooth University for their collaboration and insight with regards to the development of forecasting models and accelerating my understanding. This is in addition to Professor Phil McIver at Loughborough University for aiding me in the understanding of his integral equation solution for the breakwater diffraction problem.

Finally I would like to thank my parents Sue Monk and David Griffith, and my partner Jennifer Lewis for their unwavering support throughout the emotionally trying times and for proof reading this thesis.

# AUTHOR'S DECLARATION

At no time during the registration for the degree of Doctor of Philosophy has the author been registered for any other University award without prior agreement of the Graduate Sub-Committee.

Work submitted for this research degree at the Plymouth University has not formed part of any other degree either at Plymouth University or at another establishment.

This study was financed with the aid of a studentship from the Plymouth University.

Relevant scientific seminars and conferences were regularly attended at which work was often presented.

## **Publications:**

**Monk, K.** Zou, Q and Conley, D. Numerical and analytical simulations of wave interference about a single row array of wave energy converters. *9<sup>th</sup> European Wave and Tidal Energy Conference (EWTEC)*, Southampton, UK, 2011.

**Monk, K.** Zou, Q. and Conley, D. The effect of diffraction on the redistribution of wave energy in the lee of an overtopping type wave energy converter array, *Proceedings of the 33<sup>rd</sup> International Conference on Coastal Engineering (ICCE)*, Santander, Spain, 2012.

**Monk, K.** Zou, Q. and Conley, D. An approximate solution for the wave energy shadow in the lee of an array of overtopping type wave energy converters. *Coastal Engineering*, 73(1), pp. 115-132, 2013.

**Monk, K.** Conley, D. Lopes, M. F. P and Zou, Q. Pneumatic power regulation by wave forecasting and real-time valve control for an OWC. *Proceedings of the 10<sup>th</sup> European Wave and Tidal Energy Conference*, Aalborg, Denmark, 2013.

Vieira, M. **Monk, K.** Sarmiento, A. and Reis, L. The Pico power plant as an infrastructure for development research and graduation, *Proceedings of Congresso de ciencia e Desenvolvimento dos Acores (ACDA)*, Angra do Heroismo, Azores 2013.

Paparella, F. **Monk, K.** Winands, V. Lopes, M. F. P, Conley, D. and Ringwood, J. V. Benefits of up-wave measurements in linear short-term forecasting for wave energy applications. *Proceedings of the IEEE Multi-conference on Systems and Control*, Antibes, France, 2014

Paparella, F. **Monk, K.** Winands, V. Lopes, M. F. P, Conley, D. and Ringwood, J. V. Up-wave and autoregressive methods for short-term wave forecasting for an oscillating water column. *IEEE Transactions on Sustainable Energy*, 6(1), pp. 171-178, 2015.

## **Presentation and Conferences Attended:**

9<sup>th</sup> European Wave and Tidal Energy Conference - Southampton, UK (2011)

33<sup>rd</sup> International Conference on Coastal Engineering – Santander, Spain (2012)

4<sup>th</sup> International conference on Ocean Energy – Dublin, Ireland (2013)

10<sup>th</sup> European Wave and Tidal Energy Conference – Aalborg, Denmark (2013)

INORE European Symposium - Pembrokeshire, UK (2013)

INORE European Symposium – La Vega, Spain (2013)

**Word count of main body of thesis: 78436**

Signed..... Date.....

# FORECASTING FOR CONTROL AND ENVIRONMENTAL IMPACTS OF WAVE ENERGY CONVERTERS - KIERAN ÜMIT MONK

## Abstract

This work is divided into two distinct parts. In the first part a model is developed to assess the redistribution of wave energy about an offshore array of overtopping type wave energy converters. The model is based on a classical analytical solution for diffraction about a breakwater which is modified to consider an array of dissipating, reflecting and transmitting breakwater segments, which are used to approximate an overtopping type WEC array. The model is computationally efficient and phase resolving which allows the effect of wave scattering to be investigated for large domains with high resolution irregular wave distributions. It was found that the radial waves generated by the diffraction effect spreads and defocus wave energy away from the geometrical shadow of the array. This counteracts the rate of recovery of wave energy deficit from wave directional spreading.

In the second part, short-term wave forecasting for pneumatic power regulation through relief valve control is investigated at the Pico oscillating water column power plant, located in the Azores. Operational data from the Pico OWC is used to develop and critically assess a number of univariate and multivariate short-term wave forecast modelling approaches. A number of relief valve control strategies, which utilise a short-term wave forecast, are also developed and assessed using a numerical time-domain wave to wire system model. A system model for the Pico OWC is developed and validated using operational data from the Pico plant. The absolute performance potential resulting from control utilising a perfect forecast is considered, in addition to the realistic potential where a forecast, realisable in real-time, is used to drive control actions. One of the proposed relief valve control strategies is within the mechanical limitations of the existing relief valve adjustment system at Pico and this strategy was deployed in real field tests. Field test results of the plant's performance under this strategy closely matched the simulated performance and power enhancements of up to 29% were achieved in certain sea states and the expected annual power enhancement was projected to be around 10%. Simulations of the long term plant performance under the more advanced relief valve control strategies project far greater potential for enhanced power production although these could not be tested in the field due to the project limitations.

Keywords: Wave energy shadowing, Offshore WEC arrays, Wave diffraction, Overtopping type WEC, Wave dragon, OWC, Pico, Short-term wave forecasting, Control, Relief valve

# Contents

<b>List of Figures</b>	X
<b>List of Tables</b>	XIX
<b>Acronyms</b>	XX
<b>Chapter 1</b> Introduction	1
1.1 Scope	1
1.2 Motivation	3
1.2.1 Part one	3
1.2.2 Part two	3
1.3 Thesis structure	4
1.3.1 Part one – Wave energy shadowing from an offshore array of overtopping WEC	4
1.3.2 Part two – Short-term wave forecasting for pneumatic power control of an OWC	5
1.4 Main contributions	6
1.5 Theory of ocean waves	8
1.5.1 Regular linear waves	8
1.5.2 Irregular waves	14
1.5.2.1 Frequency spectrum	16
1.5.2.2 Directional spreading	18
1.5.2.3 Wave height distribution	19
1.5.2.4 Relationships between wave spectra and wave characteristics	19
1.5.3 Wave transformations	21
<b>Chapter 2</b> Wave energy shadowing and redistribution due to diffraction at an offshore WEC array	24
2.1 Wave energy shadowing introduction	24
2.2 Analytical solutions for wave diffraction	27
2.2.1 Semi-infinite breakwater	28
2.2.2 Breakwater gap	31
2.2.3 Detached breakwater segment	32
2.2.4 Series of detached partially transmitting and reflecting breakwater segments	36
2.2.5 Unidirectional spectral waves	38
2.2.6 Directional spectral waves	39
2.3 Comparison of approximate analytical solution to experimental data	39
2.4 Comparison of approximate analytical solution with integral equation solution	41
2.5 Diffraction and no-diffraction comparison	45
2.6 Shadow sensitivity analysis	46
2.6.1 Directional spreading	50
2.6.2 Device length	51
2.6.3 Frequency distribution	51
2.6.4 Gap length	52
2.6.5 Transmission coefficient	53
2.6.6 JONSWAP peak enhancement factor	54
2.7 Future work	54
2.8 Conclusions	55
<b>Chapter 3</b> Overview of the Pico OWC wave energy converter	56
3.1 Introduction	56
3.2 Background and history	56
3.3 System and structural specification	60
3.3.1 Relevant structural dimensions	60
3.3.2 Wells turbine	61

3.3.3 Generator	63
3.3.4 Inverter	64
3.3.5 Basic system control	64
3.3.5.1 Power take-off control	64
3.3.5.2 Pressure control using by-pass relief valve	65
3.3.6 System survival and protection	66
3.3.7 Data capture	67
3.4 Local wave climate	67
3.4.1 Hindcast metocean data	68
3.4.2 Chamber surface elevation	70
3.4.3 Near-shore hydrostatic pressure measurements	72
3.4.4 Wave climate summary	74
3.5 Basic controlled performance	78
3.6 Underperformance	79
3.6.1 Electrical power take-off	80
3.6.2 Subsurface structural damage	81
3.6.3 Performance change with tidal elevation	82
3.6.4 Pitting on turbine blade	85
3.7 Machine fatigue and longevity	86
3.8 Noise pollution	92
3.9 Summary	94
<b>Chapter 4 Literature review - OWC system and short-term wave forecast, modelling</b>	96
4.1 OWC system modelling introduction	96
4.1.1 Hydrodynamic transfer and pneumatic response	96
4.1.2 Basic equations of thermodynamics and aerodynamics for OWCs	97
4.2 OWC system modelling approaches	99
4.2.1 Frequency domain model	99
4.2.2 Stochastic analysis	101
4.2.3 Time domain model	102
4.3 Pneumatic to mechanical to electrical power transfer and losses	105
4.4 Short-term wave forecasting introduction	106
4.5 Short-term wave forecasting methods	108
4.5.1 Variable and spatial transformations using digital filters	108
4.5.2 Autoregressive model	111
4.5.3 Nonlinear Autoregressive model using Neural Networks	116
4.5.4 Cyclical model	118
4.5.5 Sinusoidal extrapolation	119
4.5.6 Nonlinear next wave estimation	120
4.6 Literature review summary	122
4.6.1 OWC system modelling summary	122
4.6.2 Short-term wave forecasting summary	122
<b>Chapter 5 Development of OWC system model and relief valve control strategies</b>	124
5.1 Introduction	124
5.2 Wave to wire system model in the time domain	125
5.2.1 Excitation flow and chamber pressure	125
5.2.2 Chamber pressure and turbine flow rate	126
5.2.3 Pneumatic to mechanical power transfer model	127
5.2.4 Electrical losses	129
5.2.5 Model performance evaluation	130
5.3 Evaluation of selected operational data	131
5.4 Relief valve control strategies	134
5.4.1 Basic relief valve control	134

5.4.2 Instantaneous relief valve control	139
5.4.3 Wave by wave relief valve control	143
5.4.4 Continuous relief valve control	145
5.4.5 Envelope relief valve control	148
5.4.6 Delayed relief valve control	153
5.5 Results summary	157
5.6 OWC system model and relief valve control strategies conclusions	161
<b>Chapter 6 Short-term wave forecast model evaluation and realisable control performance</b>	<b>163</b>
6.1 Introduction	163
6.2 Description of forecast models	164
6.2.1 FIR filter	164
6.2.2 Autoregressive forecast model	165
6.2.3 Autoregressive forecast model with exogenous input	166
6.2.4 Autoregressive forecast model with autoregressive exogenous input	167
6.2.5 Nonlinear autoregressive forecast model	168
6.2.6 Nonlinear autoregressive forecast model with exogenous input	172
6.3 Forecast model parameter selection	173
6.3.1 FIR parameter selection	174
6.3.2 Autoregressive parameter selection	175
6.3.3 Nonlinear Autoregressive neural network structure and parameter selection	176
6.4 Forecast model performance analysis	179
6.5 Forecasting causally filtered data	182
6.6 Forecast model performance analysis for relief valve control	185
6.7 Performance of control strategies using a realisable forecast	187
6.7.1 Instantaneous relief valve control	187
6.7.2 Wave by wave relief valve control	188
6.7.3 Continuous relief valve control	189
6.7.4 Envelope relief valve control	190
6.8 Forecast model retraining intervals	191
6.9 Forecast analysis for devices with phase control	193
6.10 Conclusions	194
<b>Chapter 7 Relief valve control field test results and long-term performance projections</b>	<b>197</b>
7.1 Introduction	197
7.2 Mid-term control simulations	198
7.2.1 Mid-term simulation results	199
7.3 Field tests and results	207
7.3.1 Implementation of the relief valve control system	207
7.3.2 Relief valve control testing procedure	209
7.3.3 Field test results from valve control	210
7.3.4 Comparison of simulations with field results	210
7.3.5 Divergences and further validation	217
7.4 Life time performance projection	220
7.5 Summary and conclusions	223
<b>Chapter 8 Final summary and conclusions</b>	<b>226</b>
8.1 Thesis part 1	226
8.1.1 Final summary and conclusions	226
8.1.2 Future work and extensions	227
8.2 Thesis part 2	227
8.2.1 Final summary and conclusions	227
8.2.2 Future work and extensions	229

<b>Appendix A</b> Integral equation for wave diffraction by segmented permeable breakwater	231
A.1 Context	231
A.2 Solution	231
<b>Appendix B</b> Approximate solution for the horizontal turbine axial load for the Pico Wells turbine	236
B.1 Context	236
B.2 Solution	236
<b>Appendix C</b> Method of least squares for an autoregressive forecast model	239
C.1 Context	239
C.2 Solution	239
<b>Appendix D</b> Levenberg-Marquardt learning algorithm for neural network training	241
D.1 Context	241
D.2 Solution	241
D.2.1 Method of gradient decent	241
D.2.2 Newton's method	242
D.2.3 Gauss-Newton algorithm	243
D.2.4 Levenberg-Marquardt algorithm	243
<b>Appendix E</b> Detailed field test result from control strategies <i>Basic<sub>RVC</sub></i> and <i>Envelope<sub>RVC</sub></i>	244
<b>Reference List</b>	248
<b>First Author Published Papers</b>	253

# List of Figures

**1.1** Some of the most intensely researched topics on wave energy conversion and their interrelationships. Shaded colours denote macro-topic groups.

**1.2** Regions of validity for different wave theories based on: wave steepness and the Ursell number. Figure from (Reeve, et al., 2004) with minor adaptations for homogenous symbolic usage.

**1.3** Schematic of some of the parameters used in linear wave theory derivations.  $H$  is wave height,  $a$  is wave amplitude,  $\lambda$  is wave length,  $h$  is water depth  $c_p$  is phase velocity, an infinitesimal element of the water column is described by:  $dz$  the unit height,  $dA$  the unit area and  $dV$  the unit volume.

**1.4** Example of frequency distribution as described by **(a)** Pierson-Moskowitz and **(b)** JONSWAP, spectrums, for different wind speed velocities at 19.5 (m) above the sea surface.

**1.5** Example of directional spread distribution of different frequency components as described by the function in (Misuyasu, et al., 1975), for a sea state with  $\omega_p = 0.5(\text{rad s}^{-1})$  and with wind velocities of  $U = 15(\text{ms}^{-1})$ .

**1.6** Probability density of the Rayleigh wave height distribution for  $\bar{H} = 3 (m)$

**1.7** Illustrations of different asymmetrical wave profiles.

**2.1** Definition of coordinate system, incident wave direction and calculation regions for a semi-infinite breakwater. S, O and R represent the **Shadow**, **Open**, **Reflection** region. The sign of  $\sigma$  and  $\sigma'$  to be used for the different calculations regions is shown.

**2.2** Shows the real part of the  $F(r, \theta)$  which gives the water surface elevation  $\eta$ , for: **(a)** the incident and reflected planar wave components, **(b)** the diffracted wave of the incident wave and the diffracted wave of the reflected wave, and **(c)** the complete solution which is the sum of **(a)** and **(b)** as described by (2.2).

**2.3** Definition of coordinate system, incident wave direction  $\theta$ , tip phase shift  $\varepsilon_b$ , and regions, for a gap in an infinite breakwater. The subscript  $z$  is used as a reference number for the breakwater tip for which the:  $I, R, r, \theta, \sigma$  and  $\sigma'$ , terms belong to.

**2.4** Definition of coordinate system, incident wave direction, tip phase shift and regions for a detached breakwater segment. The subscript  $z$  is used as a reference number for the breakwater tip.

**2.5** Superposition steps to create an approximate analytical solution for a disturbed field about an ideal zero reflection zero transmission overtopping type wave energy converter which we approximate as a detached breakwater segment under unidirectional monochromatic waves conditions. **(a)** semi-infinite solution with opening at the top of the domain, **(b)** semi-infinite solution with opening at the bottom of the domain, **(c)** is the sum of **(a)** and **(b)** minus the incident planar wave, which gives the approximate single WEC solution.

**2.6** Definition of coordinate system, incident wave direction, tip phase shift  $\varepsilon_B$  and breakwater phase shift  $\mu_n$ , for a series of detached breakwater segments. The subscript  $z$  is used as a reference number for the breakwater tip,  $n$  denotes the breakwater segment number.

**2.7** Superposition steps to for the approximate solution for the field about an array of overtopping type WEC converters approximated as breakwater segments, under unidirectional monochromatic wave conditions. **(a)** gives the temporary solution for single WEC, **(b)** gives multiple superpositions of the temporary solution shown in **(a)** to account for the diffracted waves (with relative phase shift) about each WEC in the array, **(c)** gives the solution shown in **(b)** with the incident wave field re-applied to give the complete approximate solution for the array.

**2.8** Layout of wave basin for the breakwater gap experiments after (Yu, et al., 2000). Transects of wave height measurements used for comparison at  $x = 0, y = 7.8$  &  $y = 16$ . The still water depth was 0.4m throughout the basin.

**2.9** Comparison of the experimental data (markers) and AAS (line) for incident waves with a mean direction of  $90^\circ$  to the breakwater plane. The incident wave parameters for each case are given in table 2.1. Individual analytical / experimental runs are grouped by the directional spread parameter  $s$ . **(a-b)** gives  $K_d$  along the transect  $x = 0$ , **(c-d)** transect  $y = 7.8(m)$  and **(e- f)** transect  $y = 16 (m)$ .

**2.10** Comparison of disturbance coefficient  $K_d$  for the AAS (red line) and integral equation solution from (McIver, 2005) (blue dashed line) along the transects;  $y = 5\lambda$ ,  $y = 50\lambda$ ,  $y = 150\lambda$  ( $+y$  is down-wave distance from the plane of the array), and  $x = 0\lambda$  ( $x = 0$  is the centre of the of the device array), for incident wave directions of  $\theta = 50^\circ, 70^\circ$  and  $90^\circ$  with permeability parameters of  $\beta = 0$  (full reflection) and  $\beta = k(1 - i)/4$  (partial reflection, transmission and dissipation).

**2.11** The disturbance coefficient  $K_d$  predicted by the AAS for **(a)** monochromatic unidirectional incident waves, **(b-f)** are spectral waves with  $T_p = 8 (s)$  and peak enhancement  $\gamma = 3.3$ , with **(b)** unidirectional, **(c)** directional with  $m = 800$  **(d)** directional with  $m = 100$ , **(e)** directional with  $m = 10$ , **(f)** directional with  $m = 2$ . In all cases the mean wave direction is  $\theta = 90^\circ$  from the plane of the array and  $c_p = 0$  and  $c_t = 0$ .

**2.12** The disturbance coefficient  $K_d$  predicted by the no-diffraction solution for **(a)** monochromatic unidirectional incident waves, **(b-f)** are spectral waves with  $T_p = 8 (s)$  and peak enhancement  $\gamma = 3.3$ , with **(b)** unidirectional, **(c)** directional with  $m = 800$  **(d)** directional with  $m = 100$ , **(e)** directional with  $m = 10$ , **(f)** directional with  $m = 2$ . In all cases the mean wave direction is  $\theta = 90^\circ$  from the plane of the array and  $c_p = 0$  and  $c_t = 0$ .

**2.13 (a)** The disturbance coefficient  $K_d$  along the transect that bisects the central WEC device of the series predicted by the AAS (solid line) and the no-diffraction solution (dot dashed line). **(b)** shows the wave directional spread probability density for discrete angular components of one degree.

**2.14** Schematic describing the direct “direct lee region” and energy summation bands, used to assess the net flux of wave energy.

**2.15** The change in total wave energy for each band of the “direct lee region” with increasing distance from the array for unidirectional monochromatic waves with  $T = 8 (s)$ , unidirectional spectral waves with  $T_p = 8 (s)$ , and directional spectral waves with  $T_p = 8 (s)$  and spread parameters  $m = 2, 10, 100$  and  $800$ . Solid lines show the AAS and dot dash lines show the no-diffraction solution.

**2.16**  $K_d$  profile along the central transect for an array with device lengths of  $B = 150 (m)$  (solid line) and  $B = 250 (m)$  (dot-dash line) for the directional spread parameter  $m = 2, 10, 100$  &  $800$  and  $T_p = 8 (s)$ .

**2.17 (a)** JONSWAP period spectrum probability density **(b)**  $K_d$  profile along the central transect for an array for peak period values of  $T_p = 8, 10, 12$  &  $14 (s)$ , for  $B = 150 (m)$  and  $m = 50$ .

**2.18**  $K_d$  profile along the central transect for an array with WEC tip to tip separation lengths of  $b = 200, 400, 600$  &  $800 (m)$ , for:  $B = 150 (m)$ ,  $T_p = 8 (s)$  and  $m = 50$ .

**2.19** Horizontal spatial distribution of  $K_d$  in the lee of an array with WEC separation length of: **(a)**  $b = 200$ , **(b)**  $b = 400$ , **(c)**  $b = 600$  and **(d)**  $b = 800 (m)$ , for:  $B = 150 (m)$ ,  $T_p = 8 (s)$  and  $m = 50$ .

**2.20**  $K_d$  profile along the central transect for an array for WEC devices with transmission coefficients of  $0, 0.25, 0.5, 0.75$ , with zero reflection, for:  $B = 150 (m)$ ,  $T_p = 8 (s)$  and  $m = 50$ .

**3.1** IGBT switch wave forms for pulse width modulation of two phases of the inverter system showing decaying trailing edge due to capacitor malfunction on the IGBT driver card of one phase polarity, resulting in a short circuit between electrical phases and damage to the inverter power electronics.

**3.2** Cross sectional schematic of the Pico OWC structure and machinery. Figure is taken from (Save\_Pico\_Powerplant.org, 2013).

**3.3** Grid representation of the local bathymetry and structure as used in (Brito-Melo, et al., 2001) for BEM analyses of the plant specific wave transfer functions.

- 3.4** Force and air velocity vector diagram for a Wells turbine blade (shown as a cross section).
- 3.5** Pico wells turbine characteristic curves for a down scaled version of the Pico Wells turbine found from laboratory testing as given in (Gato, et al., 1996) with **(a)** the relationship between non-dimensional pressure head and non-dimensional power transfer to the turbine with an indication of the threshold for turbine stall ( $\Psi_{cr}$ ), and **(b)** the relationship between non-dimensional pressure head and airflow rate past the turbine.
- 3.6** Electrical schematic of power electronics system consisting of a generator and inverter. Schematic is from (European wave energy pilot plant on the island of Pico, 1999).
- 3.7** Power take-off control laws (CL) used at Pico and the theoretical optimum as described in (Falcão, 2002).
- 3.8** Schematic of relief valve and actuating ram system.
- 3.9** Picture of actual relief valve with fully open aperture.
- 3.10** Timeline representation of the availability of different data sources for wave climate analysis. It should be noted that the metocean data extends back to 1979 but this is not shown.
- 3.11** Local area map indicating the location of the Pico plant, the location for the grid point centre of the used “GOW Azores” hindcast metocean data set, the distance between the two locations and approximate wave direction shadow lines cast by the neighbouring islands (from google maps).
- 3.12 (a, b)** Sea state occurrence frequency and **(c, d)** wave direction and significant wave height occurrence frequency, from metocean with **(a, c)** all data points considered and **(b, d)** data points with dominant wave directions that fall within the neighbouring island wave shadow zones removed.
- 3.13** Example time series comparing the observed and calculated chamber water surface elevation  $\eta$  for a time period where (towards the left) the wave amplitude is low and the recoded  $\eta$  values agree, and (towards the right) the wave amplitude is higher and the recoded  $\eta$  has clearly anomalous values and diverges from the calculated  $\eta$ .
- 3.14** Occurrence frequency of the modified sea state as described by plant chamber data for **(a)** the recoded chamber surface elevation and **(b)** the chamber surface elevation calculated from other system variables. **(c)** Gives the percentage difference of occurrence frequency between the measured and the calculated modified sea states (+ is greater occurrence from directly measured surface elevation data).
- 3.15** Sea state occurrence frequency as measured by **(a)** the near-shore hydrostatic pressure sensors and **(b)** the recoded chamber surface elevation, over the same time period.
- 3.16 (a)** Mean ratio of measured chamber wave height and up-wave wave height. **(b)** Histogram giving the total number of zero up-crossing wave periods for a 1 (s) wave period bin interval, as a percentage of the total number of wave periods, as measured in the chamber (red) and the up-wave sensor location (green).
- 3.17** Timeline comparison of sea states characterised over 1 hour time periods (except near-shore data which is 35 minutes), from; Metocean, chamber surface elevation (recoded and calculated) and near-shore hydrostatic pressure measurement, data sets. **(a)** Significant wave height, **(b)** peak wave period.
- 3.18** Mean **(a)** significant wave height and **(b)** peak period, of the calculated chamber surface elevation as a function of significant wave height and peak period, respectively, from metocean data at the corresponding times. **(c-d)** The corresponding standard deviation of all points in each data bin, which can be used to assess the confidence in the statistical association.
- 3.19** Plant life time (14 years) wave climate frequency of occurrence for chamber surface elevation sea states found by statistically linking metocean data and chamber surface elevation data. The colour bar is nonlinear to resolve the region of smaller percentages of occurrence.
- 3.20** Number of occurrence **(a,d)** total and mean **(b,e)** and max **(c,f)** power ( $W$ ) matrices using **(a-c)** the recoded chamber surface elevation and **(d-f)** the calculated chamber surface elevation, to characterise the chamber sea state.

- 3.21** Pictures of subsurface structural damage at **(a)** the west and **(b)** the south, chamber walls that both connect to a channel.
- 3.22** Picture indicating the location of a channel that connects the open ocean with the west and south walls of the plant structure.
- 3.23** Example time series showing the relationship between power take-off (1 hour mean), mean tidal elevation and surface elevation skewness as described in section 1.5.3 for a period of consistent incident wave energy.
- 3.24** Histograms of chamber surface elevation over a 1 hour period for **(a)** low tide (hour 36 in figure 3.23) and **(b)** high tide (hour 42 in figure 3.23).
- 3.25** Picture showing damage to the lip of the chamber front wall which connects the atmosphere and the chamber at larger wave troughs and at lower mean water levels.
- 3.26** Example time series showing the point (highlighted) at which the defect in the chamber front wall lip connects the chamber air pocket with the atmosphere resulting in a loss of pressure.
- 3.27** Non-dimensional chamber pressure head  $\Psi$  over a 1 hour period for **(a)** low tide (hour 36 in figure 3.23) and **(c)** high tide (hour 36 in figure 3.23) with the turbine characteristic curve (green line) given for reference.
- 3.28** Pictures showing pitting of turbine blades **(a)** and close up single blade **(b)**. A crack detection dye is used in the region where the blade meets the hub to highlight the defects in this region.
- 3.29** Analysis of vibration measured at the generator side bearing housing as a function of non-dimensional pressure and turbine angular velocity.
- 3.30** Analysis of vibration measured at the chamber side bearing housing as a function of non-dimensional pressure and turbine angular velocity.
- 3.31** Pictures of stress fractures and total detachment of guide vane blades for **(a)** original guide vane set and **(b)** new guide vane set with much thicker blades.
- 3.32** **(a)** Strain gauge placement on guide vane blade, **(b)** schematic of the orientation of the 3 axis of the strain gauge (not to scale), **(c)** Guide vane set schematic from (Vieira, et al., 2015).
- 3.33** The relationship between non-dimensional chamber pressure  $\Psi$  and peak **(a, b)** tensile and **(c, d)** compressive, strain  $\varepsilon$  recorded in three axes of the same plane ( $-45^\circ, 0^\circ, +45^\circ$ ) as measured at the generator and chamber side guide vane blades.
- 3.34** Equivalent stresses  $\sigma_v$  as a function of non-dimensional chamber pressure  $\Psi$  for **(a)** chamber side guide vane and **(b)** generator side guide vane. The guide vane stress measurements are recorded at different times and have different ranges.
- 3.35** Example curve showing the typical relationship between stress range and number of cycles before fatigue related material failure for non-corroded (blue) and corroded (steel) steel.
- 3.36** Example recorded time series showing the relationship between strain (guide vane blade) and non-dimensional chamber pressure.
- 3.37** Relationship between waterborne sound pressure level (normalised by  $1\mu Pa$ ) and non-dimensional chamber pressure with turbine stall threshold indicated.
- 3.38** Relationship between normalised airborne sound level (0 is ambient noise and 1 is loudest noise recorded in data period) and non-dimensional chamber pressure.
- 4.1** From (Brito-Melo, et al., 2001) hydrodynamic coefficients for the Pico plant: excitation volume flow coefficient  $\Gamma$  (dash dot line), radiation conductance  $B$  (solid line), and radiation susceptance  $C$  (dash line).
- 4.2** Schematic of sensor location options at the Pico OWC for the purpose of short-term forecasting.

- 5.1** Scatter plot of operational data derived (with line of best fit) and laboratory found (for small scaled turbine as given in (Gato, et al., 1996)) function  $f_m$  which relates  $\Phi$  and  $\Psi$ .
- 5.2** Scatter plot of operational data derived and laboratory found (for small scaled turbine as given in (Gato, et al., 1996)) function  $f_p$  which relates  $\Pi$  and  $\Psi$ .
- 5.3** Approximate curve relating the Pico generator mechanical to electrical power loss as a function of power take-off, and the electrical efficiency of the generator, both found iteratively from operational data and the wave to wire system model.
- 5.4** Significant wave height  $H_s$ , peak wave period  $T_p$ , and wave energy period  $T_e$  sampled at half hour intervals over a 12 hour period for the sample data set used for model validation.
- 5.5** Example half hour time series comparing the simulated **(a)** turbine angular velocity and **(b)** electrical power take-off, with the original recorded data for the respective time series.
- 5.6** Spectral analysis of the calculated chamber excitation surface elevation  $\eta_e$  and up-wave measured surface elevation  $\eta_{uw}$  (calculated from hydrostatic pressure at the sea bed) for the data sets considered, where:  $H_s$  is the significant wave height,  $T_p$  the peak wave period and  $T_e$  the energy period as measured in the chamber. The second subscript  $uw$  signifies measurements made 60(m) up-wave of the plant chamber front wall, all others refer to the chamber location.
- 5.7** Comparison of theoretical (Falcão, 2002) and data derived mean non-dimensional power transfer to turbine  $\bar{\Pi}$  as a function of the sea state defined by the standard deviation of non-dimensional pressure  $\sigma(\Psi)$  subdivided by **(a)** tidal elevation and **(b)** degree of skewness of chamber pressure.
- 5.8** Modelled mean electrical power take-off  $\bar{P}_e$ , % time spent in stall bands, vibrations above the residual and the value of  $\sigma(\Psi)$ , in response to different static relief apertures  $k_v$  ( $Basic_{RVC}$ ),
- 5.9** Modelled mean: electrical power take-off  $\bar{P}_e^*$ , %\* time spent in stall bands, mean vibrations above the residual  $\bar{V}^*$  and relief valve cycles per hour, resulting from  $Instant_{RVC}$ . All values except the number of relief valve cycles per hour are normalised by the base-line values resulting from  $Basic_{RVC}$ , for the corresponding data sets and these are denoted with the superscript \*.
- 5.10** Example time series of the simulated system response to  $Instant_{RVC}$ , compared to  $Basic_{RVC}$  for data set  $Z_{6,2}$ . **(a)** excitation chamber surface elevation  $\eta_e$ , **(b)** instantaneous non-dimensional pressure normalised by the critical value for the stall threshold  $|\Psi|/\Psi_{cr}$ , **(c)** the relief valve aperture state  $k_v$  and **(d)** instantaneous non-dimensional power transfer to turbine  $\Pi$ .
- 5.11** Comparison of simulated  $\bar{\Pi}$  as a function of  $\sigma(\Psi)$  from  $Instant_{RVC}$ , with the theoretical derived relationship between the same two parameters from combined relief valve and throttle control as given in (Falcão, 2002).
- 5.12** Modelled mean electrical power take-off  $\bar{P}_e^*$ , %\* time spent in stall bands, mean vibrations above the residual  $\bar{V}^*$  and relief valve cycles per hour, resulting from  $Wave_{RVC}$ . All values except the relief valve cycles per hour are normalised by the corresponding base-line values from  $Basic_{RVC}$ .
- 5.13** Example time series of the simulated system response to  $Wave_{RVC}$ , compared to  $Basic_{RVC}$  for data set  $Z_{6,2}$ . See figure 5.10 for parameter description.
- 5.14** Modelled mean electrical power take-off  $\bar{P}_e^*$ , %\* time spent in stall bands, mean vibrations above the residual  $\bar{V}^*$  and relief valve cycles per hour, in response to  $Continuous_{rvc}$  assessing and optimising  $\bar{\Pi}_\Gamma$  over different horizon lengths  $\Gamma$ . All values except the number of relief valve cycles per hour are normalised by the base-line values resulting from  $Basic_{RVC}$ , for the corresponding data sets.
- 5.15** Modelled mean electrical power take-off  $\bar{P}_e^*$ , %\* time spent in stall bands, mean vibrations above the residual  $\bar{V}^*$  and relief valve cycles per hour, resulting from  $Continuous_{RVC}$  using  $\Gamma_{optimum}$  to assess  $\bar{\Pi}_\Gamma$ . All values except the number of relief valve cycles per hour are normalised by the corresponding base-line values from  $Basic_{RVC}$ .

**5.16** Example time series of the simulated system response to  $Continuous_{RVC}$ , compared to  $Basic_{RVC}$  for data set  $Z_{6,2}$ . See figure 5.10 for parameter description.

**5.17** Comparison of the theoretical non-dimensional power transfer to the turbine  $\bar{\Pi}$  as a function of  $\sigma(\Psi)$  for a sea state as given in (Falcão, 2002) and the non-dimensional power transfer to the turbine  $\bar{\Pi}_{T_p}$  as a function of  $\sigma_{T_p}(\Psi)$  for the horizon time  $T_p$ , with a curve of best fit that considers all data points across all data sets.

**5.18** Modelled mean electrical power take-off  $\bar{P}_e^*$ , %\* time spent in stall bands, mean vibrations above the residual  $\bar{V}^*$  and relief valve cycles per hour, resulting from  $Envelope_{RVC}$  acting on the projected  $\sigma_{T_p}(\Psi)$ .

**5.19** Example time series of the simulated system response to  $Envelope_{RVC}$  for data set  $Z_{6,2}$ , compared to  $Basic_{RVC}$ . **(d)** gives the values of  $\sigma_{T_p}(\Psi)$  at each time step which  $Envelope_{RVC}$  is attempting to regulate. See figure 5.10 for the other parameter descriptions.

**5.20** Modelled mean electrical power take-off  $\bar{P}_e^*$ , %\* time spent in stall bands, mean vibrations above the residual  $\bar{V}^*$  and relief valve cycles per hour, resulting from  $Delayed_{RVC}$  using different values of  $\Gamma$  to assess  $\bar{\Pi}_{-\Gamma}$  in order to make the control action. All values except the number of relief valve cycles per hour are normalised by the corresponding base-line values resulting from  $Basic_{RVC}$ .

**5.21** Modelled mean electrical power take-off  $\bar{P}_e$ , and the indicators for mechanical fatigue; % time spent in stall bands and vibrations above the residual, resulting from  $Delayed_{RVC}$  using  $\Gamma = 1$  to assess  $\bar{\Pi}_{-\Gamma}$ . All values except the number of relief valve cycles per hour are normalised by the corresponding base-line values from  $Basic_{RVC}$ .

**5.22** Example time series of the simulated system response to  $Delayed_{RVC}$ , compared to  $Basic_{RVC}$  for data set  $Z_{6,2}$ . See figure 5.10 for parameter description.

**5.23** Side by side comparison of the system performance for the different data sets considered under each advanced relief valve control strategy. The relevant variables are normalised by the results from  $Basic_{RVC}$ .

**5.24** Distribution of  $\Psi$  for data set  $Z_{6,2}$  resulting from relief valve control strategies: **(a)**  $Basic_{RVC}$ , **(b)**  $Instant_{RVC}$ , **(c)**  $Wave_{RVC}$ , **(d)**  $Continuous_{RVC}$ , **(e)**  $Envelope_{RVC}$  and **(f)**  $Delayed_{RVC}$ .

**5.25** Example time series of the simulated system response to the considered control strategies for a sample period of data set  $Z_{6,2}$ . **(a)** excitation chamber surface elevation  $\eta_e$ , **(b)** instantaneous non-dimensional pressure normalised by the critical value for the stall threshold  $|\Psi|/\Psi_{cr}$ , **(c)** the relief valve aperture state  $k_p$ , **(d)** instantaneous power take-off by generator  $P_e$ . Note that a light low pass filter is applied to data to improve the plot clarity.

**6.1** Hyperbolic tangent sigmoid function.

**6.2** Univariate nonlinear autoregressive neural network process diagram. Large coloured areas are the different network layers, pink circles are the nodes containing the transfer functions, blue circles are the network inputs and output signals, orange circles are the weighting coefficients (multiplied with the signal) of the sub-signals, green circles are signal summation points.

**6.3** FIR filter GOF forecast accuracy at a horizon time  $l = 7f_s$  as a function of the filter order number  $n_b$  for the test data sets considered.

**6.4** AR modelled mean GOF forecast accuracy for all forecast points up to horizon time  $\Gamma = 13$  (s) as a function of the model order number  $n_a$  for the test data sets considered.

**6.5** ARX modelled mean GOF forecast accuracy for all forecast points up to horizon time  $\Gamma = 7$  s as a function of the model order numbers  $n_a$  and  $n_b$  for the test data sets considered. The colour scale is nonlinear to amplify the small differences for visual inspection.

- 6.6** The *NARX* neural network architectures, in terms of the number of nodes in the first  $v^1$  and second  $v^2$  layers and the number of regressors  $n_a = n_b$ , that deliver the 7 lowest 1-step ahead MSE forecast errors.
- 6.7** Visualisation of the *GOF* index in relation to different forecasted times series of  $\eta_e(t)$  for a snap shot of test data  $Z_{2,3}$ .
- 6.8** Forecast accuracy goodness of fit index (*GOF*) achieved by the different forecast models for forecast horizon times up to  $\Gamma = 20$  (s) ( $\Gamma = 7$  (s) for *FIR*), with forecast models trained and tested using raw data.
- 6.9** Forecast accuracy goodness of fit index (*GOF*) achieved by the different forecast models for forecast horizon times up to  $\Gamma = 20$  s ( $\Gamma = 7$  (s) for *FIR*), with forecast models trained and tested using zero-phase, low-pass filtered, data with cut-off angular frequency of  $\omega_c = 1.6 \text{ rads}^{-1}$ .
- 6.10** Forecast accuracy goodness of fit index (*GOF*) achieved by the different forecast models for forecast horizon times up to  $\Gamma = 20$  s ( $\Gamma = 7$  (s) for *FIR*), with forecast models trained and tested using zero-phase, low-pass filtered, data with cut-off angular frequency of  $\omega_c = 0.7 \text{ rads}^{-1}$ .
- 6.11** Frequency domain representations of the amplitude (**a, c, e and g**) and phase (**b, d, f and h**) response of the low-pass *IIR* filters; (**a, b**) Butterworth, (**c, d**) Chebyshev type I, (**e, f**) Chebyshev type II and (**g, h**) a low-pass *FIR* filter using Bartlett windows, for filter order numbers  $m = 1, 3, \dots, 15$ , with cut-off angular frequency of  $\omega_c = 0.7 \text{ rads}^{-1}$ .
- 6.12** Delay in filter's output, *GOF* when the delay is removed, and the relative goodness, as a function of filter order number and forecast horizon, when the low-pass ( $\omega_c = 0.7$ ) causal filters; (**a**) Butterworth, (**b**) Chebyshev type I, (**c**) Chebyshev type II and (**d**) *FIR* with Bartlett window, are used.
- 6.13** Mean absolute error of the forecasted standard deviation of non-dimensional pressure over different horizon times from the different forecast models considered, for the different data sets considered.
- 6.14** Power enhancement, inferred fatigue minimisation assessment, and number of full relief valve cycles per hour, when *Instant<sub>RVC</sub>* control action is made from  $\hat{\eta}_e$  from the *AR* (denoted with superscript AR) and *ARX<sub>AR</sub>* (denoted with superscript X) forecast models. All values except  $k_v^{-Hr}$  are normalised by the performance of the optimised *Basic<sub>RVC</sub>* strategy.
- 6.15** Power enhancement, inferred fatigue minimisation assessment and number of full relief valve cycles per hour, when *Wave<sub>RVC</sub>* control action is made from  $\hat{\eta}_e$  from the *AR* (denoted with superscript AR) and *ARX<sub>AR</sub>* (denoted with superscript X) models. All values except  $k_v^{-Hr}$  are normalised by the performance of the optimised *Basic<sub>RVC</sub>* strategy.
- 6.16** Power enhancement, inferred fatigue minimisation assessment and number of full relief valve cycles per hour, when *Continuous<sub>RVC</sub>* control action is made from  $\hat{\eta}_e$  from the *AR* (denoted with superscript AR) and *ARX<sub>AR</sub>* (denoted with superscript X) forecast models. All values except  $k_v^{-Hr}$  are normalised by the performance of the optimised *Basic<sub>RVC</sub>* strategy.
- 6.17** Power enhancement, inferred fatigue minimisation assessment and number of full relief valve cycles per hour, when *Envelope<sub>RVC</sub>* control action is made from  $\hat{\eta}_e$  from the *AR* (denoted with superscript AR) and *ARX<sub>AR</sub>* (denoted with superscript X) forecast models. All values except  $k_v^{-Hr}$  are normalised by the performance of the optimised *Basic<sub>RVC</sub>* strategy.
- 6.18** Forecast *GOF* achieved for data sets with increasing time from data set used to train the *AR* forecast model. Different sea states characterised by; rapidly increasing (**a**), stead (**b**) and rapidly decreasing (**b**),  $H_s$  and  $T_e$ .
- 6.19** PSD of the *AR* model coefficients  $a_j$  compared to the PSD of  $\eta$  for the: training data set, the test data set occurring immediately after the training data set and the test data set occurring 4 hour after the training data set. It should be noted that the PSD density of  $a_j$  has been amplified to contextualise it with the PSD of  $\eta_e$ .
- 6.20** Mean absolute time error of the forecasted zero-crossing and turning points, as a function of forecast horizon time, for the *AR*, *ARX* and *ARX<sub>AR</sub>* models.

- 7.1 (a)** Chamber significant wave height and peak period (from calculated excitation chamber surface elevation), **(b)** recorded tidal elevation.
- 7.2 (a)** Mean power take-off, **(b)** % time spent in stall band  $|\Psi| > 0.067$ , **(c)** % time spent in stall band  $|\Psi| > 0.1$ , from simulations for the different control strategies.
- 7.3 (a)** % time spent in stall band  $|\Psi| > 0.125$ , **(b)** % time spent in stall band  $|\Psi| > 0.15$ , **(c)** % time spent in stall band  $|\Psi| > 0.175$ , from simulations for the different control strategies.
- 7.4 (a)** mean vibrations above the residual at generator side shaft bearing, **(b)** mean vibrations above the residual at chamber side shaft bearing, from simulations for the different control strategies.
- 7.5 (a)** Mean relief valve aperture state, **(b)** number of full relief valve transit cycles per hour, **(c)** mean forecast goodness of fit over forecast horizon length, from simulations for different control strategies.
- 7.6 (a, c, e)** Un-shoaled wave **(b, d, f)** shoaled wave, **(a, b)** chamber pressure, **(c, d)** absolute non-dimensional chamber pressure, **(e, f)** power transfer to the turbine. Inspection of the effect of wave shoaling and asymmetry on the performance of the *Envelope<sub>RVC</sub>* and *Continuous<sub>RVC</sub>*.
- 7.7** Power matrix summarising the performance of each control strategy in terms of mean power take-off achieved in each unique sea state.
- 7.8** Process diagram showing the transit of analogue system sensor signals being digitised and passed to the processing suite to make the forecast and choose the control action and finally conversion back to analogue to actuate the control action.
- 7.9** Mean power take-off. **(a)** Percentage difference between *Envelope<sub>RVC</sub>* and *Basic<sub>RVC</sub>* for (blue line) simulations and (red dots) field test results (averaged over the sea state bin intervals). **(b)** Matrices of absolute values and the percentage difference between control strategies.
- 7.10** Number of full relief valve cycles per hour. **(a)** Percentage difference between *Envelope<sub>RVC</sub>* and *Basic<sub>RVC</sub>* for (blue line) simulations and (red dots) field test results (averaged over the sea state bin intervals). **(b)** Matrices of absolute values and the percentage difference between control strategies.
- 7.11** % time in stall band  $|\Psi| > 0.068$ . **(a)** Percentage difference between *Envelope<sub>RVC</sub>* and *Basic<sub>RVC</sub>* for (blue line) simulations and (red dots) field test results (averaged over the sea state bin intervals). **(b)** Matrices of absolute values and the percentage difference between control strategies.
- 7.12** % time in stall band  $|\Psi| > 0.1$ . **(a)** Percentage difference between *Envelope<sub>RVC</sub>* and *Basic<sub>RVC</sub>* for (blue line) simulations and (red dots) field test results (averaged over the sea state bin intervals). **(b)** Matrices of absolute values and the percentage difference between control strategies.
- 7.13** % time in stall band  $|\Psi| > 0.125$ . **(a)** Percentage difference between *Envelope<sub>RVC</sub>* and *Basic<sub>RVC</sub>* for (blue line) simulations and (red dots) field test results (averaged over the sea state bin intervals). **(b)** Matrices of absolute values and the percentage difference between control strategies.
- 7.14** % time in stall band  $|\Psi| > 0.15$ . **(a)** Percentage difference between *Envelope<sub>RVC</sub>* and *Basic<sub>RVC</sub>* for (blue line) simulations and (red dots) field test results (averaged over the sea state bin intervals). **(b)** Matrices of absolute values and the percentage difference between control strategies.
- 7.15** % time in stall band  $|\Psi| > 0.175$ . **(a)** Percentage difference between *Envelope<sub>RVC</sub>* and *Basic<sub>RVC</sub>* for (blue line) simulations and (red dots) field test results (averaged over the sea state bin intervals). **(b)** Matrices of absolute values and the percentage difference between control strategies.
- 7.16** Mean vibration velocities above the residual for the generator side turbine shaft bearing. **(a)** Percentage difference between *Envelope<sub>RVC</sub>* and *Basic<sub>RVC</sub>* for (blue line) simulations and (red dots) field test results (averaged over the sea state bin intervals). **(b)** Matrices of absolute values and the percentage difference between control strategies.
- 7.17** Mean vibration velocities above the residual for the chamber side turbine shaft bearing. **(a)** Percentage difference between *Envelope<sub>RVC</sub>* and *Basic<sub>RVC</sub>* for (blue line) simulations and (red dots) field

test results (averaged over the sea state bin intervals). **(b)** Matrices of absolute values and the percentage difference between control strategies.

**7.18** Example time series comparing the measured; relief valve aperture state  $k_v$ , turbine angular velocity  $N$  and generator power take-off  $P_e$ , to the simulated values of the same parameters, under ideal and realisable control condition scenarios.

**7.19** Sea state occurrence number for **(a)** mid-term simulations and **(b)** long-term statistical extrapolation using metocean data (as described in section 3.4.4).

# List of Tables

- 2.1** The sign of  $\varepsilon_b$  used with the terms associated with breakwater tip  $z$  for a breakwater gap.
- 2.2** The sign of  $\varepsilon_B$  for a region relative to breakwater tip  $z$  for a detached breakwater.
- 2.3** The sign of  $\varepsilon_B$  for the region relative to breakwater tip  $z$  for a series of breakwaters.
- 2.4** Wave parameters for tests in (Yu, et al., 2000) experiments on wave diffraction through a breakwater gap.  $H_s$  is significant wave height,  $T_p$  is peak period,  $s$  is directional spreading parameter describe by (1.59),  $\lambda_p$  is peak wavelength, and  $b$  is gap width, the significant wave height was 0.05 (m), mean direction was  $\theta_0 = 90$  which is the angle relative to the plane of the breakwater gap (x-axis) and JONSWAP peak enhancement parameter was 4 for all cases.
- 3.1** ISO 10816 standards for vibration severity ratings.
- 5.1** Mean absolute and squared error of turbine angular velocity, and mean error of power take-off, between model simulations and operational data.
- 5.2** Mean electrical power take-off and machine fatigue indicators resulting from  $Basic_{RVC}$  with the static relief aperture that achieves  $|\sigma(\Psi) - 0.05|_{min}$ , for the different data sets  $Z$  considered.
- 5.3** The horizon times  $\Gamma$  to assess  $\bar{\Pi}_\Gamma$  that resulted in the greatest performance enhancement from  $Cotinuuous_{RVC}$ , for the data sets considered with the corresponding values of chamber measured peak period  $T_p$  and energy period  $T_e$  for each data set.
- 6.1** Neural network optimisation results giving, for each data set considered, the best: architecture (number of nodes in layer one  $v_1$  and layer two  $v_2$ ), number of regressors  $n$  and the number of iterations ( $Epochs$  needed to find local minimum). Under the optimum variable the resulting 1-step ahead  $MSE$  forecast accuracy and product-moment correlation coefficient  $R$  are also given.
- 7.1** Total mean values of different performance parameters under the considered control strategies from the mid-term simulation results.
- 7.2** Total mean values of different performance parameters under the considered advanced control strategies from the mid-term simulation results, as a percentage of the mean values achieved with  $Basic_{RVC}$ .
- 7.3** Summary of mean values of system parameters resulting from  $Envelope_{RVC}$  and  $Basic_{RVC}$  with the percentage difference between them.
- 7.4** Mean power take-off during example control period under  $Envelope_{RVC}$ , with slight modifications that characterise issues encountered during control system deployment, as described by scenarios #2 to #5, as well as the percentage difference from the recoded values which is scenario #1.
- 7.5** Parameter totals (averages for the case of vibration velocities) under the different control strategies over the potential operational life time of the Pico plant to date.
- 7.6** Parameter percentage differences (totals difference for earnings) under the advanced control strategies as a percentage of that achieved with  $Basic_{RVC}$ , for the potential operational life time of the Pico plant to date.
- E1** Field test results from  $Envelope_{RVC}$  (green rows) and  $Basic_{RVC}$  (blue rows).

# Acronyms

<i>AAS</i>	Approximate analytical solution
<i>ANN</i>	Artificial neural network
<i>AR</i>	Autoregressive
<i>ARX</i>	Autoregressive with exogenous input
<i>ARX<sub>AR</sub></i>	Autoregressive with Autoregressive forecast of exogenous input
<i>Basic<sub>RVC</sub></i>	Basic relief valve control strategy
<i>BEM</i>	Boundary element method
<i>CFD</i>	Computational fluid dynamics
<i>Continuous<sub>RVC</sub></i>	Continuous relief valve control strategy
<i>Delayed<sub>RVC</sub></i>	Delayed relief valve control strategy
<i>DOF</i>	Degrees of freedom
<i>Envelope<sub>RVC</sub></i>	Envelope relief valve control strategy
<i>FIR</i>	Finite impulse response filter
<i>GOF</i>	Goodness of fit index
<i>RGOF</i>	Relative goodness of fit
<i>IIR</i>	Infinite impulse response filter
<i>ISO</i>	International organisation for standardisation
<i>Instant<sub>RVC</sub></i>	Instantaneous relief valve control strategy
<i>LRPI</i>	Long-range predictive identification
<i>MSE</i>	Mean squared error
<i>MAE</i>	Mean absolute error
<i>NACA</i>	National Advisory Committee for Aeronautics
<i>NAR</i>	Nonlinear Autoregressive
<i>NARX</i>	Nonlinear Autoregressive with exogenous input
<i>OWC</i>	Oscillating water column
<i>PE</i>	Percentage error
<i>RMS</i>	Root mean squared
<i>Wave<sub>RVC</sub></i>	Wave by wave relief valve control strategy
<i>WEC</i>	Wave energy converter

# Chapter 1

## Introduction

### 1.1 Scope

Energy from the sun is absorbed by the earth's surface and atmosphere and is converted to heat. This heat is unevenly distributed and drives convection, which is the transport of thermal energy through mass flux of fluid. In the atmosphere convection creates pressure gradients which drive the wind. As wind blows over the ocean surface kinetic energy is transferred and concentrated into the water and manifests as water waves. For centuries people have conceived ways to convert this energy into a more useful form and more recently to generate electricity. Wave energy is considered a renewable energy source because it derives from the sun's power which is limitless with respect to the life time expectancy of humanity.

As with many renewable energy sources, the wave energy resource availability in any one location or large region fluctuates with time. For an electrical grid to incorporate renewable energy from variable sources whilst meeting constant variable consumer demands, reserve capacity is needed to satisfy any intermittent short-falls in the energy provided by renewable sources. This capacity might be: traditional power plants on standby, energy storage such as pumped storage or batteries, or by energy trade arrangements with other networks. A portfolio of different renewable energy sources can help to reduce the reserve capacity because the intensity, frequency and phase is not equal between different sources, i.e. solar, wind, hydro, tidal and wave occur at different times with different intensities. This means that if the renewable energy sources are varied enough and if they contribute a similar capacity, at any one time a certain base level of energy supply will be available and this level can then be completely removed from the reserve capacity.

Solar, hydro and wind power are now highly developed and reliable technologies and tidal power looks to follow. Wave power technology on the other hand is still in its infancy and only a few full scale prototypes have been deployed thus far. This is in spite of the significant financial and human resource investment that has spanned many decades. The primary reasons for this slow progress are: the exceptionally high forces that can be exerted by breaking waves, the difficulties of achieving robust and economically viable moorings, difficulties with maintaining proper isolation between electrical components and sea water, and because of the corrosive environment in which wave energy converters (WEC) reside. The technical and physical requirements needed to survive and withstand such conditions over long time periods make economic viability difficult to achieve.

Despite the challenges wave energy presents, the topic is still passionately pursued and this is motivated in part by the consistency and predictability of the wave resource compared to some other renewable energy sources and the enormous energy potential that waves presents. It is estimated that the global wave energy resource is 2 (TW) (Cruz, 2008), which is twice the current world's energy requirements. Even if a small fraction of this was realised it would provide a significant proportion of the world's energy blend. Also, because of the high energy density associated with waves (a global average of about 2.5 (kW/m<sup>2</sup>))

compared to wind  $0.4 \text{ (kW/m}^2\text{)}$  and solar  $0.15 \text{ (kW/m}^2\text{)}$ , a large amount of energy could be extracted from a relatively small area, which could be important in an increasingly populous world.

Many WEC device types have been devised but so far none have established a very clear lead. Some devices have received greater attention in the media and within technical circles, but this has often been a result of stronger marketing and the financial resources available to the developer, rather than demonstrating significantly greater success. The market is still wide open and development continues along varied routes. If a single device type had demonstrated a clear advantage then progress is likely to have accelerated as the human resource would be more concentrated on narrower research pathway.

Three main WEC device types have been proposed, and these are:

- Oscillating water column (OWC) type – Utilisation of the relative motion between a water mass and a fixed structure or a floating structure oscillating at a different amplitude and/or phase. Grid connected example – Pico (Falcao, 2000), Mutriku (Torre-Encisco, et al., 2009)
- Floating oscillator (with a reference) type – Utilisation of the displacement difference between an oscillating floating structure in reference to a fixed point, or other oscillating structure component moving in different modes and/or amplitude and/or phase. This device type can be sub-divided into the categories: point absorbers, attenuators or terminators. Grid connected example – CETO (Mann, 2011), Pelamis (Yemm, et al., 2012)
- Overtopping type device - Utilisation of wave run up and overtopping to capture a water mass with potential energy in a floating or fixed reservoir. Grid connected example – Wave dragon (Kofoed, et al., 2000)

Research into wave energy converter technology and peripherals issues remains strong and some intensively studied research avenues are presented and interrelated in the topic web given in figure 1.1.

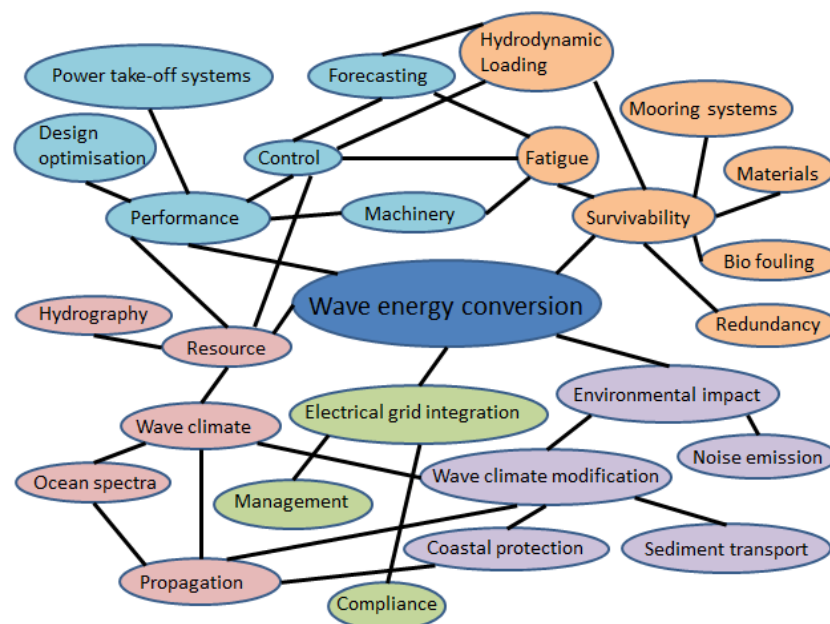


**Figure 1.1** Some of the most intensively researched topics on wave energy conversion and their interrelationships. Shaded colours denote macro-topic groups.

The research in this thesis covers a number of topics, these are:

- Wave climate modification
- Propagation
- Ocean spectra
- Performance optimisation through control
- Short-term-wave forecasting
- Fatigue
- Noise emission
- Wave climate and resource characterisation

## **1.2 Motivation**

### **1.2.1 Part one**

At the commencement of this research the Wave hub project had been approved and was gaining momentum. The Wave hub is the designation and implementation of an electrical grid connection to a far off-shore wave energy park located off the north coast of Cornwall, UK. The communities inhabiting the coastline in the direct lee of the Wave hub site are supported heavily from the income generated by tourism. A significant proportion of this comes from holidaying surfers and other sea and beach users. Serious concerns were raised by these stakeholders about the impact that wave energy extraction might have on the: local wave climate, beach formations, and ultimately their businesses and recreational resource. As such the motivation for chapter 2 of this thesis was to develop a methodology for assessing the far-field wave energy shadow cast by an array of far offshore wave energy converters. In particular, the modelling solution to tackle this question needed to be computationally efficient to handle the very large domain (associated with this case study) and to also be phase-resolving in order to provide a different perspective to an existing study that had received some criticisms about the over simplification of the problem (non-resolution of wave phase and inadequate directional spectrum representation). It was the intention, within this research framework, to compare simulation results to the wide area water surface elevation map of the region that was being sampled using HF radar. However, this final analysis did not happen because devices have yet to be deployed at the Wave hub.

### **1.2.2 Part two**

Part two of this thesis (chapters 3-7) is only loosely related to the first part and this unusual format requires a little explaining. Half way through the PhD study, the author was fortunate enough to be granted an opportunity to gain work experience in the field at the full scale Pico OWC wave energy converter project, in the Azores. To gain a more rounded perspective on wave energy conversion the author suspended his PhD for one year to take the opportunity.

Whilst working at the Pico OWC the author had first-hand experience of the low power production levels and high rates of fatigue which are both (in part) related to the Wells turbine stall phenomenon. In an early attempt to tackle this issue the author designed and fabricated a rudimentary hydrostatic pressure sensor to measure the approximate water surface elevation 60 meters up-wave of the plant in the near-

shore. The sensor provided a live data stream to the main data acquisition suite providing a small amount of lead time about the incident wave before it arrived at the plant chamber.

This lead time allowed the relief valve aperture to be adjusted based on the near-shore measured water surface elevation gradient. Adjustments were made to vent the over-pressure associated with steep water surface elevation gradient and to avoid under-pressure for temporal periods of low energy. A routine to monitor the relationship between near-shore wave surface elevation and the likelihood of stall was implemented and the control algorithm self-adapted and optimised to the sea state. Although very basic, this control system was able to significantly reduce the frequency and severity of turbine stalls, but did not significantly increase power production. More details of this earlier work is given in (Monk, et al., 2013).

The success with stall reduction using only a basic system led the author to believe that enhanced power production could also be realised with a more refined control strategy. Because of this, the author redirected the subject and research focus of his PhD (from wave energy shadowing by offshore WEC arrays) to the topic of pneumatic power regulation by short term wave forecasting and relief valve aperture control at the Pico OWC. This section of PhD research was performed on a part time basis at Plymouth University whilst the author continued to work part time at the Pico project site under the management of the WAVEC – Offshore renewables.

Unrestricted access to a full scale wave energy converter presents a unique opportunity to develop control and forecasting methodologies and, perhaps as importantly, to prove them in the field, which is something rarely found in the literature. As such, the primary overall objective of part 2 of this thesis is to contribute forecast and control methodologies that could be used with future devices to help increase performance to an economically interesting level.

## **1.3 Thesis structure**

### **1.3.1 Part one – Wave energy shadowing from an offshore array of overtopping WEC**

Part one of this thesis is concerned primarily with wave scattering from arrays of offshore wave energy converters (WEC) and how this affects the re-distribution of wave energy in their lee and ultimately the evolution of the wave energy shadow they cast, in the far-field. Chapter 2 combines the work published in a first author peer reviewed article that has been accepted to the Journal of Coastal Engineering and a first author peer reviewed article that has been accepted into the conference proceedings of the 33<sup>rd</sup> International Conference of Coastal Engineering (ICCE), which are both given in the ‘First Author Published Paper’ section. An approximate analytical solution for assessing: wave transmission, reflection, conversion and scattering, by an array of overtopping type wave energy converters, is developed. The approximate analytical solution is validated with a comparison to an existing mathematically exact integral equation solution for a very similar problem which was found to be too computationally expensive for detailed large domain analysis for high resolution directional and spectral irregular waves. The solution developed is used to show how diffraction acts to defocus wave energy away from the direct lee of the array and ultimately counteracts the recovery of the energy deficit from wave directional spreading, in the geometrical shadow of the array. To the author’s knowledge this

previously had not been considered directly in the literature. The sensitivity of the wave energy shadow to the: WEC array geometry, device size and the proportion of energy conversion, as well as the irregular wave frequency and directional distributions, is investigated.

### **1.3.2 Part two – Short-term wave forecasting for pneumatic power control of an OWC**

Chapter 3 provides a detailed overview of the Pico OWC case study. The project history, design and system specifications are reviewed. The local wave climate is analysed using a number of different data sources and a simple solution is considered to extrapolate the existing (limited) plant-side wave climate data, to give a projection of the long term chamber sea state occurrence frequency. This is done by statistically linking existing plant data with offshore metocean data, and then extrapolating in time. Some mechanisms which are responsible for the resultant short-fall in power production, when compared to early theoretical predictions, are identified. Other unexpected and significant issues stemming from turbine stall, namely; vibrations, fatigue and noise-pollution, are also investigated. It is hypothesised that regulating pneumatic power exposure to the turbine by modifying chamber pressure with by-pass relief valve control could improve power production levels as well as reducing the frequency and severity of stall and the associated undesirable effects.

In order to develop and interrogate any relief valve control methodologies a system model needs to be developed to project any performance enhancements and justify deployment. Chapter 4 provides a review of the different options, found in the literature, to simulate the power transfer stages needed to convert kinetic incident wave energy into electrical energy at the grid, for a shore mounted OWC. In addition, to perform active relief valve control a short-term wave-forecast will probably be required and a review of the existing methods and models for short-term wave forecasting, as found in the literature, is also given in chapter 4.

In chapter 5 a method is presented to generate the system model inputs indirectly from other system variables in the operational data captured at the Pico plant. The system model is developed by extracting the interrelationships needed to complete the wave to wire power transfer steps, from operational data. The resultant model is driven exclusively by operational data and the simulated system response is then validated with real data. This analysis is quite rare in the field of wave energy conversion due to the limited number of functional full scale devices. Also in chapter 5, a number of relief valve control strategies of varying technical specifications and financial commitment are proposed. Some of these control strategies require a short-term forecast of chamber excitation flow with up to one wave period of forecast horizon. It is assumed initially that a perfect forecast is available in order to assess the absolute potential of each control strategy. The performance assessment resulting from a perfect forecast is still relevant as a near perfect forecast is probably achievable (essentially) with sufficient monitoring equipment.

In chapter 6 the most promising and applicable methods for short-term wave forecasting are critically evaluated through numerical deployment using real operational data from Pico. An additional forecast model is also proposed. Univariate forecast models using data captured at the plant exclusively are compared to multivariate forecast models that also consider up-wave data having lead time. The validity

of filtering data to try to improve forecasting accuracy is investigated and additional attention is given to the forecasted phase accuracy which will be of greater relevance to other WEC device types.

Having theoretically developed a number of relief valve control strategies using a limited number of test cases, the performance of each control strategy is then simulated in the mid-term time-scale using time-domain modelling, in chapter 7. The results from this are statistically extrapolated to the long-term time scale to assess the life time-performance change under different relief valve control strategies. Finally, two proposed relief valve control strategies, which require no significant modification of the existing relief valve aperture adjustment system installed at Pico, are deployed in real field tests. These are then used to validate the numerical valve control system characterisation.

## **1.4 Main contributions**

1. In chapter 2 an approximate analytical solution is developed for assessing: wave transmission, reflection, conversion and scattering, by an array of over topping type wave energy converters. The solution is computationally efficient which allows very large grid domains to be considered and this is needed to investigate the far-field wave energy redistribution. Also, high resolution directional wave spectra can be considered, which avoids the misleading caustic patterns which result from coarser representations. The approximate analytical solution is validated using an existing computationally expensive but more mathematically exact integral equation for a very similar problem and excellent agreement is found in the region of interest. Also, the approximate analytical solution, which is phase resolving, is compared to the widely used phase averaged wave propagation modelling technique which does not fully account for diffraction. It is shown that when diffraction is more properly accounted for, the wave energy shadow recovers significantly slower for sea states with a narrow directional spread than the phase averaged solution suggests. This was found to be a result of diffraction which acts to spread energy radially and defocusing it away from the geometrical shadow of the array, which ultimately counteracts the recovery of the energy deficit from wave directional spreading.
2. In chapter 3 an unbiased and transparent review of the Pico OWC and its history is given which highlights the main issues that have interrupted and limited the project. Some of these issues have undoubtedly been experienced in other projects and the typical reluctance to share information about failures, within the wave energy community, continues to suppress the progression of wave energy conversion. It is hoped that other developers can use this information to avoid the same pitfalls.
3. In chapter 5 the well-documented methodology for simulating an OWC in the time domain is validated using operational data. Also a number of previously unconsidered control strategies for optimising pneumatic power exposure to a wells turbine by controlling the aperture of a by-pass relief valve in real time are proposed and interrogated numerically using the validated system model.
4. In chapter 6 a number of methods for short-term wave forecasting are reviewed, tailored to the problem in question and then critically assessed. In particular, the possibility of enhancing forecast accuracy by incorporating up-wave information with lead time, from a point source, is considered, which has received little attention in the literature. A new forecasting model is

proposed which is an extension of the autoregressive model with an exogenous input, where a second autoregressive model is used to forecast the exogenous input. This extends the lead time of the exogenous input and makes the multivariate method unlimited in forecast horizon time. Of the forecast models investigated, the new proposed model achieved the greatest forecast accuracy at longer forecast horizons. More generally the inclusion of up-wave information was found to give a small but notable improvement in the accuracy at longer forecast horizons, compared to univariate forecast models that consider plant-side information exclusively. This is in opposition to the conclusion in a relevant article in the literature. The possibility of improving forecasting accuracy through filtering is considered in-depth and was found to be unrealisable in on-line applications. This is contrary to what is suggested in some articles in the literature and it is important that this potential pitfall is properly understood.

5. In chapter 7 mid-term performance enhancement projections from relief valve control incorporating a realisable short-term forecast are validated using field data collected from the Pico plant. The plant achieved a notable improvement in power production and stall and vibration reductions, whilst under control in reality. Statistical projections are made for the very long term performance enhancement gains and for some control strategies these are very significant. This is possibly the first or at least one of a very limited number of successful attempts to actively control a full scale wave energy converter based on the real-time short-term wave forecasting.

A number of publications have resulted from the research conducted within this project, these are:

**Monk, K.** Zou, Q and Conley, D. Numerical and analytical simulations of wave interference about a single row array of wave energy converters. *European Wave and Tidal Energy Conference*, Southampton, UK, 2011. [poster presentation]

**Monk, K.** Zou, Q. and Conley, D. The effect of diffraction on the redistribution of wave energy in the lee of an overtopping type wave energy converter array, *Proceedings of 33<sup>rd</sup> International Conference on Coastal Engineering (ICCE)*, Santander, Spain, 2012.

**Monk, K.** Zou, Q. and Conley, D. An approximate solution for the wave energy shadow in the lee of an array of overtopping type wave energy converters. *Coastal Engineering*, vol. 73 pp. 115-132, 2013.

**Monk, K.** Conley, D. Lopes, M. F. P and Zou, Q. Pneumatic power regulation by wave forecasting and real-time valve control for an OWC. *Proceedings of 10<sup>th</sup> European Wave and Tidal Energy Conference (EWTEC)*, Aalborg, Denmark, 2013.

Vieira, M. **Monk, K.** Sarmiento, A. and Reis, L. The Pico power plant as an infrastructure for development research and graduation, *Proceedings of Congresso de Ciencia e Desenvolvimento dos Acores (ACDA)*, Angra do Heroismo, Azores 2013.

Paparella, F. **Monk, K.** Winands, V. Lopes, M. F. P, Conley, D. and Ringwood, J. V. Benefits of up-wave measurements in linear short-term forecasting for wave energy applications. *Proceedings of IEEE Multi-conference on Systems and Control (MSC)*, Antibes, France, 2014

Paparella, F. **Monk, K.** Winands, V. Lopes, M. F. P, Conley, D. and Ringwood, J. V. Up-wave and autoregressive methods for short-term wave forecasting for an oscillating water column. *IEEE Transactions on Sustainable Energy*, vol. 6, no. 1, 2015.

The following paper is in review and has been accepted pending minor revisions;

**Monk, K.** Conley, D. Winands, V. Lopes, M. F. P. Greaves, D. and Zou, Q. Simulations and field tests of pneumatic power regulation by valve control using short-term forecasting at the Pico OWC. *11<sup>th</sup> European Wave and Tidal Energy Conference*, Nantes, France, 2015.

## 1.5 Theory of ocean waves

As a precursor to the main body of this thesis a brief overview of some key aspects (with direct relevance to this research) of linear ocean wave theory, are reviewed. Some relevant nonlinear wave phenomenon will also be discussed briefly. This will simply summarise well-documented theories and is presented only to give a reader who is not familiar with the topic a foundation level of understanding that will be useful for interpreting the remainder of this thesis. Also it is presented so that reference can be made back in later chapters for fewer interruptions in the narrative. For more details, there are many books and articles on this subject group. For example (Young, 1999), (Dean & Dalrymple, 1991) and (Goda, 2010) provide good and encompassing reviews and the following sections of this chapter are primarily a summary of the parts of these literatures that are relevant to the remainder of the thesis.

### 1.5.1 Regular linear waves

When the water depth is large in comparison to the wavelength and wave height, linear wave theory can be used to describe the water surface elevation. The region of validity of linear wave theory with respect to the wave height over wave length ratio  $H/\lambda$  and the Ursell number  $H^2\lambda^2/h^3$ , where  $h$  is water depth, is shown in figure 1.2, in addition to the regions where other nonlinear wave theories are valid.

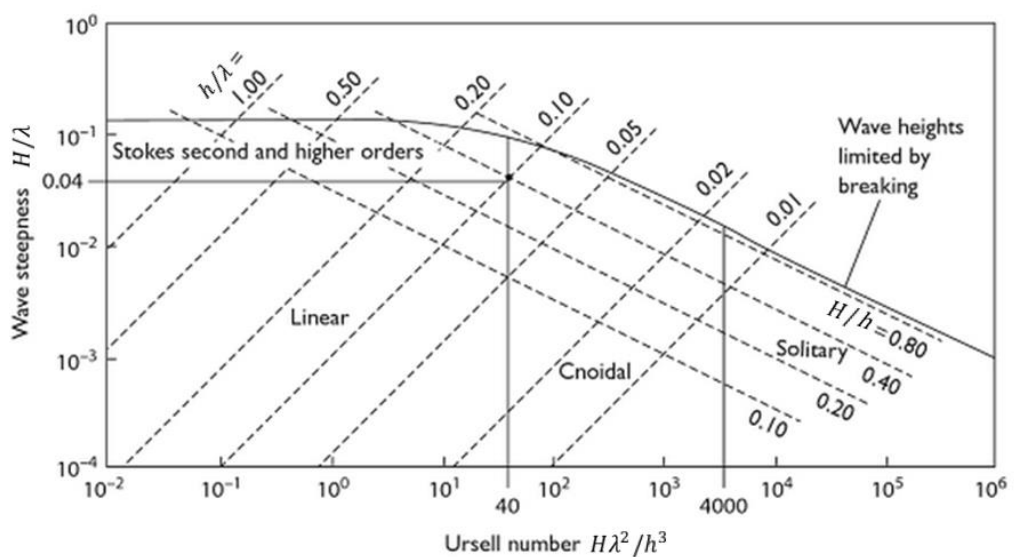


**Figure 1.2** Regions of validity for different wave theories based on: wave steepness and the Ursell number. Figure from (Reeve, et al., 2004) with minor adaptations for homogenous symbolic usage.

Linear wave theory uses the potential flow approach to describe the motion and propagation of gravity waves (long waves where surface tension effects are negligible) at the surface of a uniform fluid layer, under the assumptions that fluid flow is: inviscid, irrotational and incompressible.

In order to present the linear wave theory more easily, figure 1.3 shows the two dimensional fluid boundaries and identifies some key parameters which will be used in the following mathematical descriptions.

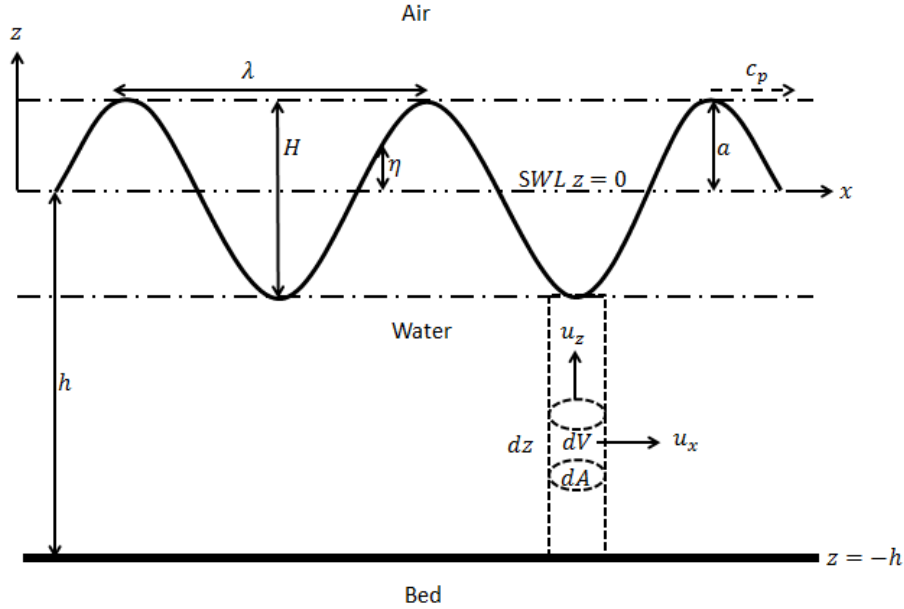


**Figure 1.3** Schematic of some of the parameters used in linear wave theory derivations.  $H$  is wave height,  $a$  is wave amplitude,  $\lambda$  is wave length,  $h$  is water depth  $c_p$  is phase velocity, an infinitesimal element of the water column is described by:  $dz$  the unit height,  $dA$  the unit area and  $dV$  the unit volume.

The continuity equation states that in a steady state process the rate of mass entering and exiting a system must be equal. When incompressibility of the fluid is assumed this concept can be defined by;

$$\nabla \cdot (\rho u) = 0 \quad (1.1)$$

where  $\rho$  is the fluid density and  $u = (\vec{u}_x + \vec{u}_z)$  is the flow velocity vector field.

If flow is assumed irrotational  $\nabla \times u = 0$  (which is valid because waves travel great distances without much dissipation), a scalar quantity called the velocity potential  $\phi$  can be defined, the gradient of which with respect to space is the fluid velocity;

$$u = \nabla \phi \quad (1.2)$$

Under the assumption of irrotational and incompressibility flow (1.2) allows us to express (1.1) in scalar form;

$$\nabla^2 \phi = 0 \quad (1.3)$$

which is the Laplace equation, which can otherwise be consider as;

$$\frac{\partial^2 \phi}{\partial x^2} + \frac{\partial^2 \phi}{\partial z^2} = 0 \quad (1.4)$$

where;

$$u_x = \frac{\partial \phi}{\partial x} \quad (1.5)$$

$$u_z = \frac{\partial \phi}{\partial z} \quad (1.6)$$

where  $x$  is the horizontal plane in the direction of wave propagation and  $z$  the vertical plane,  $u_x$  and  $u_z$ , are the velocity of fluid particles in the horizontal and vertical planes, respectively.

The system of equations is closed by defining the following boundary conditions which are needed to obtain a solution to the Laplace equation (1.3).

Fluid particles at the water free surface  $\eta$  must have vertical velocity equal to the free surface vertical velocity which gives the kinematic free-surface boundary condition;

$$\frac{\partial \eta}{\partial t} = \frac{\partial \phi}{\partial z} \quad , \quad \text{when } z = \eta \quad (1.7)$$

If the sea bed is impermeable, fluid at this location must have zero vertical velocity which gives the kinematic bed boundary condition;

$$\frac{\partial \phi}{\partial z} = 0 \quad , \quad \text{when } z = -h \quad (1.8)$$

where  $h$  is the water depth

The Navier-stokes equations are an application of Newton's second law for fluid motion and describes the conservation of momentum. For inviscid and incompressible flow, a particular Navier-stokes equations arises which is Euler's equation for steady flow;

$$\frac{\partial u}{\partial t} + (u \cdot \nabla)u + \frac{\nabla p}{\rho} - g = 0 \quad (1.9)$$

where  $p$  is fluid pressure and  $g$  is the acceleration from gravity.

Substituting the velocity potential (1.2) into (1.9) and by considering the gravitational acceleration vector with respect to space  $g = -\nabla(gz)$ , Bernoulli's equation can be derived;

$$\nabla \left( \frac{\partial \phi}{\partial t} + \frac{\nabla \phi \cdot \nabla \phi}{2} + \frac{p}{\rho} + gz \right) = 0 \quad (1.10)$$

Air and fluid pressure at their interface ( $z = \eta$ ) must be equal and this yields the dynamic free surface boundary condition;

$$\frac{\partial \phi}{\partial t} + \frac{\nabla \phi \cdot \nabla \phi}{2} + g\eta = 0 \quad , \quad \text{when } z = \eta \quad (1.11)$$

When the surface elevation and vertical velocity are both small ( $z = \eta \approx 0$ ) (1.11) becomes;

$$\frac{\partial \phi}{\partial t} + g\eta = 0 \quad , \quad \text{when } z = \eta \approx 0 \quad (1.12)$$

Using the method of separation of variables a solution to the Laplace equation (1.4), whilst considering the kinematic and dynamic boundary conditions (1.7, 1.8 and 1.12), is given in (Airy, 1845) and (Stokes, 1847) as;

$$\phi(x, z, t) = \frac{ag}{\omega} \frac{\cosh[k(h+z)]}{\cosh(kh)} \cos(kx - \omega t) \quad (1.13)$$

where  $\omega = 2\pi/T$  is the wave angular frequency ( $T$  is wave period),  $a = H/2$  is the wave amplitude (half the wave height  $H$ ) and  $k = 2\pi/\lambda$  is the wave number ( $\lambda$  the wave length)

Substituting (1.13) for the velocity potential in equation (1.12) and differentiating with respect to time, gives the formation for the surface elevation of a small amplitude regular wave;

$$\eta(x, t) = a \sin(kx - \omega t) \quad (1.14)$$

Combining (1.7) and (1.12) gives;

$$-\frac{\partial \phi}{\partial z} = \frac{1}{g} \frac{\partial^2 \phi}{\partial t^2} \quad \text{when } z = 0 \quad (1.15)$$

Then by substituting (1.15) in to (1.13) and for the condition that  $z = 0$ , we arrive at the dispersion relationship for linear waves;

$$\omega^2 = gk \tanh(kh) \quad (1.16)$$

This provides the relationship where only a unique set of values relate; wave angular velocity, wave number and water depth (or wavelength, wave period and water depth). Ultimately it describes the dispersive nature of gravity wave components, meaning each wave component propagates with a speed that is a function of frequency and water depth;

$$c_p = \omega/k = \lambda/T \quad (1.17)$$

The dispersion relationship can be simplified when certain conditions are met. In “deep water” when  $kh \gg 1$ ;

$$\omega^2 \approx gk \quad (1.18)$$

and water depth no longer significantly affects the propagation rate;

$$c_p = \sqrt{\frac{g\lambda}{2\pi}} = \frac{g}{2\pi} T \quad (1.19)$$

In “shallow water” when  $kh \ll 1$ ,  $\tanh(kh) \rightarrow kh$  and the dispersion relationship simplifies to;

$$\omega^2 = ghk^2 \quad (1.20)$$

As such the phase speed in the shallow water limit can be described by;

$$c_p = \sqrt{gh} \quad (1.21)$$

which is no longer a function of frequency and is dependent on water depth only.

In deep or intermediate water depth waves propagate with phase speed that is frequency dependent such that waves of lower frequency travel faster and overtake waves of higher frequency. The superposition of waves over-taking one another forms wave groups defined as regions in time and space where there is a net constructive or destructive interference producing a wave envelope that is harmonic in form. In deep water these wave groups propagate at a rate described by the relationship;

$$c_g = \frac{d\omega}{dk} = \frac{1}{2} \left( \frac{g}{k} \right)^{1/2} = \frac{1}{2} c_p \quad (1.22)$$

In shallow water wave propagation is no longer frequency dependent (non-dispersive) and no over-taking occurs, so;

$$c_g = c_p \quad (1.23)$$

Wave length calculations can be made by first substituting the dispersion relationship (1.16) into the version of the phase speed equation (1.17), which is a function of angular frequency and wave number, and this gives;

$$c_p^2 = \frac{g}{k} \tanh(kh) \quad (1.24)$$

Then by substituting the phase speed equation (1.17) again, this time as a function of wavelength and wave period, in to equation (1.24), gives the transcendental relationship for wave length;

$$\lambda = \frac{gT^2}{2\pi} \tanh\left(\frac{2\pi h}{\lambda}\right) \quad (1.25)$$

which can be solved by an iterative conversion.

Gravity waves have mechanical energy which is transmitted in space as they propagate. For a regular wave component, it is useful to be able to quantify the energy of the wave and the rate of transmission. This is described in (Dean & Dalrymple, 1991) for example and the mathematical formulation is given in the following;

Mechanical energy in a wave is a continuous oscillation between kinetic energy (water mass velocity) and potential energy (elevated water mass having stored energy with respect to gravity).

Consider a column of water with horizontal area  $dA$ , taking a section of this column having vertical length  $dz$  results in a volume  $dV = dAdz$ , at height  $z$  from the mean water level as shown in figure 1.3. The potential energy of the water in  $dV$  is then;

$$E_p = mgh = \rho g z dV \quad (1.26)$$

Integrating (1.26) over the full height of the water column (sea floor  $z = -h$  to water surface elevation  $\eta$ ) gives the total instantaneous potential energy of the water column;

$$E_p = \int_{z=-h}^{\eta} \rho g z dV = dA \int_{z=-h}^{\eta} \rho g z dz = dA \rho g \frac{\eta^2 - h^2}{2} \quad (1.27)$$

Since we are considering the energy of the wave, only the fluid potential energy above what would be present at still water is of interest;

$$\frac{E_p - E_p(\eta=0)}{dA} = \frac{1}{2} \rho g \eta^2 \quad (1.28)$$

To consider the average energy we must consider the average surface elevation, which for a regular wave (sinusoid) is;

$$\overline{\eta^2} = \frac{a^2}{2} \quad (1.29)$$

So that the average potential energy per unit area is

$$\frac{\overline{E_p}}{dA} = \frac{\rho g a^2}{4} \quad (1.30)$$

The kinetic energy can be found in a similar manner by again considering a unit volume  $dV$ , which gives;

$$E_k = \frac{1}{2} m v^2 = \frac{1}{2} (u_x^2 + u_y^2 + u_z^2) \rho dV \quad (1.31)$$

Similarly, by integrating over the height of the water column we find the kinetic energy in the water column is given by;

$$E_k = \int_{z=-h}^{\eta} \frac{1}{2} (u_x^2 + u_y^2 + u_z^2) \rho dV \quad (1.32)$$

Considering a regular wave in deep water as described by equation (1.14) the derivative of the squared surface elevation gives the squared velocity;

$$u_x^2 + u_y^2 + u_z^2 = (\omega a)^2 e^{2kz} \quad (1.33)$$

which when considering (1.18) leads to the formulation for the mean (because we use  $\eta^2$ ) wave kinetic energy per unit area;

$$\frac{\overline{E_k}}{dA} = \rho \omega^2 a^2 \int_{z=-h}^{\eta} \frac{1}{2} e^{2kz} dz \approx \rho \omega^2 a^2 \int_{-\infty}^0 \frac{1}{2} e^{2kz} dz = \frac{1}{2} \rho \omega^2 a^2 \frac{1}{2k} = \frac{1}{4} \rho g a^2 \quad (1.34)$$

From (1.30) and (1.34) it is seen that the average kinetic energy is equal to the average potential energy.

The total energy is the sum of kinetic and potential energy which over a specific area is;

$$E = \frac{1}{2} \rho g a^2 = \frac{1}{8} \rho g H^2 \quad (1.35)$$

The average wave energy flux  $P$  is the rate (group velocity  $c_g$ ) of average energy propagation;

$$P = E c_g \quad (1.36)$$

Which in deep water where (1.19) and (1.22) apply, gives;

$$P = \frac{\rho g^2 H^2 T}{32\pi} \quad (1.37)$$

### 1.5.2 Irregular waves

In the real ocean the wave field is not described by a single harmonic frequency component with a specific amplitude (monochromatic), instead many wave components with a probability distribution in: amplitude frequency and direction, combine and superimpose to form random irregular waves and a simplification of this process can be described by random linear wave theory.

The first step to defining irregular waves is to consider the surface elevation in time and space using the Fourier model which assumes that irregular waves can be described by a superposition of multiple regular wave components. This is achieved by summing  $n$  different regular wave components  $j$  (1.14) with a phase shift term  $\alpha$  added;

$$\eta(x, t) = \sum_{i=1}^n a_i \sin(\omega_i t - k_i x + \alpha_i) \quad (1.38)$$

where  $\omega_j$  and  $k_j$  are related through the dispersion relationship (1.16)

The wave phase angle  $\alpha_j$  relates to the origin of the axis reference. In the open ocean there is no distinct point to set an axis centre and instead the phase is considered to be random and uniformly distributed between  $0 \leq \alpha_j \leq 2\pi$  with equal probability.

At a point in time and space a wave component has phase  $\omega t - kx = \alpha_0$ . With  $d\alpha \rightarrow 0$  the expectance of the function  $\sin(\alpha_0 + \alpha)$  is;

$$E[\sin(\alpha_0 + \alpha)] = \frac{1}{2\pi} \int_{\alpha=0}^{2\pi} \sin(\alpha_0 + \alpha) d\alpha = 0 \quad (1.39)$$

The variance is the expectance of the function squared minus the square of the expectance of the function;

$$\begin{aligned} \text{Var}[\sin(\alpha_0 + \alpha)] &= E[\sin^2(\alpha_0 + \alpha)] - (E[\sin(\alpha_0 + \alpha)])^2 \\ &= \frac{1}{2\pi} \int_{\alpha=0}^{2\pi} (\sin(\alpha_0 + \alpha) - 0) d\alpha \\ &= \frac{1}{2\pi} \int_{\alpha=0}^{2\pi} \frac{1 - \cos(2(\alpha_0 + \alpha))}{2} d\alpha \\ &= \frac{1}{2} \end{aligned} \quad (1.40)$$

Since each phase components  $\alpha_j$  of the  $n$  wave components needed to consider an irregular sea state are assumed to be uniformly distributed between 0 and  $2\pi$  they can be summed as independent stochastic variables. The surface elevation variance is then found using the relationships defined in (1.39) and (1.40).

The surface elevation expectation is then;

$$E[\eta(x, t)] = \sum_{j=1}^n a_j E[\sin(\alpha_0 + \alpha_j)] = 0 \quad (1.41)$$

and the variance is;

$$\begin{aligned}\text{Var}[\eta(x, t)] &= \sum_{j=1}^n a_j^2 E[\sin^2(\alpha_0 + \alpha_j)] \\ &= \sum_{j=1}^n \frac{a_j^2}{2}\end{aligned}\tag{1.42}$$

If it is assumed that the irregular wave is a superposition of an infinite number of wave components, the sum of discrete wave components is replaced with an integral over a probability density distribution  $Q$  (centred about the wave number  $k$ ). If the wave amplitude is considered to be a function of wave number  $a_n = a(k_j)$  the substitution to make a transition from a discrete to continuous representation is;

$$\sum_{i=1}^n \frac{a(k_i)^2}{2} \rightarrow \int_{-\infty=k_x}^{+\infty} \int_{-\infty=k_y}^{+\infty} Q(k_x, k_y) dk_x dk_y = \int_k Q(k) dk^2\tag{1.43}$$

where  $k_x$  and  $k_y$  are components of wave number vector  $k$  in the  $x$  and  $y$  plane, respectively.

The function  $Q(k_x, k_y) = Q(k)$  described the probability density distribution of waves about  $k$  and is termed the wavenumber spectrum.

We recall that (1.35) describes the surface energy for a harmonic component over a unit area and is a function of the squared wave amplitude. For the irregular wave case the squared wave amplitude is described by an integral over the wave spectrum number and it follows that;

$$E = \rho g \sum_{j=1}^n \frac{a(k_j)^2}{2} = \rho g \int_k Q(k) dk^2\tag{1.44}$$

Because the wave number is a vector the surface elevation variance can be considered in polar coordinates;

$$\int_k Q(k) dk^2 = \int_{k=0}^{\infty} \int_{\theta=0}^{2\pi} Q(k, \theta) k dk d\theta\tag{1.45}$$

The dispersion relationship (1.16) states that wavenumber is a function of angular frequency so;

$$\int_{k=0}^{\infty} \int_{\theta=0}^{2\pi} Q(k, \theta) k dk d\theta = \int_{\omega=0}^{\infty} \int_{\theta=0}^{2\pi} Q(k(\omega), \theta) k(\omega) \frac{dk(\omega)}{d\omega} d\omega d\theta\tag{1.46}$$

The wavenumber spectrum considered as a function of  $\theta$  and  $\omega$  is termed the directional spectrum;

$$S(\omega, \theta) = Q(k(\omega), \theta) k(\omega) \frac{dk(\omega)}{d\omega}\tag{1.47}$$

and describes the wave energy distribution in the frequency domain and in propagation directions.

The directional spectrum function  $S(\omega, \theta)$  can also be considered as being made up of two functions that describe the distribution of wave frequencies  $S(\omega)$  and the distribution of wave directions  $D(\theta, \omega)$  (spreading function), as described;

$$S(\omega, \theta) = S(\omega)D(\theta, \omega) \quad (1.48)$$

which could also be described as a being a function of frequency  $f$  by exchanging  $\omega$  with  $f$ .

The wave directional spread  $D$  has no dimensions and is typically normalised such that;

$$\int_{\theta=0}^{2\pi} D(\theta, \omega) d\theta = 1 \quad (1.49)$$

In this format the frequency distribution describes the absolute wave energy density whilst the directional spread provides the relative magnitude of the density of directional components.

### 1.5.2.1 Frequency spectrum

As discussed in the last section sea waves can be considered as a superposition of an infinite number of regular wave components with different frequencies (and directions). The energy distribution profile of these wave components plotted against frequency describes the wave frequency spectrum. The wave frequency spectrum has been studied intensively and has been sampled from locations all over the globe. A basic spectral profile form exists and shifts in the amplitude and peak frequency results from different lengths of fetch and the locational proximity to the dominant atmospheric processes that generate the waves, as well as time.

Numerous equations to define the wave frequency spectrum have been proposed but two of the most commonly used are reviewed in the following;

The Pierson-Moskowitz (P-M) spectrum (Pierson & Moskowitz, 1964) proposes that when the wind blows steadily over a very large area for a very long period of time, waves reach an equilibrium with the driving wind. This scenario is considered as a fully developed sea.

Using data collected in the north Atlantic for periods when the wind blew steadily for long time periods they found the calculated spectrum could be approximated with the empirical equation;

$$S_{P-M}(\omega) = \frac{\alpha g^2}{\omega^5} \exp \left[ -\beta \left( \frac{\omega_0}{\omega} \right)^4 \right] \quad (1.50)$$

where  $\alpha = 8.1 \times 10^{-3}$ ,  $\beta = 0.74$  and  $\omega_0 = g/U_{19.5}$  where  $U_{19.5} \approx 1.026U_{10}$  is the wind speed ( $m/s$ ) at a height of 19.5 ( $m$ ) above the water surface.

Alternately the JONSWAP spectrum, derived from measurements of the North Sea, is proposed in (Hasselmann, et al., 1973) which better characterises the sharper spectral peak that coincides with a rapidly developing sea under strong wind conditions in a shorter water body. Unlike the P-M spectrum, the JONSWAP spectrum factors in wind fetch so that waves continue to grow with distance and time. The empirical formulation of the JONSWAP spectrum is;

$$S_J(\omega) = \frac{\alpha g^2}{\omega^5} \exp \left[ -\frac{5}{4} \left( \frac{\omega_p}{\omega} \right)^4 \right] \gamma^r \quad (1.51)$$

where;

$$r = \exp \left[ -\frac{(\omega - \omega_0)^2}{2\sigma^2\omega_p^2} \right] \quad (1.52)$$

$$\alpha = 0.076 \left( \frac{U_{10}}{Fg} \right)^{0.22} \quad (1.53)$$

$$\omega_p = 22 \left( \frac{g^2}{U_{10}F} \right)^{1/3} \quad (1.54)$$

$$\sigma = \begin{cases} 0.07 & \omega \leq \omega_p \\ 0.09 & \omega > \omega_p \end{cases} \quad (1.55)$$

where  $U_{10}$  is the wind speed at 10 (m) above sea level,  $\gamma$  is the peak enhancement factor,  $F$  is the fetch (up-wind distance to land or distance over which wind blows with constant velocity) and  $\omega_p$  is the peak wave angular frequency the value of which yields  $S(\omega) = \max$ , and is commonly interchanged with the peak wave frequency  $f_p$  and peak wave period  $T_p$  by the following relationships;

$$\omega_p = 2\pi f_p = \frac{2\pi}{T_p} \quad (1.56)$$

Using (1.50) by knowing the wind velocity, and (1.51) by also knowing the fetch, the wave spectral distribution can be forecasted. However, the spectral distribution can be defined if some key parameters of the sea state are known, namely the peak wave period  $T_p$ , significant wave height  $H_s$  (discussed later in section. 1.5.2.3), the spectral distribution. For example, the JONSWAP spectrum can be defined using;

$$s(f) = \beta_j H_s^2 T_p^{-4} f^{-5} \exp[-1.25(T_p f)^{-4}] \gamma^{\exp[-(T_p f - 1)^2 / 2\sigma^2]} \quad (1.57)$$

where  $T_p$  is the peak wave period,  $f$  the wave frequency and;

$$\beta_j = \frac{0.0624}{0.230 + 0.0336\gamma - 0.185(1.9 + \gamma)^{-1}} [1.094 - 0.01915 \ln \gamma] \quad (1.58)$$

The P-M and JONSWAP spectrums (with 500km of fetch) for a range of wind velocities is shown in figure 1.4.

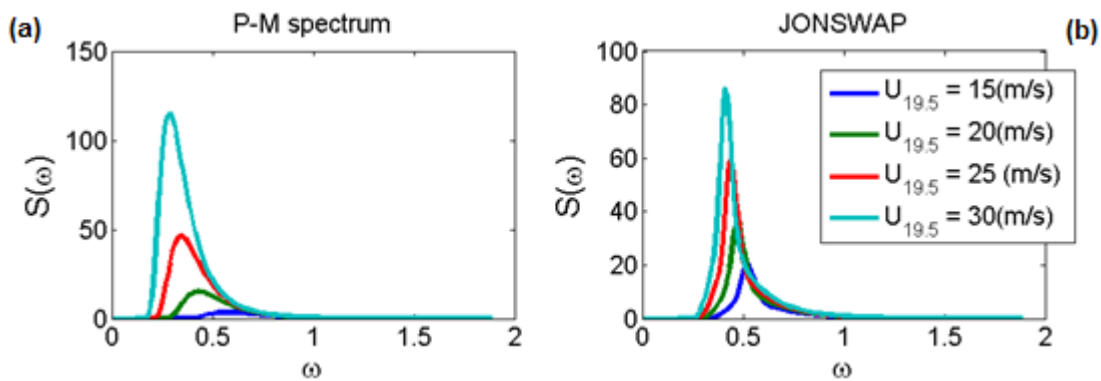


**Figure 1.4** Example of frequency distribution as described by (a) Pierson-Moskowitz and (b) JONSWAP, spectrums, for different wind speed velocities at 19.5 (m) above the sea surface.

### 1.5.2.2 Directional spreading

As well as occupying a distribution of frequencies, the wave components that combine to make ocean waves also occupy a distribution of directions known as the directional spread. The characterisation of wave directional spreading is still limited due to the technical difficulty in sampling this parameter. However, based on extensive field measurements using a cloverleaf buoy, (Misuyasu, et al., 1975) have developed a function to define the distribution of the direction of wave components;

$$D(\omega, \theta) = D_0 \cos^{2s} \left( \frac{\theta - \theta_0}{2} \right) \quad (1.59)$$

where  $\theta$  is wave direction angle,  $\theta_0$  is directional of the principle wave direction,  $D_0$  is a normalising constant;

$$D_0 = \left[ \int_{\theta_{min}}^{\theta_{max}} \cos^{2s} \left( \frac{\theta - \theta_0}{2} \right) d\theta \right]^{-1} \quad (1.60)$$

where the parameter  $s$  describes the concentration of wave directions about the principle wave direction. The degree of directional spreading between wave frequency components was found to not be equal and for engineering applications (Goda & Suzuki, 1975) propose the following relationship;

$$s = \begin{cases} (\omega/\omega_p)^5 s_{max} & \text{when } \omega \leq \omega_p \\ (\omega/\omega_p)^{-2.5} s_{max} & \text{when } \omega > \omega_p \end{cases} \quad (1.61)$$

where  $s_{max}$  is the peak value of  $s$  which was found from observations in (Misuyasu, et al., 1975) to be a function of wind speed  $U$  and  $f_p$  and described by;

$$s_{max} = 11.5(\omega_p U/g)^{-2.5} \quad (1.62)$$

To give an example of the wave directional spread of different frequency components as described by (1.59) a sea state with  $\omega_p = 0.5(\text{rad s}^{-1})$  and  $U = 15(\text{ms}^{-1})$  is considered and the relationship between wave direction  $\theta$  and directional spread  $D(\omega, \theta)$  is shown in figure 1.5.

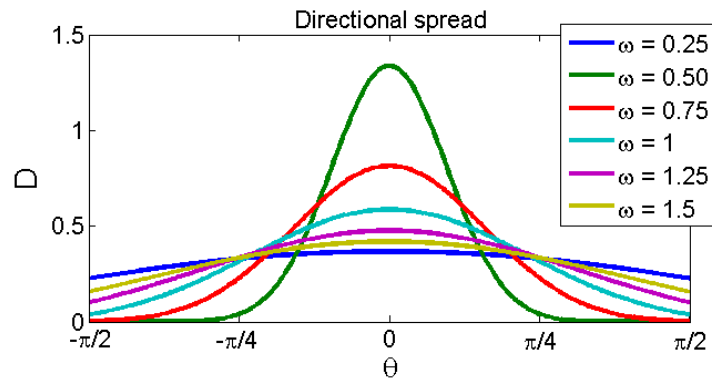


**Figure 1.5** Example of directional spread distribution of different frequency components as described by the function in (Misuyasu, et al., 1975), for a sea state with  $\omega_p = 0.5(\text{rad s}^{-1})$  and with wind velocities of  $U = 15(\text{ms}^{-1})$ .

### 1.5.2.3 Wave height distribution

The superposition of wavelets in the Fourier model also results in the distribution of wave heights which also needs to be considered when characterising irregular waves. In (Longuet-Higgins, 1952) it is shown that the Rayleigh distribution, developed originally to describe the distribution of sound intensity emitted from an infinite number of sources, also provides a good approximation of the distribution of ocean wave heights. The wave height probability density  $P$  as described by the Rayleigh distribution is;

$$P(H/\bar{H}) = \frac{\pi H}{2\bar{H}} \exp\left[-\frac{\pi}{4}\left(\frac{H}{\bar{H}}\right)^2\right] \quad (1.63)$$

where  $\bar{H}$  is the mean wave height.

For example for a sea state with  $\bar{H} = 3$  (m) the probability distribution of wave heights will take the form shown in figure 1.6.

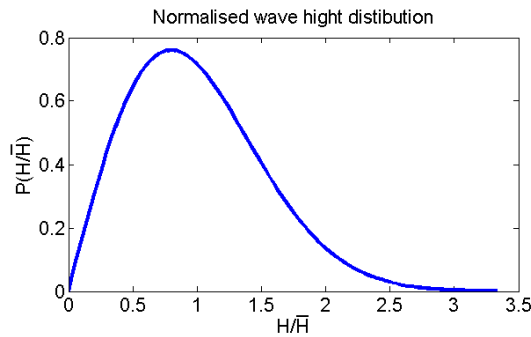


**Figure 1.6** Probability density of the Rayleigh wave height distribution for  $\bar{H} = 3$  (m)

The wave height probability distribution is normalised because the integral of  $P$  (over all wave heights) is unity;

$$\int_0^{\infty} P(H/\bar{H}) d H/\bar{H} = 1 \quad (1.64)$$

A common parameter used to describe the wave height distribution of a sea state is the significant wave height  $H_s$  which describes the mean of the highest one-third of wave heights in the distribution.

### 1.5.2.4 Relationships between wave spectra and wave characteristics

In engineering applications it is possible to obtain sea state spectral information by knowing or considering the sea state characteristics ( $H_s$  and  $T_p$ ) and by applying these values to one of the established frequency distributions, (1.57) for example, and convolving this with a proposed wave directional distribution, (1.59) for example.

In an opposing approach, the sea state characteristics can be extracted from the known spectral information or sampled wave data. For simplicity, in the description we will only consider the frequency spectrum  $S(\omega)$ . First the total wave energy  $m_0$ , also known as the zeroth spectral moment of the wave spectrum, needs to be found and this is done by integrating the frequency spectrum over the complete frequency range;

The  $n^{th}$  spectral moment is given by;

$$m_n = \int_0^\infty \omega^n S(\omega) d\omega \quad (1.65)$$

where  $n$  is the spectral moment order. The zeroth spectral moment ( $n = 0$ ) is the area under the spectral curve and is equal to the total energy density of the spectrum which is also equal to the surface elevation variance;

$$m_0 = \overline{\eta^2} = \lim_{t_0 \rightarrow \infty} \frac{1}{t_0} \int_0^{t_0} \eta^2 dt \quad (1.66)$$

The root-mean-square of the surface elevation;

$$\eta_{rms} = \sqrt{m_0} \quad (1.67)$$

holds a specific relationship with the Rayleigh wave height distribution which is defined by;

$$H_s \approx H_{m0} \approx 4\sqrt{m_0} \quad (1.68)$$

where  $H_{m0}$  signifies the significant wave height as derived from the spectral distribution

The mean wave period  $\bar{T}_0$  can be found by also considering the 2<sup>nd</sup> spectral moment;

$$\bar{T}_0 = 2\pi \sqrt{\frac{m_0}{m_2}} \quad (1.69)$$

The wave energy period, which is the mean wave period with respect to the wave energy propagation, is given by;

$$T_e = 2\pi \frac{m_{-1}}{m_0} \quad (1.70)$$

For a random wave the time averaged energy per unit area is proportional to the variance of the squared surface elevation  $E \propto \overline{\eta^2(t)}$ . From (1.65) and (1.66) we find that mean energy for an irregular wave is;

$$\bar{E} = \rho g \overline{\eta^2(t)} = \rho g \int_0^\infty S(\omega) d\omega \quad (1.71)$$

Substituting (1.68) into (1.71) yields;

$$\bar{E} = \frac{\rho g}{16} H_s^2 \quad (1.72)$$

The mean wave power for an irregular wave is found by integrating over the power of each regular wave frequency components;

$$\bar{P} = \frac{\rho g^2}{2} \int_0^{+\infty} \frac{S(\omega)}{\omega} d\omega \quad (1.73)$$

Finally by considering the energy period (1.70) and significant wave height (1.68) we find that mean wave power for an irregular wave is;

$$\bar{P} = \frac{\rho g^2}{64\pi} H_s^2 T_e \quad (1.74)$$

As an additional note, the subject of Wave groupiness will be discussed briefly. This is slightly out of place in this section but will be presented here because the method also employees spectral moments, and this subject features in a later chapter.

Wave groups are formed when wave trains come into and out of phase, constructively and destructively interfering to form distinct temporal periods of higher and lower wave energy. One commonly used method to characterise how grouped a sea state is, is the groupiness factor  $GF$  introduced by (Funke & Mansard, 1980) which is defined as the coefficient of variance of the Smoothed Instantaneous Wave Energy History ( $SIWEH$ ). The  $SIWEH$  gives the distribution of energy with time and is defined as;

$$SIWEH(t) = \frac{1}{T_p} \int_{\tau=-T_p}^{T_p} \eta^2(t + \tau) Q(\tau) d\tau \quad (1.75)$$

Where  $Q$  is the Bartlett window and  $Q = 1 - |\tau|/T_p$ , when  $-T_p \leq \tau \leq T_p$ , and  $Q = 0$  elsewhere.

The groupiness factor is then defined as;

$$GF = \sqrt{m_{E0}/m_0} \quad (1.76)$$

where  $m_{E0}$  is the zeroth spectral moment of the  $SIWEH$  spectrum, and  $m_0$  is the spectral moment of the incident wave time series.

When  $GF = 0$  the wave is a purely sinusoidal and as  $GF$  increases the wave “groupiness” is consider to be increasingly higher. Higher wave groupiness could be considered as a higher frequency wave envelope of the crests or troughs, from higher wave amplitude variance. In (Goda & Suzuki, 1976) it is seen that wave groupiness increases as the spectral band width decreases.

### 1.5.3 Wave transformations

Shoaling describes the first stage of wave transformation as waves enter shallow water. From the principle of conservation of energy, and ignoring energy dissipation, the energy of a wave propagating from deep water ( $DW$ ) to shallow water ( $SW$ ), must be equal;

$$P = E_{DW} c_{g,DW} = E_{SW} c_{g,SW} \quad (1.77)$$

Equation (1.22) states that the group velocity reduces as waves enter shallow water. If no power is dissipated an increase in energy, namely an increase in wave height, must occur to compensate for the reduction in group velocity. From equation (1.35) and equation (1.77) we find that;

$$\frac{H_{SW}}{H_{DW}} = \left( \frac{c_{g,DW}}{c_{g,SW}} \right)^{0.5} = K_s \quad (1.78)$$

where  $K_s$  is the wave shoaling coefficient which equals 1 in deep water and increase rapidly as waves enter shallow water. The frequency of a shoaling wave is unchanged but because of the slower phase speed the wavelength must decrease. This, in addition to the increase in wave height results in waves with greater steepness. Wave steepness  $S_{op}$  can be characterised by;

$$S_{op} = \frac{2\pi H}{gT^2_p} = \frac{H}{\lambda_0} \quad (1.79)$$

where  $\lambda_0$  is the deep water wavelength

In shallower water linear wave theory ceases to be valid and higher order nonlinear wave theory must be considered. The sinusoidal deep-water wave develops an increasingly asymmetrical profile when shoaling in shallow water due to nonlinear interactions between the frequency components. Initially wave asymmetry (skewness) occurs in the horizontal plane and this is characterised by a sharpening of the wave crest and an elongation and flattening of the wave trough as shown in figure 1.7. The degree of wave skewness is defined by;

$$S_k = \frac{m_3}{\sigma(\eta)^3} \quad (1.80)$$

As the water depth continues to decrease wave asymmetry also occurs in the vertical plane and is characterised by a steepening of the front face of the wave crest and a flattening of the rear face as shown in figure 1.7. Wave asymmetry in the vertical plane can be quantified by the skewness of the Hilbert transform of  $\eta(t)$ . Wave asymmetry is a departure from Gaussian statistics and the kurtosis may be used to identify the non-Gaussian characteristics of the wave field in the location of interest. The kurtosis  $C$  is defined as;

$$C = \frac{m_4}{m_2^2} - 3 \quad (1.81)$$

which for a Gaussian sea state  $C = 0$ .

Cnoidal wave theory can be used to describe nonlinear asymmetric wave transformations in shallower water but it is beyond the scope of this study to present the mathematical descriptions of this.

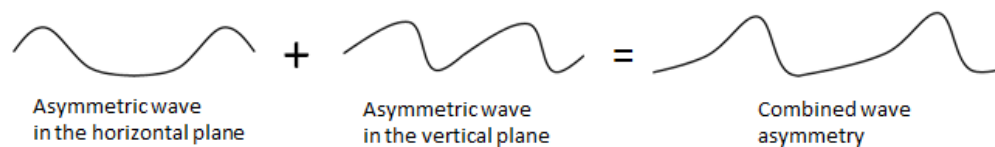


**Figure 1.7** Illustrations of different asymmetrical wave profiles.

As just shown the wave phase speed reduces as waves enter shallower water, the wave height must increase in order to maintain a constant energy density. The crest of the wave experiences a greater water depth than the trough and propagates faster. The difference in propagation rates increases as the wave height increases leading to wave asymmetry in the vertical plane. At a certain depth this speed difference becomes significant enough for the wave crest to start overtaking the remainder of the wave in front causing vertical wave asymmetry and instability. Fluid flow becomes rotational and the crest curls forward and the wave breaks and becomes highly nonlinear. The form in which the wave breaks depends on the gradient of the bathymetry with the crest projecting out further and breaking more violently with steeper bathymetry gradients

As discussed earlier in the section, wave dispersion describes how wave components propagate with a rate that is a function of water depth, except in deep water conditions. If a wave enters a region of

shallower water, unless the wave front is perfectly parallel with the bathymetric contour lines, sections of the wave front will be in water of differing depths and therefore travel with different phase velocity. The result is a bending of the wave front and this transformation is known as refraction. Refraction is not considered in this research and so the mathematical description of this effect will not be given.

As waves encounter matter that does not move with the exact phase and velocity of the water particles, reflection and diffraction occurs. If the propagation of part of the wave front is interrupted by reflection or dissipation at an object i.e. the tip of a breakwater, a sharp gradient in the velocity potential along the wave front will be formed and the point of discontinuity will act as a potential point source spreading energy in all directions, some of which will enter the geometrical energy shadow zone. The phenomenon is most easily visualised with Huygens principle which suggests that a straight wave front is actually composed of multiple point sources emitting radial waves, the interference of which (upon superposition) collectively create a straight wave front. This analogy allows the diffraction phenomenon to be more easily interpreted because at the breakwater tip (for example) the end of the wave front passing the breakwater has no other point sources (on the breakwater side) to interfere with to maintain the straight wave front, as such the underlying radial wave form is exposed and because it is a point source it spreads in all directions, but this is only easily observable in the shadow region because no other waves exist at that location to mask it. Wave diffraction is a core subject of this research and a mathematical description and an in-depth discussion is provided in the next two chapters.

In addition to diffraction, when waves encounter obstacles wave energy will be reflected unless full absorption (dissipation, conversion or capture) occurs. For the case of a fully reflecting obstacle, superposition of the incident and reflected wave will create a standing wave (with zero energy flux) in the fluid region in front of the obstacle. In the two dimensional case  $(x, z)$  the resulting surface elevation is described by;

$$\eta = \eta_I + \eta_R = a[\cos(kx - \omega t) + \cos(kx + \omega t)] = 2a \cos(kx) \cos(\omega t) \quad (1.82)$$

where  $\eta_I$  is the incident wave surface and  $\eta_R$  is the reflected wave surface elevation.

If wave energy is partially dissipated or extracted at the object, i.e. for wave energy conversion, the reflected wave will have a smaller amplitude and a partially standing wave will be formed in front of the object and the resulting surface elevation becomes;

$$\begin{aligned} \eta = \eta_I + \eta_R &= a_I \cos(kx - \omega t) + a_R \cos(kx + \omega t) \\ &= (a_I + a_R) \cos(kx) \cos(\omega t) + (a_I - a_R) \sin(kx) \sin(\omega t) \end{aligned} \quad (1.83)$$

Other wave transformations that are not relevant to the remainder of this thesis include: refraction, dissipations of energy through bottom friction and turbulence, interactions with currents, nonlinear wave-wave interactions.

## Chapter 2

# Wave energy shadowing and redistribution due to diffraction at an offshore WEC array

### Abstract

Energy conversion by overtopping type WEC arrays creates an energy deficit (shadow) in the lee of the array. Wave directional spreading has been identified in the literature as the dominant mechanism that acts to recover the wave energy deficit with increasing distance from the array. In addition to this, wave diffraction and radiation acts to scatter the incident wave energy creating a complex interference pattern. The effect of wave scattering on the wave energy shadow in the near and far-field is less obvious. To investigate the role of diffraction on wave energy re-distribution, an approximate analytical solution was constructed to find the: diffracted, reflected and transmitted wave field about a single row array of overtopping type WECs, under irregular wave conditions. The solution is constructed with multiple superpositions of the analytical solutions for monochromatic unidirectional waves about a semi-infinite breakwater, which is extended to account for directionality and partial reflection and partial transmission. This is used to approximate an overtopping type WEC array. The proposed solution is first validated with a comparison to a more mathematically exact integral equation for the same problem, as well as experimental wave tank data. It is then used to investigate the sensitivity of the far-field wave energy shadow to the array configuration, level of energy extraction, sea state characteristics, and diffraction effects. By comparison with the results from an additional proposed solution where diffraction is not considered, it is shown that diffraction acts to redistribute part of the wave energy passing through the array. This spreads energy away from the array's geometrical shadow and counteracts wave directional spreading effects, thus reducing the rate of recovery of the wave energy deficit. This chapter combines the work presented in two first author peer reviewed papers which are given in the paper appendix at the end of this thesis.

### 2.1 Wave energy shadowing introduction

The conversion of wave energy by a WEC produces a wave energy deficit or shadow down wave of the device, as well as an interference pattern about the device due to wave scattering. The ability to predict the wave energy shadow is of topical interest due to the significant stake holder concerns about the potential impacts from wave energy shadowing. Waves play a key role in mass transport, assist in mixing and force sediment transport. Quantifying the wave energy reduction and identifying induced wave height gradients would allow the environmental impacts of a WEC array on the nearby coastal ocean and shoreline, to be assessed. To minimise environmental impacts, it is desirable that the wave energy deficit redistributes over the widest area in the shortest distance from the device, or vice versa if shore protection is an additional objective of the wave energy array deployment. The ability to predict the wave shadow and interference pattern about devices could also reveal locations of low energy within the device array due to negative interference and shadowing. A specific spatial arrangement of devices that avoids placing devices in these lower energy locations could enhance the collective performance of the array.

For an overtopping type WEC the spatial redistribution of the wave energy about the device and in the far-field is affected by wave directional spreading, diffraction, wave radiation and other wave transformation such as refraction. Wave directional spreading is described in section 1.5.2.2. As shown in (Black, 2007) a broader directional spread disperses the energy deficit more rapidly with distance from

the device. This mechanism is analogous to the dull shadow cast by an object illuminated by diffuse light (broad directional spread distribution), or the sharp shadow cast by an object illuminated by a far-field point source (narrow directional spread distribution). The sharp gradient in wave height at the edge of an overtopping type WEC device from the wave termination at the device, induces diffraction which acts to re-distribute the passing wave energy. The motion of the device (if floating) will radiate part of the incident energy in all direction. Refraction due to bathymetry or ambient current changes, alter the wave front trajectory, thus altering the wave energy shadow location and its distribution at the coast.

Previous studies have investigated the wave height reduction in the lee of WEC arrays and these will be reviewed briefly. (Millar, et al., 2007) used the third generation phase averaged spectral wave model SWAN to investigate the effects of the scale of energy extraction and the incident wave parameters, on the far-field wave energy deficit. As phase is not resolved in SWAN and the individual WEC devices were not delineated, the redistribution of energy by diffraction and radiation is not properly accounted for. The wave height reduction was predicted to reduce monotonically with distance from the array. At a distance of 25 (*km*) down-wave from the array the maximum wave height reduction was projected to be less than 1% of the incident wave height. More recently (Abanades, et al., 2015) also used SWAN to investigate the wave height reductions in the lee of an offshore wave farm located closer to the coastline but for the same case study location as consider in (Millar, et al., 2007). The capabilities of the methodology are extended by coupling the wave propagation model with the coastal process model XBeach. This allows the possible shore protection benefits to be assessed in addition to the sedimentation response.

The Boussinesq wave model, Mike21 BW, was used to assess the resultant wave field about a single row of partially reflecting breakwater segments to approximate an array of overtopping WECs (Venugopal & Smith, 2007). With this approach the redistribution of wave energy from diffraction is considered but the distance from the array to the shore is only 2km which is short compared to some proposed offshore wave array installations, such as the Wavehub project.

In (Palha, et al., 2010) the parabolic mild slope wave model REF/DIF is used to assess the wave shadow in the lee of a series of large energy sinks that represent clusters of devices. Wave structure interactions and the resultant redistribution of wave energy are not considered fully. Individual devices are not delineated so that wave diffraction is only considered about the edges of the energy sink regions (WEC clusters) and not the individual devices.

In (Beels, et al., 2010) time dependent mild slope wave model MILDwave is used to assess the wave shadow in the lee of a 2D array of Wave Dragon overtopping type WEC devices. These devices were approximated in the model using porous layers, the shape of which, capture the basic geometry of the Wave Dragon device. The porous layers reflect and transmit wave energy at the (wave focusing) wings of the structure and extract, reflect, and transmit energy at the main body. The degree of reflection, absorption and transmission are dependent on the draft of the device's wings and body as well as the freeboard of the main body and the incident wave height and period.

The shore protection benefits that might be achieved by placing an array of Wave Dragon overtopping type WEC in the relatively near-shore region is assed in (Norgaard & Andersen, 2012) who also use the

Boussinesq wave model, Mike21 BW. The devices were implemented in essentially the same way as in (Beels, et al., 2010) using frequency dependent sponge layers that imitate the actual device geometry. They also considered lower resolution approximations of the devices which were rectangular porous, permeable, breakwater type structures. In this case the reflection, absorption and transmission characteristics of the detailed device were averaged across the device. It was found that in the mid-field (2 kilometres from the devices), the modelled disturbed wave field resulting from the low resolution representation of the WEC was in excellent agreement to the disturbed wave field resulting from the accurate geometrical representation with variable: absorption, transmission and reflection, across the Wave Dragon device's beam. In the very near-field there was significant local divergences in the wave fields resulting from the two device representations, however the general wave energy distribution was very similar.

The studies that consider WEC arrays located far offshore (Millar, et al., 2007), (Palha, et al., 2010) and (Abanades, et al., 2015) only approximate the wave diffraction effect. The studies that fully account for diffraction about the individual devices did not consider arrays far offshore (Venugopal & Smith, 2007); (Beels, et al., 2010); (Norgaard & Andersen, 2012). As such, the effect of wave energy re-distribution over larger distances from scattered waves remains unclear and warrants further investigation. It is also difficult to cross compare these studies to check for consistency in the results because the models and model implementations differ significantly. The present study aimed to develop an accessible engineering tool for scaling the far-field wave energy deficit in the lee of an array of overtopping type WEC devices. To achieve this, the solution/model needs to overcome the existing limitations associated with the other methods presented in the literature including the: maximum domain size, spectral and directional resolution and simulation time restrictions associated with the time-stepping phase resolving models and integral equation methods. This is in addition to the inaccurate treatment of diffraction and interference associated with phase averaged spectral models. Radiated waves associated with point absorber type WECs was not considered in order to focus on the effect of diffraction and to avoid the numerically challenging problem of near trapping of waves.

A number of analytical solutions and modelling schemes have been proposed for describing the diffracted wave field about solid, porous and dissipating type structures. These include the application of the mild-slope equations using a finite element method (Pos & Kilner, 1987) and the eigenvalue expansion approach of (Dalrymple & Martin, 1990). (McIver, 2005) presents a solution for a series of permeable or porous breakwater segments, using an application of the Green's theorem to describe the problem in terms of an integral equation.

In this study the computationally efficient classical solution for the diffracted wave field about a semi-infinite breakwater (Penny & Price, 1944) and (Penny & Price, 1952) was used as a basic building block for a full solution. By making multiple superpositions of the semi-finite solution and by applying reflection and transmission coefficients the resulting model can be used to describe the wave shadow and interference pattern in the lee of a segmented transmitting and reflecting breakwater series. A single row array of overtopping type WECs are approximated by this representation because the degree of absorption and transmission across the breakwater can be set to equal to that of the WEC. This is similar to (Norgaard & Andersen, 2012) simple overtopping WEC device geometry, which achieved the same

results as more intricate physical and geometrical descriptions of the device in the mid to far-field. The approach presented here contains some approximations that affect the accuracy of the solution in the region very close to the array and these will be discussed in detail. These approximations are justified by the comparatively low computational expense of the developed solution, which allows the wave energy shadow for high resolution spectral and directional irregular waves to be considered. However, the integral equation method of (McIver, 2005) will be used to demonstrate that the approximations associated with the analytical solution are acceptable in the far-field, which is the main region of interest of this study.

In summary, the objectives of this research part are threefold: 1) Construct an approximate analytical solution for the wave field about a single row of overtopping type WEC devices, that is sufficiently computationally efficient to scale the far-field wave energy shadow; 2) Investigate the effects of wave diffraction on the recovery of the wave energy shadow; 3) Assess the sensitivity of the wave shadow to: directional spreading, incident wave spectrum, device length and array configuration.

## **2.2 Analytical solutions for wave diffraction**

A WEC array does not capture energy uniformly across the whole wave front passing through the array as was considered in (Millar, et al., 2007), (Black, 2007) and, in part, (Palha, et al., 2010). Instead wave energy is captured from sections of the wave front by the WEC devices. As long as it has width equal to the overtopping device and a transmission coefficient equal to the energy extraction, a breakwater segment will remove the same amount of energy from the section of the wave front. It is common practice to represent an overtopping WEC device as a segmented dissipating breakwater type structure (Venugopal & Smith, 2007), (Beels, et al., 2010) and (Norgaard & Andersen, 2012).

By adapting the (Sommerfeld, 1886) solution for the diffraction of polarised light about a screen edge, (Penny & Price, 1944) and (Penny & Price, 1952) provide an analytical solution for the diffracted wave field about a semi-infinite breakwater in a domain of constant water depth for obliquely incident monochromatic waves. (Silvester & Lim, 1968) suggest that a partially reflecting semi-infinite breakwater can be approximated by applying coefficients to the reflected wave component, and the diffracted wave of the reflected wave component. This will be discussed in greater detail in section 2.2.1. (Penny & Price, 1952) also showed that the approximate diffracted wave field about a gap in an infinite breakwater can be found with a superposition of the diffracted wave field about two opposing semi-infinite breakwater sections. (Kim & Lee, 2010) extend the breakwater gap solution to account for obliquely incident waves by accounting for the phase shift of waves diffracting about the opposing tips. (Penny & Price, 1952) also propose that the diffracted wave field about a detached breakwater can be approximated with a superposition of two semi-infinite breakwater solutions. (Kim & Lee, 2010) show that approximating a breakwater segment with the superposition of two semi-infinite solutions is in good agreement with a more mathematically exact integral equation method with the two methods converging with increasing distance from the breakwater segment and being essentially the same at a distance of  $3\lambda$ . This is because of the reducing influence of the secondary diffracted waves that are not considered by the semi-finite breakwater superposition method. The solutions diverge by up to approximately 10% at closer distances to the breakwater. (Hotta, 1978) propose that the approximate solution for a detached

breakwater segment can also account for partial transmission by further superposing a modification of the breakwater gap solution. This will be discussed further in section 2.2.4.

This investigation took into account the aforementioned methods, to form an approximate analytical solution for the diffracted and transmitted wave field, about a series of partially reflecting and partially transmitting breakwater segments. The fundamental building block of the solution is the analytical solution for diffraction about a reflecting semi-infinite breakwater (Penny & Price, 1952) which derives from velocity potential theory (which is reviewed in section 1.5.1) and is calculated using the Fresnel integrals. The mathematical derivation of the semi-infinite breakwater solution is well documented. As such, the description of the full solution that is used in this study will proceed from the final solution given in (Penny & Price, 1952), which should be consulted for a full initialisation of the problem.

### 2.2.1 Semi-infinite breakwater

(Penny & Price, 1952) describe the diffracted wave field about thin fully reflecting breakwater structures in constant water depth with the complex function  $F(x, y)$ . The modulus of  $F$  describes the disturbance or diffraction coefficient  $K_d$ , which is the ratio of the resultant wave height  $H_{x,y}$  at the Cartesian coordinate point  $x, y$  and the incident undisturbed incident wave height  $H_0$ , so that;

$$K_d = H_{x,y}/H_0 = |F(x, y)| \quad (2.1)$$

The center of the Cartesian coordinate system varies with the breakwater configuration being considered but is always on the plane of the breakwater  $y = 0$ . For incident waves arriving obliquely to the plane of the breakwater it is convenient to work in polar coordinates.  $F(x, y)$  becomes  $F(r, \theta)$  with  $r = (x^2 + y^2)^{0.5}$ ,  $\theta = \tan^{-1}(y/x)$  where  $r$  is the distance from the center of the coordinate system, which is located on the plane of the breakwater or breakwater system, to the calculation point in the domain.  $\theta$  is the angle between the plane of the breakwater from the lee side and the cord that connects the calculation point in the domain with the centre of the coordinate system.

For the case of a thin semi-infinite fully reflecting breakwater, the complex function describing the diffracted wave field is (Penny & Price, 1952);

$$F(r, \theta) = f(\sigma)I + f(\sigma')R \quad (2.2)$$

where  $I$  and  $R$  are the incident and reflected planar wave components respectively which are given by;

$$I = \cos(kr \cos(\theta - \Theta)) - i \sin(kr \cos(\theta - \Theta)) \quad (2.3)$$

$$R = \cos(kr \cos(\theta + \Theta)) - i \sin(kr \cos(\theta + \Theta)) \quad (2.4)$$

where  $k$  is the wave number and is found from the dispersion relationship given by 1.16, the polar coordinate system is centred at the breakwater tip so that  $r$  is the distance from the breakwater tip to the domain calculation point,  $\theta$  is the angle between the plane of the breakwater from the lee side and the line that connects the calculation point in the domain with the breakwater tip and  $\Theta$  is the angle between the incident wave direction and breakwater plane, from the lee side (as shown in figure 2.1). Also, in (2.2);

$$f(\sigma) = 1 - f(-\sigma) = \frac{1+i}{2} \int_{-\infty}^{\sigma} e^{-\frac{\pi i u^2}{2}} du = \left(\frac{1}{2}\right) [(1 + C(\sigma) + S(\sigma)) - i(S(\sigma) - C(\sigma))] \quad (2.5)$$

where the upper limits of the integrals are given by;

$$\sigma = \pm 2 \sqrt{\left(\frac{kr}{\pi}\right)} \sin \frac{1}{2}(\theta - \Theta) \quad (2.6)$$

$$\sigma' = \pm (-2 \sqrt{\left(\frac{kr}{\pi}\right)} \sin \frac{1}{2}(\theta + \Theta)) \quad (2.7)$$

The sign of  $\sigma$  and  $\sigma'$  depends on the region S, O and R (**S**hadow, **O**pen, **R**election) about the breakwater tip that is being considered, as shown in figure 2.1. The sign of  $\sigma$  and  $\sigma'$  defines the relative phase of the diffracted wave and the presence or absence of the incident and reflected plane wave for that region due to the relationship  $f(\sigma) = 1 - f(-\sigma)$ .

In (2.5),  $C(\sigma)$  and  $S(\sigma)$  are the Fresnel integrals which are transcendental functions classically used in for the description of far-field diffraction phenomena. One might consider using the (McCormick & Kraemer, 2002) polynomial approximations for the Fresnel integrals, given by in (2.8) and (2.9). These provide excellent accuracy and reduce the computational effort considerably, which is important when numerous calculations are required to statistically represent directional and spectral wave conditions. All results presented in this chapter were calculated using these polynomial approximations;

$$C(\sigma) = -C(-\sigma) \approx \frac{1}{2} + \frac{(1+0.926\sigma) \sin\left(\frac{\pi\sigma^2}{2}\right)}{2+1.792\sigma+3.103\sigma^2} - \frac{\cos\left(\frac{\pi\sigma^2}{2}\right)}{2+4.142\sigma+3.492\sigma^2+6.670\sigma^3} + \epsilon(\sigma) \quad (2.8)$$

$$S(\sigma) = -S(-\sigma) \approx \frac{1}{2} - \frac{(1+0.926\sigma) \cos\left(\frac{\pi\sigma^2}{2}\right)}{2+1.792\sigma+3.103\sigma^2} - \frac{\sin\left(\frac{\pi\sigma^2}{2}\right)}{2+4.142\sigma+3.492\sigma^2+6.670\sigma^3} + \epsilon(\sigma) \quad (2.9)$$

with the error for both equations being  $\epsilon(\sigma) \leq 0.002$

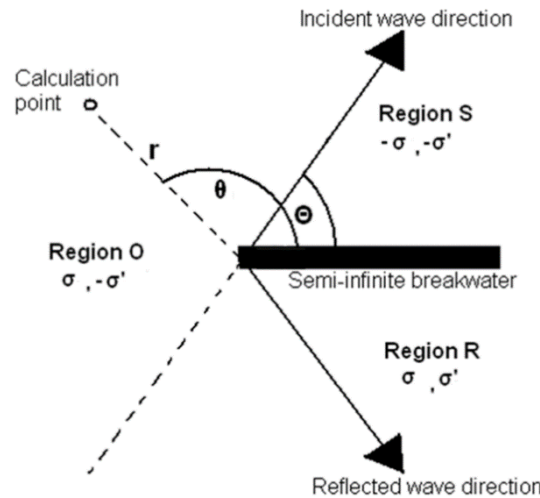


**Figure 2.1** Definition of coordinate system, incident wave direction and calculation regions for a semi-infinite breakwater. S, O and R represent the **S**hadow, **O**pen, **R**election region. The sign of  $\sigma$  and  $\sigma'$  to be used for the different calculations regions is shown.

The solution for the diffracted wave field about a semi-infinite breakwater given in (2.2) is composed of four distinct components: the incident plane parallel wave which is present in regions O and R (and S if partial transmission is considered as will be discussed later), the reflected plane parallel wave which is present in region R, and the diffracted wave of the incident wave and diffracted wave of the reflected wave, which are both present in all regions.

The diffracted wave of the incident and reflected wave can be isolated by subtracting the incident wave component  $I$  and reflected wave component  $R$ , (if present in that region) from (2.2);

$$\begin{array}{l} \text{region } S \\ \text{region } O \\ \text{region } R \end{array} \left\{ \begin{array}{ll} F(r, \theta) = f(-\sigma)I + f(-\sigma')R & \text{when } \theta < \Theta \\ F(r, \theta) = f(\sigma)I + f(-\sigma')R - I & \text{when } \Theta < \theta < 2\pi - \Theta \\ F(r, \theta) = f(\sigma)I + f(\sigma')R - I - R & \text{when } 2\pi - \Theta < \theta \end{array} \right. \quad (2.10)$$

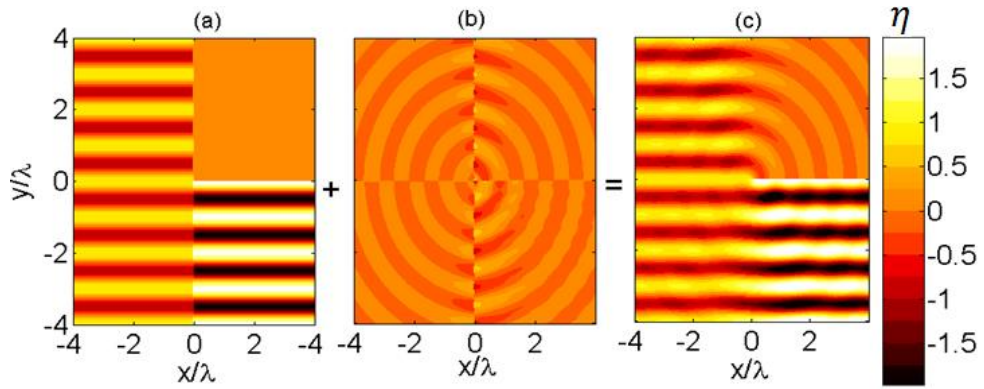


**Figure 2.2** Shows the real part of the  $F(r, \theta)$  which gives the water surface elevation  $\eta$ , for: (a) the incident and reflected planar wave components, (b) the diffracted wave of the incident wave and the diffracted wave of the reflected wave, and (c) the complete solution which is the sum of (a) and (b) as described by (2.2).

Equation (2.2) satisfies the boundary conditions of zero fluid velocity and describes a fully reflecting breakwater. As shown in figure 2.2, the solution for diffraction at a semi-infinite breakwater can be separated into the components that describe the diffraction of the incident wave and the diffraction of the reflected wave. (Silvester & Lim, 1968) suggest that by treating the reflected and incident wave components independently an approximation of a breakwater that dissipates energy (resulting in partial reflection) can be made. This is by the application of a reflection coefficient to the components that describe the reflected wave and diffraction of the reflected wave, which is the second term in (2.2). With this method, the height of reflected wave and diffracted wave of the reflected wave are reduced proportionally to the desired degree of reflection at the breakwater. With the applied reflection coefficient  $c_p$ , the original solution becomes the ‘simple solution’. This method is also used in (Hotta, 1978), (Ou, et al., 1988) and (Kim & Lee, 2010), and the “simple solution” is given by;

$$F(r, \theta) = f(\sigma)I + c_p f(\sigma')R \quad (2.11)$$

with  $c_p = 1$  for total reflection, and  $c_p = 0$  for total absorption.

As (Daemrich & Kohlhase, 1978) show, the ‘simple solution’ provides only an approximate solution as the boundary conditions are no longer fulfilled exactly. (Daemrich & Kohlhase, 1978) found experimentally that the ‘simple solution’ for partial or zero reflection under-predicts the disturbance

coefficient close to the lee side of the breakwater. They conclude that although the incident wave is fully absorbed by the breakwater, a scattered wave system must still exist. This contributes to the resultant wave field in the domain. By taking the more mathematically exact solution of diffraction at the end of a guide wall (waves travelling parallel to a breakwater) and the (Mitsui & Murakami, 1967) exact solution of wave diffraction at a wedge, (Daemrich & Kohlhasse, 1978) produced a variable weighting factor (dependent on the incident angle and reflection coefficient) that when applied to the second term in (2.2) gives very good accuracy in the down-wave region of the breakwater when compared with experimental data. However, as seen in (Daemrich & Kohlhasse, 1978) the two solutions converge with increasing distance from the breakwater tip, or when  $\theta$  gets closer to  $\Theta$ . As such the ‘simple solution’ seems a suitable approximation except for the regions very close to the lee side of the breakwater.

### 2.2.2 Breakwater gap

It is shown in (Penny & Price, 1952) that an approximate solution for the diffracted wave field about a gap in an infinite breakwater can be achieved with two superpositions of the semi-infinite solution.

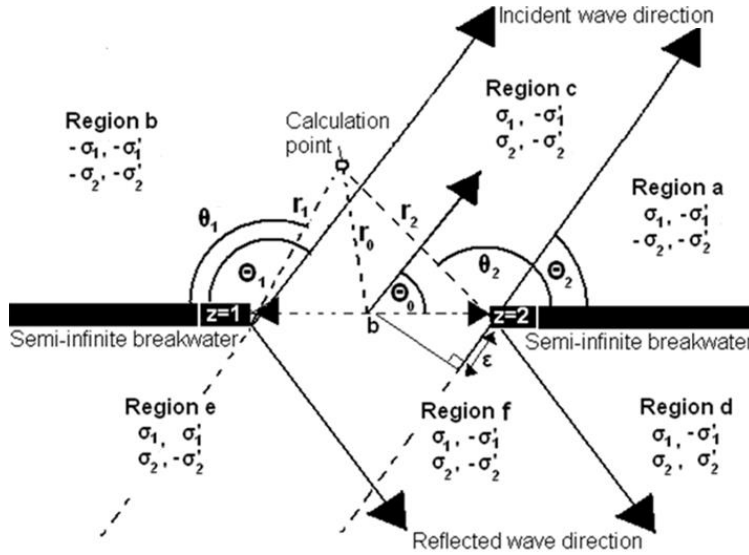


**Figure 2.3** Definition of coordinate system, incident wave direction  $\theta$ , tip phase shift  $\varepsilon_b$ , and regions, for a gap in an infinite breakwater. The subscript  $z$  is used as a reference number for the breakwater tip for which the:  $I, R, r, \theta, \sigma$  and  $\sigma'$  terms belong to.

With the partial reflection approximation (described in section 2.2.1) applied the solution describing the disturbed wave field about a gap of length  $b$  in an infinite breakwater with partial reflection, is given by;

$$\begin{aligned}
 F(r, \theta) = & \begin{aligned} & f(\sigma_1)I_1 + c_\rho f(-\sigma_1')R_1 + f(-\sigma_2)I_2 + c_\rho f(-\sigma_2')R_2 - I_0 & \text{region a} \\ & f(-\sigma_1)I_1 + c_\rho f(-\sigma_1')R_1 + f(\sigma_2)I_2 + c_\rho f(-\sigma_2')R_2 - I_0 & \text{region b} \\ & f(\sigma_1)I_1 + c_\rho f(-\sigma_1')R_1 + f(\sigma_2)I_2 + c_\rho f(-\sigma_2')R_2 - I_0 & \text{region c} \\ & f(\sigma_1)I_1 + c_\rho f(-\sigma_1')R_1 + f(\sigma_2)I_2 + c_\rho f(\sigma_2')R_2 - I_0 & \text{region d} \\ & f(\sigma_1)I_1 + c_\rho f(\sigma_1')R_1 + f(\sigma_2)I_2 + c_\rho f(-\sigma_2')R_2 - I_0 & \text{region e} \\ & f(\sigma_1)I_1 + c_\rho f(-\sigma_1')R_1 + f(\sigma_2)I_2 + c_\rho f(-\sigma_2')R_2 - I_0 & \text{region f} \end{aligned} \quad (2.12)
 \end{aligned}$$

Note that  $I_0 = \cos(kr_0 \cos(\theta_0 - \Theta_0)) - i \sin(kr_0 \cos(\theta_0 - \Theta_0))$  has been removed from the solution for all regions, otherwise the incident planar wave term would stack up. Also, the centre of the coordinate system is now at the centre of the gap between the breakwaters (as shown in figure 2.3)

In (2.6) the Fresnel integrals limits for the terms associated breakwater tip  $z$  are now given by;

$$\sigma_z = 2\sqrt{\left(\frac{kr_z}{\pi}\right)} \sin\frac{1}{2}(\theta_z - \Theta_z) \quad (2.13)$$

$$\sigma'_z = -2\sqrt{\left(\frac{kr_z}{\pi}\right)} \sin\frac{1}{2}(\theta_z + \Theta_z) \quad (2.14)$$

where  $r_z$  is the distance from the breakwater tip  $z$  to the calculation point in the domain and is given by  $r_1 = ((x + b/2)^2 + y^2)^{0.5}$ ,  $r_2 = ((x - b/2)^2 + y^2)^{0.5}$ ,  $\theta_z$  is the angle between the plane of the breakwater associated with  $z$  (from the lee side) to the line that connects the calculation point in the domain and the breakwater tip  $z$  and is given by;  $\theta_1 = \tan^{-1}(y/(-x - b/2))$  and  $\theta_2 = \tan^{-1}(y/(x - b/2))$  and  $\Theta_2$  is equal to the incident wave direction  $\Theta$  and  $\Theta_1 = \pi - \Theta$  (as described in figure 2.3).

In (Kim & Lee, 2010), the breakwater gap solution is extended to account for oblique waves by adding a phase shift term  $\varepsilon_b$  to the incident and reflected wave terms, thus accounting for the difference in phase of the incident wave at the opposing breakwater tips. The phase shift is considered relative to the centre of the breakwater gap due to the difference in path length, as shown in figure 2.3, and is given by;

$$\varepsilon_b = \pm k(b/2)\cos(\Theta_0) \quad (2.15)$$

where  $b$  is gap length and  $\varepsilon_b$  is the phase shift as shown in figure 2.3. The sign of  $\varepsilon_b$  is given in table 2.1.

**Table. 2.1** The sign of  $\varepsilon_b$  used with the terms associated with breakwater tip  $z$  for a breakwater gap.

Sign of $\varepsilon_b$	$\Theta_0 \leq 90$	$\Theta_0 > 90$
$z = 1$	-	+
$z = 2$	+	-

For oblique waves with the phase shift term applied, the incident and reflected wave terms associated with the breakwater tip  $z$  become;

$$I_z = \cos(kr_z\cos(\theta_z - \Theta_z) + \varepsilon_b) - i\sin(kr_z\cos(\theta_z - \Theta_z) + \varepsilon_b) \quad (2.16)$$

$$R_z = \cos(kr_z\cos(\theta_z + \Theta_z) + \varepsilon_b) - i\sin(kr_z\cos(\theta_z + \Theta_z) + \varepsilon_b) \quad (2.17)$$

The incident planar wave, which all other parts of the solution are considered to be relative to, is described by;

$$I_0 = \cos(kr_0\cos(\theta_0 - \Theta_0)) - i\sin(kr_0\cos(\theta_0 - \Theta_0)) \quad (2.18)$$

with the coordinate system centred at the middle of the breakwater gap requiring no phase shift.

This solution is an approximation because the boundary conditions are not completely fulfilled, because of the applied reflection coefficient (as discussed in section 2.2.1). An additional approximation is present when more than one semi-infinite break water solution is superposed. This is because the 2<sup>nd</sup> order effects of the diffracted wave from one breakwater interacting with the other breakwater are not considered.

### 2.2.3 Detached breakwater segment

In (Penny & Price, 1952), it is proposed that an approximate solution for the diffracted wave field about a detached breakwater segment can be constructed with two superpositions of the semi-infinite solution given by (2.2). This method is also used in (Hotta, 1978) and (Kim, et al., 2011).

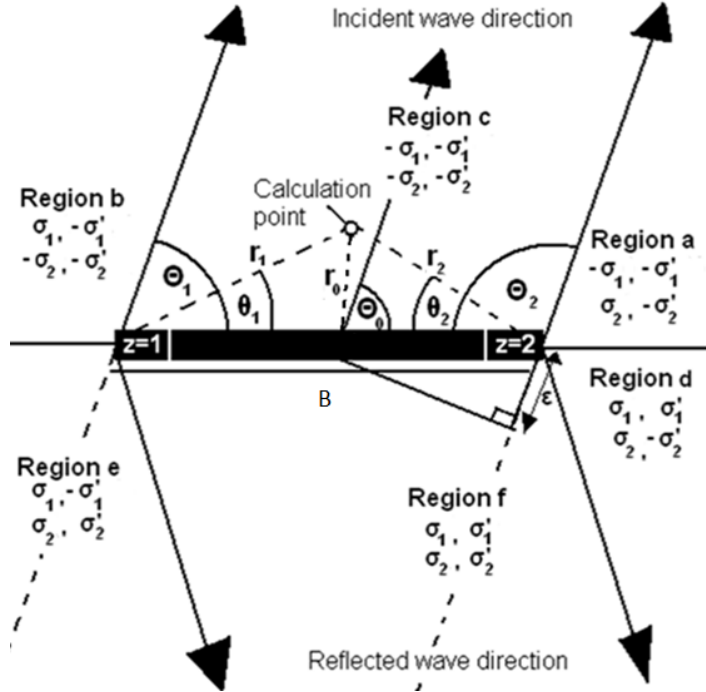


**Figure 2.4** Definition of coordinate system, incident wave direction, tip phase shift and regions for a detached breakwater segment. The subscript  $z$  is used as a reference number for the breakwater tip

The approximate complex function describing the wave field at a point  $r_0, \theta$  about a detached breakwater segment with partial transmission, where the centre of the coordinate system is now the geometrical centre of the breakwater segment, is given by;

$$\begin{aligned}
 F(r, \theta) = & \begin{aligned} & f(-\sigma_1)I_1 + c_\rho f(-\sigma_1')R_1 + f(\sigma_2)I_2 + c_\rho f(-\sigma_2')R_2 & \text{region a} \\ & f(\sigma_1)I_1 + c_\rho f(-\sigma_1')R_1 + f(-\sigma_2)I_2 + c_\rho f(-\sigma_2')R_2 & \text{region b} \\ & f(-\sigma_1)I_1 + c_\rho f(-\sigma_1')R_1 + f(-\sigma_2)I_2 + c_\rho f(-\sigma_2')R_2 & \text{region c} \\ & f(\sigma_1)I_1 + c_\rho f(\sigma_1')R_1 + f(\sigma_2)I_2 + c_\rho f(-\sigma_2')R_2 - I_0 - R_0 & \text{region d} \\ & f(\sigma_1)I_1 + c_\rho f(-\sigma_1')R_1 + f(\sigma_2)I_2 + c_\rho f(\sigma_2')R_2 - I_0 - R_0 & \text{region e} \\ & f(\sigma_1)I_1 + c_\rho f(\sigma_1')R_1 + f(\sigma_2)I_2 + c_\rho f(\sigma_2')R_2 - I_0 - R_0 & \text{region f} \end{aligned} \quad (2.19)
 \end{aligned}$$

where  $\sigma_z$  and  $\sigma_z'$  are given by (2.13) and (2.14) respectively, where  $r_z$  is the distance from the breakwater tip  $z$  to the calculation point in the domain given by  $r_1 = ((x + B/2)^2 + y^2)^{0.5}$  and  $r_2 = ((B/2 - x)^2 + y^2)^{0.5}$ .  $\theta_z$  is the angle between the plane of the breakwater (from the lee side) to the line that connects the calculation point in the domain and the break water tip  $z$  and is given by:  $\theta_1 = \tan^{-1}(y/(x + B/2))$  and  $\theta_2 = \tan^{-1}(y/(B/2 - x))$ .  $\Theta_1$  is equal to the incident wave direction  $\Theta_0$  and  $\Theta_2 = \pi - \Theta_0$ , as described in figure 2.4.

When incident waves are oblique a phase shift term  $\varepsilon_B$  (as shown in figure 2.4) is applied to account for the relative phase shift of the incident at the opposing tips of the breakwater. The phase shift is considered relative to the centre of the breakwater segment  $r_0 = 0$ , and is given by;

$$\varepsilon_B = \pm k(B/2)\cos(\theta_0) \quad (2.20)$$

where  $B$  is breakwater segment length and the sign of  $\varepsilon_B$  is given in table 2.2.

**Table. 2.2** The sign of  $\varepsilon_B$  for a region relative to breakwater tip  $z$  for a detached breakwater.

Sign of $\varepsilon_B$	$\theta_0 \leq 90$	$\theta_0 > 90$
$z = 1$	-	+
$z = 2$	+	-

For oblique waves with the phase shift term applied the incident and reflected waves associated with the breakwater tip  $z$  become;

$$I_z = \cos(kr_z \cos(\theta_z - \theta_0) + \varepsilon_B) - i \sin(kr_z \cos(\theta_z - \theta_0) + \varepsilon_B) \quad (2.21)$$

$$R_z = \cos(kr_z \cos(\theta_z + \theta_0) + \varepsilon_B) - i \sin(kr_z \cos(\theta_z + \theta_0) + \varepsilon_B) \quad (2.22)$$

The incident planar wave  $I_0$  (2.3) which all other parts of the solution are considered to be relative to, now has its coordinate system centred at the middle of the breakwater segment.

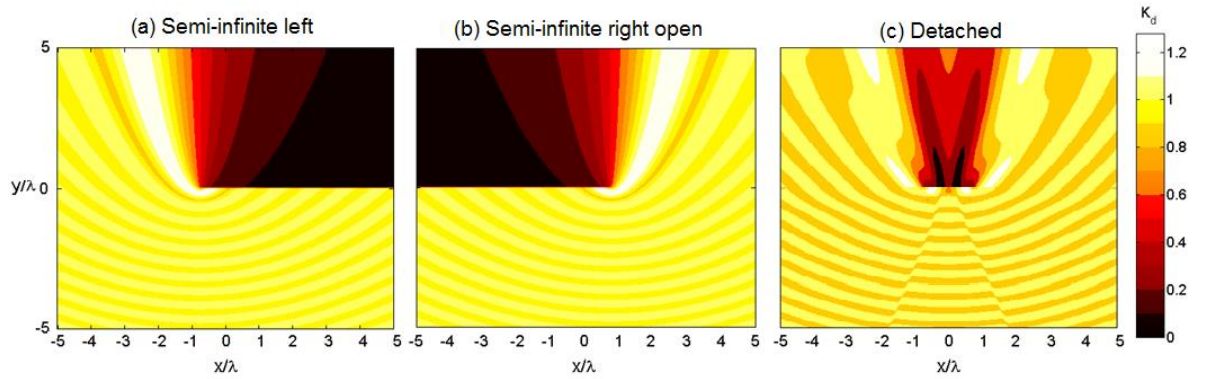


**Figure 2.5** Superposition steps to create an approximate analytical solution for a disturbed field about an ideal zero reflection zero transmission overtopping type wave energy converter, approximated as a detached breakwater segment under unidirectional monochromatic waves conditions. (a) semi-infinite solution with opening at the top of the domain, (b) semi-infinite solution with opening at the bottom of the domain, (c) is the sum of (a) and (b) minus the incident planar wave, which gives the approximate single WEC solution.

The solution for the detached partially reflecting breakwater is an approximation. This is because of the non-exact boundary conditions associated with the reflection coefficient using the ‘simple solution’ (as discussed in section 2.2.1). Another approximation exists, in that the complete system is the superposition of two systems considered in isolation. As such, the diffracted waves emanating from one breakwater tip will not register that the breakwater section is no longer present past the opposing tip, and will not perform a secondary diffraction. This results in a small discontinuity along the plane of the breakwater (a step of approximately 2% of the incident wave height for the case of zero reflection) at the open regions. This is because the diffracted wave of the incident wave and the diffracted wave of the reflected wave do not undergo a secondary diffraction at the opposing breakwater tip. This would cause a secondary redistribution and an overlap that would smooth the wave field in this region, resulting in a small error in the region close to the breakwater. Neglecting these secondary diffracted waves should have little effect

in the regions away from the immediate vicinity of the breakwater because these waves will be very small initially. Because of their radial nature, they will then have a rapidly decreasing influence with increasing distance from the breakwater array. This assumption will be supported later.

(Hotta, 1978) proposes an approximate solution for a detached breakwater segment with partial transmission. This is achieved by superposing an additional breakwater system onto the solution of a partially reflecting breakwater segment as given in (2.19). In (Hotta, 1978), the solution for the gap in the infinite breakwater given in (2.12), with a reflection coefficient  $c_\rho = 0$ , is modified by applying a transmission coefficient  $c_t$  (0 for no transmission and 1 for full transmission) to all terms related to the incident wave, and diffracted waves of the incident wave. The incident planar wave is also removed from the up wave region. In effect this gives a solution for a forward traveling wave generated in a breakwater gap. When this is superposed with the solution of a detached breakwater segment with length equal to the gap, the resulting product of the components represents the wave that has transmitted through the detached breakwater segment. The wave that transmits through the breakwater segment has an initial height of  $c_t H_0$ , and a wave front length equal to the length of the breakwater segment. Taking (2.12) with reflection coefficient  $c_\rho = 0$ , removing  $I_0$  from the up-wave region and applying  $c_t$  to all terms, yields;

$$F(r, \theta) = \begin{array}{l} c_t(f(\sigma_1)I_1 + f(-\sigma_2)I_2 - I_0) \text{ region a} \\ c_t(f(-\sigma_1)I_1 + f(\sigma_2)I_2 - I_0) \text{ region b} \\ c_t(f(\sigma_1)I_1 + f(\sigma_2)I_2 - I_0) \text{ region c} \\ c_t(f(\sigma_1)I_1 + f(\sigma_2)I_2 - 2I_0) \text{ region d} \\ c_t(f(\sigma_1)I_1 + f(\sigma_2)I_2 - 2I_0) \text{ region e} \\ c_t(f(\sigma_1)I_1 + f(\sigma_2)I_2 - 2I_0) \text{ region f} \end{array} \quad (2.23)$$

By superposing the solution of the wave transmitted through the structure given in (2.23) with the solution for the partially reflecting breakwater segment given in (2.19) the approximate solution for the wave field about a detached breakwater segment with partial reflection and transmission, is generated.

This is given by;

$$F(r, \theta) = \begin{array}{l} f(-\sigma_1)I_1 + c_\rho f(-\sigma_1')R_1 + f(\sigma_2)I_2 + c_\rho f(-\sigma_2')R_2 + c_t(f(\sigma_1)I_1 + f(-\sigma_2)I_2 - I_0) \text{ region a} \\ f(\sigma_1)I_1 + c_\rho f(-\sigma_1')R_1 + f(-\sigma_2)I_2 + c_\rho f(-\sigma_2')R_2 + c_t(f(-\sigma_1)I_1 + f(\sigma_2)I_2 - I_0) \text{ region b} \\ f(-\sigma_1)I_1 + c_\rho f(-\sigma_1')R_1 + f(-\sigma_2)I_2 + c_\rho f(-\sigma_2')R_2 + c_t(f(\sigma_1)I_1 + f(\sigma_2)I_2 - I_0) \text{ region c} \\ f(\sigma_1)I_1 + c_\rho f(\sigma_1')R_1 + f(\sigma_2)I_2 + c_\rho f(-\sigma_2')R_2 + c_t(f(\sigma_1)I_1 + f(\sigma_2)I_2 - 2I_0) - I_0 - R_0 \text{ region d} \\ f(\sigma_1)I_1 + c_\rho f(-\sigma_1')R_1 + f(\sigma_2)I_2 + c_\rho f(\sigma_2')R_2 + c_t(f(\sigma_1)I_1 + f(\sigma_2)I_2 - 2I_0) - I_0 - R_0 \text{ region e} \\ f(\sigma_1)I_1 + c_\rho f(\sigma_1')R_1 + f(\sigma_2)I_2 + c_\rho f(\sigma_2')R_2 + c_t(f(\sigma_1)I_1 + f(\sigma_2)I_2 - 2I_0) - I_0 - R_0 \text{ region f} \end{array} \quad (2.24)$$

where the regions and breakwater tip reference  $z$  are the same as in figure 2.4.

(Ou, et al., 1988) obtain wave basin experimental data for the diffracted and refracted wave field about a partially transmitting detached breakwater segment with a mildly varying bed gradient. For the test cases considered, agreement was found between the approximate solution of (Hotta, 1978) and experimental data; however, it should be noted that only a single transmission coefficient of  $c_t = 0.3$  was considered and that the approximate solution being tested has the extension for refraction. As such, further validation would be beneficial when additional data becomes available. In all but one case, this chapter considers WEC devices as perfect energy converters i.e. zero reflection and zero transmission, to assess the worst

case scenario of wave energy shadowing from an overtopping type WEC array. As such the method of partial transmission described above and the associated approximations are only relevant to the one result.

#### 2.2.4 Series of detached partially transmitting and reflecting breakwater segments

Finally, an approximate solution for the diffracted wave field about a segmented breakwater series is constructed using multiple superpositions of the detached breakwater solution given in (2.19).

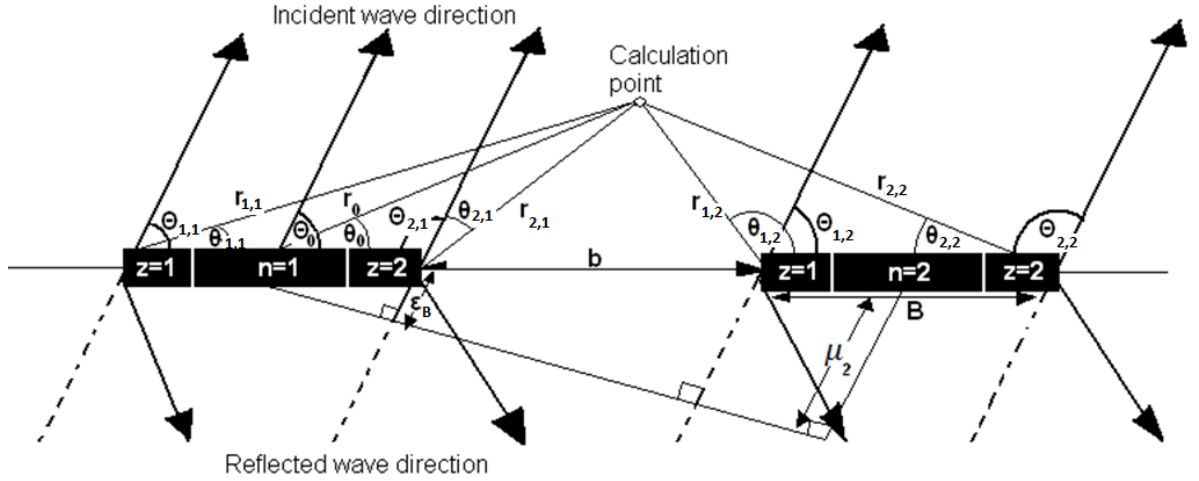


**Figure 2.6** Definition of coordinate system, incident wave direction, tip phase shift  $\varepsilon_B$  and breakwater phase shift  $\mu_n$ , for a series of detached breakwater segments. The subscript  $z$  is used as a reference number for the breakwater tip,  $n$  denotes the breakwater segment number.

By removing the incident wave described by (2.3) across the whole domain for the breakwater segment solution given in (2.24) the ‘temporary solution’ is obtained, which is shown in figure 2.7(a), and is defined by;

$$\tau(r, \theta) = F(r, \theta) - I_0 \quad (2.25)$$

The ‘temporary solution’ can now be superposed multiple times without the incident planar wave term stacking up. This is shown in figure 2.7(b) and the solution for this is given by;

$$\tau_{tot}(r, \theta) = \sum_{n=1}^n \tau(r, \theta)_n \quad (2.26)$$

where  $n$  is the number of breakwater segments and;

$$I_{z,n} = \cos(kr_{z,n} \cos(\theta_{z,n} - \Theta_{z,n}) + \varepsilon_B + \mu_n) - i \sin(kr_{z,n} \cos(\theta_{z,n} - \Theta_{z,n}) + \varepsilon_B + \mu_n) \quad (2.27)$$

$$R_{z,n} = \cos(kr_{z,n} \cos(\theta_{z,n} + \Theta_{z,n}) + \varepsilon_B + \mu_n) - i \sin(kr_{z,n} \cos(\theta_{z,n} + \Theta_{z,n}) + \varepsilon_B + \mu_n) \quad (2.28)$$

where the centre of the first breakwater of the series is also the centre of the coordinate system,  $r_{z,n}$  is the distance from the breakwater tip  $z$  on the breakwater segment  $n$  to the calculation point in the domain and is given by;  $r_{1,n} = ((x + B/2 - (n - 1)(B + b))^2 + y^2)^{0.5}$  and  $r_{2,n} = (((n - 1)(B + b) - x - B/2)^2 + y^2)^{0.5}$ .  $\theta_z$  is the angle between the plane of the breakwater  $n$  (from the lee side) to the line that connects the calculation point in the domain and the breakwater tip  $z$ , and is given by  $\theta_{1,n} = \tan^{-1}(y/(x + B/2 - (n - 1)(B + b)))$  and,  $\theta_{2,n} = \tan^{-1}(y/((n - 1)(B + b) - x - B/2))$ .  $\Theta_{1,n}$  is equal to the incident wave direction  $\Theta_0$  and  $\Theta_{2,n} = \pi - \Theta_0$ , as described in figure 2.6.

In (2.27) and (2.28)  $\varepsilon_B$  is the again the phase shift term for the tip  $z$  relative to the centre of the breakwater segment  $n$ . It is given by (2.20) and the sign of  $\varepsilon_B$  is given in table 2.3.

**Table. 2.3** The sign of  $\varepsilon_B$  for the region relative to breakwater tip  $z$  for a series of breakwaters.

Sign of $\varepsilon_B$	$\theta_0 \leq 90$	$\theta_0 > 90$
$z = 1$	-	+
$z = 2$	+	-

Also in (2.27) and (2.28), the term  $\mu_n$  is applied in the same fashion as the term  $\varepsilon_B$ . This accounts for the phase shift of the incident and reflected waves at the other breakwater segments of the series, relative to the first breakwater in the series, as shown in figure 2.6. This is done so that the phase of the incident wave arriving at each breakwater tip is considered relative to the phase of the incident wave at the centre of the first breakwater segment of the series;

$$\mu_n = \pm k(n-1)(b+B)\cos(\theta_0) \quad (2.29)$$

where the sign of  $\mu_n$  is positive when  $\theta \leq 90$  and negative when  $\theta > 90$ . This assumes a series of breakwaters segments with uniform separation distances between each segment and uniform lengths for each breakwater segment.

By re-applying the incident wave given in (2.3) to the solution for the multiple superpositions of the temporary solution given in (2.26), the approximate solution for the total wave field about a series of breakwater segments is formed, which is given by;

$$F(r, \theta)_{tot} = I_0 + \sum_{n=1}^N \tau(r, \theta)_n \quad (2.30)$$

where  $N$  is the total number of breakwater segments.

Finally the disturbance coefficient for an incident monochromatic wave of period  $T$ , in water depth  $h$ , and incident angle relative to the plane of the array  $\theta_0$ , can be obtained by taking the modulus of the complex function  $F$ . The final result is as shown in figure 2.7(c)

The solution for a segmented breakwater series appears to be complicated with multiple values for  $r_z$  and  $\theta_z$  and many different 'regions' to define (with increasing complexity for additional segments).

Practically, the solution is not complicated to implement and the end result can be achieved in the following steps;

- 1.) Calculate the domain about a single breakwater segment with (2.24)
- 2.) Remove the incident wave field  $I_0$ , in (2.3), uniformly across the domain calculated in step 1. This creates the 'temporary solution' given by (2.25)
- 3.) Repeat steps 1 and 2 for each segment of the series accounting for the phase shift of the incident wave, arriving at each segment due to its location relative to the first segment of the series.
- 4.) Superpose the 'temporary solution' for each breakwater segments into domain location that corresponds with the relative phase shift that is applied.

- 5.) Re-apply the incident wave field  $I_0$  in (2.3), relative to the first breakwater segment of the series uniformly across the domain calculated in step 4, to get the final output.

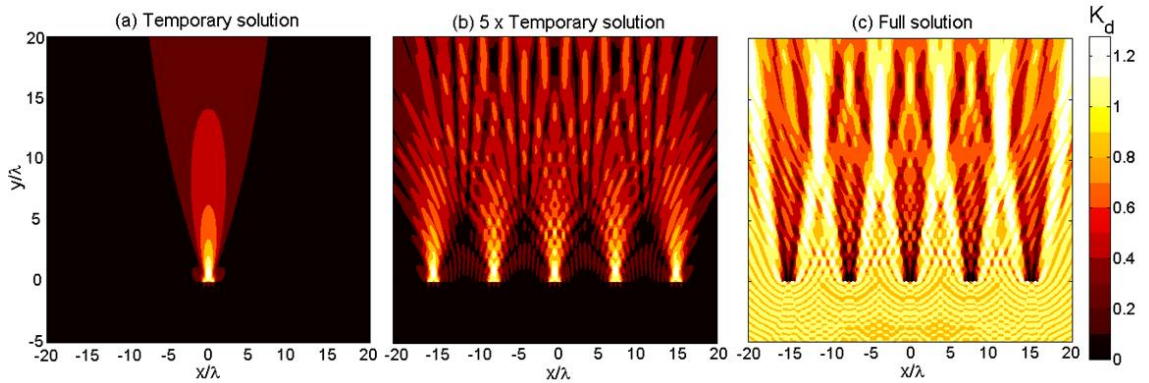


**Figure 2.7** Superposition steps to get the approximate solution for the field about an array of overtopping type WEC converters approximated as breakwater segments under unidirectional monochromatic wave conditions. (a) gives the temporary solution for single WEC; (b) gives multiple superpositions of the temporary solution shown in (a) which account for the diffracted wave components (with relative phase shift) about each WEC in the array; (c) gives the solution shown in (b) with the incident wave field re-applied to give the complete approximate solution for the disturbed wave field about the array.

The solution for a segmented series of partially transmitting, partially reflecting breakwaters is used to approximate an overtopping WEC array and will be termed the Approximate Analytical Solution (AAS).

### 2.2.5 Unidirectional spectral waves

At this stage the incident wave field is both unidirectional and monochromatic. The wavelength is discrete, creating a strong periodic interference pattern, with maxima formed when the difference in path length between two breakwater tips and a point in the domain is an integer number of wave lengths. Similarly, minima are formed when the difference in path length is a half integer number of wave lengths. A realistic wave climate is not monochromatic and the JONSWAP period spectrum  $S(T)$  is one method of statistically describing a spectral wave climate (as described in 1.5.2.1). Working in terms of wave period the JONSWAP spectrum is given by;

$$S(T) = \frac{\alpha g^2 T^5}{(2\pi)^4} \exp\left[-\frac{5}{4}\left(\frac{T_p}{T}\right)^{-4}\right] \gamma^q \quad (2.31)$$

where  $T$  is the period,  $T_p$  is the peak period of the spectrum,  $\alpha$  is the Phillip's constant ( $\alpha = 0.0081$ ),  $\gamma$  is the peak enhancement factor and  $q = \exp[-((1/T) - (1/T_p))^2 T_p^2 / 2\sigma^2]$ , with  $\sigma = 0.07$  when  $T \geq T_p$  and  $\sigma = 0.09$  when  $T < T_p$ .

The period spectrum function  $S(T)$  can be scaled to a probability density function  $P(T)$ , by;

$$P(T) = S(T) / \int_0^\infty S(T) dT \quad (2.32)$$

where  $\frac{1}{\int_0^\infty S(T) dT}$  is the normalising coefficient, and  $\int_0^\infty P(T) dT = 1$

The JONSWAP spectrum can be used to find the statistical mean diffracted wave field about the array under spectral wave conditions in the following manner. The diffracted wave energy field for each integer

period component  $T$  ( $s$ ) of the period spectrum is multiplied by the respective  $P(T)$  value for that period. This gives the scaled diffracted wave energy field for that particular value of  $T$  ( $s$ ). As  $\int_0^{+\infty} P(T)dT = 1$ . Each scaled diffracted wave energy field for each period component of the spectrum can be linearly superposed to form the mean diffracted wave field for the full JONSWAP period spectrum. A spectral resolution of one second was chosen to save computational time and a sensitivity analysis showed that only a very small amount of additional smoothing resulted from a higher frequency resolutions and that there is no appreciable effect on the trend of energy redistribution.

### 2.2.6 Directional spectral waves

The mean disturbed wave field for directional spectral waves is achieved by convolving the directional spread distribution with the frequency distribution given by (2.31). The statistical distribution of wave directions for a random wave climate is reviewed in section 1.5.2.2. For an easier comparison to the work presented in (Millar, et al., 2007) and (Black, 2007), wave directional spreading as described in the SWAN wave model was used for the main analysis. This is described by;

$$G(\theta) = \cos^m(\theta - \theta_0) \quad (2.33)$$

where  $\theta_0$  is the mean wave direction and  $m$  is the spreading parameter, whilst in section 2.3 the spreading parameter  $s$  as described by (1.59) is used to match experimental parameters used in (Yu, et al., 2000).

The spread function  $G(\theta)$  can be scaled to a probability density function, by;

$$D(\theta) = G(\theta) / \int_{-\pi}^{\pi} G(\theta)d\theta \quad (2.34)$$

where;  $1 / \int_{-\pi}^{\pi} G(\theta)d\theta$  is the normalising coefficient

As  $\int_{-\pi}^{\pi} D(\theta)d\theta = 1$ , each scaled diffracted wave energy field for each incident wave angle can be linearly superposed to give the mean diffracted wave field for the full directional spread. A directional spread resolution of one degree was chosen because a sensitivity analysis showed that no appreciable difference occurs from higher resolutions.

## 2.3 Comparison of approximate analytical solution to experimental data

Good agreement was found between wave basin experimental data in (Putnam & Arthur, 1948) and the (Penny & Price, 1952) solution for oblique wave diffraction about a semi-infinite breakwater. In addition, (Ou, et al., 1988) compare the approximate solution for the detached partially transmitting breakwater segment with experimental wave basin data and found good agreement. This leaves the breakwater gap component of the AAS, which can be validated with a comparison against the experimental wave tank data presented in (Yu, et al., 2000), for the diffracted wave field about a gap in an infinite breakwater for directional spectral waves as . This tests the method of superposing independent diffracted wave fields to form the total diffracted wave field between two neighbouring devices. It also tests the summation method for statistically representing directional and spectral wave states. The

experimental layout and tank measurement transects, which the experimental and analytical values of  $K_d$  are compared along, is shown in figure 2.8. The AAS for the breakwater gap given by (2.12), with the extensions for spectral and directional waves as given in sections 2.2.5 and 2.2.6, was calculated with full reflection ( $c_r = 1$ ) and zero transmission ( $c_t = 0$ ). This was with a period spectrum and directional spread to match the experimental parameters as described in table 2.4.

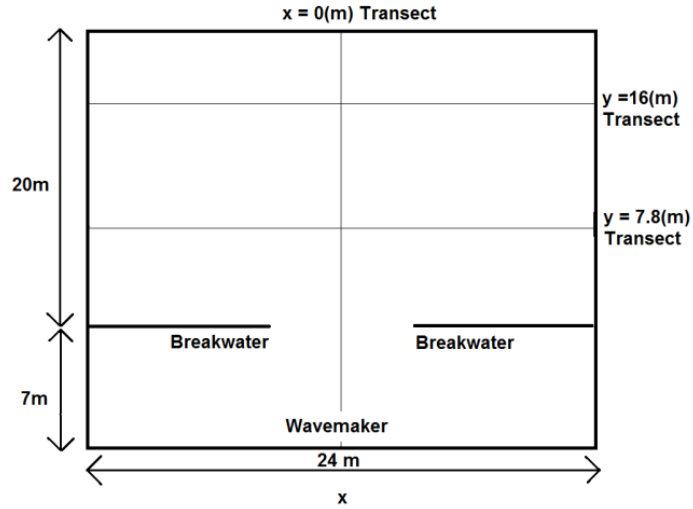


**Figure 2.8** Layout of wave basin for the breakwater gap experiments (Yu, et al., 2000). Transects of wave height measurements used for comparison at  $x = 0$ ,  $y = 7.8$  &  $y = 16$ . The still water depth was 0.4m throughout the basin.

**Table. 2.4** Wave parameters for tests in (Yu, et al., 2000) experiments on wave diffraction through a breakwater gap.  $H_s$  is significant wave height,  $T_p$  is peak period,  $s$  is directional spreading parameter describe by (1.59),  $\lambda_p$  is peak wavelength, and  $b$  is gap width, the significant wave height was 0.05 (m), mean direction was  $\theta_0 = 90$ , which is the angle relative to the plane of the breakwater gap (x-axis plane). The JONSWAP peak enhancement parameter was 4 for all cases.

Reference	$T_p(s)$	$S$	$\lambda_p(m)$	$b(m)$
a-s6	1.2	6	1.96	3.9
a-s19	1.2	19	1.96	3.9
b-s6	0.92	6	1.31	3.9
b-s19	0.92	19	1.31	3.9
c-s6	1.2	6	1.96	7.8
c-s19	1.2	19	1.96	7.8
d-s6	0.92	6	1.31	7.8
d-s19	0.92	19	1.31	7.8

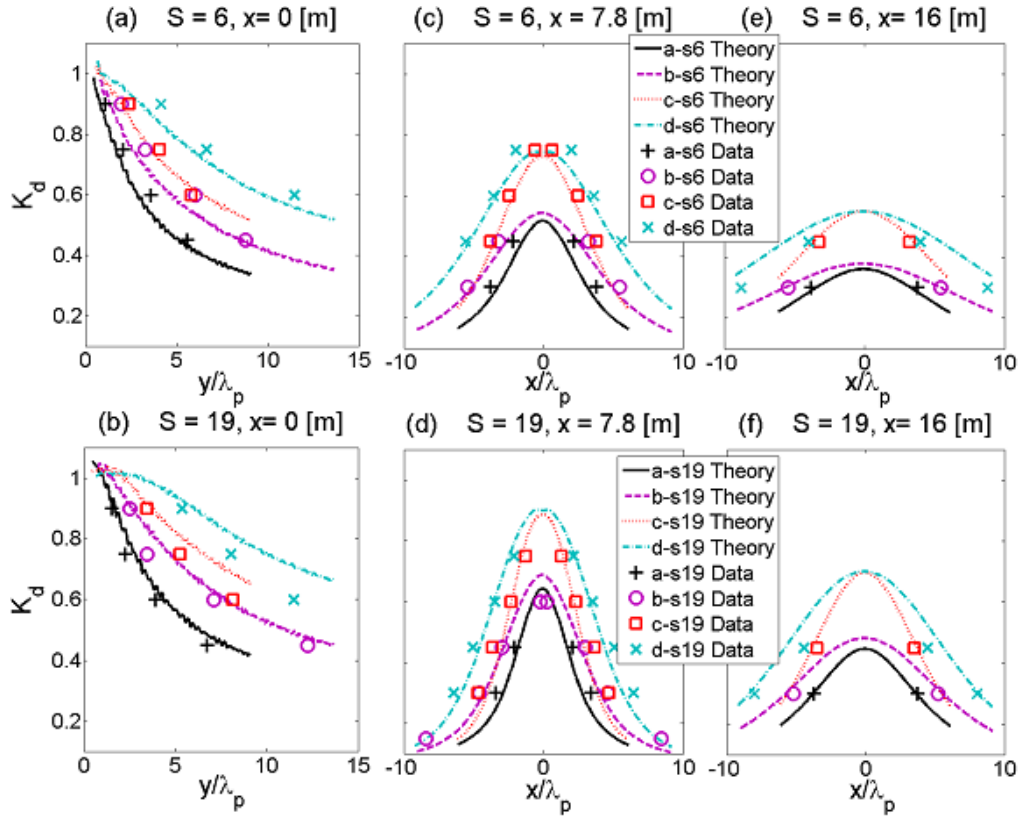


**Figure 2.9** Comparison of the experimental data (markers) and AAS (line) for incident waves with a mean direction of  $90^\circ$  to the breakwater plane. The incident wave parameters for each case are given in table 2.1. Individual analytical / experimental runs are grouped by the directional spread parameter  $s$ . (a-b) gives  $K_d$  along the transect  $x = 0$ , (c-d) transect  $y = 7.8(m)$  and (e-f) transect  $y = 16(m)$ .

The standard deviation of the difference between the measured and predicted  $K_d$  (at all wave gauge measured locations for the central, 7.8 (m), and 16 (m), transects combined) was;  $\sigma = 0.025$  when  $\theta_0 = 90^\circ$ . The same validation series was done for waves with mean incident angle  $\theta_0 = 45$  which gave a higher standard deviation of  $\sigma = 0.097$ . There is a moderate deviation between the measured and predicted diffraction coefficient at a small number of measurement locations but overall the AAS describes the diffracted wave field to a reasonable level of confidence.

## 2.4 Comparison of approximate analytical solution with integral equation solution

(McIver, 2005) gives a solution for the disturbed wave field about a series of thin permeable breakwater segments composed of discrete boundary elements, based on linear wave theory. The boundary conditions of the permeable breakwater are described by the time-harmonic motion in a porous medium (Sollitt & Cross, 1972). The problem is solved with an integral equation and an application of the Green's theorem. See appendix A for a summary of the solution or (McIver, 2005) for a fuller description. The integral solution is only used in this study to mitigate some of the approximations associated with the AAS and has not been modified.

For a partially transmitting breakwater (no dissipation)  $c_r + c_t = 1$ , and for a dissipating breakwater  $c_r + c_t < 1$ . This assumes no phase change of the wave passing through the breakwater (or below the WEC device for the intended use of the solution). For a permeable breakwater made from a porous medium the complex reflection and transmission coefficients described in (Yu & Togashi, 1996) which is reiterated in (Bowen & McIver, 2002) (for consistency with the other sections), can be adopted. These are given by;

$$c_\rho = \frac{-iks\sin\theta_0}{2\beta - iks\sin\theta_0} \quad (2.35)$$

$$c_t = \frac{2\beta}{2\beta - iks\sin\theta_0} \quad (2.36)$$

where  $\theta_0$  is the incident wave direction and

$$\beta = \frac{-i\epsilon_p}{b_y(f - is_i)} \quad (2.37)$$

where  $\epsilon_p$  is the porosity,  $f$  is a non-dimensional friction coefficient,  $s_i$  is the non-dimensional inertia coefficient and  $b_y$  is the physical thickness of the breakwater (although this is considered to be zero in the calculation domain).

Permeability of the breakwater is accounted for in (McIver, 2005) by a jump in potential across the breakwater segment. This is described by the complex parameter  $\beta$  given in (2.37) which incorporates the physical properties of the porous medium being modelled. The  $\beta$  term is used to specify the reflection, transmission and dissipation characteristics of the permeable breakwater going from full reflection to near full transmission. Only partial dissipation can be achieved through the friction and inertia terms. As discussed in (Yu & Togashi, 1996) the reflected and transmitted wave incurs a phase change, due to the representation of the inertia effects of the flow in a porous medium. The transmission of waves below an overtopping type WEC is not expected to incur the same phase change as it is not a porous medium.

The integral solution is more mathematically exact, is based on the actual boundary conditions of the breakwater series and considers the influence of multi breakwater system collectively as a whole. It is however comparatively more computationally expensive than the AAS used here and is not practical for assessing large domains with high resolution random wave sea states. The computational effort for a full large domain for a regular wave at a given discrete wave height, period and direction combination is reasonable. Also, the computational effort to find the wave field across a single transect of the domain for an irregular wave, is also acceptable. However, the computational effort to consider a large high resolution domain, with a high resolution directional and spectral wave distribution, is too excessive for general practicality. Another limitation is that the integral solution that is presented in (McIver, 2005) cannot consider high energy dissipation which is the intended approximation of wave energy conversion. The AAS on the other hand, is computationally efficient making it suitable for assessing large domains for high resolution directional and spectral wave distributions. The focus of this investigation is to assess the influence of diffraction on the evolution of the wave energy shadow, from a WEC array up to the far-field. Therefore, it is necessary to use the AAS (to assess the whole domain), but it is also important to validate the associated approximations with a comparison to the integral equation solutions output along some relevant domain transects. The approximations associated with the AAS that can be mitigated with the integral equation solution are: the omission of secondary diffraction effects between opposing breakwater tips and other breakwater segments in the series and the approximations associated with the (Hotta, 1978) application of reflection and transmission coefficients to the (Penny & Price, 1952) solution (that are not strictly based on the breakwater boundary conditions); however, the dissipation condition when  $c_\rho + c_t \neq 1$  cannot be validated by the integral solution in its published form. It can only be

assumed that the accuracy will be comparable to the validation of partial transmission when  $c_p + c_t = 1$ . This is a point of caution and should receive further attention.

A comparison of the disturbance coefficient predicted by the *AAS* and the integral equation solution in the lee of 5 overtopping type wave energy converters along the domain transects  $y = 5\lambda$ ,  $y = 50\lambda$ ,  $y = 150\lambda$ , and  $x = 0\lambda$ , is given in figure 2.10. The WEC array is located along the plane  $y = 0\lambda$ , and the middle of the central device is at  $x = 0\lambda$ . The length of each device is  $B = 250$  (m) with a tip to tip separation distance between neighbouring devices of  $b = 600$  (m). The wave period is discrete at  $T = 8$  (s), water depth is uniform at  $h = 50$  (m), the wavelength is  $\lambda = 100$  (m) (from the dispersion relationship) and this is used to normalise the dimensions of the calculation domain. Wave height is also discrete and assumed small enough for linear theory to be applicable. The incident wave directions considered are  $\theta = 50, 70$  and  $90^\circ$  and the permeability parameter used with the integral solution is  $\beta = 0$  (full reflection zero transmission) and  $\beta = k(1 - i)/4$  (partial reflection, transmission and dissipation). This translates to  $c_p = 1$ ,  $c_t = 0$ , and  $c_p = 0.6 + 0.2i$ ,  $c_t = 0.4 - 0.2i$ , respectively for the *AAS*. The computational domain is 25 (km) down-wave and 10 (km) wide which equates to  $250\lambda$  long and  $100\lambda$  wide, when normalised by the wavelength.

As seen in figure 2.10, in the moderate to far-field ( $y > 50\lambda$ ) (which is the primary area of interest for this study), the *AAS* is in excellent agreement with the integral equation solution of (McIver, 2005). At a distance closer to the breakwater array the two solutions diverge. This is significant in some regions, primarily the regions outside the geometrical shadow of the array. The divergence between the two methods enhances when the incident angle is more oblique or when the permeability increases. As such the *AAS* appears to be sufficiently accurate at predicting the disturbed wave field, in all but the region relatively close to the plane of array. The *AAS* is suitable for scaling the far-field wave energy shadow and re-distribution, but the integral solution would be required for the near-field where higher accuracy is required for spatial array optimisation studies. This result is particularly useful because the *AAS* is sufficiently computationally efficient to assess a large domain with high resolution irregular waves, and is shown to be valid for the far-field region of interest.

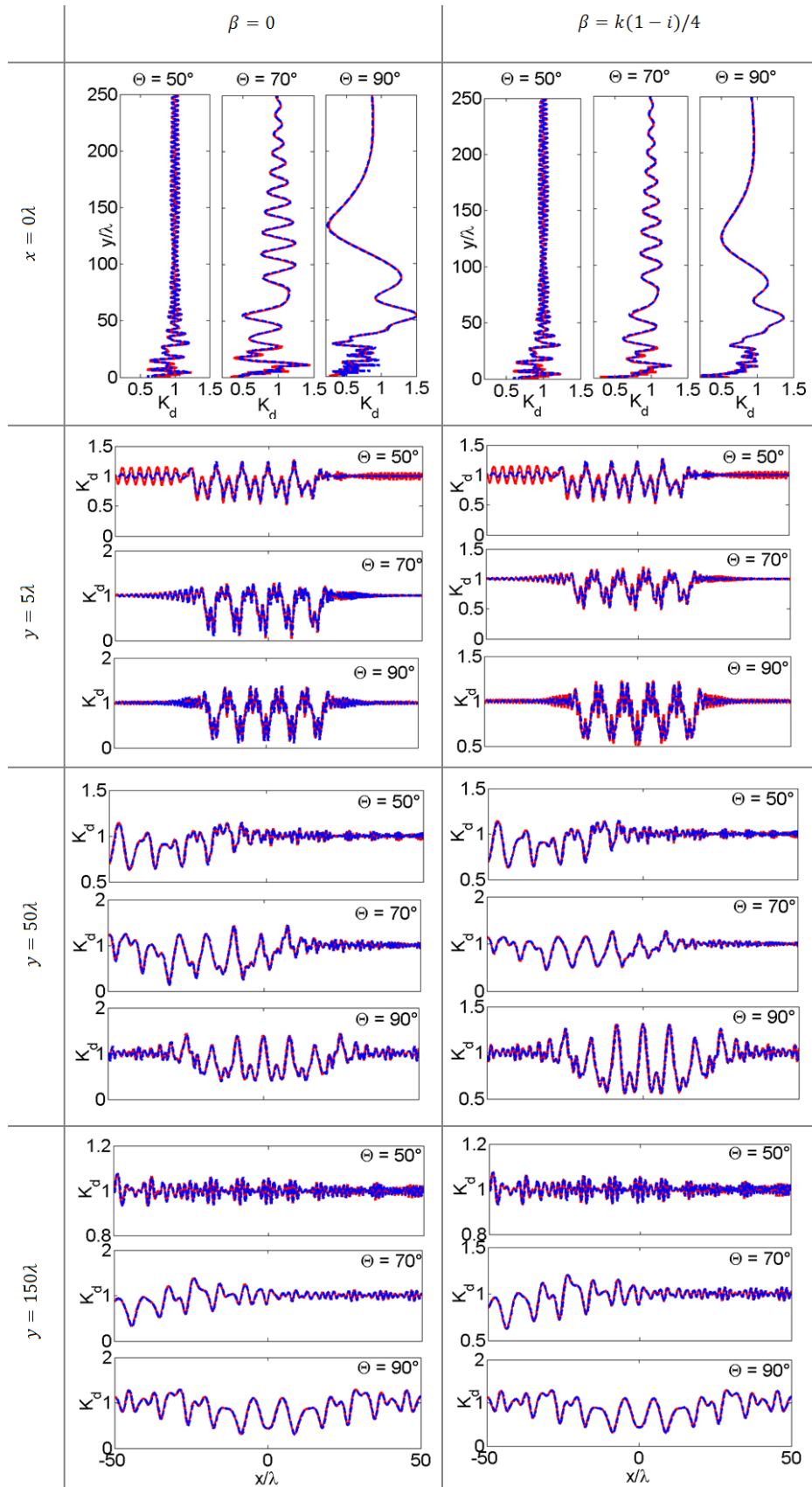


**Figure 2.10** Comparison of the disturbance coefficient  $K_d$  for the AAS (red line) and the integral equation solution from (McIver, 2005) (blue dashed line) along the transects:  $y = 5\lambda$ ,  $y = 50\lambda$ ,  $y = 150\lambda$  ( $+y$  is down-wave distance from the plane of the array), and  $x = 0\lambda$  ( $x = 0$  is the centre of the of the device array). For incident wave directions of  $\theta = 50^\circ$ ,  $70^\circ$  and  $90^\circ$  with permeability parameters of  $\beta = 0$  (full reflection) and  $\beta = k(1 - i)/4$  (partial reflection, transmission and dissipation).

## 2.5 Diffraction and no-diffraction comparison

To isolate and evaluate the effect of diffraction on the re-distribution of wave energy the hypothetical scenario where diffraction does not occur, must also be considered. This is very simple to achieve as the wave disturbance coefficient in the geometrical shadow of each device will be zero regardless of distance from the device, and will be equal to unity at all other locations. This is similar to how a phase averaged model like SWAN would interpret the wave energy shadow, provided that the diffraction approximation is off. This is demonstrated to be true in (Black, 2007), with a comparison between what is essentially described above (no-diffraction solution) and the results of using SWAN to assess the wave shadow for the wave hub project (Millar, et al., 2007).

To compare the disturbed wave field predicted by the AAS and the no-diffraction solution, the following array geometry and incident wave characteristics are considered: the WEC array is located along the plane  $y = 0\lambda$  and the middle of the central device is at  $x = 0\lambda$ . The length of each devices is  $B = 250 (m)$  the tip to tip separation distance between neighbouring devices is  $b = 600 (m)$ . For the monochromatic (regular) wave cases the period is discrete at  $T = 8 (s)$  and for the spectral cases  $T_p = 8 (s)$  with a JONSWAP frequency distribution having a peak enhancement of  $\gamma = 3.3$ . Water depth is uniform at  $h = 50 (m)$ , which from the dispersion relationship, yields a wavelength of  $\lambda = 100 (m)$  for the monochromatic cases, and a peak wavelength of  $\lambda_p = 100 (m)$ , for the spectral cases. These wave lengths are used to normalize the dimensions of the calculation domain. The incident waves are either unidirectional or directional with directional spread parameters of  $m = 2, 10, 100$  and  $800$ . The reflection coefficient is  $c_p = 0$  and the transmission coefficient is  $c_t = 0$ , so that the devices are considered to be unrealistic perfect dissipaters/converters. The computational domain is  $25 (km)$  down-wave and  $10 (km)$  wide which equates to  $250\lambda$  and  $100\lambda$  when normalised by the peak wavelength. This is a relevant domain size as the down wave distance from the Wave Hub project to the coast is approximately  $25 (km)$ .

In figure 2.11, the disturbed wave field predicted by the AAS shows a strong interference pattern when the incident waves are considered to be monochromatic and unidirectional. When spectral waves are considered, the spatial locations of the maxima and minima interference pockets change for each discrete component of the frequency distribution, resulting in a smoothing of the interference pattern. When directional spreading is considered, a stronger smoothing of the interference pattern occurs. The wave energy shadow is also seen to recover with distance from the array with a greater directional spread, resulting in a faster rate of recovery. Alternatively, in figure 2.12 the disturbed wave field for both monochromatic unidirectional and spectral unidirectional incident waves (from the no-diffraction solution), is simply a projection of the geometrical shadow of the devices. When directional spreading is accounted for, a smoothing and recovery of the wave energy shadow with increasing distance from the array occurs, and the no-diffraction solution exhibits a similar wave-field to the case where diffraction is considered. However, for narrower spread distributions, the recovery is more rapid for the no-diffraction solution.

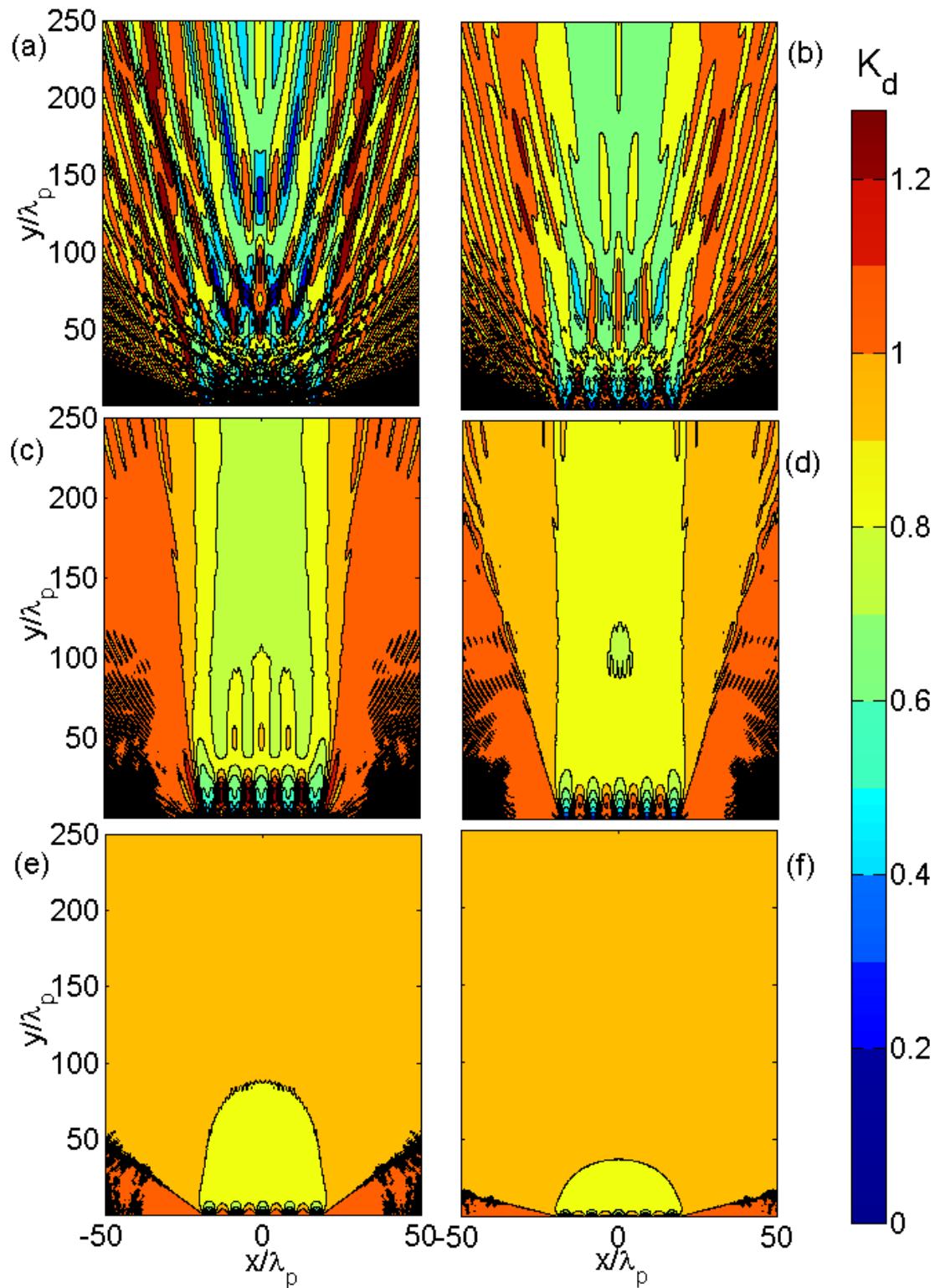


**Figure 2.11** The disturbance coefficient  $K_d$  predicted by the AAS for (a) monochromatic unidirectional incident waves, (b-f) are spectral waves with  $T_p = 8$  (s) and peak enhancement  $\gamma = 3.3$ , with (b) unidirectional, (c) directional with  $m = 800$ , (d) directional with  $m = 100$ , (e) directional with  $m = 10$  and (f) directional with  $m = 2$ . In all cases the mean wave direction is  $\theta = 90^\circ$  from the plane of the array, and  $c_p = 0$  and  $c_t = 0$ .

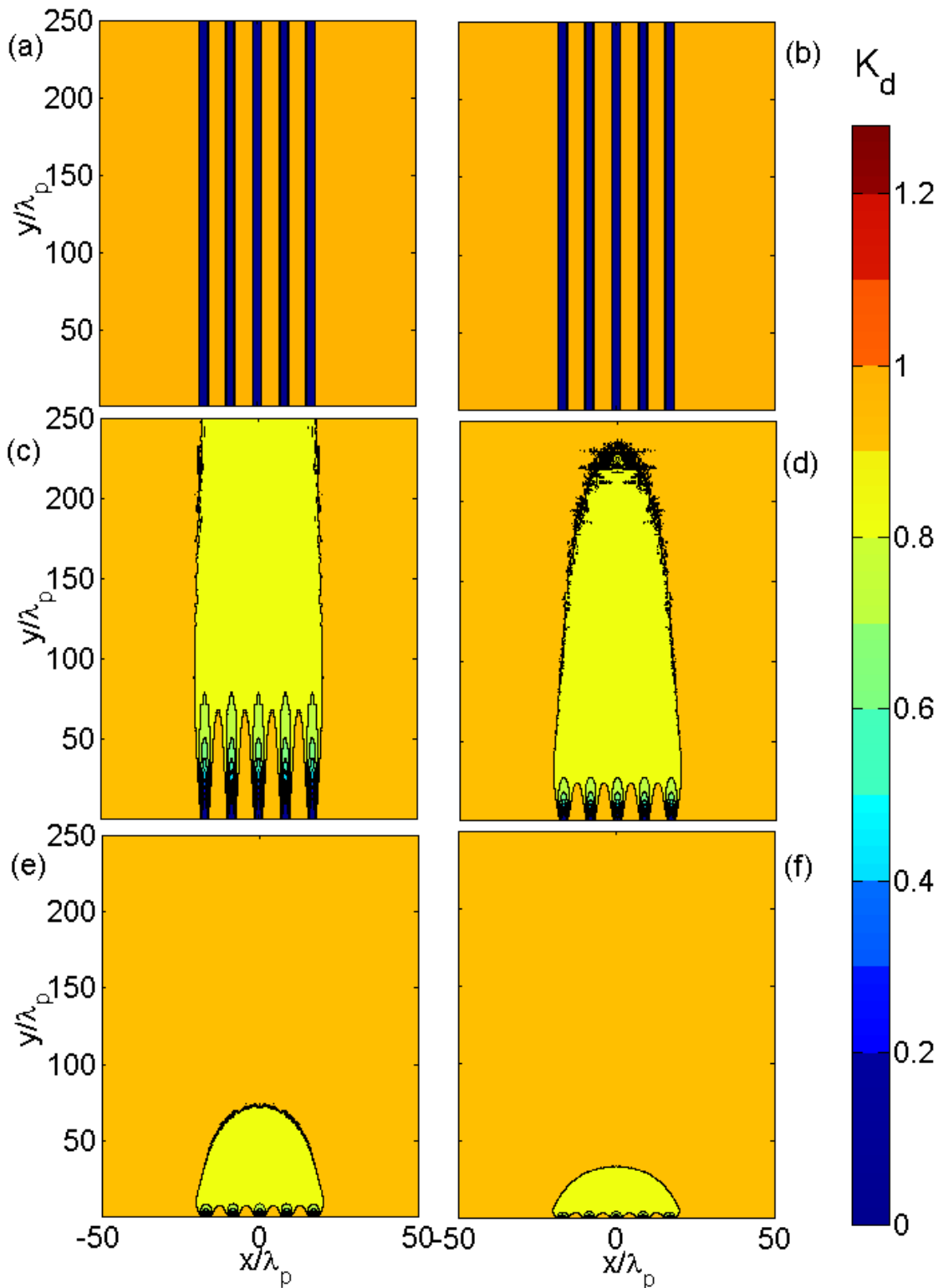


**Figure 2.12** The disturbance coefficient  $K_d$  predicted by the no-diffraction solution for (a) monochromatic unidirectional incident waves, (b-f) are spectral waves with  $T_p = 8$  (s) and peak enhancement  $\gamma = 3.3$ , with (b) unidirectional, (c) directional with  $m = 800$ , (d) directional with  $m = 100$ , (e) directional with  $m = 10$  and (f) directional with  $m = 2$ . In all cases the mean wave direction is  $\theta = 90^\circ$  from the plane of the array and  $c_p = 0$  and  $c_t = 0$ .

As the mean incident wave direction is perpendicular to the array, the greatest reduction in wave height will generally be along the transect that bisects the central device of the series ‘central transect’. This is the point at which the recovery rate of the wave energy shadow (with distance from the array) from directional spreading, is the slowest (although local interference can cause spatial fluctuations).

The disturbance coefficient along the central transect for the different cases considered is given in figure 2.13(a). It is seen that there are some appreciable differences between predictions of the AAS and the no-diffraction solution. When diffraction is considered, and directional spread is narrow (with spread parameters of  $m = 100$  and  $800$ ), a divergence in wave height is apparent in the far-field, with the no-diffraction solution showing greater wave heights with increasing distance from the array. When  $m = 800$  there is a temporary interference maxima along the central transect near the array, which provides a greater wave height at first compared to the no-diffraction solution. The divergence between the two solutions is counter-intuitive, as diffraction is often considered to be a mechanism that reduces the lateral wave height gradients. One might expect that diffraction would act to redistribute energy from the high energy region (the region outside the geometrical shadow of the array) to the low energy region (the region inside the geometrical shadow of the array), thus helping the wave energy shadow to recover more rapidly with distance from the array.

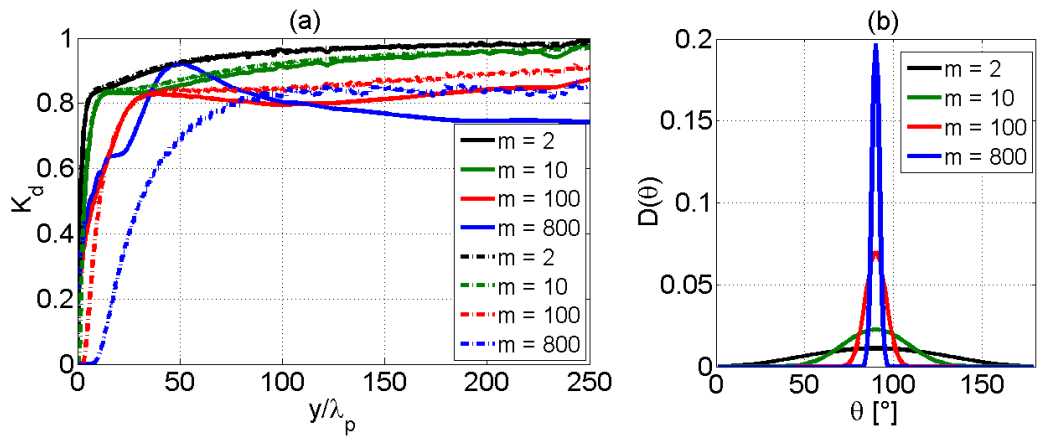


**Figure 2.13** (a) The disturbance coefficient  $K_d$  along the transect that bisects the central WEC device of the series predicted by the AAS (solid line) and the no-diffraction solution (dot dashed line). (b) shows the wave directional spread probability density for discrete angular components of one degree.

To assess the net effect of diffraction on the re-distribution of wave energy the average wave energy is found for each band of the domain  $\overline{K_{d,y}^2}$  in the ‘direct lee region’ ( $y = 0 (m), 25 (m), \dots 25000 (m)$ ). This is then normalised by the incident undisturbed wave energy  $E_0$  so that the average energy disturbance coefficient in that band is given by;

$$E_{d,y} = \overline{K_{d,y}^2} / E_0 \quad (2.38)$$

The ‘direct lee region’ is defined as the region between a half gap length before the first device in the series, to half a gap length past the last device in the series, as described in figure 2.14.

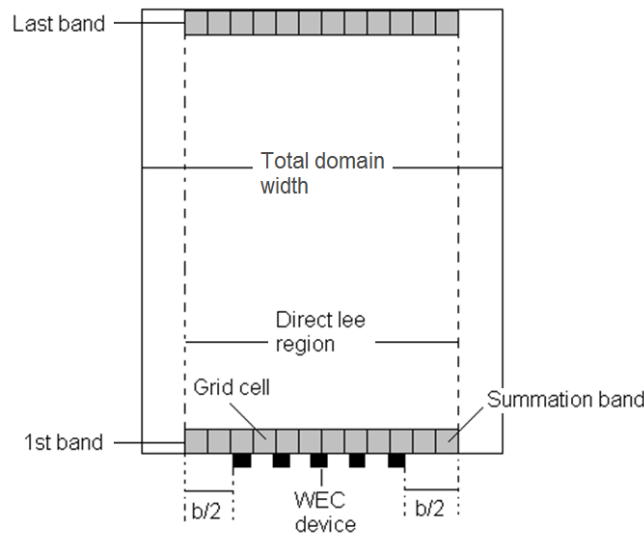


**Figure 2.14** Schematic describing the direct ‘direct lee region’ and energy summation bands, used to assess the net flux of wave energy.

As seen in figure 2.15, the wave energy in the “direct lee region”, for narrower directional spreads ( $m = 100, 800$  and  $\infty$ ), is less when diffraction effects are considered. Also for the case of a very narrow directional spread ( $m = 800$ ) the total energy in each band of the domain gets progressively less with increasing distance from the array. The energy associated with the diffracted component, which is seen in figure 2.7(a), is also given in figure 2.15.

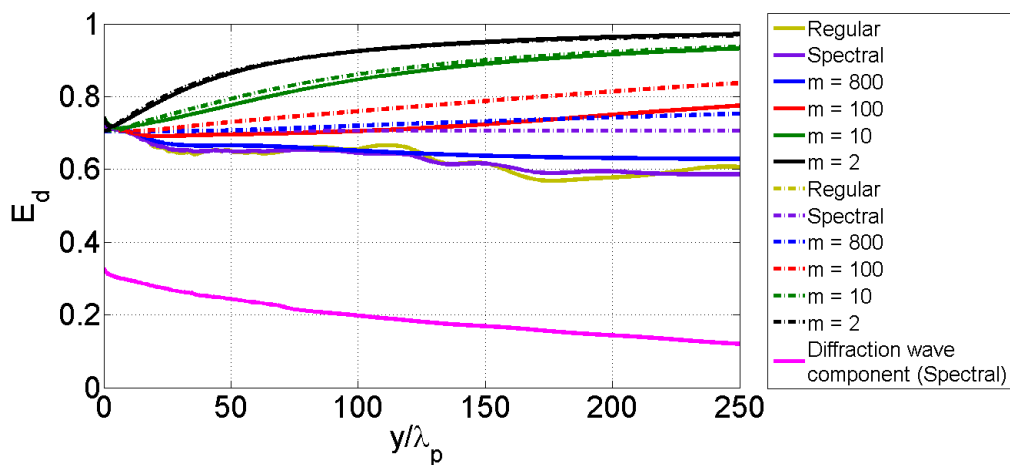


**Figure 2.15** The change in total wave energy for each band of the “direct lee region” with increasing distance from the array for unidirectional monochromatic waves with  $T = 8$  (s), unidirectional spectral waves with  $T_p = 8$  (s), and directional spectral waves with  $T_p = 8$  (s) and spread parameters  $m = 2, 10, 100$  and  $800$ . Solid lines show the AAS results and dot dash lines show the no-diffraction solution results.

As the diffraction wave components of the AAS are weighted radiation waves, it would appear that diffraction radially spreads part of the energy that passes through the array. With increasing distance, the proportion of energy of these radial waves in the geometrical shadow of the array (for that incident wave direction), diminishes. When the incident wave is more perpendicular to the plane of the array, diffraction spreads energy radially to all other regions of the domain, which would otherwise be present in the ‘direct lee region’, thus reducing the energy in this region. Conversely, when the incident wave direction is more

parallel to the plane of the array, diffraction spreads the radial wave energy from the geometrical shadow region (for the specific wave direction) into the ‘direct lee region’, which would otherwise not be present if diffraction was not considered. The result is that when the directional spread is broad, there is a cancellation of the energy redistribution and little net difference. However, when the directional spread is narrow, there is a net redistribution away from the ‘direct lee region’ and a notable reduction of energy in this region. Specifically for the cases considered, when the directional spread parameter is  $m = 800$ , the difference in average wave energy in the ‘direct lee region’ at a distance of 25 (*km*) from the array is 12% of the incident undisturbed wave energy. When  $m = 100$  this reduces to 5%, and there is no appreciable difference when  $m = 10$  or 2.

It is not completely clear whether this mechanism is physical or an artificial shortcoming of the AAS. In a similar case predictions from the AAS, the numerical Boussinesq model FUNWAVE (Wei, et al., 1995) (Kirby, et al., 2005) and the parabolic mild slope model REF/DIF (Kirby & Dalrymple, 1994) (Kirby & Ozkan, 1994), all exhibited a similar energy profile trend under unidirectional monochromatic wave conditions (Monk, et al., 2011).

## 2.6 Shadow sensitivity analysis

A series of tests were performed to investigate the sensitivity of the wave shadow to: wave directional spreading, frequency distribution, device separation length, device length and the transmission coefficients. This was performed by independently varying the parameters affecting diffraction and wave directional spreading about a set of base parameters and re-calculating the wave-field for each variation made. The base incident wave parameters were: peak period -  $T_p = 8$  (s), spread parameter -  $m = 50$ , JONSWAP peak enhancement -  $\gamma = 3.3$ . The base parameters for the WEC array and layout were: tip to tip device separation distance  $b = 600$  (m), 0% transmission and 0% reflection (perfect absorption which is independent of wave frequency and direction for the worst case scenario). The base WEC length was chosen as  $B = 150$  (m), which is changed from 250 (m) as considered in the previous section. This was to incorporate the sensitivity of the disturbed wave field to the device length, into the analysis.

In figures 2.16, 2.17(b), 2.18 and 2.20, the disturbed wave height predicted by the AAS for the different parameter permutations is given along the central transect, which is defined as a transect perpendicular to the array that bisects the central WEC device of the series. This is because in the absence of refraction and for an incident wave field with a peak wave direction perpendicular to the plane of the array, the central transect will generally show the maximum reduction in wave height. This will present the greatest potential impact.

### 2.6.1 Directional spreading

As seen in figures 2.11 and 2.13(a) for a very broad directional spread (i.e.  $m = 2$ ), the energy deficit is spread over a very wide area and the resulting disturbance coefficient is almost unity at a distance of 25 (*km*). In contrast for a very narrow directional spread (i.e.  $m = 800$ ), a significant wave height reduction persists up to 25 (*km*) away from the array. The disturbance coefficient profile at the central transect generally shows a steady recovery with increasing distance from the array, with the exception of the case of a very narrow directional spread. This is discussed in section 2.5, and appears to be a result of

the diffracted wave component spreading energy away from the geometrical shadow of the array which counteracts the recovery of the wave energy deficit from directional spreading effects. Significant fluctuations exist in the moderate to near-field due to constructive and destructive interference from the diffracted waves. The strength of these fluctuations depends primarily on the broadness of the directional spread. A single discrete incident direction will result in a complex maxima and minima pattern as shown in figure 2.11(a-b). As directional spreading is applied, the locations of these maxima and minima will shift with each discrete direction component of the spread distribution. This results in a smoothing of the interference pattern, as the maxima/minima for one discrete direction overlaps the minima/maxima for another discrete direction, thus partially cancelling each other. The narrower the spread, the smaller the range of spatial shifts of the maxima and minima locations resulting in less smoothing of the interference pattern, and vice versa. In figures 2.13(a) there exists some spatial fluctuations in the moderate to far-field and the reason for this are discussed in section 2.2.5 and 2.2.6. These fluctuations can be reduced with a higher directional and spectral resolution if required.

### 2.6.2 Device length

As shown in figure 2.11(c-f) and 2.13(a), directional spread has a strong effect on the wave energy shadow because it controls the rate of dispersion of the wave energy deficit. Decreasing the device length decreases the total array length (if the gap length is maintained) which reduces the distance from the array for direction spreading to effect the central transect. As such the sensitivity of the distributed wave field to device length will be considered in conjunction with directional spreading. As seen in figure 2.16, when the device length is shorter the energy deficit is generally lower because less wave energy is extracted. However, in the far-field the difference is marginal when the directional spread is broad. The difference is more significant when the directional spread is narrow.

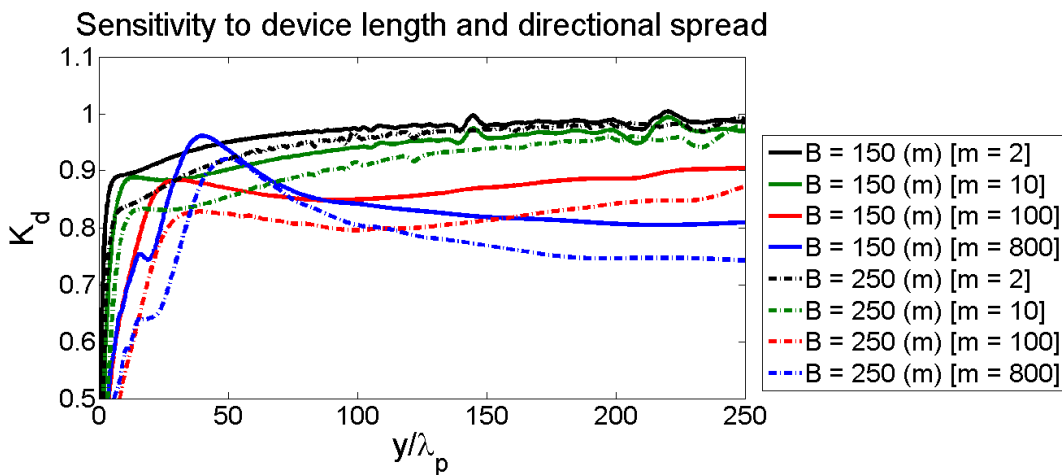


**Figure 2.16**  $K_d$  profile along the central transect for an array with device lengths of  $B = 150$  (m) (solid line) and  $B = 250$  (m) (dot-dash line) for the directional spread parameter  $m = 2, 10, 100$  &  $800$  and  $T_p = 8$  (s).

### 2.6.3 Frequency distribution

As seen in figure 2.17(b), varying the peak period  $T_p$  has very little effect on the far-field wave energy shadow, with the disturbance coefficients at  $25$  (km) being within 1% of each other for the different peak

period values considered. It should be noted that the length of each plot in figure 2.17(b) differs because a distance of 25 (*km*) is reached in fewer wavelengths when the peak period is longer, and vice versa. In the near-field there is an appreciable difference in  $K_d$ , which is a result of interference of diffracted waves. It is seen that a spectrum with a longer peak period produces maxima and minima interference with greater magnitude in the near-field. This is because the area of the domain in which two diffracted waves come into phase to produce a maxima (or vice versa for a minima), is larger when the wavelength is longer. When the wave direction changes (for each discrete component of the directional spread) the location of the interference pockets shift. Broader interference pockets for longer wavelengths are more likely to overlap for each discrete directional superposition than for narrower interference pockets for shorter wavelengths, thus stronger interference is more prevalent. Similarly, significant maxima and minima pockets are only present in the near-field because as the distance from the array increases so does the length of the shift in the location of the interference pocket between each component of the directional spread. As the distance from the array increases, the amount of overlapping of interference pockets decreases for each superposition. This results in a smoothing of the overall interference across all directions of the spread and frequencies of the spectrum, with increasing distance from the array and vice versa. For a realistic device the power take-off will be strongly dependent on the incident wave period, and so the peak period of the device will likely have a significant influence on the wave energy shadow.

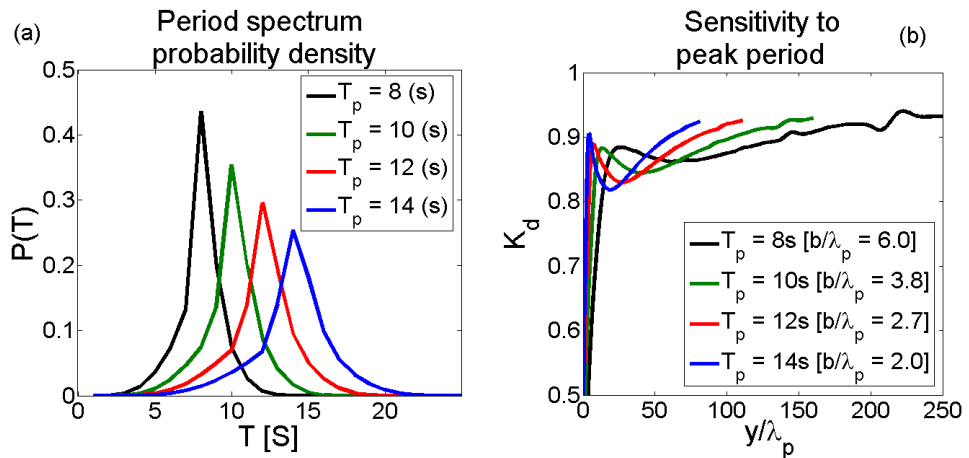


**Figure 2.17** (a) JONSWAP period spectrum probability density (b)  $K_d$  profile along the central transect for an array for peak period values of  $T_p = 8, 10, 12$  &  $14$  (s), for  $B = 150$  (m) and  $m = 50$ .

### 2.6.4 Gap length

Varying the gap length between the individual WEC devices, whilst maintaining the same energy absorption at each device and the same total energy absorption across the array, requires the length of the total WEC array to be changed. This alters the transmission ratio of the array as a whole, with a shorter gap length resulting in a lower array transmission to absorption ratio, and vice versa as seen in figure 2.18 and 2.19. Consequently, there is a greater reduction in the disturbance coefficient initially for an array with shorter gap lengths as the wave energy deficit is more concentrated. This initial enhanced reduction is countered with increasing distance from the array, as the spread of the un-attenuated waves from the open regions (to the sides of the array) requires a shorter distance to reach the central transect. This acts to reduce the disturbance coefficient closer to the array (compared to a wider array).

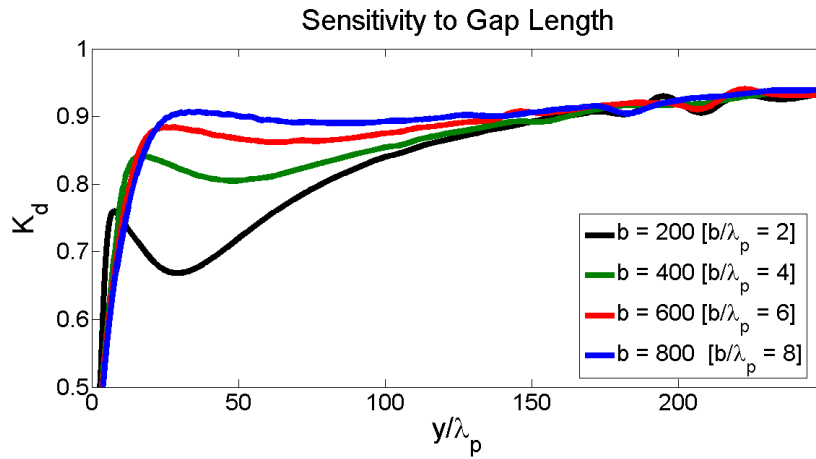


**Figure 2.18**  $K_d$  profile along the central transect for an array with WEC tip to tip separation lengths of  $b = 200, 400, 600$  &  $800$  (m), for:  $B = 150$  (m),  $T_p = 8$  (s) and  $m = 50$ .

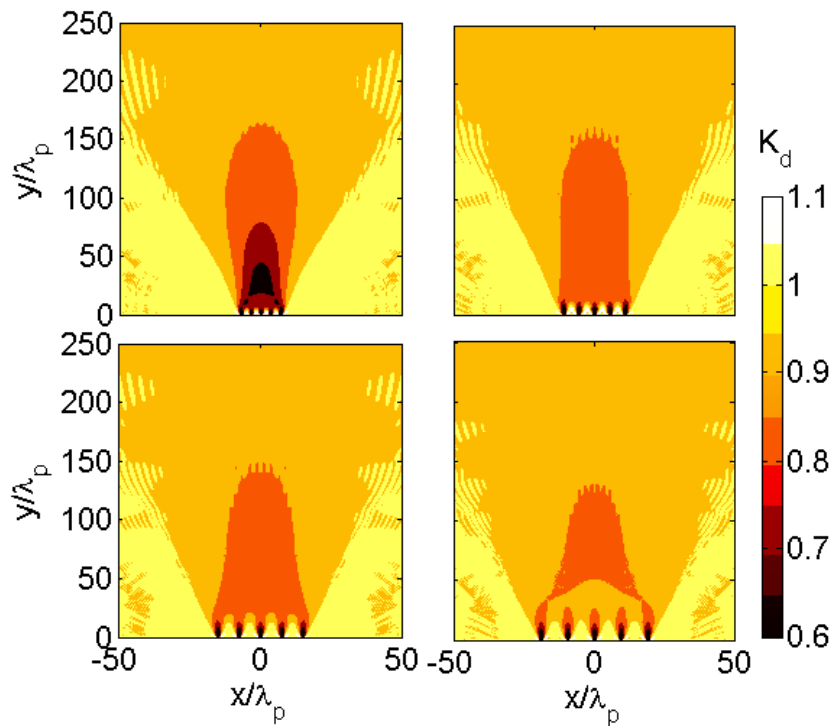


**Figure 2.19** Horizontal spatial distribution of  $K_d$  in the lee of an array with WEC separation length of: (a)  $b = 200$ , (b)  $b = 400$ , (c)  $b = 600$  and (d)  $b = 800$  (m), for:  $B = 150$  (m),  $T_p = 8$  (s) and  $m = 50$ .

### 2.6.5 Transmission coefficient

The transmission and reflection coefficient of the device defines the energy conversion by the WEC device. A higher transmission coefficient permits more wave energy to pass below the device, resulting in a smaller wave energy deficit in the lee. When wave energy is transmitted through the device, the diffracted wave reduces in magnitude as there is a smaller wave gradient along the geometrical shadow of the device and therefore less for the diffraction effect to compensate for. When the diffracted wave is smaller, its modification of the incident wave field will be reduced and the interference maxima and minima will be closer to the local mean, as shown in figure 2.20.

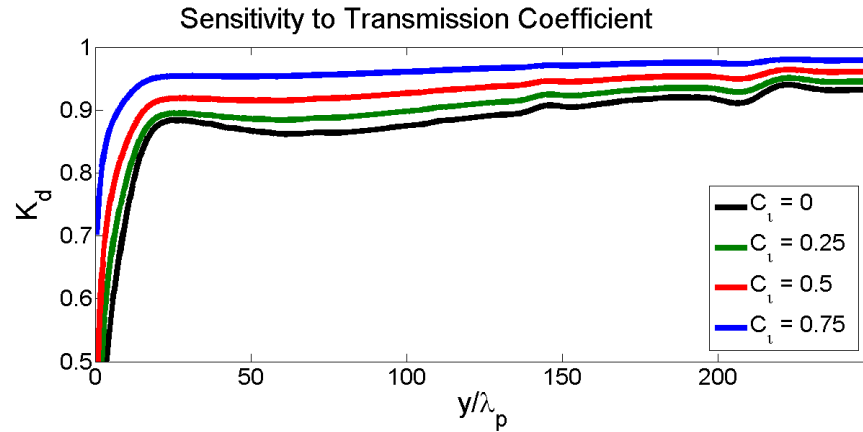


**Figure 2.20**  $K_d$  profile along the central transect for an array for WEC devices with transmission coefficients of 0,0.25,0.5,0.75, with zero reflection, for:  $B = 150$  (m),  $T_p = 8$  (s) and  $m = 50$ .

### 2.6.6 JONSWAP peak enhancement factor

The peak enhancement factor changes the shape of the period spectrum whilst maintaining the peak period value. A lower peak enhancement flattens the shape of the spectrum and vice versa. The peak enhancement factor was found to have a negligible effect on the disturbance coefficient profile. This could be a result of the change in the strength of interference from the change in the proportion of waves with a longer period than the peak wave, which is equal and opposite to the change in the strength of interference by the proportion of wave with shorter period than the peak wave.

## 2.7 Future work

The analysis presented here (except figure 2.20) assesses the worst case scenario for an ideal overtopping type device, with full absorption of the incident wave energy across the beam of the device. This was done to simplify the problem and focus on the energy redistribution mechanisms associated with wave diffraction. In reality an overtopping type WEC device would reflect, absorb and transmit a portion of the incident wave energy. These ratios would be dependent on the dimensions of the device, namely the draft, the height of the freeboard of the reservoir and the slope of the ramp. The ratios would also be dependent on the incident wavelength, height and direction. In order to assess the actual resultant wave energy shadow for a real array of overtopping type WECs, these dependencies would need also need to be considered. For a fixed Wave Dragon device, (Beels, et al., 2010) calculated the transmitted wave energy below the device for the specific device dimensions and incident wave state. This was found by integrating the wave energy from the sea floor to the draft of the device. Similarly, the absorbed wave energy is calculated by the overtopping rate based on the device draft, freeboard height, reservoir ramp width and the incident wave height and wavelength. The remaining wave energy is reflected. (Norgaard & Andersen, 2012) provide wave basin based experimental results for the wave transmission, reflection and absorption ratios for a floating and fixed 1:51.8 scale Wave Dragon device. For the sea states investigated the wave height in the lee of the floating device was approximately 23% greater than for a non-oscillating fixed device. These methods and results can be used to estimate the reflected, absorbed and transmitted wave energy at the device based on the device dimensions and incident wave parameters. These ratios could then be applied to the AAS using the reflection and transmission coefficients, which

can then be used to scale the far-field wave energy shadow prior to an actual WEC array deployment. However, a fundamental limitation at this stage exists because only domains of constant water depth can be considered which will limit the practical use of this tool for specific case studies.

## 2.8 Conclusions

An approximate analytical solution was developed to assess the disturbed wave field about a single row array of overtopping WEC devices, represented as a series of partially absorbing and transmitting breakwater segments. This provides a tool for scaling the disturbed wave field about a single row array of overtopping WEC for very large areas and for a higher resolution directional and spectral irregular waves. This might not be possible / practical with a time-stepping phase resolving numerical model. Also excellent agreement was found between the approximate analytical solution, and the more mathematically exact but computationally expensive integral equation method in the far-field region. The solution is however limited to the case of constant water depth only which will be a practical limitation for a specific case study.

For arrays placed far offshore, it was confirmed that directional spreading has the greatest influence on the maximum wave height reduction at the coast behind the WEC array. For example, an 18% drop of wave height for a very narrow directional spread compared to only 2% for a very broad directional spread were found at a distance  $x = 250\lambda_p$  behind the WEC array when the device length 150 (m) (fully absorbing across its beam). A reduction of up to 27% was found for a similar where the fully absorbing devices length was 250 (m).

The separation length between WEC devices has a strong influence on the wave energy shadow in the near-field, with a short separation length producing greater wave height reductions initially. This is because the wave energy deficit is concentrated when the gap length is shorter. This however, is counteracted with increasing distance from the array, due to the more rapid influence of directional spreading when the array length is shorter. No appreciable difference in the wave energy shadow for different gap lengths was seen in the far-field.

Under the assumption that energy extraction is independent of frequency, the peak period of the spectrum was found to not affect the maximum wave height reduction in the far-field but did have a small influence in the near-field because a longer peak period produced more amplified minima and maxima pockets, and vice versa. This is because waves of longer period have maxima and minima interference pockets that span greater areas, which results in greater overlap of interference pockets from the diffracted waves from different devices. The peak enhancement factor of the spectrum did not affect the wave shadow.

The approximate analytical solution suggests that the combined effect of diffraction about the WEC sections actually deepens the wave energy shadow with increasing distance from the array because of the radial redistribution of energy. This causes a portion of the wave energy propagating through the array to spread away from the geometrical shadow region of the array. The effect however is only significant when waves have a narrow directional spread distribution.

## Chapter 3

# Overview of the Pico OWC wave energy converter

### Abstract

An overview of the Pico oscillating water column (OWC) wave energy converter (WEC), history, issues, local wave climate and technology, is presented. The current plant performance under non-advanced control is analysed. The fatigue rate and other significant issues are investigated. A possible solution to improve performance or mitigate the related operational issues is discussed as a precursor to in depth research on relief valve control and short term wave forecasting which is presented in the following chapters.

### 3.1 Introduction

This chapter provides an overview of the Pico OWC system, the local wave climate and overview of the plant's current performance with a breakdown of the mechanisms that cause the plant to underperform. Issues such as mechanical component fatigue and noise pollution are reviewed in detail and possible solution to these issues, which may also improve the power production of the plant, are identified. One particular strategy to tackle these issues involves control of the relief valve aperture. This will be investigated in-depth in the following chapters.

### 3.2 Background and history

The Pico OWC project commenced in 1992 under the coordination of the Lisbon University Instituto Superior Tecnico (IST). The project was co-funded by the European council and the Portuguese electrical utility companies Energias De Portugal (EPD) and Energias De Açores (EDA).

As described in (European wave energy pilot plant on the island of Pico, 1999), the original project goals were;

- 1.) Demonstrate the technical feasibility of an OWC wave energy converting power plant at a commercial scale
- 2.) Provide a testing facility for different power take-off equipment
- 3.) Provide the means for assessing and validating the overall design methodology, and theoretical characterisation.
- 4.) Assess the economic feasibility of OWC power plants in small isolated electrical grids
- 5.) To gain experience in the design, construction and operation in the more controlled conditions of a shore-mounted device before deployment of offshore devices.

The plant was constructed on the shoreline of the North coast of the Pico island in the Azores archipelago at the global coordinates of N(38.560046), E (-28.441899). The location was selected because of the high

wave energy climate (excluding summer), deep water at the shoreline, and for the existing local high voltage electrical grid transformer connection.

During construction the power electronics equipment, originally housed within the plant, were installed prematurely and were damaged due to flooding in 1998 during a storm. Also the cofferdam, erected to provide wave shelter to the main construction site, was severely damaged by wave action and several thousands of cubic meters of rock were distributed on the sea bed around the entrance of the chamber. The cofferdam contractors removed most of the debris but a significant proportion collected in the chamber making extraction very difficult. This significantly reduced the chamber water depth. Also some of this material was taken further off-shore to a location out of crane reach. In addition a large section of the 2 meter thick eastern end of the chamber front lip was broken off just below the mean water line. This was suspected to be caused by defective concreting and/or from boulder impacts. Construction was completed in 1999.

The first operational tests were run in 1999-2000, but the rigidity of the turbo-generator support structure was insufficient to suppress vibrations to an acceptable level. Severe harmonics at certain frequencies and at higher turbine rotational speeds, prevented sustained operation for fear of rapid fatigue or catastrophic failure.

In 2000 a small access door at the side wall of the plant was ripped off by strong wave overtopping resulting in a second flooding of the plant and destruction of the power electronics.

The third set of power electronics was then installed on platforms inside the plant to reduce the risk of flood damage. However, due to the high humidity inside the plant because of the ineffective building encapsulation, corrosion set in rapidly and the equipment was damaged once more. Because of repeated damage of the power electronics and the unsolved issues with vibrations, the project was left dormant.

In 2003 the not for profit research company “the WAVE Energy Centre” (WAVEC) was formed to, in part, to take command of the Pico plant. This commenced a reconditioning phase of the plant. The new power electronic set was moved to an auxiliary building some distance away from the plant to avoid any further water damage.

During this period the turbine angular velocity was limited to  $N = 126 \text{ (rads}^{-1}\text{)}$  as a safety measure and basic tests were performed. At this angular velocity limit the residual *RMS* vibration velocity (with no aerodynamic loading) measured at the generator and chamber side turbine shaft bearings were  $V_G = 6 \text{ (mm s}^{-1}\text{)}$  and  $V_c = 7 \text{ (mm s}^{-1}\text{)}$ , respectively. This is considered to be in the “unsatisfactory” range of the relevant ISO 10816 vibration severity standards as seen in table 3.1. The Pico turbo-generator system is considered to be between a class II and class III machine due to the rotational speed range. With increasing rotational speed past this threshold, vibration levels increased rapidly and passed deep in to the “unacceptable” range. This maximum limitation of  $N$  was far below the initial design limit of  $N = 157 \text{ (rads}^{-1}\text{)}$ , and poor system performance resulted because of this limitation.

**Table 3.1** ISO 10816 standards for vibration severity ratings.

Vibration severity ISO 10816												
Vibration RMS velocity (mm/s)	0.28	0.45	0.71	1.12	1.8	2.8	4.5	7.1	11.2	18.0	28.0	45.9
Class II	Good				Satisfactory		Unsatisfactory		Unacceptable			
Class III												

Due to a lack of funding and the technically challenging nature of the problem the vibration issues were not resolved until 2009 when reinforcement in the form of additional support struts, designed using finite element method analysis, were retrofitted to the existing turbo generator support structure to increase the overall structural mass and stiffness. Vibrations were significantly suppressed by these reinforcements and the turbine angular velocity was extended to  $N = 157 \text{ (rads}^{-1}\text{)}$  at which speed the residual vibration velocities are  $V_G = 6 \text{ (mm s}^{-1}\text{)}$  and  $V_c = 7 \text{ (mm s}^{-1}\text{)}$ . However, the vibration levels are still in the “unsatisfactory” range at his upper rotation speed limit and the fatigue rate from prolonged periods of operation in this range is not known. Also, due to a subsequent downgrade in the power handling capacity of the power electronics a rotational speed margin is needed to more gently electromagnetically break the turbine to avoid power spikes that might cause electrical component failure. Factoring in the residual issues a power take-off control law was implemented to severely retard the machine at speeds greater than  $N = 141 \text{ (rads}^{-1}\text{)}$ , keeping the residual vibrations within the ISO 10816 “satisfactory” range at most times and giving enough rotational speed margin for electromagnetically retarding the turbine whilst staying within the power electronics limitations. However, as will be seen later vibrations velocities can still enter deep into the “unsatisfactory” range when the turbine is aerodynamically loaded during stall events.

Prior to 2009, all tests were performed manually requiring an operator to intervene to ensure the machine is properly isolated in case of failure or if warnings are detected in order to protect the machine. This was primarily because of electrical noise which distorted the signals used by the controller to monitor the system as part of the original automatic operation sequence. At the end of 2009, autonomous operation was achieved through redesign of the control system and re-wiring of the relevant sensors to ensure redundancy.

From 2010 until the present, the machine has been operational for sustained but intermittent periods of time, and electrical power is fed to the local grid and sold at a rate of €0.27 per kilowatt hour. A number of severe system failures, funding issues, lack of work force and technical support, has resulted in extended periods of machine down time. The significant system failures include:

2010 – Short circuits across the diodes of the spinning rectifier of the generator due to humidity and/or the build-up of carbon dust removed from the rotor brushes. This required a complete overhaul of the generator.

2011 – Failure of the inverter controller due to memory loss on power down resulting in unusual behaviour and destruction of power electronics components. The solution was simple (replacing the controller bios battery) but difficult to diagnose.

2012/2013 – Defect of one of the IGBT driver cards caused a decay in the pulse width modulation wave forms resulting in an overlap of electrical phases and ultimately short circuits in the inverter system and destruction of power electronics components. The IGBT gate wave forms of the non-functional and another correctly functioning IGBT is shown in figure 3.1. The solution was simple (replacement of IGBT driver card) but again it was difficult to diagnose without the appropriate technical support.

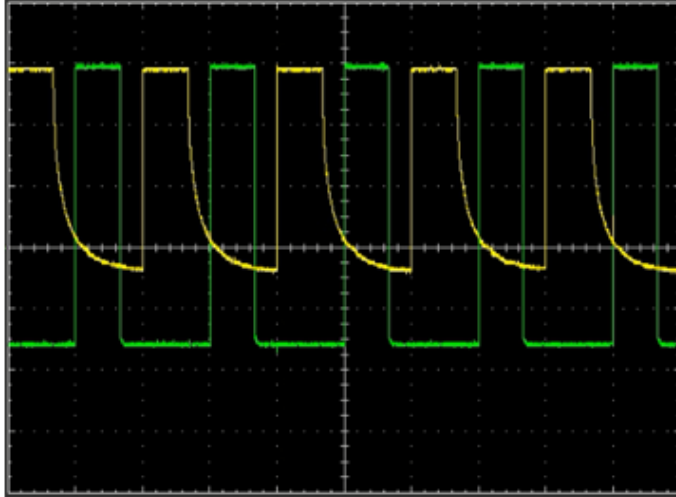


**Figure 3.1** IGBT switch wave forms for pulse width modulation of two phases of the inverter system showing decaying trailing edge due to capacitor malfunction on the IGBT driver card of one phase polarity, resulting in a short circuit between electrical phases and damage to the inverter power electronics.

2014 – Extensive damage of the data link between the plant and control centre due to a lightning strike. This required an overhaul of the data transmission and acquisition systems. Also in 2014, a second round of short cuts in the generator from carbon dust build up (from the brushes) occurred. This required a less significant overhaul of the generator rectifier.

The project is currently coordinate by WAVEC – Offshore renewables, Lisbon, and since November 2011 (when the author joined the project) the day to day operation, maintenance and progression of the plant is performed by three part-time employees:

- Victor Winands (Germany) who is responsible for coordinating the operations side of the project, research, electrical and mechanical engineering, maintenance and operational monitoring. Specialising in mechanical engineering.
- The author (UK), who is responsible for research, data acquisition and management, innovation, maintenance and operational monitoring. Specialising in coastal engineering, physics and oceanography.
- Antonio Soares (Cape Verde) who is responsible for mechanical repair and component fabrication.

### 3.3 System and structural specification

#### 3.3.1 Relevant structural dimensions

The structural dimensions of the plant are listed below and a cross sectional schematic is shown in figure 3.2 and the local bathymetry (prior to the addition of rock material from the damaged cofferdam) and structure are given in a BEM domain grid representation in figure 3.3.

- Chamber internal horizontal area –  $xy = 12 (m) \times 12 (m)$
- Chamber air volume at mean water level –  $V_0 = 1440 (m^3)$
- Turbine duct outer diameter -  $D = 2.3 (m)$
- Turbine duct inner diameter -  $D_i = 1.36 (m)$
- Chamber designed water depth\* -  $h = 7 (m)$

\*The actual depth is transient due to boulder movement but is significantly lower (between 1 and 3 meters)

Chamber front wall thicknesses at the water line is 2 (m) with a semi-circular profile.

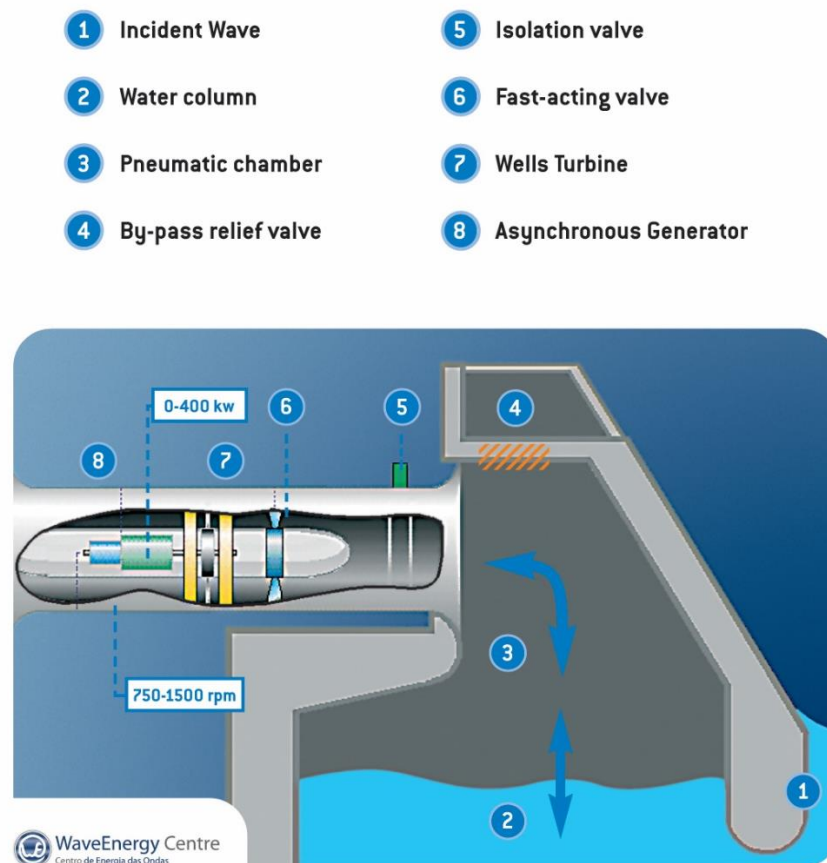


**Figure 3.2** Cross sectional schematic of the Pico OWC structure and machinery. Figure is taken from (Save\_Pico\_Powerplant.org, 2013).

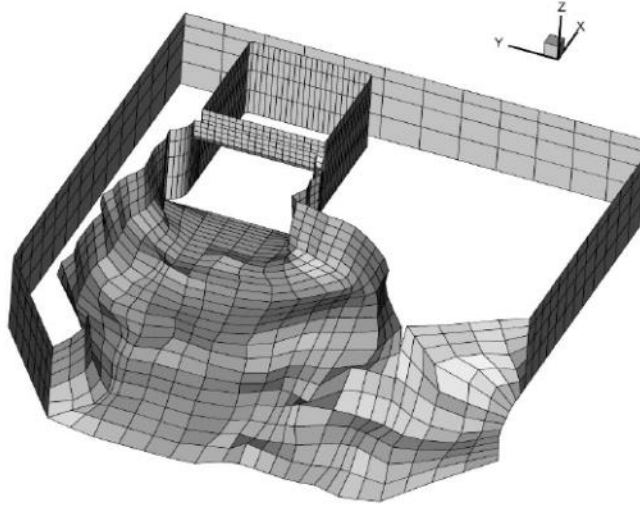


**Figure 3.3** Grid representation of the local bathymetry and structure as used in (Brito-Melo, et al., 2001) for BEM analyses of the plant specific wave transfer functions.

### 3.3.2 Wells turbine

The Pico plant uses a Wells turbine which is self-rectifying, meaning that the tangential component of lift force (driving rotation) is in the same direction regardless of the axial air flow direction. A detailed description of the Wells turbine theory can be found in (Gato & Falcao, 1988), for example. Wells turbines operate by taking advantage of the relative airflow velocity  $W$ , which is the vector sum of the driving airflow velocity  $v_a$  and turbine tip velocity  $U$  (when the turbine has a non-zero angular velocity) and the angle of attack  $\alpha$  formed between  $W$  and orientation of the turbine blade plane (which lies on a plane with  $U$ ), as shown in figure 3.4 and described by (3.1, 3.2, 3.3 and 3.4). At high speeds, this effect permits axial symmetry of the turbine blades, which is needed for force rectification of reciprocating flow.

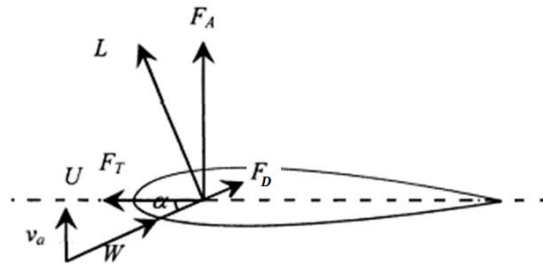


**Figure 3.4** Force and air velocity vector diagram for a Wells turbine blade (shown as a cross section).

where  $L$  is the generated lift force,  $F_t$  is the tangential force component of lift,  $F_A$  is the axial force component of lift and  $F_D$  is the aerodynamic drag force.

$$W = \sqrt{U^2 + v_a^2} \quad (3.1)$$

$$\tan \alpha = v_a/U \quad (3.2)$$

$$F_T = L \sin \alpha - F_D \cos \alpha \quad (3.3)$$

$$F_A = L \cos \alpha - F_D \sin \alpha \quad (3.4)$$

The force components  $L$  and  $F_D$  depend on the aerofoil profile and blade dimensions. The tangential force component of lift  $F_T$  is used to accelerate the turbine whilst the axial force component  $F_A$  is of no benefit and adds thrust loading to the shaft bearings and power dissipation through additional friction.

The Wells turbine at the Pico plant has the following specifications;

- 8 bladed rotor
- External diameter  $D = 2.3$  (m)
- Internal diameter  $D_i = 1.36$  (m)
- Constant cord length  $c = 0.375$  (m)
- Blade profile transitions continuously from NACA 0015 at the hub to NACA 0012 at the tip
- Moments of inertia of rotating elements  $I = 600$  (kg m<sup>2</sup>), which due to its large value acts as a flywheel for short-term energy storage and power smoothing to the grid.
- Two fixed sets of 59 cylindrically shaped, variable cord, guide vanes either side of the turbine. The generator side guide vane set is in place intermittently due to repeated fracturing from aerodynamic loading from stall (which is discussed in detail later).
- Turbine shaft is supported at either side of the turbine by bearings rated to withstand aerodynamic thrust of 22 (kN)

The turbine performance characteristic are most easily defined in non-dimensional terms (Dixon, 1978) and these were found from laboratory based testing on a small scale turbine with equal dimensional ratios to the full sized Pico turbine (Gato, et al., 1996). The non-dimensional quantities used to define the turbine characteristics are given in (3.5, 3.6 and 3.7) and the interrelationship between these non-dimensional quantities, as found for the small scaled turbine under laboratory conditions, is shown in figure 3.5.

$$\Psi = \frac{p_c}{\rho_0 N^2 D^2} \quad (3.5)$$

$$\Phi = \frac{\dot{m}_t}{\rho_0 N D^3} \quad (3.6)$$

$$\Pi = \frac{P_t}{\rho_0 N^3 D^5} \quad (3.7)$$

where  $N$  is the turbine angular velocity ( $rad\ s^{-1}$ ),  $D = 2.3$  (m) is the turbine diameter (for the Pico wells turbine),  $\dot{m}_t$  is the mass flow rate of air past the turbine,  $\rho_0$  is the density of air at atmospheric pressure,  $\Psi$  is the non-dimensional pressure head between the chamber and the atmosphere,  $\Phi$  is the non-dimensional flow rate past the turbine,  $P_t$  is the real power transfer to the turbine and  $\Pi$  is its non-dimensional equivalent.

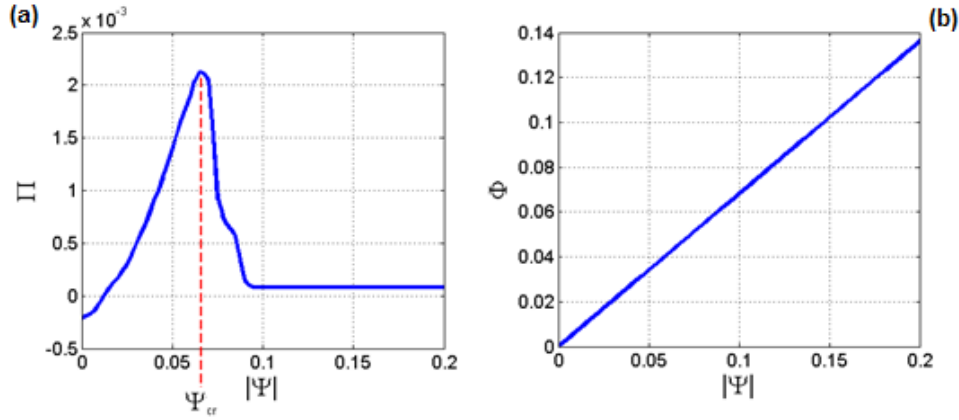


**Figure 3.5** Pico wells turbine characteristic curves for a down scaled version of the Pico Wells turbine found from laboratory testing as given in (Gato, et al., 1996) with (a) the relationship between non-dimensional pressure head and non-dimensional power transfer to the turbine with an indication of the threshold for turbine stall ( $\Psi_{cr}$ ), and (b) the relationship between non-dimensional pressure head and airflow rate past the turbine.

The main strength of the Wells turbine design is that it can be used in reciprocating flow without pivoting turbine blades or rectification of the air flow and is by far the simplest turbine design for use with OWC systems. However, the Wells turbine has a distinctly undesirable effect in that if the angle of attack exceeds the critical threshold  $\alpha > \alpha_{cr}$  flow separates over the blade and stall occurs. This results in a significant reduction or a complete loss of lift force. The angle of attack is found with;

$$\tan \alpha = \frac{v_a}{U} = \frac{v_a}{rN} \quad (3.8)$$

where  $r$  is the radius which is the distance from a point on the leading edge of the blade to the centre of rotation, and  $N$  is the turbine angular velocity.

For the Pico turbine the threshold for stall is  $\Psi_{cr} = 0.067$ , and at this level of non-dimensional pressure the flow begins to separate at the section of the blade closest to the turbine axis, as this location on the blade has the lowest  $U$  and consequently the highest  $\alpha$ . As  $|\Psi|$  increases beyond  $\Psi_{cr}$  flow separation spreads radially from the axis of rotation along the blade, until full separation occurs across the full length of the blade at  $|\Psi| \approx 0.1$ , as seen in figure 3.5. So whilst the available pneumatic power increases with chamber pressure (increases of  $|\Psi|$ ), the transfer efficiency of aerodynamic to mechanical power drops rapidly with increasing pressure past  $|\Psi| > \Psi_{cr}$ .

### 3.3.3 Generator

The turbine is connected in series (via a shaft) to a doubly fed asynchronous induction generator with a nameplate plate maximum output rating of 400 (kW). The generator is located within the inner turbine duct on the atmosphere side of the turbine. The doubly fed induction generator is used because it can act as a motor initially to speed up the turbine to its synchronous speed of 73 ( $rad\ s^{-1}$ ), which is a more receptive range for the typical airflow rate exposure. Also, the generator selection was based on the ability to operate at a broad range of rotation speeds (with a specifiable electrical power take-off) which is needed for the system to adapt to the temporal change in incident wave energy. These changes are short term fluctuations from wave grouping and longer term variations due to changes in the sea state.

To reduce current harmonics, both the "Y" and "Δ" winding configurations are present in the rotor (as shown in figure 3.6) having a 30° electrical phase difference thus damping harmonic peaks through current superposition. A 12-pulse diode rectifying bridge is located on the rotor so that the rotor output current is DC. The stator windings outputs AC which is phase and voltage matched with the local electrical grid.

### 3.3.4 Inverter

The output current from the generator rotor is single phase variable voltage DC and needs to be inverted to three-phase AC and voltage and frequency matched with the local electrical grid before delivery. To achieve this conversion 6 insulated-gate bipolar transistors (IGBTs) are used with Pulse width modulation which is driven by a controller. A schematic of the inverter system is given in figure 3.6.

\*Figure removed from this edited version because copyright authorisation was not gained\*

**Figure 3.6** Electrical schematic of power electronics system consisting of a generator and inverter. Schematic is from (European wave energy pilot plant on the island of Pico, 1999).

### 3.3.5 Basic system control

#### 3.3.5.1 Power take-off control

The electrical power take-off of the machine is prescribed through the inverter system controller as a function of turbine angular velocity  $N$ . As discussed before, because of vibrations in the turbo-generator system and the downgrade of the power electronics, the maximum turbine speed must be limited to around  $N = 141 \text{ (} \text{rads}^{-1}\text{)}$ . This is in part the reason why the theoretical optimised power take-off curves specified in (Falcão, 2002) have not yet been implemented. Only two curves have been approved for use by the power electronics supplier and electrical partner EFACEC. One is for very low energy sea states and one for medium to high energy sea states. The power take-off control laws are characterised by a rotational speed region of zero power take-off initially to allow the machine to speed up to a more optimum range than the synchronous speed achievable in motor mode. This is followed by a period of gradually increasing power take-off in the main production region, and finally a very sharp increase in power take-off acting as a strong electro-magnetic break to limit the maximum rotational speed of the machine. The power take-off control laws are seen in figure 3.7, and discussed in more detail later in this chapter.

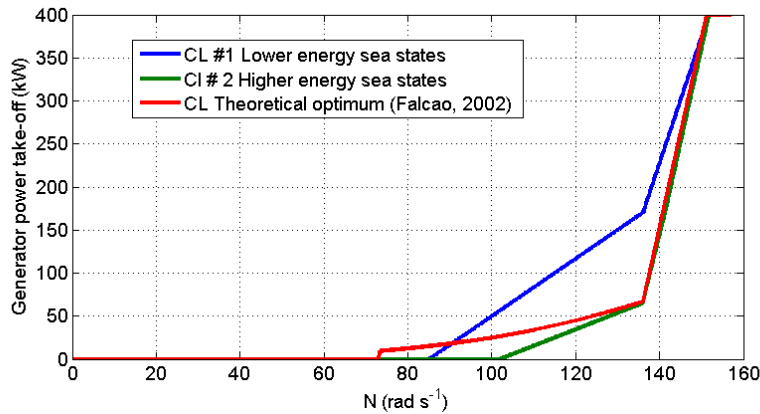


**Figure 3.7** Power take-off control laws (CL) used at Pico and the theoretical optimum as described in (Falcão, 2002).

Power take-off curve #1 was implemented primarily in reaction to the high vibrations before the turbo-generator structure was reinforced. Power take-off curve #2 is now used almost all of the time because of the increase in turbine stall events associated with power take-off curve #1, which yields low turbine speeds and a low stall threshold which is more frequently and severely breached. However, occasionally in low energy sea states, or very regular sea states (low wave groupiness) power take-off curve #1 can yield slightly higher power production.

### 3.3.5.2 Pressure control using by-pass relief valve

Rudimentary control of chamber pressure is achieved with a by-pass relief valve mounted in parallel to the turbine which connects the chamber to the atmosphere. The relief valve is similar in design to a sluice gate and is actuated by a slow moving hydraulic ram. The maximum aperture of the relief valve is  $A_v = 1.3 \text{ (m)} \times 1.3 \text{ (m)}$  and can be used to vent over-pressure, or minimise under-pressure, and to adjust the longer-term variance in chamber pressure. In this fashion the chamber pressure variance and peak values can be somewhat tailored to the optimum (which will be discussed later) with slow changes in the incident wave energy associated with varying sea states.

Although not specifically designed for continuous operation, the relief valve aperture could be adjusted slowly but continuously to improve the short-term chamber pressure variance to help optimise performance. This is one of the main focuses of this research and will be considered in detail later in chapters 5, 6 and 7. As a preliminary point of interest the existing capacity of the relief valve aperture adjustment system is reviewed in the following.

The rate of aperture adjustment is determined by the pressure and flow rate of hydraulic oil outputted by the hydraulic pump connected to the relief valve aperture adjustment ram. Also, the relative pressure difference between the chamber and the atmosphere causes a reaction force between the relief valve gate and the top and bottom flanges of the guide frame, which causes frictional resistance to the adjustment. The pumped hydraulic pressure is the same for both stroke directions but the cylinder volume for the part of the ram used to increase the valve aperture is smaller due to the presence of the internal piston rod. This results in a reduced force exerted on the valve gate in that direction as described by figure 3.8 and (3.9) and (3.10).

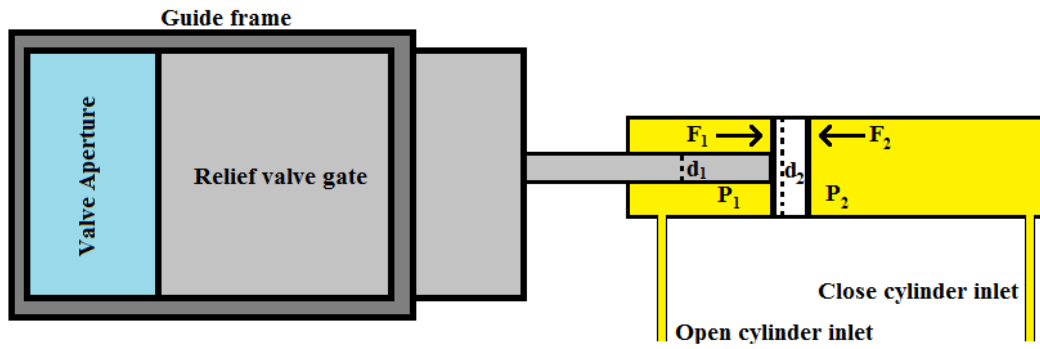


**Figure 3.8** Schematic of relief valve and actuating ram system.



**Figure 3.9** Picture of actual relief valve with fully open aperture.

$$F_1 = \frac{\pi(d_2^2 - d_1^2)P_1}{4} \quad (3.9)$$

$$F_2 = \frac{\pi d_2^2 P_2}{4} \quad (3.10)$$

Monitoring the relief valve in actuation over a broad range of chamber pressure conditions yielded a maximum of 22 (s) to pass from fully opened to fully closed aperture. If the aperture state  $k_v$  is 1 for fully opened and 0 is fully closed, the minimum aperture state closing rate is  $\dot{k}_{v,c} = 0.0454 \text{ (s}^{-1}\text{)}$ . The maximum travel time to pass from fully closed to fully open is 26 (s) giving a minimum aperture opening rate of  $\dot{k}_{v,o} = 0.0385 \text{ (s}^{-1}\text{)}$ . These times were found to be up to 6 (s) shorter because the opposing frictional resistance between the gate and the guide frame which is dependent on chamber pressure and is not constant. The maximum travel times (slowest rate of aperture change) will be used in the remainder of this study for the non-hypothetical relief valve control strategies considered, as it represents the worst case scenario.

### 3.3.6 System survival and protection

The mechanical system can be isolated from pneumatic power exposure by two valves mounted in series with the turbine, both are actuated by pneumatic rams. A slower acting ‘guillotine’ valve consisting of a large sluice gate is used to isolate the turbine duct from the chamber. It has an open stroke time of approximately 25 (s) and close stroke time of approximately 10 (s). A second faster acting “butterfly” valve consisting of a series of pivoting paddles which interlock to close the duct. This valve is located

between the guillotine valve and the turbine. The stroke time is approximately 3 (s) in both directions. The valves are used to isolate the turbine from power exposure when the machine is speeding up, when operation is to be terminated, at a grid power failure or if any system alarms are triggered. An independent security system was implemented as a redundancy for the automatic operation mode and isolates the machine using these valves in the case of any detected warning signals.

### 3.3.7 Data capture

One of the original purposes of the Pico plant project was to validate the theoretical system equations and design methodology. As such a wealth of system variables are monitored. These are;

- 1.) Water surface elevation in the chamber – Single point measurement near the centre of the chamber using an ultrasonic echo from a transducer mounted on the chamber roof. The maximum sampling frequency is low at 1 (Hz), with a maximum resolution of 0.2 (m)
- 2.) 2 x Static chamber pressure – Located at the lower step of the chamber roof
- 3.) 4 x Static duct pressure – Either side of the turbine at the inner and outer radiuses of the duct
- 4.) 4 x Dynamic duct pressure – Either side of the turbine at an outer and central radius of the duct cavity
- 5.) Turbine rotational speed
- 6.) 2x Vibration velocity – Measured at the generator side and chamber side turbine shaft bearings
- 7.) Active power
- 8.) Reactive power
- 9.) Near-shore hydrostatic pressure – Single point measured 60 (m) up wave of plant
- 10.) Near-shore water column flow velocity – Acoustic Doppler profile of water column measured 60 (m) up wave of plant

Due to the background electrical noise, significant interference exists in the data. This has been dealt with more recently by increasing the capture sampling frequency to 50Hz so that the data can be pre-filtered more effectively before logging at a frequency  $f_s = 2Hz$  (to minimise the total data size).

### 3.4 Local wave climate

It is essential to assess the local wave climate before a WEC is designed. This allows the dimensions of the device to be tailored to amplify the dominant local wave energy spectra and/or maximise the energy conversion. As with most WECs, optimisation of the energy resource is achieved primarily through the promotion of resonance resulting in amplification at the dominant frequency of the wave climate. The wave climate has been characterised for the Pico plant locality and this can be found in (Brito-Melo, et al., 2001). However, it is not stated where or how these measurements were made and only covers part of the possible sea state range known to exist at this locality i.e. no occurrences of essentially zero wave height which is often seen in summer.

Even after the initial construction, a secondary assessment of the wave climate is desirable to evaluate the modified hydrodynamic behaviour and to validate the original hydrodynamic transfer theory. A secondary assessment can also be used to aid the design of any retrofitted control strategies, which should be

optimised to the resultant modified hydrodynamics. Since the publication of (Brito-Melo, et al., 2001) new data sources have become available which need consideration to build a more complete analysis of the local wave climate and hydrodynamic response. These new data sources are the recorded chamber surface elevation and near-shore hydrostatic pressure, which both offer alternative ways to characterise the wave climate at or very close to the Pico plant site.

To assess the wave climate at the Pico plant four different data sets are considered.

- 1.) Metocean data with grid domain point located 8.8 (km) up-wave location of the Pico plant
- 2.) Hydrostatic pressure data captured at a location 60 (m) up-wave of the plant front wall
- 3.) Recorded chamber surface elevation data at the plant
- 4.) Chamber surface elevation as calculated from other plant system variables using well established OWC theory.

Each data type offers particular advantages and disadvantages, with none being ideal, and these will be discussed at the appropriate points. The data availability in time is shown in figure 3.10.

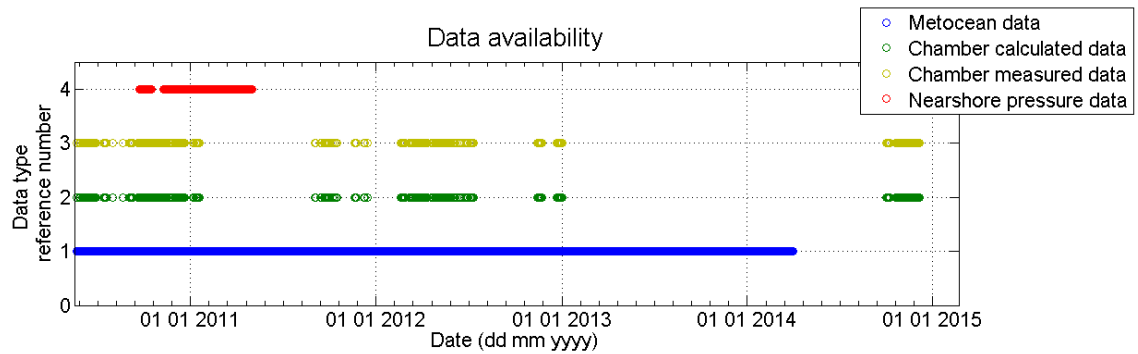


**Figure 3.10** Timeline representation of the availability of different data sources for wave climate analysis. It should be noted that the metocean data extends back to 1979 but this is not shown.

### 3.4.1 Hindcast metocean data

The Pico plant resides at the global coordinate reference of N(38.560046), E (-28.441899). The Institute of the University of Cantabria (IH Cantabria) provide a freely available numerical wind wave reanalysis data base called IHdata. The data set contains a historical time series reconstruction of hourly statistical representation of ocean wave spectra at all maritime locations on the globe, using the spectral model WaveWatch III (Tolman, 1989), (Tolman, 1991) developed at NOAA-NCEP, which solves the spectral action density balance equation for wave number directional spectra.

A 35 year hourly time series data set was selected from the GOW (Global Ocean waves) Azores regional domain dataset at the model domain grid point with its centre at N(38.625), E(-28.50), which is the closest that could be obtained due to the coarse spatial grid resolution of  $1/8^\circ$  longitude by  $1/8^\circ$  latitude ( $\sim 14\text{km}$ ). The distance between the model grid point centre and the plant site is 8.8 (km) as indicated in figure 3.11.

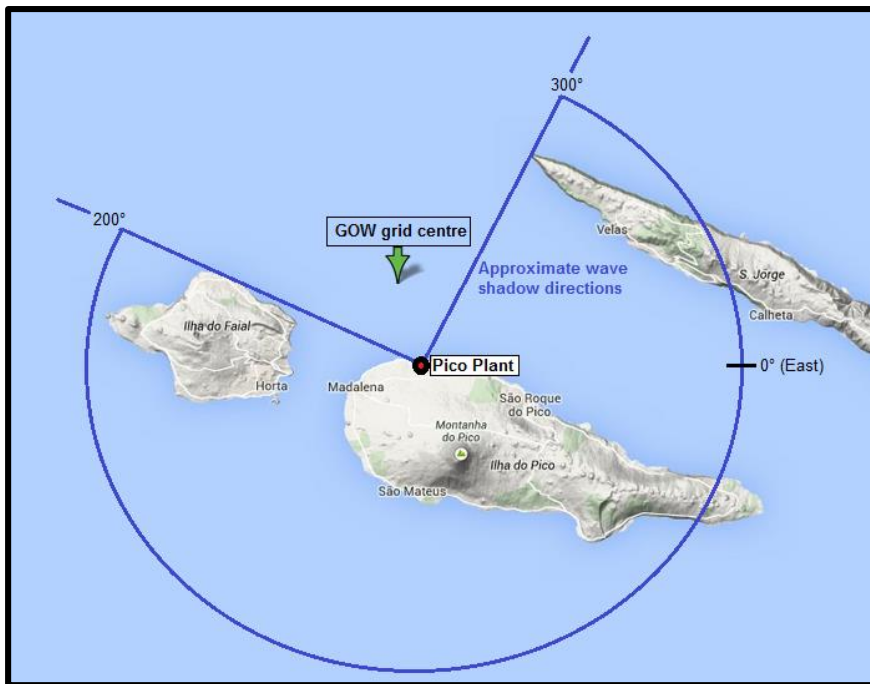


**Figure 3.11** Local area map indicating the location of the Pico plant, the location for the grid point centre of the used “GOW Azores” hindcast metocean data set, the distance between the two locations and approximate wave direction shadow lines cast by the neighbouring islands (from google maps).

The advantage of metocean data is that a very long and continuous data history is available (35 years in this case). The disadvantage is that the nearest model grid domain location is a significant distance from the plant location. Because of the complex arrangement of neighbouring islands and the wave shadows that they cast, only metocean data points with wave directions outside of the island shadow regions will have any reasonable bearing on the resultant wave climate at the plant site. Also wave transformations due to the bathymetry between the metocean data grid point location and the plant site will not be accounted for.

The 35 year wave climate in terms of wave height and directional density from metocean data is described by a wave rose diagram in figure 3.12. Also, figure 3.12 provides the occurrence frequency of sea states falling into significant wave height bin interval of 0.5 (*m*) and peak period bin interval of 1 (*s*). This analysis is given in two formats, one using all data, and the other with the removal of all data points where the dominant wave direction falls within the approximate island shadow regions. This of course is a rough approximation but is done only to illustrate the expected shift in the wave climate occurrence frequency at the plant site. A more suitable method for transferring the metocean data to the resultant wave climate at the plant site is to nest a local area wave propagation model such as SWAN, using the metocean data as the domain boundary input. In this way the wave transformation resulting from the local bathymetry can be accounted for at the same resolution as the available bathymetric data. However, this analysis has already been performed and can be found in (Le Crom, et al., 2011), which (in particular) shows as expected the importance of wave directionality with regards to the relationship between offshore and near-shore sea state transformations.

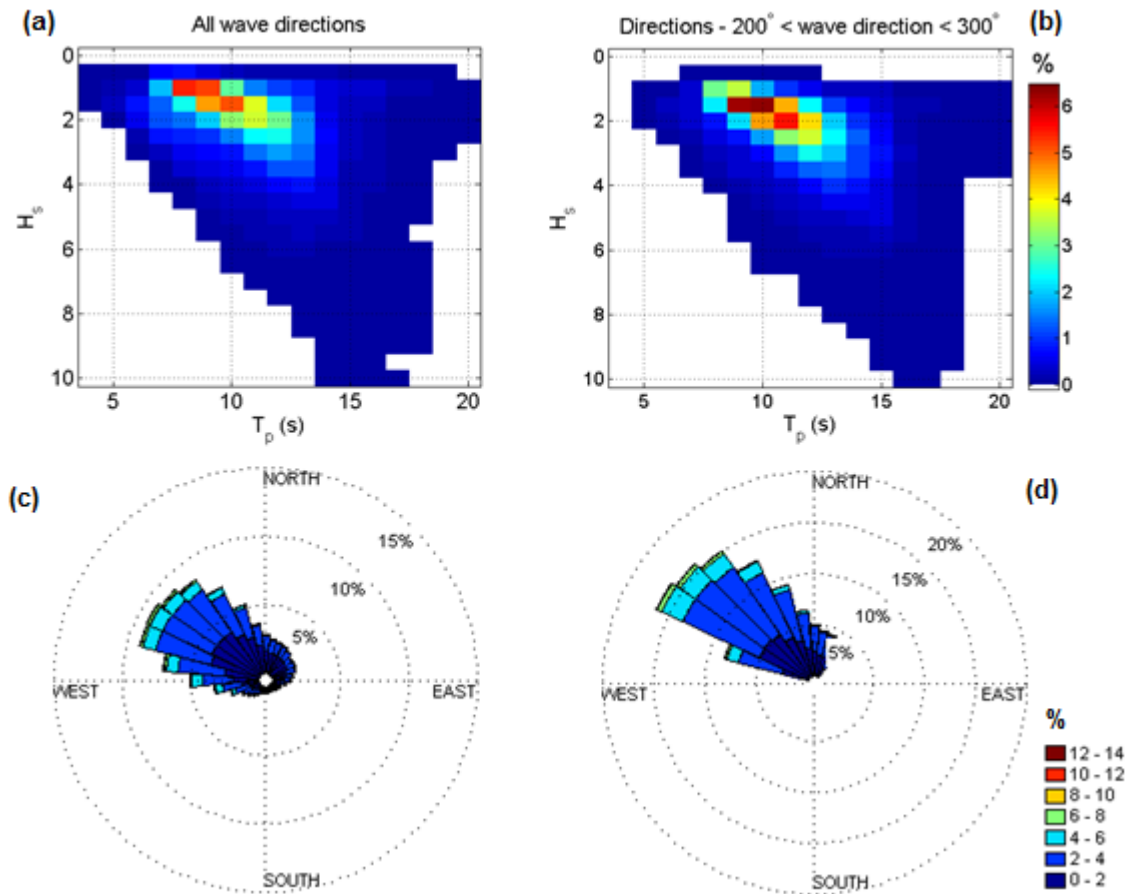


**Figure 3.12 (a, b)** Sea state occurrence frequency and **(c, d)** wave direction and significant wave height occurrence frequency, from metocean with **(a, c)** all data points considered and **(b, d)** data points with dominant wave directions that fall within the neighbouring island wave shadow zones removed.

It is seen in figure 3.12, with the removal of the dominant wave directions that fall into the island shadow zones, the sea state frequency of occurrence makes a small but notable shift towards higher  $H_s$  and longer  $T_p$  sea state characteristic pairings. The dominant wave sea states surround the  $H_s = 2 (m)$  and  $T_p = 11 (s)$  mark. However, the sea states that diverge significantly from this concentration collectively total a significant proportion of the wave climate. For example 24% of sea states fall outside the range  $[1 \leq H_s \leq 3, 8 \leq T_p \leq 14]$ . This means that the plant design can be optimised for a fairly narrow sea state range, and this will encompass a large proportion of the wave climate. But, a significant proportion of the wave climate will also be far from this optimal range. In these cases, advanced control strategies should be investigated to avoid performance depreciation.

### 3.4.2 Chamber surface elevation

A significant amount of system data has been collected at Pico. Previously data was primarily only collected when the plant was operational. More recently data is collected at all times for wave climate analysis and to gain more continuous data time-series to use as an input to drive the plant system model for long term analysis.

The chamber surface elevation can be used to characterise the modified wave climate at the plant. It is a modification because the plants structural presence and the effect of the air pocket bounded by the chamber affects the internal (chamber) wave dynamics. The surface elevation time series in the chamber

is a modification of the incident surface elevation time series (if no plant was present) due to two main mechanisms as described in (Falnes, 2002), for example. Firstly, superposition of reflected waves from the chamber back wall and incoming waves creates a frequency dependent modification of the surface elevation time series by superposition which forms a standing wave. Secondly, the chamber pressure has a spring like effect which results in radiated waves, adding further complexity and modification to the chamber surface elevation through superposition. Other more complex phenomenon like vortex shedding and dissipation, resulting from hydrodynamic flow interaction with the lip of the chamber front wall, also act to further modify the chamber hydrodynamics as investigated experimentally in (Morrison & Greated, 1992) and numerically in (Zhang, et al., 2012).

At the Pico plant, chamber surface elevation is measured using an ultrasonic transducer mounted in the roof of the chamber. A pulse is emitted and the time to receive the echo is used to calculate the distance. Unfortunately, the chamber surface elevation measurements are typically poor. Typically larger wave peaks and troughs are amplified, with the frequency of anomalous data points increasing with higher energy sea states and with lower tide levels. An example of this effect is shown in figure 3.13. The reason for this data deterioration is not known but amplification of wave troughs may be a result of the non-uniform surface level which could cause indirect backscatter of the ultrasonic pulses which miss the receiving transducer or take an indirect path. The amplification of wave peaks maybe an effect of wave breaking in the chamber which occurs for larger wave amplitudes and which becomes more significant at lower tides. This could result in a mass projection of water or an excess of airborne spray that is registered higher in the chamber and interpreted as a wave peak. The problem is exacerbated by the sensor's low minimum sampling frequency of 1Hz which limits the effectiveness of data filtering.

An alternative approach is to model the surface elevation using an inversion of the well documented OWC theory given in (Falcão & Justino, 1999) from high accuracy measurements of chamber pressure, turbine rotational speed and relief valve aperture. This method requires an extensive explanation and this will be given in detail later in section 5.2.1. However, for the readers benefit at this stage a comparison of the calculated chamber surface elevation and the recorded surface elevation is given in figure 3.13.

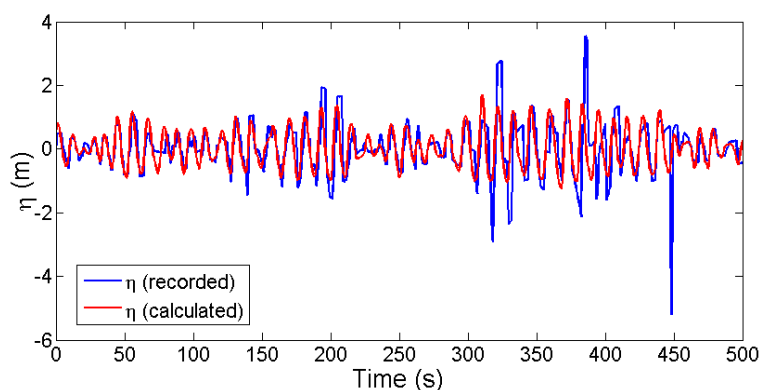


**Figure 3.13** Example time series comparing the observed and calculated chamber water surface elevation  $\eta$  for a time period where (towards the left) the wave amplitude is low and the recorded  $\eta$  values agree, and (towards the right) the wave amplitude is higher and the recorded  $\eta$  has clearly anomalous values and diverges from the calculated  $\eta$ .

The plant modified sea state occurrence frequency, calculated from the chamber surface elevation, for both the recorded and calculated data is given in figure 3.14. As expected there is a significant increase in the occurrence frequency for sea states with higher  $H_s$  when recorded data is considered (due to intermittent signal amplification).

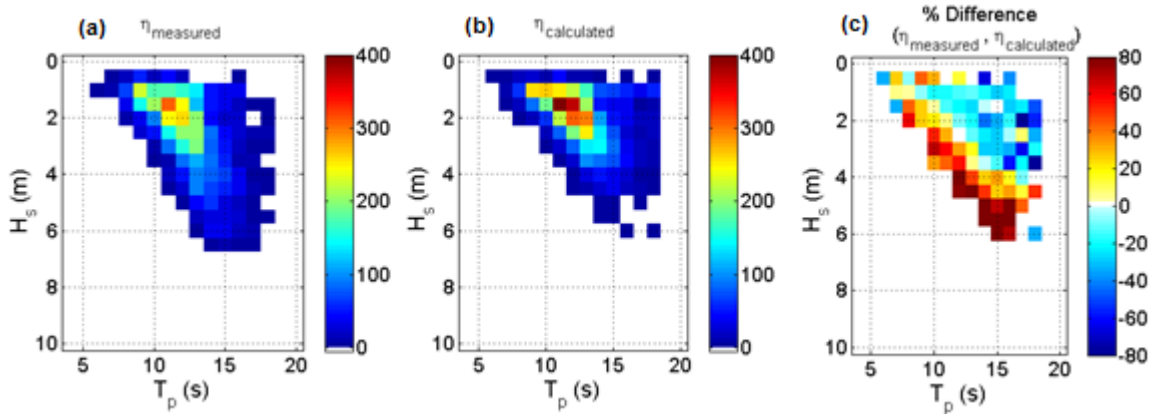


**Figure 3.14** Occurrence frequency of the modified sea state as described by plant chamber data for (a) the recorded chamber surface elevation and (b) the chamber surface elevation calculated from other system variables. (c) Gives the percentage difference of occurrence frequency between the measured and the calculated modified sea states (+ is greater occurrence from directly measured surface elevation data).

### 3.4.3 Near-shore hydrostatic pressure measurements

The final available data resource option for making a wave climate assessment is the hydrostatic pressure measurements made at the a single point on the sea bed (in approximately 8-9 meters water depth) at a location approximately 60 (m) up wave of the chamber front wall. Initially the sensor was deployed with a data communications cable but this was severed almost immediately by boulder movement. As such the sensor was deployed in a self-contained manner recording data internally. It was then retrieved at regular intervals to extract the data before re-deployment. Due to the harsh wave climate the windows of opportunity to perform the retrieval and re-deployment process were limited. Also because of the high expense involved in the operation (requiring scuba divers) it was only performed over a limited period (approximately 7 months total).

The measured hydrostatic pressure can be used to calculate the water depth at the sensor and therefore the approximate water surface elevation, vertically above the sensor as described by;

$$\eta_{uw} = z - z_0 = \frac{p_{uw}}{\rho_w g} - z_0 \quad (3.11)$$

where  $z$  is instantaneous water depth of the sensor (or water column height above the sensor),  $z_0$  is the mean water depth of the sensor at still water,  $p_{uw}$  is the hydrostatic pressure measured at the up-wave sensor location,  $\rho_w$  is the density of sea water and  $g$  is the acceleration due to gravity.

The up-wave data availability is from 21/09/2010 till 17/10/2010 and 08/11/2010 till 02/05/2011, sampled over 35 minute intervals every 3 hours. This covers the majority of the seasonal operation period for 1 year (as waves are typically too low for production between June and August). However, it is too short to make a robust assessment of the wave climate near the plant site, which requires several years of data to

account for inter-annual variability but it is still interesting to assess the sea state frequency of occurrence, as interpreted by this method, and this is seen in figure 3.15.

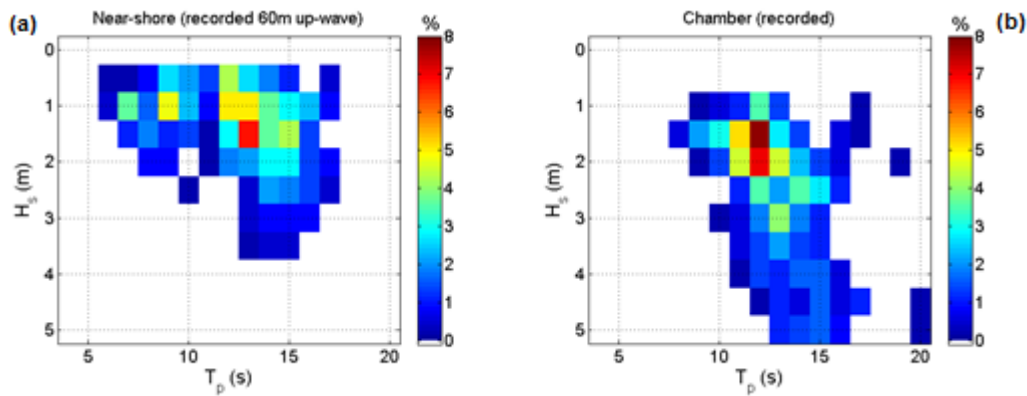


**Figure 3.15** Sea state occurrence frequency as measured by (a) the near-shore hydrostatic pressure sensors and (b) the recorded chamber surface elevation, over the same time period.

As seen in figure 3.15 the surface elevation measurements made in close proximity to the plant yield strikingly different wave climate observations. Two main effects are responsible for this deviation. Firstly, reflected and radiated wave interference at the up-wave location acts to modify the observed sea state. The peak period occurrence frequencies for the up-wave location are centralised about two wave period bin intervals;  $T_p = 9$  (s) and  $T_p = 13$  (s), whilst the chamber surface elevation has one clearer nucleus about the  $T_p = 12$  (s) data bin. Secondly, the wave height is seen to be far lower for the up-wave measurement location which is most likely to be due to wave height amplification from incident and reflected wave interference in the chamber. These effects are investigated further in the following.

The near-shore data can also be used in conjunction with the chamber surface elevation data to assess the wave transformations between the near-shore and the chamber. The relevant transformations are;

- Oscillation damping from the emission of radiated waves from non-zero chamber pressure head (Falnes, 2002)
- Wave shoaling which is the response to the retardation of group velocity as waves enter shallow water due to the non-dispersive shallower water limit, which through the conservation of wave energy flux results in an increase in wave energy density (wave height) (Phillips, 1977), (Mei, 1989)
- Attenuation from energy dissipation through friction and turbulence

In addition to these transformations, frequency dependent amplification occurs through the superposition of incident waves and waves reflected by the chamber back wall. This behaviour is described in (Lee, 1971), which shows that for a square harbour (or in this case a square chamber) the peak amplification occurs when;

$$xy = \frac{\lambda}{2\pi} \quad (3.12)$$

where  $xy$  is the horizontal internal dimensions of the square chamber and  $\lambda$  is the wave length

For the Pico plant case where  $xy = 12$  (m), and from the dispersion relationship and the chamber water depth, gives a peak amplification factor when waves have a period  $T \approx 11.5$  (s).

To assess the relationship between wave frequency and the amplification of wave height between what is measured in the near-shore  $H_{uw}$  and later in the chamber  $H$ , all existing operational data for which the corresponding up-wave pressure measurements exist (around 35,000 wave cycles recorded in the chamber) was used and the wave statistics are given in figure 3.16.

However, because the hydrostatic measurements were made at a single point only, there is no way to differentiate between the different wave directional components. As such it is impossible to extract the incident wave from the superposition formed between the incident wave and waves reflected from the plant and surrounding coastline (predominantly cliffs with high reflectivity), and radiated waves from chamber pressure. This means measured up-wave wave height  $H_{uw}$  will be a modification of the true incident wave height, and the ratio of  $H$  (chamber wave height) and the true un-modified  $H_{uw}$  will likely differ significantly.

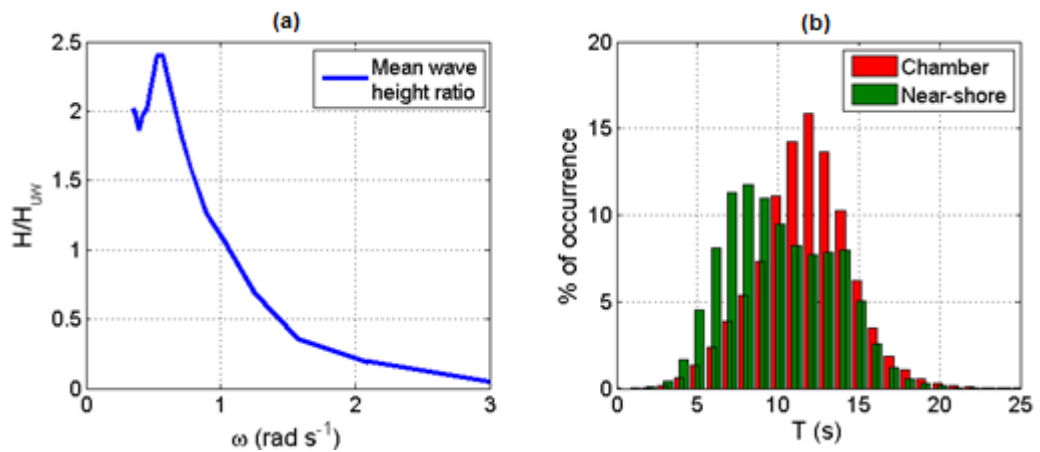


**Figure 3.16** (a) Mean ratio of measured chamber wave height and up-wave wave height. (b) Histogram giving the total number of zero up-crossing wave periods for a 1 (s) wave period bin interval, as a percentage of the total number of wave periods, as measured in the chamber (red) and the up-wave sensor location (green).

In figure 3.16 (b) a histogram shows the total number of up-crossing wave periods, for 1 (s) wave period bin intervals, as a percentage of the total number of wave cycles in the data set. This representation can also be used to qualify the effect of interference at the up-wave sensor location from waves reflected and radiated from the plant. The spectral shape is seen to differ significantly between the two locations with the up-wave location taking a bi-modal form. Waves reflected from the plant interfere with the incident waves at the up-wave sensor location causing additional zero crossings and shift the spectral profile to a high frequency.

### 3.4.4 Wave climate summary

An inter-comparison between the sea states calculated from the different data sources is presented in figure 3.17 as a sample time series between the dates 09/2010 and 02/2011 because this period has the best data overlap.

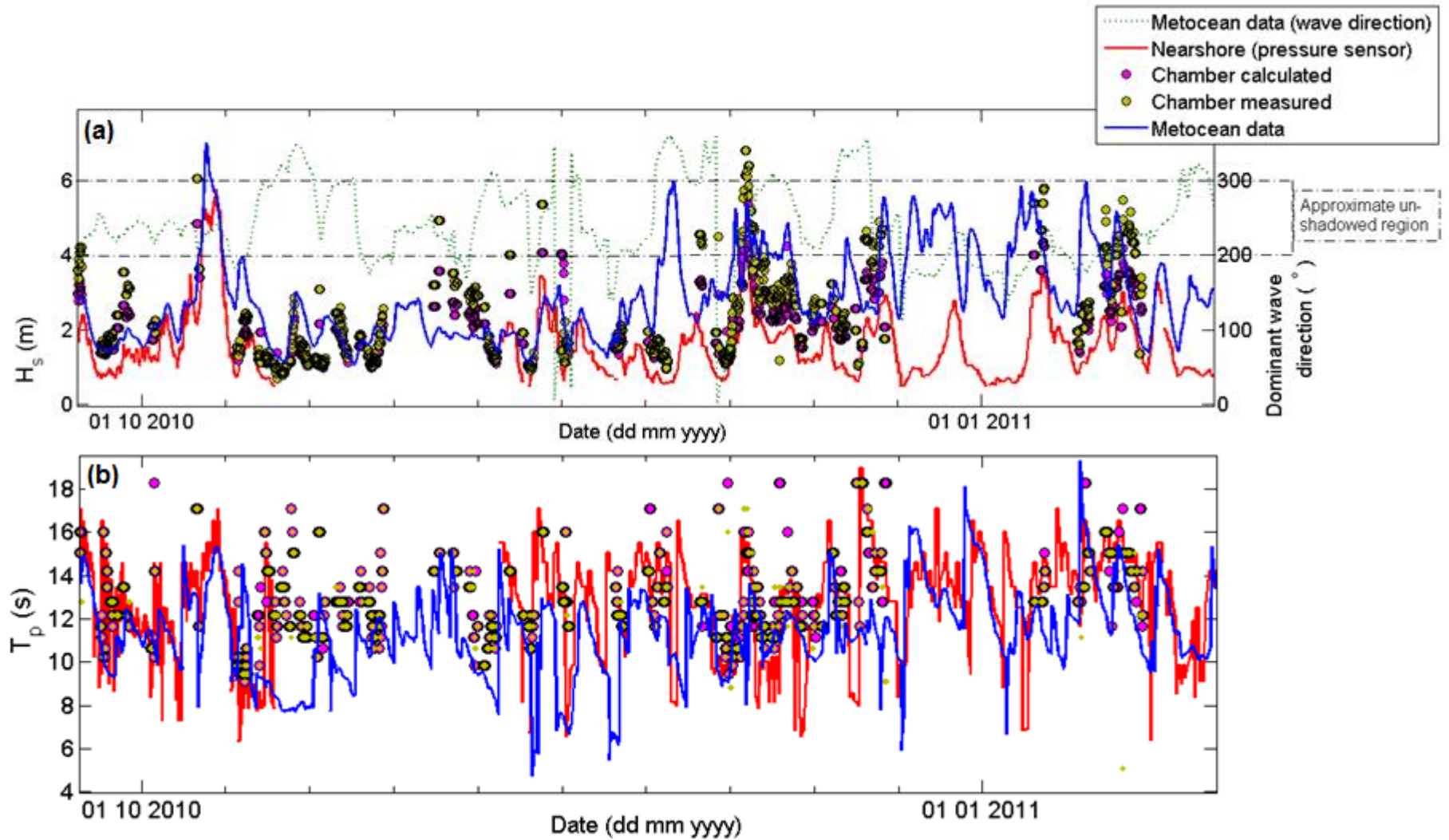


**Figure 3.17** Timeline comparison of sea states characterised over 1 hour time periods (except near-shore data which is 35 minutes), from; Metocean, chamber surface elevation (recoded and calculated) and near-shore hydrostatic pressure measurement, data sets. (a) Significant wave height, (b) peak wave period.

In figure 3.17 it is seen that the recorded and calculated chamber  $H_s$  diverge when  $H_s$  is higher but are in good agreement when  $H_s$  lower.  $H_s$  measured in the chamber is typically significantly higher than that measured in the near-shore due to frequency dependent amplification in the chamber. The relationship between the  $H_s$  for the metocean data and the data sources collected in close proximity to the plant is highly variable with a strong divergence when the dominant wave direction is within the shadow region, as would be expected, and a reasonable correlation in trend is seen when the dominant wave direction is outside the shadow zone. Generally good agreement is seen between the chamber measured and calculated  $T_p$  and that measured in the near-shore, showing that the peak period measured in the near-shore is not significantly affected despite the bi-modal frequency distribution resulting from reflected and radiated wave interference. However, the metocean data  $T_p$  diverges significantly from the other data at times. This is most true when  $H_s$  is small and this is probably because the sea state (at the metocean data location) is more susceptible to bi-modality from the combination of multiple swell which result in additional zero crossings, resulting in significantly lower values of  $T_p$ , as well as more prominent wind swell.

As seen in figure 3.16, due to the interference of reflected and radiated waves with the incident wave, the near-shore wave sensor measurements are significantly modified and are not considered to be of great value in characterising the local wave-climate or for characterising the hydrodynamic transfer between this location and the chamber. Also, because the recorded chamber surface elevation is prone to significant error in more energetic sea states and at low tide, it provides only an indication of the chamber hydrodynamics. The calculated chamber hydrodynamics seems to be the most useful option with regards to characterising the wave climate at the plant for the purpose of control strategy design, but due to the intermittent and somewhat limited data availability, long term performance analysis could be misrepresented.

In the light of these findings, it seems that the characterisation between the far off-shore metocean data and the calculated chamber hydrodynamics would be most useful. However, this transfer is complicated and will be affected by wave directionality, shallow water transformations and the chamber harmonics. As discussed before, modelling this transfer could be achieved by nesting a local area wave propagation model using the metocean data as the model boundary input, and then through the application of the plants hydrodynamic transfer functions. However, because a reasonable amount of plant data is available encompassing a broad range of sea state conditions, the far simpler alternative is to make a statistical association between the metocean data and the resulting plant hydrodynamics.

This is achieved by finding the relationship (as a function of dominant wave direction) between the significant wave height  $H_{s\ metocean}$  and peak period  $T_{p\ metocean}$  of the metocean data and the resultant mean significant wave  $H_s$  and peak period  $T_p$  of the calculated chamber surface elevation data. This relationship is given in figure 3.18 along with the respective standard deviation of all data points that falls into each data bin, so that the prediction confidence can be quantified.

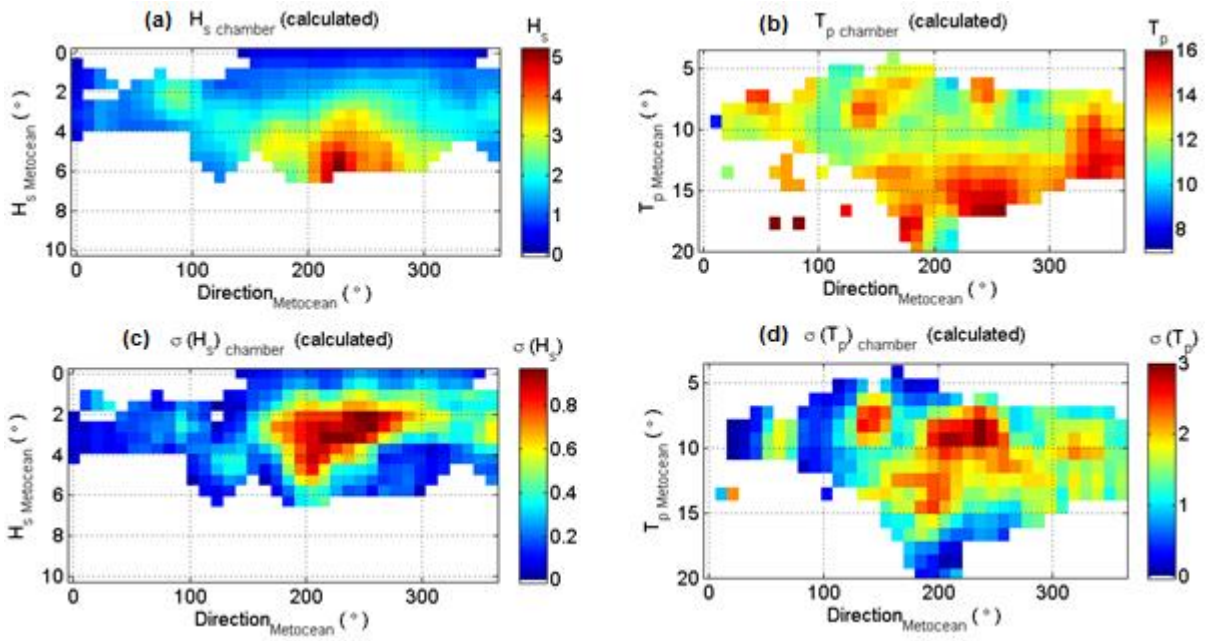


**Figure 3.18** Mean (a) significant wave height and (b) peak period, of the calculated chamber surface elevation as a function of significant wave height and peak period, respectively, from metocean data at the corresponding times. (c-d) The corresponding standard deviation of all points in each data bin, which can be used to assess the confidence in the statistical association.

It is seen in figure 3.18 that the relationship between the  $H_{s\ metocean}$  and  $H_s$  (chamber) is fairly consistent and a ratio almost equal to unity is found for the significant wave height values between the two locations when  $200^\circ < wave\ direction < 300^\circ$ , with  $H_s$  (chamber) falling significantly outside of this directional range. The relationship between the  $T_{p\ metocean}$  and  $T_p$  (chamber) is less consistent and this is almost certainly an effect of bi-modality of the wave spectra at the offshore metocean data grid point location, which will be affected more frequently and more severely by wind waves or by the overlap of ground swells propagating through the open channels between the islands (south channel about  $140^\circ$  and east channel about  $340^\circ$ ). For sea states of smaller  $H_{s\ metocean}$  the superposition of a secondary swell component will have a more notable effect on  $T_{p\ metocean}$  as it is more likely to cause additional zero crossings affecting the spectral peak frequency, and this is seen in the data. The confidence in the statistical association is indicated by the standard deviation which is seen to be quite variable and poor in some regions. As such this method is limited and will only provide an indication of the long term chamber wave climate.

Finally, the statistical association matrices in figure 3.18 can be used to extrapolate (in time) the expected long term chamber hydrodynamics characterised by the occurrence frequency of sea states, over the life of the plant so far (01/01/2000 – 31/03/2014), and this is given in figure 3.19 and will be used in the final analysis chapter to make projections of the long term performance of the proposed control strategies. The chamber sea state occurrence matrix for the life of the plant is formed by taking the occurrence frequency of all sea states for the metocean data (over the plant life period) that fall in to the data bins of size;  $H_{s\ metocean} = 0.5\ (m)$ ,  $T_{p\ metocean} = 1\ (s)$  and  $direction_{metocean} = 10\ (^\circ)$ , and then by finding the corresponding mean chamber  $\bar{H}_s$  and  $\bar{T}_p$  (as seen in figure 3.18) and then by totalling these occurrences in  $H_s = 0.5\ (m)$ ,  $T_p = 1\ (s)$  data bins.

It should be noted that in total 9% of the metocean data has been dropped because the corresponding  $H_s$  and  $T_p$  bin intervals do not exist in the available plant side data. However, it should be pointed out that the vast majority, if not all, of dropped data points corresponds to sea states where the plant would not be operational (hence the lack of data) due to either excessive or insufficient incident wave energy.

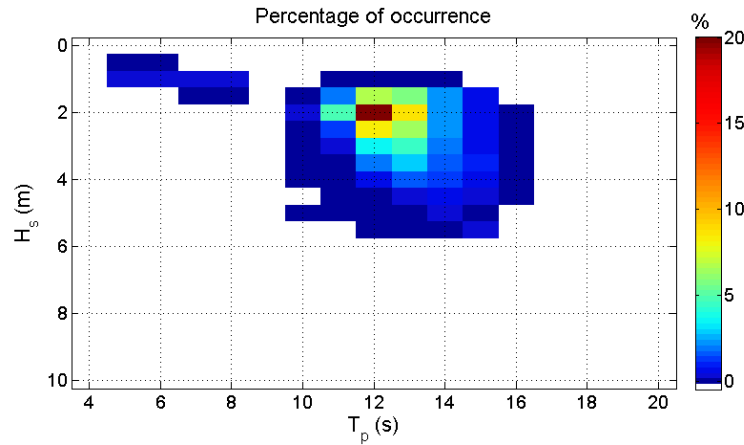


**Figure 3.19** Plant life time (14 years) wave climate frequency of occurrence for chamber surface elevation sea states found by statistically linking metocean data and chamber surface elevation data. The colour bar is nonlinear to resolve the region of smaller percentages of occurrence.

### 3.5 Basic controlled performance

Until recently the Pico plant was controlled in a rudimentary way using a basic power take-off control law and with minor adjustments ( $\pm 5\%$  of the total range) made to the relief valve aperture to keep the *RMS* real pressure within a relatively broad and somewhat optimal range. Controlling the relief valve based on *RMS* real pressure does not directly consider the turbine rotational speed which is an important factor of the system state. To improve this rudimentary control the relief valve aperture was adjusted by up to 5% increments every 15 minutes to try to match the standard deviation of non-dimensional pressure with optimum as described in (Falcão, 2002) and (Falcão & Rodrigues, 2002). Control in this fashion factors in the system state and optimises the plant performance in terms of what can be achieved without more advanced control strategies. This change was implemented in 04/2014 and a notable enhancement and stability of power output has been observed. This control strategy will be discussed in great detail later and will be used as a reference to compare the performance under more advanced relief valve control strategies.

The plant performance in terms of power production is assessed by the mean and maximum, mean power take-off achieved over 30 minute intervals, sorted by the chamber sea state in to bin intervals of  $H_s = 0.5$  (s) and  $T_p = 1$  (s) for all available operational data. The sea states are considered in two ways, firstly by using the recorded chamber surface elevation and secondly by the calculated chamber surface elevation. In order to calculate the chamber surface elevation (when operational) the relief valve aperture needs to be known, and because the sensor for this was installed more recently far less data exists for this analysis. The power matrix analysis is presented in figure 3.20.

It should be noted that to calculate the surface elevation when the machine is off-line the relief valve aperture is always fully open as part of the automatic sequence and this is why more calculated surface elevation data points are presented in figure 3.14 compared to figure 3.20.

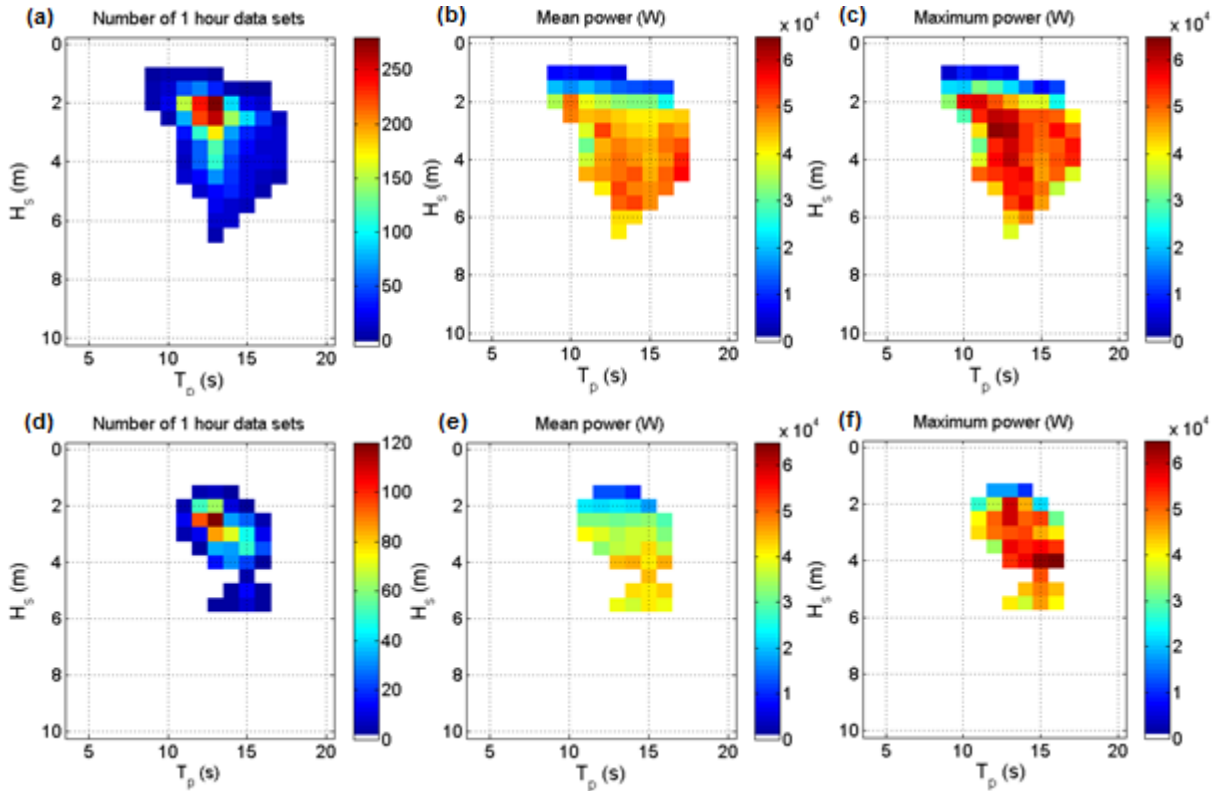


**Figure 3.20** Number of occurrence (a,d) total and mean (b,e) and max (c,f) power ( $W$ ) matrices using (a-c) the recorded chamber surface elevation and (d-f) the calculated chamber surface elevation, to characterise the chamber sea state.

In figure 3.20 the recorded chamber surface elevation suggests that the mean and maximum power production occupies a broad range of sea states  $2(m) < H_s < 5.5(m)$  and  $12(s) < T_p < 17(s)$ . In contrast the calculated chamber surface elevation suggests that the mean and maximum power production occupies a narrower range of sea states with the mean being optimum in the range  $3.5(m) < H_s < 5(m)$  and the maximum being optimum in the range  $2(m) < H_s < 4(m)$ , with a notable decline at higher  $H_s$  sea states. The power matrix associated with the calculated sea states is a more accurate representation because of the undesirable amplification issues associated with the recorded surface elevation data (as discussed before), but unfortunately has far fewer data points available because the relief valve aperture sensor was installed more recently and this is a requisite for calculating chamber surface elevation when the plant is operational. The maximum (mean over 30 minutes) power take-off is approximately  $P_e = 65(kW)$ .

### 3.6 Under-performance

The achieved power take-off levels seen in figure 3.20 are far lower than those projected in (Falcão, 2002) which predicts that the plant should achieve time averaged power take-off levels greater than  $90(kW)$  for the majority of the time, reaching levels of up to  $190(kW)$ , and averaging  $100(kW)$  over all operational periods (annually). However, the analysis in (Falcão, 2002) considers the plant to have a

maximum turbine angular velocity that is 16 ( $rad\ s^{-1}$ ) greater than the actual imposed rotational speed limit (due to vibrations). Also the analysis considers the plant with the original designed water depth (without boulder collection), no damages to the chamber subsurface structure (holes in concrete walls) and turbine blades (pitting from impacts), and with an optimised power take-off control law. Most of these deviations will be complex to characterise and could each seed a new research topic. Because of the time restrictions of this study, and the financial resource needed to correct the issues, only a brief overview of each deviation is given in the following.

### 3.6.1 Electrical power take-off

As a foreword note, the author's colleague at the Pico plant is basing his PhD research on turbine rotational speed optimisation, whilst the author is primarily concerned with chamber pressure optimisation. So as not to encroach on each other's research, the subject of rotational speed optimisation, whilst very interesting, will not be discussed past a very basic overview. Ultimately the findings of each separate study will be amalgamated and implemented at the Pico plant.

The optimum power take-off control law for the Pico case study is discussed in (Justino & Falcao, 1999) and extended in (Falcão, 2002), and a brief review of this given in the following.

If temporal variations in rotational speed, due to temporal fluctuations in incident wave power associated with wave grouping, are ignored, then from (3.7) the mean aerodynamic power transfer to the turbine is;

$$\bar{P}_a = \rho_0 D^5 \bar{\Pi}^* N^3 \quad (3.13)$$

where  $\bar{\Pi}^*$  is a characteristic of the turbine that does not depend on rotational speed or sea state. In reality this is achieved though basic relief valve control to optimise  $\sigma(\Psi)$  to give  $\bar{\Pi}_{max}$  at all times (provided the incident energy resource is sufficient), as will be discussed later.

The time-averaged turbine net-power output  $\bar{P}_n$  is then the difference between aerodynamic power transfer to the turbine and power dissipation through bearing friction loss, as described by;

$$\bar{P}_n(N) = \bar{P}_a(N) - \bar{P}_b(N) \quad (3.14)$$

where  $\bar{P}_b$  is the time averaged bearing friction losses (of turbine and generator) which is characterised mathematically in appendix B and is discussed further in the next chapter.

In (Falcão, 2002)  $\bar{\Pi}^*$  and  $\bar{P}_b(N)$  are known (for the Pico case study) and the value of  $N$  that yields the highest  $\bar{P}_n$  defines the optimum power take-off control law. The function relating  $\bar{P}_n$  and  $N$  without any rotational speed constraints, or with advanced relief valve control, was found to be;

$$\bar{P}_n = 1.224 \times 10^{-5} N^{3.1563} \quad (3.15)$$

Due to the rotational speed limitation of the machine, a condition of high power take-off that acts as an electro-magnetic break when  $N > 141$  ( $rad\ s^{-1}$ ) must also be implemented in to the curve presented in (Falcão, 2002).

The theoretically found optimum power take-off control law described in (Falcão, 2002) is compared to the non-optimised control law used at the Pico plant in figure 3.7.

There is a strong deviation between the control laws that are used at Pico and the theoretically optimum generator electrical power take-off curves. This may in part explain the under performance of the plant but for the reasons stated the subject will not be investigated further.

### 3.6.2 Subsurface structural damage

The subsurface concrete structure of the Pico plant has suffered significant damage over time and as can be seen in figure 3.21 there is a sizable hole in the western chamber wall, some smaller holes in the back chamber wall have also formed. These points of failure may have initialised due to defective concreting or by large boulder impacts and have eroded with the strong water flow and gradually expanded.

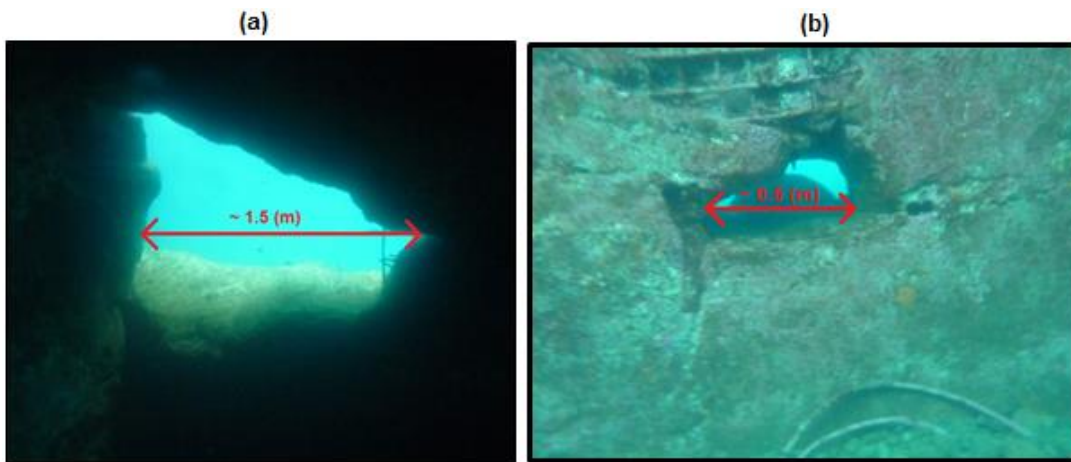


**Figure 3.21** Pictures of subsurface structural damage at (a) the west and (b) the south, chamber walls that both connect to a channel.

The holes in the chamber side walls make a connection to a channel formed between the land and a concrete breakwater with an opening to the west, as indicated in figure 3.22.



**Figure 3.22** Picture indicating the location of a channel that connects the open ocean with the west and south walls of the plant structure.

Due to the difference in wave travel time between the internal and external (fed by the channel) west side chamber walls, the surface elevation in the channel is at least partially out of phase with the chamber surface elevation. The difference in water level (and hydrostatic pressure) drives a mass flow through the holes in the chamber wall which is seen as an exit of water from the chamber to the channel during a wave peak (in the chamber) and vice versa for a wave trough. The effect can clearly be seen by the plumes of water reciprocating through the hole in even the lowest energy sea states. This will likely damp the water surface oscillation in the chamber and destructively interfere with the incident wave thus reducing the available wave power in the chamber location. As such it is recommended that the hydrodynamic transfer functions found in (Brito-Melo, et al., 2001) using BEM analysis be re-evaluated, but due to the complexity of the new situation re-evaluation could also include CFD analysis.

### 3.6.3 Performance change with tidal elevation

It was noticed that the plant performance in terms of power production (and stall frequency and severity) is highly dependent on the mean water level, with performance being best at high tide and worst at low tide. A sample time series in figure 3.23 illustrates this point. The mean power output at high tide is typically around twice that achieved at low tide (being greater for large tidal ranges and vice versa).

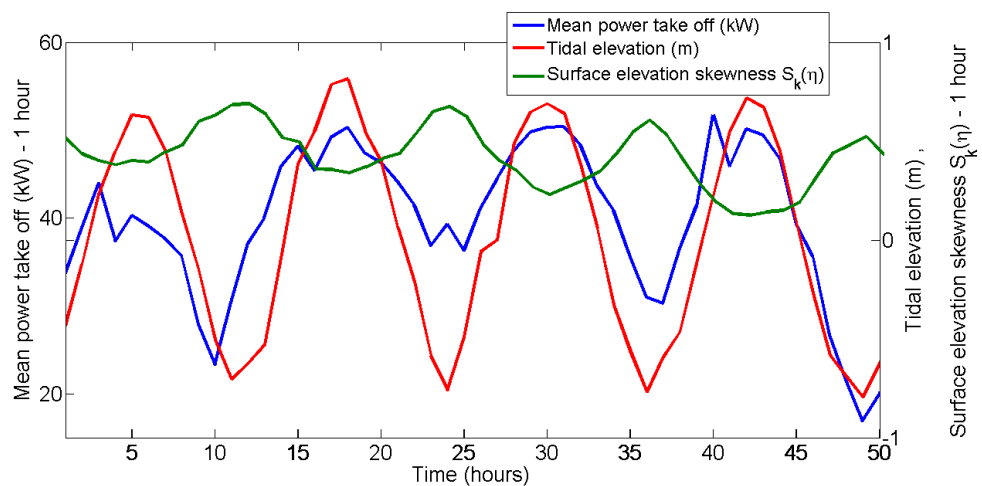


**Figure 3.23** Example time series showing the relationship between power take-off (1 hour mean), mean tidal elevation and surface elevation skewness as described in section 1.5.3 for a period of consistent incident wave energy.

The reason for this is almost certainly due to two effects as will be shown. As waves enter shallower water they begin to shoal which is characterised by a narrowing and sharpening of the wave crest and an elongation and blunting of the wave trough. This effect is clearly seen in the data and an example of this is given in figure 3.24 which shows the histograms of surface elevation at low tide (hour 36 in figure 3.23) and at high tide (hour 42 in figure 3.23). At high tide the surface elevation distribution approaches a Gaussian profile, whilst at low tide the profile is far from Gaussian and is heavily skewed and most notably there is a large concentration of data points where  $-0.9 < \eta < 0.6$  which signifies the shallower elongated wave troughs.

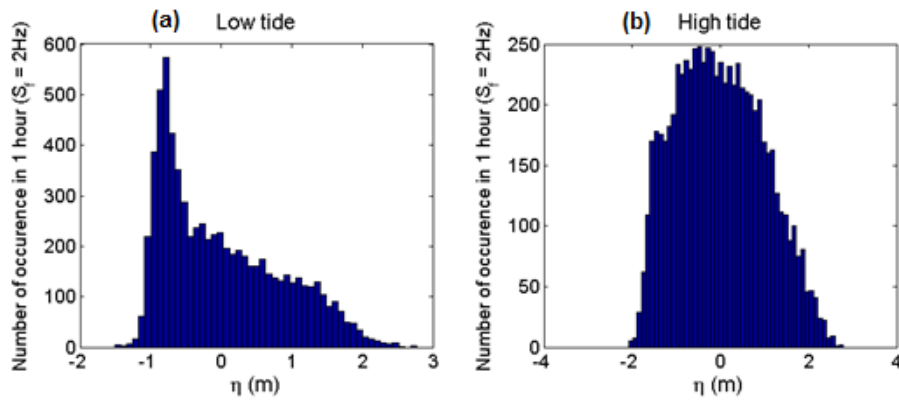


**Figure 3.24** Histograms of chamber surface elevation over a 1 hour period for (a) low tide (hour 36 in figure 3.23) and (b) high tide (hour 42 in figure 3.23).

The chamber pressure also adopts any asymmetry associated with the surface elevation profile so that within a wave cycle there is a significantly higher absolute pressure head during the exhalation cycle than during the inhalation cycle. In certain sea states this can result in more frequent and severe turbine stalls (low power transfer to the turbine) in the exhalation half of the pressure cycle, and under-pressure (lower power transfer) in the inhalation half of the pressure cycle. This effect is likely to be the main reason for underperformance of the Pico OWC, and all future devices with wells turbines should be deployed in greater local water depth and account for any subsequent sedimentation of the chamber to minimise wave shoaling.

The tidal elevation will also alter the front wall immersion depth which is shown in (Zhang, et al., 2012) to affect the hydrodynamic transfer efficacy through vortex generation. In addition, wave breaking will occur at progressively lower wave amplitudes as the tidal elevation reduces (Zou, et al., 2013). Wave breaking will dramatically modify the surface elevation profile resulting in a highly nonlinear chamber pressure profile

A further effect that is dependent on tidal elevation (which is specific to the Pico case study) and has a significant role to play is the effect of structural damage to the chamber front lip. The structural damaged is shown in figure 3.25.



**Figure 3.25** Picture showing damage to the lip of the chamber front wall which connects the atmosphere and the chamber at larger wave troughs and at lower mean water levels.

This defect means that during wave troughs at lower mean water level an air passage is exposed between the chamber and the atmosphere which can clearly be seen by the ejection of spray laden air. This, in effect, acts as a secondary relief valve (during a small part of the wave cycle) and modifies the chamber pressure profile by forming a step like profile about zero pressure head at the wave trough. This is followed by a rapid increase in pressure as the vertical water column velocity is already fast at the point of submersion of the gap. In total the issue results in a highly nonlinear pressure profile rather than the smoother sinusoid profile that would be expected, and for which the system is designed. This effect is shown in figure 3.26, which shows a sample time series of chamber pressure. The effect becomes more frequent and with greater duration with the increase in wave height and at lower tidal elevations (lower minimum water level exposing larger air passage area), and will certainly affect the system performance because less time is spent in the mid pressure range of the exhalation half cycle which is when the greatest power transfer to the turbine occurs (see figure 3.5).

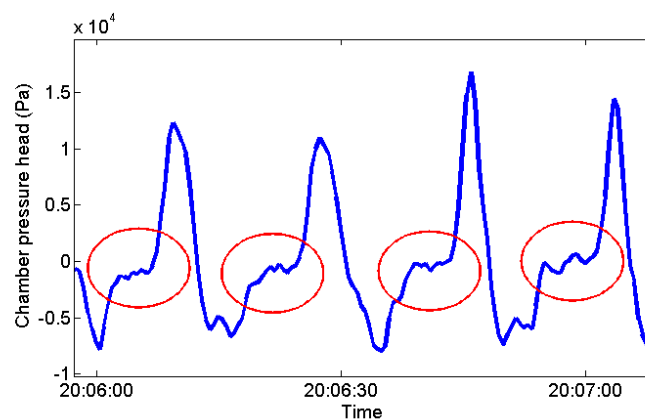


**Figure 3.26** Example time series showing the point (highlighted) at which the defect in the chamber front wall lip connects the chamber air pocket with the atmosphere resulting in a loss of pressure.

An example of the asymmetry in the non-dimensional chamber pressure head  $\Psi$  distribution resulting from wave shoaling and the defect in the chamber front lip, and its dependence on tidal elevation, is shown by the histograms in figure 3.27, which also display the turbine characteristic curve to aid interpretation. At high tide (hour 42 in figure 3.23)  $\Psi$  is more evenly distributed about the range of  $\Psi$  with a greater proportion of time spent in the  $\Psi$  range that delivers greater power transfer to the turbine compared to the low tide case. There is still significant positive skewness evident which shows that shoaling is still occurring to a degree at high tide. At low tide the distribution of  $\Psi$  is highly irregular having a significant concentration in the range  $-0.05 < \Psi < 0$  which relates to the combined loss of pressure due to chamber front lip defect (at the wave trough) and elongated wave trough from shoaling. At both tidal elevations (in this case) the bulk of power transfer to the turbine occurs in the inhalation half wave cycle.

This demonstrates the clear deviation from the stochastic methods presented in (Falcao & Rodrigues, 2002) and (Falcão, 2002) which relies on a Gaussian distribution of chamber pressure, and explains quite clearly the root causes for the under performance of the Pico plant at all times but particularly during low tide.

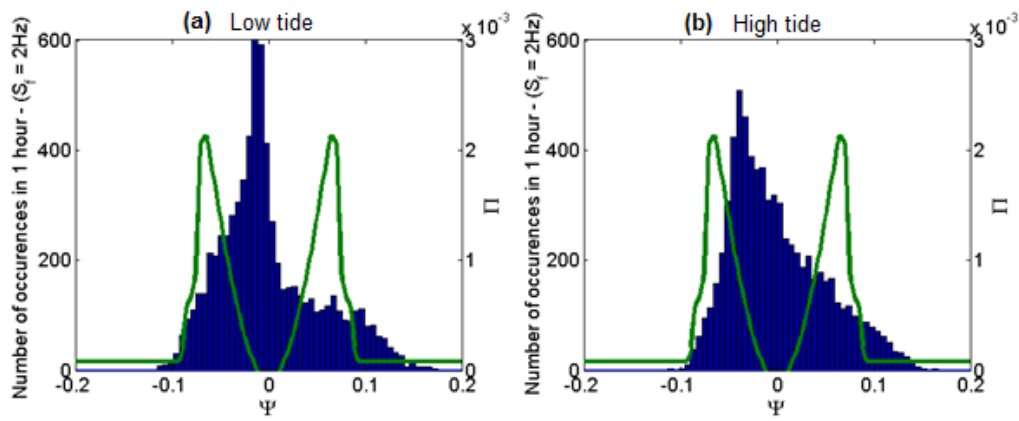


**Figure 3.27** Non-dimensional chamber pressure head  $\Psi$  over a 1 hour period for (a) low tide (hour 36 in figure 3.23) and (c) high tide (hour 36 in figure 3.23) with the turbine characteristic curve (green line) given for reference.

### 3.6.4 Pitting on turbine blade

Impacts between the turbine blades and small debris in the turbine duct air flow stream have created thousands of small pits on the surfaces of the turbine blades. Repeated salt crystallisation and dissolving cycles and corrosion have expanded these pits and some are now of considerable size (up to 1 cm). At the thinner trailing edge of the blade some sections have broken away completely, and the leading edge has the highest density of holes because this edge dissects the airflow. Polyester resin was applied to the turbine blades in an attempt to fill the holes and restore the smooth surface but this slowly broke away and ultimately did not last very long. The turbine blade damage is shown in figure 3.28 where a crack detection dye is used to highlight pitting near the hub. The roughness and non-uniformity of the turbine blade surfaces might have altered the turbine's aerodynamic characteristics. For a thorough analysis of the effect of blade pitting CFD analysis could be conducted.

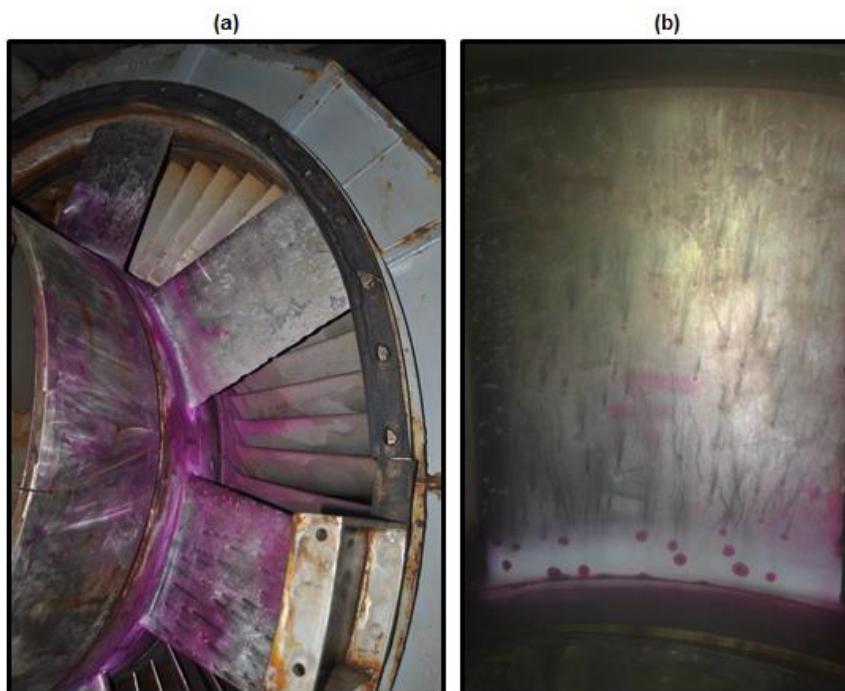


**Figure 3.28** Pictures showing pitting of turbine blades (a) and close up single blade (b). A crack detection dye is used in the region where the blade meets the hub to highlight the defects in this region.

### 3.7 Machine fatigue and longevity

The maintenance intervals of the Pico plant are short (approximately every 2 weeks of operational time). Corrosion due to improper sealing of the building and saltwater exposure to the (non-stainless) steel internal system elements is probably the primary cause of deterioration requiring intervention. The second biggest contributor that necessitates maintenance is stress and fatigue from machine vibrations. The fibreglass turbine duct covers and stainless steel guide vane sets have the highest frequency of failure and both regularly incur significant stress fractures which need to be repaired through fibre glassing and welding, respectively. Also the turbine cover bolts are frequently loosened through vibrations and fall out despite using springs and nylon threaded nuts to secure them. By simply observing the system during operation it can clearly be seen that the turbine duct covers shake violently when the turbine is in stall conditions, indicating that the root cause of failure for these components is from stress induced by turbulent airflow.

To assess machine fatigue, vibration sensors capturing *RMS* vibration velocity are mounted on the turbine shaft bearing housings. Also for a very short time strain gauges were mounted on the guide vane blades. Ideally vibration sensors would be used in all places experiencing fatigue but this has not been done and so must be inferred from the existing measurement points.

The generator *RMS* vibrations are analysed in figure 3.29 and figure 3.30, which shows;

- The mean residual vibrations (a function of turbine angular velocity only) when the turbine is not aero-dynamically loaded (zero pressure head)
- The mean vibration as a function of turbine angular velocity  $N$  and non-dimensional pressure  $\Psi$
- The mean vibration velocities above the residual vibrations (when the turbine is aerodynamically loaded) which gives the vibration contributions from air-flow interactions (as a function  $N$  and  $\Psi$ )
- The ISO 10816 vibration severity rating (for class 2 devices) as described in table 3.1 (as a function  $N$  and  $\Psi$ )

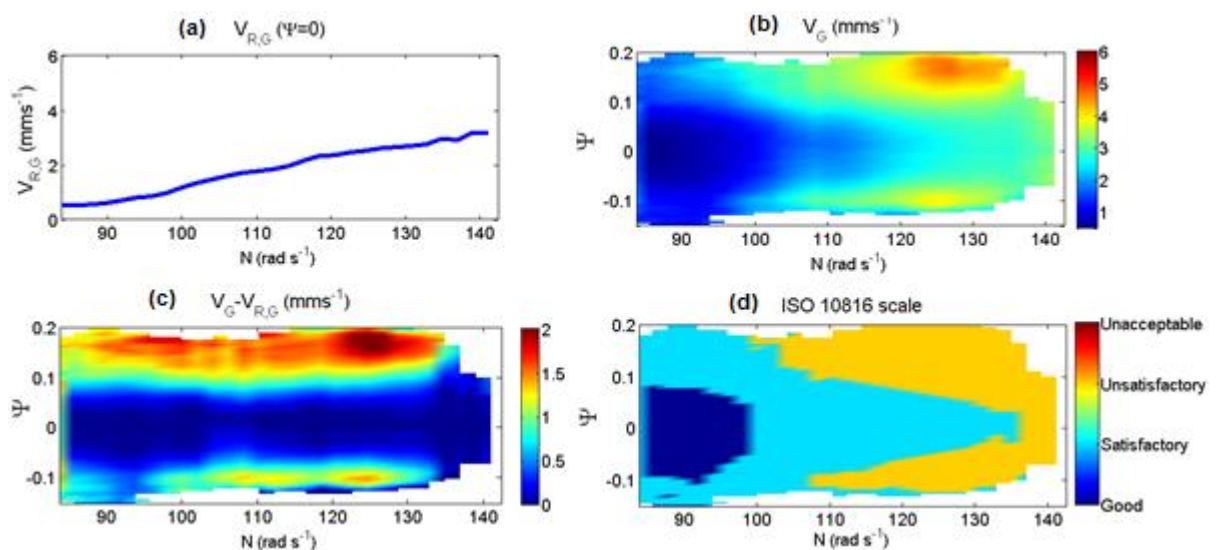


**Figure 3.29** Analysis of vibration measured at the generator side bearing housing as a function of non-dimensional pressure and turbine angular velocity.

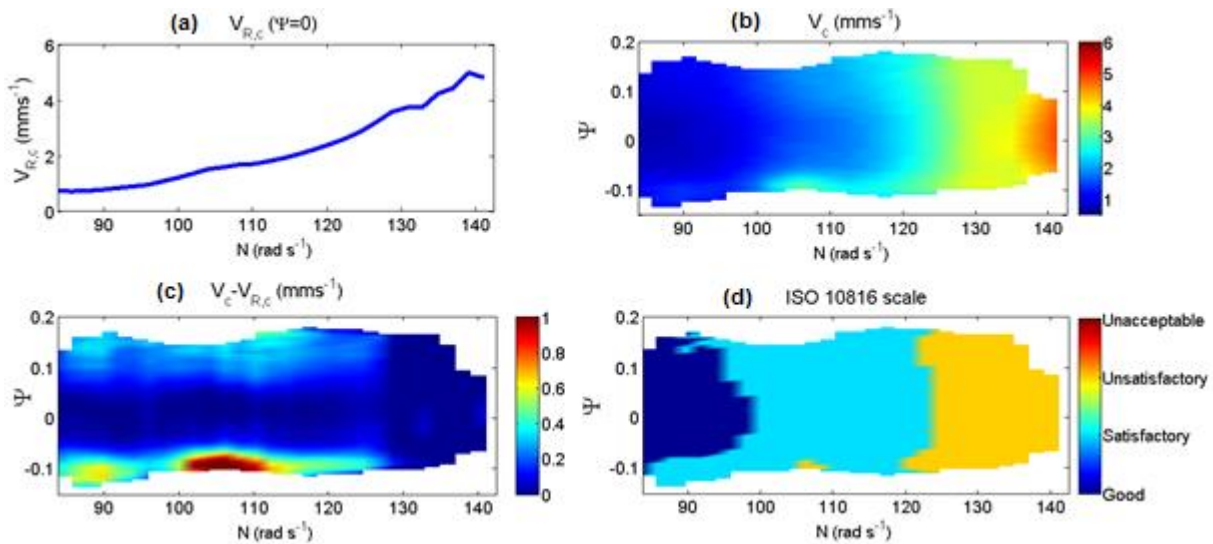


**Figure 3.30** Analysis of vibration measured at the chamber side bearing housing as a function of non-dimensional pressure and turbine angular velocity

In figure 3.29 and figure 3.30 it is seen that the residual vibrations share a fairly linear increasing relationship with increasing turbine speed as would be expected. To deal with this issue the turbine support structure could be reinforced to further increase stiffness or a more aggressive power take off curve could be implemented to reduce the turbine speed, but this would be at the expense of performance and would be counteracted in part by the increase in vibration associated with the increase in turbine stalls that would be incurred.

More interestingly, a relationship exists between non-dimensional pressure and vibrations. Past the threshold for turbine stall  $\Psi > 0.067$  a sharp increase in vibrations occurs which strengthens rapidly with the further increase in  $\Psi$ . To assess the severity and frequency of stall in the analysis given in the following chapters, some stall severity boundaries will be defined based on the turbine characteristic curves and loosely based on the vibration levels above the residual and the machine sound levels, as will be discussed later. The stall severity boundaries are defined as:

- $0.068 < \Psi < 0.1$  - Partial stall
- $0.01 < \Psi < 0.125$  – Low level stall
- $0.0125 < \Psi < 0.15$  – Medium level stall
- $0.015 < \Psi < 0.175$  – High level stall
- $\Psi > 0.175$  – Severe level stall

The interaction between the turbulent flow (from stall) and the structure significantly increases the system vibrations, and it is this mode of vibration that is expected to be the source of stress related fatigue, as will be explained. However, a deviation to this trend exists when the turbine is close to the upper angular velocity limit and in this range there is a less significant increase in vibrations from the stall effect. The reason for this is not obvious and should be investigated further. It is interesting to note that the sound emitted by the machine when stalling at high rotational speeds is quite different and less concerning than the sound emitted at the same degree of stall at lower rotational speeds. It is possible that this range lies between two harmonics.

Reducing the residual vibrations by limiting the turbine speed is not a practical option because of the poor performance and increase in stall frequency that will result, and further reinforcement of the turbo generator structure is not financially viable under the current budget restrictions. However, minimising the frequency and severity of turbine stall will reduce vibration velocity and because this is proportional to stress, the fatigue rate of the machine components will also be reduced as indicated in figure 3.35. This could be achieved by controlling the flow rate (pressure) by controlling the relief valve aperture to vent over-pressure to reduce the severity of stall.

The original generator side guide vane set comprised of a grid of thin stainless steel sheets. These rapidly incurred catastrophic failure from fracturing as shown in figure 3.31. A second guide vane set was fabricated and this is comprised of a radial fan of thick curved stainless steel blades. This also rapidly incurred severe damage and fractures formed on most of the blades as shown in figure 3.31. The fractures slowly spread across the blades width, with some being up to half the width of the blade long. As such the generator side guide vanes were removed for fear that a piece of the guide vane blade would detach and strike the turbine. Interestingly the chamber side guide vanes are so far completely un-fractured which strongly indicates that turbine stall is the root cause of the failure. This is because wave shoaling results in significantly higher airflow rates for the exhalation half cycle so that turbine stalls occurs more frequently and more severely during this part of the cycle. As such the generator side guide vanes are exposed more frequently and more severely to aerodynamic loading from turbulent flow shed from the turbine.



**Figure 3.31** Pictures of stress fractures and total detachment of guide vane blades for (a) original guide vane set and (b) new guide vane set with much thicker blades.

A student, Mario Vieira, studying for his MSc in Mechanical Engineering at IST University, was tasked with investigating the source of the guide vane failure as part of his thesis project. Strain gauges were mounted on guide vane blades to monitor the stress from aerodynamic loading. This author supervised the MSc student on the plant side of his study and the findings of the study can be found in (Vieira, et al., 2015). The data obtained by the MSc student has been re-analysed by this author in a way that is more relevant to the objectives and point of interest of this study. The objective of this secondary analysis is to try to find a clear relationship between non-dimensional pressure, turbine stall, and the resultant guide vane stress and strain, in order to qualify the fatigue reduction that might be achieved through the minimisation of turbine stall and severity.

Triple axis, rosette type strain gauges were mounted on the surface of one blade of the generator and chamber side guide vane sets. This is shown in figure 3.32 along with a schematic of the mounting orientation of the strain gauge transducers and of the total guide vane set.

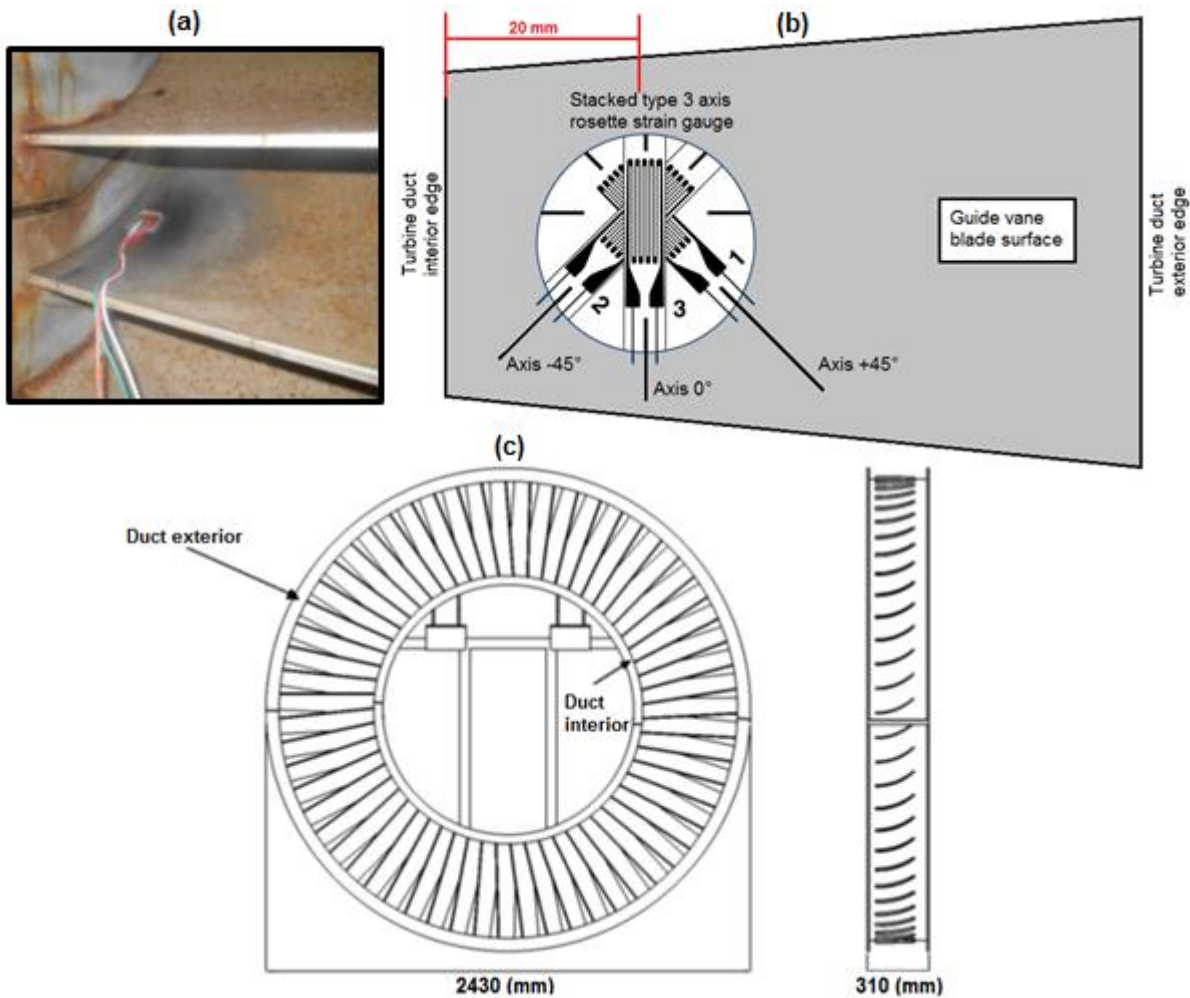


**Figure 3.32** (a) Strain gauge placement on guide vane blade, (b) schematic of the orientation of the 3 axis of the strain gauge (not to scale), (c) Guide vane set schematic from (Vieira, et al., 2015).

The strain  $\varepsilon_A$  measured by the gauge is described by;

$$\varepsilon_A = \frac{\Delta L}{L} \quad (3.17)$$

Where the subscript  $A$  is the strain gauge axis reference number (1,2 or 3) as seen in figure 3.32,  $L$  is the un-loaded length of the gauge.

The recorded strain over the very short test period (several minutes), as a function of non-dimensional pressure, is shown in figure 3.33. Past the stall threshold  $\Psi > 0.067$  strain in all axes increases with a fairly linear relationship to non-dimensional pressure. It seems likely the blades are buffeted by the chopped strong turbulent flow shed by the turbine which causes them to flex significantly.

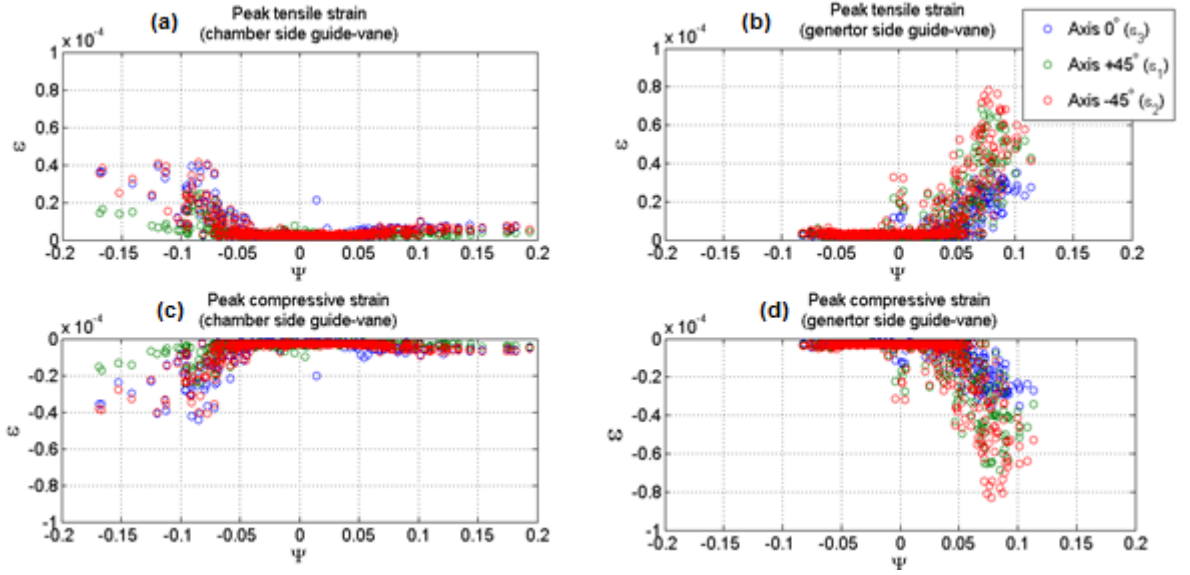


**Figure 3.33** The relationship between non-dimensional chamber pressure  $\Psi$  and peak (a, b) tensile and (c, d) compressive, strain  $\varepsilon$  recoded in three axes of the same plane ( $-45^\circ, 0^\circ, +45^\circ$ ) as measured at the generator and chamber side guide vane blades.

The maximum  $\varepsilon_{max}$  and minimum  $\varepsilon_{min}$ , principal strains can then be calculated with;

$$\varepsilon_{max} = \frac{1}{2} \left[ \varepsilon_1 + \varepsilon_2 + \sqrt{2((\varepsilon_1 - \varepsilon_2)^2 + (\varepsilon_2 - \varepsilon_1)^2)} \right] \quad (3.17)$$

$$\varepsilon_{min} = \frac{1}{2} \left[ \varepsilon_1 + \varepsilon_2 - \sqrt{2((\varepsilon_1 - \varepsilon_3)^2 + (\varepsilon_2 - \varepsilon_3)^2)} \right] \quad (3.18)$$

The maximum  $\sigma_{max}$  and minimum  $\sigma_{min}$ , principal stresses are then;

$$\sigma_{max} = \frac{E}{1-\nu^2} (\varepsilon_{max} - \nu\varepsilon_{min}) \quad (3.19)$$

$$\sigma_{min} = \frac{E}{1-\nu^2} (\varepsilon_{min} - \nu\varepsilon_{max}) \quad (3.20)$$

where  $E = 172 \text{ (GPa)}$  is the Young's modulus and  $\nu = 0.3$  is the Possion's ratio, for the AISI 316L stainless steel of which the guide vane blades are fabricated from.

Finally the equivalent stress (von Mises stress), under the principle plane stress load scenario, is found with;

$$\sigma_v = \sqrt{\sigma_{max}^2 - \sigma_{max}\sigma_{min} + \sigma_{min}^2} \quad (3.21)$$

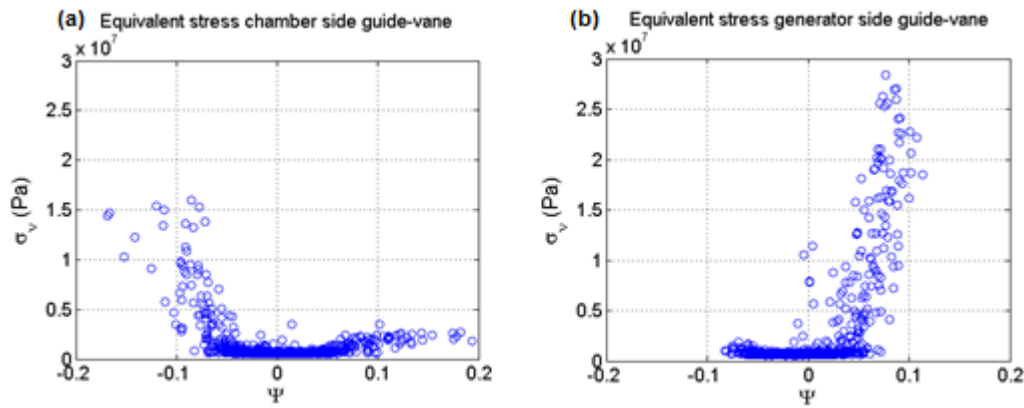


**Figure 3.34** Equivalent stresses  $\sigma_v$  as a function of non-dimensional chamber pressure  $\Psi$  for (a) chamber side guide vane and (b) generator side guide vane. The guide vane stress measurements are recorded at different times and have different ranges.

As seen in figure 3.34 wave shoaling and the increased absolute pressure head associated with the exhalation half cycle results in a far greater stress range recorded at the generator side guide vanes than the chamber side. As can be seen on a typical strain cycle graph (figure 3.35), this increase in stress amplitude and frequency leads to a lower number of flex cycles before material failure (fracture). The problem is exasperated by the mild corrosion that has set in (despite being stainless steel).

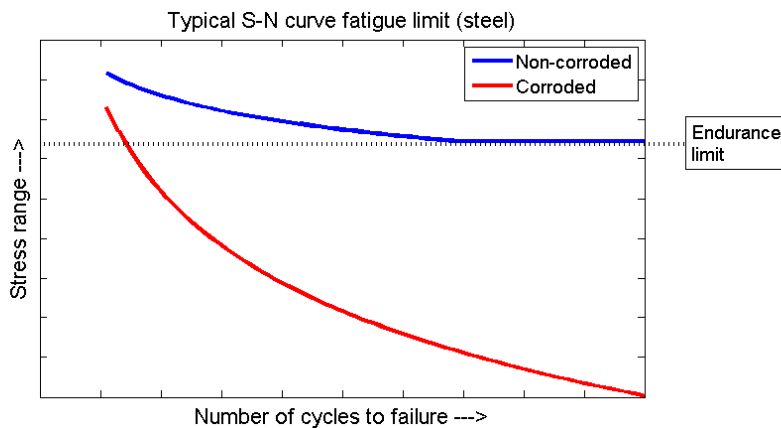


**Figure 3.35** Example curve showing the typical relationship between stress range and number of cycles before fatigue related material failure for non-corroded (blue) and corroded (steel) steel.

Inevitably because of corrosion the expected life time of the guide vane blade material is finite unlike certain non-corroded materials, which for steel has a potentially infinite life time if the stress range is kept below the endurance limit. However, the material life time (before failure) can be extended significantly by limiting the stress range which can be achieved by lowering the frequency and severity of stall events. This is validated directly by the absence of fracturing on the chamber side guide vanes, which are exposed to a lower stress range. Again it is noted that stall limitation, and therefore fatigue rate reduction, could be achieved through pressure control using the relief valve.

For finality, a sample time-series for strain along the three gauge axes and the corresponding non dimensional pressure is shown in figure 3.36.

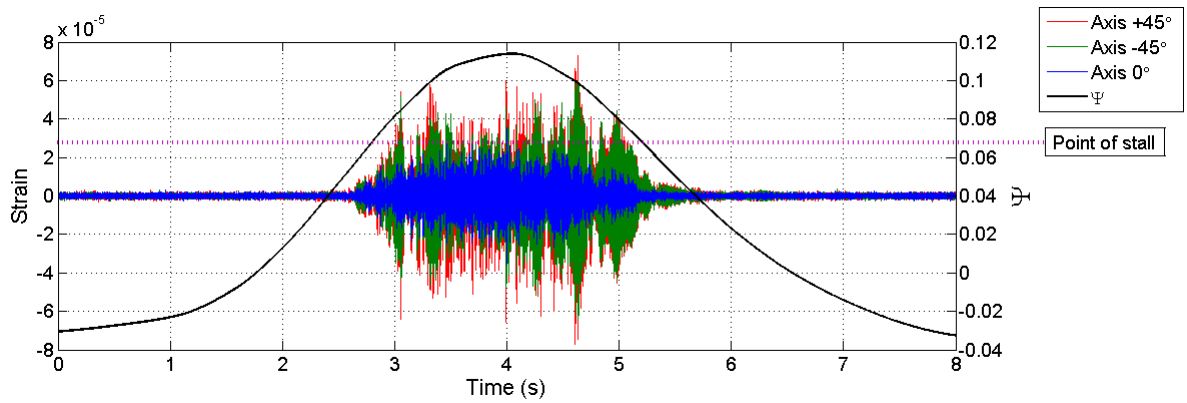


**Figure 3.36** Example recorded time series showing the relationship between strain (guide vane blade) and non-dimensional chamber pressure.

### 3.8 Noise pollution

One significant issue that tarnishes the reputation of OWC devices is the sound emitted by the device in operation. This is particularly problematic for shore mounted devices such as Pico because the noise can be very disruptive to any inhabitants in the local area. For example the Mutriku OWC project located in the province of Gipuzkoa in Spain had to be adapted after construction because the local residents (housed several hundreds of metres away) complained about the excessive noise emitted. Their solution was to vent air flow passing the turbine into the main generator hall inside the building rather than venting to the outside of the building as originally designed. This has the impact that salt and water collects around the machinery which will undoubtedly reduce the life time of components. In addition sound proofing was installed on the building walls resulting in further expense.

At Pico the noise emitted from the device is extremely loud. In operation ear defenders need to be worn when in closer proximity to the device ( $\sim < 100\text{ m}$ ), and the sound can be heard up to several kilometres away, at times.

Under non-stalled conditions the sound is similar to the low rumblings of an idling jet engine of a commercial airplane. However, the sound increases significantly during turbine stall and would be described in the following way by this author.

- $0.068 < \Psi < 0.1$  - Low rumbling sound with occasional slight screeching / grinding metal sound (partial turbine stall)
- $0.01 < \Psi < 0.125$  – High rumbling with occasional significant screeching / grinding metal sound (full turbine stall)
- $0.0125 < \Psi < 0.15$  – Unpleasant screeching / grinding metal sound (full turbine stall)
- $0.015 < \Psi < 0.175$  – Very harsh screeching sound which is troubling (full turbine stall)
- $\Psi > 0.175$  – Alarming severe screeching / grinding metal sound that can be heard at very long range along with local ground shaking (full turbine stall)

A study in 2010 was made to assess the environmental impact of the airborne and waterborne sound emitted by the Pico plant and this can be seen found (de Moura, et al., 2010). The study does not focus on the specific correlation between the system state and the noise emitted and is more concerned with the

background averages. Because the noise emitted is highly dependent on the system state the author had hoped to get the data to make a secondary analysis. Only the far less relevant waterborne acoustic data captured by a hydrophone located 10 meters up wave of the chamber front wall was available. The useful test period with respective plant data was short (5 minutes) and it was conducted during a period with a very low energy sea state [ $H_s < 1$  (m),  $T_p \sim 9$  (s)] in which only very mild turbine stall occurred occasionally.

The correlation between non-dimensional pressure and sound pressure level in decibels normalised by the reference pressure level of  $p_0 = 1$  ( $\mu Pa$ ) as described by;

$$dB_{SPL} = 20 \log_{10} \left( \frac{p_{rms}}{p_0} \right) \quad (3.22)$$

is seen in figure 3.37.

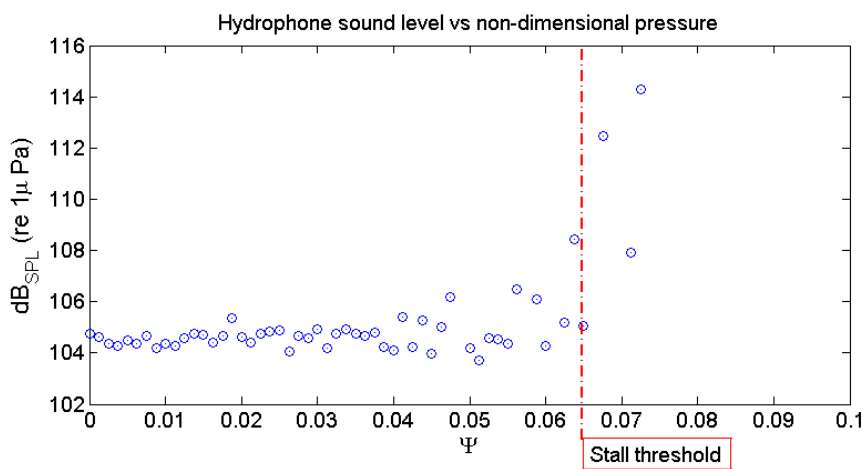


**Figure 3.37** Relationship between waterborne sound pressure level (normalised by  $1\mu Pa$ ) and non-dimensional chamber pressure with turbine stall threshold indicated.

Because of a lack of specialist sound metering equipment a new rudimentary analysis of the relationship between airborne sound intensity and system state, was made using a smartphone. A 20 minute recording of airborne sounds outside the plant at a distance of approximately 100 metres from the turbine was made during plant operation in an energetic sea state. The file was captured in a .WAV format but because a good sound reference level was not available for calibration, the conversion to decibels was not possible. Instead the sound intensity was simply normalised such that 1 represents the loudest sound recorded (during the data period) and 0 gives the minimum sound level (ambient sound when  $\Psi = 0$ ). Clearly this is a very rough method and was done simply to investigate if a clear relationship exists between sound levels and  $\Psi$ . The relationship between the normalised sound level and  $|\Psi|$  is given in figure 3.38.

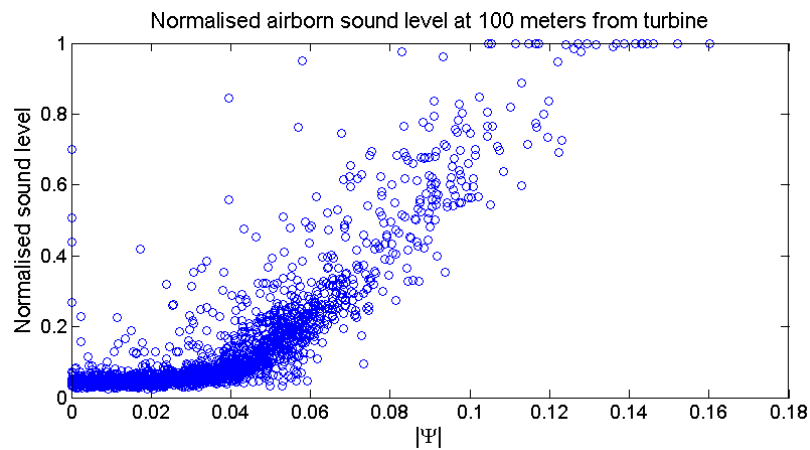


**Figure 3.38** Relationship between normalised airborne sound level (0 is ambient noise and 1 is loudest noise recorded in data period) and non-dimensional chamber pressure.

As seen in figure 3.37 despite the limited data the correlation is reasonable and there is a fairly clear and sharp increase in sound level about the point of turbine stall. Figure 3.38 shows that the airborne sound level shares a similar trend to the waterborne sound levels, but suggests that significant increases in sound levels begin before the onset of stall. In both cases the sound levels appear to increase linearly with increasing  $\Psi$  (after the approximate point of stall onset). The trends are similar to the guide vane stress measurements as seen in figure 3.34 which is expected as sound originates from vibrations and therefore is linked with stress.

Because the magnitude of the sound emitted by the machine is closely related to stall severity, clearly minimising the frequency and severity of turbine stall would be of benefit. From the authors experience more severe stalls ( $\Psi > 0.125$ ) result in a very unpleasant, and at times, alarming sounds, and the minimisation of this is likely to be positively perceived by the local residents (and plant employees). This could be achieved through relief valve control to limit stall severity and frequency as discussed earlier.

### 3.9 Summary

Despite the numerous significant failures throughout the Pico plant's history (which is often the case for prototype devices) perseverance has prevailed and the machine is now in a relatively stable state and feeds reasonably significant levels of power to the local grid. There were major issues with the original machine design and several severe failures occurred during the construction phase. These delayed the project and much has been learned from this process. In an unfortunate way this fulfils one of the original objectives of the project which was to gain experience in deploying the technology and to refine the methodology in an environment with the easy access associated with on-shore deployment before venturing to offshore locations. Although the power levels are currently too low to be commercially interesting, the availability of a functional full scale WEC with easy access presents a unique facility for research and development purposes. The knowledge of OWCs gained in these harsh, energetic and non-ideal conditions can be applied to the design and deployment of future devices to improve their chances of survival and success.

After resolution of the fundamental issues, time is afforded to concentrate on improving the system performance and extending the machine's lifetime.

The machine underperforms when compared to the theoretical projection, for the following reasons;

- Boulder collection in the chamber has lowered the water depth and increased wave shoaling. This has resulted in an asymmetric chamber pressure profile, which has a tendency to cause over pressure and stall in the exhalation half of the cycle and under-pressure in the inhalation half wave cycle. This has a particularly detrimental effect at lower tides when the degree of wave shoaling increases.
- The broken section of concreting at the chamber front lip opens an air passage to the atmosphere at the wave trough causing a loss of pressure and results in a significant modification of the chamber pressure profile.
- The residual machine vibrations levels and down-grade of the power electronics has resulted in a turbine rotational speed limited that is lower than the theoretical optimal for high energy sea states.
- Pitting of the turbine blades may have changed the aerodynamic performance but whether or not this has significantly reduced the performance is currently unknown.
- Holes in the chamber side walls result in a damping of the chamber surface elevation due to mass flow exchange with the side channel (which has a water surface elevation that is out of phase with the chamber).

With enough financial backing these issues could all be resolved which would improve the plant performance. However, without much additional financial backing (as is the current situation) the system performance might be improved by implementing more advanced system control strategies. Firstly, the turbine rotational speed can be controlled in a more optimised way for greater pneumatic to mechanical power transfer (and potential stall minimisation) using a power take-off control law. This could be achieved with a power take-off curve that encourages the turbine to occupy a narrower optimal rotational speed range based on the current sea state. However, for the reasons discussed before this is beyond the scope of this study.

The other option for optimisation through control is to regulate the turbine air flow rate. This can be achieved by regulating chamber pressure such that the instantaneous pressure or the pressure variances over a short time period, is more optimal for power transfer to the turbine. Enhancing power transfer to the turbine can be achieved by reducing the time spent in over-pressure, which causes turbine stall and low power transfer to the turbine, and the time spent in under-pressure when only a portion of the available pneumatic power, which is lower than optimal, is exposed to the turbine. Also, because pressure optimisation necessarily acts to minimise the frequency and severity of turbine stalls (as part of the power enhancement strategy), the stresses exerted on the system components will be reduced. Ultimately this should reduce the rate of component fatigue and extend the time before failure, which in turn will extend the time between maintenance intervals, thus reducing the financial and human resource burden. Chamber pressure optimisation through relief valve control is the primary focus of this study and is investigated in depth in the following chapters.

## Chapter 4

# Literature review - OWC system and short-term wave forecast, modelling

### Abstract

The main objective of the second part of this thesis is to numerically develop and validate strategies to actively control the relief valve aperture at the Pico OWC in real-time in order to regulate and optimise pneumatic power exposure to the turbine, before proceeding to the deployment of the selected control strategy in field tests. For the initial development phase, a system model for the Pico OWC plant must be selected, developed and validated, because this is needed to develop and test different control strategies and to quantify the theoretical performance enhancements. In addition because the control strategies will be active a short-term wave forecast will probably be required. The forecast will provide the information needed to make the control decisions in order to prepare the system to the up-coming wave event. This requires the selection, development and validation of short-term wave forecasting models. A literature survey must precede this development process and OWC system modelling options are reviewed in the first part of this chapter and this is followed by a review of short-term wave forecasting modelling, in the second part.

### 4.1 OWC system modelling introduction

Oscillating water column type WECs are probably the most intensively studied device type. Significant progress has been made in the theory for modelling the system dynamics of OWCs. In particular, the Pico OWC has been studied extensively and the first part of the literature review will focus primarily on work relating to the Pico plant as this is the most relevant.

To model the entire OWC system, one must consider the following power transfer steps;

- 1.) The relationship between chamber excitation flow and incident wave (hydrodynamics)
- 2.) The transfer from chamber wave power to the resultant chamber pressure (thermodynamics)
- 3.) The turbine characteristics that describes the relationship between the available pneumatic power and the turbine mechanical power transfer (turbo-aerodynamics)
- 4.) Losses of mechanical turbine power through bearing friction
- 5.) The transfer of mechanical turbine power to electrical power take-off and electrical losses
- 6.) The transfer of electrical power take-off to electrical power delivery to the grid and any further electrical losses in this process.

#### 4.1.1 Hydrodynamic transfer and pneumatic response

For a shore mounted OWC a number of processes transform the incident water surface elevation from an up wave location  $\eta_{uw}(t)$  to what later occurs inside the chamber  $\eta(t)$ . Local bathymetry and topography will modify the incident wave through refraction, diffraction, and shoaling. In addition, wave structure interactions, such as wave reflection from the plant structure and radiation from the chamber pressure, will cause interference, further modifying the observed transfer (as discussed in section 3.4.3).

Because the hydrodynamic transfer is dependent on the chamber pneumatic response, through wave radiation from chamber pressure, these two transfer steps will be reviewed simultaneously.

In reality the hydrodynamic transfer will be more complex than what can be considered with the following reviewed methods. Advanced methods such as computational fluid dynamics are required to account for complex nonlinear phenomenon. One example of this is the energy dissipation from vortex generation from the interactions of hydrodynamic flow and the chamber front lip (Morrison & Greated, 1992), (Zhang, et al., 2012). However, keeping in mind that system modelling must be performed on-line in order to direct relief valve control, only computationally inexpensive methods will be considered.

For fixed OWC systems equipped with a wells turbine, where linear water wave theory is assumed to be valid (linear water wave theory is described in section 1.5.1), three main approaches can be found in the literature to model the hydrodynamic and pneumatic response. These will be reviewed in the following sections after first introducing some relevant theory that will aid the review of the different considered approaches.

#### 4.1.2 Basic equations of thermodynamics and aerodynamics for OWCs

Before delving deeper into the options to model the hydrodynamic and pneumatic power transfer, it is convenient at this stage to introduce the basic governing equations of the problem as described in (Falcao & Rodrigues, 2002), for example.

The oscillating water free surface in the chamber, resulting from wave action, produces an oscillating volume rate of air space  $q(t)$ . In (Evans, 1982), the volume flow rate is decomposed into two components; the excitation flow rate  $q_e(t)$  where the internal chamber pressure is constant and equal to the atmosphere (an open system) and the radiation flow rate  $q_r(t)$  driven by pressure oscillations (in a closed system) driving oscillations in the free surface without incident waves, so that;

$$q(t) = q_e(t) + q_r(t) = -\frac{dV}{dt} \quad (4.1)$$

where  $V$  is the enclosed air volume between the water surface, turbine and the chamber walls and turbine duct.

The mass flow rate of air  $\dot{m}$  entering or exiting the system boundaries is given by;

$$-\frac{dm}{dt} = \dot{m} = -\frac{d(\rho_c V)}{dt} \quad (4.2)$$

where  $\rho_c$  is the air density in the chamber

If no relief valve is present  $\dot{m} = \dot{m}_t$ , or if a relief valve is mounted in parallel to the turbine  $\dot{m} = \dot{m}_t + \dot{m}_v$ , where  $\dot{m}_t$  is the mass flow rate passing the turbine, and  $\dot{m}_v$  is the mass flow rate passing the relief valve (defined in 3.3.5.2) which is described in (Falcao, et al., 2003) as;

$$\dot{m}_v = \rho_0 k_v A_v \text{sign}(p_c) \left( \frac{2|p_c|}{\rho_0} \right)^{1/2} \quad (4.3)$$

where  $k_v$  is the valve aperture state (0 for completely closed and 1 for completely open),  $A_v$  is the area of the valve aperture when completely open, and  $\rho_o$  is air density at atmospheric pressure.

Combing (4.1), (4.2) and expanding with the product rule yields;

$$\frac{\dot{m}}{\rho_c} = -\frac{V}{\rho_c} \frac{d\rho_c}{dt} + q_e + q_r \quad (4.4)$$

In order to solve the system equation the relationships between:  $q_e$  and the incident waves  $\eta_{uw}$ ,  $q_r$  and the chamber pressure  $p_c$ ,  $\rho_c$  and the combined chamber and atmospheric pressure  $p_c + p_o$ , and  $\dot{m}_t$  to  $p_c$ , need to be found.

First the relationship between  $\rho_c$  and the combined chamber and atmospheric pressure  $p_c + p_o$  will be considered. The heat transfer across the chamber boundary walls is likely to be small relative to the work done in the system and as such an adiabatic process is a reasonable assumption. If it is also assumed that viscous effects are negligible the process would also be reversible. An adiabatic reversible process can then be described by the linearized isentropic relationship which is given by;

$$\frac{p_c + p_o}{\rho_c^\gamma} = \frac{p_o}{\rho_o^\gamma} \quad (4.5)$$

where  $\gamma = 1.4$  is the ratio of the specific capacities for air of constant volume and constant pressure.

As discussed in (Justino & Falcao, 1999), in reality the turbine efficiency will be far from perfect and this means there will be aerodynamic losses at the turbine and the specific entropy of air entering the system from the atmosphere will be greater than the specific entropy of the atmospheric air. Because the change in entropy of air in the chamber is a very difficult process to model, the isentropic compression and decompression of air is commonly assumed. The error introduced by this assumption is shown in (Falcão & Justino, 1999) to be relatively low.

Rearranging (4.5) and taking the derivative gives the chamber air density rate of change;

$$\frac{d\rho_c}{dt} = \frac{1}{\gamma(p_c + p_o)} \frac{dp_c}{dt} \quad (4.6)$$

Combining (4.4), (4.5) and (4.6), gives;

$$q_e + q_r = \frac{\dot{m}}{\rho_o} \left(1 + \frac{p_c}{p_o}\right)^{1/\gamma} + \frac{V}{\gamma(p_c + p_o)} \frac{dp_c}{dt} \quad (4.7)$$

To relate  $\dot{m}_t$  to  $p_c$  the turbine characteristics need to be found. For the wells turbine (Dixon, 1978) provides convenient non-dimensional (by the turbine angular velocity  $N$ ) equations to relate chamber pressure head to the mass flow rate across the turbine, and power transfer to the turbine, as described by;

$$\Psi = \frac{p_c}{\rho_o N^2 D^2} \quad (4.8)$$

$$\Phi = \frac{\dot{m}_t}{\rho_o N D^3} \quad (4.9)$$

$$\Pi = \frac{P_t}{\rho_o N^3 D^5} \quad (4.10)$$

where  $N$  is the turbine angular velocity ( $radians\ s^{-1}$ ),  $D = 2.3\ (m)$  is the turbine diameter (for the Pico wells turbine),  $\Psi$  is the non-dimensional pressure head between the chamber and the atmosphere,  $\Phi$  is the non-dimensional flow rate past the turbine,  $P_t$  is the power transfer to the turbine and  $\Pi$  is its non-dimensional equivalent.

The functions  $f_m$  and  $f_p$  that respectively relate the instantaneous non-dimensional flow rate and non-dimensional power to the non-dimensional pressure head;

$$\Phi = f_m(\Psi) \quad (4.11)$$

$$\Pi = f_p(\Psi) \quad (4.12)$$

are to be determined experimentally or theoretically for a specific turbine design.

## 4.2 OWC system modelling approaches

### 4.2.1 Frequency domain model

The first approach, historically, is to consider the system in the frequency domain (without a relief valve) in order to analyse the system's pneumatic response to incident regular (monochromatic) waves of different amplitude and frequency. This method is presented (Evans, 1982), for example. Advantage is taken of the fact that OWCs with Wells turbines are approximately linear systems, which is a requisite for the basic assumptions of the approach.

If it is assumed that the function  $f_m$  (relating chamber pressure and airflow rate past the turbine) is linear, which is approximately true for the Wells turbine as shown in (Gato, et al., 1996) for example, and described by a constant  $K$ , then (4.4) can be linearized to give;

$$q_e + q_r = \frac{KDp_c}{\rho_0 N} + \frac{V_0}{\gamma p_0} \frac{dp_c}{dt} \quad (4.13)$$

where  $V_0$  is the total chamber volume when the water free surface is undisturbed.

Assuming a regular monochromatic incident wave, (4.13) can be converted to be a function of  $\omega$  for analysis in the frequency domain with the following substitutions;

$$p_c = P_c e^{i\omega t} \quad (4.14)$$

$$q_e = Q_e e^{i\omega t} \quad (4.15)$$

$$q_r = Q_r e^{i\omega t} \quad (4.16)$$

$$\eta_{uw} = A e^{i\omega t} \quad (4.17)$$

where  $P_c$ ,  $Q_e$  and  $Q_r$  are the complex amplitudes of the respective variables and  $A$  is the wave amplitude.

Substituting (4.14), (4.15) and (4.16) in to (4.13), and with some re-arranging can give;

$$Q_e + Q_r = \left( \frac{KD}{\rho_0 N} + \frac{i\omega V_0}{\gamma p_0} \right) P_c \quad (4.18)$$

The excitation volume flow rate can be found for a regular wave if the excitation flow coefficient  $\Gamma$  is known;

$$|Q_e| = A\Gamma(\omega) \quad (4.19)$$

where  $A$  is incident wave amplitude

As described in (Evans, 1982) radiation flow  $Q_r$  can be decomposed as;

$$Q_r = -(B + iC)P_c \quad (4.20)$$

which can be solved if the radiation conductance  $B$  and the radiation admittance  $C$  are known.

Substituting (4.20) into (4.18), and rearranging gives the equation for chamber pressure  $P_c$  as;

$$P_c = \frac{Q_e}{\left[ \frac{KD}{\rho_0 N} + B + i \left( \frac{\omega V_0}{\gamma p_0} + C \right) \right]} \quad (4.21)$$

The chamber pressure time series for regular waves of angular frequency  $\omega$  can then be obtained by;

$$p_c(t) = \text{Re}[P_c e^{i\omega t}] \quad (4.22)$$

In (Sarmiento & Falcao, 1985) the hydrodynamic coefficients are found analytically by applying the following simplifying assumptions: the device structure has a perfectly reflecting chamber back wall extending to the sea bed; it has a thin front wall of negligible draft; the chamber is constructed at the end of an infinitely long gully which is equal to the internal width of the chamber having a rectangular horizontal profile, and the system is under the exposure of unidirectional waves propagating in constant water depth with a direction perpendicular to the chamber front wall.

Alternatively if the local bathymetry and topography are intricate (not simplified to derive an analytical solution), the boundary element method (*BEM*) can be used to find the system's frequency response. This analysis has been performed for the Pico case study using an extension of the hydrodynamic simulation software AQUADYN in (Brito-Melo, et al., 2001) and the resultant hydrodynamic excitation flow coefficient  $\Gamma$ , which describes exaction flow frequency response, along with hydrodynamic coefficients  $B$  and  $C$  that describe the radiation flow response, is seen in figure 4.1. The domain grid boundary representation of the structure and surrounding area used in (Brito-Melo, et al., 2001) is seen in figure 3.3;

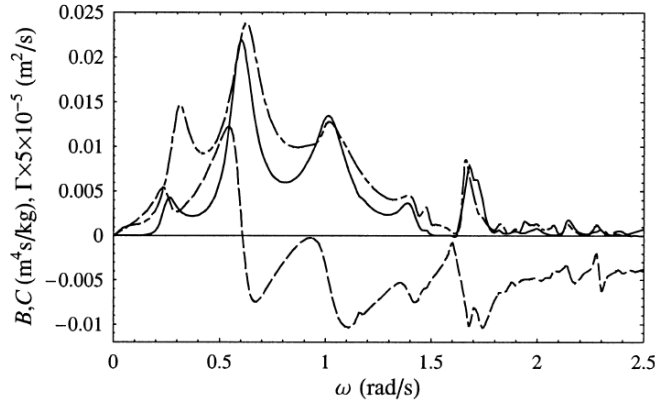


**Figure 4.1** From (Brito-Melo, et al., 2001) hydrodynamic coefficients for the Pico plant: excitation volume flow coefficient  $\Gamma$  (dash dot line), radiation conductance  $B$  (solid line), and radiation susceptance  $C$  (dash line).

The frequency domain modelling approach is useful in the design phase for matching the device geometry to the dominant local wave climate spectra. Once the hydrodynamic coefficients are known the approach is computationally efficient for single frequency based performance analysis. However, to assess the performance under irregular wave conditions, the frequency domain analysis needs to be combined with stochastic methods.

#### 4.2.2 Stochastic analysis

An extension to frequency domain analysis is the stochastic method described in (Falcao & Rodrigues, 2002). This can be used to assess the average plant performance as a function of the spectral representation of the sea state. The goal of the method is to relate the random incident wave surface elevation variance, to the resulting chamber pressure variance, and then to relate the pressure variance to the average non-dimensional power transfer to the turbine. A brief description of the method follows but (Falcao & Rodrigues, 2002) should be consulted for full details.

The stochastic method assumes that any given sea state can be represented by a spectral distribution  $S_\eta(\omega)$  which is not significantly affected by radiated waves from the chamber pressure oscillations or by the presence of the plant, and that waves are random with an approximately Gaussian probability density function (Goda, 2000), as described by;

$$\phi(\eta) = \frac{1}{\sqrt{2\pi}\sigma(\eta)} \exp\left(-\frac{\eta^2}{2\sigma^2(\eta)}\right) \quad (4.23)$$

where  $\eta$  is the surface elevation and  $\sigma(\eta)$  is its standard deviation

If the relationship between the incident wave and the resulting chamber pressure is assumed to be linear then the chamber pressure spectral distribution  $S_p(\omega)$  will also be random with a Gaussian probability density function;

$$\phi(p) = \frac{1}{\sqrt{2\pi}\sigma(p)} \exp\left(-\frac{p^2}{2\sigma^2(p)}\right) \quad (4.24)$$

where  $p$  is the chamber pressure

The variance of  $S_\eta(\omega)$  and  $S_p(\omega)$  are respectively given by;

$$\sigma^2(\eta) = \int_0^\infty S_\eta(\omega) d\omega \quad (4.25)$$

$$\sigma^2(p) = \int_0^\infty S_p(\omega) = 2 \int_0^\infty S_\eta(\omega) |\Gamma(\omega)\Lambda(\omega)|^2 d\omega \quad (4.26)$$

where  $\Lambda$  is the frequency response relating the diffraction flow rate to the chamber pressure, and is given by;

$$\Lambda = \left[ \frac{KD}{\rho_0 N} + B + i \left( \frac{\omega V_0}{\gamma p_0} + C \right) \right]^{-1} \quad (4.27)$$

Combining (4.10) and (4.12) the instantaneous power transfer to the turbine is given by;

$$P_t = \rho_0 N^3 D^5 f_p \left( \frac{p}{\rho_0 N^2 D^2} \right) \quad (4.28)$$

As the chamber pressure is assumed to have a Gaussian probability density distribution with variance  $\sigma^2(p)$ , the mean power transfer to the turbine is given by;

$$\bar{P}_t = \int_{-\infty}^{\infty} \phi(p) P_t(p) dp \quad (4.29)$$

which combined with (4.24) and (4.28) gives the full solution for mean power transfer to the turbine;

$$\bar{P}_t = \frac{\rho_0 N^3 D^5}{\sqrt{2\pi}\sigma(p)} \int_{-\infty}^{\infty} \exp\left(-\frac{p^2}{2\sigma^2(p)}\right) f_p \left( \frac{p}{\rho_0 N^2 D^2} \right) dp \quad (4.30)$$

or in dimensionless form;

$$\bar{\Pi} = \frac{1}{\sqrt{2\pi}\sigma(\Psi)} \int_{-\infty}^{\infty} \exp\left(-\frac{\Psi^2}{2\sigma^2(\Psi)}\right) f_p(\Psi) d\Psi \quad (4.31)$$

However, as shown in section 3.6.3 due to the water depth reduction in the chamber by the collection of boulders and the defect in the chamber front lip, the chamber pressure is asymmetric and the probability distribution is not Gaussian. As such the validity of using stochastic analysis for the Pico case study, in its current state, needs attention.

### 4.2.3 Time domain model

In order to assess temporal changes in the system dynamics such as: tracking the temporal turbine angular velocity fluctuations, the effects of wave grouping, or the system response to adaptive control strategies, a time series of the system variables needs to be modelled. The time domain model is tasked with generating a time-series of chamber pressure and the resulting turbine response from a known input of excitation flow rate  $q_e(t)$ , and the system starting conditions. A time domain model for a shore mounted OWC is presented in (Falcão & Justino, 1999), which follows from (Evans, 1982), and is reviewed in the following.

In (Falcao, et al., 2003), a method to synthesise the excitation flow in the time-domain is described. For regular waves propagating in a direction perpendicular to the chamber front wall, the surface elevation can be described by;

$$\eta(x, t) = a \sin(\omega t - kx) \quad (4.32)$$

where:  $a$  is the amplitude,  $k$  is the wave number and  $x$  is the horizontal coordinate parallel to the wave direction and where  $x = 0$  is the chamber back wall. Assuming the front wall is thin with negligible draft, reflection from the front wall can be neglected and the excitation flow rate is the rate of change in chamber volume (of a system open to the atmosphere) resulting from the standing wave formed by the superposition of the incident wave and the reflected wave from the back wall, which is given by;

$$q_e(t) = \frac{2ay_H\omega}{k} \sin(2kx_H) \cos(\omega t) \quad (4.33)$$

where  $x_H$  is the horizontal separation distance between the chamber front and back wall and  $y_H$  is the horizontal separation distance between the chamber side walls

As discussed in section 1.5.2, the synthesise of irregular waves is achieved with a superposition of a number of  $n$  regular waves  $j$  so that the expression for surface elevation of the incident wave in time and space becomes;

$$\eta(x, t) = \sum_{j=1}^n a_j \sin(\omega_j t - k_j x) \quad (4.34)$$

The excitation flow rate for irregular waves then becomes;

$$q_e(t) = 2y_H \sum_{j=1}^n \frac{a_j \omega_j}{k_j} \sin(2k_j x_H) \cos(\omega_j t) \quad (4.35)$$

The radiation flow rate  $q_r(t)$ , is a response to  $q_e(t)$  and depends on the instantaneous chamber pressure, which is also dependent on the chamber pressure history. Following (Falcão & Justino, 1999) a memory function term or added damping term  $g_r(t)$  is introduced to account for the pressure history in the expression that defines the radiation flow rate. The radiation flow rate is then described by the convolution integral of the pressure history and memory function, given by;

$$q_r(t) = \int_{-\infty}^t g_r(t - \tau) p(\tau) d\tau \quad (4.36)$$

$g_r(t)$  is a function of radiation conductance which in turn is a function of the specific system geometry being considered and needs to be found. Relating  $g_r(t)$  to the radiation conductance  $B(\omega)$  is done by substituting in (4.14), (4.16) into (4.20), and taking the Fourier transform, under the assumption that  $g_r(t)$  is an even function, and inverting the result (see (Falcão & Justino, 1999) for more details), which yields;

$$g_r(t) = \frac{2}{\pi} \int_{-\infty}^{\infty} B(\omega) \cos(\omega t) d\omega \quad (4.37)$$

where radiation conductance  $B(\omega)$  is to be found for the specific system geometry as described in section 4.2.1.

Numerically evaluating (4.37) is not trivial due to a logarithmic singularity at  $t = 0$  and the procedure for evaluating  $g_r(t)$  is described in (Justino, 1993) and (Falcão & Justino, 1999).

Applying (4.36) to (4.7), yields the integro-differential equation of the time-domain model for the chamber pressure;

$$\frac{dp_c}{dt} = \frac{\gamma p_0}{V_0} \left[ q_e + \int_{-\infty}^t g_r(t - \tau) p(\tau) d\tau - \frac{\dot{m}_t + \dot{m}_v}{\rho_0} \right] \quad (4.38)$$

Expanding (4.38) with (4.3), (4.8), (4.9) and with  $f_m = K$ , yields;

$$\frac{dp_c}{dt} = \frac{\gamma p_0}{V_0} \left[ q_e + \int_{-\infty}^t g_r(t - \tau) p(\tau) d\tau - \frac{K p_c D}{\rho_0 N} - A_v k_v \text{sign}(p_c) \left( \frac{2|p_c|}{\rho_0} \right)^{\frac{1}{2}} \right] \quad (4.39)$$

which is to be solved numerically.

The solution in (4.39) assumes that  $q_e$  is a known function of time. This is of little concern if the theoretical simulations are to be made using a synthesised irregular input wave time series as described by (4.36). However, a problem presents itself if the model is to be driven from operational data as it will be very difficult to sample  $q_e$  directly because it will need to be decomposed from the superposition it forms with radiation flow. This is in addition to the difficulties with measuring the change in chamber volume.

At Pico, the water surface elevation inside the chamber is captured at a single point near the horizontal centre of the chamber by an ultrasonic backscatter distance measurement sensor. As such an alternative option for driving the time domain model, using real field data as the input, is to assume that at any time instant the chamber water surface elevation is equal at all points inside the chamber (like a flat piston plate) and this is equal to the surface elevation measured by a sensor. This approach is described in (Count, et al., 1981), for example. Under this assumption, and with the condition that other system variables remain constant, the following equation is formed;

$$q_e(t) + q_r(t) = q_e + \int_{-\infty}^t g_r(t - \tau) p(\tau) d\tau = -\frac{dV}{dt} = \frac{d(\eta \gamma_H x_H)}{dt} \quad (4.40)$$

where  $\eta$  is the chamber surface elevation, can be substituted into (4.39), to yield;

$$\frac{dp_c}{dt} = \frac{\gamma p_0}{V_0} \left[ \frac{d(\eta \gamma_H x_H)}{dt} - \frac{K p_c D}{\rho_0 N} - A_v k_v \text{sign}(p_c) \left( \frac{2|p_c|}{\rho_0} \right)^{\frac{1}{2}} \right] \quad (4.41)$$

However, if the objective is to model the system response to control, as is the case in this study, adjustments to the system variables will be made as part of the control strategy. As such this method would no longer be valid because control will modify the chamber pressure, modifying the radiation flow  $q_r(t)$  and subsequently the time series of  $\dot{V}$  which is being used as the input to drive the model, unless it is assumed that the modification to  $q_r(t)$  has a negligible effect on  $\dot{V}$ . Alternatively the  $q_r(t)$  could be calculated from chamber pressure and subtracted from the sampled  $\dot{V}$ , to give  $q_e$  needed to drive the model (in a similar manner to the first time-domain model approach, discussed). However, only long waves have a flat water surface profile and sloshing is not considered. Furthermore, as seen in the chamber surface elevation data from Pico (seen in figure 3.13), the wave elevation measurements are

difficult to obtain accurately (for the possible reasons discussed in section 3.4.2). These effects are seen (in the data) to get significantly worse in larger waves and at lower tidal elevations because of the increasingly nonlinearity of the chamber hydrodynamics in the shallow water.

### 4.3 Pneumatic to mechanical to electrical power transfer and losses

Once the pneumatic response is known the remaining power transfer stages can be considered to yield the full system response simulation. These remaining power transfer stages are modelled with the integration of the following power balance equation which is described in (Falcão, 2002), for example;

$$\frac{dN}{dt} = \frac{P_a - P_e - P_b - P_{el}}{IN} \quad (4.42)$$

where  $P_e$  is the electrical power taken off the turbine, which is known and is specified by the implemented electrical power take-off curve (the power take-off curves for the Pico case study are given in figure 3.7),  $P_a$  is the instantaneous aero-dynamic power transfer to the turbine, which is found by the value of  $\Pi(k)$  that corresponds with  $\Psi(p_c(k), N(k))$  (if the turbine characteristic curve is known), and with (4.10),  $P_b$  is the power dissipation from bearing friction (to be found) and  $P_{el}$  is other electrical losses (also to be found).

If aerodynamic losses (drag) are factored into the turbine characteristic curve (which is true for the Pico case study and manifests by negative values of  $\Pi$  at zero values of  $\Psi$ , in figure 3.5), the remaining turbine mechanical power losses will be dominated by the conversion of kinetic energy to heat from friction in the bearings that support the turbo-generator axel. The load on the bearings is comprised of two components namely; the vertical force due to the mass of the turbine resulting in a frictional force  $F_m$  and a torque opposing rotation  $\tau_m$  and a horizontal force due to thrust from air flow across the turbine resulting in a frictional force  $F_a$  and a torque opposing rotation  $\tau_a$ .

The torque  $\tau_m$  can be found by analysing the rotational speed decay of the turbine at low rotational speeds so that the aerodynamic drag is negligible. This was performed for the Pico case study using plant data in (Falcão, 2002) yielding  $\tau_m = 12.8 (Nm)$ .

As discussed in (Falcão, 2002)  $\tau_a$  is far more difficult to measure because the system cannot be isolated for analysis as air flow is required to generate the axial thrust force. All other components of the pneumatic to mechanical to electrical transfer would need to be known exactly in order to make this calculation, which could be performed with;

$$\tau_b = \frac{P_a - P_e - P_{el}}{N} - I \frac{dN}{dt} - \tau_m \quad (4.43)$$

Alternatively, the generator could be isolated electrically in which case electrical power and electrical losses are eliminated, leaving just the balance between aerodynamic torque as described by the turbine characteristic curve (which accounts for aerodynamic resistance) and the opposing torque from the bearings;

$$\tau_b = \frac{P_a}{N} - I \frac{dN}{dt} - \tau_m \quad (4.44)$$

Removing the resistive electromagnetic torque whilst maintaining the driving pneumatic power would be considered to be a risky experiment as the machine could accelerate quickly with the potential for it to lose control. Also,  $\tau_a$  is likely to be comparatively small and the trend will most likely be lost in the error due to data noise and any error in the turbine characteristic curve.

An alternative solution to find (very approximately) the value of  $\tau_a$  using theoretical aerodynamic flow modelling is presented in (Falcão, 2002) and the derivation of the following equation is given in appendix B;

$$|F_a| = \rho_0 N^2 D^4 \left( \frac{\pi}{4} |\Psi| - \frac{1}{2(1-(D_i/D)^2)^2} [1 + 4H(|\Psi| - \Psi_{cr}) \cot^2 \alpha_1] \Phi^2 \right) \quad (4.45)$$

where  $\Psi_{cr} = 0.067$  is the critical non-dimension pressure threshold after which point turbine stall occurs,  $H$  is a Heavyside step function where  $H = 0$  when  $|\Psi| - \Psi_{cr} < 0$  or  $H = 1$  when  $|\Psi| - \Psi_{cr} > 0$ , and  $\alpha_1 = 62.5^\circ$  relates to the radial averaged guide vane angle.

The constant  $c_b$  to characterise the bearing system, can be defined as the ratio of the applied reaction force, and resulting opposing torque from friction.

$$c_b = \frac{\tau_m}{gm_{turbine}} = 0.458 \times 10^{-3} (m) \quad (4.46)$$

where  $m_{turbine} = 2850(kg)$  is the mass of the turbine, shaft and generator rotor, and  $g$  is acceleration from gravity.

Assuming that the constant characterising the bearing system is equal in the vertical force direction as it is in the horizontal force direction, the aerodynamic torque from bearing friction is given by;

$$\tau_a = c_b |F_a| \quad (4.47)$$

and the mechanical power loss from bearing friction is then;

$$P_b = (\tau_a + \tau_m)N \quad (4.48)$$

Finally, electrical losses from electrical conversion inefficiency also need to be considered. The plant system model is affected by the generator efficiency because the true power taken off the generator is  $P_e + P_{el}$  but only  $P_e$  reaches the power electronics because  $P_{el}$  is lost due to inefficiencies in the generator. To determine the power to grid the power electronics efficiency must also be known and factored in, although this does not affect the turbine response. The power to grid  $P_G$  is then described by;

$$P_G = P_e - P_{pel} \quad (4.49)$$

where  $P_{pel}$  is the power electronics power losses.

#### 4.4 Short-term wave forecasting introduction

In order to control and alter the WECs behaviour or response for the purposes of performance optimisation or survival, a forecast of the incident wave parameters or a wave time-series will be needed, unless the control elements are passive, have negligible actuation time or control is based on wave

activity that occurred in the recent past. The forecast horizon needed for control is dependent on: the type of control strategy, the response rate of the device's motion or inertial components, and the actuation rate of controlling mechanisms. Some examples of WEC control strategies in the literature include: switching turbines on or off to maintain an optimum pressure head for an overtopping type WEC (Tedd & Frigaard, 2007), latching or declutching to promote resonance of floating oscillating devices such as a point absorbers (Budal, et al., 1982), turbine rotational speed regulation using generator torque control for an OWC (Falcão, 2002). To obtain advanced knowledge of the incoming wave time series for the Pico case study, the following options are available.

Deploy a sensor or sensor array some distance up-wave of the device (figure 4.2) in order to measure the incident wave time-series and then transform this information to what is later expected to occur at the device. The transfer of up-wave measurements to the resulting behaviour at the device is considered in (Tedd & Frigaard, 2007), (Ferri, et al., 2012), (Fernandez, et al., 2013) and (Paperella, et al., 2015). For the Pico case study this transfer is complicated by the following processes: frequency dependent resonance of the water oscillation in the chamber, damping from the pressure in the chamber (Folley & Whittaker, 2005), shoaling, wave directionality and viscous loss from turbulence induced by the chamber front wall (Morrison & Greated, 1992). In addition, reflected waves from the chamber back wall or surrounding coastline, and radiated waves from the chamber pressure, will propagate up-wave and interfere with the incident wave, modifying the observations. A spatial array of wave sensors could be used to extract the incident wave from the incident and scattered wave superposition (Goda & Suzuki, 1976) and deal with any wave directionality (Davis & Regier, 1977), (Isobe & Kondo, 1984). This, however, will add financial and computational cost, complexity and additional points of potential failure.

Alternatively the wave prediction can be made using only the past measurements made at the device location as described in (Paperella, et al., 2015), (Korde, et al., 2001), (Fusco & Ringwood (b), 2010), (Sheng & Lewis, 2010) and (Fischer, et al., 2012). This removes the issues associated with wave interference (from reflected and radiated waves), wave directionality and wave dispersion effects. Additionally, the cost and potential for failure associated with placing sensors in a hard to access and harsh environment is avoided. However, performance of the forecast will be exclusively dependent on the strength of correlation between the future behaviour and the measurements of the recent past.

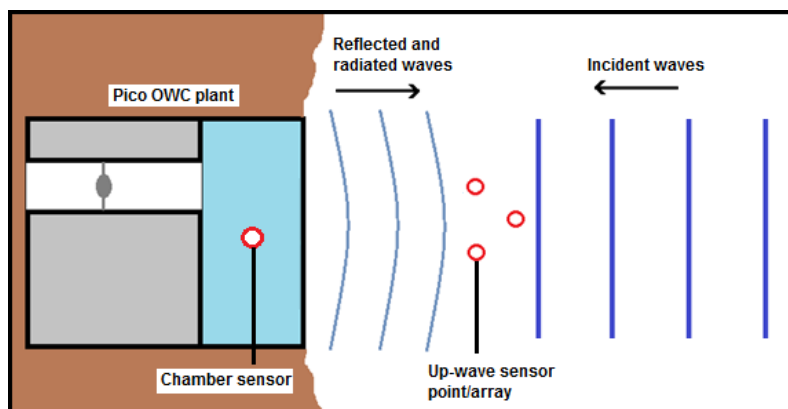


**Figure 4.2** Schematic of sensor location options at the Pico OWC for the purpose of short-term forecasting.

The final option is a multivariate approach which combines measurements made up-wave (with a lead time), and past measurements made at the device. This approach is less well documented in the literature, probably due to the lack of relevant data for this configuration.

## 4.5 Short-term wave forecasting methods

The most promising and relevant methods (for the Pico case study) for short-term wave forecasting, as found in the literature, are presented in following subsections.

### 4.5.1 Variable and spatial transformations using digital filters

If up-wave information is available a digital filter can be used to transform the up-wave measurements to what is expected to occur at the device. This method is used in (Tedd & Frigaard, 2007) to forecast the wave elevation at the reservoir ramp of the “Wave dragon” over-topping type WEC.

In (Tedd & Frigaard, 2007) the digital filter serves two functions 1.) Translate the pressure measured by a transducer attached to the mooring pile 52 *m* up-wave, to the resulting surface elevation at the device and 2.) Translate the alteration in wave phase measured at the up-wave sensor location to the resulting phase at the device location due to the wave propagation time and frequency dispersion effects.

From linear wave theory, the pressure  $p(z)$  measured at a depth  $z$ , is related to the surface elevation  $\eta_{uw}$  vertically above the sensor by;

$$\eta_{uw} = \frac{p(z) \cosh(kh)}{\rho g \cosh(kz+kh)} \quad (4.50)$$

where  $h$  is the water depth,  $k$  the wave number,  $\rho$  the water density and  $g$  the acceleration due to gravity.

As (4.50) is a function of frequency, the relationship could be described by the amplitude response of a filter  $|H(\omega)|$ , which applies gain to each frequency component  $\omega$ . The filter can then be used to deliver the corresponding surface elevation vertically above the pressure sensor. The phase response of the filter can be used to translate the wave phase measured at the sensor, to what later occurs at the device. In the time-domain the filter’s phase response equates to a time delay  $t(\omega)$ . The time delay imposed on each frequency component needs to factor in the propagation rate and travel time  $\tau_{tr}$  of the different wave frequency components between the up-wave sensor and the device;

$$\tau_{tr} = \frac{xk}{\omega} \quad (4.51)$$

where  $x = 52 \text{ m}$  is the distance between up-wave measurement point and device,  $k$  is the wave-number, and  $\omega$  the angular frequency of the wave component.

All causal filters have a negative non-zero phase response, which in the time-domain equates to a delay. For a finite impulse response filter (*FIR*) this phase response is linear and is a function of the filter order number  $m$  and the sampling frequency  $f_s$ . The time delay introduced by the *FIR* filter  $\tau_{df}$ , is given by;

$$\tau_{df} = \frac{m}{2f_s} \quad (4.52)$$

If  $\Gamma$  is the total forecast horizon time needed for control, taking into account the wave travel time  $\tau_{tr}$  and the time delay imposed by the filter is  $\tau_{df}$ , then the required frequency component time shift  $t(\omega)$  is;

$$t(\omega) = \Gamma - \tau_{tr} - \tau_{df} \quad (4.53)$$

which translates to a phase shift of;

$$\angle H(\omega) = \omega(\Gamma_c - \tau_{tr} - \tau_{df}) \quad (4.54)$$

The ideal target filter  $H(\omega)$ , that describes the transfer in both phase and amplitude, was discretised by sampling at  $n$  equally spaced frequency intervals between 0 and the numerically down-sampled sampling frequency  $f_s$ ;

$$H[n] = |H(\omega)|e^{\angle H(\omega)} \quad \text{for } n = 0, \dots, m-1 \quad (4.55)$$

where  $\omega = f_s 2\pi n/m$

A real-filter was then designed around the discretised points of the ideal filter. They conclude that a filter with an order number of  $m = 64$  provided a suitable representation of the ideal filter (in the dominant frequency band of interest) when comparing the filter's amplitude and phase response in the frequency domain. At this filter order number the time delay incurred by the filter is  $\tau_{df} = 12.8$  s (for the peak frequency component) so that the actual forecast horizon for the lead time they require  $t_{tr} = 11.2$  (s), is  $\Gamma_c = 24$  (s). As this horizon time is outside the time range for waves to propagate between the up-wave sensor and the device it seems the intended placement of the up-wave sensor is further from the device but it is assumed that the transfer accuracy is the same.

For use in real-time forecasting the inverse discrete-time Fourier transform generates the filter's impulse response  $h[k]$ ;

$$h[k] = \frac{1}{m} \sum_{k_1=0}^{m-1} H(n) e^{i \frac{2\pi n k}{m}} \quad \text{for } k = 0, \dots, m-1 \quad (4.56)$$

Unfortunately they were unable to gain surface elevation data at the device due to technical issues and ultimately compared the forecast accuracy to another forecast using an off-line filter with a very high filter order number (that converges with the ideal filter) that would make  $\Gamma_c$  too large to be used in practice (up-wave sensor would be very far from the device). Good accuracy was found in this test, but uncertainty is present as the actual physical scenario being considered was not tested.

The same approach is adopted in (Ferri, et al., 2012) to forecast the surface elevation and excitation force on the one degree of freedom, point absorber the “Wavestar”, using an *FIR* filter. Small scale laboratory testing was performed with the up-wave sensor located 2.55 m from the device with regular and irregular waves with;  $0.7 \text{ s} \leq T_p \leq 2 \text{ s}$ ,  $0.02 \text{ m} \leq H_s \leq 0.2 \text{ m}$ , and in intermediate water depth  $\lambda/20 < h < \lambda/2$ . Good forecast accuracy, with a correlation factor  $> 95\%$ , was achieved for low steepness linear waves (low  $H_s$  and high  $T_p$ ).

In (Paperella, et al., 2015) an alternative solution to forecasting using an *FIR* filter is proposed. If the water depth  $h$  between the up-wave sensor is much less than the wavelength ( $h < \lambda/20$ ), the wave phase velocity is not dependent on frequency and dispersion effect can be ignored. In this scenario the phase shift between the up-wave sensor location and the devices is constant and undistorted by frequency dispersion. This simplifies the problem greatly. The proposed *FIR* filter model in (Paperella, et al., 2015) assumes that the surface elevation at the device  $\eta(k)$ , at a data point in time  $k$ , can be described by a linear combination of the  $n$  past up-wave measurements, starting at a data time point  $k - n_k$  where  $n_k$  is a data point delay that accounts for the uniform wave propagation travel time  $t_{tr} = n_k f_s$  between the up-wave measurement point and the device. The filter’s impulse response is found by applying  $n$  weighting coefficients  $b_j$  (where  $j = 1, 2, \dots, n$ ) to the past  $n$  up-wave values. The values of the weighting coefficients  $b_j$  are found through the minimisation of the error between the sum of the weighted  $n$  past up-wave values and the corresponding surface elevation at the device (after the travel time  $t_{tr}$ ). This approach circumvents the need to perform the Fourier transform and design the filter in the frequency domain through comparison with an ideal target filter as in (Tedd & Frigaard, 2007). It also implicitly accounts for the phase shift due to the wave travel time and the phase delay imposed by the filter. Using this method the *FIR* filter takes the form;

$$\eta(k) = \sum_{j=1}^n b_j u(k - j + 1 - n_k) + \varepsilon(k) \quad (4.57)$$

Where  $u$  is the up-wave measurement relating to the surface elevation,  $b_j$  is the weighting coefficients and  $\varepsilon(k)$  is the error.

In (4.57) the input data, which is the up-wave measurement  $u$ , is delayed by  $n_k$  time steps (equal to the propagation time between up-wave sensor and device), which achieves a phase match between the first filter input and its output. From the filter’s perspective the up-wave sensor now resides at the same location as the device and the travel time is considered to be zero ( $n_k = 0$ ). Any transformations between the up-wave location and the device are linearly approximated by the filter’s impulse response.

From a batch training data set of length  $L$ , the model coefficients  $b$  are found as those that result in the least squares minimisation of the cost function  $J$ . The algorithm for the method of least squares is described in appendix C. The cost function is defined as the variance of the error between the measurements made up-wave and measurements made at the device.

$$J = \sum_{k=1}^L (\eta(k) - \hat{\eta}(k))^2 \quad (4.58)$$

When the model coefficients  $b_j$  that minimise the cost function are found the *FIR* forecast model can be deployed. In real-time use, if the most recent data (instead of the delayed data that was used for designing the filter) is input to the filter, the  $l_{max} = t_{tr}/f_s$  steps ahead prediction is automatically generated and outputted by filter. Any point  $l$  between the present time and the  $l_{max}$  steps ahead point, can be generated by delaying the filter input time series by  $(l - l_{max})$ .

The  $l$  steps ahead prediction of the surface elevation at the device  $\hat{\eta}$  is then given by the *FIR* filter output;

$$\hat{\eta}(k + l|k) = \sum_{j=1}^n b_j u(k + l - l_{max} - j + 1) \quad (4.59)$$

This method will depreciate with increasing phase modification from dispersion effects and is only suitable for shallow water applications or when the separation distance is very short. Because the model is linear its performance will likely depreciate with increasing nonlinear transformations that occur during the propagation between the up-wave measurement location and the device. Also, interference of up-wave measurements from the superposition of the incident waves with the radiated and reflected waves from the device will likely have a detrimental effect on the performance unless an up-wave array of sensors is used to decompose the superposition to extract the incident wave.

#### 4.5.2 Autoregressive model

If no up-wave information is available, the challenge of wave forecasting is limited to predicting the future events from the past and present measurements made at the device. If there is a linear relationship between past and present observations and the future events then an autoregressive (*AR*) model might be considered.

In (Korde, et al., 2001) an *AR* model is used to predict the velocity of a spherical buoy moving in heave only. If  $k$  is a data point in time, the *AR* model assumes the velocity  $v(k)$  of the buoy is equal to a number  $n$  (model order) of its past values each weighted by a autoregression coefficients  $a_j$  (where  $j = 1, \dots, n$ ) plus an error term  $\varepsilon(k) = v(k) - \hat{v}(k)$ , which is assumed to be white noise, with a Gaussian profile and zero mean;

$$v(k) = \sum_{j=1}^n a_j v(k - j) + \varepsilon(k) \quad (4.60)$$

To implement the forecast model first the autoregression coefficients  $a_j$  must be found. To achieve this a known training data set of length  $L$  (they used  $L = 1005$  data points) is divided in to sets of length  $n$  containing successive data points in time. These samples are placed into a matrix giving a one data point staggered windowing of the data;

$$\mathbf{V} = \begin{bmatrix} v(n) & v(n-1) & \dots & v(1) \\ v(n+1) & v(n) & \dots & v(2) \\ \vdots & \vdots & \ddots & \vdots \\ v(L-1) & v(L-2) & \dots & v(L-n) \end{bmatrix} \quad (4.61)$$

If the autoregression coefficients  $a_j$  and the targets  $v$  are described by the following vectors;

$$A = \begin{bmatrix} a_1 \\ \vdots \\ a_n \end{bmatrix} \quad (4.62)$$

$$\Xi = \begin{bmatrix} v(n+1) \\ \vdots \\ v(L) \end{bmatrix} \quad (4.63)$$

then (4.60) can be described in matrix notation as;

$$\Xi = VA + \varepsilon \quad (4.64)$$

The cost function  $J$  is a quantification of the total error and they define the cost function as the error variance of the entire training data set;

$$J = \varepsilon^T \varepsilon = (\Xi - VA)^T (\Xi - VA) \quad (4.65)$$

The linear least-squares minimisation of  $J$  (appendix C) gives the best estimate of the autoregression coefficients;

$$\hat{A} = (V^T V)^{-1} V^T \Xi \quad (4.66)$$

The predicted velocity  $\hat{v}(k+1)$  of the buoy at the next data sampling point is then found by summing  $n$  past values weighted with a corresponding autoregression coefficients  $a_j$  found with (4.66).

$$\hat{v}(k+1) = \sum_{j=1}^n a_j v(k+1-j|k) \quad (4.67)$$

For multi-step ahead prediction the process is repeated so that for each new iteration (to predict the next time step) the most recent input value to the model is the predicted velocity  $\hat{v}$  from the previous iteration, and the oldest is discarded. The forecasted velocity at future point  $k+l$  is then given by;

$$\hat{v}(k+l|k) = \sum_{j=1}^n a_j \hat{v}(k+l-j|k) \quad (4.68)$$

In (4.68)  $\hat{v}$  becomes  $v$  when  $k+l-j \leq k$ .

The autoregression coefficients  $a_j$  are found from a known training data set and are static while being used to forecast the unseen test data. The model is self-adaptive to the most recent phase and amplitude information because each of the autoregression coefficients is coupled with an input data point holding this information. However, the model is not self-adaptive to the most recent spectral information because the autoregression coefficients, optimised from the training data, are fixed until they are updated by the process of re-training with the most recent available data to redefine the optimum regression coefficients. This up-date is not intrinsic to the forecast model and retraining intervals need to be defined in order to adjust the model to temporal spectral changes.

In (Korde, et al., 2001) a forecast horizon of only two time steps equating to 0.8 (s) is considered, and the model order was said to be found by trial and error but the value is not disclosed.

In (Fusco & Ringwood (b), 2010) the *AR* model (amongst many other forecasting models) is used to forecast the surface elevation measured by wave buoys located offshore at the Pico Island in the Azores (conveniently) and Galway bay, Ireland. The *AR* model is configured in same way as (Korde, et al., 2001) but the forecast target variable was the surface elevation  $\eta$  measured by a wave rider buoy instead of a point absorber's heave velocity. Also the model coefficients were found using a different cost function than (Korde, et al., 2001), called the long-range predictive identification (*LRPI*), which factors in the error incurred for all forecasted data points of the multi-step ahead forecast instead of just the 1-step ahead forecast. This cost function is defined as;

$$J_{LRPI} = \sum_{k=1}^L \sum_{j=1}^{l_{max}} [\eta(k) - \hat{\eta}(k|k-j)]^2 \quad (4.69)$$

where  $L$  is the total number of data points in the training data set,  $l_{max}$  is the maximum data point forecast horizon length.

A method to estimate the predictability (the dependency of future values on past values) of the data is also proposed, and quantified by the predictability index  $R^2$  ( $R^2 = 1$  means full dependency of future value  $k + l$  on past values and  $R^2 = 0$  meaning no dependency), given by;

$$R^2(l) \triangleq \frac{E\{\hat{\eta}(k+l)^2\}}{E\{\eta(k)^2\}} \quad (4.70)$$

where  $\hat{\eta}(k + l)$  is the optimal  $l$  step ahead prediction, and  $E$  is the expectation operator.

This predictability index is used to assess the relationship between the spectral bandwidth and the achievable forecast accuracy. It was found that the predictability significantly increases when the spectral bandwidth is shortened by removing the low energy high frequency waves (and noise) with a low pass filter. Based on this finding, the training data used to define the *AR* coefficients and the data used to query the model were heavily low pass filtered with a cut off frequency of  $\omega_c = 0.7 \text{ rad s}^{-1}$ . A Chebyshev type I filter of order 15 and maximum error in the pass band of  $10^{-3}$  was used. They justify the use of such a low cut off frequency because it still preserves the lower frequency wave components, which contain the bulk of the incident wave energy, whilst discarding the high frequency components that are of little interest to wave energy conversation and potentially degrade the forecast accuracy.

Filtering was performed offline with a zero-phase filter so that no phase delay or distortion is incurred by the filtering process. To achieve zero-phase filtering, the data set must first be passed through the filter forward in time in its entirety. Because all filters impose a phase-delay the forward in time filtered data must then be filtered again backwards in time to counter the delay incurred in the first pass (to preserve the original phase). Mathematically this method is described most easily in the frequency domain and is commonly found in the literature, for example (Stearns & Hush, 2011);

Taking the z-transform of the excitation surface elevation time series  $\eta_{e_t}$ , gives the frequency domain representation  $H(z)$ , given by;

$$H(z) = \sum_{t=0}^{\infty} \eta_{e_t}(z)^{-t} \quad (4.71)$$

where  $z$  is a complex number given by  $z = e^{i\omega}$ ,  $\omega$  is the angular frequency, and  $i = \sqrt{-1}$  is the imaginary unit.

For a single (causal) pass of the frequency domain representation of the chamber excitation surface elevation  $H(e^{i\omega})$  with some filter  $F(e^{i\omega})$ , yields;

$$H(e^{i\omega})F(e^{i\omega}) \quad (4.72)$$

The imaginary term translates to a phase distortion. The time reverse of this filter's output is given by;

$$H(e^{-i\omega})F(e^{-i\omega}) \quad (4.73)$$

If this is then passed through the filter  $F(e^{i\omega})$  (anti-causal) a second time the result is;

$$H(e^{-i\omega})F(e^{-i\omega})F(e^{i\omega}) \quad (4.74)$$

Taking the time reverse of the second filter pass yields;

$$H(e^{i\omega})F(e^{i\omega})F(e^{-i\omega}) = H(e^{i\omega})|F(e^{i\omega})|^2 \quad (4.75)$$

Thus the output spectrum is obtained with a filter with response  $|F(e^{i\omega})|^2$ , which because of the squared term means it is purely real valued and zero phase distortion is achieved.

However, to effectively apply this technique, future values must be known making the filter non-causal and is therefore not realisable in real time applications where only the known data points, up to the point of interest, are available for the filter input.

The use of a non-causal zero-phase filter is justified by the authors of (Fusco & Ringwood (b), 2010) because although wave rider buoy data is used, the target system under evaluation is a floating point absorber. The motion of a floating point absorber naturally rejects higher frequency components due to: inertia, viscosity, power take-off damping and non-uniform pressure acting on the device. In essence the device has a physical low-pass filtering effect (Faltinsen, 1990) between the driving water surface elevation and its resultant motion. This is used to support the validity of the results obtained through non-causal digital filtering. Generally excellent forecast accuracy was achieved, especially for the narrow banded sea-states associated with the Pico wave buoy location. At this degree of filtering a near perfect forecast was achieved up to a forecast horizon of 20 seconds (the maximum forecast horizon considered). A model order of 24 which, due to the sampling frequency of  $f_s = 1.28$  (Hz) equates to 18.75 (s) of past data used to influence and make the forecast, was found to give the best forecast accuracy in the specific application. However, this approach has the possibility of being valid only if the device has a natural low-pass filtering effect that is equal to the non-causal digital filter being applied.

In (Fusco & Ringwood (a), 2010) the validity of filtering data digitally is more critically evaluated by considering the forecast performance of data that has been filtered with a single forward pass in time, which makes it causal and realisable in real-time (as no future values are considered). Unlike the non-causal zero-phase filter, all causal filters introduce a non-zero phase response which equates to a time delay in the filter's output. The phase response is a function of the filter order number and the greater the filter order number the greater the time delay in the filter's output. If the filter's output is delayed then a forecast made using this data will also be delayed, resulting in lost time in the forecast.

Also all real filters introduce an error in the output signal amplitude because the filter has a magnitude response transition region which is non-instantaneous in the frequency domain and spans the specified cut-off frequency. The amplitude of frequency components lower than the cut-off frequency will be partially attenuated in this transition band. Similarly the amplitude of frequency components that are higher than the cut-off frequency will only be partially attenuated. Increasing the filter order number narrows the transition band, thereby minimising the amplitude error of the output, but this of course increases the time delay in the filter's output. Ultimately choosing a filter order number will be a trade-off between incurring a time delay or amplitude error in the filter output. A lower order filter will minimise the output delay, but will increase the amplitude error and vice versa. The output delay is lost time in the forecast and will need to be correct through post processing by applying a phase shift

It is shown in (Fusco & Ringwood (a), 2010) that the sensitivity of the *AR* model to the amplitude errors introduced to the wave elevation time series by filtering, even if very small, have a very significant effect on the prediction because they feed back into each successive iteration of the multi-step prediction, and rapidly accumulate. The authors concede that the *AR* model presented is not robust enough to deal with the errors imposed by on-line filtering. Unfortunately, the article stops short of directly analysing how this amplitude and phase error translates to the achievable on-line forecast accuracy and indeed if there are any enhancements at all to be had by filtering data. This is a critical point which needs clarification.

The *AR* model is extended in (Fusco, 2009) to be fully adaptive by updating the autoregression coefficients to the most recent spectral information on-line. This was achieved using recursive least squares method with a forgetting factor and the Kalman filter (Kalman, 1960). However, with static autoregression coefficients, the *AR* forecast model did not suffer any degradation in forecasting the test data sampled more than 2 hours away from the training data, even in the case of rapidly changing spectral sea state. As such, on-line adaptivity of the autoregression coefficients appears to be of little concern provided it is performed at regular intervals i.e. less than 2 hours in this case.

The *AR* forecast model is also used in (Fischer, et al., 2012) to forecast the surface elevation of a wave rider buoy located in the North Sea. They propose an alternative approach to forecasting with the *AR* model. The measured past values are used to make a prediction of a single value  $l$  steps ahead. This *AR* model variant is termed "direct" and is given by;

$$\hat{\eta}(k + l|k) = \sum_{j=0}^{l-1} a_{j,l}(k)\eta(k - j) \quad (4.76)$$

where the autoregressive coefficients  $a_{j,l}$  are again found with the least squares minimisation of the cost function. With this method, if a time series is to be predicted, a bank of autoregressive coefficient sets

must be compiled with each set responsible for predicting a corresponding data point interval  $l = 1, 2, \dots, l_{max}$  up to the specific forecast horizon time  $\Gamma = l_{max}/f_s$ . Concatenation of these independent prediction outputs provides the forecasted time series. For each new data point collected in real-time the autoregressive coefficients were updated, and as such this method implicitly adapts to slow spectral variations of the sea state. In (Fischer, et al., 2012) valuable information is gained because emphasis is put on the real-time on-line performance and as such avoids the uses of non-causal filtering. The forecast performance is much poorer than the results achieved in (Fusco & Ringwood (b), 2010) with heavy non-causal low pass filtering. Reasonable forecast accuracy is only achieved up to about 3 seconds (in larger sea states) with a rapid decline in performance thereafter. However, it should be noted that the North Sea wave climate is dominated by short period broad banded spectral sea states. As shown in (Fusco & Ringwood (b), 2010) the performance of the *AR* model is far better in very narrow banded sea states which are typical at the Pico plant location.

#### 4.5.3 Nonlinear Autoregressive model using Neural Networks

The *AR* model discussed in section (4.5.2) assumes the output (forecast) is linearly related to the sum of inputs (past data) each weighted by a coefficient that is found through error minimisation. If relationship is actually nonlinear to a significant degree, a nonlinear Autoregressive model could be considered. Defining the nonlinear relationship between the inputs and outputs of the forecast model can be achieved by a nonlinear function found using an Artificial Neural-Network (*ANN*) learning structure.

*ANN* are widely documented (see for example (Gurney, 1997), (Nørgaard, et al., 2003)) powerful, versatile but inherently black-box models for translating input/s to output/s. It mimics in a numerical way, the transfer and transformation of electrical signals through networks of neurons in the brain of a mammal.

Much of the literature on oceanographic forecasting with *ANNs* is concerned with forecasting the slow variations in the sea-state i.e. the significant wave height, see for example (Deo, et al., 2001), (Reikard & Rogers, 2011), (Makarynskyy, 2004) and (Mandal & Prabakaran, 2010). However, a smaller number of studies consider the surface elevation time-series forecasting problem using neural networks with the Nonlinear AutoRegressive (*NAR*) forecast model application. These are reviewed in the following.

In (Fusco & Ringwood (b), 2010) a closed loop *NAR* type forecast model is compared to several other forecast models. The *NAR* shares many similarities to the *AR* model (section 4.5.2) in that a number of past values of a variable are used to make a one step ahead forecast of the same variable. This forecasted data point is then fed back as the most recent input value and the process is repeated until the desired forecast horizon length is achieved. However, unlike the *AR* model which weights the past values with coefficients found through the least squares minimisation of the cost function, the *NAR* applies a nonlinear function  $\varphi$  (which is found using the Neural Network learning structure) to the past values of the target variable. This is described by;

$$\hat{\eta}(k + 1) = \varphi[\eta(k), \eta(k - 1), \dots, \eta(k - n)] \quad (4.77)$$

where  $\eta$ , is the surface elevation recorded at a wave buoy.

In (Fusco & Ringwood (b), 2010) the *NAR* is tasked with a multi-step ahead prediction of the surface elevation measured by wave-rider buoys located near the Pico island and in Galway bay. Forecasts are made with up to 20 seconds horizon time using only past measurements made at the device. The *ANN* structures considered had two hidden layers with between 3 and 7 nodes in each layer. The input surface elevation time series had lengths of between 12 and 32 data points with a sampling frequency of  $f_s = 2.56$  (Hz) for the Galway bay site and  $f_s = 1.28$  Hz for the Pico site. For the typically narrow banded spectral wave climate at the Pico location, excellent forecast accuracy was achieved with up to about 10 (s) forecast horizon. The performance was much lower for the typically broad banded sea states occurring at the Galway bay location with excellent accuracy being achieved up to about 4 (s) horizon time only.

Of the forecast models considered in (Fusco & Ringwood (b), 2010) only the *AR* model out-performed the *NAR*. In some instances the *NAR* outperformed the *AR*, but these were limited to very broad, highly nonlinear sea-states. As discussed in section 4.5.2, uncertainty in this otherwise excellent study is introduced by the fact that data was filtered with a heavy zero-phase non-causal low-pass filter.

In (Fernandez, et al., 2013) an extension to the *NAR* forecast model is considered where an eXogenous input is included making it a closed loop *NARX* forecast model (which will be described in more detail in the next chapter). The forecast target is the down-wave surface elevation  $\eta_{dw}$  in the GWK large scale wave flume (Hannover) and estimates of this value are fed back to be included in the input vector for a multistep ahead prediction. The exogenous input is only the known values of up-wave surface elevation  $\eta_{uw}$ , so the forecast horizon is restricted by the wave propagation time between the two points. Surface elevation measurements of irregular waves with a JONSWAP spectrum were made by a wave gauge 140 (m) from the wave generator paddle. The *NARX* model was then tasked with forecasting the surface elevation down-wave at a location with 10 (s) wave propagation time (for the peak wave period of the spectrum). A range of sea-states ( $0.175 \text{ m} < H_s < 0.9 \text{ (m)}$  and  $2.5 \text{ (s)} < T_p < 10 \text{ (s)}$ ) and neural network architectures, having a single hidden layer with between 1 and 7 nodes, were considered. The number of data points in the input time-series (order of regression) was not disclosed.

In all cases a near perfect forecast (at 10s forecast horizon) was achieved with only a slight under-prediction of the extremities of the larger amplitude peaks. The forecast accuracy was marginally better for sea states with higher  $T_p$ . The mean squared error for the 1-step ahead prediction (which is commonly used as indicator for the model performance) was in the range of  $4.0 \times 10^{-5}$  to  $1.2 \times 10^{-3}$ . The forecast accuracy far surpasses any other study (except for when non-causal filtering is performed). Treatment of the data and specifically pre-processing by filtering is not discussed and the exceptionally high accuracy might be because the data is non-causal filtered. Alternatively it might be because of the idealised conditions of the wave flume and, as one would expect, will likely have exceptional data quality with minimal noise. Also, because no wave structure interactions occur and if the dissipating beach is functioning correctly (minimal reflection), the model is only forecasting the more simplistic process of frequency dispersion (if the water depth is sufficiently deep) and wave attenuation through friction. The final possibility is that the *NARX* model has simply learned the wave paddle wave generation sequence. If wave generation is not random and the same test sequence is repeated, then the training test data will

essentially be identical to test set data. In effect this would be the same as model over-fitting. However, without further information these are just speculations.

In (Sheng & Lewis, 2010) experiments are made with a small scale simple representation of a floating OWC devices in a laboratory wave flume with irregular waves. A closed loop Neural Network *NAR* type forecast model is employed to forecast the air-flow (through a restriction orifice), the device motion in the 6 degrees of freedom (*DOF*), and the surface elevation in the chamber. Forecasts of each variable are made from the past and (after 1-step ahead forecast) predicted values of the same variable. Forecasts were made with up to 5 data sampling periods of horizon (the sampling frequency is not disclosed exactly but looking at the data it appears to be *2Hz*). Reasonable forecast accuracy is achieved for forecast horizon length considered. The forecast accuracy of the lower frequency *DOF* motions of the device was superior to the higher frequency: heave motion, air-flow rate and surface elevation in the chamber. However, the forecast accuracy achieved is less than perfect for the low frequency motions, even with only 1.5 (s) forecast horizon, the findings in (Sheng & Lewis, 2010) contradict the arguments made in (Fusco & Ringwood (b), 2010) for the validity of using non-causal zero-phase filtered data to approximate the low-pass filtering effect between the driving water surface elevation and the resultant heave motion of a point absorber.

#### 4.5.4 Cyclical model

In (Fusco & Ringwood (b), 2010) a cyclical model is proposed which attempts to more directly replicate the physical formation of irregular waves, which are the product of a non-discreet combination of directional regular wave components (as discussed in section 1.5.2). The cyclical model simplifies this phenomenon by expressing the water surface elevation as a superposition of *m* specific linear non-directional harmonic components. The phase and amplitude of each harmonic component is specified by the model coefficients that must be found by fitting with the available data. This is expressed mathematically as;

$$\eta(k) = \sum_{j=1}^m a_j \cos(\omega_i k) + b_j \sin(\omega_i k) + \varepsilon(k) \quad (4.78)$$

where  $a_j$  and  $b_j$  are the model coefficients and  $\varepsilon(k)$  is an error term.

The frequency components being considered need to be chosen and in (Fusco & Ringwood (b), 2010) small equally spaced values of  $\omega_i$  that span the spectral range were considered. As discussed in (Fusco & Ringwood (b), 2010), more complex specification of the  $\omega_i$  values, such as a non-homogenous concentration of the frequency components in the region of interest, could be made. Each component is weighted with the model coefficients  $a_j$  and  $b_j$  which provide an on-line update of the current amplitude and phase information. However, the  $\omega_i$  values are fixed in time so that the output will always be a product of the specific frequency components considered. The amplitude model presented in (Harvey, 1989) was employed and this is described by;

$$\eta(k) = \sum_{j=1}^m \psi_j(k) + \varepsilon(k) \quad (4.79)$$

and

$$\begin{bmatrix} \psi_j(k+1) \\ \psi_j^*(k+1) \end{bmatrix} = \begin{bmatrix} \cos(\omega_j/f_s) & \sin(\omega_j/f_s) \\ -\sin(\omega_j/f_s) & \cos(\omega_j/f_s) \end{bmatrix} \begin{bmatrix} \psi_j(k) \\ \psi_j^*(k) \end{bmatrix} + \begin{bmatrix} \omega_j(k) \\ \omega_j^*(k) \end{bmatrix}, \quad j = 1, \dots, m \quad (4.80)$$

where the vector containing  $\psi_j(k)$  and its complex conjugate is the model of the cyclical components.

In state space form (4.80) becomes;

$$x(k+1) = Ax(k) + w(k) \quad (4.81)$$

and (4.79) becomes;

$$\eta(k) = Cx(k) + \varepsilon(k) \quad (4.82)$$

where;

$$x(k) = \begin{bmatrix} \psi_1(k)\psi_1^*(k) \\ \vdots \\ \psi_m(k)\psi_m^*(k) \end{bmatrix} \quad (4.83)$$

$$A = \begin{bmatrix} \cos(\omega_1/f_s) & \sin(\omega_1/f_s) & 0 & 0 \\ -\sin(\omega_1/f_s) & \cos(\omega_1/f_s) & 0 & 0 \\ 0 & 0 & \dots & 0 \\ 0 & 0 & 0 & \begin{bmatrix} \cos(\omega_m/f_s) & \sin(\omega_m/f_s) \\ -\sin(\omega_m/f_s) & \cos(\omega_m/f_s) \end{bmatrix} \end{bmatrix} \quad (4.84)$$

$$w(k) = \begin{bmatrix} \omega_1(k)\omega_1^*(k) \\ \vdots \\ \omega_m(k)\omega_m^*(k) \end{bmatrix} \quad (4.85)$$

$$C = [1 \ 0 \ 1 \ 0 \ \dots \ 1 \ 0] \quad (4.86)$$

Least squares estimates of a number of past observations are used to initialise the model and a Kalman filter (Kalman, 1960) is applied online for recursive adaptation. The  $l$  step ahead prediction of the surface elevation is made using the estimate of the model's parameters  $\hat{x}(k|k)$ , and;

$$\hat{\eta}(k+l|k) = CA^l \hat{x}(k|k) \quad (4.87)$$

The cyclical model presented in (Fusco, 2009) depends on the specification of a number of harmonic frequencies. This will approach a spectral representation of the sea state as the discretisation resolution increases, at the cost of increased complexity. Also the full range of the frequencies components present in the sea state must be encompassed

The cyclical model, in the structure that the authors propose, achieved inferior forecast accuracy compared to the *AR* model which implicitly defines the frequency components of the sea-state in the training data and avoids the issues related to using discretised representation. The *NAR* forecast model also outperformed the cyclical model, in the same study.

#### 4.5.5 Sinusoidal extrapolation

In (Fusco, 2009) a modification of the cyclical model is considered, which assumes that at any instant the short-term wave time series is dominated by a single harmonic component of frequency  $\omega$ , and the

forecast is made with a single component of the cyclical model. The dominant frequency component obviously varies rapidly in time and online up-dating of this single time-dependent frequency component  $\omega(k)$  is required. This approach is called a sinusoidal extrapolation, and is defined by;

$$\eta(k) = \psi(k) + \varepsilon(k) \quad (4.88)$$

and

$$\begin{bmatrix} \psi(k+1) \\ \psi^*(k+1) \\ \omega(k+1) \end{bmatrix} = \begin{bmatrix} \cos(\omega(k)/sf) & \sin(\omega(k)/sf) & 0 \\ -\sin(\omega(k)/sf) & \cos(\omega(k)/sf) & 0 \\ 0 & 0 & 1 \end{bmatrix} \cdot \begin{bmatrix} \psi(k) \\ \psi^*(k) \\ \omega(k) \end{bmatrix} + \begin{bmatrix} \xi(k) \\ \xi^*(k) \\ \kappa(k) \end{bmatrix} \quad (4.89)$$

where  $\omega(k)$  is the adaptive frequency component at a data point in time  $k$ ,  $\varepsilon(k)$  and  $\xi(k)$  are error terms and  $\kappa(k)$  is a white noise disturbance term.

An estimate of the state vector is achieved through the extended Kalman filter, based on the truncation of the first order Taylor expansion of (4.89) (full details can be found in (Fusco, 2012)), which is used to make the  $l$  step ahead forecast;

$$\hat{\eta}(k+l|k) = \hat{\psi}(k+l|k) \quad (4.90)$$

The forecast accuracy achieved with sinusoidal extrapolation using the extended Kalman filter was found to degrade rapidly with increasing spectral bandwidth because of the complete dependence on a single frequency component to characterise an increasingly complex superposition. The model achieved further inferior accuracy to the cyclical model and was worsened by an attempt to consider multiple frequencies through superposition of single frequency sub-models, each dedicated to a different frequency component.

#### 4.5.6 Nonlinear next wave estimation

Unlike the forecast methods reviewed so far, which aim to deliver a time-series forecast of the desired target variable, (Price & Wallace, 2007) consider the forecast of discrete parameters such as the time until the next wave peak or trough which could be used for latching control of a point absorber, or the time and magnitude of the next peak excitation force, for declutching control. Depending on the control strategy, selective discrete values of the relevant variables might be sufficient. This approach was termed nonlinear next wave estimation in (Price & Wallace, 2007).

The forecast model inputs were a number of carefully extracted scalars from the recorded time series made at the device (past measurements only). These were: wave excitation force, time of last wave zero crossing, magnitude and duration of the past wave peak and trough, mean and variance of magnitude and duration of the excitation force of the past 14 waves. The forecast target was the time until the next wave peak, but this could easily be changed to another feature of interest such as the peak wave excitation force.

An extremely simple model termed the quadrant approach was considered, which dissects the wave cycle into 4 parts with the boundary for each part being defined by the unique combination of the polarity of the wave excitation force and its first derivative. The estimated time length of each part (of the future wave cycle)  $\hat{T}_{1/4}$  is simply taken as one quarter of the mean of the last 14 wave cycles;

$$\hat{T}_{1/4} = \frac{1}{14*4} \sum_{n=1}^{14} T_n \quad (4.91)$$

where  $n$  is the number of past wave periods used to find the estimate of the next wave period.

The estimate of time of the wave cycle part  $\hat{T}_{1/4}$ , minus the time between the last wave part boundary and the current point in time, plus the estimate of the time of each wave cycle part  $\hat{T}_{1/4}$  that remains until the point of interest (wave peak) occurs, gives the total time until the next point of interest. The model assumes that the wave period has little short term variation and changes occur slowly over longer time ranges.

A linear regression model was also considered in (Price & Wallace, 2007), which defines a linear-relationship between the input vector (a number of selected scalar values of interest relating to different features as listed previously) and the target, by finding the regression weights that minimise the least square error when applied to a training data set. Finally, an *ANN* was employed to find, through directed trial and error, a nonlinear function that relates the input vector, which is the selected scalar values extracted from the recent past time-series that might hold information about the future event, to the target (time until next wave peak, in this case).

The three forecast models were used to forecast the time until the next wave peak, for a noisy sinusoidal wave and a sea-state characterised by the Pierson-Markowitz wave spectrum. For the noisy sinusoid, the quadrant method performed best but this is not surprising because of the fact that the wave period and amplitude are essentially static in time. For the irregular sea state the *ANN* significantly outperformed the quadrant and linear regression approach. However, the quadrant approach did not perform too poorly showing that the assumption of slow spectral variations (on the scale of 14 waves) has some validity.

Next wave estimation using a similar method to the Neural Network approach given in (Price & Wallace, 2007) was performed by this author and specific details can be found in (Monk, et al., 2013) which can be seen in the last paper appended to this thesis. A brief overview of this work will be given in the following.

The forecast objective was to predict the maximum (Pico OWC plant ) chamber vertical water surface velocity  $\dot{\eta}_c$  over the upcoming wave cycle. Repeating this procedure in real-time delivers the upper bound envelope of the first derivative of the chamber water surface elevation. This forecast, with lead time from the event, would then be used to identify and attempt to prescribe a specific relief valve aperture that would vent over pressure (associated with upper bound envelope of  $\dot{\eta}_c$ ), via relief valve control, in order to avoid turbine stall.

A Neural Network was employed to find a nonlinear function that related the desired output  $\dot{\eta}_c$ , to a number of input values selected for their potential to influence the transfer of waves measured up-wave of the device to waves measured at the device. The input vector comprised of the following scalar values;

1. Current zero up-crossing wave period 60  $m$  up-wave of the plant  $T_{uw}$
2. Preceding zero up-crossing wave period 60  $m$  up-wave of the plant  $T_{uw-1}$
3. Preceding zero up-crossing wave period in the chamber  $T_{c-1}$

4. Current wave peak vertical water surface velocity 60 m up-wave of the plant  $\dot{\eta}_{uw}$
5. Preceding peak vertical water surface vertical velocity 60 m up-wave of the plant  $\dot{\eta}_{uw-1}$
6. Preceding peak vertical water surface vertical velocity in chamber  $\dot{\eta}_{c-1}$

Obviously  $\dot{\eta}_{uw}$  has a direct relationship with the target output  $\dot{\eta}_c$ . In addition  $T_{uw}$  will also have a strong influence on  $\dot{\eta}_c$  because of frequency dependent resonance of the oscillating water column. The values of:  $T_{uw-1}$ ,  $T_{c-1}$ ,  $\dot{\eta}_{uw-1}$  and  $\dot{\eta}_{c-1}$ , provide information relating to the amplitude, phase and frequency of the wave that occurred before the wave of interest (for control). These values were included because the wave that occurred before the wave of interest would subsequently reflect and radiate from the plant and interfere with the incoming wave of interest, and therefore influence the up-wave observation of the incident wave.

The forecast target and model output  $\dot{\eta}$  directly relates to the peak pressure  $p_{max}$  in the chamber. A look-up table, constructed from operational data, was used to translate  $\hat{\eta}$  and the current turbine angular velocity, to a relief valve aperture that would result in  $p_{max}$  being close to but not exceeding the threshold for turbine stall.

## 4.6 Literature review summary

### 4.6.1 OWC system modelling

A number of methods to model the first stage of the wave to wire system model, namely the transfer from incident wave power to pneumatic power, are reviewed with respect to their suitability to ultimately simulate the system dynamics under relief valve control. The models based in the frequency domain, although computationally efficient allowing long term analysis to be performed, do not allow the temporal variations from device control to be assessed. Also the stochastic approach which can be used to consider irregular sea states depends on a Gaussian chamber pressure distribution which deviates from that which actually occurs at Pico because of wave asymmetry and additional chamber pressure asymmetry arising from the chamber lip defect. Models in the time domain are far more computationally expensive but yield a time series of the variables relating to the system response. This is critical when considering the effect of an active control strategy, as well as other temporal fluctuations such as wave grouping. As such the time domain system model presented (Falcão & Justino, 1999) was selected as a tool for further investigation.

### 4.6.2 Short-term wave forecasting

The forecasting models proposed in the literature can be grouped by three distinct approaches;

- 1.) The transfer of measurements made up wave of the device, to the expected behaviour that will later occur at the device
- 2.) Predicting future behaviour at the device based entirely on past measurements made at the device
- 3.) A combination of the above

There are a number of undesirable factors associated with transferring measurements made up-wave of the device to what later occurs at the device (approach 1). The forecast horizon time is in part restricted by the separation distance between the device and the up-wave sensor and the propagation velocity of the incident wave. Decreasing the separation distance decreases the maximum forecast horizon time and increases the influence of interference (with the up-wave measurements) resulting from reflected and radiated waves propagating up-wave from the device. To rectify this, an array of sensors is required to decompose the incident and scattered wave superposition which will incur cost and potential for failure as well as computational expense. Increasing the separation distance will increase the maximum forecast horizon but propagation transformations will become stronger. However, this approach might be more favourable for the identification of extreme events, for survival, as they will be measured directly instead of being inferred from the residual behaviour.

The univariate approach to forecasting considers future behaviour at the device exclusively from past measurements made at the device (approach 2). This approach removes the complications associated with: wave directionality, the need to directly model wave propagation, interference of up-wave measurements from waves reflected and radiated from the device, forecasted phase accuracy in the very near future, limited forecast horizon time and the cost and risk of deploying additional sensors away from the relative safety and convenience of the device. For these reasons this approach is very appealing, provided the forecast accuracy is sufficient for the application. Exceptional forecasting accuracy has been achieved in the literature using univariate forecast models, but only when the spectral bandwidth is artificially narrowed with a zero-phase non-causal filter which is not realisable in real-time. The forecast accuracy that can be achieved on-line using raw data, or with data that has been causally filtered, is still unclear and this is a critical point that needs clarification. The most promising univariate models found in the literature are *AR* and *NAR* models.

The combination of regressive forecasting methods using past measurements made at the device and measurements made up wave (option 3) has received far less attention in the literature and needs further consideration.

## Chapter 5

# Development of OWC system model and relief valve control strategies

### Abstract

A time-domain model is constructed for the Pico plant case study. A method to calculate the excitation flow, from other measured system variables, is presented. The calculated excitation flow is used as an input to drive the system model and the model results are compared with measured operational data for model validation. The Pico plant system model is used to develop a number of control strategies, which aim to regulate and optimise chamber pressure by adjusting the relief valve aperture in response to the temporal variations of incident wave energy and changes in the system state. Performance enhancement is achieved by minimising unusable pneumatic over-power. The simulated performance of each control strategy is evaluated by the change in: resultant power take-off from the generator, the frequency and severity of turbine stalls, the vibrations of the turbo generator structure from pneumatic power exposure and the number of relief valve aperture adjustments required to achieve control in the proposed ways. Some control strategies considered are hypothetical because the valve actuator system requirements exceed those of the existing relief valve system installed at Pico. Also some control strategies require a short-term wave forecast and in these cases it is assumed that a perfect forecast of the chamber excitation surface elevation is available. This is done in order to evaluate the maximum potential performance of each control strategy and is still relevant, as a near perfect forecast could be achieved if sufficient monitoring equipment was available. However, such equipment is not available to this project and as such the expected performance of control using a realisable short-term forecast is addressed in the next chapters.

### 5.1 Introduction

As discussed in section 3.3.5.2, one of the two main options for control of an OWC to enhance performance is to regulate pneumatic power exposure to the turbine using valve control. One way to achieve this, and the only way possible with the existing mechanical infrastructure at Pico, is to control the by-pass relief valve aperture thereby controlling the mass flow rate of air through the valve. This can be used to regulate chamber pressure and ultimately the pneumatic power exposure to the turbine. Alternative options that are not possible with the existing mechanical infrastructure at Pico include throttle valve control using a valve in series with the turbine, or by implementing a pressure accumulator in series to convert the oscillating pressure head to a single pressure head polarity, or to smooth out extreme pressure head peaks and troughs.

In the following subsections a number of control strategies to regulate and optimise chamber pressure with a relief valve control are introduced. In all cases, the control strategy design focuses on simplicity and robustness for practical deployment. Some of the control strategies considered are hypothetical because they require the: design, fabrication and installation of a new relief valve actuator system. Consideration of these strategies is done to assess their merit for possible future development, but will not be tested in the field. For the simulation of non-hypothetical control strategies (which could be achieved with the existing infrastructure at Pico) the maximum real relief valve aperture adjustment rates (described in section 3.3.5.2) are adhered to in the model characterisation of this element.

Firstly, in order to develop and theoretically assess the performance of each control strategy, a system model must be constructed and validated.

## 5.2 Wave to wire system model in the time domain

As reviewed in section 4.2.3, only the time domain model yields a time series of the variables, which is essential for assessing the system response to active control. However, the time-domain model is far more computationally expensive than the frequency domain models, making long term performance analysis more demanding.

### 5.2.1 Excitation flow and chamber pressure

As discussed in section 4.2.3, the system model can potentially be driven with either the recorded time series of surface elevation  $\eta(t)$  or by the excitation flow  $q_e(t)$  (or its conceptually related excitation surface elevation flow  $\eta_e(t)$ ). The purpose of the investigation and limitations of the available sensors installed at Pico can be used to select the appropriate method.

As discussed in section 3.4.2, the sensor measuring surface elevation in the chamber is prone to inaccuracies for a number of reasons. Inaccuracies are clearly visible in the data as shown in figure 3.13. In addition the mode of operation of the sensors (acoustic pulse emission) limits the maximum sampling frequency to a very low value of  $1Hz$ . Both of these issues make the time-series of  $d\eta/dt$ , needed to drive the model described by (4.41), unreliable. In addition, driving the model with the recorded surface elevation requires the assumption that this input time series is not modified by changes in chamber pressure resulting from control. As such it is not desirable to use the recorded surface elevation to drive a model to assess the system response to control.

The alternative, which is the time-domain model driven by diffraction flow rate  $q_e$ , also has associated complications. It will be difficult to measure directly the incident wave time-series, which will require an expensive and complex sensor system capable of extracting the incident wave from the superposition it forms with the reflected and radiated waves from the plant. The hydrodynamic transfer must also then be applied.

One way around all of these complications is to obtain  $q_e(t)$  indirectly by calculating it from the other higher quality measured system variables. If the chamber pressure (and pressure history), turbine angular velocity, turbine characteristic curves, tidal elevation and relief valve aperture are known then (4.39) can be rearranged to make  $q_e(t)$  the subject;

$$q_e(t) = \frac{V_0}{\gamma p_0} \frac{dp_c(t)}{dt} + \frac{K p_c(t) D}{\rho_0 N(t)} + A_v k_v(t) \text{sign}(p_c(t)) \left( \frac{2|p_c(t)|}{\rho_0} \right)^{\frac{1}{2}} - \int_{-\infty}^t g_r(t - \tau) p(\tau) d\tau \quad (5.1)$$

In this fashion the difficult task of measuring the incident up-wave surface elevation  $\eta_{uw}(t)$  and then performing the transfer of this to  $q_e(t)$  by factoring in complex hydrodynamic transfer process, can be avoided entirely because only the chamber pressure (and history), mass flow rates past the turbine and through the relief valve, and tidal elevation, are needed to find  $q_e(t)$ . This seems to be the most valid and

achievable option available under the condition that field data is to be used to drive all simulation which is a core principle of this study.

The resultant calculated chamber surface elevation, which is a conceptual variable that describes the surface elevation if it were horizontally uniform, is then found numerically with;

$$\eta_{calculated}(t) = \frac{1}{y_H x_H} \int (q_e(t) + q_r(t)) dt \quad (5.2)$$

The recorded and calculated surface elevations for a sample time series were compared earlier in figure 3.13. It is seen that when the recorded surface elevation is small and sensible the calculated surface elevation matches very well. When the recorded surface elevation is clearly in error during large amplitude wave cycles  $\eta_{calculated}(t)$  provides sensible values. As the recorded surface elevation is poor and in error much of the time it is not possible to use this to validate, in a quantitative way, the performance of the calculated surface elevation. Instead we must rely on the strength of the theory.

After  $q_e(t)$  is found, the hydrodynamic to pneumatic power transfer model in (4.39) can be integrated to find  $p_c(t)$ . Obviously, without making changes to the system i.e. from control, the chamber pressure time series  $p_c(t)$  will be exactly the same as the input to (5.1) which was used to find  $q_e(t)$ . However, if changes to the system are made i.e. the relief valve aperture which effects  $\dot{m}_v$  and subsequently  $q_r(t)$ , the resultant chamber pressure from these changes/control can be evaluated.

### 5.2.2 Chamber pressure and turbine flow rate

The model given in (4.39) requires knowledge of the dependency of mass flow rate of air passing the turbine, on the chamber pressure. The relationship between chamber pressure and turbine mass flow is most easily interpreted with the non-dimensional counterparts of these variables given in (4.8) and (4.9). The task is then to find the function  $f_{\dot{m}}$  as described in (4.11).

In (Gato, et al., 1996)  $f_{\dot{m}}$  was found through laboratory tests using an isotropic scaled-down turbine sharing the same proportional dimensions to the full scale Wells turbine installed at the Pico OWC. The Pico turbine dimensions are described in section 3.3.2. It was found that  $f_{\dot{m}}$  is approximately a linear function (except at very high values of  $\Psi$ ), and is described by;

$$f_{\dot{m}} = 0.68 = K \quad (5.3)$$

It is important to validate  $f_{\dot{m}}$  found in (Gato, et al., 1996) using real operational data from the Pico plant, as any significant divergences could affect the model accuracy considerably. In particular, pitting of the turbine blade surfaces from impacts with debris in the airflow stream, as described in section 3.6.4, might affect the aerodynamic flow characteristic. The Pico plant is equipped with both static and dynamic pressure sensors to capture the turbine duct static pressure  $p_D$  and the turbine duct dynamic pressure  $q_D$ . The turbine duct air velocity can be found from these variables and with the relationship;

$$v_a = \left( \frac{2q_D}{\rho_c} \right)^{0.5} \quad (5.4)$$

where  $\rho_c$  is the chamber air density given by;

$$\rho_c = \frac{p+p_0}{RT} \quad (5.5)$$

where  $R$  is the specific gas constant for air and  $T$  is the absolute air temperature.

The turbine mass flow rate is then given by;

$$\dot{m}_t = v_a A_D \rho_c \quad (5.6)$$

where  $A_D = \pi(D^2 - D_i^2)/4$  is the turbine duct cross sectional area, with  $D = 2.3$  (m) being the outside diameter of the turbine and  $D_i = 1.36$  (m) being the inside diameter of the turbine.

These measurements, along with the turbine rotational speed, can then be used to visualise the function that describes  $\Phi = f_m(\Psi)$ , using (4.9), which is shown in figure 5.1.

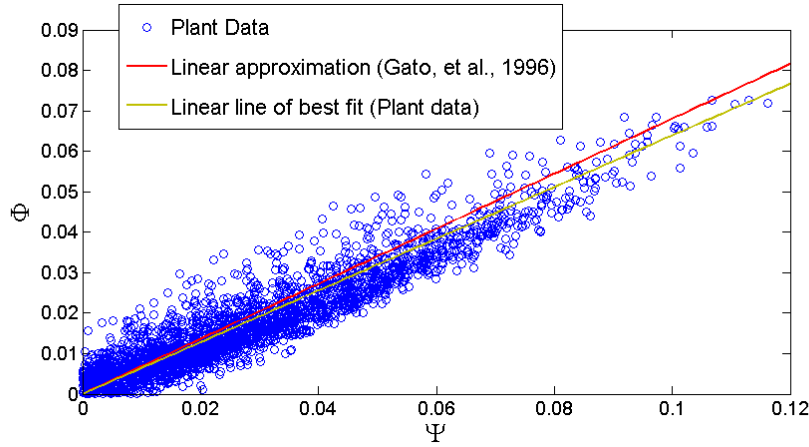


**Figure 5.1** Scatter plot of operational data derived (with line of best fit) and laboratory found (for small scaled turbine as given in (Gato, et al., 1996)) function  $f_m$  which relates  $\Phi$  and  $\Psi$ .

As seen in figure 5.1, there is good agreement between the data derived  $f_m$  and that given (Gato, et al., 1996), being almost linear with a very similar gradient, but being perhaps slightly milder suggesting the air-flow rate is actually slightly slower than previously thought, but the difference is marginal.

### 5.2.3 Pneumatic to mechanical power transfer model

The model given in (4.39) also requires knowledge of the dependency of power transfer to the turbine, on the mass flow rate of air passing the turbine or, in effect (as shown in section 5.2.2), the chamber pressure. Again, the relationship between power transfer to the turbine and chamber pressure is most easily interpreted with the non-dimensional counterparts of these variables given in (4.8) and (4.10). The task is then to find the function  $f_p$  as described in (4.12).

The function  $f_p$  for a geometrically scaled down version of the full size Wells turbine installed at Pico is also presented in (Gato, et al., 1996). However, again due to the high dependency of the system model on this relationship, it is important to validate this turbine characteristic using operational data for the full scale turbine.

The ideal way to find this relationship would be with a torque meter at the coupling between the turbine shaft and the generator shaft. In this case the aerodynamic power transfer to the turbine  $P_a$  is simply given by;

$$P_a = \tau N \quad (5.7)$$

where  $\tau$  is the aero dynamic torque

Unfortunately this type of sensor was not available so the only option remaining was to calculate  $P_a$  as the missing element of a power balance equation by considering the change in rotational speed  $\dot{N}$ , which describes positive power transfer to the turbine whilst accounting for the negative power transfer from the turbine from electrical power take-off and the mechanical and electrical power losses, as described by the re-arrangement of (4.42);

$$P_a = IN \frac{dN}{dt} + P_e + P_b + P_{el} \quad (5.8)$$

However, because of the high inertia of the turbine, changes in the angular velocity over short time scales ( $dt = 1/f_s = 0.5$  (s)) will be very small and any noise in the data of  $N$ , even if very weak, will obscure the underlying relationship. Electrical noise in the sensor data is a consistent problem at Pico and new data with sufficient clarity could not be obtained using the available equipment, for the purposes of this analysis. However, some data was captured in 2011 during an operational period using a former data acquisition system with isolated channels for the relevant system variables and with isolated power supplies. This data set is very short and does not span the whole  $\Psi$  range of interest but was found to be the only option available. This analysis (using the same data) was previously performed in (Le Crom, 2010) but for some reason was compared to an entirely different Wells turbine characteristic curve. The data derived characteristic curve for the Pico Wells turbine, which is the relationship between  $\Pi$  and  $\Psi$ , is given in figure 5.2.

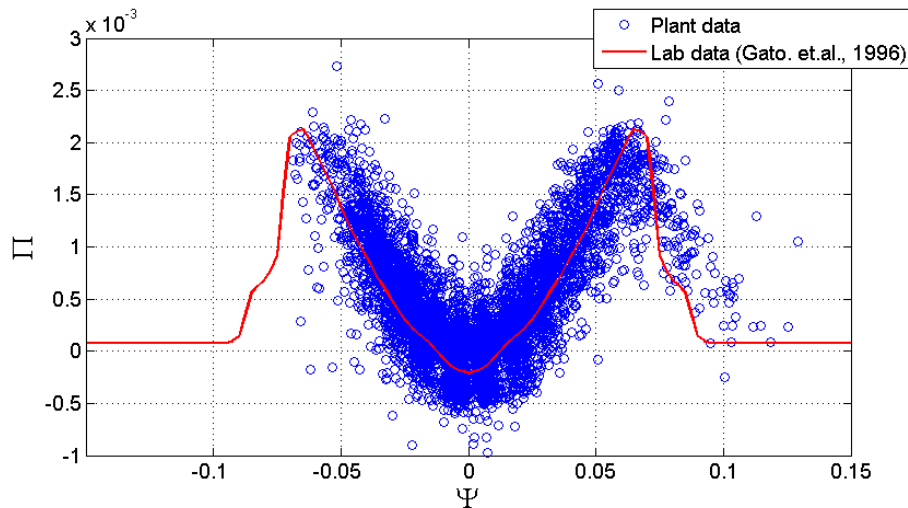


**Figure 5.2** Scatter plot of operational data derived and laboratory found (for small scaled turbine as given in (Gato, et al., 1996)) function  $f_p$  which relates  $\Pi$  and  $\Psi$ .

As seen in figure 5.2 there is quite a good agreement between the characteristic curve given in (Gato, et al., 1996) and the data derived relationship. However, the data derived relationship suggests that the curve

is somewhat less peaked and that the power transfer to the turbine does not decline as rapidly with increasing pressure head past the threshold for the onset of turbine stall. The reason for this disparity might be because of the extensive pitting of the turbine blades which could affect the aerodynamic performance. But because of the poor correlation due to noise in the data and because of the incomplete data range, this observation is not conclusive and it seems most appropriate to continue with the turbine characteristic curve found in (Gato, et al., 1996) until more data with greater clarity can be obtained.

#### 5.2.4 Electrical losses

The final element needed to construct the system model for the Pico plant is the electrical power losses. The power take-off  $P_e$  by the generator is dictated by a control law implemented in the power electronics controller which is a function of the rotational speed as described by figure 3.7. As with any generator the conversion efficiency between mechanical and electrical power is not perfect and there will be some associated losses in this transfer. This author was unable to find the specific efficiency curve for the doubly fed asynchronous generator used at Pico. As such an approximation of the generator efficiency curve was found by simulating the system response, using the turbine characteristic curve given in (Gato, et al., 1996). Simulations were made over a 12 hour period of continuous data which spans a period of rapidly increasing energy period  $T_e$  (so as to consider a wide range of rotational speeds and consequently power-take off and electrical losses) using the calculated excitation flow time series  $q_e(t)$  for that period to drive the model. The electrical losses  $P_{el}$  were considered to be a function of electrical power take-off  $P_e$  only, as defined by;

$$P_{el} = \alpha P_e^\beta \quad (5.9)$$

The range of  $\alpha = 0.1, 0.2, \dots, 20$ , and  $\beta = 0.05, 0.1, \dots, 10$  were considered with the optimum generator efficiency curve being the simulation output of rotational speed having the least mean absolute error, as described by;

$$MAE_{ab}(N) = \frac{1}{L} \sum_{k=1}^L |N_o(k) - N_s(k)| \quad (5.10)$$

where  $L$  is the data time series length, with  $N_o$  and  $N_s$  being the originally recorded and simulated turbine angular velocities, respectively.

The generator efficiency curve that resulted in the minimum  $MAE_{ab}(N)$  was described by;

$$P_{el} = P_e^{0.8} \text{ (W)} \quad (5.11)$$

and this efficiency curve is shown in figure 5.3.

The generator percentage efficiency is then given by;

$$Efficiency = \frac{P_e - P_{el}}{P_e} \times 100 \quad (5.12)$$

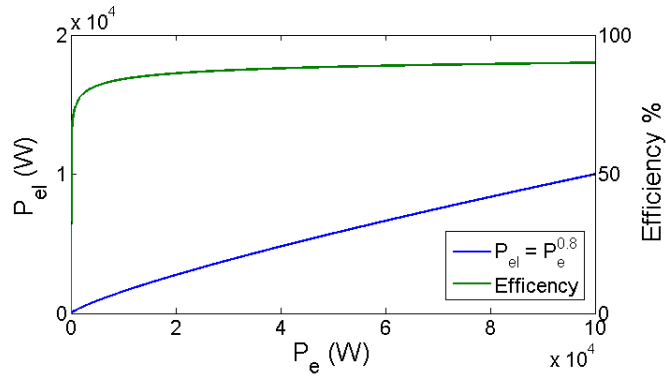


**Figure 5.3** Approximate curve relating the Pico generator mechanical to electrical power loss as a function of power take-off, and the electrical efficiency of the generator, both found iteratively from operational data and the wave to wire system model.

This generator efficiency curve was also used in the process to find the operational data derived turbine characteristic curve shown in figure 5.2. This method, in part, will counteract any error in the turbine characteristic curve. Ultimately it is a rough approximation and might not be accurate, but as will be seen in the next section the results are more than satisfactory.

### 5.2.5 Model performance evaluation

Another operational data set of length 12 hours, that spanned a period of sea states that are rapidly increasing then rapidly decreasing in energy, was selected to validate the Pico system model, because it covers a significant proportion of the systems operational range. This was different to the 12 hour data set used to find the generator efficiency curve in the previous section to ensure fitting to the specific data had not occurred. The characteristics of the sea states within this period, sampled at half-hour intervals, is shown in figure 5.4.

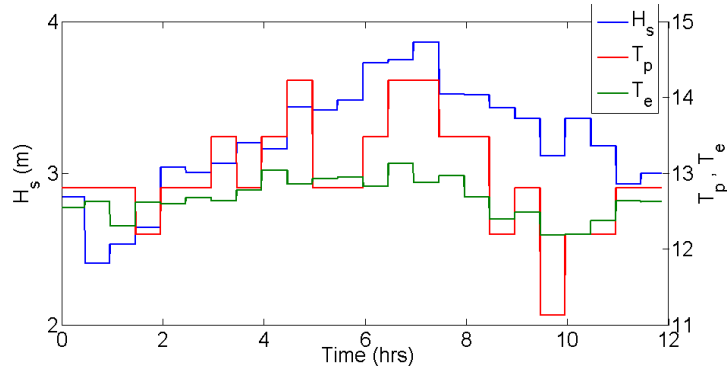


**Figure 5.4** Significant wave height  $H_s$ , peak wave period  $T_p$ , and wave energy period  $T_e$  sampled at half hour intervals over a 12 hour period for the sample data set used for model validation.

The characteristic curve in (Gato, et al., 1996) and shown in figure 5.2 was employed in the model. The model performance is evaluated by the mean absolute and squared error of the simulated turbine angular velocity time series when compared to the original turbine angular velocity time series, also the percentage error of mean power take-off is considered, as described by;

$$PE(\bar{P}_e) = 100 * \frac{\sum_{k=1}^L P_e(k) - P_{e,s}(k)}{\sum_{k=1}^L P_e(k)} \quad (5.13)$$

where  $P_{e,s}$  is the simulated power take-off.

The analysis of these performance evaluators is given in table 5.1.

**Table 5.1** Mean absolute and squared error of turbine angular velocity, and mean error of power take-off, between model simulations and operational data.

	$MAE(N)$	$MSE(N)$	$PE(\bar{P}_e)$
Using turbine characteristic curve in (Gato, et al., 1996)	1.63	4.38	-2.25%

For completeness a half hour sample time series, comparing the original turbine angular velocity and electrical power take-off time series against the simulated time series using the turbine characteristic curve as given in (Gato, et al., 1996), is given in figure 5.5.

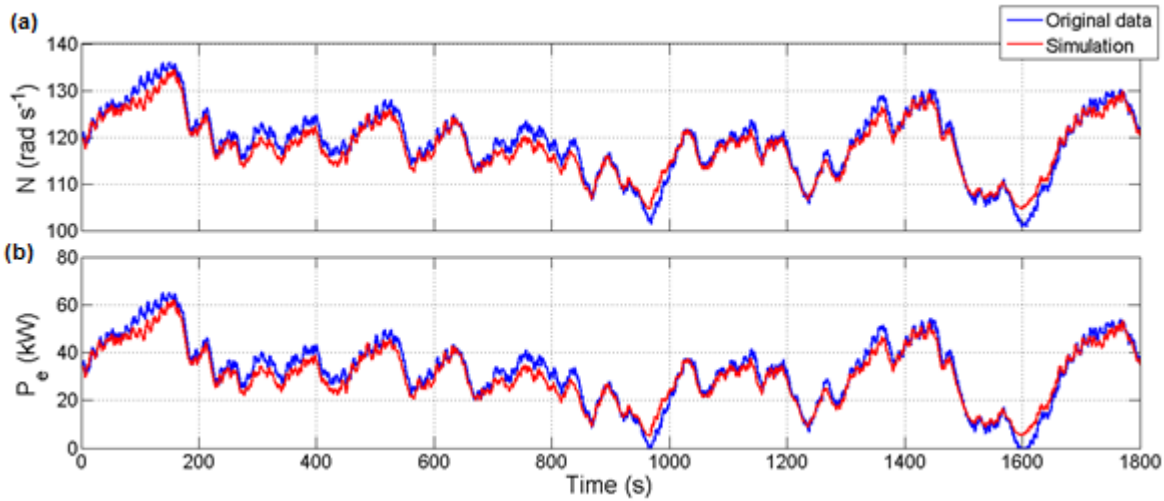


**Figure 5.5** Example half hour time series comparing the simulated (a) turbine angular velocity and (b) electrical power take-off, with the original recorded data for the respective time series.

As seen in figure 5.5 the simulation results of angular velocity and electrical power take-off are very good, though sharp peaks and troughs are slightly under predicted or over predicted, respectively. However, the percentage error in the mean power take-off is below 3% for the extended data set considered. Overall the wave-to-wire system model achieves a high level of accuracy and is considered suitable for the next stage, which is modelling the changes from the proposed relief valve control strategies.

### 5.3 Evaluation of selected operational data

The wave to wire power transfer model in the time-domain described in the preceding sections is used to simulate the system response to relief valve control in the remainder of this chapter. The model requires only the input of the chamber wave excitation flow data time-series  $q_e$  and the system starting conditions. Wave excitation flow  $q_e$  is convertible to surface elevation excitation flow  $\eta_e$  by (5.14) and this alternative term will be used primarily (over the alternative  $q_e$ ) because it is more intuitive.

$$q_e = -\frac{dV_{open}}{dt} = \frac{d(\eta_e \mathcal{V}_{H^*H})}{dt} \quad (5.14)$$

where  $V_{open}$  is the open chamber volume (bound by the imaginary top wall) and  $\eta_e$  is the excitation surface elevation which is a conceptual variable only and describes the water surface elevation if it had

uniform height at all locations within the chamber.  $y_H x_H$  is the horizontal internal chamber where  $x_H$  is the total internal length of the chamber, and  $y_H$  is the total internal width of the chamber.

To assess the performance of the different relief valve control strategies, input model data needs to be selected and this will be discussed first. 12 data sets of  $\eta_e$  time-series were selected that encompass a broad range of chamber significant wave heights  $H_s$  sea states. Each data set has a length of  $L = 4200$  data points at a sampling frequency of  $f_s = 2Hz$ , equating to a total time length of 35 minutes. The 12 data sets are separable in to 6 data set pairs with each set-pair containing two data sets that were recorded with a 3 hours separation time between their start points. Data sets were selected in pairs primarily because of the need for distinct training and test data sets for the training and querying of the short term wave forecasting models, respectively. The 3 hours separation between data set pairs is an unfortunate restriction of the available up-wave data. Previously hydrostatic pressure data time series, 35 minute in length, were recorded internally (no live data feed to main data acquisition suite) on a disconnected Nortek “Aquadopp” sensor at 3 hour intervals, at a location approximately 60 meters up-wave of the chamber front wall. The up-wave hydrostatic pressure  $p_{uw}(z)$  at depth  $z$  can be converted to the approximate up-wave surface elevation  $\eta_{uw}$  as described by (3.11).

Because it was anticipated that near-shore up-wave data could enhance the accuracy of the short-term wave forecast, data set pairs containing near-shore wave data, but incurring a separation time of 3 hours, were selected. The alternative would be data sets that are concurrent in time but would not have the corresponding near-shore wave information in one of the data set pairs. More generally, considering data in set-pairs also allows a comparison to be made between the results obtained under similar sea state conditions in order to evaluate the consistency of the results. However, it should be noted that the tidal elevation may not be consistent between the data set pairs and for the reasons discussed in section 3.6.3 the degree of wave asymmetry between the data sets in pairs, may differ significantly. In these cases a difference in performance is expected between the data sets that are in pairs even when the sea state characteristics are consistent. The spectral analysis of each data set as recorded in the chamber and the up-wave sensor location is given in figure 5.6.

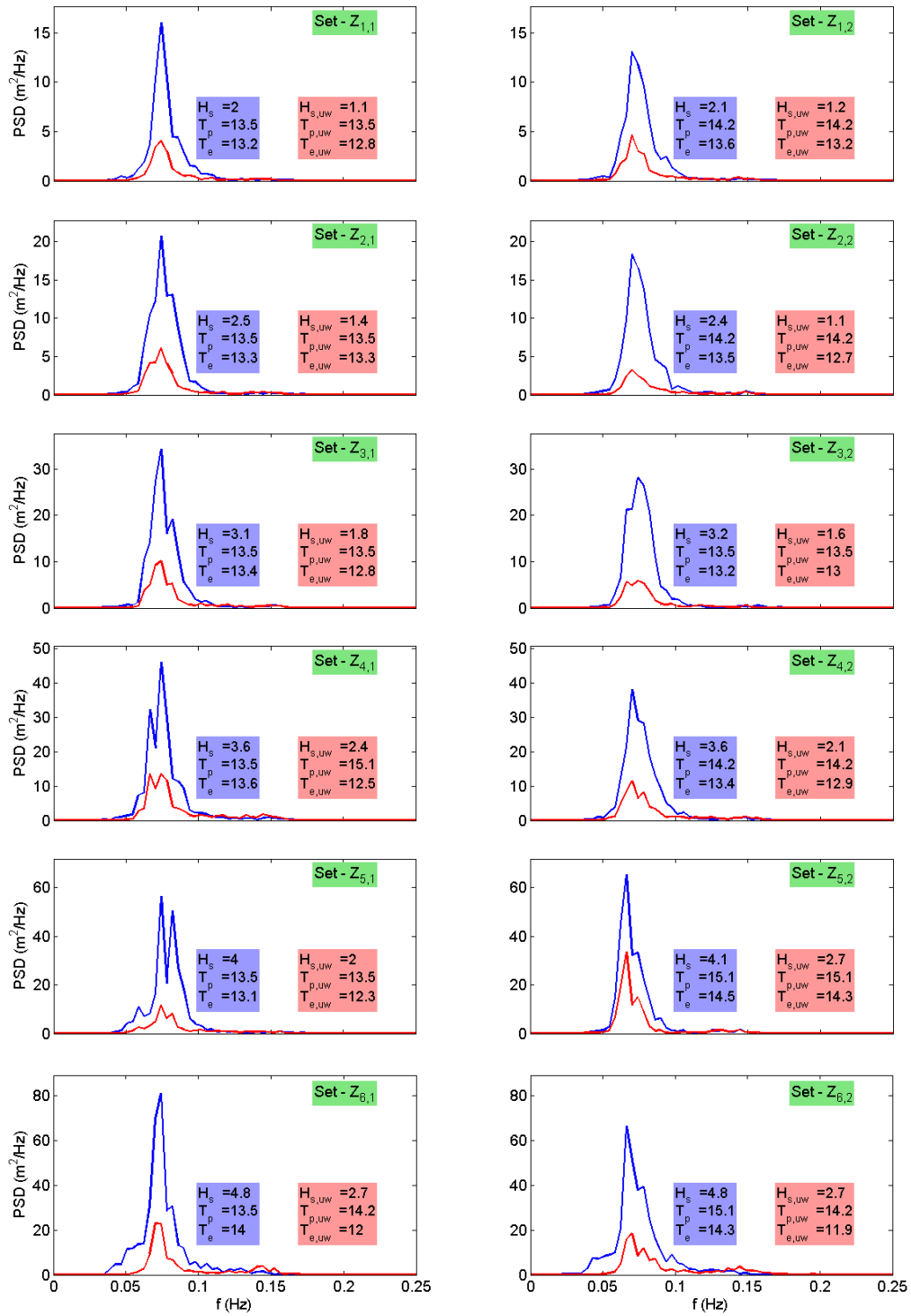


**Figure 5.6** Spectral analysis of the calculated chamber excitation surface elevation  $\eta_e$  and up-wave measured surface elevation  $\eta_{uw}$  (calculated from hydrostatic pressure at the sea bed) for the data sets considered, where:  $H_s$  is the significant wave height,  $T_p$  the peak wave period and  $T_e$  the energy period as measured in the chamber. The second subscript  $uw$  signifies measurements made 60(m) up-wave of the plant chamber front wall, all others refer to the chamber location.

As seen in figure 5.6, there are substantial differences between  $H_s$  and  $H_{s,uw}$  and the reason for this are discussed in section 3.4.3.

## 5.4 Relief valve control strategies

In the following, a number of relief valve control strategies are introduced and these strategies will be referred to by the following shortened names:

1. ‘Basic relief valve control’ ( $Basic_{RVC}$ )
2. ‘Instantaneous relief valve’ ( $Instant_{RVC}$ )
3. ‘Wave by wave relief valve control’ ( $Wave_{RVC}$ )
4. ‘Continuous relief valve control’ ( $Continuous_{RVC}$ )
5. ‘Envelope relief valve control’ ( $Envelope_{RVC}$ )
6. ‘Delayed relief valve control’ ( $Delayed_{RVC}$ )

Strategies  $Basic_{RVC}$  and  $Instant_{RVC}$  exist theoretically in the literature and are defined in (Falcão, 2002), (Falcao, et al., 2003). To the authors knowledge the control strategies  $Wave_{RVC}$ ,  $Continuous_{RVC}$ ,  $Envelope_{RVC}$  and  $Delayed_{RVC}$  are concepts that have not previously been discussed in the literature.

The control strategies  $Instant_{RVC}$  and  $Wave_{RVC}$  will be hypothetical in this study because the mechanical requirements of the relief valve actuator (namely the aperture adjustment rate) do not currently exist at the Pico project to perform valve control in the proposed manner. Also to the author’s knowledge they have not been implemented in any other project of this sort. The control strategies:  $Basic_{RVC}$ ,  $Envelope_{RVC}$  and  $Delayed_{RVC}$  are within the mechanical limitations of the existing relief valve actuator system installed at the Pico plant.  $Continuous_{RVC}$  could be within the mechanical limitations of the existing system with a small minor modification requiring the instillation of a new hydraulic pump capable of more continues operation without overheating or by adding a cooling system to the existing hydraulic pump.

### 5.4.1 Basic relief valve control

Because the Wells turbine has a highly nonlinear relationship between power transfer to the turbine and chamber pressure, with a significant reduction in transfer efficiency associated with the stall regime as shown in figure 5.2, exposing the maximum amount of available pneumatic power to the turbine, especially in very high energy sea states, will not necessarily result in the greatest power transfer to the turbine.

As such, the most basic relief valve control strategy is to set an essentially static relief valve aperture that optimises the pressure variance over longer periods of time to partially optimise power transfer to the turbine. This control strategy will be referred to as  $Basic_{RVC}$  and will be used as a base-line for evaluating the comparative performance of the more advanced control strategies introduced later.

The temporal variances in the incident wave time series over a certain period of time will be different even under the same classification of the sea state. As such, knowing what this optimum relief valve aperture would have been over a certain period of time can only be achieved through post event analysis with time domain modelling. This of course has little benefit for real operation practice because the event period has already passed unless it is assumed that the future incident wave time series characteristics are sufficiently similar to what occurred in the recent past.

Alternatively, a statistical approach can be adopted. As shown theoretically in (Falcão, 2002) from stochastic analysis there exists a peak in the relationship between the standard deviation of non-dimensional chamber pressure  $\sigma(\Psi)$ , and the resultant mean non-dimensional power delivery to the turbine  $\bar{\Pi}$ . This relationship is shown in figure 5.7 for the wells turbine installed at Pico and shows that  $\bar{\Pi}_{max}$  occurs at a value of  $\sigma(\Psi) \approx 0.05$ . This statistical analysis can be used as a guide in tuning the optimum and temporally static relief valve aperture. In this fashion the relief valve aperture is used to try to achieve the optimum value of  $\sigma(\Psi)$  in the future, based on the value of  $\sigma(\Psi)$  that occurred in the recent past i.e. reduce the relief valve aperture in the future if in the recent past  $\sigma(\Psi) \ll 0.05$ , and vice versa. In this way the plant performance is optimised through Gaussian statistics.

Considering that (for the Pico case study) chamber pressure does not have a Gaussian distribution and is skewed due to the shallow chamber water depth and the defect in the chamber front lip (as discussed in section 3.6.3), it is important to validate the theoretical relationship between  $\sigma(\Psi)$  and  $\bar{\Pi}$  given in (Falcão, 2002). For this purpose the same value pairs of  $\sigma(\Psi)$  and  $\bar{\Pi}$  were calculated using all operational data between 01/10/2014 and 02/02/2015. Each data set is 35 minutes which corresponds to around 100 wave cycles of the maximum wave period expected at the site and is a standard minimum length for classifying a sea state. For each data set the data time-series of instantaneous non-dimensional pressure  $\Psi$  is calculated with (4.8). The non-dimensional power transfer to the turbine is found from the function  $f_p$  given in (Gato, et al., 1996) and validated in figure 5.2.

The time series of  $\Psi(k)$ , having a data point length  $L$ , is then used to find the mean non-dimensional power:

$$\bar{\Pi} = \frac{1}{L} \sum_{k=1}^L \Pi(k) \quad (5.15)$$

In addition to the standard deviation of non-dimensional pressure;

$$\sigma(\Psi) = \sqrt{\frac{1}{L} \sum_{k=1}^L \left( \Psi(k) - \frac{1}{L} \sum_{k=1}^L \Psi(k) \right)^2} \quad (5.16)$$

The data and theory derived curves of  $\bar{\Pi}$  vs  $\sigma(\Psi)$  are compared in figure 5.7. Although the full range of  $\sigma(\Psi)$  data points is not available in the real operational data because higher  $\sigma(\Psi)$  values results in excessive turbine stall and is not permitted by the operator, and lower  $\sigma(\Psi)$  does not result in high enough power production to be worthwhile. For the points that do exist, the plant data is in quite good agreement with the projection from stochastic methods, although there is significant variability about the mean. To uncover the source of this variability the data is subdivided by tidal elevation which will influence the degree of wave shoaling and therefore wave asymmetry. This is in addition to a second subdivision of the data which is based on the degree of skewness of chamber pressure (as defined in section 1.5.3). As seen at higher tidal elevations, the operational data is distributed more closely about the stochastic theoretical relationship with a tendency for higher tidal elevations to exceed this. At lower tidal elevations the resultant  $\bar{\Pi}$  has a tendency to fall notably below the theoretical value. The degree of skewness is seen to be dependent on the achieved value of  $\sigma(\Psi)$ , showing skewness increases with  $H_s$  as would be expected. On average, the inaccurate assumptions (for the Pico case study) of a Gaussian

probability density function of chamber pressure, and linear oscillations in the free surface, do not appear to have a significant impact on the overall relationship between  $\sigma(\Psi)$  and  $\bar{\Pi}$ .

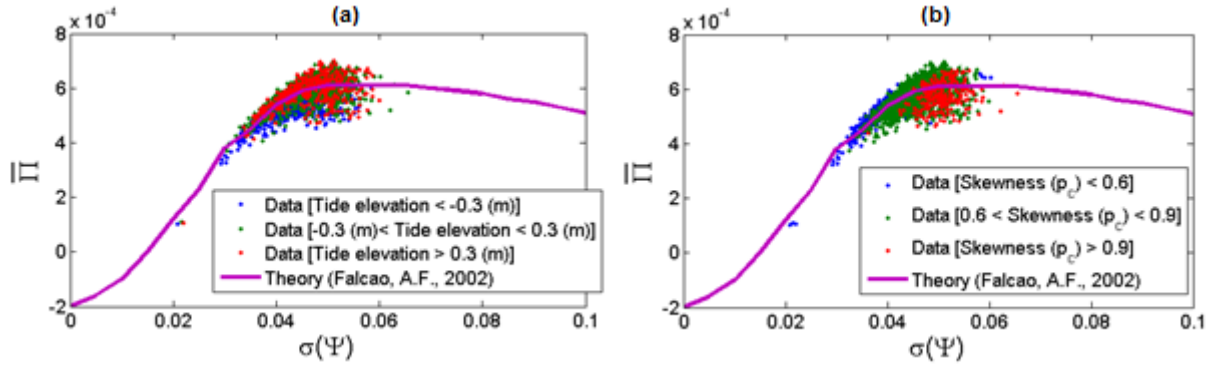


**Figure 5.7** Comparison of theoretical (Falcão, 2002) and data derived mean non-dimensional power transfer to turbine  $\bar{\Pi}$  as a function of the sea state defined by the standard deviation of non-dimensional pressure  $\sigma(\Psi)$  subdivided by (a) tidal elevation and (b) degree of skewness of chamber pressure.

As seen in figure 5.7 both the theory and data show  $\bar{\Pi}_{max}$  occurs when  $\sigma(\Psi) \approx 0.05$ . As such, without utilising time-domain analysis on-line to project the optimum static relief valve aperture for a certain time period, the realistic operational practice for performance optimisation is to try to converge with  $\sigma(\Psi) \approx 0.05$ .

Optimising  $\sigma(\Psi)$  in order to optimise  $\bar{\Pi}$  does not guarantee that the greatest power production will be achieved because these are mean non-dimensional quantities from stochastic analysis and the system response to the temporal variance in the incident wave envelope is not considered. But because of the added complications and computational expense associated with online time-domain analysis, this statistical approach has been adopted at the Pico plant and has been found to be a robust and reliable operational practice. From operational experience, optimising  $\sigma(\Psi)$  with respect to the optimisation of  $\bar{\Pi}$  has been found to give a consistent and reasonable balance between power production and the frequency and severity of stalls which as discussed in section 3.7, are detrimental to the longevity of the machine. As such the simulated system response that occurs when the relief valve aperture achieves  $|\sigma(\Psi) - 0.05|_{min}$  will be used as a base line for comparison and evaluation of the other relief valve control strategies considered. This control strategy will be termed *Basic<sub>rvc</sub>* and is a relevant way to consider the base-line performance as this is how the plant would be (and is currently) controlled under normal operational conditions.

To assess the influence of *Basic<sub>RVC</sub>* on the system performance, the time-domain model of the chamber pressure (4.39) is used. At each data point in time  $k$ , the chamber pressure in the next time step  $p_c(k + 1)$  is found with the integration of (4.39) between data time points of  $k$  and  $k + 1$ , using  $q_e(k + 1)$ . The assumption is made that, in terms of a single time step in the pressure model, the turbine angular velocity is constant  $N(k) = N(k + 1)$ . This is justified due to the huge inertia of the turbine  $I = 600 \text{ kg m}^2$ , making angular acceleration over a data time-step (0.5 seconds in this case), very low, and because of the very low dependency of the pressure model on small differences in  $N$ . This assumption is seen to be more than acceptable from the system model analysis given in section 5.2.5. After  $p_c(k + 1)$  is found, the

turbine response in the next time step  $N(k + 1)$  is then found with the integration of (4.42). The process repeats to evolve the full time series simulation.

For each data set the system response to the static relief valve states of  $k_v = [0, 0.05, \dots, 1]$  are considered. Figure 5.8 shows, for each static relief valve state and for each data set considered, the mean electrical power take-off  $\bar{P}_e$ , % time spent in the different stall bands (which were defined in section 3.7), mean additional vibrations above the residual  $\bar{V}$  (from aerodynamic effects) found from the data derived figures 3.29 and 3.30. Also the value of  $\sigma(\Psi)$  resulting from  $k_v$ , is presented.

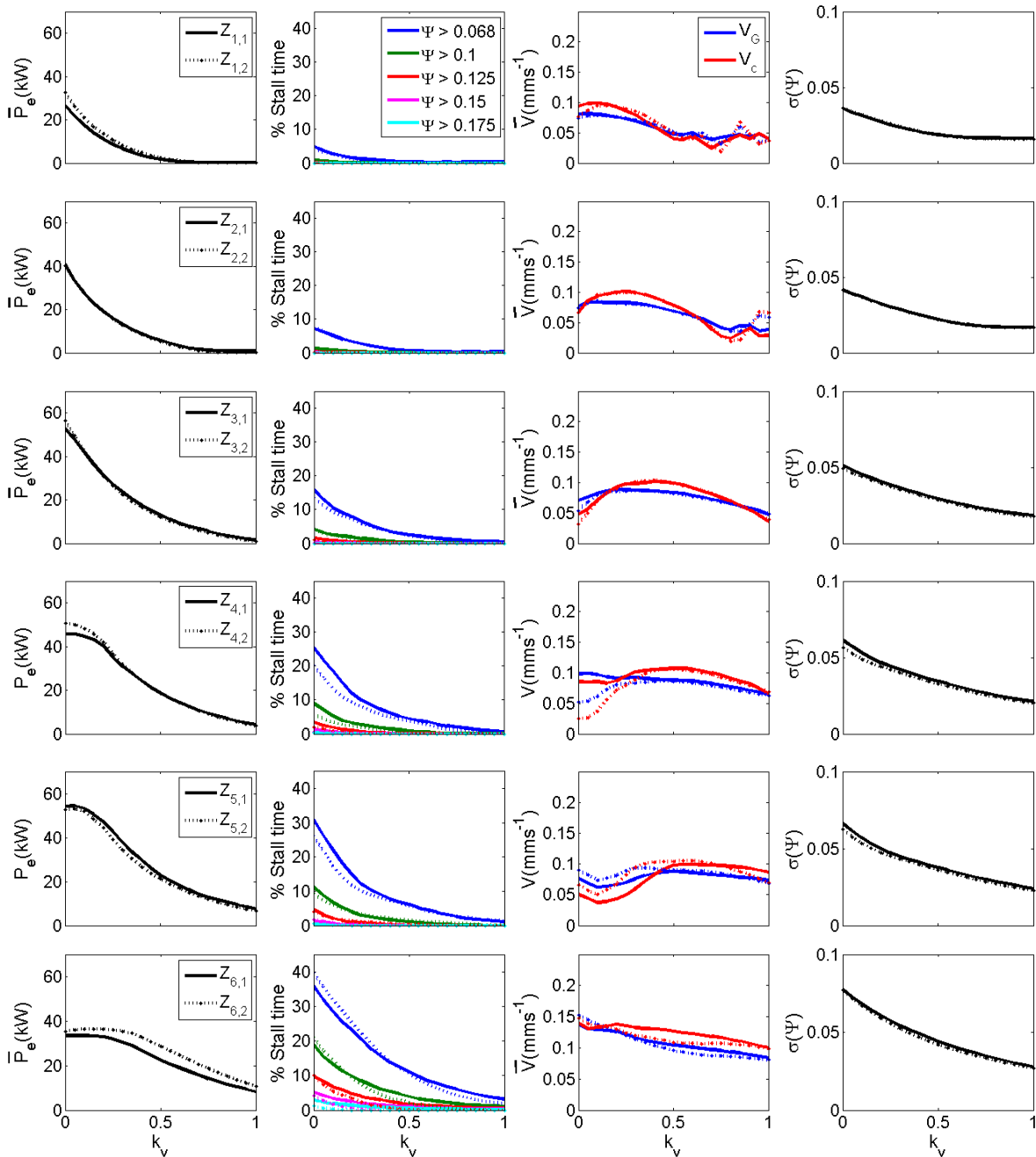


**Figure 5.8** Modelled mean electrical power take-off  $\bar{P}_e$ , % time spent in stall bands, vibrations above the residual and the value of  $\sigma(\Psi)$ , in response to different static relief apertures  $k_v$  (*Basic<sub>RVC</sub>*),

In figure 5.8 it is seen that, as expected, the system performance is strongly dependent on the relief valve state  $k_v$ . In most cases a larger  $k_v$  results in lower mean electrical power take-off because a greater mass

flow rate through the relief valve reduces the chamber air density gradient to the atmosphere and subsequently the mass flow rate past the turbine, thus reducing the available pneumatic power. It is also seen that when  $\sigma(\Psi) > 0.05$  the power production plateaus. At best only very small increases in  $\bar{P}$  can be achieved at the expense of large increases in the % time spent in stall when  $\sigma(\Psi) > 0.05$ . For higher power sea states than the ones considered, the maximum  $\bar{P}_e$  would be expected to occur with increasing values of  $k_v$ . By increasing  $k_v$  in higher energy sea states, the oscillations in pneumatic power exposure to the turbine will be shifted into a range that has an overall greater proportion of power transfer to the turbine because the proportion of time spent in deep stall (un-transferable power), is reduced. Reducing the turbine power exposure also reduces the proportion of time that the turbine spends in the stall regime. The effect of  $k_v$  on the additional turbine shaft vibrations is more complex because of the nonlinear relationship between rotation speed, chamber pressure and vibrations (as seen in figures 3.29 and 3.30)

As stated earlier, achieving  $\sigma(\Psi) \approx 0.05$  does not guarantee the greatest performance in terms of power production, but in normal operational practice without knowing the future the relief valve would be controlled to try to achieve  $|\sigma(\Psi) - 0.05|_{min}$ . As such the relief valve states  $k_v$  that result in  $|\sigma(\Psi) - 0.05|_{min}$  are selected to generate the base line performance level for later comparison against the simulations resulting from the more advanced relief valve control strategies. The corresponding system performance statistics, namely the: mean power production  $\bar{P}_e$ , the % time in stall bands and the mean vibrations above the residual  $\bar{V}$ , for these base line simulations, are given in table 5.2.

**Table 5.2** Mean electrical power take-off and machine fatigue indicators resulting from  $Basic_{RVC}$  with the static relief aperture that achieves  $|\sigma(\Psi) - 0.05|_{min}$ , for the different data sets  $Z$  considered.

	$Z_{1,1}$	$Z_{1,2}$	$Z_{2,1}$	$Z_{2,2}$	$Z_{3,1}$	$Z_{3,2}$	$Z_{4,1}$	$Z_{4,2}$	$Z_{5,1}$	$Z_{5,2}$	$Z_{6,1}$	$Z_{6,2}$
$\bar{P}_e$ (kW)	26.2	32.5	41.0	40.1	52.8	56.5	43.3	48.2	47.0	48.4	29.1	34.6
$\bar{V}_G$ (mms <sup>-1</sup> )	0.08	0.07	0.08	0.07	0.07	0.05	0.1	0.06	0.07	0.08	0.11	0.11
$\bar{V}_c$ (mms <sup>-1</sup> )	0.09	0.08	0.07	0.07	0.05	0.03	0.09	0.04	0.04	0.06	0.13	0.12
$\Psi > 0.068$ (% time)	4.9	4.2	7.1	7.6	15.9	13.3	15.1	16.5	18.2	14.3	15.6	16.3
$\Psi > 0.1$ (% time)	0.77	0.32	1.3	1.3	4.0	3.7	3.9	4.3	5.2	4.8	6.1	4.6
$\Psi > 0.125$ (% time)	0.30	0.0	0.3	0.1	1.6	1.0	1.3	1.5	1.4	1.6	3.0	1.5
$\Psi > 0.15$ (% time)	0.0	0.0	0.1	0	0.4	0.1	0.2	0.6	0.1	0.4	1.5	0.5
$\Psi > 0.175$ (% time)	0.0	0.0	0.0	0.0	0.0	0.0	0.1	0.1	0	0.1	0.8	0.1
$k_v$	0	0	0	0	0	0	0.15	0.10	0.20	0.15	0.35	0.35

Provided the sea state does not change too rapidly  $Basic_{RVC}$  will be able to prescribe a value of  $k_v$ , that results in  $\sigma(\Psi) \approx 0.05$  in the near future (if the wave power resource is sufficiently great). In reality it may be difficult to exactly achieve  $\sigma(\Psi) = 0.05$  due to the short term wave variability and over-shoot in relief valve aperture adjustment (due to a minimum adjustment percentage). As such  $Basic_{RVC}$  would cause the value to oscillate marginally about the target value unless a range is defined i.e.  $0.048 < \sigma(\Psi) < 0.052$ .

## 5.4.2 Instantaneous relief valve control

As seen in the characteristic curve for the Pico Wells turbine in figure 5.2, there exists a critical value of non-dimensional pressure  $\Psi_{cr} \approx 0.067$  where  $\Pi_{max}$  occurs. The reason for this maximum and subsequent rapid decline with  $|\Psi| > \Psi_{cr}$  is described in the following.

The angle of attack  $\alpha$  between the driving aerodynamic flow and the blade profile is described by;

$$\tan \alpha = \frac{v_a}{U} = \frac{v_a}{rN} \quad (5.17)$$

where;  $v_a$  is aerodynamic flow-velocity past the turbine (which increases with  $|\Psi|$ ),  $U$  is the tangential turbine tip speed at a point on the blade,  $r$  is the radius, which is the distance from a point on the blade to the axis of rotation, and  $N$  is the turbine angular velocity.

As  $|\Psi|$  increases with the increase in pressure head  $p_c$  or decrease in angular velocity  $N$ ,  $\alpha$  increases. There is a critical threshold  $\alpha_{cr}$  when  $|\Psi| = \Psi_{cr}$ , past which point flow begins to separate over the blade and becomes turbulent and a loss of lift force is incurred. This is known as the threshold for turbine stall. So whilst the available pneumatic power increases with the increases of  $|\Psi|$ , the transfer efficiency of aerodynamic to mechanical power, drops rapidly when  $|\Psi| > \Psi_{cr}$ .

In (Falcão & Justino, 1999) a hypothetical control strategy using either a relief valve or throttle valve control with negligible actuation time is considered. Alternatively, in (Falcao, et al., 2003) an array of smaller relief valves with negligible aperture adjustment time is described. The method of optimising the instantaneous pressure with just a relief valve having negligible aperture adjustment time will be termed ‘instantaneous relief valve control’ or *Instant<sub>RVC</sub>* for short. If this type of valve was available the relief valve control strategy would be of the following form.

When  $|\Psi| < \Psi_{cr}$ , a valve aperture of zero area is prescribed in order to build up chamber pressure as quickly as possible to try to achieve the optimum  $|\Psi| = \Psi_{cr}$  as soon as possible, because this results in  $\Pi_{max}$ . When  $|\Psi| = \Psi_{cr}$  is achieved a non-zero relief valve aperture is prescribed so that the mass flow rate through the relief valve  $\dot{m}_v$ , and the mass flow rate through the turbine  $\dot{m}_t$ , balances the volumetric flow rate  $\dot{V}_c$  from the oscillating water surface elevation such that the chamber pressure (relative to the atmospheric pressure) is maintained at its critical value;

$$p_{c_{cr}} = \frac{RT(\dot{m}_t + \dot{m}_v)}{\dot{V}_c} = \Psi_{cr} \rho_0 N^2 D^2 \quad (5.18)$$

where  $R$  is the specific gas constant and  $T$  is the absolute temperature.

Control of the relief valve in this manner maintains  $|\Psi| = \Psi_{cr}$  (after it has been achieved) whilst  $p_{c_{cr}} < RT\dot{m}_{turb}/\dot{V}_c$ . When  $p_{c_{cr}} > RT\dot{m}_t/\dot{V}_c$  (with  $\dot{m}_v = 0$  for  $k_v = 0$ ) the achievable  $\Psi$  is less than  $\Psi_{cr}$ . During this portion of the wave cycle  $k_v = 0$  is maintained so that  $\dot{m}_v = 0$ , to minimise  $\Psi_{cr} - |\Psi|$ .

Physically implementing *Instant<sub>RVC</sub>* was not achievable within the time frame or financial and resource limitations of this study because it involves engineering a complex, fast and powerful, relief valve actuator system. It has also been evaluated theoretically in the time domain in (Falcão & Justino, 1999)

with synthesised waves and stochastically in (Falcao & Rodrigues, 2002) but in combination with a throttle valve to maintain a Gaussian distribution of chamber pressure which is necessary for the stochastic modelling approach.

Despite this, it is still interesting to re-simulate  $Instant_{RVC}$  in the time domain specifically for the Pico case-study because now real input wave data can be used rather than synthesised waves as in (Falcao, et al., 2003). Significantly different results are expected because of the previously unforeseen wave asymmetry. Also the time-series model delivers a time-series of the real electrical power take-off, rather than a mean non-dimensional power  $\bar{\Pi}$  from stochastic analysis as seen (Falcão, 2002). This allows the theoretical maximum real power that could be achieved with relief valve control for the selected data sets and with the current angular velocity dependent electrical power take-off (by the generator) curves that are currently used at Pico (as shown in figure 3.7). This will also serve as a useful case comparison for evaluating the performance of other less demanding relief valve control systems, which are presented in the following subsections.

To evaluate  $Instant_{RVC}$  a time-series model for the pressure system dynamics and wave to wire power transfer is constructed and driven with the time-series of excitation flow  $q_e$  from the selected data sets. The model for chamber pressure and turbine response is described by (4.39) and (4.42) respectively and is similar to the model used in the analysis of  $Basic_{RVC}$ , but with the following differences. At each data time step  $k$ ,  $p_c(k+1)$  and  $N(k+1)$  are calculated using the relief valve states  $k_v(k+1) = 0, 0.01, \dots, 1$ . The value of  $k_v$  that delivers the lowest positive value of  $\Psi_{cr} - |\Psi(k+1)|$  is selected and set for continuation in the model at the next time step. This process is repeated until a full simulation of the time-series is achieved. The transition from one relief valve state to the next occurs in one data time step  $dt = 0.5(s)$  and there are no other restraints on the rate of aperture adjustment. The maximum aperture area  $A_v = 1.69 (m^2)$ , which is equal to the relief valve dimensions at Pico, was selected. The model also assumes that a perfect forecast of  $\hat{q}_e$  with one data point of horizon, is available and that computational time is negligible (no delay).

A statistical analysis of the performance of  $Instant_{RVC}$  is given in figure 5.9 which, for the data sets considered, gives the mean: electrical power take-off  $\bar{P}_e^*$ , %\* of time spent in stall bands, and vibrations above the residual  $\bar{V}^*$ . The variable values marked with the superscript \* are normalised by the corresponding base-line values achieved with  $Basic_{RVC}$ , as given in table 5.2. The number of complete relief valve cycles per hour  $k_v^{-Hr}$  if all relief valve state adjustments were summed, is also given. This evaluation parameter is defined by;

$$k_v^{-Hr} = \frac{3600 f_s \sum_{k=1}^L |k_v(k) - k_v(k-1)|}{L} \quad (5.19)$$

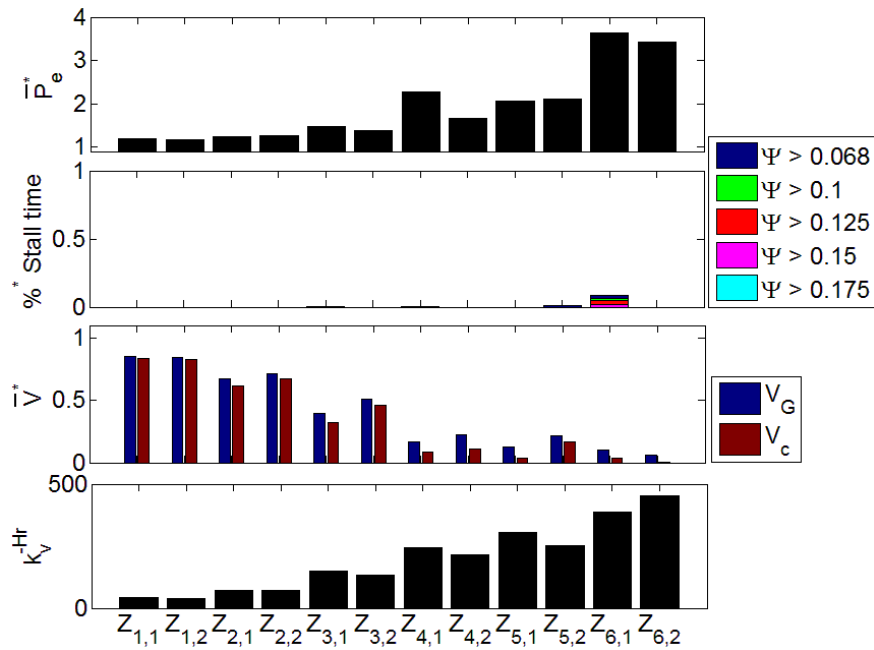


**Figure 5.9** Modelled mean: electrical power take-off  $\bar{P}_e^*$ , %\* time spent in stall bands, mean vibrations above the residual  $\bar{V}^*$  and relief valve cycles per hour, resulting from  $Instant_{RVC}$ . All values except the number of relief valve cycles per hour are normalised by the base-line values resulting from  $Basic_{RVC}$ , for the corresponding data sets and these are denoted with the superscript \*.

As might be expected the mean electrical power take-off  $\bar{P}_e$  increases significantly with the incident wave power because the maximum power transfer condition ( $\Psi = \Psi_{cr}$ ) is more frequently achieved and sustained for longer periods of time. For the data sets considered,  $Instant_{RVC}$  achieves electrical power take-off levels  $\bar{P}_e$  up to about 270% greater than value achieved with  $Basic_{RVC}$ . Of course, if the limitations imposed on maximum rotational speed due to vibrations were removed, and a more optimal electrical power take-off curve were deployed, the power enhancement could be higher still. The model projects that turbine stall can still occur because of the maximum valve aperture restrictions. However, these are so infrequent that they can be dismissed entirely. Mean vibrations above the residual are also dramatically reduced especially in the higher energy sea states. These gains however are at the expense of a very large number of relief valve adjustment cycles which would likely cause serious complications in the real application.

For completeness, a snapshot time series from the simulation of  $Instant_{RVC}$  for data set  $Z_{6,2}$  is given in figure 5.10 to visualise the relief valve aperture adjustments and the response of  $\Psi$  and  $\Pi$ .

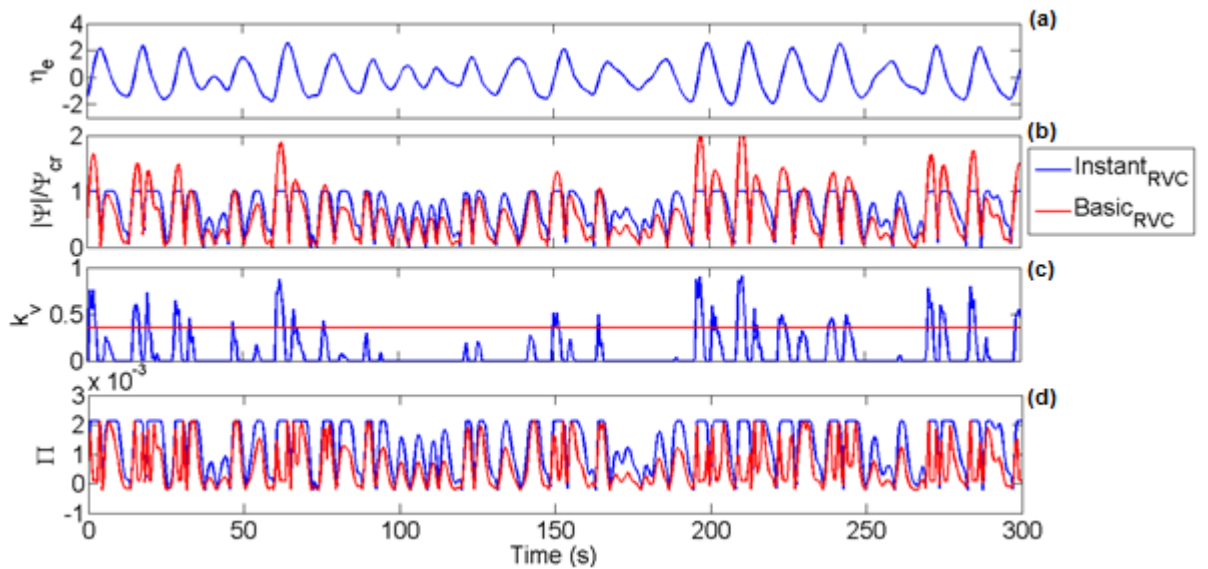


**Figure 5.10** Example time series of the simulated system response to  $Instant_{RVC}$ , compared to  $Basic_{RVC}$  for data set  $Z_{6,2}$ . (a) excitation chamber surface elevation  $\eta_e$ , (b) instantaneous non-dimensional pressure normalised by the critical value for the stall threshold  $|\Psi|/\Psi_{cr}$ , (c) the relief valve aperture state  $k_v$  and (d) instantaneous non-dimensional power transfer to turbine  $\Pi$ .

The mean non-dimensional power  $\bar{\Pi}$  as a function of  $\sigma(\Psi)$  resulting from  $Instant_{RVC}$  is given in figure 5.11. The curve resulting from the combined instantaneous control of the relief and throttle valve for the Pico plant case study is given in (Falcão, 2002) and is also shown in the figure 5.11. However, the two curves necessarily diverge because, for the combined relief valve and throttle valve scenario, the throttle valve acts to restrict the instantaneous mass flow rate passing the turbine so that  $\Pi_{max}$  occurs when  $\Psi > \Psi_{cr}$ , whilst the relief valve acts to maintain a Gaussian probability density function of chamber pressure, which is a basic requirement of the stochastic method used in that study. In contrast, relief valve control on its own acts to restrict the instantaneous chamber pressure so that at all times the non-dimensional chamber pressure is  $\Psi \leq \Psi_{cr}$ . This causes a clipping of the chamber pressure and the probability density function of chamber pressure is no longer Gaussian (even if it were Gaussian without  $Instant_{RVC}$ ). This difference is evident in the curve  $\bar{\Pi}$  vs  $\sigma(\Psi)$  in (Falcão, 2002), where combined valve control has values of  $\sigma(\Psi) > \Psi_{cr}$ , whereas for relief valve control only,  $\sigma(\Psi)$  can only converge asymptotically with  $\Psi_{cr}$  if it is functioning correctly.

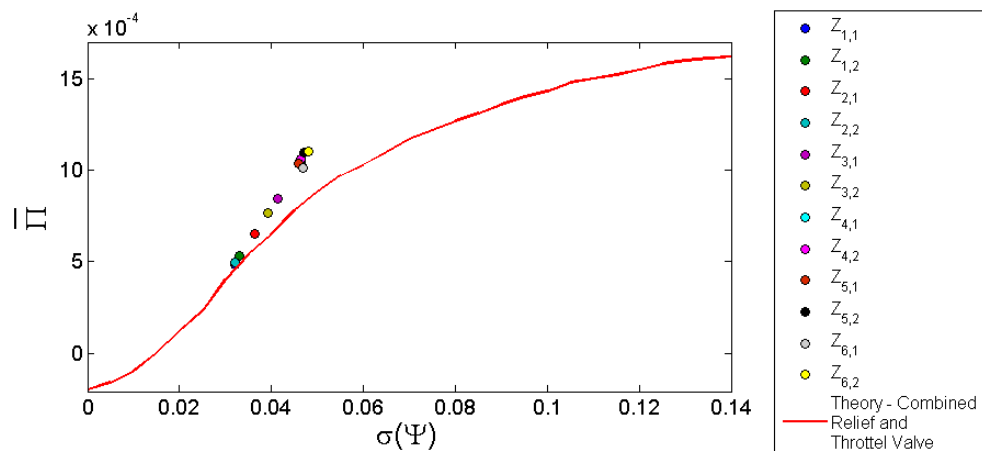


**Figure 5.11** Comparison of simulated  $\bar{\Pi}$  as a function of  $\sigma(\Psi)$  from  $Instant_{RVC}$ , with the theoretical derived relationship between the same two parameters from combined relief valve and throttle control as given in (Falcão, 2002).

Active *Instant<sub>RVC</sub>*, where the relief valve aperture is actively set will require a short-term prediction of the chamber excitation flow  $\hat{q}_e(k + 1)$  or the excitation surface elevation  $\hat{\eta}_e(k + 1)$  in order to model the chamber pressure response with different values of  $k_v$  and then set the optimum, in the next data time step. The horizon requirements for a hypothetical *Instant<sub>RVC</sub>* will be of the order of a fraction of a second and assumes the combined time for: computational processing, electrical delays, mechanical response of the valve actuator and the rate of aperture adjustment are negligible. Alternatively a semi-passive system could be implemented so that no forecast is required. Such a system could be a valve that passively opens at rotational speed dependent pressure threshold  $p_{cr}$ , defined as;

$$p_{cr} = \Psi_{cr} \rho_0 N^2 D^2 \quad (5.20)$$

### 5.4.3 Wave by wave relief valve control

To the author's knowledge, relief valve control strategies other than *Basic<sub>RVC</sub>* and *Instant<sub>RVC</sub>* (with either a relief valve, throttle valve or a combination of both) have not been considered in the literature. Regulating the chamber pressure profile over time scales shorter than that needed to characterise a sea state (which we consider to be 35 minutes in this study) as performed with *Basic<sub>RVC</sub>*, but over longer periods than at each data time instant as performed with *Instant<sub>RVC</sub>*, might also yield some performance enhancements and require less intensive relief valve aperture adjustments. Because of the significant degree of wave asymmetry, the obvious choice is to try to optimise the mean power delivery to the turbine over a half wave cycle from the points of zero chamber pressure head, which occurs (with a very slight delay) with the wave peak or trough. At the point of zero chamber pressure head there will be no additional thrust loading on the relief valve and therefore no additional frictional resistance opposing the valve's movement. This would reduce the required force needed to make the aperture adjustments, lowering the demands of the valve actuator system. We shall define this control strategy as 'Wave by wave' relief valve control, or *Wave<sub>RVC</sub>* for short.

To its detriment, a system of this sort requires a short term forecast of the incident excitation flow  $\hat{q}_e(k + l)$  with data horizon time equal to  $l$ , which is the data time length of the up-coming half wave period. This forecast is required to model the pressure profile resulting from different values of  $k_v$  in order to identify the optimum for power transfer to the turbine over the half wave period.

As with *Instant<sub>RVC</sub>*, because the valve actuator system currently installed at Pico does not meet the requirements needed for *Wave<sub>RVC</sub>* control, namely the aperture adjustment rate is far too slow, *Wave<sub>RVC</sub>* is purely hypothetical at this stage.

To assess the system response to *Wave<sub>RVC</sub>* in terms of enhancements to electrical power production and to infer any fatigue reductions, another time-domain model is required to perform a simulation of control and this is constructed as follows. Again as with *Instant<sub>RVC</sub>* we assume that a perfect forecast of the chamber excitation flow  $\hat{q}_e(k + l)$  is available, but this time the forecast spans the data time period  $k, k + 1, \dots, k + l$  where  $l$  is the data point time length between the adjacent (in time) instances of  $q_e(k) = 0$ . (which occur at the turning point of the wave crest or trough, in the chamber). When  $q_e(k) \approx 0$  a time series of  $p_c(k + l)$ , and turbine response  $N(k + l)$ , is modelled with (4.39) and (4.42), respectively. This is performed for a range of relief valve state  $k_v = [0, 0.05, \dots, 1]$ , and the relief valve state providing the

highest mean non-dimensional power transfer to turbine  $\bar{\Pi}_{max}$  is selected and prescribed in the model over the next half wave time period. To reduce the computational time required to perform this scan (to find the optimum  $k_v$ ) to an acceptable level would require significant computational power but due to the hypothetical nature of this control strategy (at this stage) it is assumed that this computational resource is available. The model simulation requires  $k_v$  to be changed within 1 data time step between the data points where  $q_e$  changes sign. The valve aperture range is considered to be the same as the relief valve currently installed at Pico which is  $A_v = 1.69 (m^2)$ .

Again, for each data set considered, the modelled values of: mean electrical power take-off  $\bar{P}_e^*$ , %\* time spent in the stall bands, mean vibrations above the residual  $\bar{V}^*$ , all normalised by the optimised base-line found from  $Basic_{RVC}$ , are shown in figure 5.12 along with the number of relief valve cycles per hour  $k_v^{-Hr}$ .

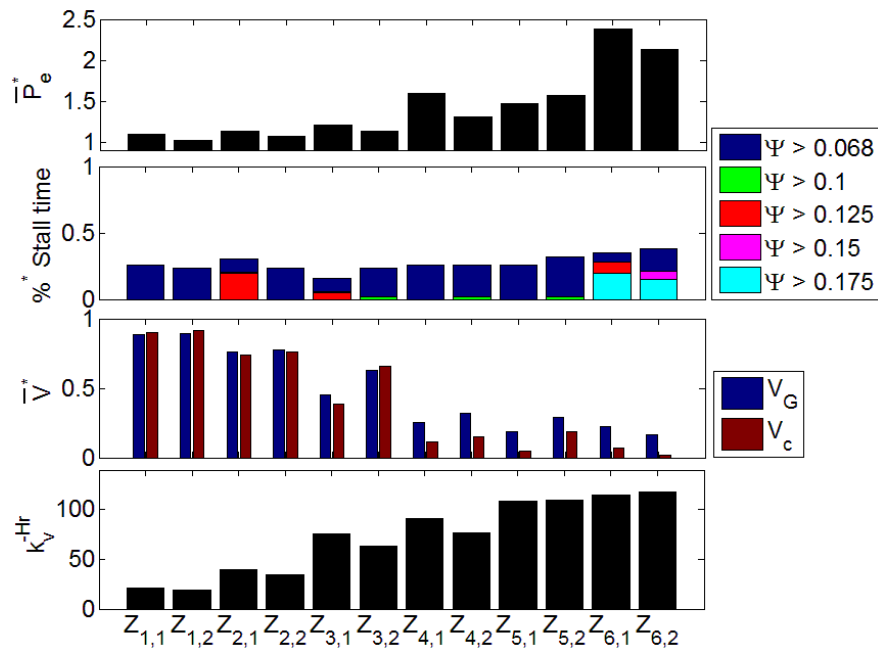


**Figure 5.12** Modelled mean electrical power take-off  $\bar{P}_e^*$ , %\* time spent in stall bands, mean vibrations above the residual  $\bar{V}^*$  and relief valve cycles per hour, resulting from  $Wave_{RVC}$ . All values except the relief valve cycles per hour are normalised by the corresponding base-line values from  $Basic_{RVC}$ .

As seen in figure 5.12, for the sea states  $Z_1, Z_2$  and  $Z_3$  there is little difference in performance between  $Wave_{RVC}$  and  $Basic_{RVC}$ , except for the % time spent in the different stall bands. This is because the incident wave power resource results in minimal time spent in the stall regime under  $Basic_{RVC}$  leaving little room for  $Wave_{RVC}$  to have a notable effect. However, significant performance enhancements are achieved with sea states  $Z_4, Z_5$  and  $Z_6$ , where there is sufficient wave power resource for relief valve control to be significantly influential. Electrical power take-off is enhanced by up to 140% and there are substantial relative reductions in stalls and vibrations above the residual. Again these performance enhancements are at the expense of a high number of relief valve cycles but far less than incurred with  $Instant_{RVC}$ .

For completeness, a snapshot time series from the simulation of  $Wave_{RVC}$  for data set  $Z_{6,2}$  is given in figure 5.13 to visualise the relief valve aperture adjustments and the response of  $\Psi$  and  $\Pi$ .

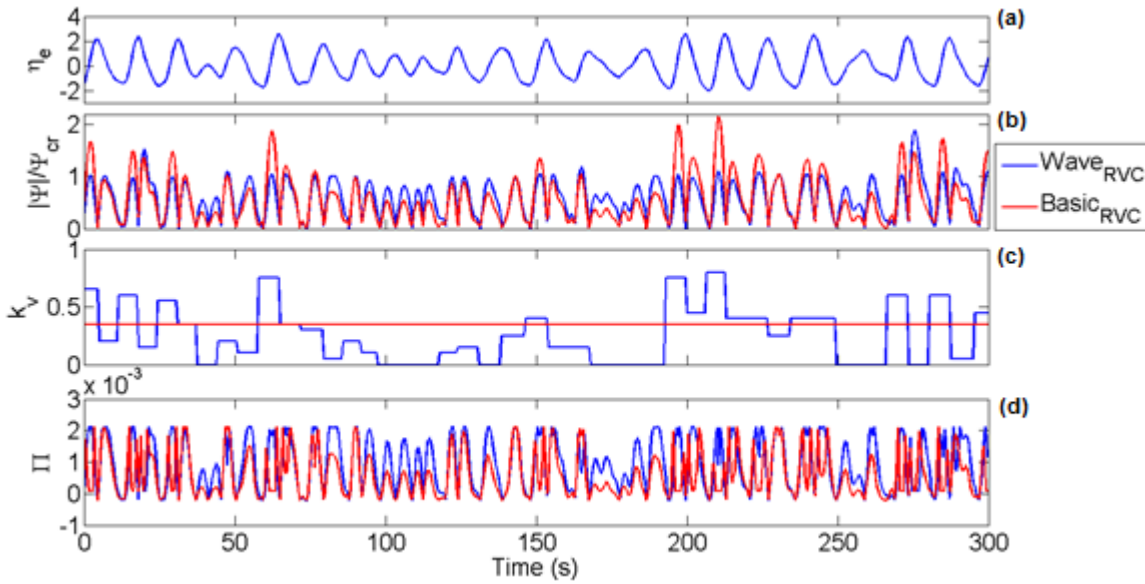


**Figure 5.13** Example time series of the simulated system response to  $Wave_{RVC}$ , compared to  $Basic_{RVC}$  for data set  $Z_{6,2}$ . See figure 5.10 for parameter description.

#### 5.4.4 Continuous relief valve control

As seen in section 5.4.3, optimising power transfer to the turbine strictly on a half wave cycle using  $Wave_{RVC}$  requires large and almost instantaneous relief valve adjustments to be made. This is not achievable with the existing relief valve adjustment system installed at Pico. However, it would be possible to adjust the relief valve aperture slowly but continuously in order to regulate the chamber pressure profile over the next specific time period  $\Gamma$ , in order to optimise power transfer to the turbine. Although it is not clear if the existing hydraulic pump used to make aperture adjustments is robust enough for constant operation and may need a minor upgrade. This strategy will be called  $Continuous_{RVC}$ .

At each data point  $k$  a time series of  $p_c(k+l)$ , and turbine response  $N(k+l)$ , where  $l = 1, 2, \dots, \Gamma f_s$ , that would result if the relief valve aperture was maintained or if it was increased or decreased by the current relief valve aperture adjustment rates, is modelled with (4.39) and (4.42). The new relief valve states considered are described by;

- Maintain the current aperture -  $k_v(k+l) = k_v(k)$
- Increase the aperture -  $k_v(k+l) = k_v(k) + \dot{k}_{v,o} / f_s$
- Decrease the aperture -  $k_v(k+l) = k_v(k) - \dot{k}_{v,c} / f_s$

where  $\dot{k}_{v,o}$  and  $\dot{k}_{v,c}$  are described in section 3.3.5.2.

The adjustment or maintenance of the relief valve state  $k_v$  that delivers the greatest  $\bar{\Pi}_\Gamma$  over the upcoming time period  $\Gamma$  is set in the model for the next time step and the process is repeated to evolve the full time series of the system response to this valve control strategy. Because this control strategy is not hypothetical, two additional conditions are implemented to make the model more representative of what might occur in reality. Firstly the computational time required to make the assessment is factored in as a time delay to the aperture adjustment and secondly the valve aperture is not permitted to transfer directly from an open stroke to a closing stroke and must spend one data time point interval at its current aperture. This condition was implemented, based on observations of the actual valve aperture adjustment response.

Again, in order to project of mean power transfer of the up-coming time period  $\Gamma$  a short term forecast of the incident excitation flow  $\hat{q}_e(k+l)$  will be required, and a perfect forecast is assumed at this stage.

To investigate the effect of  $\Gamma$  on the performance of *Continuous<sub>RVC</sub>* the horizon times  $\Gamma = 1, 2, \dots, 20$ , which are used to evaluate  $\bar{\Pi}_\Gamma$ , are considered. For each data set and  $\Gamma$  permutation, the values of mean electrical power take-off  $\bar{P}_e^*$ , %\* time spent in the stall bands and vibrations above the residual  $\bar{V}^*$ , normalised by the corresponding optimised base-line values found from *Basic<sub>RVC</sub>*, in addition to the total number of relief valve cycles per hour  $k_v^{-Hr}$ , is shown in figure 5.14.

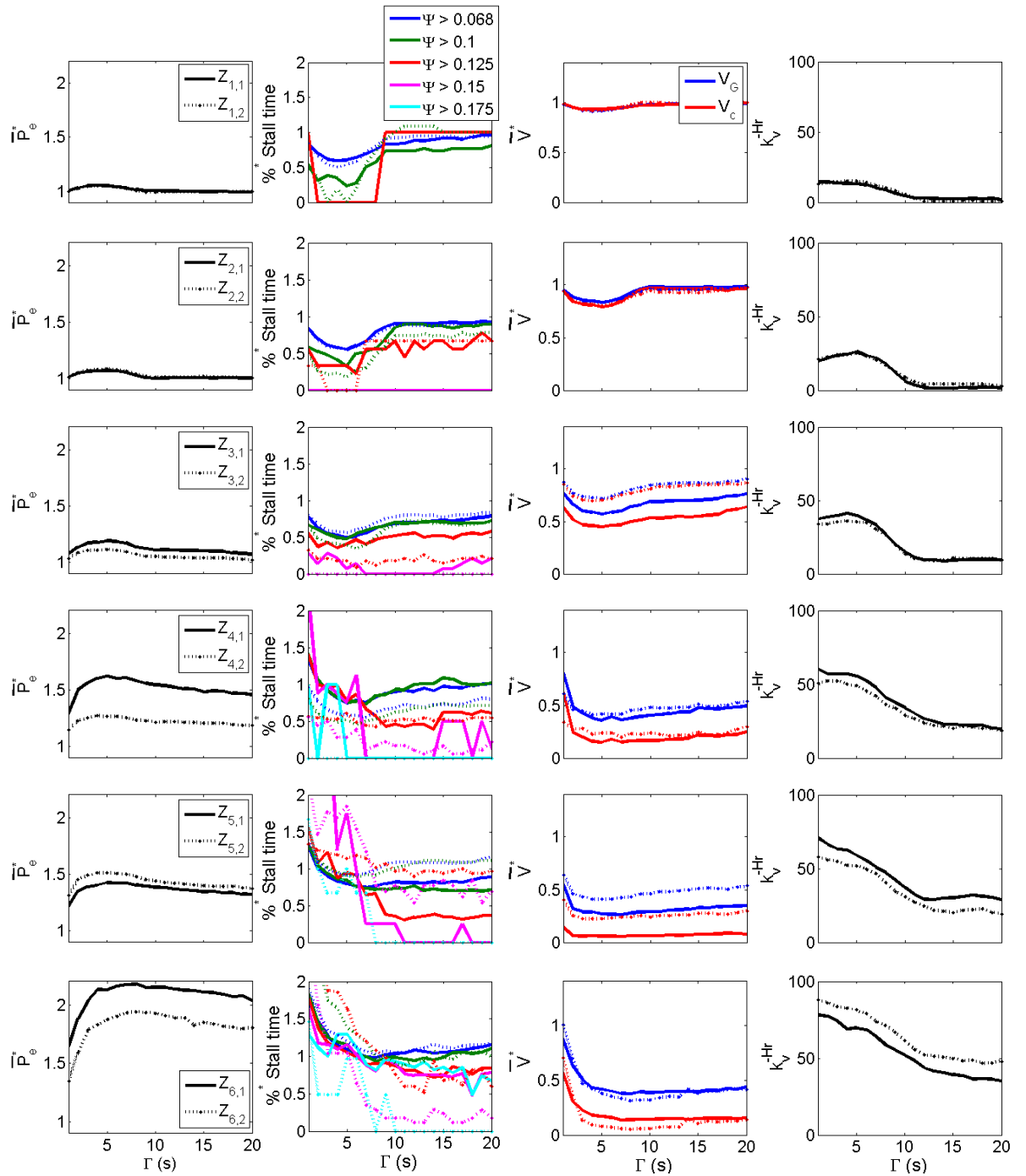


**Figure 5.14** Modelled mean electrical power take-off  $\bar{P}_e^*$ , %\* time spent in stall bands, mean vibrations above the residual  $\bar{V}^*$  and relief valve cycles per hour, in response to *Continuous<sub>rvc</sub>* assessing and optimising  $\bar{\Pi}_\Gamma$  over different horizon lengths  $\Gamma$ . All values except the number of relief valve cycles per hour are normalised by the base-line values resulting from *Basic<sub>RVC</sub>*, for the corresponding data sets.

The optimum time horizon  $\Gamma_{optimum}$  for each data set, is considered as the one that gives the best compromise between  $\bar{P}_e^*$  and %\* time spent in stall bands and these values are given in table 5.3.

**Table 5.3** The horizon times  $\Gamma$  to assess  $\bar{\Pi}_\Gamma$  that resulted in the greatest performance enhancement from  $Continuous_{RVC}$ , for the data sets considered with the corresponding values of chamber measured peak period  $T_p$  and energy period  $T_e$  for each data set.

	$Z_{1,1}$	$Z_{1,2}$	$Z_{2,1}$	$Z_{2,2}$	$Z_{3,1}$	$Z_{3,2}$	$Z_{4,1}$	$Z_{4,2}$	$Z_{5,1}$	$Z_{5,2}$	$Z_{6,1}$	$Z_{6,2}$
$\Gamma_{optimum}[s]$	5	5	5	5	6	6	7	7	7	7	7	7
$T_p$	13.5	14.2	13.5	14.2	13.5	13.5	13.5	14.2	13.5	15.1	13.5	15.1
$T_e$	13.2	13.6	13.3	13.5	13.4	13.2	13.6	13.4	13.1	14.5	14.0	14.3

It is seen in table 5.3 that  $\Gamma_{optimum}$  is 0 to 3 (s) less than  $T_p/2$  (because the mean wave period is less than the peak period), but considering  $\Gamma_{optimum} = T_p/2$  would achieve almost the same result. Alternatively, as seen in figure 5.14 the lowest relief valve adjustment cycle frequency is associated with a horizon of  $\Gamma \approx T_p$ . Although the greatest power enhancement is achieved by optimising chamber pressure over the half peak wave period because of wave asymmetry, significant performance enhancements are also gained by optimising chamber pressure over the peak wave period and far fewer relief valve aperture adjustments are required to achieve this. Pressure optimisation over a time period similar to the peak wave period will be investigated further in the next subsection.

For an easier comparison of the result in figures 5.9 and 5.12, the statistical analysis of the resultant performance using the optimum control horizon time as described in table 5.3, for each data set, is given in figure 5.15.

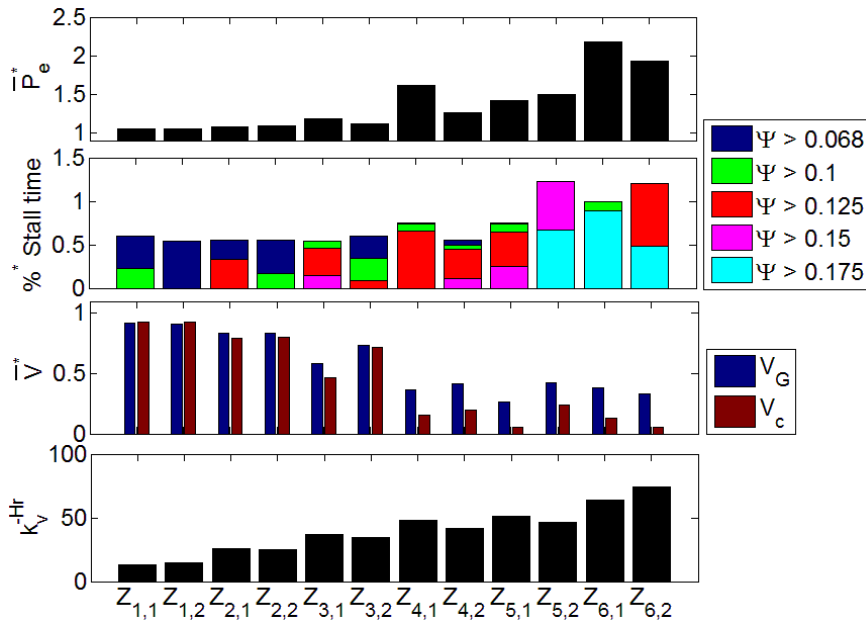


**Figure 5.15** Modelled mean electrical power take-off  $\bar{P}_e^*$ , %\* time spent in stall bands, mean vibrations above the residual  $\bar{V}^*$  and relief valve cycles per hour, resulting from  $Continuous_{RVC}$  using  $\Gamma_{optimum}$  to assess  $\bar{\Pi}_\Gamma$ . All values except the number of relief valve cycles per hour are normalised by the corresponding base-line values from  $Basic_{RVC}$ .

For completeness a snapshot time series from the simulation of  $Wave_{RVC}$  for data set  $Z_{6,2}$  is given in figure 5.16 to visualise the relief valve aperture adjustments and the response of  $\Psi$  and  $\Pi$ .

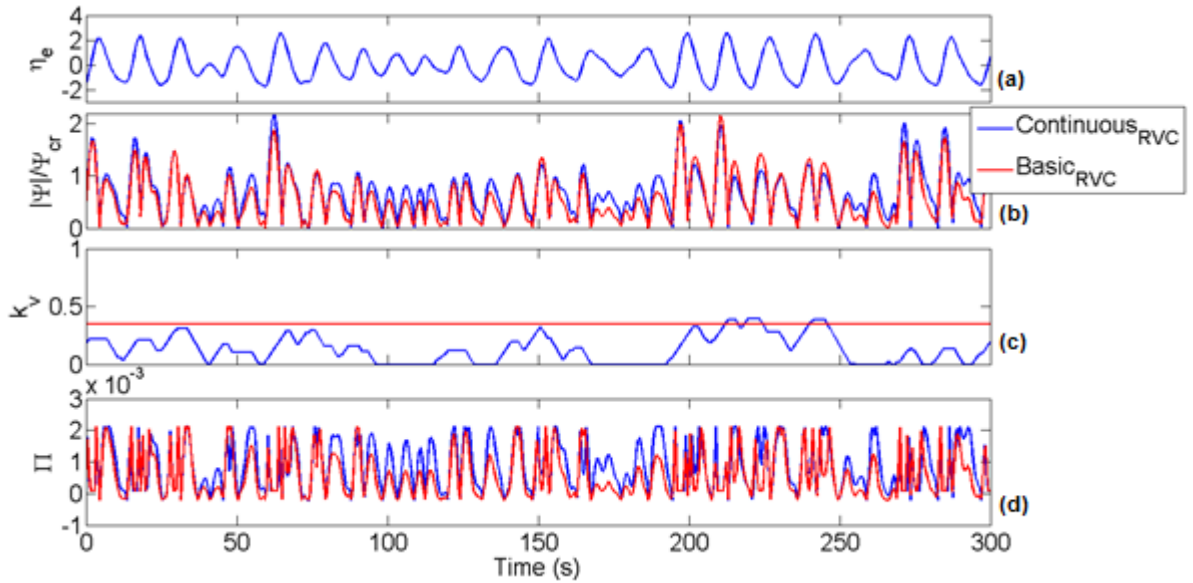


**Figure 5.16** Example time series of the simulated system response to  $Continuous_{RVC}$ , compared to  $Basic_{RVC}$  for data set  $Z_{6,2}$ . See figure 5.10 for parameter description.

#### 5.4.5 Envelope relief valve control

As seen in section 5.4.4, continuously adjusting the relief valve aperture, to optimise the chamber pressure profile over a time period approximately equal to half the peak wave period, achieves significant enhancements to power production and reductions in stalls and vibrations in higher energy sea states. Although this method is technically feasible using the existing relief valve aperture (because the real valve aperture adjustment rates are used in the model) it is seen that a very high number of relief valve cycle adjustment cycles are required to perform control in this way. In reality the existing relief valve actuator system (at Pico) was not designed for this purpose and it is likely that it would not be able to tolerate such constant demand for very long before overheating. Alternatively, as seen in figure 5.14, relief valve adjustments can be significantly reduced by optimising chamber pressure over a period approximately equal to the full peak wave period, although a small but significant reduction in power enhancement is incurred.

Another potential issue with  $Continuous_{RVC}$  is the on-line computational modelling time required to identify the optimum aperture adjustment. To model the three different scenarios associated with opening, closing and maintaining the relief valve aperture, requires around 1 (s) computational time using a similar computer to the one that would need to be used at Pico (without implementing a computer system overhaul). This computational time delay is likely to have a detrimental effect on the controlled performance. For these reasons another relief valve control strategy, similar to  $Continuous_{RVC}$ , but with some additional conditions that aim to reduce the relief valve cycle frequency and the computational effort, is considered.

Firstly, in order to reduce the computational time, an evaluation parameter could be developed and used to determine statistically whether it would be beneficial to open, close or maintain the current relief valve aperture in the next data time step. If only a single short-term model pass is required, at each data time

step, the computational time needed to evaluate the control action can be reduced below the data sampling period (which is  $T_s = 0.5$  (s) at Pico). This would result in no additional delay in the relief valve control response.

Secondly, this statistical evaluation parameter could be used to define an optimum range so that minor fluctuations in the incident short-term excitation flow profile would not result in minor adjustments to the relief valve aperture, thus reducing the aperture adjustment frequency. In this fashion the current relief valve aperture would be maintained at its current aperture until more significant changes in the up-coming excitation flow profile occur.

Thirdly, the aperture adjustment rate for the closing stroke can be reduced, whilst the aperture adjustment rate for the opening stroke is maintained at the maximum. With this modification the relief valve aperture will be able to increase at the maximum rate in order to vent over-pressure associated with the arrival of a higher energy wave groups, thus avoiding turbine stalls, but will only close again more slowly so as to slowly track the excitation flow envelope of the wave group, rather than strongly accounting for small fluctuations within the wave group. A reduced closing rate could be achieved in reality by slowly pulsing the electrical signal delivered to the hydraulic ram pump.

With these additional conditions applied to  $Continuous_{RVC}$ , the resulting new valve control will be called  $Envelope_{RVC}$  because relief valve aperture adjustments are made so as to track the wave envelope rather than the half-wave cycle. These additional conditions are likely to reduce the system performance in terms of power production, because an approximate optimum pressure variance range will be targeted, rather than the exact optimum. However, far less intensive valve aperture adjustments will be required, which is probably an important constraint when deployment is performed in reality (using the existing relief valve actuator). To realise  $Envelope_{RVC}$ , first a control evaluation parameter needs to be developed. After, the system response to this new mode of control will be evaluated with a simulation.

The standard deviation of non-dimensional pressure over a wave period considers the variance of the pressure oscillation over this time frame, whilst factoring in the system state (turbine speed) and this could be used as a control evaluation parameter. To investigate this idea the mean non-dimensional power transfer to the turbine  $\bar{\Pi}_{T_p}$ , resulting from the standard deviation of non-dimensional pressure  $\sigma_{T_p}(\Psi)$  over an evaluation horizon time which is equal to the sea state peak period  $T_p$ , is evaluated. This is compared to the values of  $\bar{\Pi}$  and  $\sigma(\Psi)$  resulting from a longer durations (a 35 minute evaluation of the sea state), to infer the potential enhancement.

The standard deviation of non-dimensional pressure over a horizon period equal to  $T_p$ , is defined by;

$$\sigma_{T_p}(\Psi) = \sqrt{\frac{1}{T_p f_s} \sum_{l=1}^{k+T_p f_s} \left( \Psi(k+l) - \frac{1}{T_p} \sum_{l=1}^{k+T_p f_s} \Psi(k+l) \right)^2} \quad (5.21)$$

The mean non-dimensional power transfer to the turbine over time  $T_p$  is given by;

$$\bar{\Pi}_{T_p} = \frac{1}{T_p f_s} \sum_{l=1}^{k+T_p f_s} \Pi(\Psi(k+l)) \quad (5.22)$$

To examine the relationship between  $\bar{\Pi}_{T_p}$  and  $\sigma_{T_p}(\Psi)$  more closely 6 data sets, as described in section 5.3, are considered ( $Z_{1,1}, Z_{2,1}, \dots, Z_{6,1}$ ). The relationship between  $\bar{\Pi}_{T_p}$  and  $\sigma_{T_p}(\Psi)$  for each data set is given as a scatter plot with a polynomial line of best fit for all data sets in figure 5.17. This is compared to the mean non-dimensional power transfer to the turbine  $\bar{\Pi}$  as a function of the standard deviation of non-dimensional pressure  $\sigma(\Psi)$  over a length of time sufficiently long to define a sea state, i.e. 100 wave periods.

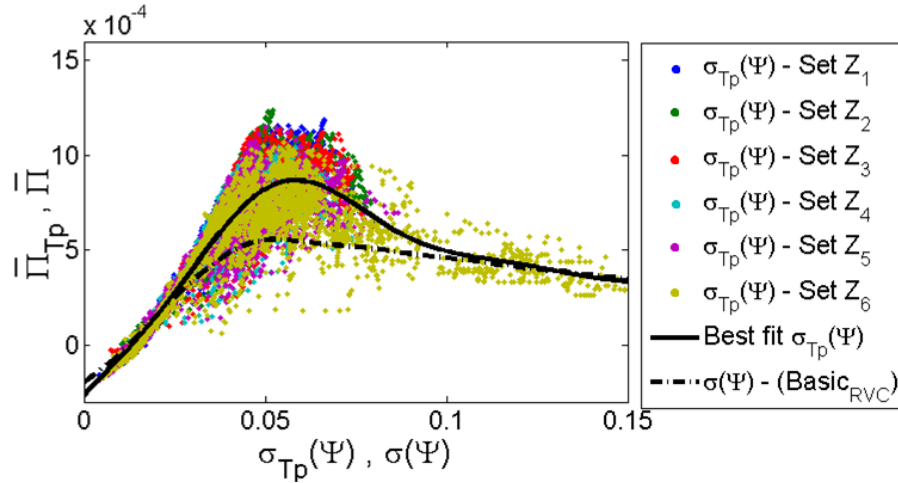


**Figure 5.17** Comparison of the theoretical non-dimensional power transfer to the turbine  $\bar{\Pi}$  as a function of  $\sigma(\Psi)$  for a sea state as given in (Falcão, 2002) and the non-dimensional power transfer to the turbine  $\bar{\Pi}_{T_p}$  as a function of  $\sigma_{T_p}(\Psi)$  for the horizon time  $T_p$ , with a curve of best fit that considers all data points across all data sets.

As seen in figure 5.17, the correlation in the relationship between  $\bar{\Pi}_{T_p}$  and  $\sigma_{T_p}(\Psi)$  is far from ideal. This is due to the fact that a specific time period  $T_p$  is being used to evaluate  $\sigma_{T_p}(\Psi)$ . As such, unless the wave cycle in question actually has a period of  $T = T_p$  the consideration of  $\sigma_{T_p}(\Psi)$  will span part of a wave-cycle if  $T > T_p$ , or a wave cycle and a part of the next wave cycle if  $T < T_p$ . The result is that in any instance a greater proportion of the higher  $\Pi$  data points of the wave cycle might be captured in the span leading to a higher value of  $\bar{\Pi}_{T_p}$  and vice versa. This effect is additional to the variability of the excitation flow profile over a wave cycle and the strength of wave asymmetry as discussed before.

However, the best fit curve for mean non-dimensional power  $\bar{\Pi}_{T_p}$  diverges from the mean non-dimensional power over a longer time period (sea state)  $\bar{\Pi}$ , and is seen to achieve greater levels in the range  $0.04 \leq \sigma_{T_p}(\Psi) \leq 0.08$ , than the maximum for the sea state  $\bar{\Pi}_{max}$ . Most notably there is a significant increase in  $\bar{\Pi}_{T_p,max} = 0.0009$  for the curve of best fit for a wave cycle compared to  $\bar{\Pi}_{max} = 0.00055$ , for the sea state which occurs at  $\sigma(\Psi) \approx 0.05$ . This is promising with regards to using  $\sigma_{T_p}(\Psi)$  as a statistical evaluation parameter because significant enhancements in the mean non-dimensional power can be achieved from the consistent minimisation of  $|\sigma_{T_p}(\Psi) - 0.055|$  with valve control over a time period equal to the most probable wave period. This means a single model pass can be used to project the value of  $\sigma_{T_p}(\Psi)$  at the current valve aperture, and if  $\sigma_{T_p}(\Psi) \ll 0.055$  then it is statistically advantageous to reduce the valve aperture to increase  $\sigma_{T_p}(\Psi)$ , and vice versa. This avoids the alternative

of performing three model passes to assess the response of  $\bar{\Pi}_{T_p}$  to increasing, decreasing or maintaining the current aperture.

It has been identified that there is some potential benefit to be had by minimising  $|0.055 - \sigma_{T_p}(\Psi)|$  with  $Envelope_{RVC}$  over a time period equal to one wave period, compared to minimising  $|0.05 - \sigma(\Psi)|$  for a sea state time scale as done with  $Basic_{RVC}$ . As such it is justified to go further and simulate  $Envelope_{rvc}$  with another time-series model and assess the real enhancements to power production and infer any reductions in the indicators for machine fatigue. The time-series model is again formed with (4.39) and (4.42). At the data point in time  $k$  the chamber pressure time-series  $p_c(k + l)$  and then the turbine response  $N(k + l)$ , where  $l = 1, 2, \dots, T_p f_s$ , is found if the current relief valve state  $k_v(k)$  were maintained at its current value.

If the valve aperture was instructed to try to achieve  $\sigma_{T_p}(\Psi) = 0.055$  the relief valve would oscillate about the optimum and many relief adjustment valve cycles would be incurred. The alternative is to try shift  $\sigma_{T_p}(\Psi)$  to within a certain range. When it is in this range the relief valve aperture is maintained until more significant changes in the incident energy occur, thus minimising the relief valve adjustment cycles. The broader the range the lower the relief valve adjustment frequency, but this will be at the expense of more frequent and significant divergences from the statistical optimum value of  $\sigma_{T_p}(\Psi)$ . From figure 5.17, it is seen that significant enhancements in  $\bar{\Pi}_{T_p}$  occur when  $0.04 < \sigma_{T_p}(\Psi) < 0.08$ . As more frequent and severe stalls will occur with increasing values of  $\sigma_{T_p}(\Psi)$  it seems more appropriate to target the lower half of this range. As such,  $0.04 < \sigma_{T_p}(\Psi) < 0.06$  is selected for the control action limits and this will be considered as the optimum range for balancing performance, relief valve adjustment cycles, and turbine stalls.

Valve control is specified in the model in the following way; if it is projected that  $\sigma_{T_p}(\Psi) > 0.06$  will occur over up-coming time period  $T_p$  (with the current relief valve state), the relief valve is instructed to start opening at the maximum opening rate so that  $k_v(k + 1) = k_v(k) + \dot{k}_{v,o} / f_s$ . Alternatively, if  $\sigma_{T_p}(\Psi) < 0.04$  is projected, the relief valve is instructed to start closing at the reduced closing aperture adjustment rate which was selected as half the maximum rate (to reduce the adjustment cycle frequency) so that  $k_v(k + 1) = k_v(k) - \dot{k}_{v,c-slow} / 2f_s$ . Finally, if  $0.04 < \sigma_{T_p}(\Psi) < 0.06$ ,  $\sigma_{T_p}(\Psi)$  is projected, the valve aperture is considered to be already in the approximate optimum range and no adjustment is made (also to reduce the adjustment cycle frequency).

As with  $Continuous_{RVC}$ , in order to make the simulation closer to reality, the computational time required to make the assessment is factored in as a time delay to the aperture adjustment. Also the valve aperture is not permitted to directly transfer from an open stroke to a closing stroke and must spend one data sampling period interval at its current aperture, to reflect reality.

With the relief valve state chosen for the next time step  $k_v(k + 1)$ , a second iteration of the model is performed, but for one time step in order to find  $p_c(k + 1)$  and then the turbine response  $N(k + 1)$ . The

process repeats at each data point to evolve the full time-series simulation. The simulation results for each data set are given in figure 5.18.

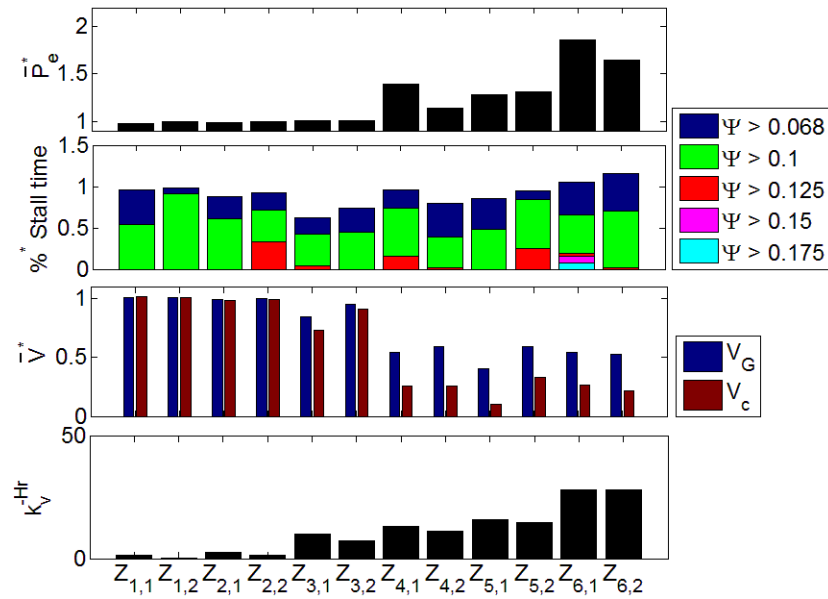


**Figure 5.18** Modelled mean electrical power take-off  $\bar{P}_e^*$ , %\* time spent in stall bands, mean vibrations above the residual  $\bar{V}^*$  and relief valve cycles per hour, resulting from  $Envelope_{RVC}$  acting on the projected  $\sigma_{T_p}(\Psi)$ . All values except the number of relief valve cycles per hour are normalised by the corresponding base-line values from  $Basic_{RVC}$ .

As seen in figure 5.18 when compared with figure 5.15, although the performance of  $Envelope_{RVC}$  is notably inferior to  $Continuous_{RVC}$  in terms of power production, far fewer relief valve adjustment cycles were required. Also the frequency and intensity of stalls in the higher energy sea states is reduced compared to  $Continuous_{RVC}$ . Because of wave asymmetry,  $Continuous_{RVC}$  has a tendency to reduce the aperture in the weaker inhalation wave half cycle and as a consequence it is then not able to increase the valve aperture fast enough to properly damp the more powerful exhalation half wave cycle, thus incurring more significant stall. Notable power gains of up to 80% and reductions in vibration in the higher energy sea states, as well as notable reductions in stall frequency and severity in all cases, when compared to  $Basic_{RVC}$ , were achieved. Because of the reduced relief valve adjustment cycles and computational effort,  $Envelope_{RVC}$  might be a more practical option than  $Continuous_{RVC}$  when considering the limitations of the existing equipment at Pico. However,  $Envelope_{RVC}$  requires a longer forecast horizon which will incur greater error and this could be a limiting factor.

For completeness and to visualise the relief valve adjustments under  $Envelope_{RVC}$  and the effect on the chamber pressure, power and attempted convergence with the optimum range  $0.04 < \sigma_T(\Psi) < 0.06$ , a sample time-series of the simulated valve control and its effect on  $\sigma_{T_p}(\Psi)$  compared to  $Basic_{RVC}$  with  $k_v = 0.35$ , for a portion of the data set  $Z_{6,2}$  is given in figure 5.19.

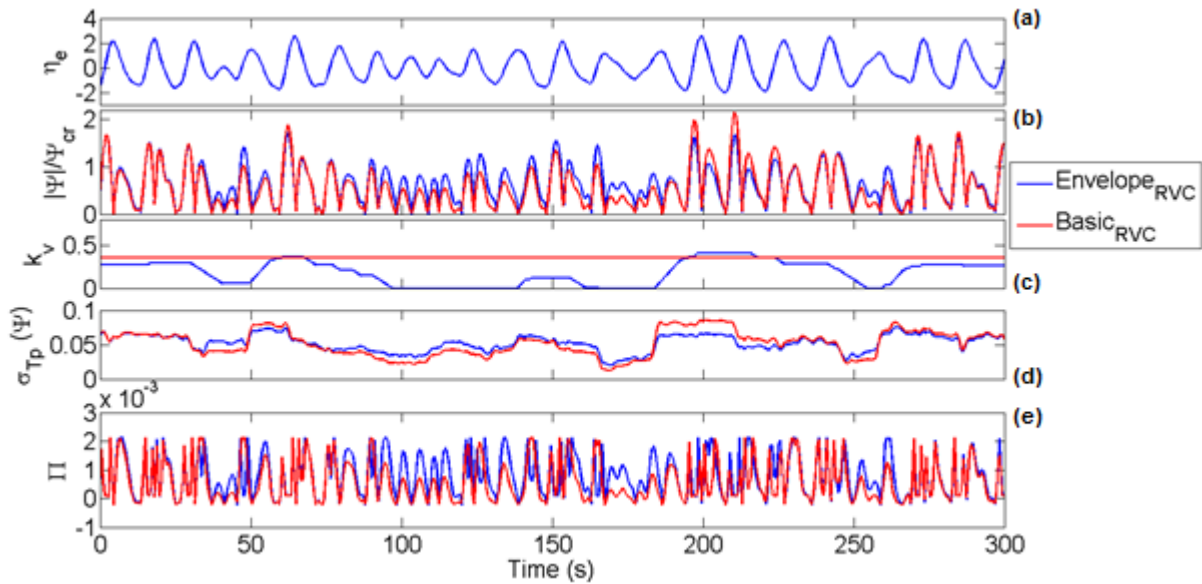


**Figure 5.19** Example time series of the simulated system response to  $Envelope_{RVC}$  for data set  $Z_{6,2}$ , compared to  $Basic_{RVC}$ . (d) gives the values of  $\sigma_{T_p}(\Psi)$  at each time step which  $Envelope_{RVC}$  is attempting to regulate. See figure 5.10 for the other parameter descriptions.

In figure 5.19, it is seen that  $Envelope_{RVC}$  optimises  $\sigma_{T_p}(\Psi)$  (to a degree) when there is sufficient incident wave power, but  $Envelope_{RVC}$  converges with  $Basic_{RVC}$  when the incident wave power reduces. As such, in higher energy sea states or if the plant had been designed with a greater horizontal chamber area to increase the pneumatic power from the same incident wave energy density,  $Envelope_{RVC}$  would in theory be able to optimise  $\sigma_{T_p}(\Psi)$  at all times provided the aperture adjustment rate can keep up with the wave energy variance.

#### 5.4.6 Delayed relief valve control

Wave groups are formed when wave trains come into and out of phase, constructively and destructively interfering to form distinct temporal periods of higher and lower wave energy. For a sea state with high groupiness (wave groupiness is defined in section 1.5.2.4), which describes the degree of distinct temporal periods of lower and higher wave energy, the characteristic of neighbouring waves might exhibit greater similarity than waves compared from a random selection over a longer time period. Controlling the relief valve, based on the assumption that wave behaviour over the next short time period is the same as the wave behaviour over the recent past short time period (of equal length), might be more optimal than assuming essentially regular waves, as  $Basic_{RVC}$  does.

Controlling the relief valve under the assumption that the near future is equal to the recent past will be called “Delayed relief valve control” or  $Delayed_{RVC}$  for short. For this control strategy to be effective (compared to  $Basic_{RVC}$ ) the sea state might need a certain level of wave groupiness, where the relative transitions between periods of high and low energy are distinct and persist for suitably long periods of time. This is because the valve will not respond to the initial change in incident wave energy as it is only considering the recent past, but if that change is somewhat stable and persist for a while, the valve aperture could be more optimal for the remainder of that higher or lower energy temporal period.

It should be noted that  $Delayed_{RVC}$  has the distinct advantage over the other control strategies introduced previously (excluding  $Basic_{RVC}$ ) because no forecast of the chamber excitation flow  $\hat{q}_e$  is required for control. This significantly simplifies the control strategy methodology and control algorithm.

Though many methods to achieve  $Delayed_{RVC}$  could be devised, the control strategy that is considered here is almost identical to  $Continuous_{RVC}$  but with control decisions being based on the recent past information instead of the near future information. In this way, the system response to possible valve aperture changes, had the changes been made in the past, is evaluated. The optimum aperture adjustment (had it been performed in the past) is then simply assumed to be the optimum adjustment for the near future.

Specifically, at each data point  $k$  a time series of  $p_c(k+l)$ , and turbine response  $N(k+l)$ , where  $l = -\Gamma f_s + 1, -\Gamma f_s + 2, \dots, 0$ , that would result if the relief valve aperture was maintained or if it was increased or decreased, is modelled with (4.39) and (4.42). The maximum aperture adjustment rate was selected for the opening stroke, but as was done with  $Envelope_{RVC}$ , half the maximum aperture adjustment rate was selected for the closing stroke to try to reduce the total relief valve adjustments cycles per hour. The new relief valve states considered are described by;

- Maintain the current aperture -  $k_v(k+l) = k_v(k)$
- Increase the aperture -  $k_v(k+l) = k_v(k) + \dot{k}_{v,o} / f_s$
- Decrease the aperture -  $k_v(k+l) = k_v(k) - \dot{k}_{v,c} / 2f_s$

where  $\dot{k}_{v,o}$  and  $\dot{k}_{v,c}$  are described in section 3.3.5.2.

The adjustment or maintenance of the relief valve state  $k_v$  that would have delivered the greatest  $\bar{\Pi}_{-\Gamma}$  over the past time period  $\Gamma$ , is then set in the model for the next future data point and a second model iteration to simulate the system response in the next future time step is performed. The process is repeated at every time step to evolve the full time series of the system response to this mode of control. Again because this control strategy is not hypothetical, the computational time required to make the assessment is factored in as a time delay to the aperture adjustment and the valve aperture is not permitted to transfer directly from an open stroke to a closing stroke and must spend one data time point interval at its current aperture.

As it is not immediately obvious what the optimal past time period to consider will be, simulations were run using the delay horizons  $\Gamma = 1, 2, \dots, 20$  to consider  $\bar{\Pi}_{-\Gamma}$ . For each data set the values of:  $\bar{P}_e^*$ , %\* time spent in the stall bands,  $|\bar{F}_a^*|$  and  $\bar{V}^*$  (again normalised by the base-line values found from  $Basic_{RVC}$ ) are found for each value of  $\Gamma$  considered, and these are given in figure 5.20.

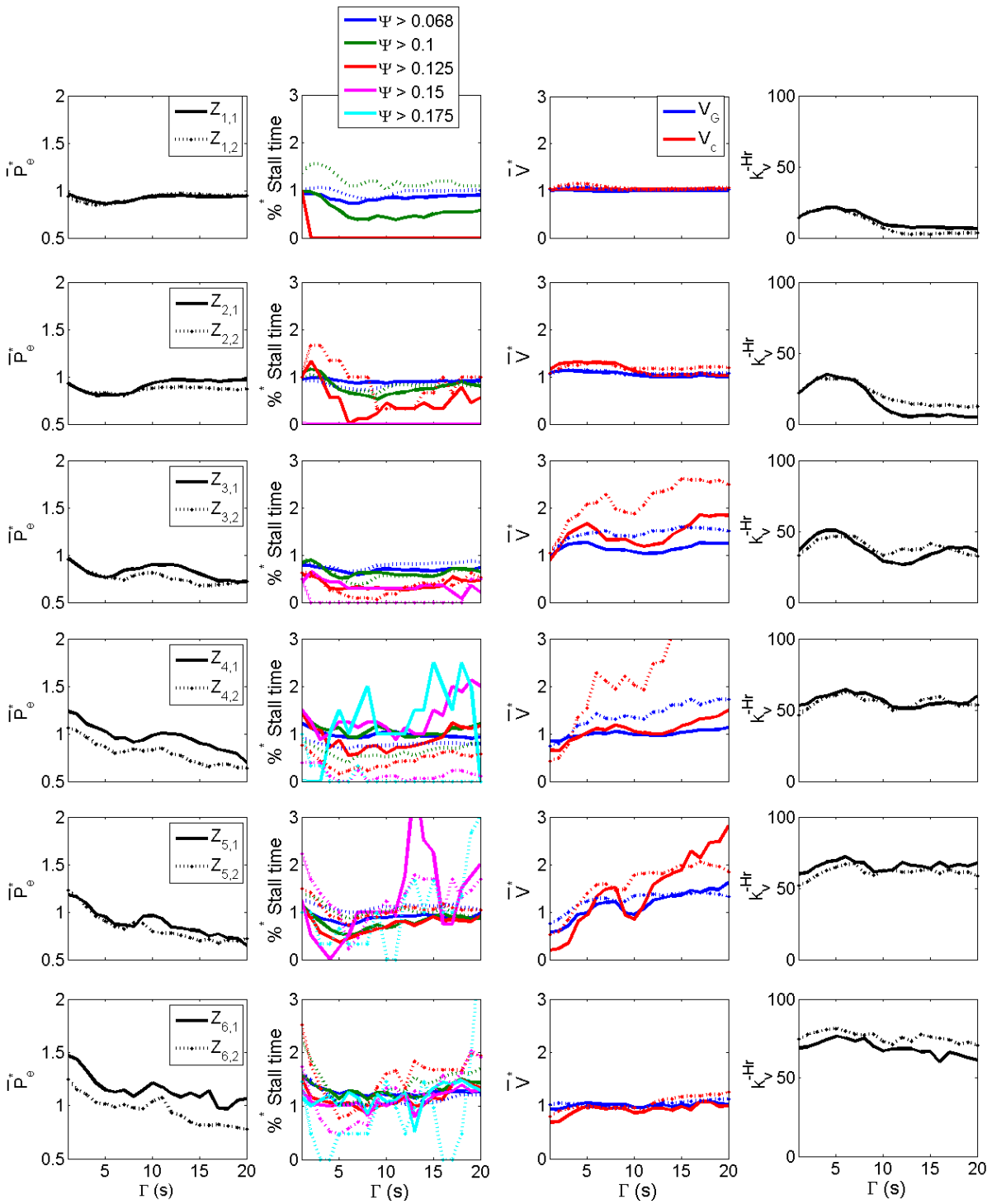


**Figure 5.20** Modelled mean electrical power take-off  $\bar{P}_e^*$ , % time spent in stall bands, mean vibrations above the residual  $\bar{V}^*$  and relief valve cycles per hour, resulting from *Delayed<sub>RVC</sub>* using different values of  $\Gamma$  to assess  $\bar{P}_{-\Gamma}$  in order to make the control action. All values except the number of relief valve cycles per hour are normalised by the corresponding base-line values resulting from *Basic<sub>RVC</sub>*.

It was anticipated that a value of  $\Gamma$  equal to the wave peak period would be optimal because *Delayed<sub>RVC</sub>* was conceived under the premise that neighbouring wave cycles could exhibit similar characteristics. This is seen to be true to a degree in figure 5.20 because a small peak in performance occurs when  $\Gamma \approx T_p$ . Control with  $\Gamma \approx T_p/2$  (like *Continuous<sub>RVC</sub>*) was not expected to perform well because there is no foundation on which to assume that the inhalation half wave cycle is similar to the exhalation half wave cycle, because of wave asymmetry. What was not expected was that the greatest power performance

would result when only  $\Gamma = 1$  was considered. This shows that controlling the valve aperture to just tail the excitation flow profile can achieve some significant power enhancements, but this is at the expense of a high number of relief adjustment cycles and also generally a greater frequency and severity of stall.

For an easier comparison of the result in figures 5.9, 5.12, 5.15 and 5.18, the statistical analysis of the resultant performance using the optimum control horizon time ( $\Gamma = 1$ ) for each data set, is given in figure 5.21.

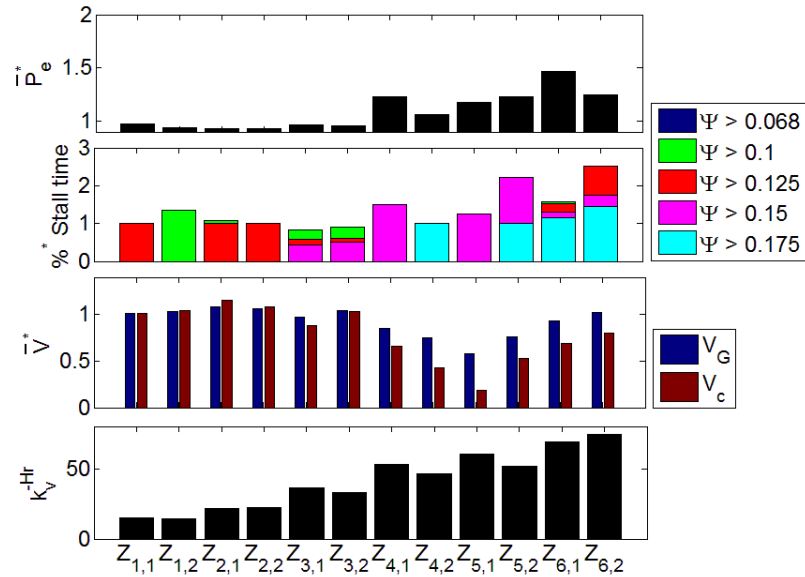


**Figure 5.21** Modelled mean electrical power take-off  $\bar{P}_e$ , and the indicators for mechanical fatigue; % time spent in stall bands and vibrations above the residual, resulting from  $Delayed_{RVC}$  using  $\Gamma = 1$  to assess  $\bar{\Pi}_{-\Gamma}$ . All values except the number of relief valve cycles per hour are normalised by the corresponding base-line values from  $Basic_{RVC}$ .

For completeness and to visualise the response of  $Delayed_{RVC}$ , a sample time-series of the simulated valve control for a portion of the data set  $Z_{6,2}$  is given in figure 5.22. The time series resulting from  $Basic_{RVC}$  with  $k_v = 0.35$ , is also shown for comparison.

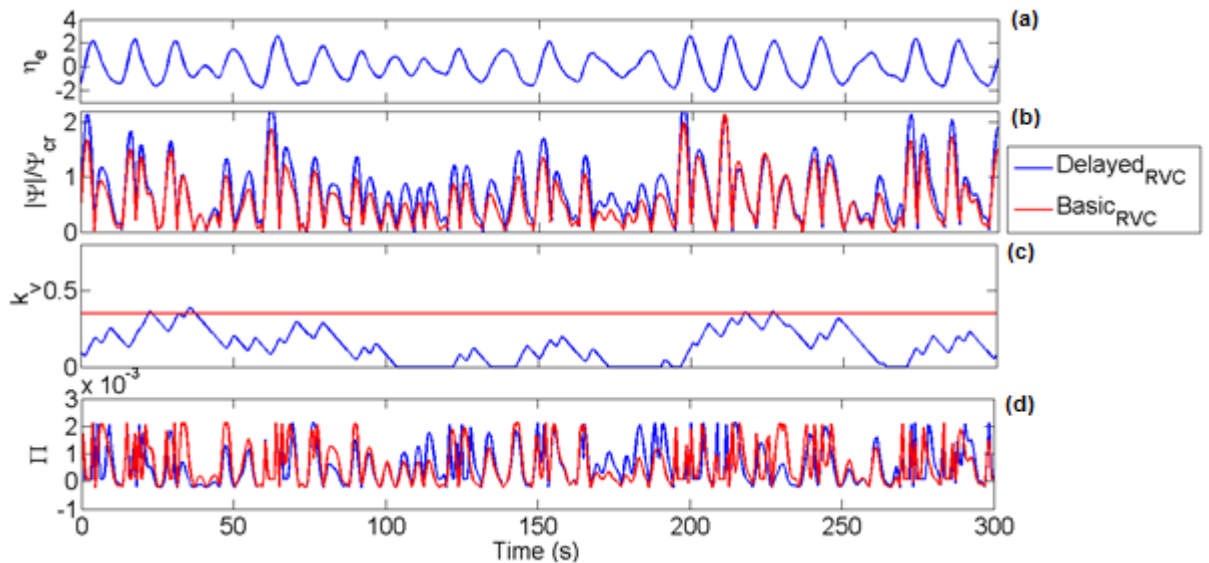


**Figure 5.22** Example time series of the simulated system response to  $Delayed_{RVC}$ , compared to  $Basic_{RVC}$  for data set  $Z_{6,2}$ . See figure 5.10 for parameter description.

Overall *Delayed<sub>RVC</sub>* produces less impressive enhancements to power production than the other more advanced control strategies and any power enhancements are at the expense of many relief valve cycles and increased stall. However, because no forecast is required its simplicity could make it viable in other situation where stall and valve wear rate are not an issue.

## **5.5 Results summary**

The simulation results from each control strategy were presented in the relevant sections of this chapter in order to help explain the development process. To provide an easier cross comparison some of the results will be repeated in this section in a side by side fashion, and this in addition to some additional analysis.

The results for the best system performance achieved, for each data set considered under each valve control strategy presented (as shown in figures 5.9, 5.12, 5.15, 5.18 and 5.21), are displayed side by side in figure 5.23, with the same axis limits.

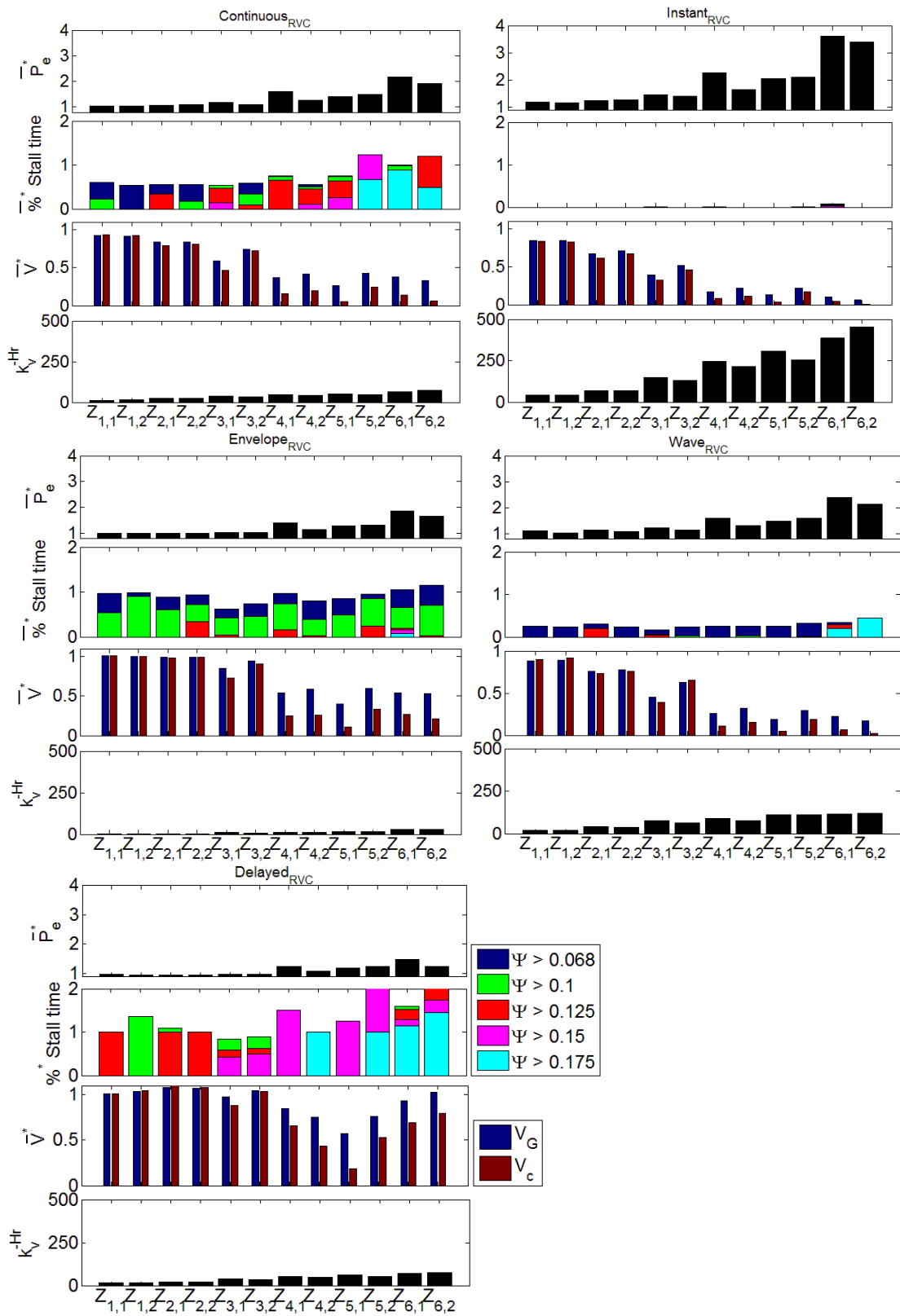


**Figure 5.23** Side by side comparison of the system performance for the different data sets considered under each advanced relief valve control strategy. The relevant variables are normalised by the results from *Basic<sub>RVC</sub>*.

To further summaries the effect of each relief valve control strategy, a side by side comparison of the resultant distribution of  $\Psi$  for data set  $Z_{6,2}$  in response to each relief valve control strategy is given in figure 5.24. This analysis can be used in conjunction with figure 5.2 to interpret the performance.

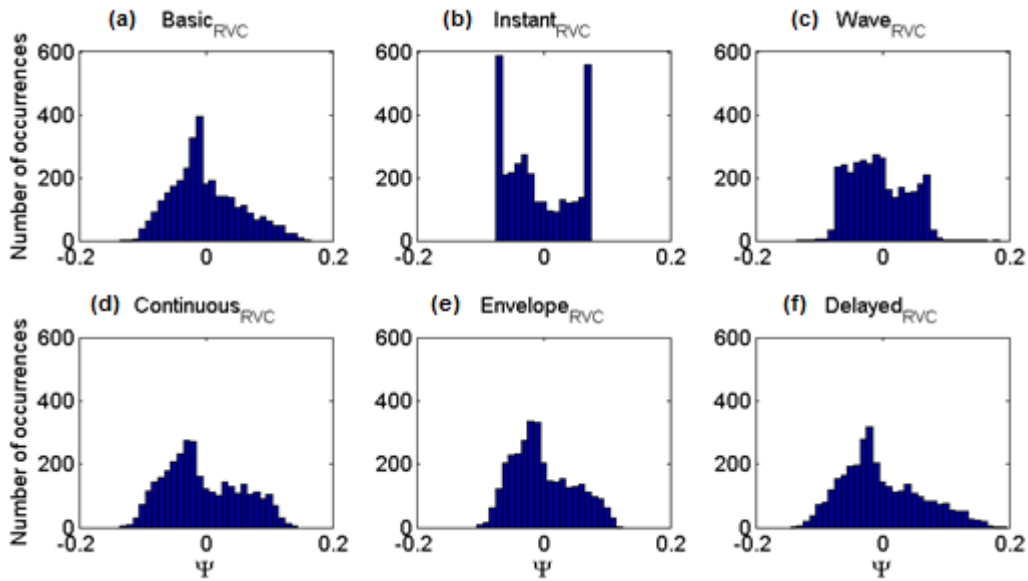


**Figure 5.24** Distribution of  $\Psi$  for data set  $Z_{6,2}$  resulting from relief valve control strategies: (a)  $Basic_{RVC}$ , (b)  $Instant_{RVC}$ , (c)  $Wave_{RVC}$ , (d)  $Continuous_{RVC}$ , (e)  $Envelope_{RVC}$  and (f)  $Delayed_{RVC}$ .

Finally, for a sample time period of data set  $Z_{6,2}$ , the simulated time series of: non-dimensional chamber pressure normalised by the stalled threshold  $|\Psi|/\Psi_{cr}$ , relief valve aperture state  $k_v$  and instantaneous power take-off by generator  $P_e$ , resulting from each control strategy is compared in figure 5.25.

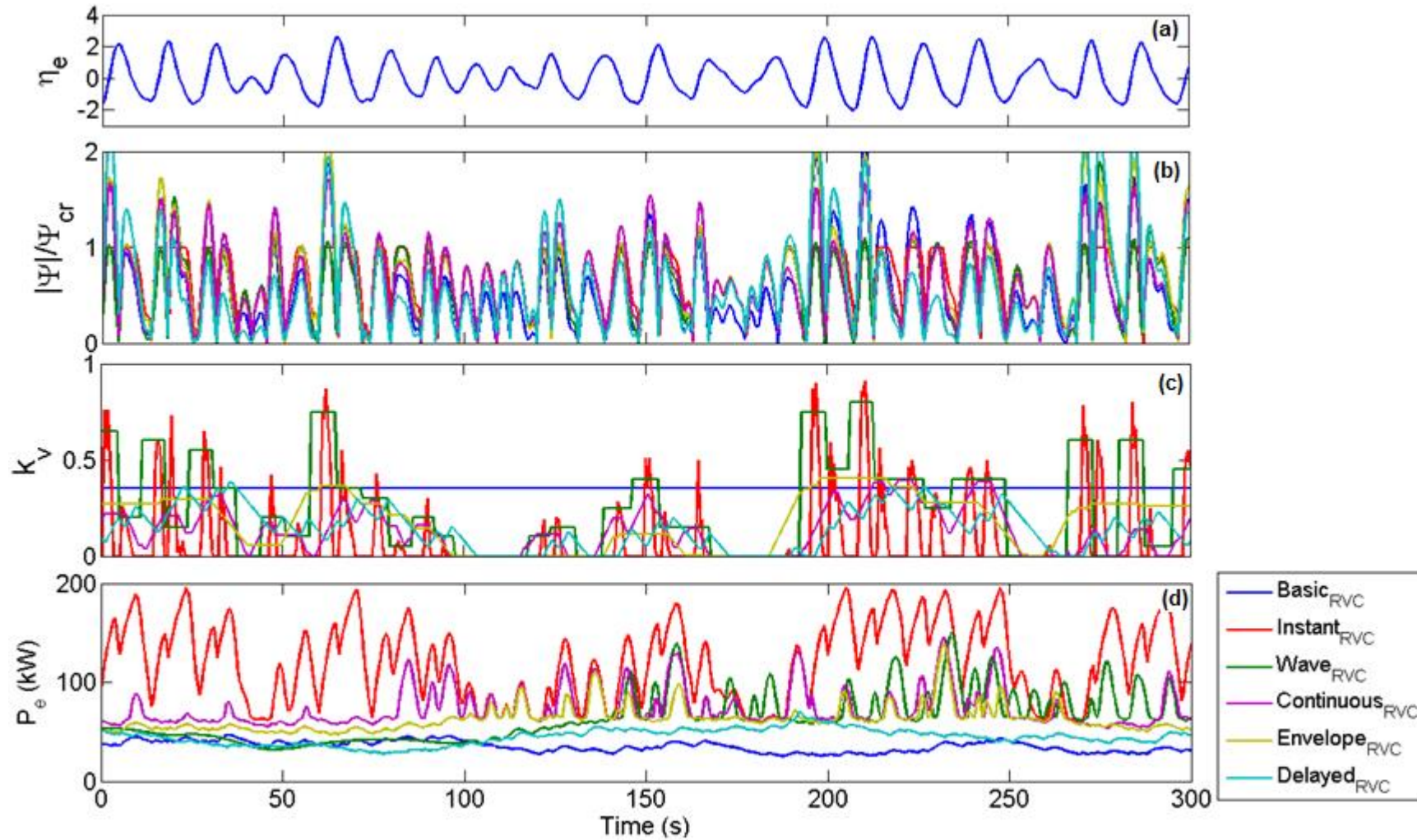


**Figure 5.25** Example time series of the simulated system response to the considered control strategies for a sample period of data set  $Z_{6,2}$ . (a) excitation chamber surface elevation  $\eta_e$ , (b) instantaneous non-dimensional pressure normalised by the critical value for the stall threshold  $|\Psi|/\Psi_{cr}$ , (c) the relief valve aperture state  $k_v$ , (d) instantaneous power take-off by generator  $P_e$ . Note that a light low pass filter is applied to data to improve the plot clarity.

## 5.6 OWC system model and relief valve control strategies conclusions

The time domain model requires an input time series of the excitation flow to drive the model. As the excitation flow is not a recorded parameter at the Pico plant it must be calculated indirectly using the high accuracy measurements of chamber pressure, turbine angular velocity, tide elevation and relief valve aperture. This was selected over the alternative, which is to drive the model with the low quality surface elevation time series data under the assumption that chamber pressure, and ultimately the radiation flow, have a negligible effect on the chamber water column oscillations, and that the water surface elevation is perfectly flat. The choice was made because any relief valve control strategy will alter the chamber pressure, which in turn alters the chamber surface elevation through the radiation flow component, and because chamber surface elevations measurements are not reliable. The excitation flow alone is not measured to validate this component of the model, but the combined excitation and radiation flow was found to be in good agreement with the measured (when clearly not in error) surface elevation.

The turbine characteristic curve found under laboratory conditions for a small scaled version of the Pico turbine given in (Gato, et al., 1996) was compared to the full scale operational data derived curve calculated indirectly as the missing term in a power balance equation between available positive pneumatic power and the negative power take-off and mechanical and electrical losses. The operational data derived curve suggests that the relationship between non-dimensional pressure and power, is less sharp about its peak, and that the reduction in efficiency at the point of stall is more gradual (with increasing pressure) than previously thought. However, the laboratory found turbine characteristic curve was utilised as part of the full time domain system model yields satisfactory results.

The full system model was assessed by comparing the model output for turbine angular velocity and power take-off against the true value, over a long and varied operational data period. Even though some elements of the system model could not be validated directly and may not be entirely accurate, the overall performance was high and the simulated turbine speed and power take-off had very little error.

The system response to a number of relief valve control strategies (some of which are new valve control concepts) was simulated numerically using a time domain model driven by the incident wave excitation flow for a number of real operational data periods. These covered a broad range of incident wave energy densities but because of the computational effort involved with time domain modelling, assessing the full spectrum of possible wave climates is not practical at this early stage.

Unsurprisingly  $Instant_{RVC}$  was found to be by far the optimal relief valve control strategy considered and significant amplification of electrical power take-off (in higher power sea states) and the complete removal of turbine stall, was projected. However, the relief valve actuator demands to achieve control in this manner would require an extraordinary feat of engineering, as well as enduring a very high duty cycle, but possibly a worthwhile investment for OWCs with wells turbines.

By optimising the chamber pressure profile over half wave periods,  $Wave_{RVC}$  delivered some significant enhancements to electrical power production and reductions in vibrations, especially in higher power sea states. Turbine stall frequency and severity was dramatically reduced in all cases considered. However,  $Wave_{RVC}$  also requires a high number of relief valve aperture adjustment cycles and the fabrication of a

fast acting relief valve actuator. However, because valve aperture adjustments are made at slack pressure the valve actuator requirements would be far lower than those needed for *Instant<sub>RVC</sub>*.

By adjusting the relief valve slowly but continually to optimise the chamber pressure profile over a half-wave period, *Continuous<sub>RVC</sub>* was able to achieve similar power performance enhancements to *Wave<sub>RVC</sub>*. Because the relief valve actuator requirements are within the physical limitations of the existing relief valve actuator at Pico it might be a preferable strategy to *Wave<sub>RVC</sub>*. It is even possible that no further modification is required (at least for short term testing) but this remains to be seen.

By adjusting the relief valve to continually target an optimum non-dimensional chamber pressure variance range, over a time period equal to the peak period of the sea state, *Envelope<sub>RVC</sub>* delivered notable but less dramatic enhancements to electrical power production compared to *Instant<sub>RVC</sub>*, *Wave<sub>RVC</sub>* and *Continuous<sub>RVC</sub>*. However, *Envelope<sub>RVC</sub>* required the lowest relief valve duty cycle (omitting *Basic<sub>RVC</sub>*) which, considering the limitations of the existing relief valve aperture adjustment system at Pico, makes *Envelope<sub>RVC</sub>* the most realistic control strategy for deployment at this stage. Because of this *Envelope<sub>RVC</sub>* will be the primary focus of the remainder of this study.

*Delayed<sub>RVC</sub>* is by far the easiest control strategy to implement (omitting *Basic<sub>RVC</sub>*) as no wave forecast is required. However, control in this manner showed power performance enhancements at the expense of a high number of relief valve cycles and increases in stall frequency and severity. This is in spite of the typically narrow banded, highly grouped, wave climate that is dominant at the Pico site location and for which the hypothesis of the control strategy depends. As such *Delayed<sub>RVC</sub>* will not be considered further.

The: *Instant<sub>RVC</sub>*, *Wave<sub>RVC</sub>*, *Continuous<sub>RVC</sub>* and *Envelope<sub>RVC</sub>*, control strategies depended on short-term forecast of the incident chamber excitation flow. The results presented in this chapter for these control strategies consider the potential performance that could be realised if sufficient monitoring equipment were available to make high accuracy short-term forecasts. As a perfect forecast is not expected to be achieved with the current monitoring equipment available at Pico, the realisable performance is uncertain. In the remaining chapters the realisable forecast that can be achieved at Pico with the existing monitoring equipment is evaluated and the resulting performance from relief valve control using this achievable forecast is reconsidered.

## Chapter 6

# Short-term wave forecast model evaluation and realisable control performance

### Abstract

The most promising short-term forecasting models identified from the literature review in chapter 4 are evaluated both for general performance and suitability with other WEC control systems, and for their direct suitability to the proposed relief control strategies as described in chapter 5. In some instances these forecast models are adapted and extended to suit the specific application and resource availability. In addition a new forecast model arrangement is proposed. Issues related to data filtering, causality and spectral bandwidth are addressed in detail and the focus of the performance analysis is placed on the achievable on-line forecast accuracy, which is required for actual deployment of the proposed relief valve control system.

The theoretical maximum performance of the relief valve control strategies, achieved from a perfect forecast as found in chapter 5, is compared to the theoretical achievable performance using an on-line output from the selected forecast models. This gives the theoretically achievable performance of the proposed control systems at the current state of development.

### 6.1 Introduction

This chapter is dedicated to: selecting, modifying, extending and critically evaluating the most promising and relevant short-term wave forecast models found in the literature. The forecast models selected for further investigation are chosen for their: performance in other applications, capability to deliver the forecast requirements primarily of the proposed *Envelope<sub>RVC</sub>* strategy, which is the control strategy being focused upon (described in section 5.4.5), and because they are within the sensor resource limitations that are available at the Pico project.

The simplest approach to forecasting is the univariate approach where only the past measurements made at the device are used to make the future forecast. This approach is attractively simple, robust and economical. Also the univariate approach also has no restrictions on the maximum forecast horizon.

From the performance analysis presented in the literature and particularly in (Fusco & Ringwood (b), 2010), the most promising univariate forecasting models made only with past measurements at the device, are AutoRegressive models (*AR*) and neural network found Nonlinear AutoRegressive models (*NAR*). Forecast models of this type will be the main focus of the investigation because they do not require up-wave measurements and it was not clear if an up-wave sensor would be available for new field tests.

As discussed in section 3.4.3, a small amount of up-wave data exists for the Pico case study and the multivariate approaches, which consider a combination of both past measurements at the device and up-wave measurements with a finite lead time, are investigated with extensions to the *AR* and *NAR* forecast models to include an exogenous input (the up-wave measured hydrostatic pressure time series). These forecast models will then be considered as AutoRegressive models with an eXogenous input (*ARX*) and neural network found Nonlinear AutoRegressive models with an eXogenous input (*NARX*), respectively. For the Pico case study, the exogenous input variable, which is the up-wave hydrostatic pressure, has a

finite lead time, which for some of the proposed control strategies, is shorter than the forecast horizon needed. This means that when the lead-time of the forecast expires the *ARX* and *NARX* models will drop the exogenous input and revert to *AR* and *NAR* models respectively, in order to continue the forecast to the required horizon time. As such it is interesting to propose and consider a final forecast method which utilises the *AR* model to first forecast the exogenous input time series, thus extending its lead time. This allows the *ARX* model to be used for any forecast horizon time length. This model will be called  $ARX_{AR}$  because of the autoregressive forecast of the exogenous input.

Finally, a simplified *FIR* forecast model which takes advantage of the fact that waves are non-dispersive in shallow water, is considered as a point of interest. However, again the maximum forecast horizon time using the *FIR* model is dependent on the separation distance between the up-wave sensor and the device. For the existing data and sensor placement, this distance is too short for some of the proposed strategies.

## 6.2 Description of forecast models

In the following subsections a mathematical description is given for the forecast models considered, developed and assessed in this chapter.

### 6.2.1 FIR filter

Up-wave measurements can be transformed to the subsequent expected behaviour at the device using a Finite Impulse Response (*FIR*) filter. If the filter is designed using the up-wave hydrostatic pressure as the input and chamber excitation surface elevation as the forecast target output, the *FIR* filter's impulse response will linearly approximate the conversion between hydrostatic pressure and surface elevation at the up-wave sensor location and the hydrodynamic transformations between the up-wave location and the chamber. This avoids the need to directly consider the physical processes involved. The *FIR* filter's phase response can also be used to account for the phase transformations that occur between the input up-wave measurement and the target output which is the measurement at the device, due to the travel time.

For the Pico case study the water depth between the up-wave sensor and the plant chamber is between 5 and 8 meters, which is approaching the shallow water condition  $h < \lambda/20$ . This is especially true because the dominate wave climate has a long peak period and is narrow banded. Based on the water depth and separation distance between the up-wave sensor and the chamber the wave propagation time between these two locations is approximately  $t_{tr} = 7$  (s), which was found from (1.21). Assuming the water depth is considered to be within the shallow water limit threshold for all frequency components that comprise the irregular wave time series, the propagation time will be independent of frequency. Under this assumption phase distortion from frequency dispersion can be ignored and a constant phase shift can account for the phase difference between the up-wave sensor location and the chamber. This circumvents the need to design the *FIR* filter's phase response in the frequency domain.

The phase shift between the up-wave sensor location and the chamber is dependent on the wave propagation time  $t_{tr}$  given by;

$$t_{tr} = \frac{x}{v_p} = \frac{l_{max}}{f_s} \quad (6.1)$$

where  $x$  is the separation distance,  $v_p$  is the phase velocity,  $l_{max}$  is a maximum number of lead time data points between the two locations, and  $f_s$  is the sampling frequency.

If it is assumed that the chamber excitation surface elevation  $\eta_e$  is linearly related to a number  $n_b + 1$  recent up-wave surface elevation measurements, and that the up-wave surface elevation is linearly related to the hydrostatic pressure  $p_{uw}$  vertically below the water at the same point, then a linear function  $F$  relates  $\eta_e$  and  $p_{uw}$  by;

$$\eta_e(k) = F[p_{uw}(k - l_{max}), p_{uw}(k - l_{max} - 1), \dots, p_{uw}(k - l_{max} - n)] \quad (6.2)$$

This function can be approximated by the impulse response of an  $n^{th}$  order *FIR* filter. The *FIR* filter's impulse response (which needs to be found) applies a specific weight  $b_j$  to each of the  $n_b + 1$  delayed entries (taps) of the input signal  $p_{uw}$ . The convolution of the impulse response with the delayed input signal  $[p_{uw}(k - l_{max}), p_{uw}(k - l_{max} - 1), \dots, p_{uw}(k - l_{max} - n)]$  plus some error  $\varepsilon(k)$  delivers the filter output  $\eta_e(k)$  at the point in-time  $k$ . Mathematically the *FIR* filter is described by;

$$\eta_e(k) = \sum_{j=0}^{n_b} b_j p_{uw}(k - l_{max} - j) + \varepsilon(k) = \hat{\eta}(k) + \varepsilon(k) \quad (6.3)$$

where  $\hat{\eta}_e(k)$  is the predicted chamber surface excitation elevation.

Before the *FIR* filter can be deployed in real-time the impulse response of the filter needs to be defined. The impulse response can be found before deployment using a recent batch training data set of length  $L$ . The best impulse response will minimise some quantification of the total error (cost function) between the predicted  $\hat{\eta}_e$  and the true value  $\eta_e$  of the target, for the training data set. The cost function  $J$  used to find the estimates of the filter coefficients was selected as the variance of the zero step ahead error;

$$J = \sum_{k=n_b+l_{max}}^L \varepsilon(k)^2 = \sum_{k=n_b+l_{max}}^L (\eta_e(k) - \hat{\eta}_e(k))^2 \quad (6.4)$$

The least squares method can then be used to efficiently find the coefficients of the impulse response  $[b_0, b_1, \dots, b_{n_b}]$  that minimises the cost function, and this coefficient set defines the best impulse response achievable with this method. The method of least squares is given in appendix C.

Once the coefficients are defined the filter is immediately ready to be used with an un-seen data set on-line because the filter was constructed using up-wave pressure data delayed by  $l_{max}$  data points in order to achieve a phase match with the chamber excitation surface elevation data. If the data input to the filter is not delayed the  $l_{max}$  steps ahead forecast is automatically output by the filter thus providing the forecast. The forecast of any point with  $l$  sampling periods of horizon is achieved by delaying the input to the filter by  $(l_{max} - l)$ , and this can be used to construct a time series forecast.

### 6.2.2 Autoregressive forecast model

The Auto-Regressive (*AR*) forecast model assumes that a measurement made at the device is linearly dependent on a weighted number  $n_a$  of the past measurements made at the device plus an error. In this

case the target variable regressors is the chamber excitation surface elevation  $\eta_e$  time series. The *AR* model is defined as;

$$\eta_e(k) = \sum_{j=1}^{n_a} a_j \eta_e(k-j) + \varepsilon(k) = \hat{\eta}_e(k) + \varepsilon(k) \quad (6.5)$$

As with the *FIR* filter the model coefficients  $a_j$  need to be found. Their values are determined in the same manner as the *FIR* filter using a batch training data set of length  $L$  with a least squares minimisation of the cost function  $J$  which is the 1-step ahead error variance;

$$J = \sum_{k=n_a+1}^L (\eta_e(k) - \hat{\eta}_e(k))^2 = \sum_{k=n_a}^L \varepsilon(k)^2 \quad (6.6)$$

After the optimum regression coefficients  $a_j$  are found, the one step ahead prediction is given by;

$$\hat{\eta}_e(k+1) = \sum_{j=1}^{n_a} a_j \eta_e(k-j+1) \quad (6.7)$$

For a multi-step ahead prediction the forecast model is closed in a loop so that the one step ahead prediction is fed back to the input to become the most recent data point for the next iteration. The oldest input is discarded so that the input signal has constant length. This gives the two step ahead prediction. Successive iterations in this fashion can be made to give an unlimited steps ahead forecast horizon. This is described by;

$$\hat{\eta}_e(k+l) = \sum_{j=1}^{n_a} a_j \eta_e(k-j+l) \quad (6.8)$$

where on the right side of the equation  $\eta_e = \hat{\eta}_e$  when  $j < l$

Any error in the output incurred by the previous iteration is passed to the input of the next iteration. As such the error accumulates with increasing forecast horizon. The 1-step ahead prediction error must be very small for accurate longer range forecasts.

### 6.2.3 Autoregressive forecast model with exogenous input

The *AR* forecast model can be extended to include an eXogenous input variable and is then considered an *ARX* forecast model. The exogenous input can be any other variable that might provide additional information that helps to reduce the forecast error. In this case the most relevant variable is the up-wave hydrostatic pressure information but other variables such as tidal elevations which affects the wave profile by the shoaling effect, could also be considered.

The *ARX* model assumes that the target variable  $\eta_e(k)$  can be described by a sum of  $n_a$  past values of the same variable, weighted by the model coefficients  $a_j$ , plus the sum of  $n_b$  past values of the exogenous input  $p_{uw}$ , delayed by the lead-time  $l_{max}$  as described by (6.1), weighted by the model coefficients  $b_j$ . The *ARX* forecast model is then described by;

$$\eta_e(k) = \sum_{j=1}^{n_a} a_j \eta_e(k-j) + \sum_{j=0}^{n_b} b_j p_{uw}(k-j-l_{max}) + \varepsilon(k) = \hat{\eta}_e(k) + \varepsilon(k) \quad (6.9)$$

Again the model coefficients  $a_j$ ,  $b_j$  need to be determined which is achieved using a batch training data set with a least squares minimisation of the cost function which was chosen to be the 1-step ahead error variance, as described by (6.6).

In the same fashion as the *AR* forecast model described in section 6.2.2, a multi-step ahead forecast is achieved through a closed loop feed-back of the 1-step ahead prediction. However, because the exogenous input  $p_{uw}$  has been delayed, the known values of  $p_{uw}$ , in the second term of the right side of (6.9), are used with each new iteration of the multi-step ahead forecast (the oldest is discarded). When a data forecast horizon of  $k + l_{max}$  is reached the finite lead time of the delayed exogenous input expires and the *ARX* inputs no longer meet the requirements of the model and no additional forecast horizon can be made. The  $l$  step ahead *ARX* forecast model is given by;

$$\hat{\eta}_e(k+l) = \sum_{j=1}^{n_a} a_j \eta_e(k-j+l) + \sum_{j=0}^{n_b} b_j p_{uw}(k-j-l_{max}+l) \quad (6.10)$$

where on the right side of the equation  $\eta_e = \hat{\eta}_e$  when  $j < l$  and at all times  $l \leq l_{max}$

If a forecast of data points with horizon greater than  $l_{max}$  (which is the limitation set by the separation distance between the up wave sensor and plant as well as the wave propagation speed) is required the *AR* model described in section. 6.2.2 can be used to continue the iterations to an unlimited forecast horizon using only the forecast of the chamber excitation surface elevation and its past known values. This will method will be performed in the analysis.

#### 6.2.4 Autoregressive forecast model with autoregressive exogenous input

As the *ARX* model is limited by the lead-time of the exogenous input, a further extension is to forecast the exogenous input  $p_{uw}$ . The forecast of  $\hat{p}_{uw}$  can be made using another *AR* forecast model dedicated to this variable and by following the same steps described in section 6.2.2. The *AR* model of the exogenous input is described by;

$$\hat{p}_{uw}(k+l) = \sum_{j=1}^{n_a} \alpha_j p_{uw}(k-j+l) \quad (6.11)$$

where on the right side of the equation  $p_{uw} = \hat{p}_{uw}$  when  $j < l$ , and the  $\alpha_j$  is the regression coefficient

Because the future values of the exogenous input have been forecasted using (6.11), the exogenous input values can now have an unlimited lead time over the chamber excitation surface elevation measurement and as such the *ARX* model is not confined to the data point horizon limit  $l \leq l_{max}$ . Because the exogenous input  $p_{uw}$  has been forecasted using an *AR* forecast model this new variant of the *ARX* model will be called the *ARX<sub>AR</sub>* forecast model and is described by;

$$\hat{\eta}_e(k+l) = \sum_{j=1}^{n_a} a_j \eta_e(k-j+l) + \sum_{j=0}^{n_b} b_j p_{uw}(k-j-l_{max}+l) \quad (6.12)$$

where on the right side of (6.12)  $\eta_e = \hat{\eta}_e$  when  $j < l$ , and  $p_{uw} = \hat{p}_{uw}$  when  $l > l_{max}$ .

## 6.2.5 Nonlinear autoregressive forecast model

The *FIR*, *AR*, *ARX* and *ARX<sub>AR</sub>* forecast models introduced so far assume that the inputs and the target outputs to the model share some linear relationship which is approximated from observations of the training data set. However, nonlinearities will be present and the strength of these will determine how well the linear approximation performs. In the case of the forecast models that consider past measurements at the device only, this nonlinearity might be due to: sloshing in the chamber, wave breaking, frequency dependent resonance and radiative damping, for example. For the forecast models that considered up-wave measurements additional nonlinearity in the transfer might be due to: shoaling, refraction, multi-directionality, dissipation, wave-wave interactions and dispersion, for example. Furthermore, the up-wave measurement might be subjected to interference from waves reflected and radiated from the device. As such the forecast models presented so far will at best provide a linear approximation of these nonlinearities. This might be an oversimplification if nonlinear effects are significant.

Because nonlinearity will be present it is also interesting to consider a Nonlinear AutoRegressive (*NAR*) forecast model, where a nonlinear function  $\varphi$  is used to estimate the nonlinear relationship between a number  $n_a$  of past values to future values of the same variable, which in this case is the chamber excitation surface elevation  $\eta_e$ . This relationship is described by;

$$\eta_e(k) = \varphi[\eta_e(k-1), \eta_e(k-2), \dots, \eta_e(k-n_a)] \quad (6.13)$$

where  $\varphi$  is a nonlinear function to be found,  $k$  is the present data point in time and  $n_a$  is the number of past values used to make the regression.

The nonlinear function  $\varphi$  that describes the relationship must first be found from a batch training data set before the forecast model can be deployed to forecast unseen data. Artificial Neural Networks (*ANN*) are particularly suited to the task of learning nonlinear relationships between inputs and known outputs. The key steps to finding  $\varphi$  using *ANN* is described in the following;

- 1.) First an *ANN* architecture must be defined. There are no specific guidelines to what the optimum architecture is and there are infinite possible permutations (only limited by computational resource) and must be found by experimentation through trial and error.
- 2.) Propagate the input batch training data sub-sets, which are the horizontal entries of the matrix;

$$Inputs = \begin{bmatrix} \eta_e(n_a) & \eta_e(n_a-1) & \dots & \eta_e(1) \\ \eta_e(n_a+1) & \eta_e(n_a) & \dots & \eta_e(2) \\ \vdots & \vdots & \ddots & \vdots \\ \eta_e(L-1) & \eta_e(L-2) & \dots & \eta_e(L-n) \end{bmatrix} \quad (6.14)$$

through the network, modifying each set by the same weights (chosen at random initially) and by applying nonlinear transfer functions.

- 3.) Collect the processed input signal sets to deliver an output signal which is the networks' estimate of the known target.
- 4.) Compare the output signal with the known target and assess the error.

- 5.) Based on the error, selectively adjust the networks weights using a learning algorithm.
- 6.) Iteratively repeat steps 2-5 to try to reduce the prediction error.
- 7.) When the error can be reduced no further training is complete and the nonlinear function  $\varphi$ , that describes the network structure with optimum final weights, is generated for deployment.

The ANN architecture considered in this study comprises the following layers, which the inputs migrate through and are cycled through for each iteration (epoch) of the learning procedure;

- 1.) An input layer containing the discretised input signal of finite length  $n_a$
- 2.) A specified number of hidden layers  $l = 1, 2, \dots, h$  that modifies the signal by applying weighting coefficients and a nonlinear transfer function
- 3.) An output layer that receives and sums all signals propagating through the network to give an estimate of the target variable and assess the error.

The process for propagating a single training data sub-set through the network, for one learning iteration, is given in the following. Matrix notion is used for an easier description and relevant steps are illustrated in the process diagram given in figure 6.2.

In the following, the superscripts signify the layer number in question, as described above.

The first layer of the network contains the network input vector holding the training data sub-set which is the  $n_a$  past observations of the excitation elevation time series at a data point in time  $k$ ;

$$\mathbf{p} = \begin{bmatrix} \eta_e(k-1) \\ \eta_e(k-2) \\ \vdots \\ \eta_e(k-n_a) \end{bmatrix} = \begin{bmatrix} \eta_{e1} \\ \eta_{e2} \\ \vdots \\ \eta_{e_{n_a}} \end{bmatrix} \quad (6.15)$$

If there are  $v^1$  nodes in the first hidden layer (superscript signifies layer number not power) then the network will have  $w^1_{i,j}$  weighting coefficients between the input layer and the first hidden layer, where  $i = 1, 2, \dots, v^1$  and  $j = 1, 2, \dots, n_a$ . In the first iteration all network weights are chosen at random. As a matrix the weighting coefficients are given by;

$$W^1 = \begin{bmatrix} w^1_{1,1} & w^1_{1,2} & \dots & w^1_{1,n_a} \\ w^1_{2,1} & w^1_{2,2} & \dots & w^1_{2,n_a} \\ \vdots & \vdots & \ddots & \vdots \\ w^1_{v^1,1} & w^1_{v^1,2} & \dots & w^1_{v^1,n_a} \end{bmatrix} \quad (6.16)$$

The weighting coefficients are applied to the inputs  $\mathbf{p}$  and summed to give the vector of the node entry signals  $\mathbf{n}^1$ ;

$$\mathbf{n}^1 = W^1 \mathbf{p} = \begin{bmatrix} w^1_{1,1}\eta_{e1} + w^1_{1,2}\eta_{e2}, \dots, + w^1_{1,n_a}\eta_{e_{n_a}} \\ w^1_{2,1}\eta_{e1} + w^1_{2,2}\eta_{e2}, \dots, + w^1_{2,n_a}\eta_{e_{n_a}} \\ \vdots \\ w^1_{v^1,1}\eta_{e1} + w^1_{v^1,2}\eta_{e2}, \dots, + w^1_{v^1,n_a}\eta_{e_{n_a}} \end{bmatrix} \quad (6.17)$$

The entry signal  $n^1_i$  to the node  $i$  has a nonlinear sigmoid transfer function  $\varphi^1$  applied. A standard hyperbolic tangent sigmoid transfer function was selected, and the output from each node after the transformation is;

$$a^1_i = \frac{2}{1+e^{-2n^1_i}} - 1 = \varphi^1(n^1_i) \quad (6.18)$$

The form of the hyperbolic tangent sigmoid function is shown in figure 6.1.

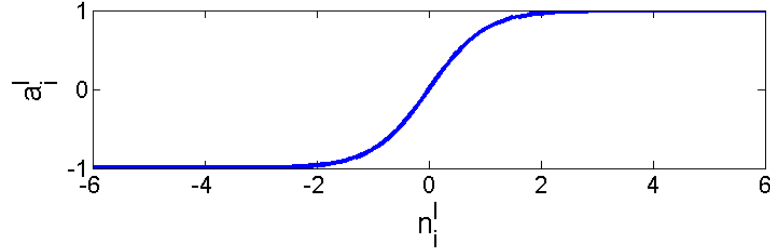


**Figure 6.1** Hyperbolic tangent sigmoid function.

The vector of nonlinearly transformed exit signals, from all nodes in the first hidden layer, is then given by;

$$a^1 = \varphi^1(n^1) \quad (6.19)$$

If there are  $v^2$  nodes in the second hidden layer (superscript signifies layer number not power) then the network will have  $w^2_{i,j}$  weighting coefficients between the first hidden layer and the second hidden layer, where  $i = 1, 2, \dots, v^1$  and  $j = 1, 2, \dots, v^2$ . As a matrix the 2<sup>nd</sup> hidden layer weighting coefficients are given by;

$$W^2 = \begin{bmatrix} w^2_{1,1} & w^2_{1,2} & \dots & w^2_{1,v^2} \\ w^2_{2,1} & w^2_{2,2} & \dots & w^2_{2,v^2} \\ \vdots & \vdots & \ddots & \vdots \\ w^2_{v^1,1} & w^2_{v^1,2} & \dots & w^2_{v^1,v^2} \end{bmatrix} \quad (6.20)$$

In the same fashion as the last layer transfer, the new weighting coefficients are applied to the outputs of the first hidden layer and summed to give the vector of the node entry signals  $n^2$  to the second hidden layer;

$$n^2 = W^2 a^1 \quad (6.21)$$

Again, in this design, the hyperbolic tangent sigmoid transfer function  $\varphi^2 = \varphi^1$  is applied at the node and the vector of the transformed exit signals from the nodes in the second layer is;

$$a^2 = \varphi^2(n^2) \quad (6.22)$$

This process repeats for all hidden layers up to layer  $h$  so that vector of the exit signals from the nodes in the last hidden layer is;

$$a^h = \varphi^h(W^h \varphi^{h-1}(\dots, \varphi^2(W^2 \varphi^1(W^1 p)))) \quad (6.23)$$

The final output layer contains a signal node with a linear transfer function  $F$ . The exit signals from the hidden layers are weighted a final time by  $W^o$  and summed to give the output which is the networks estimate of the target variable  $\hat{\eta}_e(k)$ ;

$$\hat{\eta}_e(k) = F(W^o a^h) \quad (6.24)$$

This series of events associated with a single training iteration of the ANN found NAR is depicted in the process diagram in figure 6.2.

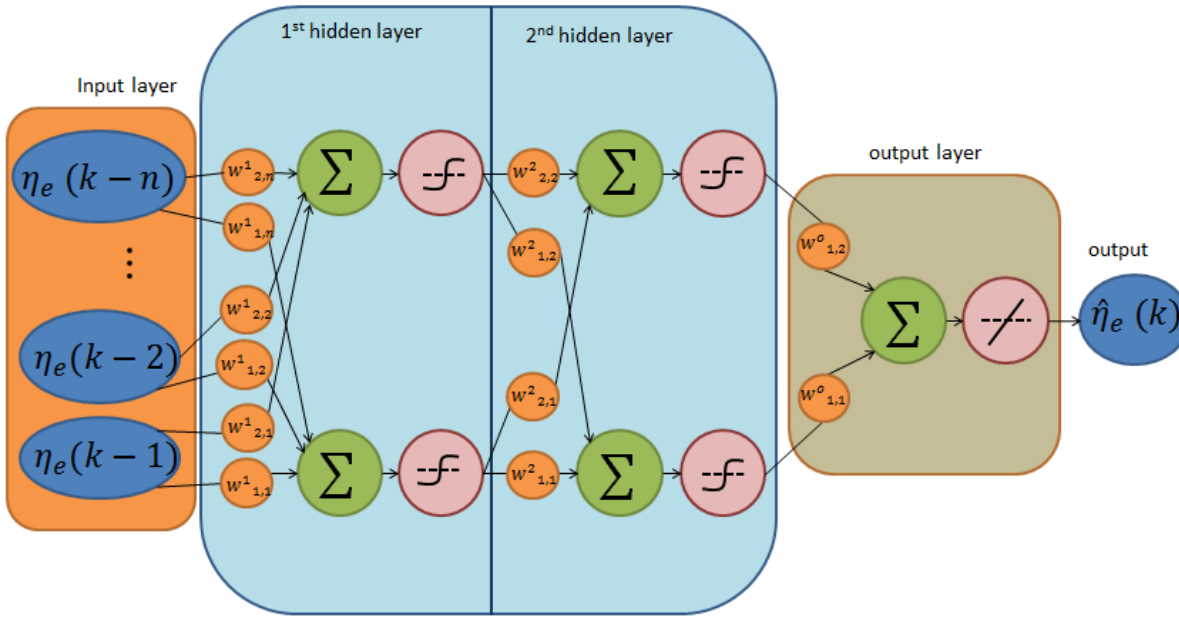


**Figure 6.2** Univariate nonlinear autoregressive neural network process diagram. Large coloured areas are the different network layers, pink circles are the nodes containing the transfer functions, blue circles are the network inputs and output signals, orange circles are the weighting coefficients (multiplied with the signal) of the sub-signals, green circles are signal summation points.

The process is repeated for all training data sub-sets until a vector of the estimates of the target variable time series is found;

$$\hat{\eta}_e = [\hat{\eta}_e(L), \hat{\eta}_e(L-1), \dots, \hat{\eta}_e(n_a + 1)] \quad (6.25)$$

Subtracting the vector of the estimates of the target variable with the true values gives the error vector;

$$\varepsilon = [(\eta_e(L) - \hat{\eta}_e(L)), (\eta_e(L-1) - \hat{\eta}_e(L-1)), \dots, (\eta_e(n_a) - \hat{\eta}_e(n_a))] \quad (6.26)$$

Unless one is very lucky the random values of the weights chosen for the first training iteration (epoch) are unlikely to be the optimum and the total error can probably be reduced. As such the process described above is repeated with the weights being adjusted in order to find more optimum values. To find the network's weights that result in the network output at the local error minimum more rapidly, a supervised learning algorithm is employed. The learning algorithm is used to solve the nonlinear least-squares error minimisation of the network's output. In this study, after assessing many learning algorithms (as discussed later), the Levenberg-Marquardt (LM) learning algorithm was selected as described in (Levenberg, 1944) and (Marquardt, 1963), which is a combination of the Gauss-Newton algorithm and

the method of gradient descent. The algorithm is presented in a way that is applicable to the Neural Network learning application in Appendix. D.

If more than one local error minimum exists, convergence of the network to the global minima is not guaranteed. To mitigate this, the network can be trained multiple times with different initial conditions in the hope that at least one network will have converged with the global minima.

When training is complete the performance of the final network structure is typically assessed by the mean squared error (MSE) between the networks estimates of the 1-step ahead chamber excitation surface elevation and its true value;

$$MSE = \frac{1}{L-n_a-1} \sum_{k=n_a+1}^L (\eta_e(k) - \hat{\eta}_e(k))^2 \quad (6.27)$$

If multiple networks are trained, the one achieving the lowest  $MSE$  is selected as it is assumed that the function related to this trained network describes the global minimum, although in reality this might not be the case.

When deploying the  $NAR$ , just like the  $AR$  forecast model, an  $l$  steps ahead forecast is achieved by closing the loop and, in an iterative way, feeding back the 1-step ahead forecast from the previous pass as the most recent input data point for the next pass. Again the oldest input is discarded to maintain a constant input data point length for compatibility with the designed model. The  $l$  steps ahead  $NAR$  forecast model is described by;

$$\hat{\eta}_e(k+l) = \varphi[\eta_e(k+l-1), \eta_e(k+l-2), \dots, \eta_e(k+l-n_a-1)] \quad (6.28)$$

where on the right side of the equation  $\eta_e$  becomes  $\hat{\eta}_e$  when  $k+l-n_a > k$

This is just one example of how a  $NAR$  type Neural Networks could be used for a multi-step ahead prediction. Alternatively, an open loop Network that is directed to make the  $l^{th}$  step ahead prediction using only known past data, could be used. For this method a bank of networks is trained with each network dedicated to forecasting one of the future steps ahead data points  $l = 1, 2, \dots, l_{max}$ . Concatenation of the outputs from each individual trained network is used to build up a time series forecast up to  $l_{max}$ . This is similar to the “direct”  $AR$  model described in (Fischer, et al., 2012). This method was investigated in this research and provided marginally better forecast accuracy but, due to the large increase in the computational cost and increased susceptibility to poorly trained functions, it was not considered to be a practical or worthwhile option for on-line forecasting in this application and was discarded.

### 6.2.6 Nonlinear autoregressive forecast model with exogenous input

As with the  $ARX$  forecast model the  $NAR$  forecast model can be extended to include the information contained in an exogenous input to become a  $NARX$  forecast model. For this study a  $NARX$  forecast model is considered with a series parallel architecture in the learning phase. The target variable is the chamber excitation surface elevation  $\eta_e$  and the exogenous input is the up-wave hydrostatic pressure  $p_{uw}$ . If the up-wave data is delayed by  $l_{max}$  data point based on the wave travel time between the up-wave sensor and the device  $l_{max} = t_{tr}f_s$ , then, when the network is closed to make a parallel architecture (for a

multistep ahead forecast), the exogenous inputs will be real known values up to a forecast horizon of  $\Gamma = l_{max}/f_s$ . After which point, the lead time of the exogenous input expires and, as was done with the  $ARX_{AR}$  model, the exogenous input also needs to be forecasted or the  $NARX$  must revert to the  $NAR$  model in order to forecast to greater horizon times.

First let's consider the  $NARX$  forecast model for a 1-step ahead forecast. As with the  $NAR$  model the  $NARX$  operates by first learning a nonlinear function  $\varphi$  that relates the current value of  $\hat{\eta}_e$  to the past  $n_a$  values of  $\eta_e$ , but unlike the  $NAR$ , the delayed  $n_b$  past values of  $p_{uw}$  are also considered with equal weight initially. The neural network in the training phase takes the form;

$$\eta_e(k) = \varphi[\eta_e(k-1), \eta_e(k-2), \dots, \eta_e(k-n_a), p_{uw}(k-l_{max}), p_{uw}(k-1-l_{max}), \dots, p_{uw}(k-n_b-l_{max}+1)] \quad (6.29)$$

The nonlinear function  $\varphi$  is learned by the neural network from a batch training data set by minimising the error described by (6.26) and by following the same steps described in section. 6.2.5.

Once  $\varphi$  is found the  $NARX$  network is converted from a series parallel architecture to a parallel architecture to make a multistep ahead forecast. This means that for each forecast iteration, the estimate of the 1-step ahead value of  $\hat{\eta}_e$  is feedback and becomes the most recent input value. As the up-wave data was delayed for each iteration up to the forecast horizon of  $l_{max}$ , real know data points are used as the exogenous input.

This  $l$  steps ahead  $NARX$  forecast model is then described by;

$$\hat{\eta}_e(k+l) = \varphi[\eta_e(k+l-1), \eta_e(k+l-2), \dots, \eta_e(k+l-n_a-1), p_{uw}(k-l_{max}+l), p_{uw}(k-1-l_{max}+l), \dots, p_{uw}(k-n_b-l_{max}+1+l)] \quad (6.30)$$

where on the right side of the equation  $\eta_e$  becomes  $\hat{\eta}_e$  when  $k+l-n_a > k$ .

Like the  $ARX$ , when  $l > l_{max}$  the lead time of  $p_{uw}$  data expires and if this is not also forecasted the  $NARX$  no longer has the data input requirements to function. A  $NARX_{NAR}$  model could also be considered, where a forecast of  $p_{uw}$  is made using a separate  $NAR$  model. Unlike the  $ARX_{AR}$ , which is more computationally efficient, this additional complexity incurs a level of computational processing time that is more difficult to realise in a real-time application. As such the  $NARX_{NAR}$  approach was not considered. The alternative is to revert to the  $NAR$  model described as by (6.28) when the forecast data point horizon requires  $l > l_{max}$ , and this method was performed.

### 6.3 Forecast model parameter selection

Each forecast model considered has at least one influential model parameter that needs to be specified. Little guidance is available in the literature as to what optimum values of these parameters might be and

will likely differ significantly for different applications. It is necessary to first analyse the sensitivity of forecast model performance to these parameters and find the optimums for this application.

Each forecast model considered was trained with un-filtered raw data (the specific reason for this is explained later in this chapter) with a range of model parameters encompassing all reasonable parameter permutations. The forecast models were trained using the data in the first set of each respective data set pair  $(Z_{1,1}, Z_{2,1}, \dots, Z_{6,1})$  which are described in section 5.2. After, the trained forecast models were used to predict the chamber excitation surface elevation time series of the unseen corresponding second data set of the data set pair  $(Z_{1,2}, Z_{2,2}, \dots, Z_{6,2})$ . At each time instant, a forecast up to the horizon time of  $\Gamma = 13$  (s) was made for the univariate models (due to the approximate forecast length requirements of *Envelope<sub>RVC</sub>*), and  $\Gamma = 7$  (s) for the multivariate models (due to the finite up-wave data lead time).

Training the forecast model with different data to the test data ensures that over-fitting has not occurred. Over-fitting is when the forecast model simply learns the training data time-series including the intricacies such as random noise. If this occurs, the forecast model will not be able to generalise the underlying dynamics needed to forecast the un-seen test data, and may be volatile to minor fluctuations. Over-fitting can occur if the forecast model is too complex and as such it is necessary to select the forecast models carefully rather than just making it as complex as the computing resource will allow.

The average forecast accuracy at each horizon time step can be quantified by the goodness of fit index (*GOF*) which considers the forecast accuracy of phase and amplitude. This statistical measure is also used in (Fusco & Ringwood (b), 2010) and (Paperella, et al., 2015) and the *GOF* index is also used here for easier cross comparison with these articles. This index is used in this section to assess the influence of the different model parameters, and is defined by;

$$GOF_l = 100 * \left( 1 - \frac{\sqrt{\sum_{k=n}^{L-l} (\eta_e(k+l) - \hat{\eta}_e(k+l))^2}}{\sqrt{\sum_{k=n}^{L-l} \eta_e(k+l)^2}} \right) \quad (6.31)$$

where  $n$  is the model order number and  $l$  is the data point forecast horizon being considered.

### 6.3.1 FIR parameter selection

The *FIR* forecast model requires the specification of the filter order number  $n_b$ , which describes the length of the impulse response which in effect defines how many past values of  $p_{uw}$  influence the forecast. The range of  $n_b = 1, 2, \dots, 100$  was considered. The optimum  $n_b$  is considered as the value that results in the highest *GOF* for the specific data point forecast horizon  $l = 7f_s$  (which equates to a forecast time horizon of time of  $\Gamma = 7$  (s)) as this is the approximate lead time between the near-shore surface-elevation sensor location and the chamber (as discussed in section. 6.2.1)

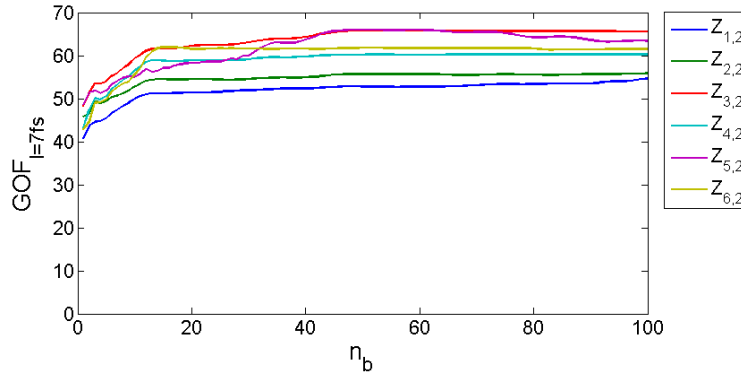


**Figure 6.3** FIR filter  $GOF$  forecast accuracy at a horizon time  $l = 7f_s$  as a function of the filter order number  $n_b$  for the test data sets considered.

As seen in figure 6.3 the  $GOF$  at  $\Gamma = 7$  (s) increases notably with  $n_b$  until  $n_b > 15$ . After this point the forecast accuracy gradient plateaus. For all data sets considered,  $n_b = 50$  seems to be a marginally optimum value when balancing accuracy and computational expense.

### 6.3.2 Autoregressive parameter selection

The  $AR$  forecast model requires the specification of the model order number  $n_a$ , which is the number of past  $\eta_e$  values used to make the forecast. The range of  $n_a = 1, 2, \dots, 100$  was considered. In this case the optimum  $n_a$  was considered as the value that delivered the highest mean goodness of fit across all horizon data points up to  $\Gamma = 13$  (s) (data point forecast horizon of  $l_{max} = 13f_s$ ). This value is selected because it is the approximate forecast horizon length needed for the  $Envelope_{RVC}$  control strategy (as shown in section 5.4.5 for the data sets considered) and because the control strategy is dependent on the accuracy of all forecast points up to  $l_{max}$ .

$$\overline{GOF} = \frac{1}{l_{max}} \sum_{l=1}^{l_{max}} GOF_l \quad (6.32)$$

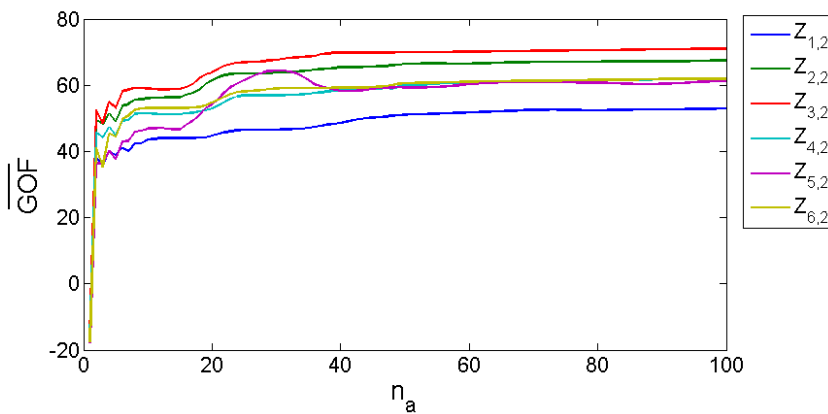


**Figure 6.4**  $AR$  modelled mean  $GOF$  forecast accuracy for all forecast points up to horizon time  $\Gamma = 13$  (s) as a function of the model order number  $n_a$  for the test data sets considered.

As seen in figure 6.4 the trend in the  $AR$  forecast model accuracy is fairly consistent across all data sets considered and increases with the model order number. The gradient in the forecast accuracy improvement rapidly reduces after about  $n_a \geq 7$ . However minor improvements continue until  $n_a \approx 50$ . As the  $AR$  is computationally inexpensive the value  $n_a = 50$ , which represents the smallest order number

with maximum forecast accuracy, was selected.  $n_a = 50$  with a sampling frequency of  $2Hz$  equates roughly to around 2 wave cycles at the peak period.

The  $ARX$  model requires the specification of the model order number  $n_a$  and  $n_b$ , which describe how many past values  $\eta_e$  and  $p_{uw}$ , respectively, are used to make the forecast. The ranges of  $n_a = 1, 2, \dots, 100$  and  $n_b = 1, 2, \dots, 100$  were considered. The optimum combination of  $n_a$  and  $n_b$  was considered to be the value that resulted in the highest average goodness of fit across all six of the test data sets considered, for all forecast horizon times up to  $\Gamma = 7s$  (data point forecast horizon up to  $l_{max} = 7f_s$ ) as this is the approximate lead time between the up-wave sensor and the device.

$$\overline{GOF} = \frac{1}{6} \sum_{set=1}^6 \frac{1}{l_{max}} \sum_{l=1}^{l_{max}} GOF_l(\eta_{e_{set}}) \quad (6.33)$$

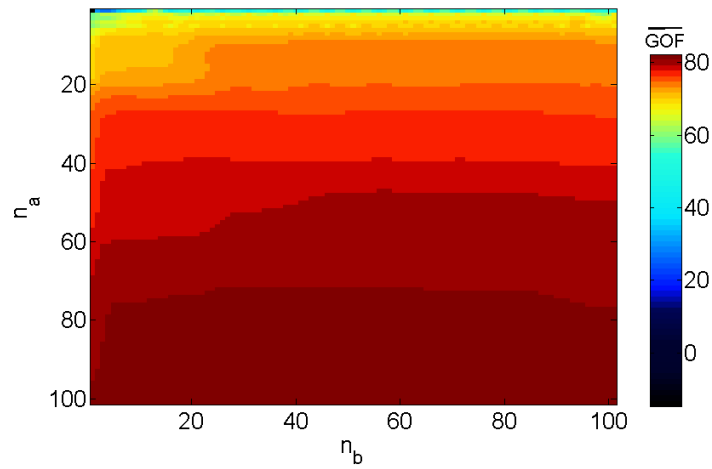


**Figure 6.5**  $ARX$  modelled mean  $GOF$  forecast accuracy for all forecast points up to horizon time  $\Gamma = 7s$  as a function of the model order numbers  $n_a$  and  $n_b$  for the test data sets considered. The colour scale is nonlinear to amplify the small differences for visual inspection.

Figure 6.5 shows the  $ARX$  forecast accuracy benefits by considering a greater number of  $\eta_e$  data points than the number of  $p_{uw}$  data points. Again the forecast accuracy essential plateaus when  $n_a > 50$  with very marginal improvements when  $n_b > 50$ . Because of the computational efficiency of the forecast model, the marginal optimum is taken as  $n_a = 50$  and  $n_b = 50$  and these values were selected for deployment.

As the  $ARX_{AR}$  forecast model is a combination of the  $ARX$  and  $AR$  forecast models, the model order numbers found to optimise the respective models were also selected as the model parameters for the  $ARX_{AR}$  forecast model. These are;  $n_a = 50$ ,  $n_b = 50$  and  $n_{aX} = 50$  (and was confirmed, but the analysis does not reveal anything new so it is not presented).

### 6.3.3 Nonlinear Autoregressive neural network structure and parameter selection

Selecting the forecast model parameters and structure for the  $NAR$  and  $NARX$  is significantly more complicated because at a minimum, the optimum: learning algorithm, number of epochs, number of hidden layers, the number of neurons in each hidden layer and the model order numbers, needs to be found and specified. Again there appears to be no definitive guide in the literature for selecting these variables, which differ for different applications. One could spend a lifetime investigating every conceivable permutation. As such the problem of optimising the model comes down to selective trial and

error guided by the literature. Also the following basic principles should be kept in mind: over-fitting will occur if the model structure is too complex, sufficient complexity is needed to characterise the underlying dynamics, and sufficient past information that significantly effects future values needs to be provided.

First the learning algorithm needs to be selected. Two learning algorithms, Levenberg-Marquardt (Marquardt, 1963) and Resilient back propagation (Riedmiller & Braun, 1992) repeatedly appear in similar applications in the literature for example; (Valério, et al., 2008), (Fernandez, et al., 2013), (Mandal & Prabakaran, 2010), (Fusco & Ringwood (b), 2010) and (Makarynsky, 2004).

It was found that the Levenberg-Marquardt learning algorithm generally resulted in marginally better forecast accuracy but that Resilient back propagation incurred significantly less computational expense. A number of other leaning algorithms were considered but these all performed marginally worse than the Levenberg-Marquardt and Resilient back propagation algorithms in this application. As computational cost was not a significant factor and within the margins for the proposed control strategy, the Levenberg-Marquardt algorithm was selected and the description of the algorithm is given in appendix D.

The number of epochs (learning iterations) can be dealt with more intelligently by sub-dividing the training data into training data and unseen validation data. A random division of the all data points was made such that 85% were used for training whilst the reaming 15% where used for validation. After each epoch the forecast accuracy of the training data and the validation data is assessed and compared. If at a certain number of epochs the forecast accuracy improves for the training data points, but worsens for the unseen validation data points, it can be concluded that the model is beginning to over-fit. This means the function is learning the intricacies of training data set but not the underlying dynamics, thus performing poorly with test data. If this diversion continues for a defined number of epochs (6 was selected), to ensure the divergence it is not just a fluctuation, training is halted. This represents the point of optimum generalisation of the *NAR* and that the local minima is found.

Finally the number of hidden layers, number of neurons or nodes in each hidden layer and the model order number, need to be selected. The optimum values of these parameters is found by trial and error. Two hidden layers were considered with  $v^1 = 1,3, \dots, 9$  neurons in the first layer and  $v^2 = 1,3, \dots, 9$  neurons in the second layer. The model order numbers of  $n_a = 1,5,10, \dots, 100$  were considered for the *NAR*, and this is in addition to  $n_b = 1,5,10, \dots, 100$  for the *NARX*. A network was trained for every permutation of  $v^1, v^2$  and  $n_a = n_b$ (for the *NARX*). The model order numbers for the input  $n_a$  and the exogenous input  $n_b$  were set equal to reduce the number of parameter permutations to an acceptable limit based on computational expense. Again, the first set of each respective data set pair  $(Z_{1,1}, Z_{2,1}, \dots, Z_{6,1})$  was used for training and the respective second data set pair  $(Z_{1,2}, Z_{2,2}, \dots, Z_{6,2})$  was used for testing. The model performance is evaluated by the mean squared error (*MSE*) for the 1-step ahead prediction as defined by (6.34). The accuracy of the 1-step ahead prediction indicates the performance of the multi-step ahead prediction because the error will accumulate with successive feedback iterations.

$$MSE = \frac{1}{L-n_a-1} \sum_{k=n_a+1}^L (\eta_e(k) - \hat{\eta}_e(k))^2 \quad (6.34)$$

The permutations of the model structure and model parameters that achieved the 7 lowest (to observe clustering about the optimum) 1-step ahead *MSE* for each data set, is given in figure 6.6.

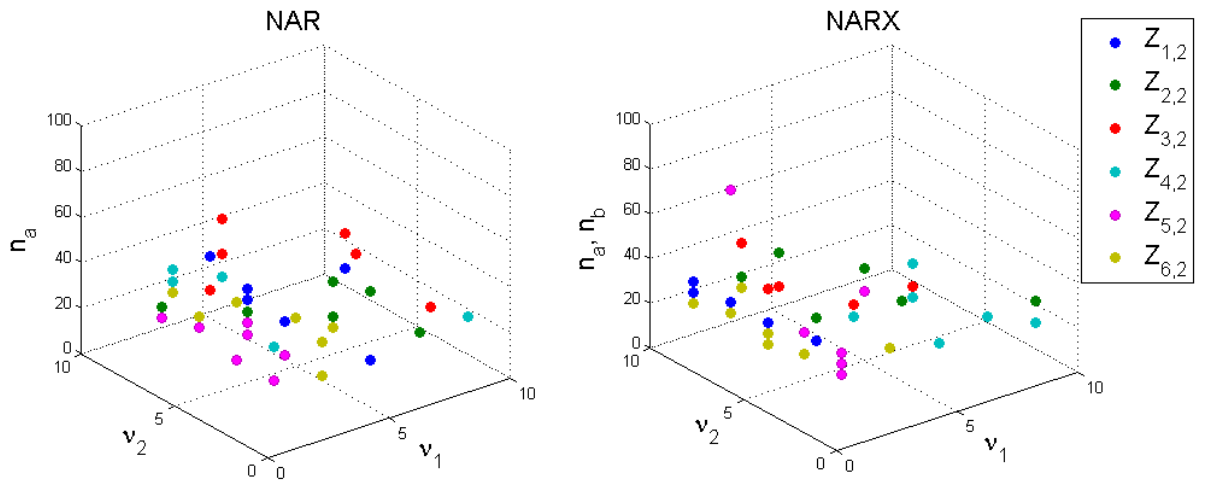


**Figure 6.6** The *NARX* neural network architectures, in terms of the number of nodes in the first  $v^1$  and second  $v^2$  layers and the number of regressors  $n_a = n_b$ , that deliver the 7 lowest 1-step ahead *MSE* forecast errors.

As seen in figure 6.6 there is not a clear optimum network structure and model order combination. But, there is a reasonably distinct clustering of data points in the regions that translate to a smaller number of neurons in one hidden layer, a larger number of neurons in the other hidden layer, with a tendency for the larger number of neurons to be in the second hidden layer. The 1-step ahead *MSE* was found to be slightly more sensitive to the model order number which was found to be optimal in the range  $n_a = n_b = 20, \dots, 40$ . There is also some sub-clustering seen for the points of individual data sets indicating that different network structures perform better with different data periods, but the computational expense of the exercises makes it impractical to perform as a precursor to deployment in real-time operation. However, the difference in forecast accuracy was found to be marginal in the optimal region (i.e. smaller  $v^1$ , larger  $v^2$  and  $20 \leq n_a = n_b \leq 40$ ) the network structure of  $v_1 = 3$  neurons in the first layer and  $v_2 = 7$  neurons in the second was selected as a universal structure for deployment. The model order  $n_a = n_b = 30$ , was selected. The best achieved forecast accuracy defined by the 1-step ahead *MSE* is lowest for smaller energy sea states and when the exogenous input is included. This is to be expected because as the wave energy increases highly nonlinear and unpredictable events, such as wave breaking and extreme sloshing in the chamber, occur more frequently and with more severity. The best achieved *MSE* values and the corresponding Pearson product-moment correlation coefficient (Pearson, 1895) (a measure of the correlation between the real and forecasted chamber excitation surface elevation) defined as;

$$R = \frac{c(\eta_e, \hat{\eta}_e)}{\sigma_{\eta_e} \sigma_{\hat{\eta}_e}} \quad (6.35)$$

where  $c$  is the covariance.

along with the training parameters that produced the result, are given in table. 6.1 for each data set and for both the *NAR* and *NARX*.

**Table 6.1** Neural network optimisation results giving, for each data set considered, the best: architecture (number of nodes in layer one  $v_1$  and layer two  $v_2$ ), number of regressors  $n$  and the number of iterations

(*Epochs* needed to find local minimum). Under the optimum variable the resulting 1-step ahead *MSE* forecast accuracy and product-moment correlation coefficient *R* are also given.

	NAR						NARX						
	$v_1$	$v_2$	$n_a$	<i>MSE</i>	<i>Epochs</i>	<i>R</i>	$v_1$	$v_2$	$n_a$	$n_b$	<i>MSE</i>	<i>Epochs</i>	<i>R</i>
$Z_{1,2}$	3	7	35	0.018	23	0.9662	3	7	30	30	0.017	12	0.9666
$Z_{2,2}$	3	3	30	0.019	13	0.9697	3	7	25	25	0.018	18	0.962
$Z_{3,2}$	7	3	35	0.023	16	0.9827	3	3	25	25	0.021	73	0.9783
$Z_{4,2}$	3	7	30	0.062	9	0.9726	7	1	35	35	0.059	27	0.9762
$Z_{5,2}$	3	5	25	0.095	50	0.0973	7	3	35	35	0.088	82	0.9737
$Z_{6,2}$	3	3	25	0.090	9	0.9772	3	7	30	30	0.088	15	0.9761

This result is substantially poorer than some other results found in the literature. For example in (Fernandez, et al., 2013) a  $MSE = 3.3 \times 10^{-5}$  was achieved with data from large scale WCG wave flume. Without more detailed information of the test procedure conducted in (Fernandez, et al., 2013) some speculative reasons for this discrepancy are given in section 4.5.3. However, this is an important result because it presents what might be achievable in the field with non-idealised truly random conditions. This is far more relevant for practical use with wave energy in the field.

## 6.4 Forecast model performance analysis

Each forecast model considered was first trained using unfiltered raw data using the excitation surface elevation time series in the chamber and, where applicable, the up-wave hydrostatic pressure time series. Training was made using the data in the first set of each respective data set pair ( $Z_{1,1}, Z_{2,1}, \dots, Z_{6,1}$ ). After, the trained models were used to predict the chamber excitation surface elevation time series of the corresponding unseen second data set of the data pair ( $Z_{1,2}, Z_{2,2}, \dots, Z_{6,2}$ ). The *GOF* index was selected for a preliminary evaluation of the forecast accuracy.

Firstly, the *GOF* index is contextualised by visualising how it can translate to the forecasted time series. Different *GOF* levels are compared against  $GOF = 100$  which represents a perfect forecast (original data) and this is seen for a snapshot time series of data set  $Z_{2,3}$  in figure 6.7.

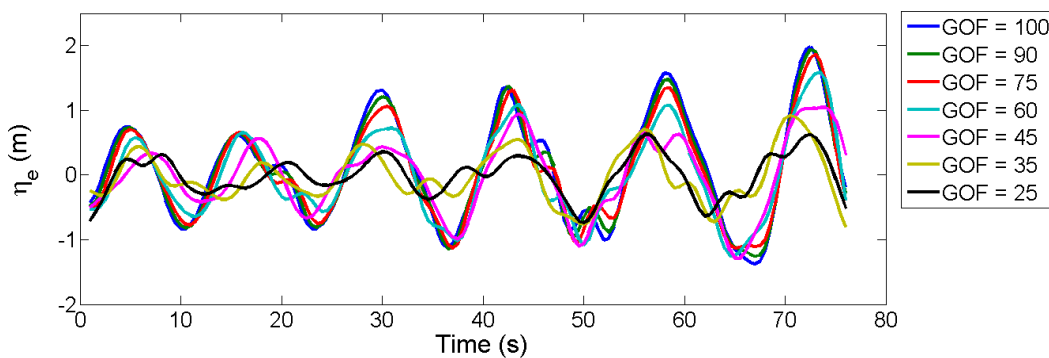


**Figure 6.7** Visualisation of the *GOF* index in relation to different forecasted times series of  $\eta_e(t)$  for a snap shot of test data  $Z_{2,3}$ .

The *GOF* achieved by each forecast model considered for the forecast horizon times of  $\Gamma = 0.5, 1, \dots, 20$ , using unfiltered raw data to both train and test the forecast model, is given in figure 6.8.

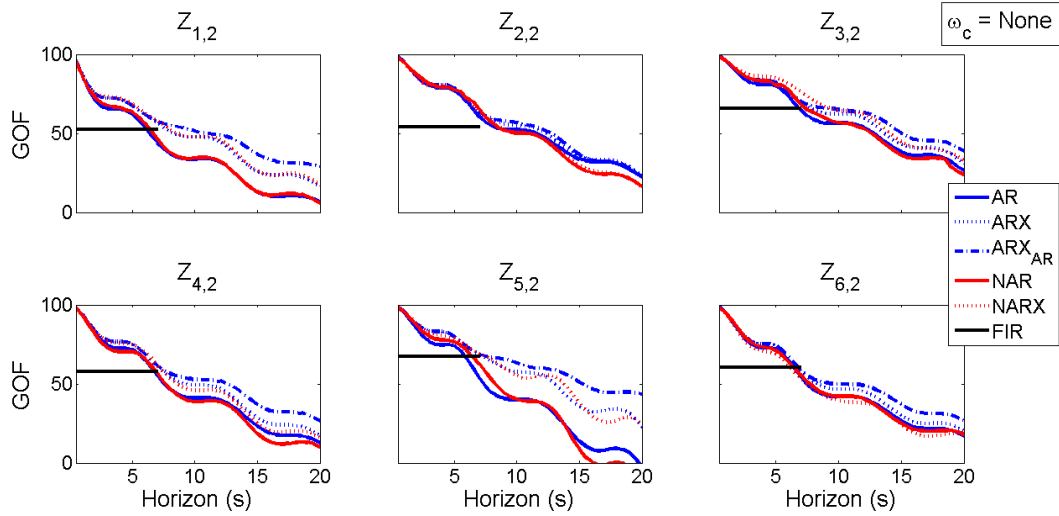


**Figure 6.8** Forecast accuracy goodness of fit index (*GOF*) achieved by the different forecast models for forecast horizon times up to  $\Gamma = 20$  (s) ( $\Gamma = 7$  (s) for *FIR*), with forecast models trained and tested using raw data.

As seen in figure 6.8 the *GOF* of the *AR*, *ARX*, *NAR* and *NARX*, decays fairly consistently with increasing horizon time. The models that include the up-wave data as an exogenous input generally have a slower decay in forecast accuracy when  $\Gamma > 3$  (s) achieving a notably greater accuracy in this time region. There is little difference in the accuracy between the *AR* and *NAR*, and the same is true between the *ARX* and *NARX*, which suggests that either nonlinearity in  $\eta_e$  is not an important factor, or that it is not possible to characterise it even with a nonlinear function. The *ARX\_{AR}* model generally performed best especially at longer forecast horizons ( $\Gamma > 10$  (s)) where it diverges from the next best competitors which are *ARX* and *NARX* models. The *FIR* model necessarily has a constant *GOF* with horizon time because no information from the chamber is included so it is a static time-independent transfer of the reading at the up-wave location to the chamber. It is also noted that all forecast are immediately in error (when  $\Gamma = 0.5$  (s)). This error was found to be due primarily to random electrical noise in the original data, which is not forecasted by the models.

In (Fusco & Ringwood (b), 2010) and (Paperella, et al., 2015) the forecast accuracy was greatly improved by artificially reducing the spectral bandwidth. To confirm this, the training and test data sets were filtered offline with a zero-phase low pass Butterworth filter of order 10 and a cut off angular frequency of  $\omega_c = 1.6 \text{ rad s}^{-1}$  which translate to a cut off wave period of  $T_c = 4$  s. This value was chosen from the spectral analysis (in figure 5.6) to remove electrical noise but preserve all real wave information. The forecast model's performance is seen in figure 6.9.

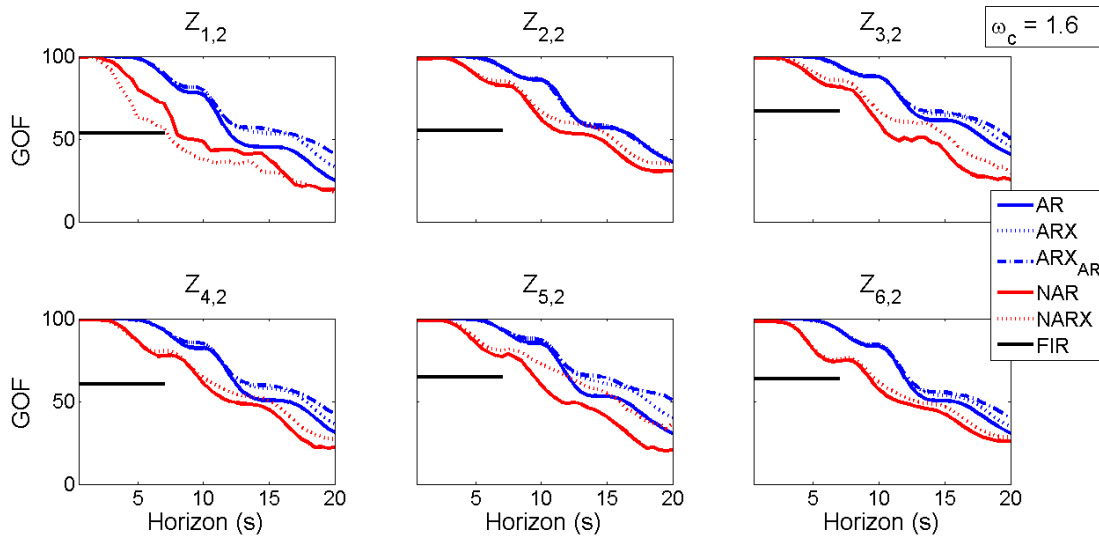


**Figure 6.9** Forecast accuracy goodness of fit index (*GOF*) achieved by the different forecast models for forecast horizon times up to  $\Gamma = 20$  s ( $\Gamma = 7$  (s) for *FIR*), with forecast models trained and tested using zero-phase, low-pass filtered, data with cut-off angular frequency of  $\omega_c = 1.6$   $rad\,s^{-1}$ .

Comparing figures 6.8 and 6.9 shows a significant improvement in forecast accuracy when electrical noise is filtered out (except the *FIR*). The accuracy of *AR*, *ARX* (and *ARX<sub>AR</sub>*), which were previously comparable to the *NAR* and *NARX* models, respectively, have improved even more significantly.

The Pico OWC and most wave energy devices are designed to be receptive and resonate with longer period waves that hold the bulk percentage of the incident wave energy. As such, it could be argued that in this context there is little benefit to be gained from forecasting the higher frequency wave components that contain only a small proportion of the total energy. For this reason a second zero-phase low pass filter was considered with  $\omega_c = 0.7$   $rad\,s^{-1}$ , equating to a cut off period of  $T_c = 9$  s. This value was chosen by inspection from the spectral analysis in figure 5.6. This cut off frequency represents the point (for the data sets considered) that preserves the vast majority of the incident energy, removing only the very small high frequency tail of the spectrum.

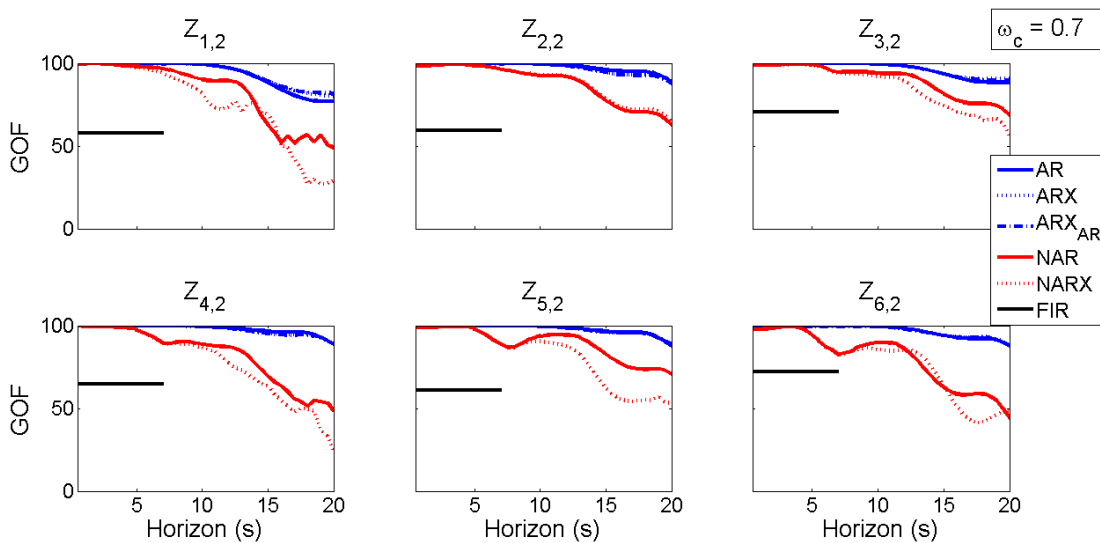


**Figure 6.10** Forecast accuracy goodness of fit index (*GOF*) achieved by the different forecast models for forecast horizon times up to  $\Gamma = 20$  s ( $\Gamma = 7$  (s) for *FIR*), with forecast models trained and tested using zero-phase, low-pass filtered, data with cut-off angular frequency of  $\omega_c = 0.7$   $rad\,s^{-1}$ .

By preserving only the wave frequencies that contain the bulk of the incident wave energy, the forecast accuracy for all forecast models improves significantly. Again the accuracy of *AR*, *ARX* and *ARX<sub>AR</sub>*, far surpasses the accuracy of the *NAR* and *NARX* models, respectively, giving a perfect forecast up to  $\Gamma = 10$  (s). With this filter little difference is seen in the *GOF* between the *AR*, *ARX* and *ARX<sub>AR</sub>*, models. Filters with different  $m$  and  $\omega_c$  were investigated and it was found that progressively higher  $m$  and/or lower  $\omega_c$  achieved a perfect forecast at increasingly longer horizons.

## 6.5 Forecasting causally filtered data

As seen in the previous subsection, significant improvements in forecasting accuracy can be achieved by artificially reducing the spectral bandwidth to consider the main frequency range of interest using a near ideal zero-phase filter. An ideal filter has an amplitude response of 1 in the pass band and 0 in the stop band so that all undesired frequencies are perfectly removed and all desired frequencies are perfectly preserved. A real filter converges with an ideal filter with increasing filter order number  $m$  because a shorter transition band is achieved. A short transition band minimises the attenuation of desired frequencies and maximise the attenuation of undesired frequencies, thus minimising the amplitude error.

All causal filters incur a non-zero phase delay which equates to a time lag in the filter output. For a typical *FIR* filter the phase response is linear so that all frequency components are delayed by the same data-time length and there is no phase distortion in the signal. However, for infinite impulse response filters (*IIR*) the phase response is nonlinear, meaning different frequency components are delayed by different amounts of time and the filter's output will have a phase that is distorted when compared to the input, as well as a delay. This phase distortion effect is comparable to wave dispersion in non-shallow water. The phase response (time delay in the filter output) generally gets larger as the filter order number increases. This means that choosing a filter order number is a trade-off between reducing the amplitude error of the filter's output but increasing the delay, and vice versa.

However, the phase distortion and phase delay imposed by the filter can be corrected by first filtering the signal forward in time and then backwards in time, so that the delay and distortion is cancelled. This process is described by (4.71-4.75). The zero-phase filtering method was used in the analysis in section 6.4. To achieve zero-phase filtering future values must be known which makes the filter non-causal and is therefore not realisable in real time applications. No solution to this issue was found in the literature and a solution was not developed in this work, despite much effort. As such, the results achieved in (Fusco & Ringwood (b), 2010) and (Paperella, et al., 2015) might only be possible if the device has a natural low pass filtering effect on the target variable. This needs to be confirmed with physical evidence because the forecast model could simply be replicating the filter used to process the data. This is a logical conclusion because at the heart of an *AR* model is an *IIR* filter.

If digital filtering is to be utilised in real-time, only a signal forward pass causal filter can be used, which unfortunately incurs a delay of the output in the time domain. To use a causal filter in real time, the delay imposed by the filter will have to be corrected. This means that in order to forecast a point at horizon time  $\Gamma$ , ultimately a forecast of  $\Gamma + \tau_{df}$  is required, where  $\tau_{df}$  is the time delay of the filter's output. When the delay is removed the forecast at horizon  $\Gamma$  is obtained. If an *FIR* filter is used this phase shift should allow

for perfect phase re-alignment but if an *IIR* filter is used phase distortion will only permit partial phase realignment.

It remains to determine if causally filtering the forecast model input data can yield any forecast accuracy enhancements. For this analysis some of the most widely used filters in digital signal processing, were selected. Specifically these are the *IIR* filters: Butterworth, Chebyshev type I and Chebyshev type II, and a *FIR* filter with Bartlett windowing. A mathematical description of the different filters can be found for example in (Stearns & Hush, 2011).

For the Chebyshev type I filter the maximum error in the stop-band was selected as 0.001 and for the Chebyshev type II the maximum error in the stop-band was selected as 20. The *FIR* filter was implemented with a Bartlett window with length  $m + 1$ . The amplitude and phase response of the low-pass filters considered, with low pass cut-off frequency  $\omega_c = 0.7$ , is given in figure 6.11, as a function of the filter order numbers.

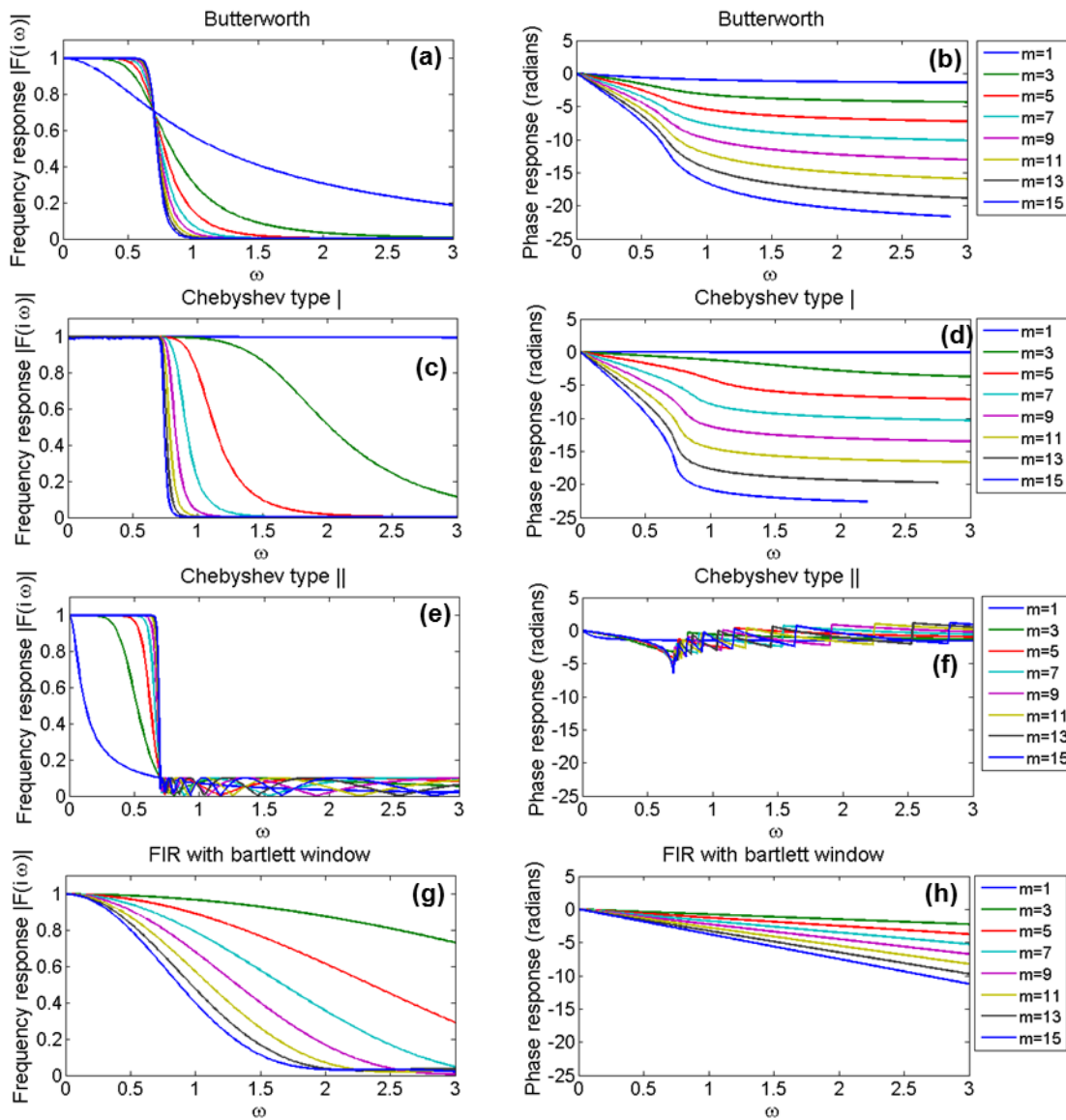


**Figure 6.11** Frequency domain representations of the amplitude (**a, c, e and g**) and phase (**b, d, f and h**) response of the low-pass *IIR* filters; (**a, b**) Butterworth, (**c, d**) Chebyshev type I, (**e, f**) Chebyshev type II and (**g, h**) a low-pass *FIR* filter using Bartlett windows, for filter order numbers  $m = 1, 3, \dots, 15$ , with cut-off angular frequency of  $\omega_c = 0.7 \text{ rads}^{-1}$ .

As seen in figure 6.10 the *AR* forecast model delivered the greatest forecast accuracy when data is non-causally filtered. As such the *AR* forecast accuracy that is achievable using a signal forward pass of the causal filter described in figure 6.11, is considered. Achievable forecast accuracy is assessed by first finding the delay by shifting the forecast output  $\hat{\eta}_e(t)$  in time to minimise the error with the original signal  $\eta_e(t)$ . When the delay is found it is removed thus achieving a phase re-alignment with the target data (phase re-alignment is approximate for the *IIR* filtered data). Finally the resultant forecast *GOF* is assessed. This is then compared to the *GOF* forecast accuracy when no filter is used (requiring no phase shift) and the difference is evaluated in terms of the relative goodness of fit *RGOF*. This analysis is given in figure 6.12, and the relative goodness of fit is defined as;

$$RGOF = GOF_{filter} - GOF_{no\ filter} \quad (6.36)$$

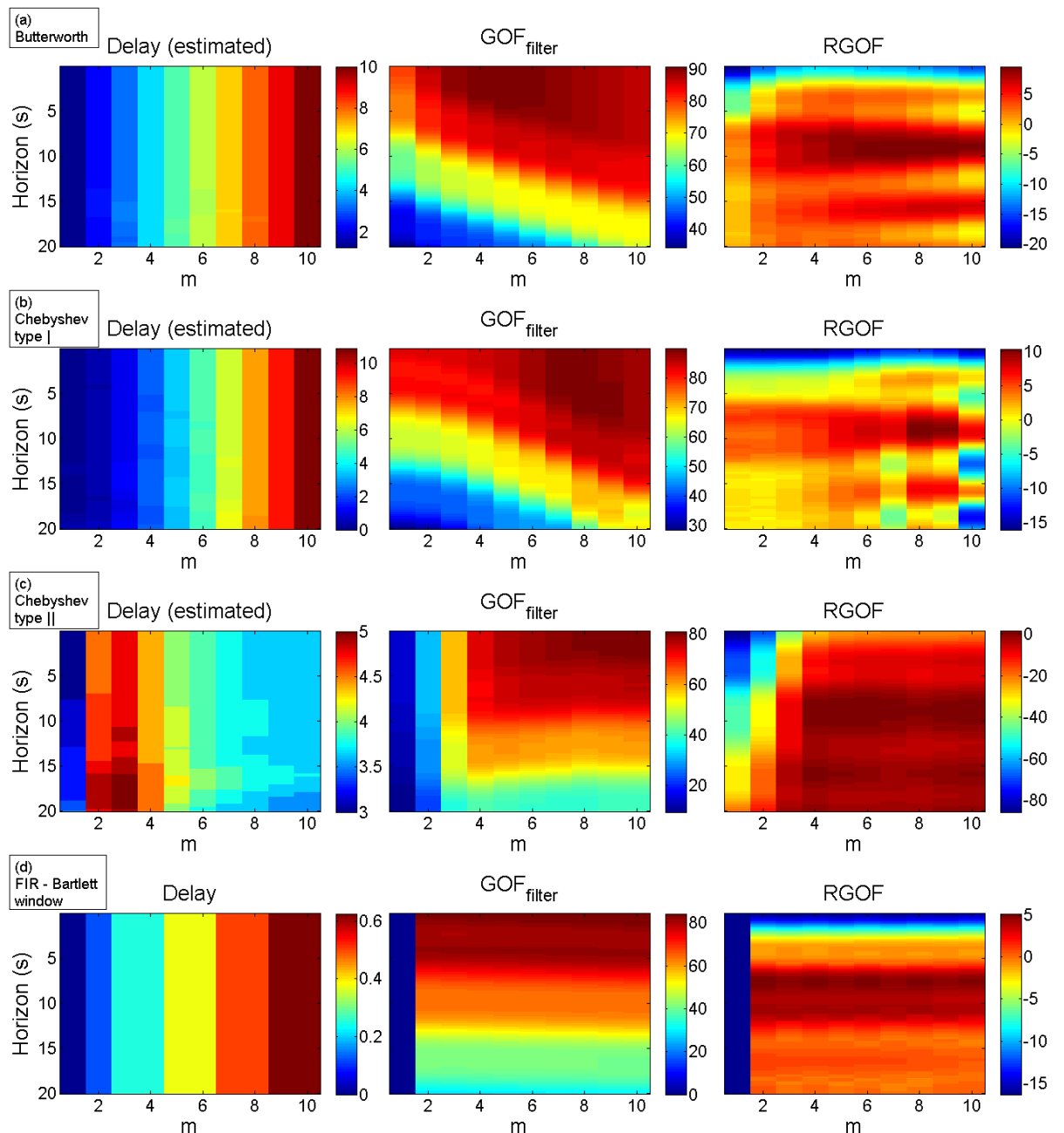


**Figure 6.12** Delay in filter's output, *GOF* when the delay is removed, and the relative goodness, as a function of filter order number and forecast horizon, when the low-pass ( $\omega_c = 0.7$ ) causal filters; **(a)** Butterworth, **(b)** Chebyshev type I, **(c)** Chebyshev type II and **(d)** FIR with Bartlett window, are used.

As seen in figure 6.12, after the delay is removed, temporal improvements in the forecast accuracy at certain forecast horizon times and (generally) lower filter order numbers, is achieved. However, at best these are cancelled out almost completely by reductions in forecast accuracy at other forecast horizon times and at worst the mean accuracy is worse or even significantly worse. The Butterworth and Chebyshev type I filters were capable of increasing the mean *RGOF* by up to 3% but the improvement does not justify the computational effort and potential for mistakes to be made in the post processing. It is noted that for higher order Butterworth and Chebyshev type I filters the accuracy decreases significantly due to an increasingly nonlinear phase distortion. Low order Chebyshev type II performed particularly poorly because of the attenuation of frequencies in the pass-band as seen in figure 6.11.

Ultimately there appears to be no significant gain to be had by filtering input data for forecasting. This means the exceptional forecast accuracies achieved by off-line zero-phase filtering are not realisable in on-line real-time applications and as such could only have value if low pass filtering of target variable occurs naturally. This effect is seen in the motion of a point absorber, for example. However, it needs to be confirmed that natural low pass filtering is representable by a zero-phase digital filter and disprove the argument made here that the forecast model is simply replicating the non-causal filter. As such the forecast accuracies shown in figures 6.9 and 6.10 and reported in (Fusco & Ringwood (b), 2010) and (Paperella, et al., 2015) are, at best, only achievable if the spectral band-width of the forecast models input data is truly contained within limits that were inferred using a digital filtering. At this point data filtering for the purposes of improving the realisable on-line forecast accuracy will be discarded and will not feature in any of the remainder of this work.

## 6.6 Forecast model performance analysis for relief valve control

In section 6.4, the forecast accuracy is assessed by the goodness of fit (*GOF*) index because it is commonly used in the literature. The *GOF* index assesses the root of the sum of squared errors between each real and forecasted data point, normalised by the standard deviation. As such, *GOF* is highly dependent on phase alignment. A forecast with good amplitude accuracy but with a small misalignment in phase will result in a poor *GOF*. For WEC control requiring high phase accuracy, such as the excitation force phase for latching or declutching control for a point absorber, the *GOF* is a highly relevant evaluation parameter. Alternatively,  $Envelope_{RVC}$  proposed in section 5.4.5 is dependent on the standard deviation of non-dimensional chamber pressure head  $\sigma_{T_p}(\Psi)$  over a relatively long time period and will be insensitive to small errors in the forecasted phase. The same is true for  $Continuous_{RVC}$ . As such, the *GOF* might be a misleading error quantification parameter for some of the control strategies proposed because the quantification of the forecast accuracy might be disproportionately weighted by the phase error, which is less important in some of the proposed application. Assessing the forecast accuracy of the standard deviation of pressure allows the suitability of the different forecast models to be directly evaluated for use with  $Envelope_{RVC}$  (the primary control strategy under investigation).

To perform this secondary forecast accuracy assessment, first the time series of chamber pressure  $p_c(t)$ , resulting from a perfect forecast of chamber excitation surface elevation, needs to be found for a baseline comparison. This was done for each data set considered using (5.14) and (4.39) with the original time-series of: calculated chamber excitation surface elevation  $\eta_e(k)$  and turbine angular velocity  $N(k)$ , where

$k = 1, 2, \dots, L$ . For consistency, the relief valve was considered to be static having zero aperture ( $k_v = 0$ ) for all data sets.

Next, at each data time instant  $k$  the forecasted chamber pressure time series  $\hat{p}_c(k)$  is found using (5.14) and (4.39) again with the original turbine angular velocity  $N(k)$ , and a relief valve state of  $k_v = 0$ , but with the forecasted chamber excitation surface elevation  $\hat{\eta}_e(k + l)$  provided by the different forecast models considered. Here  $l = 1, 2, \dots, \Gamma_{max} f_s$ , where  $\Gamma_{max} = 20$  s is the maximum forecast horizon time considered.

The mean absolute error between the standard deviation of non-dimensional pressure using the perfect forecast  $\sigma_\Gamma(\Psi, k)$ , and the real forecast  $\sigma_\Gamma(\hat{\Psi}, k)$ , for each increment of forecast Horizon time  $\Gamma$  is found with;

$$MAE(\sigma_\Gamma(\Psi)) = \frac{1}{L} \sum_{k=1}^L |\sigma_\Gamma(\Psi, k) - \sigma_\Gamma(\hat{\Psi}, k)| \quad \text{for } \Gamma = 0.5, 1, \dots, \Gamma_{max} \quad (6.37)$$

The  $MAE(\sigma_\Gamma(\Psi))$  for each permutation of: test data set, forecast horizon increment and forecast model, is shown in figure 6.13.

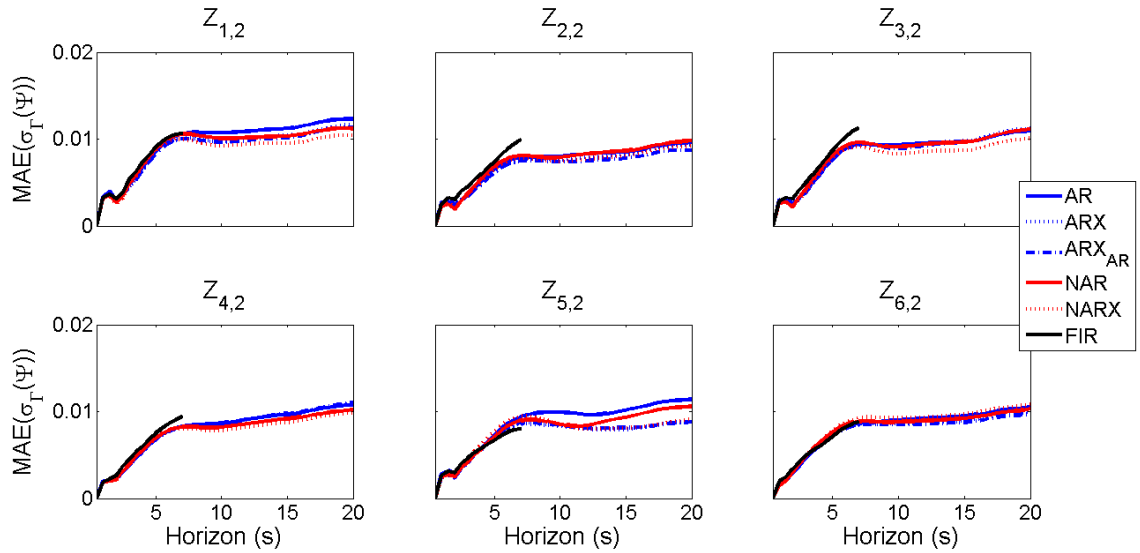


**Figure 6.13** Mean absolute error of the forecasted standard deviation of non-dimensional pressure over different horizon times from the different forecast models considered, for the different data sets considered.

Considering the forecast accuracy in terms of  $MAE(\sigma_\Gamma(\Psi))$  reveals some additional conclusions that were not apparent when considering the  $GOF$  index only, these are:

1. The  $MAE(\sigma_\Gamma(\Psi))$  nearly plateaus when  $\Gamma > 7$  s, whereas the  $GOF$  in figure 6.8 steadily declines with increasing forecast horizon. This translates to a stabilisation of the amplitude error of the forecast, but a continued increase in the phase error with increasing horizon time  $\Gamma$ .
2. The  $FIR$  model achieves essentially the same  $MAE(\sigma_\Gamma(\Psi))$  as the multivariate models ( $ARX$ ,  $NARX$  and  $ARX_{AR}$ ). In contrast making the same comparison with  $GOF$  index shows that the  $FIR$  model achieves much lower accuracy for shorter horizon times. This shows that the difference in  $GOF$  between the  $FIR$  and the;  $ARX$ ,  $NARX$  and  $ARX_{AR}$ , is primarily due to error in

the forecasted phase, but that this phase error is not as significant for the forecast of  $\sigma_T(\Psi)$ . The phase error might be due to frequency dispersion and/or interference from reflected and radiated waves from the device, which is not, in part, corrected by the chamber data input to the model as with the  $ARX$ ,  $NARX$  and  $ARX_{AR}$  models.

3. In general there is very little difference in the forecast accuracy of  $\sigma_T(\Psi)$  between all forecast models. As there were significant differences in the  $GOF$  between the different forecast models it can be concluded that the difference in  $GOF$  forecast accuracy is primarily due to forecasted models having different levels of phase error.

As seen in figure 6.13, the forecast accuracy of  $\sigma_T(\hat{\Psi})$  (needed for  $Envelope_{RVC}$ ) is essentially the same between the linear and nonlinear models in this application. However, the linear autoregressive models are far quicker to train and less prone to over fitting and the nonlinear models are susceptible to instabilities associated with the neural network found nonlinear function. Because of this the  $AR$  and  $ARX_{AR}$  (for the situation where up-wave measurements are available) are considered to be the favourable option in this application where a nonlinear relationship, between future and past data points, or between up-wave and plant side data, is either not important or cannot be characterise by this method. Also, they were selected because of the robust and rapid deployment requirements of real-time operation. As such only the  $AR$  and  $ARX_{AR}$  forecast models will be considered from this point on.

## 6.7 Performance of control strategies using a realisable forecast

As the achievable forecast accuracy of  $\sigma_T(\hat{\Psi})$  in section 6.6 was found to be far from perfect it is now important to re-asses the performance of the different control strategies proposed in chapter 5 for the scenario when valve control action is based on the information delivered by a realisable forecast of the chamber excitation surface elevation. In all cases the simulations are the same as in chapter 5, except that at each data time point a forecast of  $\hat{\eta}_e$  is made using the  $AR$  and  $ARX_{AR}$  models. This is then used to make the control decision, but the modelled system dynamics evolve from the original time series of  $\eta_e$ . Also simulations are made from the second data set pairs ( $Z_{1,2}, Z_{2,2}, \dots, Z_{6,2}$ ) only because the first data set pairs ( $Z_{1,1}, Z_{2,1}, \dots, Z_{6,1}$ ) are used to train the forecast models.

### 6.7.1 Instantaneous relief valve control

As described in section 5.4.2, the  $Instant_{RVC}$  strategy requires a short forecast horizon which we consider to be 0.5 (s) (one data sampling period for the current setup). As seen in figure 6.8, the realisable forecast accuracy is immediately in error at one time-step of horizon. The forecast error at one time step is small but because of the high tolerance of the strategy due to the sharp drop in power transfer efficiency at the point of turbine stall, the error could have a significant effect on the performance of the system and requires re-evaluation. Although the technology for the valve actuator system for control in this manner is not available to continue this line of research further than a theoretical study, it is still interesting to project how such a system might perform with the achievable forecast accuracy.

Due to the small forecast error it was found that the optimum performance (for power production) is achieved by reducing the critical threshold of non-dimensional chamber pressure (that valve control tries to achieve but not exceed) from  $\Psi_{cr} = 0.067$  to  $\Psi_{cr} = 0.06$ . This is because the forecast error, at times,

results in an overshoot in the chamber pressure so that a significantly detrimental portion of time is spent in the poorer power transfer efficiency stall regime  $\Psi > \Psi_{cr}$ , if the target  $\Psi_{cr}$  is not reduced to account for the forecast error. All other aspects of the simulation are consistent with the analysis in section 5.4.2.

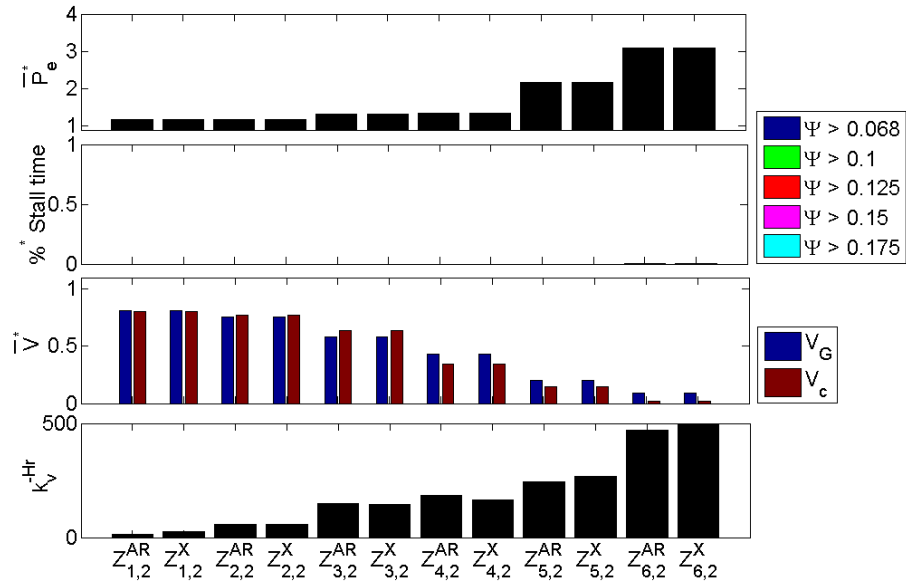


**Figure 6.14** Power enhancement, inferred fatigue minimisation assessment, and number of full relief valve cycles per hour, when  $Instant_{RVC}$  control action is made from  $\hat{\eta}_e$  from the AR (denoted with superscript AR) and  $ARX_{AR}$  (denoted with superscript X) forecast models. All values except  $k_v^{-Hr}$  are normalised by the performance of the optimised  $Basic_{RVC}$  strategy.

Comparing the plant performance under  $Instant_{RVC}$ , using a realisable forecast as shown in figure 6.14, to that with a perfect forecast as shown in figure 5.9, shows a small drop in power production. This is due to the very narrow efficiency peak of the wells turbine power transfer curve seen in figure 5.2, so a small error in the forecast results in more frequent deviations from this peak and ultimately a notable reduction in the transfer efficiency. The indicators for machine fatigue did not change significantly because the reduction of the target  $\Psi_{cr}$  maintains stall avoidance despite the small forecast error. The relief valve cycle frequency is only marginally increased, relatively speaking. Also, it is noted that there is almost no notable difference in performance when the forecast is made with the AR or  $ARX_{AR}$  forecast models. This is expected as the forecast accuracy between the two models only deviates at longer forecast horizons. Overall the performance enhancement is still very impressive but this is at the expense of a high number of relief valve adjustment cycles.

### 6.7.2 Wave by wave relief valve control

$Wave_{RVC}$ , along with  $Continuous_{RVC}$  and  $Envelope_{RVC}$ , all depend on much longer forecast horizons than  $Instant_{RVC}$ , in order to determine the optimum control action. As the forecast accuracy depreciates much more significantly with greater forecast horizon (as seen in figure 6.8 and 6.13), the performance of these control strategies will likely incur greater degradation and there is an even stronger need for reevaluation.  $Wave_{RVC}$  depends more heavily on the phase accuracy of the forecast because the half-wave period length needs identifying. This is in addition to the chamber excitation surface elevation profile contained within this period, which is needed to identify the optimum chamber pressure amplification or damping. The performance of  $Wave_{RVC}$  is shown in figure 6.15.

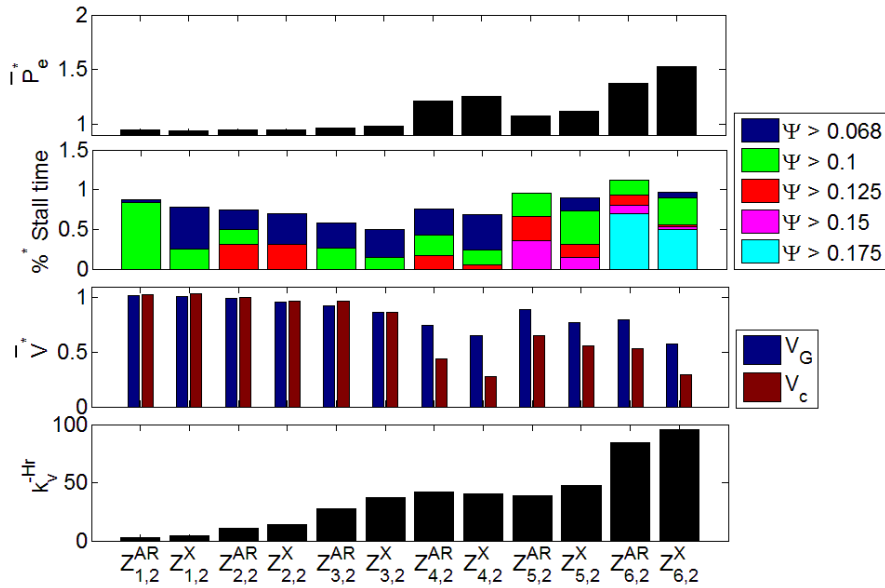


**Figure 6.15** Power enhancement, inferred fatigue minimisation assessment and number of full relief valve cycles per hour, when  $Wave_{RVC}$  control action is made from  $\hat{\eta}_e$  from the AR (denoted with superscript AR) and  $ARX_{AR}$  (denoted with superscript X) models. All values except  $k_v^{-Hr}$  are normalised by the performance of the optimised  $Basic_{RVC}$  strategy.

The plant performance under  $Wave_{RVC}$  from a realisable forecast as shown in figure 6.15 incurs a significant decline in performance compared to the case where a perfect forecast is available, as seen in figure 5.12. Power enhancements fall by around 50% and the frequency of stalls and the vibrations increase significantly. The relief valve cycle frequency has reduced and this is likely to be due to the forecast model's tendency to under predict the amplitude which results in more conservative aperture adjustments. However, for the higher energy sea states there is still a notable improvement in performance using  $Wave_{RVC}$  compared to  $Basic_{RVC}$ , and in all cases the stall frequency and severity is significantly reduced. In most cases it is seen that the performance of  $Wave_{RVC}$  improves when the forecast is made with  $ARX_{AR}$  model compared to the AR, with small increases in power production and reductions in stall frequency. This is likely to be caused by the enhanced phase forecast accuracy associated with the  $ARX_{AR}$  forecast model which is needed to identify the future half wave cycle.

### 6.7.3 Continuous relief valve control

Using a realisable forecast,  $Continuous_{RVC}$  was found to be optimised with the same forecast horizon  $\Gamma \approx T_p/2$  (used to assess  $\bar{\Pi}_\Gamma$ ) as was found for the perfect forecast case in section 5.4.4 and given in table 5.3. Using a realisable forecast to assess  $\hat{\Pi}_\Gamma$  and with relief valve control being based on this prediction, the performance of  $Continuous_{RVC}$  for each data set is given in figure 6.16.

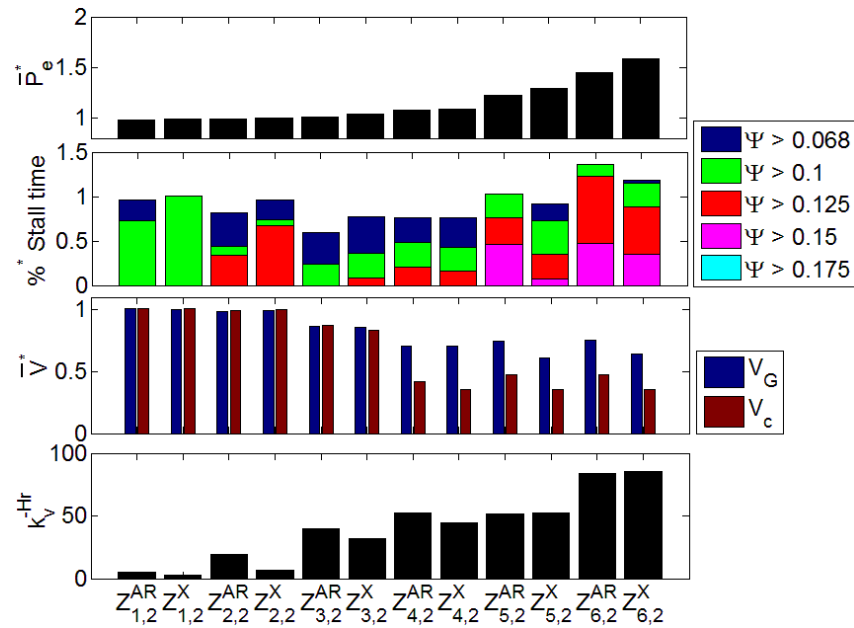


**Figure 6.16** Power enhancement, inferred fatigue minimisation assessment and number of full relief valve cycles per hour, when *Continuous<sub>RVC</sub>* control action is made from  $\hat{\eta}_e$  from the *AR* (denoted with superscript *AR*) and *ARX<sub>AR</sub>* (denoted with superscript *X*) forecast models. All values except  $k_v^{-Hr}$  are normalised by the performance of the optimised *Basic<sub>RVC</sub>* strategy.

Comparing figures 6.16 and 5.15 it is again seen that a significant reduction in performance is incurred when *Continuous<sub>RVC</sub>* is based on a reliable forecast. In general the enhancement to power production is about 40% less than that achieved with a perfect forecast. The stall frequency has incurred mixed changes with an increase in the lower energy sea states, but a decrease in the higher level stall bands for the highest energy sea states. Vibrations have increased notably but there are still significant relative reductions in the higher energy sea states. The relief valve adjustment frequency has also increased slightly in the higher energy sea states. There is a small but notable improvement in performance when the forecast is made with *ARX<sub>AR</sub>* model compared to the *AR*.

Overall there are still notable enhancements in performance when the *Continuous<sub>RVC</sub>* strategy is driven with a realisable forecast compared to *Basic<sub>RVC</sub>* with up to 60% power production increase (for the data sets considered). Also *Continuous<sub>RVC</sub>* is seen to perform at least as well and perhaps marginally better than *Wave<sub>RVC</sub>*. To implement *Continuous<sub>RVC</sub>* at the Pico plant requires only a small modification to the relief valve actuator system, which would be the replacement of the hydraulic pump for one that is capable of continues operation without over-heating, or by adding a pump motor cooling system. As such, *Continuous<sub>RVC</sub>* is a strategy that should be considered in the future and *Wave<sub>RVC</sub>* should be discarded unless the short-term forecast accuracy can be improved.

#### 6.7.4 Envelope relief valve control

Using a realisable forecast, *Envelope<sub>RVC</sub>* was also found to be optimised with a horizon equal to  $T_p$  (used to assess  $\sigma_{T_p}(\Psi)$ ) as was found in section 5.4.5. The performance of *Envelope<sub>RVC</sub>* acting on information delivered by a realisable forecast is shown in figure 6.17.

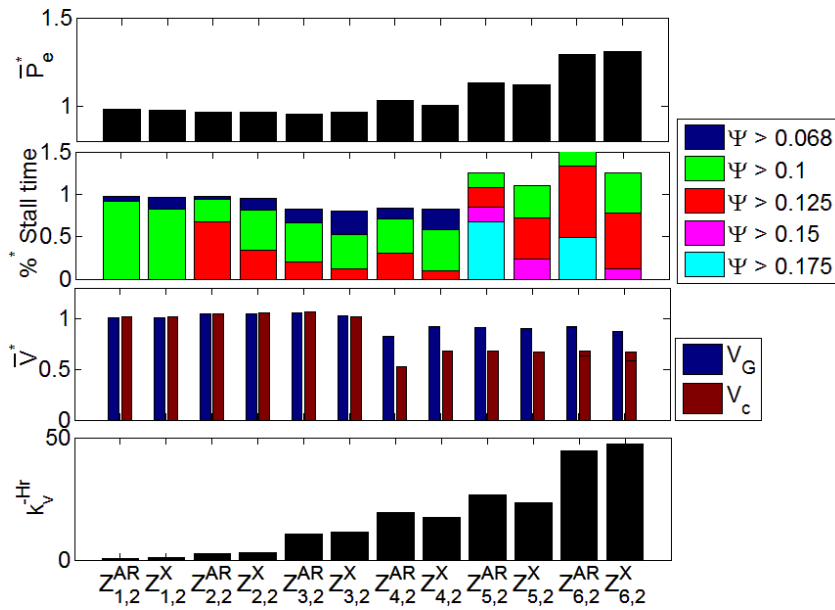


**Figure 6.17** Power enhancement, inferred fatigue minimisation assessment and number of full relief valve cycles per hour, when  $Envelope_{RVC}$  control action is made from  $\hat{\eta}_e$  from the AR (denoted with superscript AR) and  $ARX_{AR}$  (denoted with superscript X) forecast models. All values except  $k_v^{-Hr}$  are normalised by the performance of the optimised  $Basic_{RVC}$  strategy.

Comparing figures 6.17 and 5.18 it is seen that, in a similar fashion to  $Continuous_{RVC}$ , a significant reduction in performance is incurred when the  $Envelope_{RVC}$  strategy operates from a reliable forecast. In general the enhancement to power production is about 40% less than that achieved with a perfect forecast. The stall frequency has increased slightly for the lower energy sea states and more significantly for the higher energy sea states. In some cases the proportion of time spent in the lower level stall bands is actually greater under  $Basic_{RVC}$ . The stall pattern resulting from  $Envelope_{RVC}$  would still be considered as preferable to the stall pattern from  $Basic_{RVC}$  because severe stalls are consistently reduced and these are expected to cause the greatest rate of fatigue and failure. Vibrations have increased notably but there are still significant reductions in the higher energy sea states. The relief valve adjustment frequency has increased quite notably due to forecasting error which results in frequent changes of the relief valve aperture trajectory.

In all cases it is seen that the stall frequency improves when the forecast is made with  $ARX_{AR}$  model compared to the AR, but the enhancements to power production are not consistent between the two modelling approaches, although the differences are only slight. Overall there is still a notable enhancement in performance when the  $Envelope_{RVC}$  strategy is driven with a realisable forecast compared to  $Basic_{RVC}$  with up to 30% increases in power production (for the data sets considered), and requiring no modification to the existing relief valve actuator system installed at the Pico plant. As such  $Envelope_{RVC}$  is selected for real deployment at the Pico plant and the results from field tests will be presented in the next chapter.

## 6.8 Forecast model retraining intervals

Training and test data sets have been separated by 3 hour intervals (due to restrictions in the available data as described in section 5.3) for all forecast performance analysis up to this point. As such it is important to confirm that forecast model accuracy has not suffered significantly from this data time

separation. It is also interesting to investigate how frequently the forecast model parameters should be updated. To this end three continuous data sets, of chamber excitation surface elevation only, spanning 4.5 (*hrs*), were selected. The selection was made based on the time varying trend of sea state. These were;

1. Rapidly increasing incident wave energy
2. Steady incident wave energy
3. Rapidly decreasing incident wave energy.

The first 0.5 (*hrs*) of each data set was used for training and the forecast was performed on the remaining 4 (*hrs*) of data broken in to subsets of 0.5 (*hrs*) in length. The forecast was made using the *AR* model with the accuracy being assessed by the *GOF* index. The analysis is presented in figure 6.18.

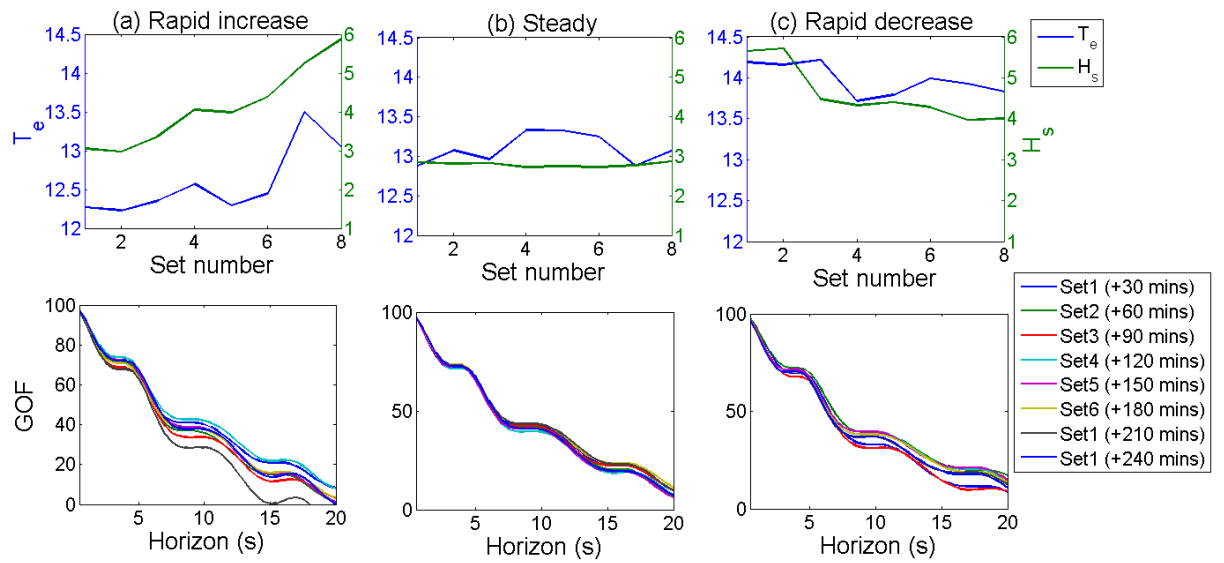


**Figure 6.18** Forecast *GOF* achieved for data sets with increasing time from data set used to train the *AR* forecast model. Different sea states characterised by; rapidly increasing (a), stead (b) and rapidly decreasing (c),  $H_s$  and  $T_e$ .

It is seen in figure 6.18 that, in general, the forecast accuracy is rather consistent with increasing time between the test data set and the data set used to train the *AR* model. However, for the changing sea states the forecast tends to be marginally more consistent for the test set closest in time from the training set. The steady sea state showed the greatest consistency in the forecast accuracy, as would be expected.

Going further, a spectral analysis can be made of the autoregressive coefficients. The autoregressive power spectral density equation is given in (Schlindwein & Evans, 1992), for example, and is defined as;

$$PSD(f) = \frac{\sigma(\varepsilon)^2}{f_s \left| \sum_{j=0}^n a_j e^{-i2\pi j f / f_s} \right|^2} \quad (6.38)$$

where  $f$  is a discrete frequency component,  $\sigma(\varepsilon)^2$  is the variance of the noise term,  $a_0 = 1$  and  $f_s$  is the data sampling frequency.

A comparison between the spectral density of the *AR* models and the spectral density of the chamber excitation surface elevation, for the: training set, test set that immediately proceeded the training set, and the test set that started 4 hours after the first point in the training set, is given in in figure 6.19.

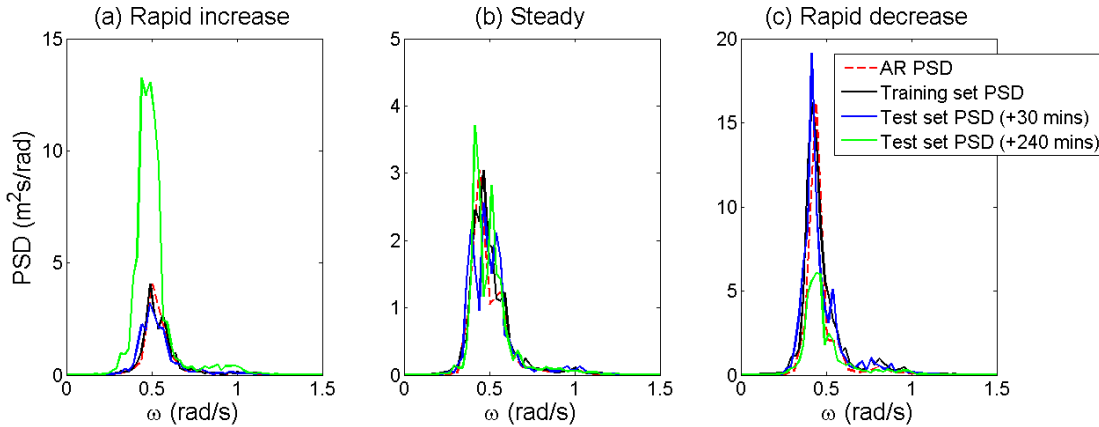


**Figure 6.19** PSD of the *AR* model coefficients  $a_j$  compared to the PSD of  $\eta$  for the: training data set, the test data set occurring immediately after the training data set and the test data set occurring 4 hours after the training data set. It should be noted that the PSD density of  $a_j$  has been amplified to contextualise it with the PSD of  $\eta_e$ .

As seen in figure 6.19, for the periods of rapidly increasing and rapidly decreasing energy period  $T_e$ , the spectrum of the *AR* coefficients gives a good representation of the wave spectrum that immediately proceeds the training data. However, as the sea state is changing rapidly the *AR* spectrum gives a poorer representation when the test data set that is 4 hours away from the training data set. For the period having a steady energy period the *AR* spectrum maintains a good representation for the duration. In other cases it was found that the *GOF* performance of the *AR* model suffers more significantly from variations in spectral peak frequency than variations in the magnitude of the power spectral density peak.

As the computational effort for training the *AR* is low (a few seconds of processing time), it seems marginally beneficial to regularly update the *AR* coefficients based on the most recent data. If the updating of the forecast model coefficients is done in series to the forecasting algorithm, a short period of no forecast output will occur. No time delay can be achieved if the coefficients are up-dated in parallel, but a bump due to the change in model coefficients will occur. As such it seems optimal to update the forecast model coefficients in parallel at a medium time interval. Every hour seems reasonable.

## 6.9 Forecast analysis for devices with phase control

The *Envelope<sub>RVC</sub>* strategy adjusts the relief valve aperture based on the forecast of the standard deviation of non-dimensional chamber pressure  $\sigma_{T_p}(\hat{\Psi})$  over a time scale equivalent to the spectral peak period. As such it is not particularly sensitive to errors in the forecasted phase. Alternatively *Wave<sub>RVC</sub>* functions in part by forecasting the half-wave period and will suffer more greatly from any forecasted phase error. Other wave energy converter control strategies, such as latching and declutching of a floating point absorber, will be highly reliant on the phase accuracy of the forecasted excitation force. For control in this manner the phase forecast provides the information on when to latch or declutch the device and the duration of latching or declutching. This is based on the period of the upcoming half-wave cycle. As such a final assessment of the realisable forecast accuracy is made with focus on the forecasted phase. The

forecasted phase accuracy is assessed by the mean absolute time error  $MAE_{zc}(s)$  of the forecasted zero crossing  $\eta_e = 0$  events, as described by;

$$MAE_{zc}(s) = \frac{1}{K_{zc}} \sum_{zc=1}^{K_{zc}} |t_{zc}(\eta_e = 0) - t_{zc}(\hat{\eta}_e = 0)| \quad \text{for } \Gamma = 0.5, 1, \dots, \Gamma_{max} \quad (6.39)$$

where  $K_{zc}$  is the total number of zero crossings in the test data set, and the mean absolute time error  $MAE_{tp}(s)$  for the forecasted turning points  $\dot{\eta}_e = 0$  (or  $q_e = 0$ ) at the wave peak or trough, as described by;

$$MAE_{tp}(s) = \frac{1}{K_{tp}} \sum_{tp=1}^{K_{tp}} |t_{tp}(\dot{\eta}_e = 0) - t_{tp}(\hat{\dot{\eta}}_e = 0)| \quad \text{for } \Gamma = 0.5, 1, \dots, \Gamma_{max} \quad (6.40)$$

where  $K_{tp}$  is the total number of turning points in the test data set

The assessment of  $MAE_{zc}(s)$  and  $MAE_{tp}(s)$  as a function of forecast horizon is made using the forecasts from the  $AR$ ,  $ARX$  and  $ARX_{AR}$  models, for the 6 test sets of the data set pairs, and this is shown in figure 6.20.

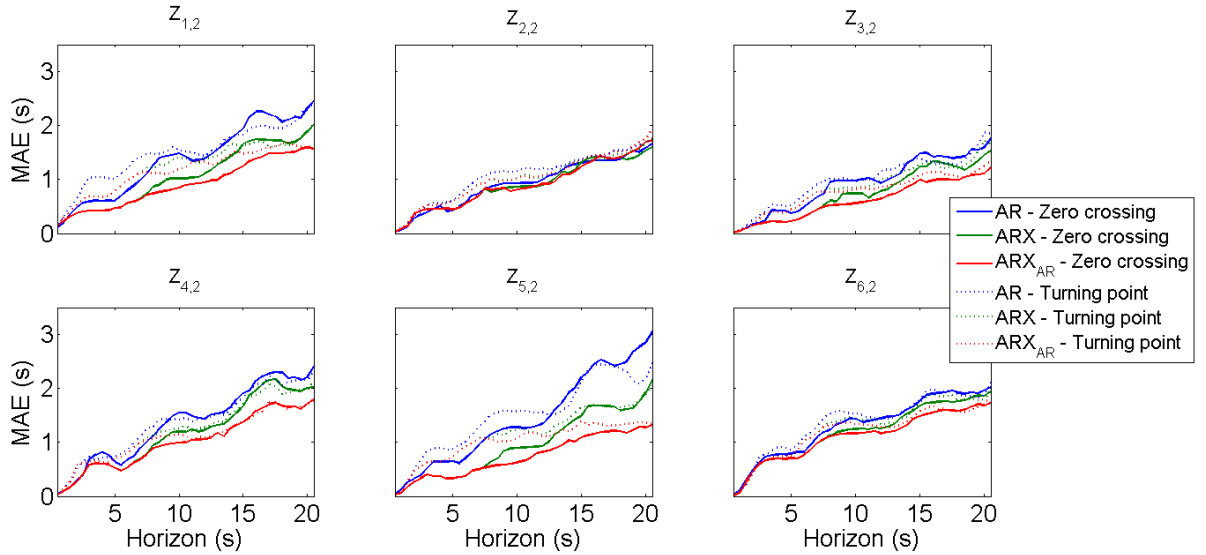


**Figure 6.20** Mean absolute time error of the forecasted zero-crossing and turning points, as a function of forecast horizon time, for the  $AR$ ,  $ARX$  and  $ARX_{AR}$  models.

As seen in figure 6.20, the forecast time error of the zero-crossing and turning point events (relevant for phase control of a WEC), increases with forecast horizon. The  $ARX_{AR}$  shows the greatest phase accuracy which also confirms why the  $GOF$  achieved with the  $ARX_{AR}$  was substantially greater than the other forecast models (at longer horizon times), whilst the  $MAE(\sigma_T(\Psi))$  (less dependent on phase accuracy) is similar between the models. In all cases the accuracy is only very high for short forecast horizon times which could be useful for identifying the point of latching. However, for phase control based on the upcoming half wave period an error of between 0.5 - 2 seconds would be incurred on average.

## 6.10 Conclusions

Six forecast models were considered to make short-term forecasts of the chamber excitation surface elevation for the Pico OWC case study. The  $AR$  and  $NAR$  models considered past measurements at the

device exclusively, while the *FIR* models considered measurements at the device and up-wave measurements in the model training phase but exclusively used the up-wave measurements with a specific lead time in the forecasting phase. The *ARX*, *NARX* and *ARX<sub>AR</sub>* consider both past measurements and up-wave measurements simultaneously throughout the training and forecasting phases.

When the forecast horizon is less than three seconds there was no difference in forecast accuracy between the: *AR*, *ARX*, *NAR*, *NARX* and *ARX<sub>AR</sub>* models, but the *FIR* model performed poorer as a result of phase error due to a lack of phase correction from the plant side data input. For the forecast horizon range of between three to seven seconds, with seven seconds being the finite lead time due to the separation between the up-wave sensor and the device, the forecast models that considered both plant side measurements and up-wave information: *ARX*, *NARX*, *ARX<sub>AR</sub>*, out-performed the *AR* and *NAR* models that consider just past measurements. The difference in error between these two groups increasingly diverged with the further increases in forecast horizon. For forecast horizons greater than seven seconds, the: *ARX*, *NARX* and *ARX<sub>AR</sub>* continued to outperform the *AR* and *NAR* models, and the *ARX<sub>AR</sub>* performed best and diverged from the next best competitors with increasing forecast horizon primarily because of the greater phase accuracy of the forecast. Forecast models which utilise an exogenous input variable having lead time were considered and in this specific case the forecast accuracy benefitted a small but notable amount from this additional information. The multivariate forecast model analysis should be conducted again using the true incident wave time-series (extracted from the resulting superposition using a multi-point sensor array) as an exogenous input because the forecast accuracy is expected to enhance further.

There was little difference in performance between the linear and nonlinear autoregressive models. As the: *AR*, *ARX* and *ARX<sub>AR</sub>*, are far more computationally efficient and resilient to training error, compared to the *NAR* and *NARX* models, they are considered to be the preferable choice. In this application the up-wave sensor positioning meant that the maximum forecast horizon of the *FIR* model was insufficient for the proposed *Envelope<sub>RVC</sub>* control strategy. This is of little concern as the *FIR* was found to be the (marginally) weakest of the forecast models considered.

By applying a zero-phase filter to the query data, the forecast accuracy from all models (except the *FIR*) could be dramatically enhanced. This is especially true for the linear autoregressive models. However, unless the device has a naturally occurring low-pass filtering effect on the forecast target variable, this method cannot be considered as it is non-causal. The validity of forecasting non-causally filter data to replicate a device that has a natural filtering effect needs to be proven with real tests, because the forecast model could simply be replicating the non-causal filter. Causally filtering the data incurs a delay in the filter's output. When the delay was corrected no significant enhancement in forecast accuracy could be achieved because any improvement in forecast accuracy from narrowing the spectral bandwidth was counteracted at least almost completely by the forecast delay. The process also adds further complexity to the forecasting procedure and as such this approach is not considered to be worthwhile.

The time length between the forecast model retraining intervals was found to be not very critical but should be done more frequently if the sea state spectral distribution is changing rapidly. Re-training every

hour in this application seems a good option considering the computational effort and forecast accuracy gains to be had.

Because of the short forecast horizon requirements of *Instant<sub>RVC</sub>*, the degradation of the performance whilst using a realisable forecast was relatively small. In contrast, the longer forecast horizons required by; *Wave<sub>RVC</sub>*, *Continuous<sub>RVC</sub>* and *Envelope<sub>RVC</sub>* incurred a greater average forecast error. As such a more notable relative reduction in the performance was incurred by these strategies when compared to the hypothetical case considered in chapter 5 where a perfect forecast is available. When using a realisable forecast, *Wave<sub>RVC</sub>* and *Continuous<sub>RVC</sub>* achieved similar performance enhancements, but because the relief valve aperture adjustment system required for *Continuous<sub>RVC</sub>* requires only a small modification to the existing system it is deemed the preferable solution. *Envelope<sub>RVC</sub>* performed the poorest but still showed some desirable performance enhancements. Because it is the only system requiring no modification to the relief valve actuator system, it is the only control system that can be deployed and tested in reality at Pico (within the limitations of this research project), and will be considered further.

## Chapter 7

# Relief valve control field test results and long-term performance projections

### Abstract

The results from field testing of the envelope relief valve control strategy at the Pico OWC are presented. The performance of the plant under *Envelope<sub>RVC</sub>* control was found to be in generally good agreement with model simulations and in some cases a notable enhancement in power production is achieved which coincides with a reduction in the frequency and severity of turbine stall and the associated machine vibrations above the residual levels. The *Continuous<sub>RVC</sub>* and *Instant<sub>RVC</sub>* valve control strategies could not be tested in reality because of the required modifications of the relief valve actuator and because of the current financial and resource limitations associated with the project. A mid-term projection of the performance of: *Basic<sub>RVC</sub>*, *Envelope<sub>RVC</sub>*, *Continuous<sub>RVC</sub>* and *Instant<sub>RVC</sub>* relief valve control is made with a simulation of each strategy in the time domain, driven by real operational data which spans a period of about one month. A sufficient variety of sea states were encompassed in this model input data range to enable a statistical extrapolation in time to estimate the long-term system behaviour under each control strategy over the plant's life time so far. This is then used to assess the long term potential financial gains as well as the performance enhancements and fatigue reductions to be gained from all considered relief valve control strategies.

### 7.1 Introduction

In the chapters 5 and 6, a number of relief valve control strategies were developed using a limited number of example data sets that span a broad range of  $H_s$  sea states but only a narrow range of  $T_p$  values. It was necessary to develop the control strategies using only a small number of short data sets because of the associated computational cost associated with investigating the different variable permutations of the control system and forecast models. Now that the methodology has been refined and optimised parameters have been found, mid-term simulations of high but acceptable computational cost can be performed to investigate the performance of each control strategy under a much broader range of sea state conditions.

Also, and perhaps most importantly, it remains to validate the simulation results with results from real field testing to ensure confidence in the projections. Because of the financial and resource limitations, only *Envelope<sub>RVC</sub>* (and *Basic<sub>RVC</sub>*) can be validated from field testing because these strategies require no modification to the existing relief valve actuator system and *Instant<sub>RVC</sub>* and *Continuous<sub>RVC</sub>* will not be validated. However, because essentially the same model and forecasting method are used in the analysis of all advanced control strategies, the validation of one (*Envelope<sub>RVC</sub>*) in part validates the others. This is true only if the relief valve aperture adjustment rate and response time, as characterised in the models in chapter 5 and 6, can be achieved in reality. This will be particularly questionable for *Instant<sub>RVC</sub>* which requires fast and numerous relief valve actuation cycles to operate effectively.

The final task is to extend the mid-term simulation results, obtained with the system time domain model, to the long-term projections of performance, in order to assess the significance of each control strategy. The computational cost of the time-domain model is too great to execute long term simulation, and in any

case there is not enough operational data available (to drive the model) for this method to be robust against inter-annual variability. As an alternative, long-term projections are made in a statistical way by extrapolating the results from the mid-term simulation to the long-term using the plant's life time chamber sea state occurrence frequency, defined in section 3.4.4, which was found using long-term metocean data.

## 7.2 Mid-term control simulations

To make the mid-term performance simulation, all available data over the time period 09/10/2014 to 26/11/2014 was selected because this spans the autumn period which has a high degree of sea state variability. This data was divided into 30 minute sections providing 1240 unique data sets (26 days in total). The data is fairly continuous in time, having only a few breaks where the machine was off-line for an extended period. However, if any breaks in data occurred, the first 30 minutes of data (after the break) was used to train the forecasting models (where applicable) and perform the spectral analysis, which is used with some of the control strategies for certain parameter selections. The end point of this initial 30 minutes data set was used as the starting conditions for the simulation over the subsequent 30 minutes, and then this first 30 minute of each continues data set was discarded.

The relief valve control strategies:  $Basic_{RVC}$ ,  $Envelope_{RVC}$ ,  $Continuous_{RVC}$  and  $Instant_{RVC}$  were simulated with the time domain model including on-line forecasting, as described in chapter 6. The calculated wave excitation flow from the plant data was used as the input to drive all models. The model parameters that needed to be specified had the following values:

- For  $Basic_{RVC}$ , the standard deviation of non-dimensional  $\sigma(\Psi)$  was evaluated every 15 minutes and if it was found that  $\sigma(\Psi) < 0.048$  the relief valve aperture would be decreased by 5% in order to increase  $\sigma(\Psi)$  over the next 15 minute period, and vice versa if  $\sigma(\Psi) > 0.052$  where the relief valve aperture was increased by 5%. This was done to try to continuously converge with  $\sigma(\Psi) \approx 0.05$ , This process was repeated throughout the duration of the simulation.
- For  $Envelope_{RVC}$ ,  $Continuous_{RVC}$  and  $Instant_{RVC}$  the autoregressive forecast model was trained using the half hour data set that preceded the data set that was being used in the simulation, to reflect the model training procedure that can be achieved in reality.
- For  $Envelope_{RVC}$  the forecast horizon length of  $\Gamma = T_p$  was used (as this was found to be approximately optimal in sections 5.4.5 and 6.7.4) in the model control algorithm to assess and attempt to optimise  $\sigma_{T_p}(\Psi)$ .  $T_p$  was found from the spectral analysis of the data set that preceded the data set that was being used in the simulation to reflect the control procedure in reality.
- For  $Continuous_{RVC}$  the horizon length of  $\Gamma = T_p/2 - 1$  was used (as this was found to be approximately optimal in sections 5.4.4 and 6.7.3) in the model control algorithm to assess and attempt to optimise  $\bar{\Pi}_\Gamma$ . Again  $T_p$  was found from the spectral analysis of the data set that preceded the data set that was being used in the simulation to reflect the control procedure in reality.

### 7.2.1 Mid-term simulation results

The characteristics of chamber hydrodynamics (which are equal between all simulations for the different control strategies) as described by the following parameters for each half hour data set is given in figure 7.1;

- Significant wave height in the chamber calculated from the excitation surface elevation  $H_s$
- Peak wave period in the chamber calculated from the excitation surface elevation  $T_p$
- Tide elevation calculated from the measured chamber surface elevation  $\bar{\eta}$

The system performance under the different relief valve control strategies is characterised by the following parameters and this is given in figures 7.2, 7.3 and 7.4;

- Mean electrical power take-off  $\bar{P}_e$
- Percentage of time spent in excess of the stall severity levels  $\Psi > [0.068, 0.1, 0.125, 0.15, 0.175]$
- Mean vibrations above the residual at the generator side  $\bar{V}_G$  chamber side  $\bar{V}_c$ , turbine shaft bearing

In addition to the following parameters of interest are evaluated and these are given in figure 7.5;

- Mean relief valve state  $\bar{k}_v$
- Number of full relief valve cycles per hour  $k_v^{-hr}$
- Mean forecast goodness of fit over the horizon range  $\Gamma$  (where applicable)  $\overline{GOF}$

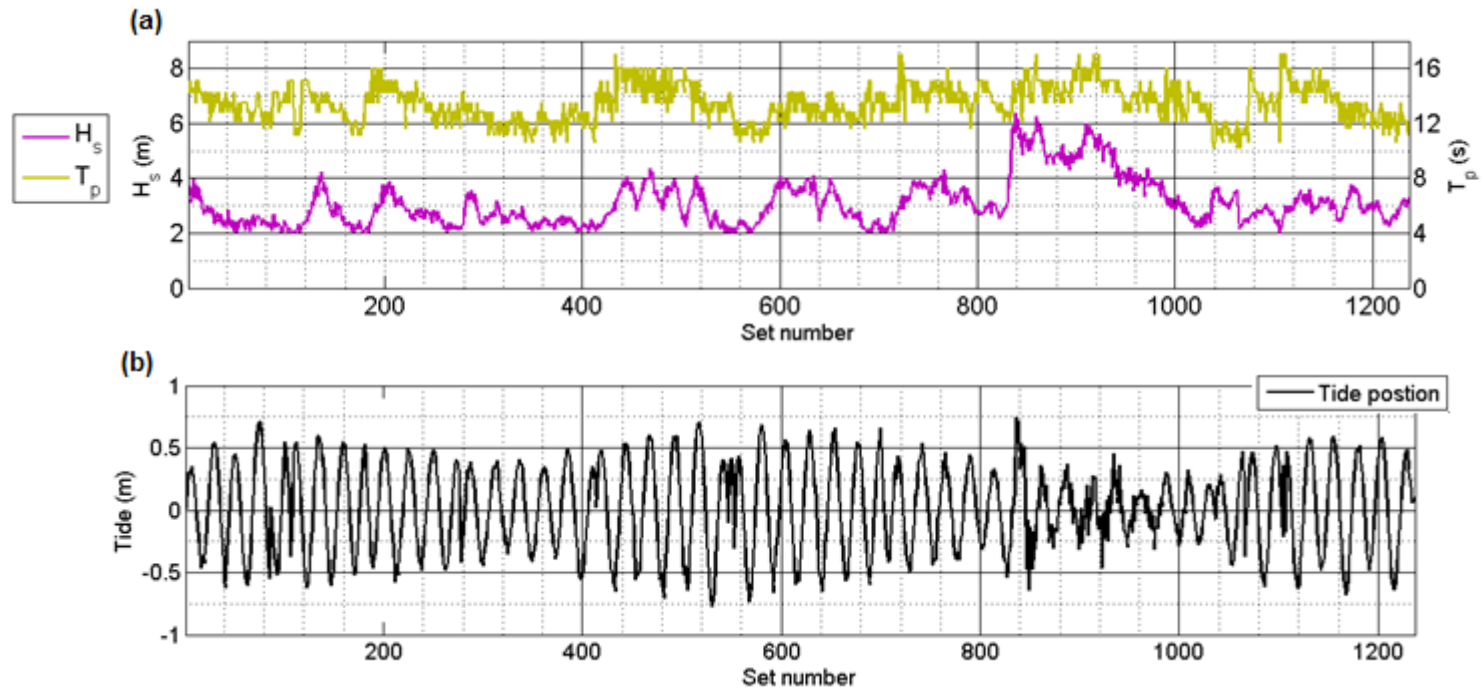


**Figure 7.1** (a) Chamber significant wave height and peak period (from calculated excitation chamber surface elevation), (b) recorded tidal elevation.

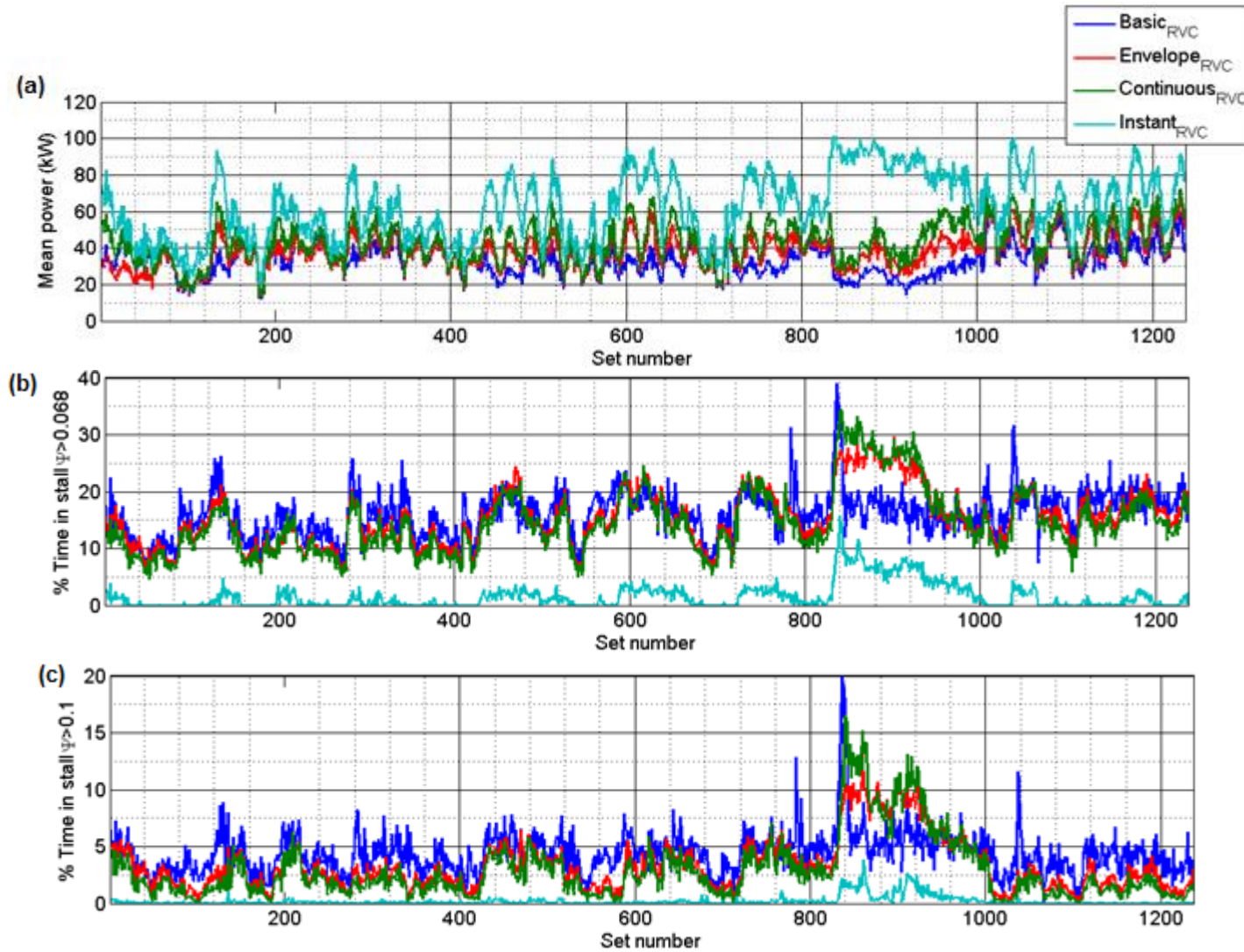


**Figure 7.2** (a) Mean power take-off, (b) % time spent in stall band  $|\Psi| > 0.067$ , (c) % time spent in stall band  $|\Psi| > 0.1$ , from simulations for the different control strategies.

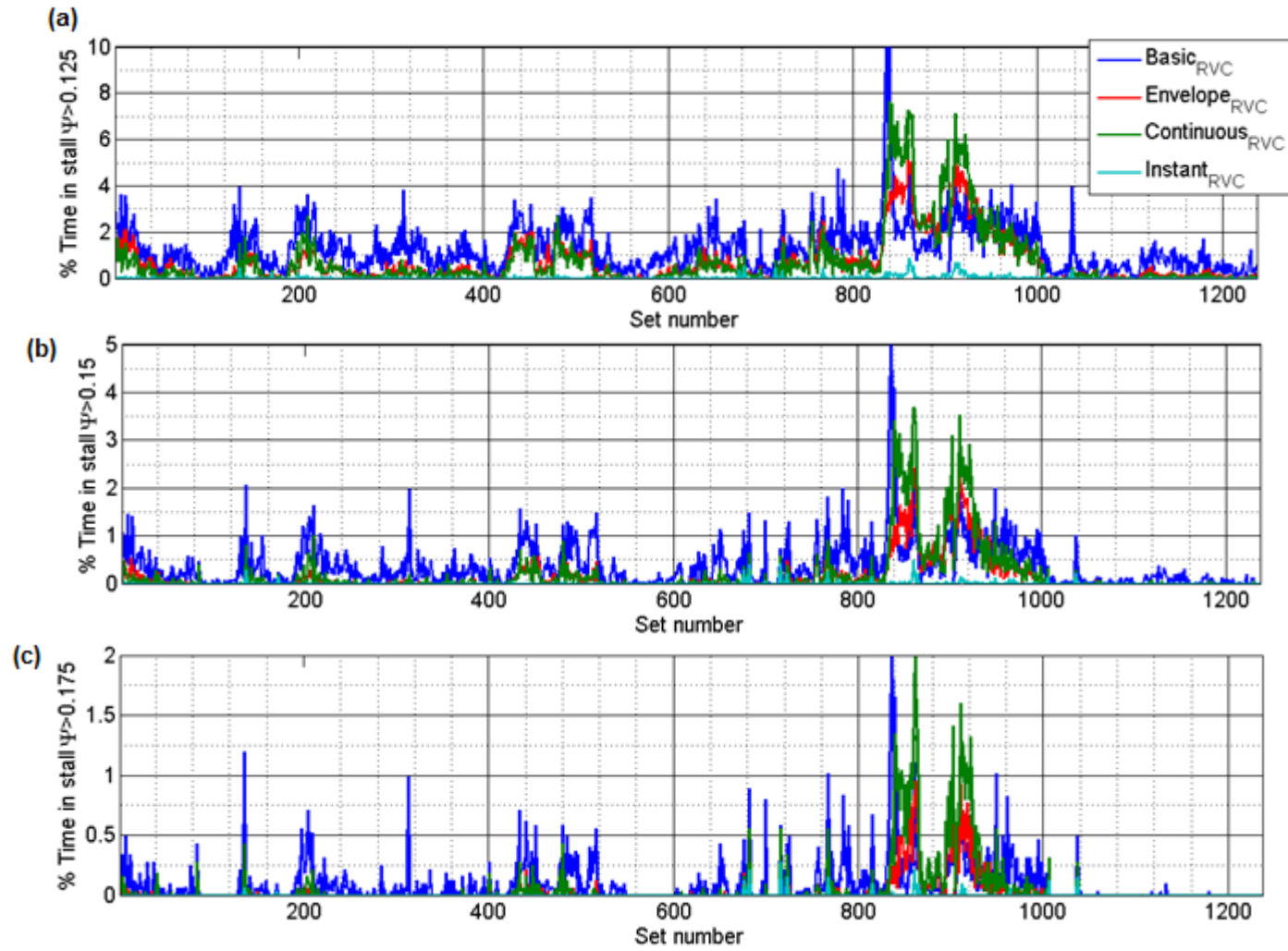


**Figure 7.3** (a) % time spent in stall band  $|\Psi| > 0.125$ , (b) % time spent in stall band  $|\Psi| > 0.15$ , (c) % time spent in stall band  $|\Psi| > 0.175$ , from simulations for the different control strategies.

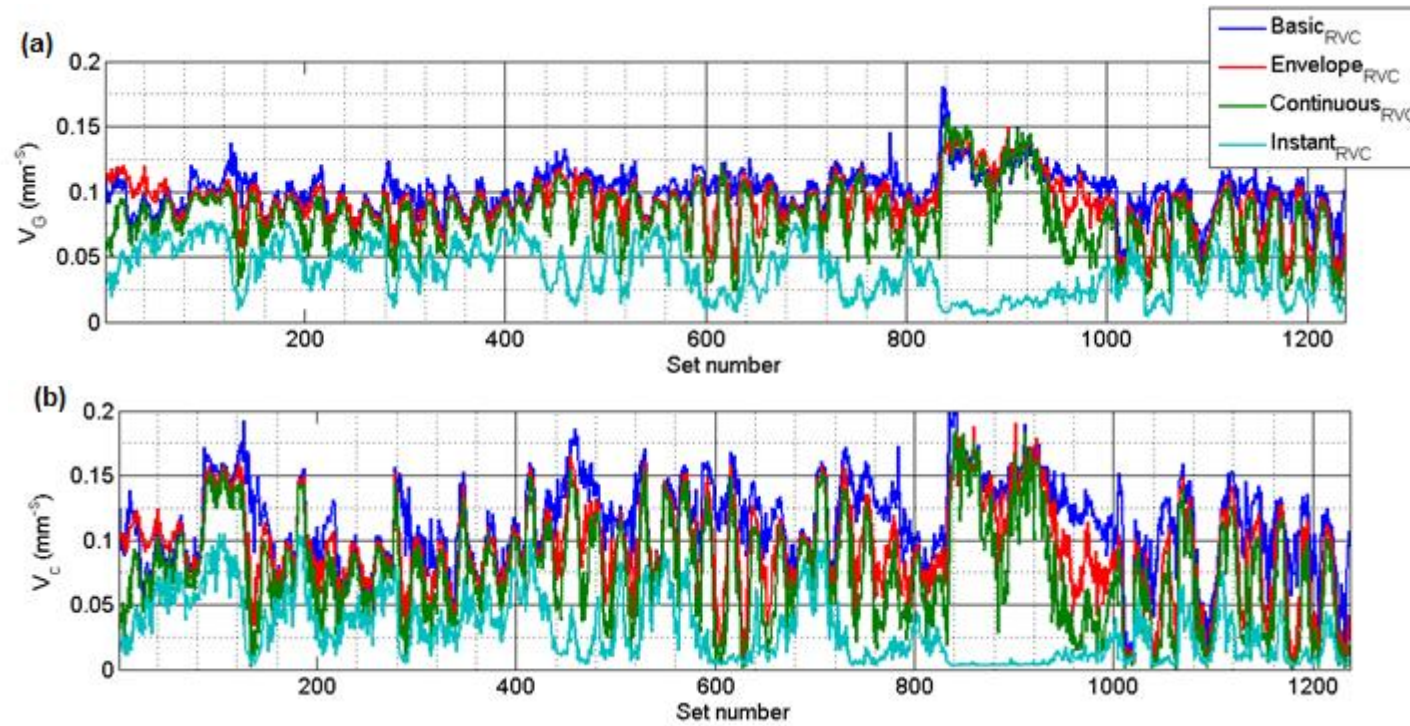


**Figure 7.4** (a) mean vibrations above the residual at generator side shaft bearing, (b) mean vibrations above the residual at chamber side shaft bearing, from simulations for the different control strategies.

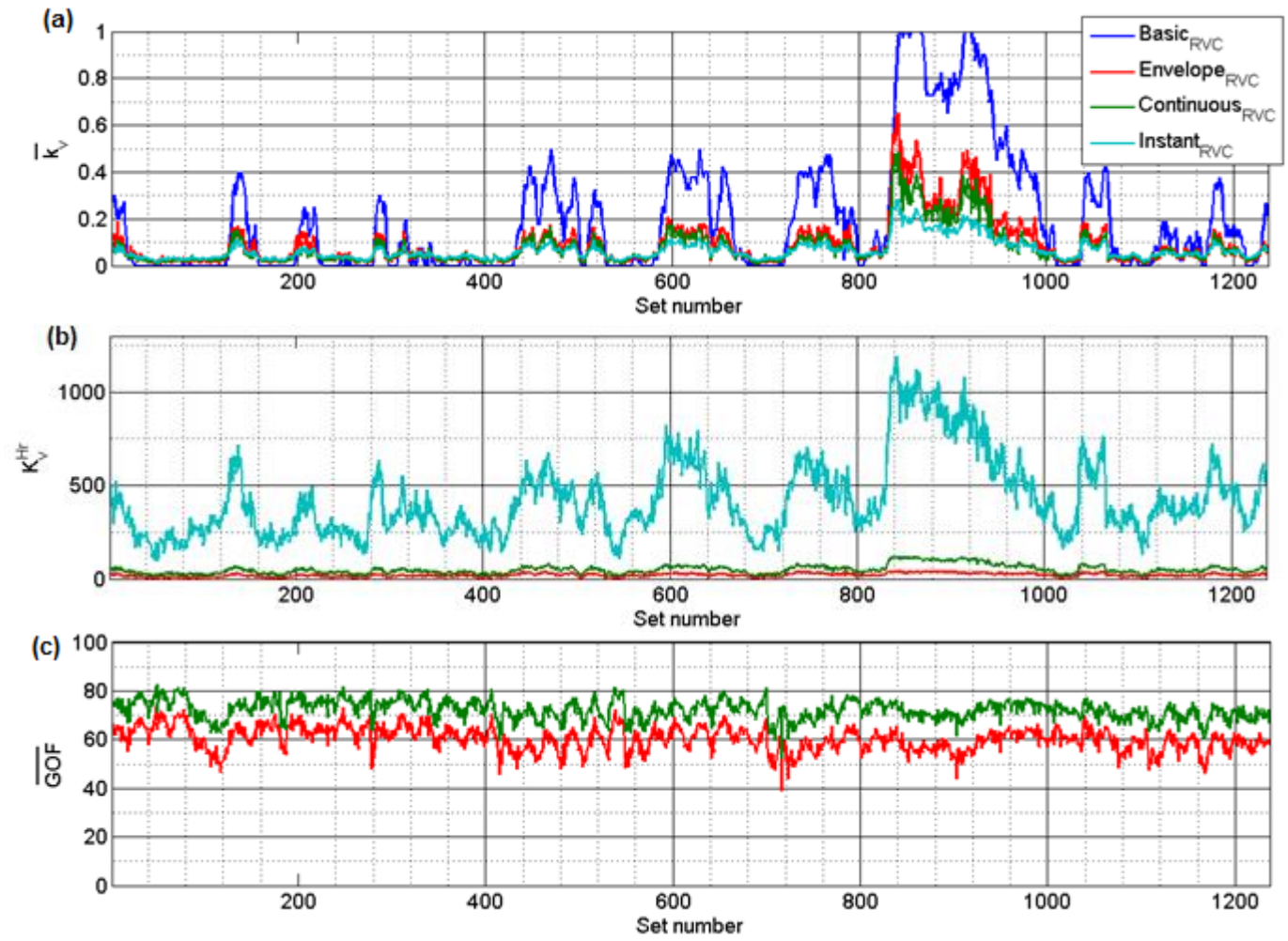


**Figure 7.5** (a) Mean relief valve aperture state, (b) number of full relief valve transit cycles per hour, (c) mean forecast goodness of fit over forecast horizon length, from simulations for different control strategies.

As expected, the performance of *Instant<sub>RVC</sub>* is far superior to the other control strategies with *Continuous<sub>RVC</sub>* slightly out-performing *Envelope<sub>RVC</sub>*. What was not anticipated is that there appears to be an upper limit in the effectiveness of *Continuous<sub>RVC</sub>* and *Envelope<sub>RVC</sub>*, because during the period of very high energy sea states less significant increases in power production were achieved and this was at the expense of a significant increase in stall frequency and severity. Clearly, during these very high energy periods the surface elevation variance was so great that the rate of aperture adjustment could not keep up with the wave energy envelope. Also this period of high variance resulted in a lower performance of the forecast model projection, which will reduce the accuracy of the control decisions. Also, it was not anticipated how strongly the tidal elevation would affect the relative performance of each control strategy. At lower tide levels and in higher energy sea states *Continuous<sub>RVC</sub>* and *Envelope<sub>RVC</sub>* only marginally outperform *Basic<sub>RVC</sub>* (in terms of power take-off and vibration levels), whereas at higher tide the difference (improvement) can be quite significant.

Firstly, it is noted that the forecast  $\overline{GOF}$  reduces with lower tidal elevations. This is likely to be, in part, a response to the defect in the chamber front wall which opens the chamber to the atmosphere during a wave trough and modifies the chamber pressure profile (used to calculate the excitation flow) as described in section 3.6. This occurs more frequently and more severely at lower tides and / or high wave amplitude and the result is that the calculated excitation flow will appear to be more nonlinear and erratic and therefore harder to forecast, and this results in poorer control performance. Also the shoaling effect strengthens at lower tidal elevations and wave breaking is more likely to occur, which will enhance the excitation flow variability and degree of nonlinearity, making it harder to forecast.

The increase in wave shoaling results in a chamber pressure profile that has a shorter and sharper positive pressure head and a longer and blunter negative pressure head. This asymmetry gets stronger as the mean water depth decreases. To illustrate the impact of wave shoaling and the limitations this imposes on control performance, an extreme case is considered where two waves are synthesised, one is a pure sinusoid (un-shoaled) and the other is a strongly asymmetrical sinusoid (shoaled wave). The resulting chamber pressure, absolute non-dimensional pressure and power transfer to the turbine are simulated and this is shown in figure 7.6. As can be seen in figure 7.6, for the pure sinusoid (un-shoaled) case, when the pressure is damped with relief valve control, an equal increase in power transfer to the turbine results for both the inhalation and exhalation half wave cycles. In contrast, in the case of the shoaled wave, whilst an increase in power transfer to the turbine occurs on the exhalation half wave cycle, which is attained by damping the chamber pressure to avoid over-pressure, a decrease in power transfer to the turbine occurs over the inhalation half wave cycle because of under-pressure. Ultimately this means relief valve control by *Envelope<sub>RVC</sub>* is less effective when wave shoaling is stronger, because the cancellation is stronger. This is also true for *Continuous<sub>RVC</sub>* but to a lesser extent because this strategy attempts to optimise the pressure over a half wave cycle, which would counteract this effect. However, because of the aperture limited adjustment rate of the valve the effectiveness is also limited for heavily shoaled waves which requires a rapid change in aperture to properly influence the pressure profile over each half wave cycle

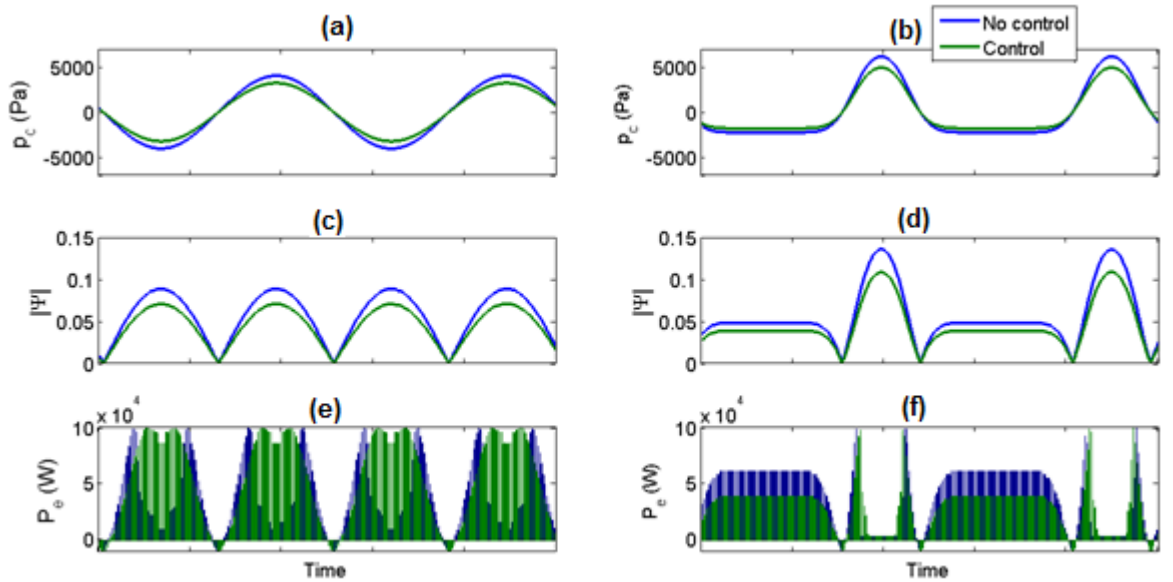


**Figure 7.6** (a, c, e) Un-shoaled wave (b, d, f) shoaled wave, (a, b) chamber pressure, (c, d) absolute non-dimensional chamber pressure, (e, f) power transfer to the turbine. Inspection of the effect of wave shoaling and asymmetry on the performance of the  $Envelope_{RVC}$  and  $Continuous_{RVC}$ .

The stall frequency and severity is found not to be significantly affected by tidal elevation and all control strategies generally achieve a significant reduction with  $Instant_{RVC}$  performing exceptionally well.

The performance from the mid-term simulations in terms of mean power production over each unique sea state bin, under each relief valve control strategy, is summarised by the power matrices in figure 7.7. The total mean values for all the system variables of interest, is given in table 7.1. This is in addition to the percentage difference between the advanced control strategies and  $Basic_{RVC}$  which is given in table 7.2. As discussed before there appears to be an upper limit (dependent on  $H_s$ ) to the effectiveness of  $Envelope_{RVC}$  and  $Continuous_{RVC}$ . As  $H_s$  increases the wave envelope variance becomes greater and the current relief valve adjustment rate is too slow to match this rate of change. As such the plant performance under  $Envelope_{RVC}$  and  $Continuous_{RVC}$  does not continue to increase with incident wave energy past a certain threshold which is approximately  $H_s > 3.5$  (m), unlike  $Instant_{RVC}$ .

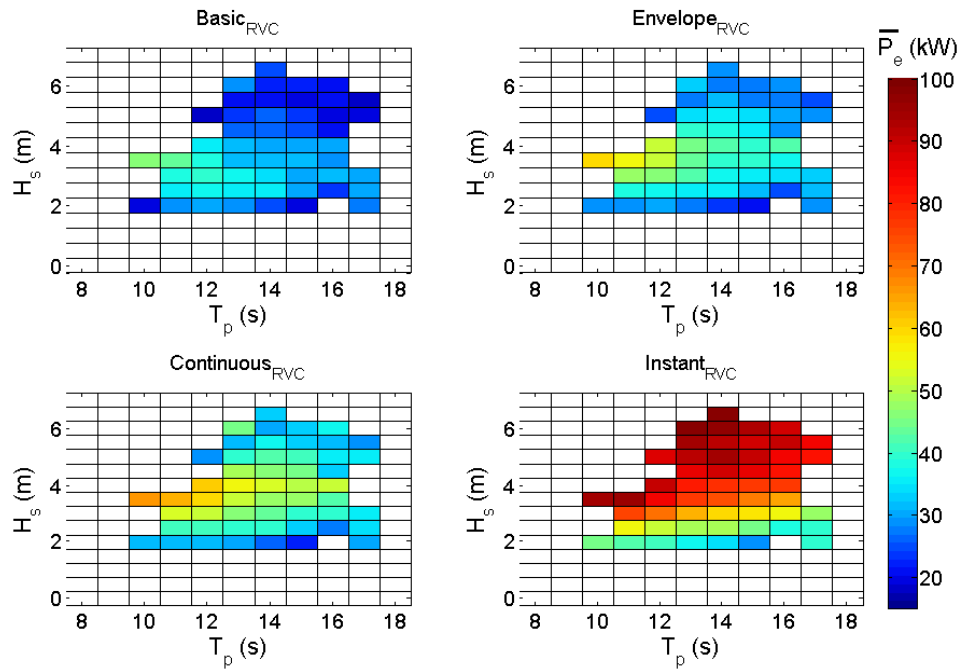


**Figure 7.7** Power matrix summarising the performance of each control strategy in terms of mean power take-off achieved in each unique sea state.

**Table 7.1** Total mean values of different performance parameters under the considered control strategies from the mid-term simulation results

	$\bar{P}_e$ (kW)	$\Psi > 0.068$ (% time)	$\Psi > 0.1$ (% time)	$\Psi > 0.125$ (% time)	$\Psi > 0.15$ (% time)	$\Psi > 0.175$ (% time)	$\bar{V}_G$ ( $mms^{-1}$ )	$\bar{V}_c$ ( $mms^{-1}$ )
<i>Basic<sub>RVC</sub></i>	32.8	15.92	4.28	1.25	0.34	0.08	0.100	0.11
<i>Envelope<sub>RVC</sub></i>	37.9	15.13	3.24	0.70	0.15	0.03	0.091	0.092
<i>Continuous<sub>RVC</sub></i>	42.8	14.44	2.83	0.71	0.19	0.06	0.079	0.073
<i>Instant<sub>RVC</sub></i>	62.2	1.53	0.19	0.02	0.00	0.00	0.038	0.028

**Table 7.2** Total mean values of different performance parameters under the considered advanced control strategies from the mid-term simulation results, as a percentage of the mean values achieved with *Basic<sub>RVC</sub>*.

% Difference vs <i>Basic<sub>RVC</sub></i>	$\bar{P}_e$ (kW)	$\Psi > 0.068$ (% time)	$\Psi > 0.1$ (% time)	$\Psi > 0.125$ (% time)	$\Psi > 0.15$ (% time)	$\Psi > 0.175$ (% time)	$\bar{V}_G$ ( $mms^{-1}$ )	$\bar{V}_c$ ( $mms^{-1}$ )
<i>Envelope<sub>RVC</sub></i>	+15.4	-4.93	-24.35	-43.74	-56.80	-59.42	-9.310	-18.28
<i>Continuous<sub>RVC</sub></i>	+30.7	-9.28	-33.90	-43.20	-43.85	-28.08	-21.425	-34.767
<i>Instant<sub>RVC</sub></i>	+89.3	-90.42	-95.62	-98.26	-100	-100	-61.702	-74.767

## 7.3 Field tests and results

To validate the simulations of relief valve control, *Envelope<sub>RVC</sub>* was deployed at the Pico OWC and the format of these field tests and the results are presented in this section.

### 7.3.1 Implementation of the relief valve control system

For long term use the relief valve control system would benefit from a dedicated programmable logical controller which would increase response speed and overall stability. However, due to the

financial and resource limitations the relief valve control system was implemented in rudimentary way for short term testing and the method used is described in the following and presented as a process diagram in figure 7.8.

At the point of initialising the  $Envelope_{RVC}$  control algorithm, the most recent 1 hour of plant data is imported into MATLAB® where training of the autoregressive forecast model is made. If control was to be made over a period longer than 1 hour a second routine was set to run automatically in parallel to the main control algorithm to update the autoregressive model coefficients using the most recently obtained system data so that the forecast model reflects the most recent sea state spectra. In addition a spectral analysis was performed using the training data to characterise the chamber sea state. The chamber sea state peak period was then recorded for use in the main control algorithm to optimise the forecast horizon time used to evaluate the standard deviation of non-dimensional pressure. This is the parameter which the relief valve strategy is attempting to optimise and is used in the limits of the control action.

At the Pico plant data is captured using the DAQ-factory data acquisition suite, which is fed with data from a labjack analogue to digital converter. Because the DAQ-factory suite is rather limited in its options for on-line data processing, a routine was implemented to write (to file) short segments of the most recent data history having length equal to the autoregressive model order. This process was performed at a frequency of 2Hz. The data was then imported into the MATLAB® programming suite where the short-term forecast of wave excitation flow and chamber pressure was made using the pre-trained autoregressive model. In addition, the relevant processing required to make the relief valve control decision was performed in this phase. The control action (open, close or hold) is then written to file and imported back into DAQ factory. Digital to analogue conversion is instructed by DAQ factory and the labjack then provides the voltage signals that actuate the relays directing the hydraulic pump that feeds the relief valve aperture adjustment ram. A process diagram describing this sequence is seen in figure 7.8.

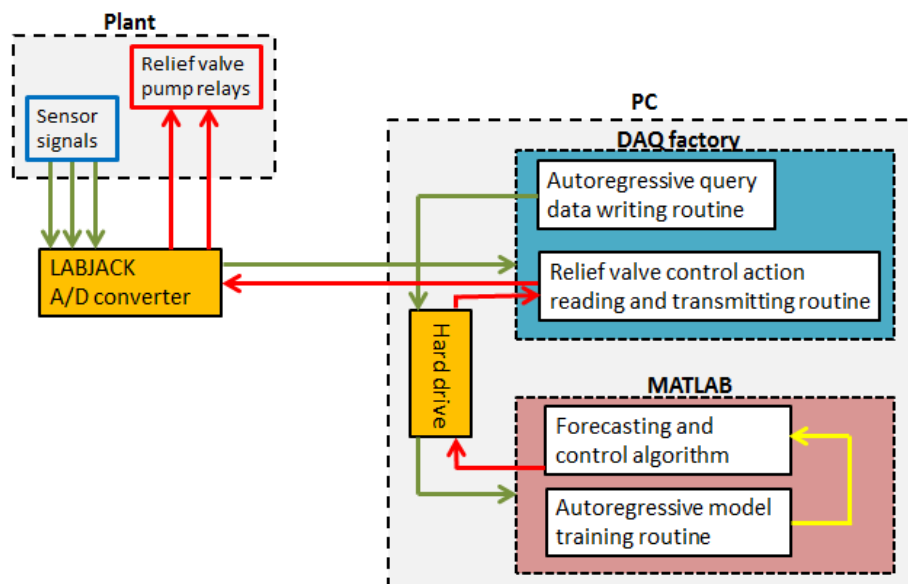


**Figure 7.8** Process diagram showing the transit of analogue system sensor signals being digitised and passed to the processing suite to make the forecast and choose the control action and finally conversion back to analogue to actuate the control action.

This forward and backward pass of data between the two data processing suits resulted in up to 0.5 (s) of lost time in the forecast horizon which was not accounted for in the control system evaluation made in chapters 5-7, or indeed in any of the simulations. Also the PC at the plant that was used to perform the online forecast, was not as powerful as the PC that was used to make the simulations in chapters 5-7. Although computational time was factored into the simulation made in chapters 5-7, for field tests this time was found to be greater because of the lower frequency CPU of the plant PC and this resulted in an additional processing delay of approximately 0.2 - 0.5 (s), which again is lost time in the forecast horizon. The implication of these additional delays needs evaluating and this is performed in section 7.3.5.

### 7.3.2 Relief valve control testing procedure

To evaluate the performance of *Envelope<sub>RVC</sub>* the control strategy was deployed alternately with *Basic<sub>RVC</sub>*, so that *Envelope<sub>RVC</sub>* was deployed for 1 hour 15 minutes and this was followed immediately by one hour and 15 minutes of *Basic<sub>RVC</sub>* control, and this sequence was repeated. The alternation between *Envelope<sub>RVC</sub>* and *Basic<sub>RVC</sub>* test periods would be continued for as long as possible and would only be terminated if there was an issue with the plant that affected the data or timing integrity of the test series. Tests would also be terminated if the author, who was conducting the tests sequence (alone), had to leave the plant site for any reason, because the control system had not yet been tested to an adequate level to leave unattended with sufficient confidence. The last one hour of data of each sub-test of the two different control strategies was then logged and used for the results. The first 15 minutes of each subtest was discarded as this time was considered to be a generous transition period between the two routines, allowing the system to settle into the new mode of control. With this testing structure, the system performance under *Envelope<sub>RVC</sub>* could be directly compared and validated by the system performance resulting from *Basic<sub>RVC</sub>*, with the sea state conditions being very similar between the alternating tests.

Initially the optimisation limits of  $0.04 < \sigma_r(\Psi) < 0.06$  were set for *Envelope<sub>RVC</sub>*, which matches the simulation methodology in sections 5.4.5 and 6.7.4. The first *Envelope<sub>RVC</sub>* control test was performed in a high energy sea state, which incurred a high number of relief valve aperture adjustments. This caused the relief valve hydraulic pump to overheat and the pump electrically isolated itself as part of its protection mechanism. Fortunately it was not damaged but it meant, rather disappointingly, that the optimisation range had to be broadened to  $0.03 < \sigma_r(\Psi) < 0.06$  so as to reduce the relief valve aperture adjustment frequency. The result of this change is that the relief valve closes later when a temporal period of lower incident wave energy occurs. This is a further deviation from the simulation in sections 5.4.5 and 6.7.4 and the implication of this change requires evaluation and this is given in section 7.3.5. However, this adjustment resolved the overheating issue which did not occur again. The originally considered optimisation limits could be restored by installing a more robust hydraulic pump or cooling system.

In total 11 test periods were conducted and these covered a reasonably broad range of sea state condition as seen in appendix E table E1. It was hoped that enough test periods would be conducted to essentially encompass the full wave climate spectra at the Pico plant site, but unfortunately during the window of opportunity for testing the generator suffered a major short circuit due to the accumulation of carbon dust from the brushes, which caused a bridge across the rectifier poles. The short circuit resulted in significant

damage to the isolation material in the generator and diodes and significant intervention was required to correct the issue. This put the machine out of action for the remainder of the available testing period.

### 7.3.3 Field test results from valve control

Field testing of *Envelope<sub>RVC</sub>* was executed towards the end of 2014. An extra ordinary effort spanning several years was needed to: recover the previously damaged and non-functional machine, resolve the numerous and significant issues that followed, deal with data quality and delay issues and implement a relief valve control system just to get to the point at which field testing could be conducted. The effort required to achieve this should not be underestimated, particularly when compared to the relative ease at which similar tests might be conducted under laboratory conditions.

The results from field testing of the *Envelope<sub>RVC</sub>* (green rows) and *Basic<sub>RVC</sub>* (blue rows), control strategies is presented in appendix E, which provides the mean values and percentage differences of the following parameters used to evaluate the system performance under the two control strategies;

- Standard deviation of non-dimensional chamber pressure  $\sigma(\Psi)$  (where *Basic<sub>RVC</sub>* is instructed to try to achieve  $\sigma(\Psi) = 0.05$  and *Envelope<sub>RVC</sub>* has no resections)
- Mean relief valve aperture state  $\bar{k}_v$
- Mean electrical power take-off  $\bar{P}_e$
- Percentage of time spent in excess of the stall severity levels  $\Psi > [0.068, 0.1, 0.25, 0.15, 0.175]$
- Mean vibrations above the residual at the generator side  $\bar{V}_G$  chamber side  $\bar{V}_c$ , turbine shaft bearing
- Significant wave height in the chamber calculated from the excitation surface elevation  $H_s$
- Peak wave period in the chamber calculated from the excitation surface elevation  $T_p$
- Mean tidal elevation calculated from the recoded chamber surface elevation

The field tests results given in appendix table E1 are summarised in table 7.3, but it should be remembered that control was conducted over a relatively small range of sea states and as such will be only partially representative of the long term performance from control.

**Table 7.3** Summary of mean values of system parameters resulting from *Envelope<sub>RVC</sub>* and *Basic<sub>RVC</sub>* with the percentage difference between them.

	$\bar{P}_e$ (kW)	$\Psi > 0.068$ (% time)	$\Psi > 0.1$ (% time)	$\Psi > 0.125$ (% time)	$\Psi > 0.15$ (% time)	$\Psi > 0.175$ (% time)	$\bar{V}_G$ ( $\text{mms}^{-1}$ )	$\bar{V}_c$ ( $\text{mms}^{-1}$ )
<i>Envelope<sub>RVC</sub></i>	38.5	11.19	3.05	0.99	0.21	0.03	0.080	0.070
<i>Basic<sub>RVC</sub></i>	34.9	11.73	3.32	1.18	0.33	0.08	0.087	0.083
% Differece	+10.2	-4.62	-8.11	-16.14	-36.39	-66.85	-8.81	-15.39

### 7.3.4 Comparison of simulations with field results

In order to validate the performance of *Envelope<sub>RVC</sub>* projected by the simulations in section 7.2, a comparison between the simulated and real field test results of *Envelope<sub>RVC</sub>* needs to be made. This will also help to enhance the confidence in the performance projections of *Continuous<sub>RVC</sub>* and *Instant<sub>RVC</sub>*

because the forecasting model, and essentially the same wave to wire model, is used in the analysis of the different control strategies.

It was found in section 7.2 from simulations, that the performance of the *Envelope<sub>RV</sub>* (and the other strategies) in terms of: mean power take-off, mean vibrations above the residual and the total number of relief valve cycles, is more significantly affected by tidal elevation than previously identified and this was an oversight when developing the relief valve control strategy methodology. This is primarily the result of wave asymmetry for the reasons discussed in section 3.6 and section 7.2. In contrast, stall frequency and severity is seen to not be affected significantly by tidal elevation.

As such, the results from each 1 hour field test period were collated in different ways. For: mean power take-off, mean vibrations above the residual and the total number of relief valve cycles, data is divided into data bins based on  $H_s$ ,  $T_p$  and tidal elevation, in the data bin intervals 0.5 (m), 1 (s) and 0.5 (m), respectively.

Because stall frequency and severity was found to be only marginally influenced by tidal elevation, the percentage time spent in excess of the different stall severity levels was divided into data bins based on  $H_s$  and  $T_p$  only (with the same data bin interval), because this results in a greater number of data point matches between real tests and the simulations.

All field data collated into the different data bins was averaged in order to make the comparison with the simulations.

Because of the variability in performance associated with tidal elevation, the forecast model performance and because field test were cut short meaning *Envelope<sub>RV</sub>* was used in only a limited number of sea states, this statistical analysis will be limited.

As such, it was decided to compare and validate *Envelope<sub>RV</sub>* in two formats. Firstly, a time-series is given which can be used to visualise the trend with the change in sea state and perhaps most importantly, with the change in the tidal elevation. Secondly, a comparison is made using a statistical matrix, which is the common practice, to analysis the performance response of control to the sea state characteristics only. This omits the influence of tide, which is important for: mean power take-off, mean vibrations above the residual and the total number of relief valve cycles, because to include this would require a 4D graph, which was found to be hard to interpret because of the limited number of data points. As such, the matrix for these parameters does not give the full picture and should be considered with a degree of cautiousness, whereas the matrices for stall frequency and severity do not have the same strength of limitation (because of the low influence of tidal elevation).

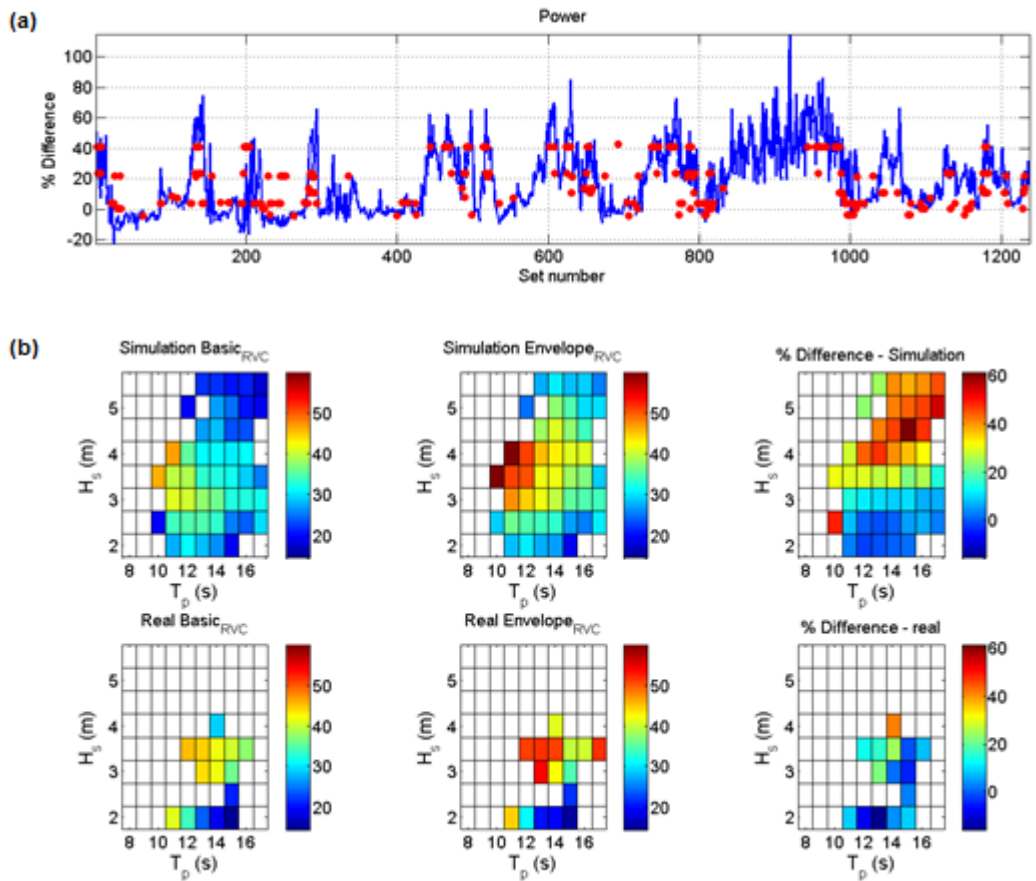


**Figure 7.9** Mean power take-off. (a) Percentage difference between  $Envelope_{RVC}$  and  $Basic_{RVC}$  for (blue line) simulations and (red dots) field test results (averaged over the sea state bin intervals). (b) Matrices of absolute values and the percentage difference between control strategies.

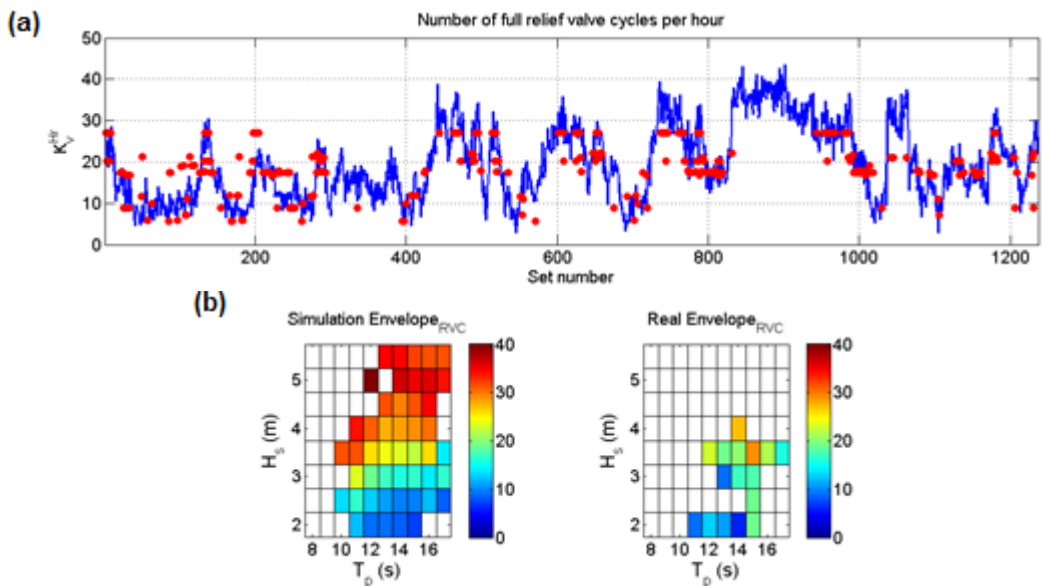


**Figure 7.10** Number of full relief valve cycles per hour. (a) Percentage difference between  $Envelope_{RVC}$  and  $Basic_{RVC}$  for (blue line) simulations and (red dots) field test results (averaged over the sea state bin intervals). (b) Matrices of absolute values and the percentage difference between control strategies.

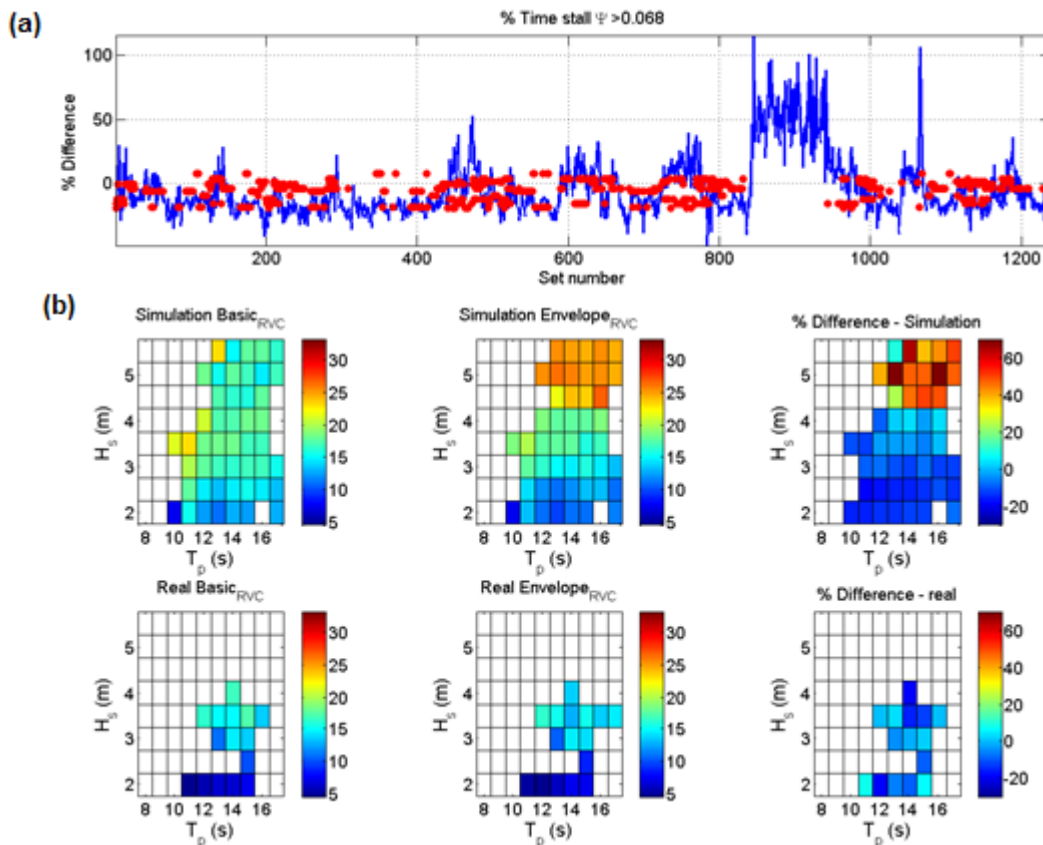


**Figure 7.11** % time in stall band  $|\Psi| > 0.068$ . (a) Percentage difference between  $Envelope_{RVC}$  and  $Basic_{RVC}$  for (blue line) simulations and (red dots) field test results (averaged over the sea state bin intervals). (b) Matrices of absolute values and the percentage difference between control strategies.

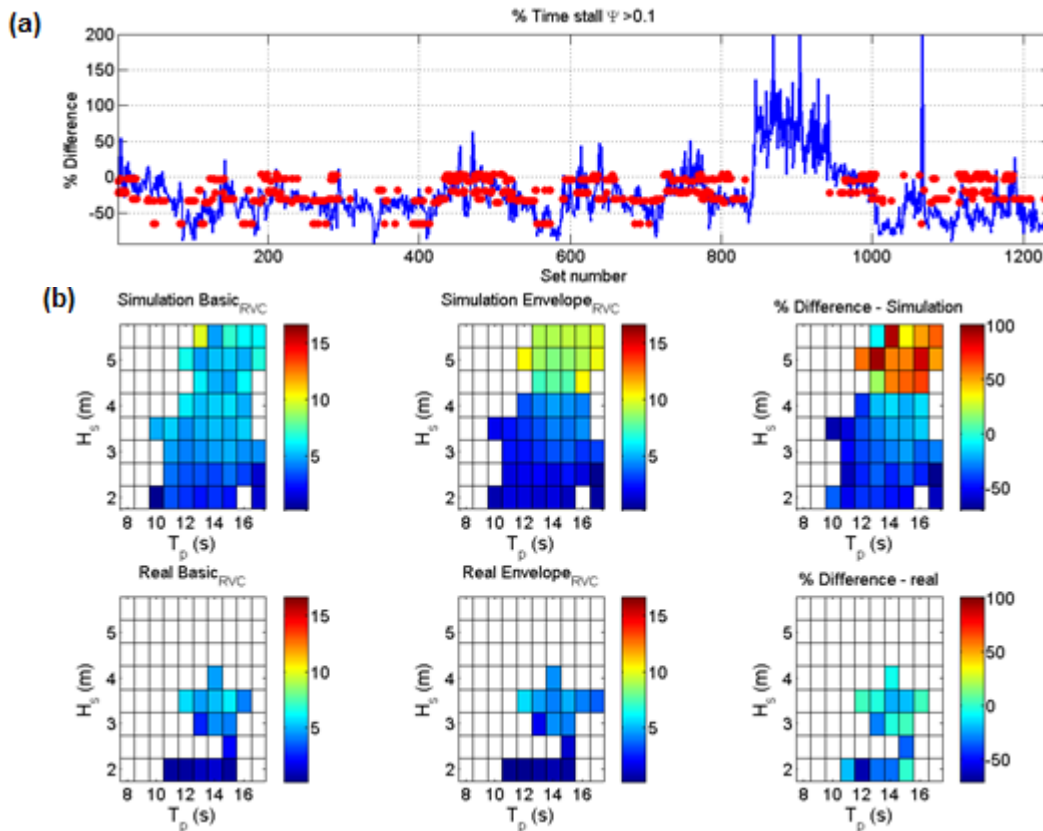


**Figure 7.12** % time in stall band  $|\Psi| > 0.1$ . (a) Percentage difference between  $Envelope_{RVC}$  and  $Basic_{RVC}$  for (blue line) simulations and (red dots) field test results (averaged over the sea state bin intervals). (b) Matrices of absolute values and the percentage difference between control strategies.

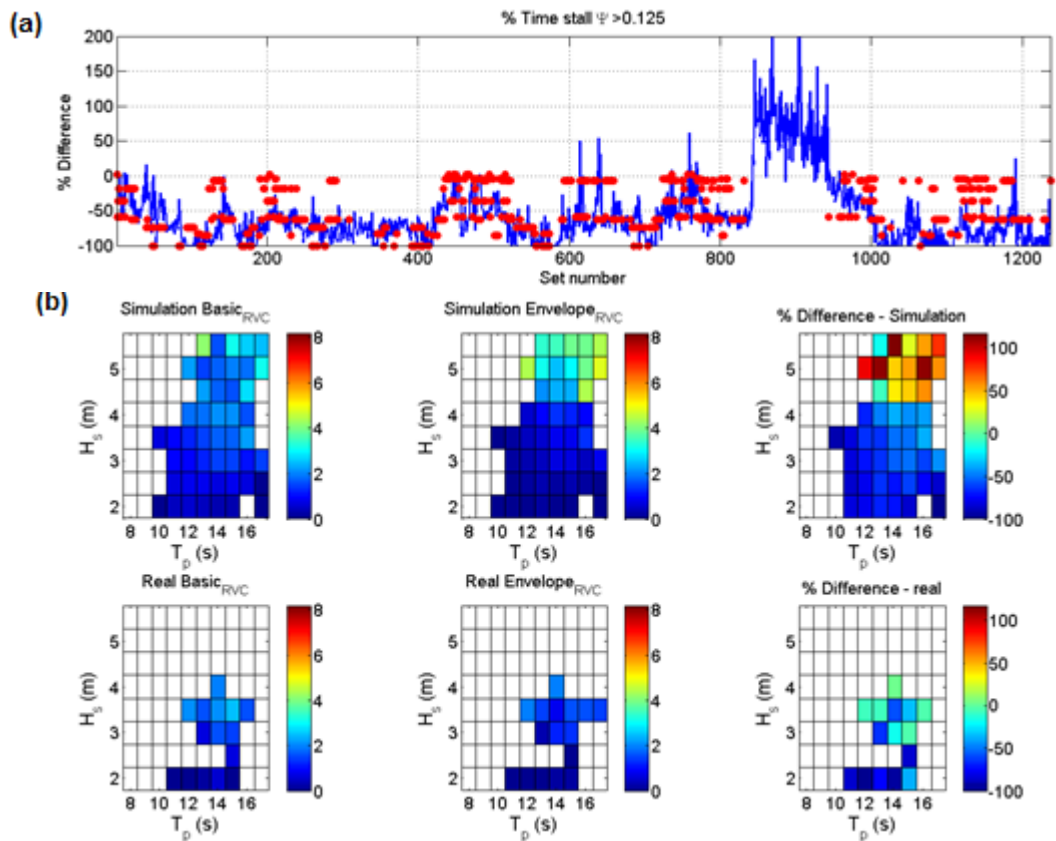


**Figure 7.13** % time in stall band  $|\Psi| > 0.125$ . (a) Percentage difference between  $Envelope_{RVC}$  and  $Basic_{RVC}$  for (blue line) simulations and (red dots) field test results (averaged over the sea state bin intervals). (b) Matrices of absolute values and the percentage difference between control strategies.

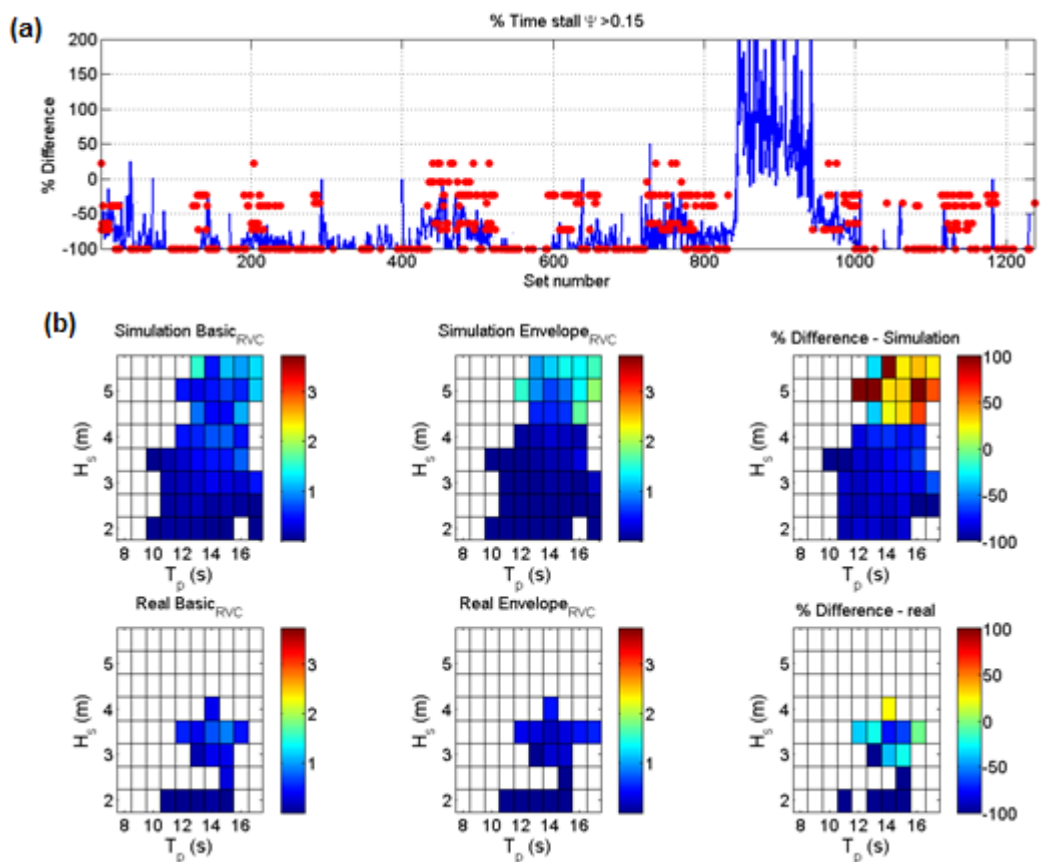


**Figure 7.14** % time in stall band  $|\Psi| > 0.15$ . (a) Percentage difference between  $Envelope_{RVC}$  and  $Basic_{RVC}$  for (blue line) simulations and (red dots) field test results (averaged over the sea state bin intervals). (b) Matrices of absolute values and the percentage difference between control strategies.

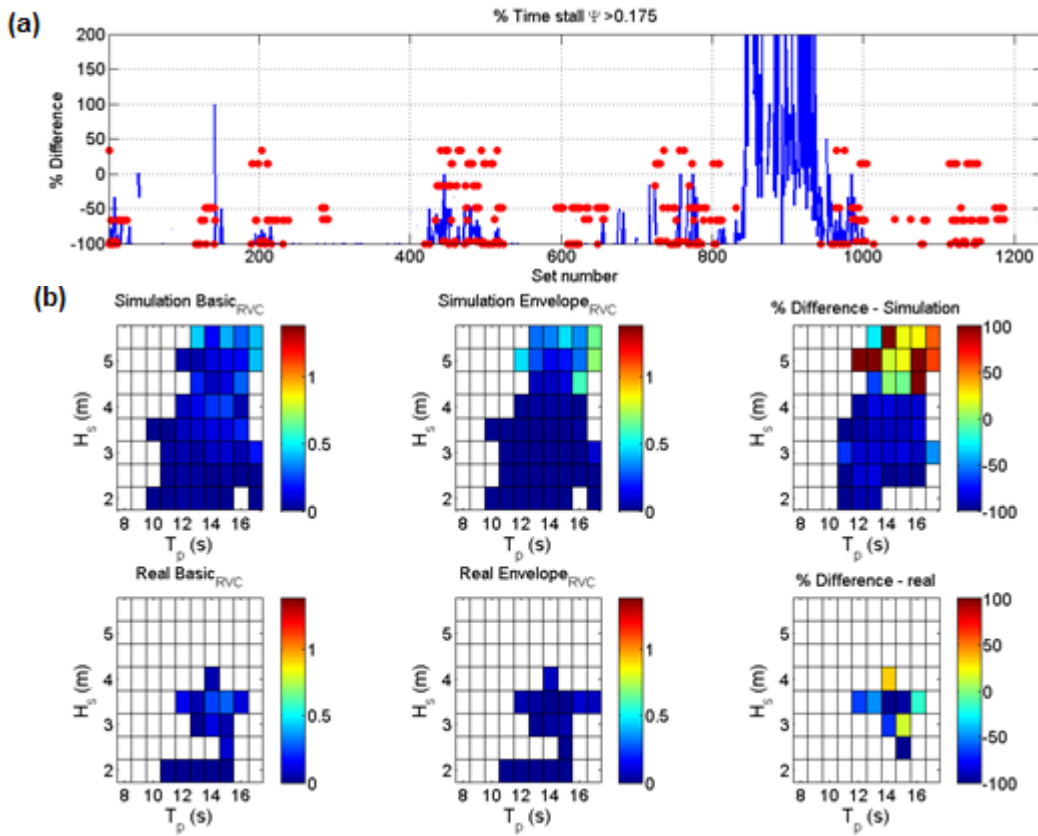


**Figure 7.15** % time in stall band  $|\Psi| > 0.175$ . (a) Percentage difference between  $Envelope_{RVC}$  and  $Basic_{RVC}$  for (blue line) simulations and (red dots) field test results (averaged over the sea state bin intervals). (b) Matrices of absolute values and the percentage difference between control strategies.

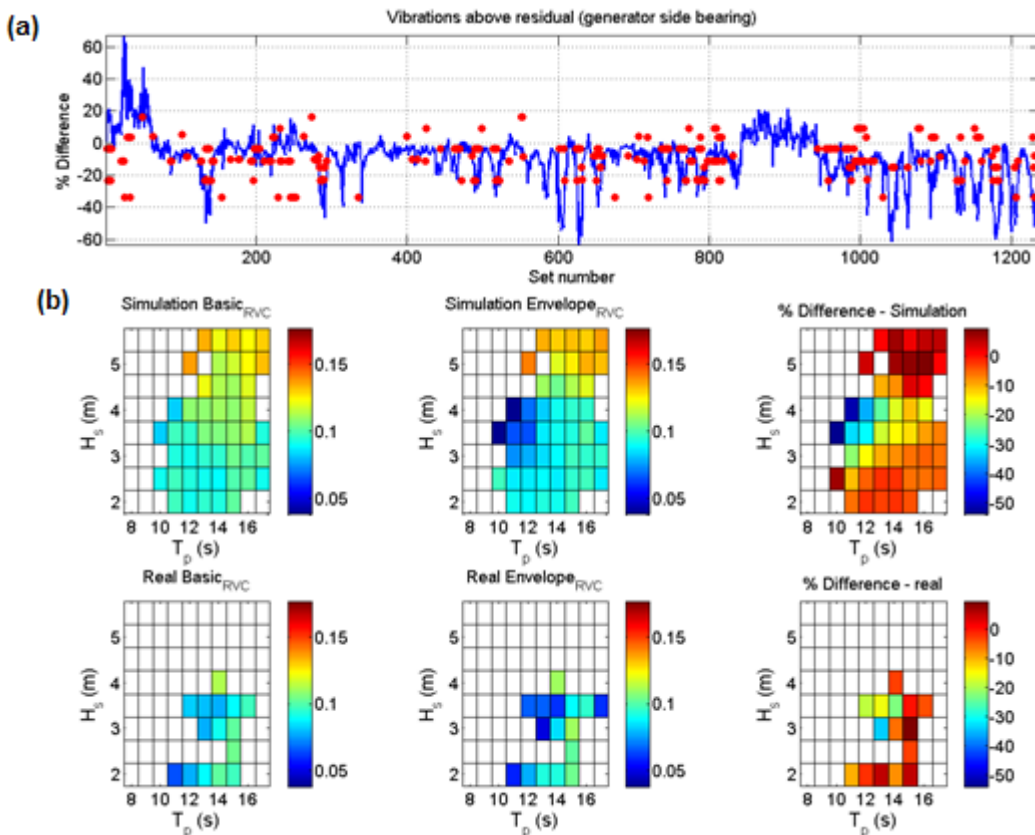


**Figure 7.16** Mean vibration velocities above the residual for the generator side turbine shaft bearing. (a) Percentage difference between  $Envelope_{RVC}$  and  $Basic_{RVC}$  for (blue line) simulations and (red dots) field test results (averaged over the sea state bin intervals). (b) Matrices of absolute values and the percentage difference between control strategies.

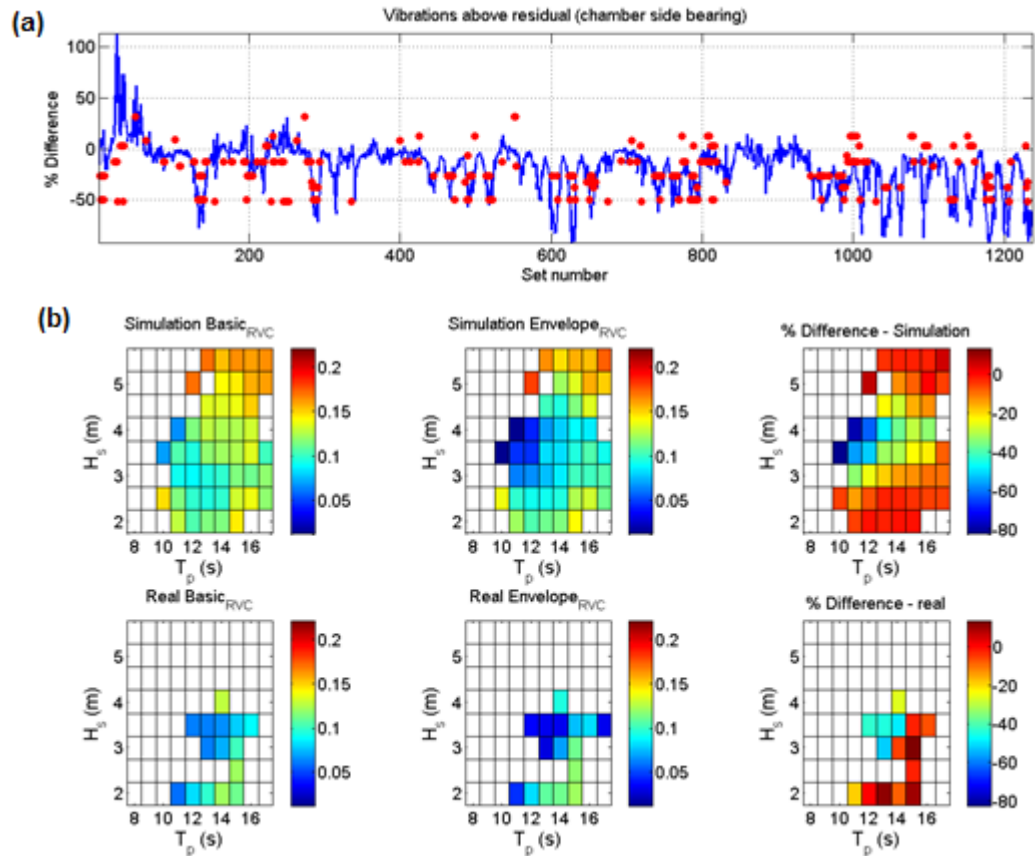


**Figure 7.17** Mean vibration velocities above the residual for the chamber side turbine shaft bearing. (a) Percentage difference between  $Envelope_{RVC}$  and  $Basic_{RVC}$  for (blue line) simulations and (red dots) field test results (averaged over the sea state bin intervals). (b) Matrices of absolute values and the percentage difference between control strategies.

As seen in figures 7.9 to 7.17, power take-off, relief valve cycles and the percentage of time in the lower stall severity regions are all in good agreement with the simulations. The percentage of time in the higher stall severity regions is predicted less well but because of the infrequent occurrence it would only take a small number of more severe stalls (slight mistake in control sequence) to result in a significant divergence. Vibrations are also predicted less well, suggesting that vibrations might have a more complex relationship than defined in the matrices given in figures 3.29 and 3.30 and might need reconsidering.

Note that because only a small amount of field data was collected the data might be disproportionately weighted by an unusual test series / sea state and are not long enough to benefit from longer term averaging that could mitigate the error. Also, other than  $H_s$ ,  $T_p$  and tidal elevation other factors will affect the performance. These include: variance in wave envelope (wave groupiness), forecast accuracy, current state of boulder placement on the sea floor (water depth), and possibly incident wave direction. Finally, it should be remembered that some unavoidable divergences from the simulations were incurred. These were computational time delays and the increases in the separation between the control action trigger limits.

Considering the potential variability and incurred divergences, the results validate the simulation results and methodology quite well and the general trends agree.

### 7.3.5 Divergences and further validation

As stated in section 7.3.1 whilst implementing the relief valve control system at Pico some unavoidable divergences between the simulation and real deployment of the relief valve control system were incurred, these were;

- The optimum range of standard deviation of non-dimensional over horizon time  $\Gamma$  (that  $Envelope_{RVC}$  is trying to achieve) as used in sections 5.4.5 and 6.7.4, had to be changed from;  $0.04 < \sigma_{\Gamma}(\Psi) < 0.06$  to  $0.03 < \sigma_{\Gamma}(\Psi) < 0.06$ , because the relief valve pump over heated due to the high cycle frequency. This modification made the relief valve adjustment react slower and less likely to initiate a closing stroke. This reduces the aperture adjustment cycles but also makes control less responsive to the potential optimisation.
- Up to 0.5 (s) in the forecast horizon was lost due to the need to transfer data between the data acquisition suite (DAQ-factory) and the forecasting and control suite (MATLAB®).
- Between 0.2 (s) and 0.5 (s) in additional forecast horizon (compared to what was considered in sections 5.4.5 and 6.7.4) was lost because of the lower processing power of the integrated computer at Pico, when compared to the computer used to make the simulations.

These issue can be resolved quite easily with a more robust relief valve pump, or cooling system, and a dedicated PLC, but as these were not available. The impact of these divergences needs investigation.

To make this assessment, a period of recorded data from field tests (test number 5) with relief valve control (Scenario #1) is compared to the simulated system response under the following alternative scenarios;

- #2 - Simulation using original control conditions in methodology ( $0.04 < \sigma_{\Gamma}(\Psi) < 0.06$  and no additional time delay)
- #3 - Simulation using achievable field control conditions, ( $0.03 < \sigma_{\Gamma}(\Psi) < 0.06$  and additional time delay of 1 second)
- #4 - Simulation using original control conditions but with the additional processing and data transfer time delay
- #5 - Simulation using achievable field control conditions without additional processing and data transfer time delay

By comparing the simulation time series of relief valve aperture, RPM and power take-off, against what occurred in reality, the impact of these unforeseen issues can be identified. This can be used to interpret the field test results when compared to simulations and to prioritise the issues for future testing. In addition, this assessment will provide a powerful validation of all the simulation results given so far. The comparison between scenarios #1, #2 and #3 is seen in figure 7.18 and the mean power and percentage different from the recoded value, for all scenarios, is given in table 7.4.

**Table 7.4** Mean power take-off during example control period under  $Envelope_{RVC}$ , with slight modifications that characterise issues encountered during control system deployment, as described by scenarios #2 to #5, as well as the percentage difference from the recorded values which is scenario #1.

Scenario number	#1	#2	#3	#4	#5
$\bar{P}_e$ (kW)	50.17	52.69	50.18	51.91	50.80
% Difference from #1	N/A	+5.03%	+0.02%	+3.47%	+1.26%

As seen in figure 7.18, scenario #3, which is the model simulation that most accurately accounts for the divergences between the original methodology and what could be achieved in field test conditions, agrees extremely well with the recorded data (Scenario #1) in terms of turbine angular velocity and power take-off. The simulated relief valve aperture is less precise but is still good. An exact match would not be expected because it is more difficult to characterise exactly how the relief valve aperture will change. This is because of the mildly chaotic nature of this part of the model and because of the sharp limits used in deciding the control action. The system is mildly chaotic because a small difference in relief valve aperture (between reality and the model) will have a knock on effect resulting in a small difference in forecasted chamber pressure, which could result in a different relief valve control action being taken.

The chaotic effect will have a tendency to reset (in part) when  $k_v = 0$ , as reality and the simulation re-align at this lower limit, provided the modelled RPM is not significantly different to reality (which is much less sensitive to chaotic effects). This is why the track of the opening relief valve aperture (after  $k_v = 0$ ) is simulated with the greatest accuracy.

Also it is shown in figure 7.18 that the projection under scenario #2, which is the model simulation under the same conditions used in the rest of this study, results in a notably better performance in all system variables and in particular the relief valve aperture state (faster response). It should also be noted from figure 7.18 that the rate of aperture adjustment between scenario #1 (real data) and scenario #3 (simulation accounting for divergences) is in very good agreement. This shows that the original characterisation of the relief valve adjustment rates and response times was surprisingly accurate, despite having the tendency to be slightly nonlinear as the motion is affected by variable levels of resistance resulting from changes in chamber pressure as discussed in section 3.3.5.2.

From table 7.4 it is seen that, by removing the time delay to account for additional processing time and data transfer times between the software packages, a small increase in performance results. A slightly more significant performance enhancement results if the control action limits of  $0.04 < \sigma_r(\Psi) < 0.06$  are restored. In this specific example, the difference in power take-off between the optimum case and the achievable case is 5%. This in part explains the small short-fall seen in section 7.3.4 between the results from field tests and the simulation results.

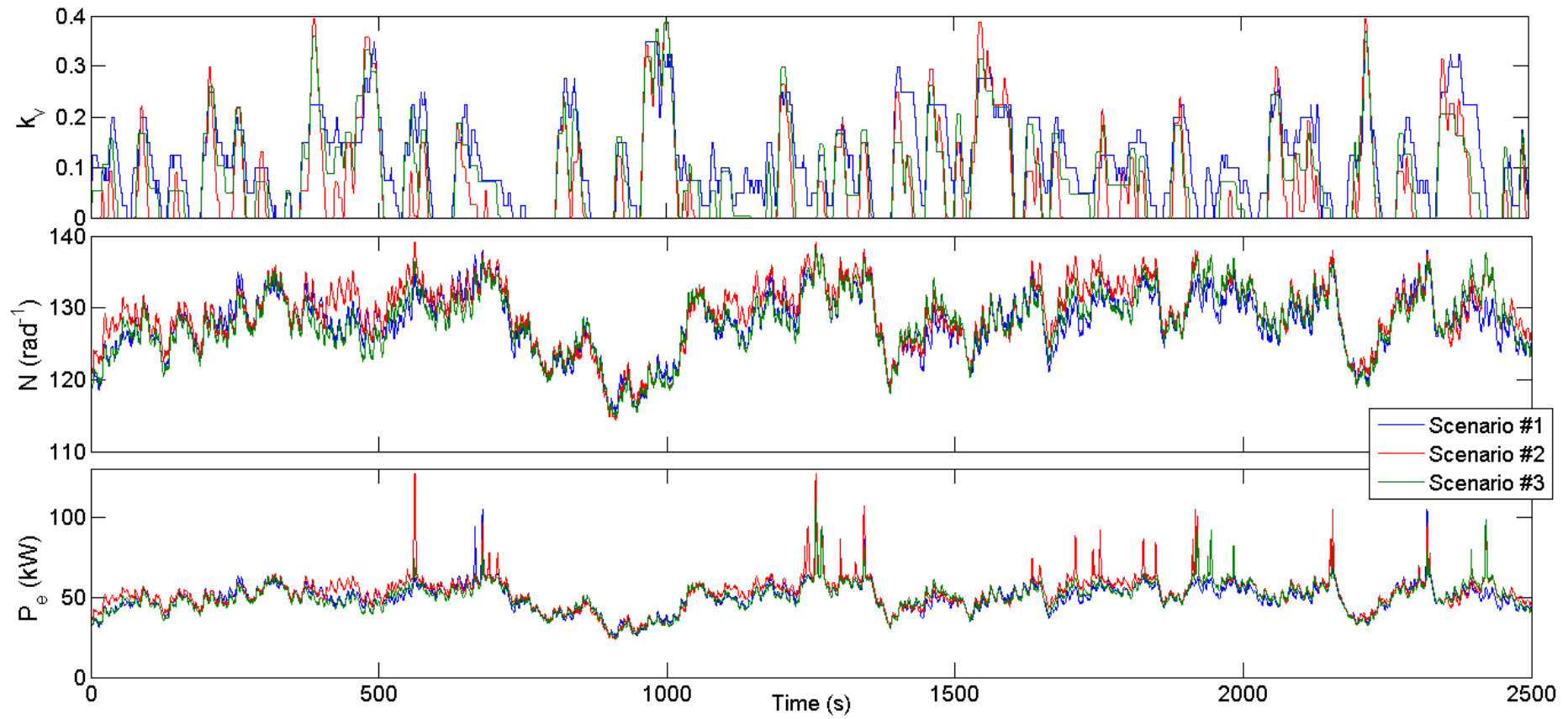


**Figure 7.18** Example time series comparing the measured; relief valve aperture state  $k_v$ , turbine angular velocity  $N$  and generator power take-off  $P_e$ , to the simulated values of the same parameters, under ideal and realisable control condition scenarios.

## 7.4 Life time performance projection

It is too computationally expensive to perform long term simulations of relief valve control at the Pico plant in the time domain. Also the plant has not been operational for long enough to provide the input data needed to drive the system model for a very long term analysis. Instead a statistical approach to long term performance analysis is made. In section 3.4.4 the long term continuous metocean data set was statistically related to the calculated chamber sea state (from operational data) in order to give an approximation of the chamber sea state number of occurrences, over the plant's lifetime to date. Because the chamber sea state number of occurrences from the mid-term simulations span a broad range of sea states, there is sufficient overlap to relate the two, as can be seen in figure 7.19. In fact if the sea states where  $H_s \leq 1.5$  are discounted (where the plant is usually not operational due to low incident energy and was not considered in the mid-term analysis) only 480 hours out of 93587 potential operational hours are lost due to an absence in chamber sea state overlap between the mid-term and long-term data sea state occurrences.

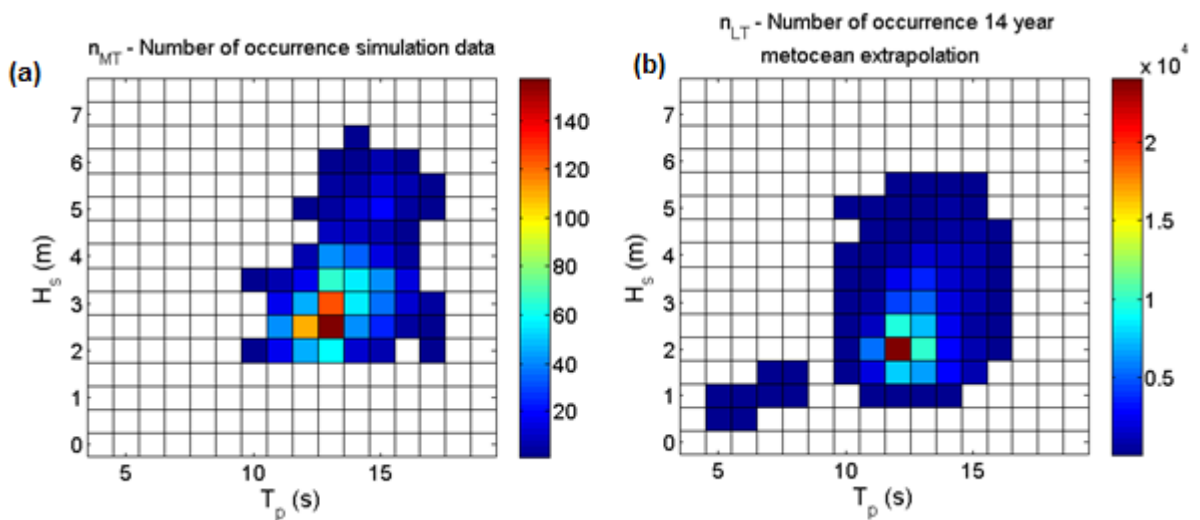


**Figure 7.19** Sea state occurrence number for (a) mid-term simulations and (b) long-term statistical extrapolation using metocean data (as described in section 3.4.4)

Combining the long-term sea state occurrence number with the mid-term time domain simulation results (as described in section 3.4.4), the long term performance enhancements under the different relief valve control strategies can be projected over the plant's life time to date. This of course is under the ideal hypothetical scenario where the plant had been fully functional from the point of project completion (2000) until the present (2014).

The extrapolation of the mid-term simulation results to the statistical long-term performance results is performed as follows;

Long-term statistical extrapolation of the following performance parameters: power take-off  $\bar{P}_e$ , % time spent in different stall bands, mean vibrations above the residual  $\bar{V}_g \bar{V}_c$ , and number of full relief valve cycles per hour  $k_p^{-Hr}$ , is achieved by finding all data sets from the mid-term simulation results that fall into the same sea state bin interval (the bin interval is show in figure 7.19). These are summed and

averaged using the number of occurrences  $n_{M,T}[H_s, T_p]$  (shown in figure 7.19), giving the parameter average;

$$\overline{Parameter}[H_s, T_p] = \frac{\sum_{set=1}^{n_{MT}} Parameter_{set}[H_s, T_p]}{n_{MT}[H_s, T_p]} \quad \text{for } [H_s = 0, 0.5, \dots, 10, T_p = 4, 5, \dots, 20] \quad (7.1)$$

Next for  $\bar{P}_e, k_v^{-Hr}$  and time spent in excess of each stall severity band, each sea state averaged parameter from the mid-term simulations  $\overline{Parameter}[H_s, T_p]$  is multiplied by corresponding long-term occurrences  $n_{L,T}[H_s, T_p]$  (shown in figure 7.19) for the respective sea state bin interval and then all sea state totals are summed to give the long-term parameter total for the plant's life time to date;

$$Parameter\ total_{L,T} = \sum_{H_s=0,0.5,\dots}^{10} \sum_{T_p=4}^{20} n_{L,T} \times \overline{Parameter}[H_s, T_p] \quad (7.2)$$

The vibrations velocities above the residual levels are treated differently and for these parameters the long-term average is found;

$$\bar{V}_{L,T} = \frac{\sum_{H_s=0,0.5,\dots}^{10} \sum_{T_p=4}^{20} n_{L,T}[H_s, T_p] \times \bar{V}[H_s, T_p]}{\sum_{H_s=0,0.5,\dots}^{10} \sum_{T_p=4}^{20} n_{L,T}[H_s, T_p]} \quad (7.3)$$

Because sea states with  $H_s \leq 1.5[m]$  were not simulated in the mid-term simulations, as the plant typical does not produce worthwhile levels of power in these conditions, any sea state occurrence in this range (for the long-term extrapolation) is considered to be time that the plant would be off-line and these do not influence the totals.

The long term performance projections in terms of the total values of the consider parameters, from each control strategy, are present in table 7.5. The percentage difference between the total from *Basic<sub>RVC</sub>* and the other advanced control strategies is presented in table 7.6.

**Table 7.5** Parameter totals (averages for the case of vibration velocities) under the different control strategies over the potential operational life time of the Pico plant to date.

	Online time (Hrs)	Offline time (Hrs)	$P_e$ (GWHrs)	$\Psi > 0.068$ (Hrs x 10 <sup>3</sup> )	$\Psi > 0.1$ (Hrs x 10 <sup>3</sup> )	$\Psi > 0.125$ (Hrs x 10 <sup>3</sup> )	$\Psi > 0.15$ (Hrs x 10 <sup>3</sup> )	$\Psi > 0.175$ (Hrs x 10 <sup>3</sup> )	$\bar{V}_G$ (mms <sup>-1</sup> )	$\bar{V}_c$ (mms <sup>-1</sup> )	Total full relief valve cycles	Total earnings
<i>Basic<sub>RVC</sub></i>	93107	21660	2.99	13.46	3.31	0.812	0.185	0.041	0.089	0.10	low	€806,500
<i>Envelope<sub>RVC</sub></i>	93107	21660	3.24	12.17	2.16	0.325	0.048	0.009	0.082	0.088	1415700	€875,100
<i>Continuous<sub>RVC</sub></i>	93107	21660	3.60	11.30	1.67	0.283	0.059	0.015	0.073	0.075	3543200	€971,200
<i>Instant<sub>RVC</sub></i>	93107	21660	4.90	0.68	0.08	0.009	0.000	0.000	0.046	0.040	19763000	€1,322,400

**Table 7.6** Parameter percentage differences (totals difference for earnings) under the advanced control strategies as a percentage of that achieved with *Basic<sub>RVC</sub>*, for the potential operational life time of the Pico plant to date.

<i>Difference Basic<sub>RVC</sub> vs</i>	$P_e$	$\Psi > 0.068$	$\Psi > 0.1$	$\Psi > 0.125$	$\Psi > 0.15$	$\Psi > 0.175$	$\bar{V}_G$	$\bar{V}_c$	$\Delta$ Total earnings
<i>Envelope<sub>RVC</sub></i>	+8.5%	-9.6%	-34.7%	-60.0%	-73.7%	-78.8%	-8.0%	-13.3%	€68,600
<i>Continuous<sub>RVC</sub></i>	+20.4%	-16.0%	-49.5%	-65.1%	-68.25%	-64.1%	-18.1%	-26.0%	€164,800
<i>Instant<sub>RVC</sub></i>	+64.0%	-95.0%	-97.7%	-99.0%	-100%	-100%	-49.2%	-60.4%	€515,900

## 7.5 Summary and conclusions

The plant system response under the different relief valve control strategies considered was simulated in the time-domain over a period of one month (mid-term) using operational data as the model input. The results were validated with field test results where a suitable match in the chamber sea state occurred. The mid-term simulation results also provided a database of average performance levels under a wide range of sea state conditions in order to make statistical long term performance projections.

It was found that the performance of the advanced control strategies, relative to the basic relief valve control strategy, is highly dependent on the tidal elevation. This was found to be, in part, a response to wave shoaling and wave asymmetry resulting in a partial cancelation of the benefits gained from control in one wave half cycle by losses in the other half wave cycle. If the Pico OWC did not have the collection of boulders in the chamber or had been deployed in deeper local water depth, the performance of the advanced relief valve control strategies would likely have achieved a greater overall performance relative to the basic control strategy. This is an important point to note as new devices deployed in deeper water or offshore devices could benefit more significantly from relief valve control. The performance from relief valve control under less shoaled wave conditions needs evaluation and this could be done using more idealised (more sinusoidal) synthesised waves. However, the forecast performance would not be factored into this analysis unless wave randomness was accurately represented in the wave synthesis.

The envelope relief valve control strategy was deployed in the field at the Pico plant in alternating test periods with the basic relief valve control strategy, which was used as a reference to evaluate performance enhancements. Only a limited number of tests series were conducted due to technical issues with the plant, which prevented a more complete set of test results from being obtained. Also, some additional milder informatics and mechanical issues resulted in a small time delay in the relief valve control response and a reduction in the allowable relief valve aperture adjustment frequency, and therefore a divergence from the original control methodology used in the simulations.

The field tests spanned a reasonably broad range of sea states and the results averaged over each sea state were compared to the simulation results. Considering the limited number of field tests conducted and the potential additional variability associated with other parameters that were not considered in the data division, as well as the additional divergences that were incurred due to technical issues during the field test, a reasonable correlation with the simulation results was found.

The small short-fall in performance from the field tests results was found to be due to the incurred time delay and the need to broaden the optimum control range to reduce the aperture adjustment cycle frequency. The valve aperture track recorded from a field test was compared to a simulation and a very good agreement was found when the additional incurred issues were characterised and implemented in the model. Also, the turbine angular velocity and power take-off time series were in very strong agreement. Removing the characteristics of the incurred issues from the model and restoring the original considered control methodology resulted in a notable enhancement in performance. As such it is recommended that a dedicated PLC and relief valve pump cooling system be installed to realise the full performance benefits of the envelope relief valve control strategy.

The continuous and instant relief valve control strategies could not be tested in reality because a modification of the relief valve actuator system was required. This was beyond the budget limitations of the project. However, the validation of the envelope relief valve control, in part, validates the simulations of these other control strategies because they are all based on the same modelling methodology.

The long term performance of the plant under each control strategy was considered for the hypothetical scenario where the Pico plant had been continuously operational from the point of completion of the construction, to the present. The long term performance was projected in a statistical way by extrapolating the mid-term simulation results, averaged by sea state, based on the expected long-term chamber sea state occurrence frequency. The expected occurrence frequency was found by statistically associating metocean data with chamber surface elevation measurements. This extrapolation indicates that the: envelope, continuous and instant, control strategies have the potential to increase the average annual electrical energy sales of €57000 (if full-time operation was achieved), by approximately €5000, €12000 and €37000, respectively per year. In addition, the significant reductions in stall frequency and severity, and vibrations above the residual are expected to significantly reduce the rate of mechanical component fatigue thus decreasing the maintenance interval frequency and the operational and human resource costs. This, however, might be at the expense of accelerated wear of the relief valve actuator system and this requires longer term observations to quantify. Also the reduction in stall frequency and severity will reduce the noise emitted by the plant and this could improve the public perception of the project as well as reducing the environmental impact.

The following recommendations for relief valve control at Pico are listed in order of ascending financial commitment and potential performance gain;

1. Permanently deploy the envelope control strategy at the current state of development
2. Implement a dedicated control PLC and relief valve pump cooling system and restore the original proposed control conditions for the envelope control strategy.
3. Implement a relief valve hydraulic pump that is capable of near continuous operation and deploy the continuous relief valve control strategy.
4. Develop and implement a fast acting relief valve actuator and the instant relief valve control strategy.

Because the advanced relief valve control necessarily incurs a high number of relief aperture adjustment cycles to be effective, the sustainability of this, in terms of wear and fatigue rates, remains to be evaluated. The envelope control strategy should be deployed initially for an extended period and the rate of wear and fatigue should be monitored and characterised for long term extrapolation to assess the practicality of relief valve control.

Given the poor performance of the Pico plant in terms of power production, the potential financial gains from envelope control in this scenario are somewhat less interesting despite the notable relative percentage increases. Also, the possible reduction of machine component fatigue rate is hard to quantify. Because of this, perhaps the main thrust of this study is to demonstrate that short-term forecasting, using only the information collected at the device, can be used to successfully achieve notable performance enhancements of a full-scale WEC in the field using only rudimentary control equipment. The short-term

wave forecasting methodology developed in this study is applicable to all wave energy converters and device types that have a greater capacity for optimisation through control based on short-term forecasting could benefit more significantly from the findings and methodologies developed in this study.

## Chapter 8

# Final summary and conclusions

### 8.1 Thesis part 1

#### 8.1.1 Final summary and conclusions

There have already been some examples of the deployment of small offshore WEC arrays. These include the Pelamis Aguçadoura wave park in Portugal, the CETO 5 Perth wave energy project in Australia and soon the Wavehub project in the UK will receive its first devices. It seems that large arrays of WECs will be deployed offshore in the not too distant future and this will be the next necessary step if wave energy is to play a significant role in meeting global energy demands. If this happens, careful consideration should be given to the potential impacts that large scale wave energy extraction could have on the down-wave open-ocean and shoreline wave climates. In chapter 2 the wave energy deficit in the lee of a single row array of overtopping type wave energy converters, is considered. The analysis of this situation was achieved by developing a computationally inexpensive approximate analytical solution for the problem, which is capable of assessing large, high resolution domains with high resolution directional and spectral irregular sea states. This solution was created using multiple superpositions of the classical analytical solution for diffraction about a semi-infinite breakwater with reflection and transmission coefficients applied in order to approximate energy extraction and transmission at the device. The approximations associated with the developed solution were mitigated with a comparison to the results from a computationally expensive but more mathematically exact integral equation solution for the same problem, with excellent agreement being achieved in the far-field region of interest. The developed solution suggests that the diffraction effect, induced by energy extraction at the devices, causes wave energy to disperse radially thus defocusing energy away from the geometrical shadow of the array. By comparing the wave energy shadows predicted by a solution that considers diffraction and a solution that omits diffraction, it was demonstrated that the redistribution of energy from diffraction counteracts the recovery of the wave energy deficit from wave directional spreading and that the net contribution of this effect is significant for narrowly distributed wave directional spread sea states. This adds to the existing knowledge because previously, wave energy shadowing had only been considered either by phase averaged models, which are incapable of correctly considering the diffraction effect, or by computationally expensive phase resolving models, for the consideration of smaller domains which did not consider the far-field where local interference diminishes and where the effect of diffraction emerges more clearly.

Sensitivity analysis also revealed that, in the far-field, the wave energy deficit is highly sensitive to the broadness of wave directional spreading and the scale of energy extraction (when spreading is narrower), but is insensitive to device spacing and the wave spectral distribution (under the assumption that energy extraction is independent of frequency). In the near-field it was found that the interference pattern from wave scattering was sensitive to changes in the array geometry, incident wave frequency and directional distributions. This will be important if additional rows of WECs are to be placed within the array because

local interference minima should be avoided. Furthermore if the array is located close to shore, significant local spatial wave disturbances may occur at the coastline.

### **8.1.2 Future work and extensions**

In chapter 2 overtopping type WECs were considered in a simplistic way. The dependency of energy conversion on the wave frequency, direction and height, was not considered and the device movement, which will result in wave radiation waves, was also omitted. This was done primarily to isolate and investigate the effect of diffraction on the re-distribution of wave energy. The next step could be to implement these features into the solution and perform a reanalysis to scale the wave energy shadow about a more realistic representation of an overtopping WEC array. In addition the refraction effect and the bathymetry of a specific case study could be incorporated to assess the expected wave height disturbance at the coast of a proposed WEC array deployment. This could be achieved by applying the dispersion relationship to each wave component of the solution. Finally, an array of point absorbers could be considered with a similar approximate analytical solution (omitting secondary wave radiation). Because of radiated wave emission by the motion of the device, a similar process of wave defocusing is expected. All of these possible extensions were considered (by the author) and early stage implementation was achieved but this work remains incomplete due to the change in topic part way through the PhD programme.

## **8.2 Thesis part 2**

### **8.2.1 Final summary and conclusions**

The Pico OWC has overcome many of the early technical challenges that resulted in extended machine down-time and is now intermittently operational. However, interest in the project has dwindled and this is regrettable because it presents a unique platform for the preliminary testing of power take-off systems and the development of control strategies. Also, because of the harsh wave climate it is the ideal candidate for fatigue and loading analysis as well as survivability studies. The author has attempted to rejuvenate interest in the project by demonstrating a field application of short term wave forecasting. More generally, the motivation of this research was to also demonstrate that effective short-term forecasting could be achieved in the field using only the past measurement made at the device and that real-time active control can be achieved using only rudimentary equipment and minimal additional cost.

Forecasting was used to provide information about the up-coming incident chamber excitation flow time-series, with lead time, in order to regulate and optimise pneumatic power exposure to the turbine with bypass relief valve control. The motivation for control stems from the plants underperformance (compared to early theoretical projections) which, as shown in chapter 3, is a primary result of the chamber pressure asymmetry. Asymmetry is a product of the reduction of chamber water depth (from boulder collection) and wave shoaling. This is in addition to defects in the chamber walls that cause intermittent pressure loss and further chamber pressure asymmetry. Pressure asymmetry has a particularly detrimental effect on the performance of Wells turbines because of the associated stall effect. Without advanced control, pressure variance can only be optimised during one of the wave half-cycles, or partially optimised over a full wave

cycle. Also the aerodynamic flow separation during turbine stall incurs additional undesirable effects which include increased vibrations, machine component stress and severe noise emission.

A number of relief valve control strategies of varying technical demand and financial commitment were developed in chapter 5 to try to counteract the degradation in system performance resulting from chamber pressure asymmetry and to reduce the frequency and severity of turbine stall. Firstly, a relief valve control strategy was considered which attempts to deliver the pneumatic power conditions that result in the maximum possible power transfer to the turbine (from the available power) at every time instant ( $Instant_{RVC}$ ) through rapid relief valve aperture adjustments. A second relief valve control strategy was devised to counteract pressure asymmetry and optimise the pressure variance over each half wave-cycle ( $Wave_{RVC}$ ) by making a single rapid valve aperture adjustment at the point of zero pressure head (that occurs at the wave crest or trough). The third strategy also attempts to optimise chamber pressure variance over each half wave cycle but through slow continuous aperture adjustments ( $Continuous_{RVC}$ ), thus incurring much lower demands of the aperture adjustment system. The final control strategy considered attempts to optimise the chamber pressure variance over each wave cycle thus tracking the wave energy envelope ( $Envelope_{RVC}$ ) by making slow intermittent aperture adjustments over time. This control strategy factored in the mechanical limitations of the existing relief valve aperture adjustment system installed at Pico so that field tests could be conducted with the resources available.

The relief valve control strategies proposed are all active and require prior knowledge of the incident excitation flow time-series with varying amounts of lead time (between 0.5 and 16 seconds). To gain this knowledge a number of short-term wave forecasting methods were investigated and developed in chapter 6. These were the univariate linear ( $AR$ ) and nonlinear autoregressive ( $NAR$ ) feedback forecast models using just the information recorded at the device and the multivariate derivatives ( $ARX$  and  $NARX$ ) of the same models which also incorporate the information from a point source measurement of hydrodynamic pressure, made 60 ( $m$ ) up-wave of the device having a finite lead time. To extend the forecast range of the multivariate model a new method was proposed in which the exogenous input is first forecasted to remove the forecast horizon limitations ( $ARX_{AR}$ ). Finally a finite impulse response filter was considered to make spatial and temporal transformations of the up-wave information exclusively. It was found that little difference in the achievable forecast accuracy resulted when the future wave behaviour is considered to have either a linear or nonlinear relationship with the recent past behaviour. Forecast accuracy at longer horizon times was found to be improved by also considering the up-wave information with the  $ARX_{AR}$  performing best, but the gain in forecast accuracy was primarily due to a reduction in the forecasted phase error. As the proposed control strategies depend more heavily on the forecast amplitude accuracy, and are mostly insensitive to small phase error, it was concluded that, considering a compromise between computational effort, model stability, reliability and financial cost, the  $AR$  forecast model was the most suitable candidate for this application. It was reported in the literature that very significant enhancements to the forecast accuracy could be achieved by filtering out higher frequency wave components that are of little interest to control and wave energy conversion. However, this was only achieved with non-causal filtering which is not realisable in real-time. As demonstrated, no significant improvement in forecast accuracy could be gained by causally filtering data because the phase delay of the filter's output, when removed, counteracted any enhancements.

The mid-term performance (one month in autumn) of each control strategy was projected with a wave to wire time-domain model of the Pico OWC system, which was validated using operational data. Field tests of  $Envelope_{RVC}$  were performed at the Pico plant and these results showed that the achieved power production enhancements and stall reductions are in good agreement with the model projections. The long-term performance enhancements resulting from each control strategy was extrapolated statistically using long-term hindcast metocean data at a nearby location. It was found that the  $Instant_{RVC}$ ,  $Continuous_{RVC}$  and  $Envelope_{RVC}$  strategies had the potential to increase the annual power production by 64%, 20% and 9% respectively. This is in addition to significant reductions in the frequency and intensity of stalls and machine vibrations.

Because of the financial and resource limitations associated with the project only the least effective advanced valve control strategy considered was tested and validated in the field. The results from this strategy, although interesting, are unlikely to have a very significant change to the overall performance of the Pico project. However, the short-term forecast methodologies developed in this research are applicable to all WECs and other device types that have a greater capacity for enhancing the performance through control, could benefit more significantly from the findings of this study. The expected forecast accuracy at a device located in the field, with different sensor arrangements, was presented and this would give control system developers information and guidance on the expected restraints of any proposed strategies, in the early stages of development.

### 8.2.2 Future work

In chapter 6 it is shown that the forecast phase accuracy can be enhanced by also considering up-wave information from a point source. At Pico it was found that the up-wave measurements are significantly affected by reflected and radiated wave interference and it would be interesting to see how much the forecast accuracy could improve if the true incident wave information, extracted from this superposition, is used with the multivariate forecast models. The incident wave extraction could be achieved using an up-wave multi-point sensor array. With this information it could be interesting to compare the up-wave measured wave power spectral density convolved with the plants hydrodynamic volume flow coefficient, to the  $ARX$  power spectral density.

Because of wave asymmetry at Pico, it would also be interesting to consider a control strategy that can influence chamber pressure more significantly over each half wave cycle, without incurring high mechanical demands of the aperture adjustment system. This could be achieved by combing an active control strategy, such as  $Envelope_{RVC}$ , with a passive element such as a flap which is drawn across and closes a proportion of the valve aperture during inhalation. This would amplify the weaker inhalation half wave cycle without the need to make fast active aperture adjustments.

It was shown that very significant enhancements to power production could be achieved with  $Instant_{RVC}$  and that these strategy might shift the performance of the Pico plant into the range of commercial viability. However, to achieve control in this manner, a powerful fast-acting relief valve aperture adjustment system, capable of a high duty cycle, needs to be developed. It remains to be seen if this is more economically and practically viable than an alternative solution such as the replacement of the Wells turbine with a bi-radial turbine, which appears to not have the issues associated with stall and is likely to

be less sensitive to performance degradation from wave asymmetry. A comparison study should be made to identify the most likely route to success.

A reanalysis of the plant performance using a time-domain model driven with synthesised un-shoaled waves could be used to validate the stochastic frequency domain modelling approach. This would also provide an indication of the expected performance of the Pico plant if a significant investment were made to repair the structural defects and dredge the chamber as well as the potential performance of other shoreline OWC plants provided that sedimentation issues are addressed.

# Appendix A

## Integral equation for wave diffraction by a segmented permeable breakwater (McIver, 2005)

### A.1 Context

The integral equation for diffraction about a segmented permeable breakwater series proposed in (McIver, 2005) is used without any modification to validate a computationally efficient approximate analytical solution (for the same problem) developed and presented in chapter 2. For this reason the integral equation solution is summarised in the following (in the format it is used in this study) for the readers reference and (McIver, 2005) should be consulted for a more detailed description.

### A.2 Solution

The solution presented in (McIver, 2005) considers a series of  $B$  thin porous breakwater segments with each segment assigned a reference number  $m$ , initially breakwaters are considered to be of arbitrary shape and standing in water of constant depth  $h$ . Incident waves are considered to be monochromatic with small amplitude and flow is irrotational, inviscid and incompressible and may be described by linear wave theory and the velocity potential as described in section 1.5.1.

In Cartesian coordinates the velocity potential for flow exterior to the breakwater can be expressed as;

$$\phi = \text{Re} \left\{ \frac{-iga}{\omega \cosh(kh)} \phi_T \cosh k(z+h) e^{-\omega t} \right\} \quad (\text{A1})$$

where  $a$  is wave amplitude,  $k$  is the wave number,  $\omega$  is wave angular frequency,  $g$  is gravitational accelerating and  $\phi_T$  is the total velocity potential and is a complex function (of  $x$  and  $y$  horizontal coordinates only due to the breakwater uniformity in the  $z$  plane) that satisfies the Helmholtz equation;

$$\frac{\partial^2 \phi_T}{\partial x^2} + \frac{\partial^2 \phi_T}{\partial y^2} + k^2 \phi_T = 0 \quad (\text{A2})$$

If the cross section of breakwater segment number  $m$  is denoted  $\Gamma_m$  and has two faces  $\Gamma_m^+$  and  $\Gamma_m^-$ . The breakwater segment is considered by a number of points  $p$  on  $\Gamma_m^+$ . Each point has a normal  $n_p^+$  with direction into the breakwater face  $\Gamma_m^+$ , and another normal  $n_p^-$  directed into the breakwater face  $\Gamma_m^-$ .

At each point on the breakwater conservation of mass requires;

$$\frac{\partial \phi_T}{\partial n_p^+}(p^+) = -\frac{\partial \phi_T}{\partial n_p^-}(p^-) \quad (\text{A3})$$

At all points on the breakwater the velocity of flow through it is proportional to the pressure difference across it;

$$\frac{\partial \phi_T}{\partial n_{p^+}}(p^+) = -\beta[\phi_T(p)] \quad (\text{A4})$$

where the complex parameter  $\beta$  is described by;

$$\beta = \frac{-i\epsilon}{b(f-is)} \quad (\text{A5})$$

where  $\epsilon$  is the breakwater porosity,  $f$  and  $s$  are non-dimensional friction and inertia coefficients, respectively.

The total velocity potential  $\phi_T$  is a combination of the incident potential  $\phi_I$ ;

$$\phi_I = \exp[-ikr \cos(\theta - \alpha)] \quad (\text{A6})$$

and the diffracted wave field velocity potential  $\phi$ , which satisfies the radiation wave condition;

$$\lim_{r \rightarrow \infty} r^{1/2} \left( \frac{\partial \phi}{\partial r} - ik\phi \right) \quad (\text{A7})$$

such that;

$$\phi_T = \phi_I + \phi \quad (\text{A8})$$

where  $r$  and  $\theta$  are polar coordinates and  $\alpha$  is the incident wave direction (normal to the wave plane) with respect to the  $x$  coordinate

In order to find the wave height of the scattered field in the considered domain due to the presence of the breakwater series an integral equation is needed to solve  $\phi(x, y)$  which is obtained through an application of Green's theorem to  $\phi$  and the Green's function;

$$\phi_0(P, Q) \equiv \frac{1}{4i} H_0^{(1)}(kR_{PQ}) \quad (\text{A9})$$

where  $\phi_0$  is a solution to (A2),  $H_0^{(1)}$  is the 0<sup>th</sup> order Hankel function of the first kind,  $P$  is a point in the domain (with coordinates  $x_P, y_P$ ) exterior to the breakwater,  $Q$  is the source point (with coordinates  $x_Q, y_Q$ ),  $R_{PQ}$  is the distance between points  $P$  and  $Q$  such that;

$$R_{PQ} = (x_P - x_Q)^2 + (y_P - y_Q)^2 \quad (\text{A10})$$

Applying green's theorem over the domain outside the breakwater and simplifying with (A3) and the continuity of the derivatives of  $\phi_0$ , results in;

$$\phi(P) = \int_{\Gamma} \phi(q) \frac{\partial \phi_0}{\partial n_{q^+}}(P, q) ds_q \quad (\text{A11})$$

where  $\Gamma$  is the line that connects all points  $p$  on the breakwater,  $s_q$  is the arc length as the source point  $q$  varies along  $\Gamma$ .

Considering (A4), (A8) and (A11), gives;

$$\frac{\partial \phi_I}{\partial n_{p^+}}(p^+) + \beta[\phi_T(p)] = \frac{\partial \phi}{\partial n_{p^+}} = -\frac{\partial}{\partial n_{p^+}} \int_{\Gamma} \phi(q) \frac{\partial \phi_0}{\partial n_{q^+}}(p, q) ds_q \quad (\text{A12})$$

Due to the singularity in the intergraded in (A12) which arises from the second derivative of the Green's function, a finite-part integral is required. The finite-part integral of a sufficiently smooth function  $F$  is defined by;

$$\mathcal{F} \frac{F(t)}{(s-t)^2} = \lim_{\epsilon \rightarrow 0} \left\{ \int_a^{s-\epsilon} \frac{F(t)}{(s-t)^2} dt + \int_{s+\epsilon}^b \frac{F(t)}{(s-t)^2} dt - \frac{2F(s)}{\epsilon} \right\} \quad (\text{A13})$$

Applying (A13) to (A12) provides an equation for the unknown jump in potential at  $\phi(p)$ ;

$$\beta[\phi_T(p)] + \mathcal{F}_{\Gamma} \phi(q) \frac{\partial^2 \phi_0}{\partial n_{p^+} \partial n_{q^+}}(p, q) ds_q = -\frac{\partial \phi_I}{\partial n_{p^+}} \quad (\text{A14})$$

A solution for (A14) allows the velocity potential for every point in the fluid domain to be found from (A11).

Using the general solution for diffraction about arbitrary shaped breakwaters, as described in the above, the specific case of a series of  $m = 1, 2, \dots, B$  straight breakwater segments positioned along the  $x$  axis each having a length of  $2a$ , is considered. Breakwater segment  $\Gamma_m$  is centered at  $(x = x_m, y = 0)$ , and the co-ordinates of its tips are  $(x_m, +au, 0)$  where  $u = [-1, 1]$ . Because the breakwater segments are aligned along the  $x$  axis the normals  $n_{p^+}$  and  $n_{q^+}$  are equivalent to  $y_p$  and  $y_q$ , respectively, and;

$$\frac{\partial^2 \phi_0}{\partial n_{p^+} \partial n_{q^+}}(p, q) = \frac{k}{4iR_{pq}} H_1^{(1)}(kR_{pq}) \quad (\text{A15})$$

If on breakwater segment  $m$ , at point  $p$ , the a jump in velocity potential  $\phi(p)$  is described by the function  $\mathcal{P}_m(u)$ , (A14) becomes;

$$\frac{i\beta}{k} \mathcal{P}_m(u) + \frac{1}{4} \sum_{n=1}^B \mathcal{F}_{-1}^1 \mathcal{P}_n(u) \frac{H_1^{(1)}(ka|x_m - x_n|/a+u-v)}{|(x_m - x_n)/a+u-v|} dv = \sin \alpha \exp[-ika(x_m/a + u - v) \cos \alpha] \quad (\text{A16})$$

As shown in (Linton & McIver, 2001) for a straight breakwater segment aligned along the  $x$  axis the diffraction velocity potential in the fluid domain at two mirrored points about the  $x$  axis share the relationship;

$$\phi(x, -y) = -\phi(x, y) \quad (\text{A17})$$

and it follows that for each  $p^+$  point on the breakwater segment  $\Gamma_m$ ;

$$\mathcal{P}_m(u) = 2\phi(p^+) \quad (\text{A18})$$

For any point in the fluid domain on the  $x$  axis that is not on a breakwater segment;

$$\phi(x, 0) = 0 \quad (\text{A19})$$

which means that on the breakwater;

$$\mathcal{P}_m(u) \rightarrow 0 \quad \text{when } u \rightarrow \pm 1 \quad (\text{A20})$$

The Chebyshev polynomials of the second kind [ $U_s(u)$  for  $s = 0, 1, \dots$ ] are complete over the range  $u = (-1, 1)$  and have a weighting function  $(1 - u^2)^{0.5}$ . The diffracted velocity potential derivatives have singularities at the breakwater segment tips and an approximate solution for  $\mathcal{P}_m(u)$  across the breakwater segment is need which takes the form;

$$\mathcal{P}_m(u) = (1 - u^2)^{0.5} \sum_{s=0}^S a_{ms} U_s(u) \quad (\text{A21})$$

where the coefficients  $a_{ms}$  are to be found and  $S$  is an integer.

Applying (A21) to (A16) yields;

$$\begin{aligned} & \frac{i\beta}{k} (1 - u^2)^{0.5} \sum_{s=0}^S a_{ms} U_s(u) + \frac{1}{4} \sum_{s=0}^S a_{ms} \mathfrak{f}_{-1}^1 (1 - v^2)^{0.5} U_s(v) \frac{H_1^{(1)}(ka|u-v|)}{|u-v|} dv + \\ & \frac{1}{4} \sum_{n=1, n \neq m}^B \sum_{s=0}^S a_{ns} \int_{-1}^1 (1 - v^2)^{0.5} U_s(v) \frac{H_1^{(1)}(ka|x_m - x_n|/a+u-v|)}{|(x_m - x_n)/a+u-v|} dv = \sin \alpha \exp[-ika(x_m/a + u - v) \cos \alpha] \end{aligned} \quad (\text{A22})$$

Collocation at the points;

$$u_s = \cos \left[ \frac{(2s+1)\pi}{2S+2} \right] \quad \text{for } s = 0, 1, \dots, S \quad (\text{A23})$$

is used to obtain a set of simultaneous equations for the coefficients  $a_{ms}$  which are the zeros of the Chebyshev polynomial of the first kind.

By introducing the following;

$$L(z) = H_1^{(1)}(z) + \frac{2i}{\pi z} - \frac{1}{\pi} z \log z \quad (\text{A24})$$

and by using the following result given in (Frenkel, 1983), to evaluate the finite-part integral in (A23);

$$\mathfrak{f}_{-1}^1 \frac{(1-v^2)^{0.5} U_s(v)}{(u-v)^2} dv = -\pi(s+1)U_s(v) \quad (\text{A25})$$

leads to the following;

$$\begin{aligned} & \mathfrak{f}_{-1}^1 (1 - v^2)^{0.5} U_s(v) \frac{H_1^{(1)}(ka|u-v|)}{|u-v|} dv = \frac{2i}{ka} (s+1)U_s + \frac{ika}{\pi} \mathfrak{f}_{-1}^1 (1 - v^2)^{0.5} U_s(v) \log(ka|u - v|) dv + \\ & \int_{-1}^1 (1 - v^2)^{0.5} U_s(v) \frac{L(ka|u-v|)}{|u-v|} dv \end{aligned} \quad (\text{A26})$$

where  $\mathfrak{f}$  is a principle-value integral.

The step velocity potential across each breakwater allows the velocity potential in the remainder of the fluid domain to be determined. This is achieved with (A11) and (A21) and the following result;

$$\frac{\partial \phi_0}{\partial n_q^+}(P, q) = \frac{1}{4} iky \frac{H_1^{(1)}(kR_{Pq})}{R_{Pq}} \quad (\text{A27})$$

The velocity potential the fluid domain is given by;

$$\phi(x, y) = \frac{1}{4} ikay \sum_{m=1}^B \int_{-1}^1 \mathcal{P}_m(v) \frac{H_1^{(1)}(kR_m)}{R_m} dv \quad \text{when } y \neq 0 \quad (\text{A28})$$

which expands to;

$$\phi(x, y) = \frac{1}{4} ikay \sum_{m=1}^B \sum_{s=0}^S a_{ms} \int_{-1}^1 (1 - v^2)^{0.5} U_s(v) \frac{H_1^{(1)}(kR_m)}{R_m} dv \quad \text{when } y \neq 0 \quad (\text{A29})$$

which can solved numerically using Gauss-Chebyshev quadrature and where;

$$R_m^2 = (x - x_m - av)^2 + y^2 \quad (\text{A30})$$

The solution for the remaining domain not considered in (A29) is;

$$\phi = \frac{\mathcal{P}_m((x-x_m)/a)}{2} \quad (\text{A31})$$

at the surface of segment  $\Gamma_m^\pm$  except for the region outside the breakwater surface along the line  $y = 0$  in the fluid domain where  $\phi = 0$ .

In the far-field when  $r = (x^2 + y^2) \rightarrow \infty$  (A29) can be simplified using the following result from (Abramowitz & Stegun, 1964);

$$H_1^{(1)}(z) \sim \left(\frac{2}{\pi z}\right)^{0.5} \exp\left[i\left(z - \frac{3\pi}{4}\right)\right] \quad (\text{A32})$$

and

$$\begin{aligned} R_m &= \{(x - x_m - av)^2 + y^2\}^{0.5} = r(1 - 2x(x_m + av)/r + O(r^{-2}))^{0.5} \\ &= r - (x_m + av) \cos \theta + O(r^{-1}) \end{aligned} \quad (\text{A33})$$

So that;

$$\phi(x, y) \sim \frac{\exp[i(kr - 3\pi/4)]}{(2\pi kr)^{0.5}} K_d(\theta, \alpha) \quad \text{as } kr \rightarrow \infty \quad (\text{A34})$$

where the diffraction coefficient is described by;

$$K_d(\theta, \alpha) = \frac{1}{2} ika \sin \theta \sum_{s=0}^S \left[ \int_{-1}^1 (1 - v^2)^{0.5} U_s \exp(-ikav \cos \theta) dv \sum_{m=1}^B a_{ms} \exp(-ikx_m \cos \theta) \right]$$

## Appendix B

# Approximate solution for the horizontal turbine axial load for the Pico Wells turbine (Falcão, 2002)

### B.1 Context

As part of the OWC wave to wire power transfer model the mechanical losses from bearing friction need to be accounted for. In order to do this the turbine variable reciprocating horizontal axial load  $F_a$  resulting from aerodynamic thrust needs to be known.  $F_a$  is a difficult quantity to measure but a theoretical solution to make a very approximate calculation of the axial load for a Wells turbine using; chamber pressure, air flow past the turbine and turbine angular velocity, is presented in (Falcão, 2002) and this solution is summarised in the following.

### B.2 Solution

The chamber pressure head  $p$  is the difference between chamber pressure and atmospheric pressure;

$$|p| = p_{0A} - p_{0B} \quad (\text{B1})$$

where  $p_{0A}$  is the chamber pressure and  $p_{0B}$  is atmospheric pressure if  $p_{0A} > p_{0B}$ , and vice versa when  $p_{0A} < p_{0B}$ .

If  $p_1$  and  $p_2$  are the up-stream and down-stream pressures at the rotor, respectively, and flow is taken as being incompressible, the axial force on the rotor is;

$$|F_a| = \int (p_1 - p_2) dA \quad (\text{B2})$$

where  $A$  is the duct area given by;

$$A = \frac{\pi(D^2 - D_i^2)}{4} \quad (\text{B3})$$

where  $D$  is the turbine diameter which is also the outer duct diameter and  $D_i$  is the inner duct diameter.

If one dimensional flow is assumed (B2) simplifies to;

$$|F_a| = (p_1 - p_2)A \quad (\text{B4})$$

If no guide vanes are present and the stagnation pressure loss between  $p_{0A}$  and  $p_1$  is zero, then;

$$p_1 = p_{0A} - \frac{\rho_0 v_a^2}{2} \quad (\text{B5})$$

where  $\rho_0$  is air density at atmospheric pressure and  $v_a$  is the air flow rate passed the turbine (with direction perpendicular to the turbine plane), which is given by;

$$v_a = \frac{\dot{m}_t}{\rho_0 A} \quad (\text{B6})$$

where  $\dot{m}_t$  is the mass flow rate of air past the turbine.

If it is assumed that all kinetic energy is lost at the turbine duct exit to the atmosphere  $p_{0B} = p_2$ , (B1) and (B5), lead to;

$$p_1 - p_2 = |p| - \frac{\rho_0 v_a^2}{2} \quad (\text{B7})$$

As discussed in section 4.1.2, the non-dimensional pressure head  $\Psi$  and non-dimensional flow rate  $\Phi$  past the turbine are given by;

$$\Psi = \frac{p_c}{\rho_0 N^2 D^2} \quad (\text{B8})$$

$$\Phi = \frac{\dot{m}_t}{\rho_0 N D^3} \quad (\text{B9})$$

If the whole turbine rotor, not just that exposed to the air-flow, is considered to be exposed to the same pressure differences  $p_1 - p_2$ , the turbine axial load is given by combing (B5), (B5), (B8) and (B9), to give;

$$|F_a| = \rho_0 N^2 D^4 \left[ \frac{\pi}{4} |\Psi| - \frac{1}{2(1-D_r^2)^2} \Phi^2 \right] \quad (\text{B10})$$

where  $D_r = D_i/D$ .

If guide vanes are present, so that flow passes a triple cascade blade systems, it is now necessary to considered two-dimensional flow. If the turbine is in un-stalled conditions then irrotational and incompressible flow assumptions are still applicable.

The upstream flow angle at the inlet of the turbine is;

$$\alpha_1 = \tan^{-1} \left( \frac{v_a}{v_{1c}} \right) \quad (\text{B11})$$

and downstream flow angle at the outlet of the turbine is;

$$\alpha_2 = \tan^{-1} \left( \frac{v_a}{v_{2c}} \right) \quad (\text{B12})$$

where  $v_{1c} = -v_{2c}$  are the circumferential air flow velocity components.

The angular deflection of flow from the interaction with the turbine is;

$$\Delta\alpha = \alpha_2 - \alpha_1 = \pi - 2\alpha_1 \quad (\text{B13})$$

For un-stalled conditions  $\alpha_1$  and  $\alpha_2$  are independent of  $\dot{m}_t$  and  $N$ . If the aerodynamic losses at the guide vanes are neglected it can be shown that;

$$p_1 = p_{0A} - \frac{\rho_0 v_a^2 \csc^2(\alpha_1)}{2} \quad (\text{B14})$$

$$p_2 = p_{0B} - \frac{\rho_0 v_a^2 \cot^2(\alpha_1)}{2} \quad (\text{B15})$$

which yields the same  $F_a$  as given in (B10).

In stalled conditions  $\Psi > \Psi_{cr}$ , the turbine torque reduces and becomes very small with increasing  $\Psi$ . The flow deflection by the turbine also becomes small and the angular deflection of flow from the interaction with the turbine is now;

$$\Delta\alpha = \alpha'_2 - \alpha_1 \quad (\text{B16})$$

where  $\alpha'_2$  is the outlet flow angle for stalled conditions.

If it is assumed that  $\alpha'_2 \approx \alpha_1$  and  $v'_{2c} \approx v_{1c} = v_a \tan(\alpha_1)$  the flow angle at the downstream guide vanes is no longer in-line with the guide vane's blade angle  $(\pi - \alpha_1)$  and a significant loss is expected because of the large angle of incidence, which is estimated in (Pfleiderer & Petermann, 1991) as;

$$\frac{\rho_0(v_{1c}-v'_{2c})^2}{2} = 2\rho_0 v_a^2 \cot^2(\alpha_1) \quad (\text{B17})$$

Taking in to account the expected difference in stalled conditions the turbine axial load with guide vanes is given by;

$$|F_a| = \rho_0 N^2 D^4 \left( \frac{\pi}{4} |\Psi| - \frac{1}{2(1-D_r^2)^2} [1 + 4H(|\Psi| - \Psi_{cr}) \cot^2 \alpha_1] \Phi^2 \right) \quad (\text{B18})$$

where  $H$  is the Heaviside a step function where  $H = 0$  when  $|\Psi| - \Psi_{cr} < 0$  or  $H = 1$  when  $|\Psi| - \Psi_{cr} > 0$ , and  $\alpha_1 = 62.5^\circ$  relates to the radial averaged guide angle.

## Appendix C

# Method of least squares for an autoregressive forecast model

### C.1 Context

In chapters 6 and 7 the autoregressive forecast model is used to make short-term wave forecasts of the chamber excitation surface elevation  $\eta_e$ . In order to use an autoregressive model, first training must be performed to find the models optimum coefficients of regression through the minimisation of the cost function  $J$  which describes the sum of squared errors of the forecast when compared to the real data. The method of linear least squares is one way to find these optimal model regression coefficients. The method of least squares will be presented in the context of the autoregressive model format because this has the most relevance to the problem being considered. The method of least squares is a common technique and described widely but the first published example of the method is said to be in (Legendre, 1805), although other sources state that it was first discovered by Gauss in 1795.

### C.2 Solution

Let's consider a sampled data time series of  $\eta_e$ , and assume that at any data time instant  $k$ ,  $\eta_e(k)$  is dependent on the total of  $n - 1$  past values of  $\eta_e$  each multiplied by a linear coefficient  $a_j$  with some additive noise  $\varepsilon(k)$ ;

$$\eta_e(k) = a_1\eta_e(k - 1) + a_2\eta_e(k - 2) + \dots + a_n\eta_e(k - n + 1) + \varepsilon(k) \quad (C1)$$

where  $\eta_e(k)$  is the  $k^{th}$  observation of the dependent variable  $\eta_e$ ,  $\eta_e(k - j)$  is the  $k^{th}$  observation of the  $j^{th}$  independent variable, and  $a_j$  (coefficient of regression in this case) is the  $j^{th}$  coefficient of the  $j^{th}$  independent variable.

If a number of observations  $k = n, n + 1, \dots, L$  are made of the data set described in (C1) we have;

$$\begin{aligned} \eta_e(n) &= a_1\eta_e(n - 1) + a_2\eta_e(n - 2) + \dots + a_n\eta_e(1) + \varepsilon(n - 1) \\ \eta_e(n + 1) &= a_1\eta_e(n) + a_2\eta_e(n - 1) + \dots + a_n\eta_e(2) + \varepsilon(n) \\ &\vdots \\ \eta_e(L) &= a_1\eta_e(L - 1) + a_2\eta_e(L - 2) + \dots + a_n\eta_e(L - n + 1) + \varepsilon(L - 1) \end{aligned} \quad (C2)$$

which in matrix form is;

$$\begin{bmatrix} \eta_e(n) \\ \eta_e(n + 1) \\ \vdots \\ \eta_e(L) \end{bmatrix} = \begin{bmatrix} \eta_e(n - 1) & \eta_e(n - 2) & \dots & \eta_e(1) \\ \eta_e(n) & \eta_e(n - 1) & \dots & \eta_e(2) \\ \vdots & \vdots & \ddots & \vdots \\ \eta_e(L - 1) & \eta_e(L - 2) & \dots & \eta_e(L - n + 1) \end{bmatrix} \begin{bmatrix} a_1 \\ a_2 \\ \vdots \\ a_n \end{bmatrix} + \begin{bmatrix} \varepsilon(n - 1) \\ \varepsilon(n) \\ \vdots \\ \varepsilon(L - 1) \end{bmatrix} \quad (C3)$$

Or in matrix notation

$$Y = HA + E \quad (C4)$$

For a given estimate of the regression coefficients  $\hat{A}$  the difference (or error) between the past observations  $H\hat{A}$  and the target  $Y$  is found from;

$$E = Y - H\hat{A} \quad (C5)$$

A cost function  $J$  can be used to characterise the total error and if the cost function is set to the sum of the squared error the values of  $\hat{A}$  that minimise the cost function can be found using the least squares method;

$$J(\hat{A}) = E^T E \quad (C6)$$

$$J(\hat{A}) = (Y - H\hat{A})^T (Y - H\hat{A}) \quad (C7)$$

Expanding the above yields;

$$J(\hat{A}) = Y^T Y - H^T \hat{A}^T Y - Y^T H \hat{A} + \hat{A}^T H^T H \hat{A} \quad (C8)$$

The cost function can be interpreted as a curved surface or three-dimensional parabola describing the total error as a function of  $\hat{A}$ . The lowest point of the parabola  $\partial J / \partial \hat{A} = 0$  is the point at which  $\hat{A}$  results in the lowest possible  $J(\hat{A})$ . Taking the derivative of (C8), we find;

$$\frac{\partial J}{\partial \hat{A}} = -2Y^T H + 2\hat{A}^T H^T H = 0 \quad (C9)$$

Re-arranging (C9) and taking the transpose gives the equation of  $\hat{A}$  that gives the least squares minimisation of  $J(\hat{A})$ ;

$$\hat{A} = (H^T H)^{-1} H^T Y \quad (C10)$$

To verify this solution we consider the case where we want to predict  $Y$  from  $H\hat{A}$  which from (C4) leads to;

$$\hat{Y} = H\hat{A} = H(H^T H)^{-1} H^T Y \quad (C11)$$

$$\hat{Y} = H H^{-1} H^T H^{-T} Y = Y \quad (C12)$$

## Appendix D

# Levenberg-Marquardt learning algorithm for neural network training

### D.1 Context

In chapter 6 nonlinear autoregressive functions, found using artificial neural networks, are investigated for use with short-term wave forecasting. A learning algorithm can be used to selectively adjust the neural network parameters in order to more quickly find the optimal nonlinear autoregressive function. The Levenberg-Marquardt learning (LM) was used for this purpose and this learning algorithm is an amalgamation of method of gradient descent and the Gauss-Newton algorithm, which is an extension of Newton's Method and needs to be described first in order to describe the latter. The algorithm was first published in (Levenberg, 1944) and then rediscovered and published in (Marquardt, 1963). In the following, the LM algorithm is summarised from (Yu & Wilamowski, 2011) in manner that describes the optimisation of the weights of artificial neural networks in the training phase.

### D.2 Solution

If  $\varepsilon_{k,p}$  is a vector containing all the errors between the networks output  $\hat{\eta}_k$  and targets  $\eta_k$  for a number of data points  $k$ , using a specific training pattern, the sum square error is given by;

$$E(\eta, w) = \frac{1}{2} \sum_{k=1}^L \varepsilon_{k,p}^2 \quad (D1)$$

where  $\eta$  is the past surface elevation input vector,  $w$  is a vector containing all the network weights,  $L$  is the total length of the output/target error vector.

#### D.2.1 Method of gradient decent

The method of gradient decent considers the first derivative of the total error with respect to each network weight. The gradient vector  $g$  is given by;

$$g = \frac{\partial E(\eta, w)}{\partial w} = \left[ \frac{\partial E}{\partial w_1} \quad \frac{\partial E}{\partial w_2} \quad \dots \quad \frac{\partial E}{\partial w_n} \right]^T \quad (D2)$$

where  $n$  is the total number of network weights.

With  $g$  found the network's weights are updated for the next iteration  $\iota + 1$  where  $\iota$  is the iterations index, based on the steepest descent;

$$w_{\iota+1} = w_{\iota} - cg_{\iota} \quad (D3)$$

where  $c$  is step size learning constant

### D.2.2 Newton's method

If each of the  $n$  weights in the network have the index  $i$  and the gradient components  $g_1, g_2, \dots, g_n$  are nonlinear functions of all weights with each weight being linearly independent, the first order approximation of the Taylor series of the gradient components, is given by;

$$g_i \approx g_i + \frac{\partial g_i}{\partial w_1} \Delta w_1 + \frac{\partial g_i}{\partial w_2} \Delta w_2 + \dots + \frac{\partial g_i}{\partial w_n} \Delta w_n \quad (D4)$$

From (D2) the gradient vector with respect to the weights can be described by;

$$\frac{\partial g_i}{\partial w_j} = \frac{\partial^2 E}{\partial w_i \partial w_j} \quad (D5)$$

where  $j = 1, 2, \dots, n$  is a second index for the weights

Inputting (D5) into (D4) gives

$$\begin{aligned} g_1 &\approx g_1 + \frac{\partial^2 E}{\partial w_1^2} \Delta w_1 + \frac{\partial^2 E}{\partial w_1 \partial w_2} \Delta w_2 + \dots + \frac{\partial^2 E}{\partial w_1 \partial w_n} \Delta w_n \\ g_2 &\approx g_2 + \frac{\partial^2 E}{\partial w_2 \partial w_1} \Delta w_1 + \frac{\partial^2 E}{\partial w_2^2} \Delta w_2 + \dots + \frac{\partial^2 E}{\partial w_2 \partial w_n} \Delta w_n \\ &\quad \vdots \\ g_n &\approx g_n + \frac{\partial^2 E}{\partial w_n \partial w_1} \Delta w_1 + \frac{\partial^2 E}{\partial w_n \partial w_2} \Delta w_2 + \dots + \frac{\partial^2 E}{\partial w_n^2} \Delta w_n \end{aligned} \quad (D6)$$

The local minimum of the total error is found when the gradient vectors equal zero, applying this to (D6) and rearranging gives;

$$\begin{aligned} -\frac{\partial E}{\partial w_1} = -g_1 &\approx \frac{\partial^2 E}{\partial w_1^2} \Delta w_1 + \frac{\partial^2 E}{\partial w_1 \partial w_2} \Delta w_2 + \dots + \frac{\partial^2 E}{\partial w_1 \partial w_n} \Delta w_n \\ -\frac{\partial E}{\partial w_2} = -g_2 &\approx \frac{\partial^2 E}{\partial w_2 \partial w_1} \Delta w_1 + \frac{\partial^2 E}{\partial w_2^2} \Delta w_2 + \dots + \frac{\partial^2 E}{\partial w_2 \partial w_n} \Delta w_n \\ &\quad \vdots \\ -\frac{\partial E}{\partial w_n} = -g_n &\approx \frac{\partial^2 E}{\partial w_n \partial w_1} \Delta w_1 + \frac{\partial^2 E}{\partial w_n \partial w_2} \Delta w_2 + \dots + \frac{\partial^2 E}{\partial w_n^2} \Delta w_n \end{aligned} \quad (D7)$$

There are  $m$  equations which can be used to calculated the change in all the weights  $\Delta w_i$ .

If the all the second order differential equations of (D7) are described by the Hessian matrix  $H$ , all the  $g_i$  gradients are described by the vector  $g$ , and all weights changes  $\Delta w_i$  are described by the vector  $\Delta w$ , which allows (D7) to be presented in Matrix notation as;

$$-g = H \Delta w \quad (D8)$$

Rearranging (D8) gives;

$$\Delta w = H^{-1} g \quad (D9)$$

This is the update rule for Newton's method, so that the weight of each new iteration  $\iota + 1$  is;

$$w_{\iota+1} = w_{\iota} - H^{-1} g_{\iota} \quad (D10)$$

### D.2.3 Gauss-Newton algorithm

To ease the calculations of the all the second-order derivatives of the total error function for weight updating with the Newton's method, the Jacobian matrix  $J$  is introduced;

$$J = \begin{bmatrix} \frac{\partial \varepsilon_{1,1}}{\partial w_1} & \frac{\partial \varepsilon_{1,1}}{\partial w_2} & \dots & \frac{\partial \varepsilon_{1,1}}{\partial w_n} \\ \frac{\partial \varepsilon_{1,2}}{\partial w_1} & \frac{\partial \varepsilon_{1,2}}{\partial w_2} & \dots & \frac{\partial \varepsilon_{1,2}}{\partial w_n} \\ \vdots & \vdots & \ddots & \vdots \\ \frac{\partial \varepsilon_{1,m}}{\partial w_1} & \frac{\partial \varepsilon_{1,m}}{\partial w_2} & \dots & \frac{\partial \varepsilon_{1,m}}{\partial w_n} \end{bmatrix} \quad (\text{D11})$$

Substituting  $J$  into the gradient decent equation (D2) gives;

$$g = J\varepsilon \quad (\text{D12})$$

where  $\varepsilon$  is a vector containing all errors;

Because the multiplication of  $J$  by its transpose gives an approximation of the Hessian matrix  $H$ , (D10) using (D12), gives;

$$w_{t+1} = w_t - (J_t^T J_t)^{-1} J_t \varepsilon_t \quad (\text{D13})$$

### D.2.4 Levenberg-Marquardt algorithm

Finally the Levenberg-Marquardt algorithm combines the method of gradient descent and the Gauss-Newton algorithm by adding a positive combination coefficient  $\mu$  to the approximation of the Hessian matrix;

$$H \sim J^T J + \mu I \quad (\text{D13})$$

where  $I$  is the identity matrix

Substituting the new approximation of the Hessian matrix into (D13), gives;

$$w_{t+1} = w_t - (J_t^T J_t + \mu I)^{-1} J_t \varepsilon_t \quad (\text{D14})$$

By prescribing a large value for  $\mu$ , (D14) gives an estimate of (D3), which is the gradient decent method. Because the gradient decent method asymptotical converges to the local minimum, when it gets close the weight adjustments are very small and convergence slows. By prescribing progressively small value for  $\mu$  (D14) approaches (D13), which is Newton's method which has faster convergence near the minimum and is more accurate. In effect the Levenberg-Marquardt learning algorithm interpolates between the gradient decent and Newton's method to utilise the strengths of each at different stages of the error minimisation process to give a faster and more accurate convergence.

## Appendix E

### Detailed field test result from control strategies

#### *Basic<sub>RVC</sub>* and *Envelope<sub>RVC</sub>*

The hourly averages in performance from field test results under the *Basic<sub>RVC</sub>* and *Envelope<sub>RVC</sub>* control strategies along with the corresponding sea state characteristics and tidal elevation are given in in table E1. The results from each test group are order in descending power enhancement from *Envelope<sub>RVC</sub>* when compared to *Basic<sub>RVC</sub>*.

**Table E1** Field test results from *Envelope<sub>RVC</sub>* (green rows) and *Basic<sub>RVC</sub>* (blue rows).

Set #	$\sigma(\Psi)$	$\overline{k_v}$	$\overline{P_e}$ (kW)	% $\Psi > 0.068$	% $\Psi > 0.1$	% $\Psi > 0.125$	% $\Psi > 0.15$	% $\Psi > 0.175$	$\overline{V_G}$ (mms <sup>-1</sup> )	$\overline{V_c}$ (mms <sup>-1</sup> )	$H_s$ (m)	$T_p$ (s)	Tide
#1	0.048	0.17	41.5	10.49	2.25	0.51	0.10	0.00	0.079	0.067	3.5	13.6	0.45
	0.049	0.08	51.3	14.16	3.60	1.10	0.22	0.00	0.061	0.034	3.5	13.6	0.34
	0.048	0.11	35.1	11.86	2.99	0.74	0.22	0.00	0.093	0.094	3.6	12.8	0.25
	0.051	0.06	48.6	12.90	3.29	0.85	0.14	0.01	0.067	0.041	3.6	12.8	0.10
	0.049	0.03	44.5	13.49	4.08	1.29	0.27	0.05	0.083	0.063	3.6	13.2	-0.07
	0.049	0.03	53.8	12.48	3.08	0.82	0.08	0.01	0.055	0.026	3.6	13.2	-0.19
	0.048	0.12	38.2	9.97	2.29	0.47	0.10	0.00	0.084	0.079	2.9	13.1	-0.32
	0.050	0.04	53.6	10.43	1.79	0.28	0.00	0.00	0.051	0.030	2.9	13.1	-0.42
	0.049	0.16	42.0	11.75	2.85	1.03	0.18	0.00	0.074	0.062	3.7	12.8	-0.38
	% Difference			28.8	8.6	1.7	-5.7	-36.1	-29.9	-29.4	-55.2		
#2	0.050	0.35	29.2	16.62	4.71	1.94	0.40	0.06	0.113	0.127	3.9	14.4	0.48
	0.056	0.10	41.3	13.45	4.47	1.99	0.49	0.07	0.109	0.094	3.9	14.4	0.54
	0.055	0.23	29.9	18.68	6.29	2.89	1.39	0.54	0.121	0.123	3.5	15.5	0.43
	0.052	0.09	36.1	17.58	5.35	2.04	0.50	0.03	0.114	0.113	3.5	15.5	0.21
	0.049	0.16	27.0	15.35	4.55	1.35	0.28	0.06	0.112	0.130	3.2	14.6	-0.08
	0.053	0.05	31.3	18.32	5.93	2.26	0.58	0.08	0.119	0.127	3.2	14.6	-0.17
% Difference			26.2	-2.6	1.2	1.8	-23.9	-71.6	-1.1	-12.0			
#3	0.049	0.06	51.9	14.46	4.51	1.76	0.56	0.11	0.060	0.033	3.5	16.5	0.10
	0.046	0.15	42.3	12.69	3.70	1.24	0.41	0.11	0.081	0.068	3.4	15.5	0.16
	0.048	0.07	46.7	12.58	3.76	1.36	0.43	0.08	0.070	0.048	3.3	16.0	0.23
	0.049	0.16	43.3	14.44	4.34	2.05	0.62	0.12	0.085	0.069	3.6	15.1	0.10
	0.049	0.04	49.8	14.50	4.43	1.75	0.47	0.11	0.070	0.043	3.2	14.2	0.03
	0.048	0.10	41.5	12.44	3.56	1.18	0.35	0.07	0.085	0.074	3.2	15.1	-0.11
% Difference			16.9	5.0	9.6	9.1	5.8	0.9	-20.7	-41.3			
#4	0.049	0.22	40.9	15.47	5.19	1.92	0.44	0.04	0.093	0.078	3.5	12.2	0.29
	0.052	0.13	52.5	16.72	5.85	2.03	0.21	0.04	0.064	0.027	3.5	12.2	0.44
	0.051	0.18	45.9	16.29	5.71	1.86	0.62	0.06	0.079	0.052	3.4	12.6	0.49
	0.053	0.12	50.4	18.21	6.04	2.26	0.57	0.03	0.071	0.034	3.4	12.6	0.41
	0.053	0.25	42.8	18.78	6.50	2.43	0.64	0.10	0.094	0.075	3.6	12.6	0.32
	0.055	0.17	48.3	21.14	7.75	2.89	0.64	0.04	0.088	0.052	3.6	12.6	0.16
	0.051	0.27	40.3	17.75	5.92	2.08	0.39	0.01	0.098	0.085	3.4	13.1	0.01
	0.053	0.17	48.1	19.40	6.05	1.85	0.28	0.03	0.083	0.050	3.4	13.1	-0.02
	0.052	0.27	45.1	17.89	6.10	2.24	0.46	0.06	0.086	0.064	3.6	11.8	-0.09
	% Difference			15.9	9.5	9.2	7.2	-17.1	-34.5	-14.9	-42.3		

**Table E1** (continued)

Set #	$\sigma(\Psi)$	$\bar{k}_v$	$\bar{P}_e$ (kW)	% $\Psi > 0.068$	% $\Psi > 0.1$	% $\Psi > 0.125$	% $\Psi > 0.15$	% $\Psi > 0.175$	$\bar{V}_G$ (mms <sup>-1</sup> )	$\bar{V}_c$ (mms <sup>-1</sup> )	$H_s$ (m)	$T_p$ (s)	Tide
#5	0.048	0.21	45.6	14.10	4.42	1.67	0.37	0.04	0.071	0.050	3.6	12.2	-0.17
	0.051	0.18	50.4	15.75	5.60	1.90	0.39	0.06	0.069	0.039	3.6	12.2	-0.08
	0.052	0.24	47.0	16.94	6.05	2.75	0.86	0.26	0.080	0.055	3.4	11.7	0.22
	0.050	0.19	47.4	14.65	5.07	1.74	0.33	0.07	0.076	0.049	3.4	11.7	0.36
	0.055	0.25	47.1	18.87	7.07	2.78	0.78	0.32	0.081	0.062	3.5	12.2	0.49
	0.051	0.18	54.4	15.25	5.40	1.72	0.17	0.00	0.058	0.024	3.5	12.2	0.57
	0.049	0.17	51.3	14.32	4.64	1.40	0.29	0.08	0.061	0.036	3.5	12.6	0.55
	0.051	0.15	57.1	15.69	5.24	1.81	0.46	0.08	0.050	0.017	3.5	12.6	0.43
	0.050	0.13	52.8	15.47	4.83	1.94	0.53	0.07	0.059	0.031	3.5	13.1	0.34
	0.051	0.13	54.6	15.62	5.33	1.96	0.46	0.07	0.057	0.023	3.5	13.1	0.18
	0.051	0.13	49.9	16.07	5.90	2.06	0.46	0.15	0.070	0.044	3.2	12.6	-0.10
	% Difference			7.8	-3.6	-2.9	-13.1	-34.2	-64.2	-12.0	-34.0		
#6	0.036	0.03	28.9	5.74	0.42	0.00	0.00	0.00	0.082	0.091	2.1	13.5	-0.19
	0.037	0.00	25.8	5.83	0.86	0.03	0.00	0.00	0.085	0.096	2.0	13.5	-0.57
	0.036	0.01	19.8	5.97	0.47	0.00	0.00	0.00	0.092	0.111	1.9	12.5	-0.74
	0.036	0.00	16.0	6.05	0.82	0.19	0.03	0.00	0.095	0.112	1.8	13.1	-0.58
	0.035	0.02	18.1	5.21	0.35	0.01	0.00	0.00	0.090	0.105	1.9	13.1	-0.25
	0.036	0.00	20.3	5.71	0.75	0.07	0.00	0.00	0.089	0.102	1.8	12.8	0.05
% Difference			7.5	-3.9	-49.1	-95.2	-100.0	N/A	-1.6	-1.3			
#7	0.036	0.02	43.8	4.92	0.21	0.00	0.00	0.00	0.060	0.049	1.8	10.9	0.02
	0.035	0.00	39.3	4.71	0.40	0.06	0.01	0.00	0.065	0.061	1.7	10.7	0.30
	0.032	0.02	31.1	2.50	0.06	0.00	0.00	0.00	0.068	0.077	1.5	10.7	0.48
	0.035	0.00	32.1	4.97	0.29	0.08	0.04	0.01	0.075	0.083	1.4	10.7	0.26
% Difference			5.0	-23.4	-62.0	-100.0	-100.0	-100.0	-8.4	-12.8			

**Table E1** (continued)

Set #	$\sigma(\Psi)$	$\bar{k}_v$	$\bar{P}_e$ (kW)	% $\Psi > 0.068$	% $\Psi > 0.1$	% $\Psi > 0.125$	% $\Psi > 0.15$	% $\Psi > 0.175$	$\bar{V}_G$ ( $mms^{-1}$ )	$\bar{V}_c$ ( $mms^{-1}$ )	$H_s$ (m)	$T_p$ (s)	Tide
#8	0.037	0.00	14.4	6.24	0.90	0.12	0.04	0.00	0.098	0.111	2.2	14.6	0.16
	0.038	0.06	15.6	7.05	0.92	0.08	0.00	0.00	0.103	0.121	2.2	14.6	0.11
	0.043	0.00	21.5	9.90	2.18	0.67	0.30	0.10	0.104	0.120	2.5	14.6	0.08
	0.042	0.06	22.1	8.94	1.41	0.10	0.00	0.00	0.101	0.117	2.5	14.6	-0.07
	0.040	0.00	10.9	8.82	1.31	0.24	0.04	0.00	0.116	0.126	2.1	13.5	-0.37
	0.041	0.02	15.5	9.11	1.26	0.11	0.00	0.00	0.115	0.136	2.1	13.5	-0.59
	0.040	0.00	19.0	8.73	1.40	0.28	0.01	0.00	0.103	0.122	2.0	13.8	-0.48
	0.037	0.01	19.8	6.19	0.85	0.08	0.00	0.00	0.094	0.112	2.0	13.8	-0.15
	0.039	0.00	26.1	7.37	1.17	0.31	0.06	0.00	0.092	0.105	1.9	13.1	0.10
	0.035	0.03	17.9	4.71	0.33	0.00	0.00	0.00	0.088	0.102	1.9	13.1	0.19
0.034	0.00	13.7	4.71	0.58	0.03	0.00	0.00	0.089	0.101	1.7	12.8	0.25	
% Difference			3.4	-5.6	-24.1	-72.3	-100.0	-100.0	-0.2	3.1			
#9	0.033	0.00	17.9	3.47	0.32	0.07	0.00	0.00	0.082	0.100	1.6	11.6	0.45
	0.032	0.03	17.9	2.67	0.11	0.00	0.00	0.00	0.082	0.105	1.6	11.6	0.23
	0.034	0.00	13.7	4.47	0.24	0.00	0.00	0.00	0.085	0.097	1.4	11.1	-0.05
	0.030	0.03	14.0	2.46	0.07	0.00	0.00	0.00	0.083	0.103	1.4	11.1	-0.48
	% Difference			1.0	-35.5	-67.5	-100.0	N/A	N/A	-1.2	5.8		
#10	0.035	0.07	38.7	4.58	0.21	0.00	0.00	0.00	0.068	0.065	2.1	11.6	0.31
	0.036	0.00	44.0	5.33	0.76	0.08	0.00	0.00	0.059	0.049	2.0	12.8	0.35
	0.036	0.03	45.4	5.43	0.49	0.01	0.00	0.00	0.058	0.045	2.0	11.4	0.24
	0.036	0.00	40.8	4.92	0.44	0.03	0.00	0.00	0.066	0.058	1.9	11.1	-0.12
	0.034	0.03	35.6	4.45	0.19	0.00	0.00	0.00	0.071	0.072	1.9	12.5	-0.34
	0.036	0.00	34.1	5.75	0.36	0.00	0.00	0.00	0.079	0.082	1.9	12.2	-0.45
	% Difference			0.7	-9.6	-43.9	-87.5	N/A	N/A	-3.5	-4.2		
#11	0.050	0.08	36.8	14.97	5.21	2.14	0.71	0.25	0.092	0.086	3.6	15.1	0.48
	0.048	0.11	39.6	12.62	4.07	0.89	0.19	0.00	0.089	0.076	3.6	15.1	0.59
	0.053	0.08	40.8	16.82	5.65	2.64	1.14	0.37	0.093	0.078	3.7	15.5	0.44
	0.050	0.11	39.1	14.82	5.01	2.00	0.42	0.00	0.100	0.090	3.7	15.5	0.21
	0.053	0.07	39.2	18.19	6.40	2.64	0.76	0.17	0.102	0.088	3.2	14.2	-0.08
	0.049	0.10	32.1	13.35	4.04	0.81	0.06	0.00	0.105	0.107	3.2	14.2	-0.35
	0.051	0.02	35.8	16.00	5.61	1.89	0.33	0.10	0.108	0.106	3.0	14.6	-0.59
	% Difference			-3.1	-17.6	-23.5	-47.1	-69.8	-100.0	-0.9	1.4		

# References List

- Abanades, J., Greaves, D. & Iglesias, G., 2015. Coastal defence using wave farms: The role of farm-to-coast distance. *Renewable energy*, Volume 75, pp. 527-582.
- Abramowitz, M. & Stegun, I. A., 1964. *Handbook of mathematical functions*. New York: National bureau of standards.
- Airy, G. B., 1845. Tides and Wavec. In: *Encyclopaedia Metropolitana*. s.l.:art 192, pp. 241-396.
- Beels, C. et al., 2010. Numerical implementation and sensitivity analysis of a wave energy converter in a time-dependent mild-slope equation model. *Coastal Engineering*, 57(5), pp. 471-492.
- Black, K., 2007. *Review of wave hub technical studies: Impact on inshore surfing beaches*, s.l.: Report for South West of England Regional Development Agency by ARS ltd.
- Bowen, M. K. & McIver, P., 2002. Diffraction by a gap in an infinite permeable breakwater. *Journal of Waterway, Port, Coastal and Ocean Engineering*, Volume 128, pp. 2-9.
- Brito-Melo, A. et al., 2001. Numerical modelling of OWC-shoreline devices including the effect of surrounding coastline and non-flat bottom. *Journal of Offshore and Polar Engineering*, 11(2), p. 147-154.
- Budal, K. et al., 1982. *The Norwegian wave-power buoy project*. Trondheim, The 2nd International Symposium on Wave Energy Utilization.
- Count, B. M., Fry, R., Haskell, J. & Jackson, N., 1981. *The MEL Oscillating water column*, s.l.: C.E.Q.B report no. RD/M/1157N81.
- Cruz, J., 2008. *Ocean wave energy. Current status and future perspectives*. 1 ed. Berlin: Springer-Verlag.
- Daemrich, K. F. & Kohlhasse, S., 1978. *Influence of breakwater reflection on diffraction*. Honolulu, 16th International Conference on Coastal Engineering.
- Dalrymple, R. A. & Martin, P. A., 1990. Wave diffraction through offshore breakwaters. *Journal of Waterway, Port, Coastal, and Ocean Engineering*, 116(6), pp. 727-741.
- Davis, R. E. & Regier, L. A., 1977. Methods for estimating directional wave spectra from multi-element arrays. *Journal of Marine Research*, 35(3), pp. 453-477.
- de Moura, A. C. et al., 2010. *Airborne and underwater noise assessment at the Pico OWC wave power plant*. Bilbao, 3rd International Conference on Ocean Energy.
- Dean, R. G. & Dalrymple, R. A., 1991. *Water wave mechanics for engineers and scientists*. 2nd ed. Singapore: World Scientific.
- Deo, M. C., Jha, A., Chaphekar, A. S. & Ravikant, K., 2001. Neural networks for wave forecasting. *Ocean Engineering*, 28(7), pp. 889-898.
- Dixon, S. L., 1978. *Fluid Mechanics, Thermodynamics of Turbomachinery*. 3rd ed. Oxford: Pergamon.
- European wave energy pilot plant on the island of Pico, a. P. P. t. E., 1999. *European wave energy pilot plant on the island of Pico, azores, Portugal. Phase two: Equipment*, Lisbon: JOR3-CT95-0012, Contract.
- Evans, D. V., 1982. Wave power absorption by systems of oscillating surface pressure distributions. *Journal of Fluid Mechanics*, Volume 114, p. 481-499.
- Falcao, A. F., 2000. *The shoreline OWC wave power plant at the Azores*. Aalborg, Denmark, 4th European wave and Tidal Energy Conference.
- Falcão, A. F. d. O., 2002. Control of an oscillating-water-column wave power plant for maximum energy production. *Applied Ocean Research*, 24(2), p. 73-82.

- Falcão, A. F. d. O., 2002. Control of an oscillating-water-column wave power plant for maximum energy production. *Applied Ocean Research*, 24(2), p. 73–82.
- Falcão, A. F. d. O. & Justino, P. A., 1999. OWC wave energy devices with airflow control. *Ocean Engineering*, 26(12), p. 1275–1295.
- Falcao, A. F. d. O., Vieira, L. C., Justino, P. A. P. & Andre, J. M. C. S., 2003. By-pass Air-Valve Control of an OWC Wave Power Plant. *Journal of Offshore Mechanics and Arctic Engineering*, pp. 205 - 210.
- Falcao, A. F. d. & Rodrigues, R. J. A., 2002. Stochastic modelling of OWC wave power plant performance. *Applied Ocean Reserch*, Volume 24, pp. 59-71.
- Falnes, J., 2002. *Ocean waves and oscillating systems*. 1st ed. Cambridge: Cambridge University press.
- Faltinsen, O. M., 1990. *Sea Loads on Ships and Offshore Structures*. Cambridge: Cambridge University press.
- Fernandez, H., Vousdoukas, M. I., Schimmels, S. & Allajbej, I., 2013. *Real time wave prediction for WEC control system optimization using a dynamic neural network*. Aalborg, 10th European Wave and Tidal Energy Conference.
- Ferri, F., Sichani, M. T. & Frigaard, P., 2012. *A Case study of short-term wave forecasting based on FIR filter: optimization of the power production for the wave star device*. Rhodes, 22nd International Offshore and Polar Engineering Conference, pp. 628-351.
- Fischer, B., Kracht, P. & Perez-Becke, S., 2012. *Online-Algorithm using Adaptive Filters for Short-Term Wave Prediction and its Implementation*. Dublin, 4th International Conference on Ocean Energy.
- Folley, M. & Whittaker, T., 2005. *The effect of plenum chamber volume and air turbine hysteresis on the optimal performance of oscillating water columns*. Halkidiki, 24th International Conference on Offshore Mechanics and Arctic Engineering.
- Frenkel, A., 1983. *External modes of two-dimensional thin scatterers*. s.l., IEE proceedings H, Microwaves, optics and antenas , pp. 209-214.
- Funke, E. R. & Mansard, E. P. D., 1980. *On the Synthesis of Realistic Sea States*. Sydney, 17th International Conference on Coastal Engineering, pp. 2974-2991.
- Fusco, F., 2009. *Short-term Wave Forecasting as a Univariate Time Series Problem*, Maynooth: Research report department of Electronic Engineering NUI Maynooth.
- Fusco, F., 2012. *Real-time Forecasting and Control for Oscillating Wave Energy Devices*, Maynooth: PhD thesis, National University of Ireland Maynooth.
- Fusco, F. & Ringwood (a), J. V., 2010. *Short-Term Wave Forecasting with AR models in Real-Time Optimal Control of Wave Energy Converters*. Bari, ISIE 2010, 2010 IEEE International Symposium on Industrial Electronics.
- Fusco, F. & Ringwood (b), J. V., 2010. Short-Term Wave Forecasting for Real-Time Control of Wave Energy Converters. *IEEE Transactions on Sustainable Energy*, 1(2), pp. 99-106.
- Gato, L. M. C. & Falcao, A. F. d. O., 1988. Aerodynamics of the Wells turbine. *International Journal of Mechanical Sciences*, 30(6), pp. 383-395.
- Gato, L. M. C., Warfield, V. & Thakker, A., 1996. Performance of a High-Solidarity Wells Turbine for an OWC Wave Power Plant. *ASME Journal of Energy Resources Technology*, Volume 118, pp. 263-268.
- Goda, Y., 2000. *Random seas and design of maritime structures*. 2nd ed. Singapore: World Scientific.
- Goda, Y., 2010. *Random seas and design of martime structures*. 3rd ed. Singapore: World Scientific.
- Goda, Y. & Suzuki, Y., 1975. Computations of refraction and diffraction of sea waves with Mitsuyasu's directional spectrum. *Technical Note of the Port and Harbour Research institute*, Volume 230, p. 45.
- Goda, Y. & Suzuki, Y., 1976. *Estimation of incident and reflected waves in random wave experiments*. Honolulu, Hawaii, 15th International Conference on Coastal Engineering.

- Goda, Y. & Suzuki, Y., 1976. *Estimation of incident and reflected waves in random wave experiments*. Honolulu, Hawaii, 15th International Conference on Coastal Engineering, pp. 828-845.
- Gurney, K., 1997. *An Introduction to Neural Networks 1997*. London: University College London Press.
- Harvey, A. C., 1989. *Forecasting, structural time series and the Kalman filter*. 1st ed. Cambridge: Cambridge University Press.
- Hasselmann, K. et al., 1973. Measurements of wind-wave growth and swell decay during the Joint North Sea Wave Project (JONSWAP). *Ergänzungsheft zur Deutschen Hydrographischen Zeitschrift Reihe*, a8(12), pp. 1-93.
- Hotta, S., 1978. *Wave height distribution around permeable breakwaters*. Honolulu, 16th International Conference on Coastal Engineering.
- Isobe, M. & Kondo, K., 1984. *Methods for estimating directional wave spectrum in incident and reflected wave field*. Houston, 19th International Conference on Coastal Engineering.
- Justino, P. A. P., 1993. *Phase control of oscillating water column systems for wave energy absorption*, Lisbon: Master's thesis, Instituto Superior Tecnico.
- Justino, P. A. P. & Falcao, A. F. d. O., 1999. Rotational speed control of an OWC wave power plant. *Journal of Offshore Mechanics and Arctic Engineering*, Volume 121, pp. 65-70.
- Kalman, R. E., 1960. A new approach to linear filtering and prediction problems. *Transactions of the ASME journal of basic engineering*, 82(D), pp. 35-45.
- Kim, H., Do, K. D. & Suh, K., 2011. Scattering of obliquely incident water waves by partially reflecting nontransmitting breakwaters. *Ocean Engineering*, 38(1), pp. 148-158.
- Kim, S. & Lee, H. J., 2010. The comparison of analytical and numerical solutions for wave diffraction due to insular breakwaters. *International Journal of Physical Sciences*, 5(3), pp. 226-237.
- Kirby, J. T. & Dalrymple, R. A., 1994. *Combined refraction/diffraction model REF/DIF 1, version 2.5 User manual - Technical report CACR-94-22*, Newark: University of Delaware.
- Kirby, J. T., Long, W. & Shi, F., 2005. *FUNWAVE 2.0 Fully Nonlinear Boussinesq Wave Model On Curvilinear Coordinates Part I: Model Formulations*, Newark: Center for Applied Reserch University of Delaware - Report number CRC-03-xx.
- Kirby, J. T. & Ozkan, H. T., 1994. *Combined refraction/diffraction model for spectral wave conditions, REF/DIF S*, Newark: Deptment of Civil and Enviromental Engineering, University of Delaware.
- Kofoed, J. P., Frigaard, P., Sorenson, H. C. & Friis-Madsen, E., 2000. *Development of the wave energy converter - Wave Dragon*. Seattle, Washington, 10th international offshore and polar engineering conference.
- Korde, U. A., Schoen, M. P. & Lin, F., 2001. *Time Domain Control of a Single Mode Wave Energy Device*. Stavange, 21st International Society of Offshore and Polar Engineers.
- Le Crom, I., 2010. *Engineering, analysis and monitoring of full-scale and prototype plants (performance safety and environmental impacts)*, s.l.: Wave train 2 report deliverable 6.
- Le Crom, I. et al., 2011. *Incident wave climate at the OWC Pico plant: Validation of a feed-forward based propagation method (ANN) and a numerical simulation (SWAN) with measured data*. Southampton, 9th European Wave and Tidal Energy Conference.
- Lee, J. J., 1971. Wave-induced oscillations in harbours of arbitrary geometry. *Journal of Fluid Mechanics*, Volume 45, pp. 375-394.
- Legendre, A. M., 1805. *Nouvelles Méthodes pour la Détermination des Orbites des Comètes*. 1st ed. Paris: F. Didot.
- Levenberg, K., 1944. A Method for the Solution of Certain Non-Linear Problems in Least Squares. *Quarterly of Applied Mathematics*, Volume 2, p. 164-168.

- Linton, C. M. & McIver, P., 2001. *Handbook of mathematical techniques for wave/structure interactions*. Boca Raton: Chapman & Hall/CRC.
- Longuet-Higgins, M. S., 1952. On the statistical distribution of the heights of sea waves. *Marine research*, 9(3), pp. 245-266.
- Makarynsky, O., 2004. Improving wave predictions with artificial neural networks. *Ocean Engineering*, 31(5-6), pp. 709-724.
- Mandal, S. & Prabakaran, N., 2010. Ocean Wave Prediction Using Numerical and Neural Network Models. *The Open Ocean Engineering journal*, Volume 3, pp. 12-17.
- Mann, L. D., 2011. Application of ocean observations and analysis: The CETO wave energy project. In: G. B. A. Schiller, ed. *Operational Oceanography in the 21st century*. s.l.:Springer Netherlands, pp. 721-729.
- Marquardt, D., 1963. An Algorithm for Least-Squares Estimation of Nonlinear Parameters. *SIAM Journal on Applied Mathematics*, 11(2), pp. 431-441.
- Marquardt, D., 1963. An Algorithm for Least-Squares Estimation of Nonlinear Parameters. *SIAM Journal on Applied Mathematics*, 11(2), p. 431-441.
- McCormick, S. D. & Kraemer, D. R. B., 2002. Polynomial approximations for the Fresnel integrals in diffraction analysis. *Coastal Engineering*, 44(3), pp. 261-266.
- McIver, P., 2005. Diffraction of water waves by a segmented permeable breakwater. *Journal of Waterway, Port, Coastal and Ocean Engineering*, Volume 131, pp. 69-76.
- Mei, C. C., 1989. *The applied dynamics of ocean surface waves*. 1st ed. Singapore: Singapore World Scientific.
- Millar, D. L., Smith, H. C. M. & Reeve, D. E., 2007. Modelling analysis of the sensitivity of shoreline change to a wave farm. *Ocean Engineering*, 34(5-6), pp. 884-901.
- Misuyasu, H. et al., 1975. Observations of the directional spectrum of ocean waves using a cloverleaf buoy. *Physical Oceanography*, 5(4), pp. 750-760.
- Mitsui, H. & Murakami, H., 1967. *Wellenhöhenverteilung an diskontinuierlichen teilen von kustenbauwerken*. s.l., Kaigan Kogaku Koenkai Koenshu.
- Monk, K., Conley, D., Lopes, M. & Zou, Q., 2013. *Pneumatic Power Regulation by Wave Forecasting and Real-Time Relief Valve Control for an OWC*. Aalborg, 10th European Wave and Tidal Energy Conference.
- Monk, K., Zou, Q. & Conley, D., 2011. *Numerical and Analytical Simulations of Wave Interference about a Single Row Array of Wave Energy Converters*. Southampton, 9th European Wave and Tidal Energy Conference.
- Morrison, G. & Greated, C. A., 1992. *Oscillating Water Column Modelling*. Venice, 23rd International Conference on Coastal Engineering.
- Morrison, I. & Greated, C., 1992. *Oscillating water column modelling*. Venice, 23rd International Conference on Coastal Engineering.
- Norgaard, J. H. & Andersen, T. L., 2012. *Investigation of wave transmission from a floating Wave Dragon wave energy converter*. Rhodes, 22nd International Offshore and Polar Engineering Conference.
- Nørgaard, M., Ravn O, O., Poulsen, N. K. & Hansen, L. K., 2003. *Neural networks for modelling and control of dynamic systems: A practitioner's handbook*. London: Springer-Verlag.
- Ou, S. H., Tzang, S. Y. & Hsu, T. W., 1988. *Wave field behind the permeable detached breakwater*. Torremolins, 21st International Conference on Coastal Engineering.
- Palha, A. et al., 2010. The Impact Of Wave Energy Farms In The Shoreline Wave Climate: Portuguese Pilot Zone Case Study Using Pelamis Energy Wave Devices. *Renewable Energy*, 35(1), pp. 62-77.
- Paperella, F. et al., 2015. Up-wave and autoregressive methods for short-term wave forecasting for an oscillating water column. *IEEE Transactions on Sustainable Energy*, 6(1), pp. 171-178.

- Pearson, K., 1895. Notes on regression and inheritance in the case of two parents. *Proceedings of the Royal Society of London*, 58(1), pp. 240-242.
- Penny, W. G. & Price, A. T., 1944. *Diffraction of water waves by breakwaters*, s.l.: Misc. Weapons development technical history, Artificial Harbours, Sec 3D.
- Penny, W. G. & Price, A. T., 1952. The diffraction theory of sea waves and the shelter afforded by breakwaters. *Philosophical Transactions of The Royal Society*, Volume Ser. A244, pp. 236-253.
- Pfleiderer, C. & Petermann, H., 1991. *Stromungsmaschinen*. 6th ed. Berlin: Springer.
- Phillips, O. M., 1977. *The dynamics of the upper ocean*. 2nd ed. Cambridge: Cambridge University press.
- Pierson, W. J. & Moskowitz, L. A., 1964. Proposed spectral form for fully developed wind seas based on the similarity theory of S. A. Kitaigorodskii. *Journal of Geophysical Research*, 69(1), pp. 5181-5190.
- Pos, J. D. & Kilner, F. A., 1987. Breakwater gap wave diffraction: An experimental and numerical study. *Journal of Waterway, Port, Coastal, and Ocean Engineering*, 113(1), pp. 1-21.
- Price, A. & Wallace, A. R., 2007. *Non-linear methods for next wave estimation*. porto, 7th European Wave and Tidal Energy Conference.
- Reeve, D., Chadwick, A. & Fleming, C., 2004. *Coastal Engineering: Processes, Theory and Design Practice*. 1st ed. New York: Spoon Press.
- Reikard, G. & Rogers, E. W., 2011. Forecasting ocean waves: Comparing a physics-based model with statistical models. *Journal of Coastal Engineering*, 58(5), pp. 409-416.
- Riedmiller, M. & Braun, H., 1992. *Rprop - A Fast Adaptive Learning Algorithm*, 1992. s.l., Proceedings of the 7th International Symposium on Computer and Information Science.
- Sarmiento, A. J. N. A. & Falcao, A. F. d. O., 1985. Wave generation by an oscillating surface-pressure and its application in wave energy extraction. *Journal of Fluid Mechanics*, Issue 150, p. 467-485.
- Save\_Pico\_Powerplant.org, 2013. s.l.: <http://www.save-pico-powerplant.org/index.php/the-pico-plant/technology/>.
- Schindwein, F. S. & Evans, D. H., 1992. Autoregressive spectral analysis as an alternative to fast Fourier transform analysis of Doppler ultrasound signals. In: Edward Arold, editor. *Diagnostic Vascular Ultrasound*, Volume 8, pp. 74-84.
- Sheng, W. & Lewis, T., 2010. *Artificial Neural Network Application in Short-Term Prediction in an Oscillating Water Column*. Beijing, 20th International Society of Offshore and Polar Engineers.
- Silvester, R. & Lim, T. K., 1968. *Application of wave diffraction data*. London, 11th International Conference of Coastal Engineering.
- Sollitt, C. K. & Cross, R. H., 1972. *Wave transmission through permeable breakwaters*. Vancouver, 13th International Conference on Coastal Engineering.
- Sommerfeld, A., 1886. Mathematische theorie der diffraction. *Math Annalen*, Volume 47, pp. 317-374.
- Stearns, S. D. & Hush, D. R., 2011. *Digital Signal Processing with Examples in MATLAB®*. 2nd ed. Boca Raton: CRC press.
- Stokes, G. G., 1847. On the theory of oscillatory waves. *Transactions of the Cambridge Philosophical Society*, 8(1), pp. 441-455.
- Tedd, J. & Frigaard, P., 2007. *Short term wave forecasting, using digital filters, for improved control of Wave Energy Converters*. Lisbon, 17th International Offshore and Polar Engineering Conference, pp. 388-394.
- Tolman, H. L., 1989. *The numerical model WAVEWATCH: a third generation model for the hindcasting of wind waves on tides in shelf seas*. Delft, Communications on Hydraulic and Geotechnical Engineering, Delft University of Technology, pp. 1 - 72.

- Tolman, H. L., 1991. A third-generation model for wind waves on slowly varying, unsteady and inhomogeneous depths and currents. *Journal of Physical Oceanography*, Volume 21, pp. 782-797.
- Torre-Encisco, Y., Ortubia, I., Lopez de Aguilera, L. I. & Margues, J., 2009. *Mutriku wave power plant from the thinking out to the reality*. Uppsala, Sweden, 8th European Wave and Tidal Energy Conference.
- Valério, D., Mendes, M. J. G. C., Beirão, P. & Costa, J., 2008. Identification and control of the AWS using neural network models. *Applied Ocean Research*, 30(3), pp. 178-188.
- Venugopal, V. & Smith, G. H., 2007. *Wave climate investigation for an array of wave power devices*. Porto, 7th European wave and tidal energy conference.
- Vieira, M., Sarmiento, A. & Reis, L., 2015. Failure analysis of the guide vanes of the Pico wave power plant wells turbine. *Engineering Failure Analysis*, p. In Press.
- Wei, G., Kirby, J. T., Grilli, S. T. & Subramanya, R., 1995. A fully nonlinear Boussinesq model for surface waves. Part 1: highly nonlinear unsteady wave. *Journal of Fluid Mechanics*, Volume 294, pp. 71-92.
- Yemm, R., Pizer, D., Retzler, C. & Henderson, R., 2012. Pelamis: experience from concept to connection. *Philosophical transactions of the royal society*, Volume 370, pp. 365-380.
- Young, I. R., 1999. *Wind generated ocean waves*. 2nd ed. Oxford: Elsevier.
- Yu, H. & Wilamowski, B. M., 2011. Levenberg-Marquardt Training. In: *The Industrial Electronics Handbook Vol. 5 Intelligent Systems*. 2nd ed. Boca Raton: CRC Press.
- Yu, X. & Togashi, H., 1996. *Combined diffraction and transmission of water waves around a porous breakwater gap*. Orlando, 25th International Conference of Coastal Engineering.
- Yu, Y. X., Liu, S. X., Li, Y. S. & Wai, O. W., 2000. Refraction and diffraction of random waves through breakwater. *Ocean Engineering*. *Ocean engineering*, 27(5), pp. 489-509.
- Zhang, Y., Qing-Ping, Z. & Greaves, D., 2012. Air water two-phase flow modelling of hydrodynamic performance of an oscillating water column device. *Renewable Energy*, Volume 41, pp. 159-170.
- Zou, Q. et al., 2013. Ensemble prediction of coastal flood risk arising from overtopping by linking meteorological, ocean, coastal and surf zone models. *Quarterly Journal of the Royal Meteorological Society*, 139(671), pp. 298-313.

## First Author Published Papers

- 1.) **Monk, K.** Zou, Q. and Conley, D. An approximate solution for the wave energy shadow in the lee of an array of overtopping type wave energy converters. *Coastal Engineering*, vol. 73 pp. 115-132, 2013.
  
- 2.) **Monk, K.** Zou, Q. and Conley, D. The effect of diffraction on the redistribution of wave energy in the lee of an overtopping type wave energy converter array, *Proceedings of 33<sup>rd</sup> International Conference on Coastal Engineering (ICCE)*, Santander, Spain, 2012.
  
- 3.) **Monk, K.** Conley, D. Lopes, M. F. P and Zou, Q. Pneumatic power regulation by wave forecasting and real-time valve control for an OWC. *Proceedings of 10<sup>th</sup> European Wave and Tidal Energy Conference (EWTEC)*, Aalborg, Denmark, 2013.

\*Papers removed from this edited version because copyright authorisation was not gained\*